Topics in Current Chemistry 369

Roman Boulatov *Editor*

Polymer Mechanochemistry

Springer

369
Topics in Current Chemistry

Aims and Scope

The series Topics in Current Chemistry presents critical reviews of the present and future trends in modern chemical research. The scope of coverage includes all areas of chemical science including the interfaces with related disciplines such as biology, medicine and materials science.

The goal of each thematic volume is to give the non-specialist reader, whether at the university or in industry, a comprehensive overview of an area where new insights are emerging that are of interest to larger scientific audience.

Thus each review within the volume critically surveys one aspect of that topic and places it within the context of the volume as a whole. The most significant developments of the last 5 to 10 years should be presented. A description of the laboratory procedures involved is often useful to the reader. The coverage should not be exhaustive in data, but should rather be conceptual, concentrating on the methodological thinking that will allow the non-specialist reader to understand the information presented.

Discussion of possible future research directions in the area is welcome.

Review articles for the individual volumes are invited by the volume editors.

Readership: research chemists at universities or in industry, graduate students.

More information about this series at http://www.springer.com/series/128

Roman Boulatov
Editor

Polymer Mechanochemistry

With contributions by

R.D. Astumian · A. Balan · A. Barge · M.J. Buehler · B. Cheng · P. Cintas · J.M. Clough · G. Cravotto · S. Cui · A.P. Haehnel · G.S. Heverly-Coulson · G. Jung · G.S. Kochhar · Y. Li · Y. Lin · K. Martina · N.J. Mosey · Z. Qin · Y. Sagara · M.J. Serpe · S.S. Sheiko · R.P. Sijbesma · Y.C. Simon · C. Weder · W. Weng · Y. Xu · H. Zhang · Q.M. Zhang

Springer

Editor
Roman Boulatov
Department of Chemistry
University of Liverpool
Liverpool, United Kingdom

ISSN 0340-1022 ISSN 1436-5049 (electronic)
Topics in Current Chemistry
ISBN 978-3-319-22824-2 ISBN 978-3-319-22825-9 (eBook)
DOI 10.1007/978-3-319-22825-9

Library of Congress Control Number: 2015953644

Springer Cham Heidelberg New York Dordrecht London

Printed on acid-free paper

Springer International Publishing AG Switzerland is part of Springer Science+Business Media (www.springer.com)

Preface

Few people realize that when they stretch a rubber band – or inflate tires on their cars – they do chemistry. In this example of vulcanized rubber, the chemistry is simple – homolysis of C–C, C–S, or S–S bonds, but the underlying principle is anything but simple. The probability of ethyl disulfide spontaneously dissociating into radicals at room temperature is negligible. Yet this probability can increase by many orders of magnitude for the same molecular moiety when it is as part of amorphous material under mechanical load. In other words, translation of macroscopic objects (e.g., our hands) that compress, stretch, or twist polymeric material can directly control reaction rates of material building blocks. Such control of course is not seen in the vast majority of reactions studied by chemists and as a result is not accommodated in any of the existing models of chemical kinetics.

This coupling between macroscopic motion (or mechanical loads) and chemical reactivity is called mechanochemistry [1]. Load-induced fragmentation of polymers was discovered almost as soon as the nature of polymers had been recognized [2]. Polymer mechanochemistry is thought to be an important (but poorly understood) determinant of how polymeric materials respond to mechanical loads [3–5]. Because polymers are subject to such loads throughout their lifecycles, from production to recycling, polymer mechanochemistry pervades our everyday lives. Mechanochemical phenomena are thought to affect the generation, growth, and propagation of microcracks which are responsible for catastrophic failure of polymeric materials, desalination membranes, impact-resistant materials (e.g., bullet-proof vests), and tires, and the stabilities of surface-anchored polymers in microfluidic diagnostics and high-performance chromatography. Polymer mechanochemistry may be important in jet injection (e.g., during inkjet printing of organic electronics), polymer melt processing, high-performance lubrication, enhanced oil recovery (e.g., polymer flooding), and turbulent drag reduction. Exploiting mechanochemical phenomena may yield remarkable new materials and processes, including polymer photoactuation (i.e., direct conversion of light into motion to power autonomous nanomechanical devices, control information flow in optical computing, position mirrors or photovoltaic cells in solar capture schemes) [6, 7]),

efficient capture of waste mechanical energy, materials capable of autonomous reporting of internal stresses and self-healing, and tools to study polymer dynamics at sub-nanometer scales [8].

Until about 10 years ago, unambiguous examples of mechanochemical reactions were limited to simple backbone fragmentations that resulted when biological or synthetic polymers were subject to tensile loads in solids, melts, or solutions. Early attempts to interpret rates of bulk polymer failures under various conditions as governed by mechanochemical acceleration or inhibition of reactions of their monomers, such as amide hydrolysis, are now considered unreliable and unlikely to reflect true load-induced changes in the intrinsic kinetic stabilities of stretched polymer chains [9, 10]. In contrast, the past decade has seen impressive progress in designing polymers whose stretching at the single-chain level accelerates reactions more complex than simple bond hemolysis with the ultimate goal of both understanding the fundamental aspects of mechanochemical energy coupling and designing stress-responsive materials of the types discussed above.

To understand the current state of polymer mechanochemistry and to try to guess the directions of its evolution, it is useful to divide the phenomena studied by polymer mechanochemists (Fig. 1) into those where:

1. The coupling between macroscopic mechanical effects and atomistically localized reactivity is mediated by interactions between multiple polymer chains as in amorphous materials, melts, and load-bearing biological tissues

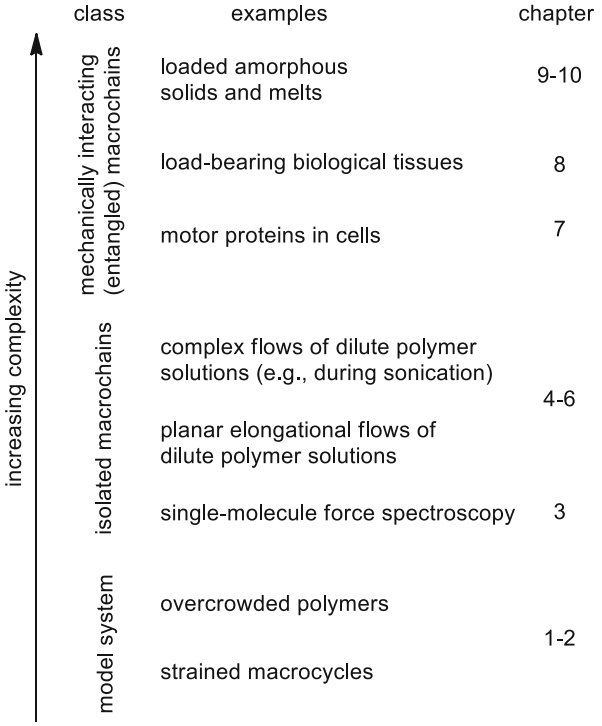

Fig. 1 Hierarchy of mechanochemical phenomena and the volume chapters devoted to specific categories

2. *Individual* polymer chains are stretched either by interaction with non-polymeric environment (e.g., solvent flows, see chapters "Mechanochemistry of Topologically Complex Polymer Systems", "Force induced Reactions and Catalysis in Polymers", and "The Interplay of Mechanochemistry and Sonochemistry") or because they are bound directly to translating macroscopic objects, such as in single-molecule force spectroscopy (see chapter "Supramolecular Chemistry and Mechanochemistry of Macromolecules at the Single Chain Level")

Molecular interpretation of mechanochemical phenomena in amorphous materials and melts remains largely qualitative and the main effort and success to date in this area has been primarily in empirical exploration and some tentative exploitation of materials obtained by incorporating force-sensitive reactive sites in otherwise inert polymer chains and matrices (see chapters "Mechanochemistry in Polymers with Supramolecular Mechanophores" and "Responsive Polymers as Sensors, Muscles, and Self-Healing Materials"). This work has the potential to expand greatly our presently primitive quantitative understanding of mechanochemistry of entangled polymer chains by providing experimental tools to quantify how and how fast mechanical loads propagate through amorphous polymer matrices to reactive sites, and the range of local forces (or molecular strains) and their temporaspatial distributions that reactive sites experience in response to macroscopic load. In comparison, the mechanism and dynamics of mechanochemical energy transduction that underlies the operation of motor proteins is well understood (see chapter "Understanding the Directionality of Molecular Machines: The Importance of Microscopic Reversibility") as is the response of biological tissue to mechanical loads. The reason is, at least in part, the primarily non-covalent nature of mechanochemistry of biological tissues, which makes it amenable to usefully accurate large-scale computational simulations, as described in the chapter "Mechanical Properties and Failure of Biopolymers: Atomistic Reactions to Macroscale Response".

Such simulations are often performed by "attaching" a virtual spring between the terminal atoms of a biopolymer, changing the parameter(s) of this spring to impose a time-varying tensile force on the biopolymer, and "watching" how the polymer evolves under this force. The experimental analog of this set-up is single-molecule force spectroscopy (SMFS) in which a single polymer chain bridges a tip of an atomic force microscope and a retracting surface (see chapter "Supramolecular Chemistry and Mechanochemistry of Macromolecules"). SMFS is the least intractable manifestation of polymer mechanochemistry and is responsible for some of the most important conceptual developments in polymer mechanochemistry [11]. Unfortunately, SMFS is technically demanding and only a handful of laboratories worldwide combine sufficient expertise of synthetic polymer chemistry, micromanipulation techniques, and physical analysis to design, perform, and interpret cutting-edge SMF experiments. Unlike SMFS, mechanochemistry of isolated polymer chains in flow fields of dilute polymer solutions have broad industrial applications (e.g., see chapter "Mechanochemistry of Topologically Complex Polymer Systems"). The absence of chain entanglement potentially makes these systems

atomistically more tractable than mechanochemistry in amorphous polymers and melts. Indeed, the value of planar elongational flow fields for studying the fundamental aspects of polymer dynamics in solution has long been recognized [12]. However, the technical challenges of achieving sufficient strain-rate gradients to induce mechanochemistry in moderately long macrochains (with the contour lengths below 10 μm) are daunting and planar elongational flows remain largely unexploited in polymer mechanochemistry.

In contrast to SMFS and planar elongational flows, which provide perhaps the best opportunities to develop a physically sound, general, and predictive model of mechanochemical kinetics (see below), sonication of dilute polymer solutions is a very simple and popular technique routinely used to mimic the response of polymer chains to stretching (see chapters "Force Induced Reactions and Catalysis in Polymers" and "The Interplay of Mechanochemistry and Sonochemistry"). Sonication creates transient elongational flows when bubbles generated by propagating sound waves suddenly collapse. Because the solvent flow rate in close proximity to a collapsing bubble decreases very rapidly with distance from the bubble surface, the two termini of the same chain located at different distances from this surface experience very different flow rates and the chain becomes stretched. The dynamics of bubble collapse, which can be extraordinarily complex [13], determines the temporaspatial flow rate gradients and hence loading rates and maximum forces that polymer chains experience, thus directly affecting the apparent (macroscopic) mechanochemical kinetics. However, little is known about how this dynamics is governed by macroscopic control parameters (sound frequency and power density, temperature, durations of on/off cycles), solvent and polymer characteristics (vapor pressure, viscosity, and solvation capacity for the former; molecular mass distribution for the latter), and environmental variables (shape and size of the ultrasound horn and of the reaction vessel). Consequently, studies of polymer mechanochemistry in sonicated solutions should be viewed as at best qualitative and the results may vary from one laboratory to another simply because of the difficulty of controlling key kinetic variables (or even identifying them). Quantitative interpretations of sonication experiments are further complicated by the very modest chemical selectivity of mechanochemical reactions, which manifests itself in reactions of very different strain-free activation energies (e.g., C–C bond homolysis and ring-opening of dichlorocyclopropanes) occurring at competitive rates during sonication. They are also complicated by the contribution of radicals from solvent sonolysis to any observed polymer chemistry, by the uncertain distribution of strain (or equivalently, restoring force, see below) along individual stretched polymer chains, and by the (presumably) strong dependence of the forces experienced by a stretched polymer chain on its contour length. These limitations of sonication-induced mechanochemistry have long been acknowledged in the literature [4], but the number of reported studies designed to clarify them remains disappointingly small [14, 15].

The vast majority of reported studies in polymer mechanochemistry are on linear polymers. Mechanochemistry of topologically complex polymers, which is of increasing industrial importance (see chapter "Mechanochemistry of Topologically

Complex Polymer Systems"), is an area where sonication, despite all its limitations, has a chance to make an outsize impact. Unfortunately, the very few reports on the subject are contradictory, warranting further detailed research.

Model studies have and continue to be critical for developing the conceptual foundation of polymer mechanochemistry and for rationalizing and systematizing the existing observations. Experimental model studies (see chapter "Mechanochemistry Driven by Intermolecular Forces") use molecules which attempt to strain reactive sites by means of molecular architecture rather than the application of mechanical loads. The most prominent examples include strained macrocycles based on stiff stilbene and overcrowded polymers. They are distinct from the large number of strained molecules which chemists have studied over the past 100 years in that their architectures are designed specifically to reproduce the highly anisotropic molecular strain that localized reactive sites in polymers experience in mechanochemical phenomena and to facilitate quantitation of such local strain as restoring force (as opposed to strain energy). Likewise, computational mechanochemistry (see chapter "Theoretical Approaches for Understanding the Interplay Between Stress and Chemical Reactivity") uses models, such as small reactive moieties in which one non-bonding internuclear distance is constrained to a non-equilibrium value by an external potential of varying stiffness, because direct quantum-chemical calculation of mechanochemical response of polymer chains remains beyond reach. As is the case in any model studies, an outstanding problem with this approach is to learn how to map the measurements and trends observed (or computed) in such models onto bona fide mechanochemical systems [16]. To date, extrapolating results of model studies to even the simplest manifestations of polymer mechanochemistry (i.e., a single-molecule force experiment) has had mixed success [11, 16].

With the exception of motor proteins (see chapter "Understanding the Directionality of Molecular Machines: The Importance of Microscopic Reversibility"), the significant increase in the diversity of empirical data in polymer mechanochemistry and the development of quantum-chemical methods of calculating force-rate correlations in small-molecule reactants have not yet been matched by comparable progress in developing the conceptual foundation of mechanochemical kinetics. A key component of this foundation is a general and predictive relationship between the macroscopic control parameters that define mechanical loads (e.g., stress or strain tensors and loading rates) and the changes in reaction rates in the same way that the transition state theory and the Eyring equation relate reaction temperature and rate. One of the earliest (empirical) models of kinetics of mechanochemical fragmentation of polymer chains was put forth by Eyring [17], who postulated a direct proportionality between the activation energy of the fragmentation and the force exerted on the stretched polymer chain by its surroundings. The model was silent on what the proportionality constant might be or how to derive the single-chain force from the flow rate gradient, which was the control parameter in the system considered by Eyring. The same idea was subsequently applied by Bell to cell adhesion [18] and extended to time-varying single-chain force by Evans [19], who derived it within the Kramers formulation of chemical kinetics. This Evans

model has probably become the most widely used variant of mechanochemical kinetics because it enabled rationalization of single-molecule force experiments and has been elaborated extensively since its publication [20–22]. By replacing the force with stress, the Eyringansatz was extended from the single-chain level to a polymer solid [10, 23], albeit at the cost of further obscuring the molecular origin of the proportionality between the control parameter (stress) and reaction rates.

Although these related models have certainly facilitated the development of polymer mechanochemistry, they offer no explanation for their empirical parameters and as such resemble the role of the Arrhenius equation in standard chemical kinetics. As it appears unlikely that a fundamental physical law exists that determines the dependence of the energy of a strain molecule on force straining the molecule (or any other plausible quantifier of the external perturbation), a plausible approach to moving beyond the Eyring–Bell–Evans ansatz and its variants is to use Taylor expansion. In other words, the activation energy of a chemical reaction, $\Delta G^{\ddagger}$, in an externally strained polymer is estimated as a Taylor expansion of the strain-free activation energy with respect to the straining force, f (see (1), where *is* and *ts* subscripts refer to the initial and transition states of the reaction) [24]. In this approach, the Eyring–Bell–Evans models are simply the Taylor expansion to the first order. Provided that the expansion coefficients have clear molecular meanings and can be estimated from strain-free initial and transition state geometries (which are derived from quantum-chemical calculations), the reactivity of a molecule under force can be predicted, at least in theory, without resource-intensive optimizations of molecular geometries coupled to force.

$$\Delta G^{\ddagger} \approx \underbrace{\left(f\frac{\partial G_{ts}}{\partial f}\bigg|_{f=0} + \frac{f^2}{2}\frac{\partial^2 G_{ts}}{\partial f^2}\bigg|_{f=0} + \cdots \right)}_{\text{transition-state(ts)energy}} - \underbrace{\left(f\frac{\partial G_{is}}{\partial f}\bigg|_{f=0} + \frac{f^2}{2}\frac{\partial^2 G_{is}}{\partial f^2}\bigg|_{f=0} + \cdots \right)}_{\text{initial-state(is)energy}}. \tag{1}$$

Practical application of (1) depends critically on the specific molecular definition of force f. With the possible exceptions of single-molecule force spectroscopy, in mechanochemical phenomena polymers are not stretched by pulling apart a pair of atoms. Instead, the non-equilibrium (stretched) geometry of a chain (or its part) is maintained by interactions of multiple atoms of the chain with multiple atoms of its environment. Under such circumstances, no single force is stretching a chain. Fortunately, however, if the chain is in mechanical equilibrium with its environment, a mathematical relationship exists between restoring forces of all the internal molecular degrees of freedom (e.g., internuclear distances) of the chain, at least within the (local) harmonic approximation [25]. The restoring force of a strained object is the force that attempts to recover the original, unstrained shape of this object: for example, when we stretch a rubber band, the restoring force of the band is what pulls our hands closer together. When the force in (1) is defined as the restoring force of an internal molecular degree of freedom, it is plausible to equate the first-order ($\partial G/\partial f$) and second order ($\partial^2 G/\partial f^2$) Taylor coefficients to the strain-free values of this molecular coordinate and of its harmonic compliance,

respectively. (This equality is exact if, instead of free energies of states, the electronic energy of a single conformer were used. However, chemical reactivity is determined by free energies and most molecules have multiple conformers contributing to initial or transition states, obscuring the molecular identification of the Taylor coefficients.)

The validity of the Taylor-expansion approach is typically tested computationally by comparing $\Delta G^{\ddagger}$ correlations calculated explicitly with the values predicted by (1) truncated at the second order using either single-conformer or ensemble-averaged distances and compliances of various internal coordinates in the strain-free initial and transition states. These tests indicate that the predictive capacity of the Taylor expansion approach depends critically on the selection of the internal molecular coordinate whose restoring force is used in the equation [26–28]. Fortunately, it appears that the same type of coordinate is appropriate for all reactions of the same mechanism (e.g., S_N2 displacements) [29]. This approach can also be used to predict the critical force at which mechanochemical reactivity is observed in single-molecule force experiments. In this application, an extra step is needed to relate the force applied by the AMF to termini of the polymer chain and the force of a local internal degree of freedom of the reactive moiety [30]. This relationship ("chemomechanical coupling coefficient") can be estimated from technically simple molecular-mechanics calculations.

It has not yet been possible to extend this approach to mechanochemical systems more complex than single-molecule force spectroscopy. The reason is not the inapplicability of the fundamental assumptions of the transition state theory to mechanochemical reactions, but rather the lack of established means of converting macroscopic control parameters (e.g., stress) into single-chain forces (which can then be converted to local molecular restoring forces as shown previously). The molecular definitions of temperature and pressure offered by the equipartition theorem and the kinetic theory of gases underlie the general and predictive relationship between the macroscopic control parameters (temperature and pressure) and the reaction rate by means of a molecular (rather than continuum) parameter (free energy) embodied by the Eyring equation [31]. In the absence of a broadly useful and theoretically sound molecular definition of mechanical stress, the problem of deriving a predictive model of mechanochemical kinetics may be solved by defining the correct hierarchy of mechanochemical phenomena (Fig. 1) so that existing models that perform reasonably well within individual rungs of the hierarchy (e.g., chemical kinetics, continuum mechanics, etc.) could be systematically integrated into an overarching multiscale model. Such mechanochemical Eyring equations could be expected to have as profound an impact on the design and studies of polymers as transition state theory has had on chemistry. Although we are very far from the mechanochemical Eyring equation, important progress towards this goal, particularly from the "small-scale" end of the hierarchy (model compounds and single-molecule force experiments), is evident in the chapters of this volume.

The development of a general, quantitative conceptual framework which can guide the evolution of polymer mechanochemistry would revolutionize polymer

science but the multiscale nature of mechanochemical phenomena makes this task exceedingly challenging. Yet, even fairly incremental progress in the field has a chance of making great technological, scientific, and societal impact, given the importance of polymers to modern society, the central role that mechanotransduction plays in life as we know it, and the opportunity arising from applying the tools and ideas of chemistry to polymer physics and engineering. For example, the ability to map the distribution of single-chain forces in amorphous materials and melts using simple mechanochromic reactions designed with the help of quantum-chemical force/rate calculations and calibrated in single-molecule force experiments greatly advances our capacity to rationalize mechanical properties of polymers at the molecular level, and eventually enables us to design new materials with pre-determined responses to mechanical loads by selecting proper monomers, their ratios, and connectivities. Likewise, further evolution of our understanding of the operation of motor proteins – by means of theory, computations, single-molecule force experiments, and model studies – could help us design practically useful actuating materials capable of converting the free energy of chemical reactions (including photoisomerizations) directly into macroscopic motion, without the intermediacy of thermal or electrostatic gradients. The development of physically sound and at least semi-quantitative models of mechanochemical kinetics in sonicated dilute polymer solutions would enable rapid low-cost screening of reactions and monomers to identify candidates likely to give desired mechanochemical responses when incorporated in amorphous materials in analogy to high-throughput screening in medicinal chemistry and solid-state catalysis. Continued development of efficient algorithms for quantum-chemical calculation of force-rate correlations of diverse chemical reactions may lead to "virtual" single-molecule force spectroscopy, potentially increasing vastly our ability to understand in intricate detail how energy flows across the formidable gap between 10 and 100 nm where the molecular and the continuum meet.

References

1. Boulatov R (2013) Demonstrated leverage. Nat Chem 5:84–86
2. Staudinger H, Heuer W (1934) Über hochpolymere verbindungen, 93. Mitteil.: Über das zerreißen der faden-moleküle des poly-styrols. Ber Dtsch Chem Ges 1159
3. Ribas-Arino J, Marx D (2012) Covalent mechanochemistry: theoretical concepts and computational tools with applications to molecular nanomechanics. Chem Rev 112:5412
4. Kean ZS, Craig SL (2012) Mechanochemical remodeling of synthetic polymers. Polymer 53:1035–1048
5. Brown CL, Craig SL (2015) Molecular engineering of mechanophore activity for stress-responsive polymeric materials. Chem Sci 6:2158–2165
6. Kucharski TJ, Boulatov R (2012) In: Knopf GK (ed) Optical nano and micro actuator technology. CRC, Boca Raton, pp 83–106. Chap. 3
7. White TJ (2012) Light to work transduction and shape memory in glassy, photoresponsive macromolecular systems: trends and opportunities. J Polym Sci B50:877

8. Gossweiler GR, Kouznetsova TB, Craig SL (2015) Force-rate characterization of two spiropyran-based molecular force probes. J Am Chem Soc 137:6148–6151
9. Rapoport N, Zaikov GE (1983) Kinetics and mechanism of the oxidation of polymers in a stressed state. Rus Chem Rev 52:897
10. Tyler DR (2004) Mechanistic aspects of the effects of stress on the rates of photochemical degradation reactions in polymers. J Macromol Sci Pol Rev 44:351
11. Wang J et al. (2015) Inducing and quantifying forbidden reactivity with single-molecule polymer mechanochemistry. Nat Chem 7:323–327
12. Schroeder CM, Babcock HP, Shaqfeh ESG, Chu S (2003) Observation of polymer conformation hysteresis in extensional flow. Science 301:1515
13. Lauterborn W, Kurz T (2010) Physics of bubble oscillations. Rep Prog Phys 73:106501
14. Groote R, Jakobs RTM, Sijbesma RP (2012) Performance of mechanochemically activated catalysts is enhanced by suppression of the thermal effects of ultrasound. ACS Macro Lett 1:1012
15. Kean ZS, Gossweiler GR, Kouznetsova TB, Hewage GB, Craig SL (2015) A coumarin dimer probe of mechanochemical scission efficiency in the sonochemical activation of chain-centered mechanophore polymers. Chem Commun 51:9157
16. Craig SL (2012) Mechanochemistry: a tour of force. Nature (London, UK) 487:176–177
17. Kauzmann W, Eyring H (1940) The viscous flow of large molecules. J Am Chem Soc 62:3113
18. Bell GI (1978) Models for the specific adhesion of cells to cells. Science 200:618
19. Evans E, Ritchie K (1997) Dynamic strength of molecular adhesion bonds. Biophys J 72:1541
20. Evans E (2001) Probing the relation between force — lifetime — and chemistry in single molecular bonds. Ann Rev Biophys Biomol Struct 30:105
21. Dudko OK, Hummer G, Szabo A (2008) Theory, analysis, and interpretation of single-molecule force spectroscopy experiments. Proc Natl Acad Sci USA 105:15755
22. Friddle RW, Noy A, De Yoreo JJ (2012) Interpreting the widespread nonlinear force spectra of intermolecular bonds. Proc Natl Acad Sci USA 109:13573
23. Leffler JE, Grunwald E (1963) Rates and equilibria of organic reactions. Wiley, New York
24. Huang Z, Boulatov R (2010) Chemomechanics with molecular force probes. Pure Appl Chem 82:931–951
25. Kucharski TJ, Boulatov R (2011) The physical chemistry of mechanoresponsive polymers. J Mater Chem 21:8237–8255
26. Hermes M, Boulatov R (2011) The entropic and enthalpic contributions to force-dependent dissociation kinetics of the pyrophosphate bond. J Am Chem Soc 133:20044–20047
27. Tian Y, Boulatov R (2013) Comparison of the predictive performance of the Bell–Evans, Taylor-expansion and statistical-mechanics models of mechanochemistry. Chem Commun 49:4187–4189
28. Tian Y, Kucharski TJ, Yang QY, Boulatov R (2013) Model studies of force-dependent kinetics of multi-barrier reactions. Nat Commun 4:2538
29. Boulatov R (2011) Reaction dynamics in the formidable gap. Pure Appl Chem 83:25–41
30. Akbulatov S, Tian Y, Boulatov R (2012) Force-reactivity property of a single monomer is sufficient to predict the micromechanical behavior of its polymer. J Am Chem Soc 134:7620–7623
31. Klippenstein SJ, Pande VS, Truhlar DG (2014) Chemical kinetics and mechanisms of complex systems: a perspective on recent theoretical advances. J Am Chem Soc 136:528

Contents

Top Curr Chem (2015) 369: 1–36
DOI: 10.1007/128_2015_627

Published online: 25 March 2015

Molecular Mechanochemistry: Engineering and Implications of Inherently Strained Architectures

Yuanchao Li and Sergei S. Sheiko

Abstract Mechanical activation of chemical bonds is usually achieved by applying external forces. However, nearly all molecules exhibit inherent strain of their chemical bonds and angles as a result of constraints imposed by covalent bonding and interactions with the surrounding environment. Particularly strong deformation of bonds and angles is observed in hyperbranched macromolecules caused by steric repulsion of densely grafted polymer branches. In addition to the tension amplification, macromolecular architecture allows for accurate control of strain distribution, which enables focusing of the internal mechanical tension to specific chemical bonds and angles. As such, chemically identical bonds in self-strained macromolecules become physically distinct because the difference in bond tension leads to the corresponding difference in the electronic structure and chemical reactivity of individual bonds within the same macromolecule. In this review, we outline different approaches to the design of strained macromolecules along with physical principles of tension management, including generation, amplification, and focusing of mechanical tension at specific chemical bonds.

Keywords Bond tension · Mechanical activation · Mechanochemistry · Mechanophores · Molecular force probes · Molecular tensile machines · Self-strained molecules

Contents

Y. Li and S.S. Sheiko (✉)
Department of Chemistry, University of North Carolina, Chapel Hill, NC 27599-3290, USA
e-mail: sergei@email.unc.edu

1 Introduction

Mechanical activation of chemical bonds is a vital instrument in synthetic chemistry [1] and molecular biology [2]. Strain at molecular length scales controls rates of chemical reactions [3, 4], activates latent catalysts [5, 6], and steers reaction pathways [7, 8]. More recently, it has been shown that mechanical force can also trigger depolymerization of low-ceiling-temperature polymers [9]. Strained molecular architectures and assemblies govern most of the physiological processes including enzyme activities [10–13], motion of molecular motors [14–19], division of cells [20–22], and contraction of muscles [23]. Given the vector character of force, mechanochemical reactions follow specific pathways, yielding products different from that of non-directional thermal and photonic activation [1, 7]. Strained chemical bonds also play an important role in the materials design. In addition to activation of chemical reactions, significant numbers of experimental studies were devoted to the effect of molecular strain on electronic structure along with the corresponding implications for electronic and optical properties of materials [24–30]. Mechanical control of structure, orientation, and interactions of individual molecules was applied to the design of mechanically responsive nanomaterials and nanosystems [31]. Various mechanophores were purposely synthesized and incorporated into polymers to create stress-responsive materials [32–34]. Activation of latent catalysts opens interesting opportunities for the rational design of new mechano-catalytic systems for truly autonomous (e.g., self-healing) applications [35]. These advances in materials engineering do not dismiss the traditional challenges in fundamentals of mechanochemistry related to understanding the transduction of macroscopic strain to individual bonds. In addition to conventional mechanochemistry tools (grinding, ultrasonic irradiation, and elongational flows), advanced techniques, such as optical tweezers [36], magnetic tweezers [37, 38], atomic force microscopy (AFM)-based force spectroscopy [39–41], micro-needle manipulation [42], biomembrane force probes [43], and targeted incorporation of mechanophores [44–46], have been developed to control forces on a single-molecule scale. Simultaneously, theoretical frameworks for mechanochemistry undergo continuous development, from early work by Eyring [47], Kramers [48], Zhurkov [49], and Bell [50] to more recent fundamental studies

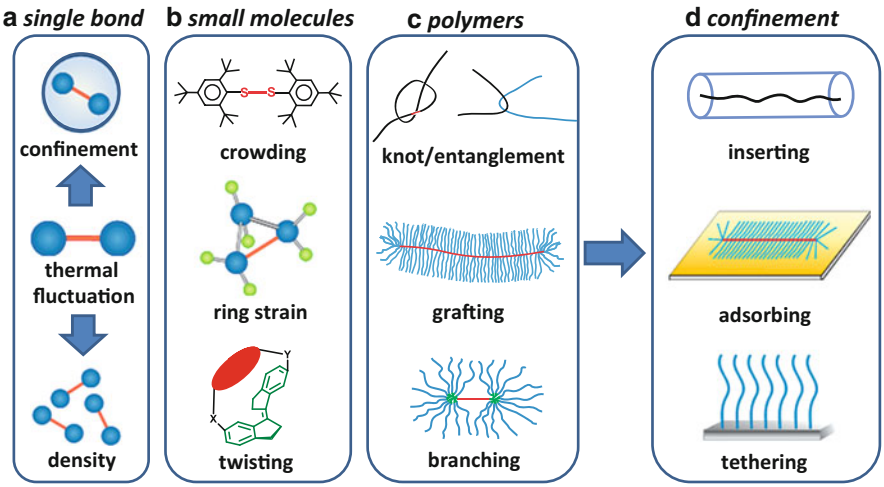

Fig. 1 Strained molecular architectures in the order of the increasing length scale involved into bond tension amplification: (**a**) diatomic molecules strained by thermal fluctuation depending on density and confinement; (**b**) locally strained configurations of small molecules; (**c**) large polymer molecules strained by unfavorable conformations and steric repulsions between dense branches; (**d**) bond length (hence, tension) is affected by topographic constraints

by Evans [51], Klein [52], Beyer [53], Hummer [54], Dudko [55], Marx [56], Martinez [8], and many others reviewed in [57].

Traditional mechanochemistry deals with externally applied forces. However, there is a distinct class of mechanochemistry where strained bonds and angles are inherent to a given molecular architecture. The internal strains are introduced during synthesis and determined by the architectural design, which may involve sterically unfavorable constructions such as cycles and branches. Figure 1 outlines general categories of strained molecular structures in the order of increasing length scale involved in stress generation, ranging from diatomic molecules to spatially constrained macromolecular systems. It is remarkable that even a basic diatomic molecule may be strained by thermal fluctuations depending on mass density and geometric confinement (Fig. 1a). Additional contributions to bond tension result from connecting small chemical groups into sterically hampered molecular constructs (Fig. 1b). The bond tension can be further amplified by introducing additional hindrances on larger length scales such as knots, grafts, and branches (Fig. 1c). Bonds and angles may also change when molecules either spontaneously penetrate or are forced into a geometric confinement such as pores, channels, and slits (Fig. 1d). Additional deformations of bonds within large macromolecules can be introduced by conformational transitions induced by heating, swelling, and interaction with light [58]. The study of intrinsically strained (or self-strained) molecules, which encompasses generation, distribution, amplification, and the physical impact of intramolecular forces, is viewed by us as a distinct subclass of mechanochemistry – *molecular mechanochemistry*.

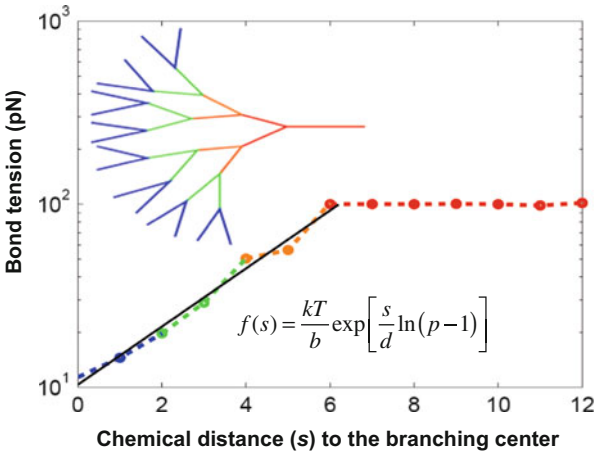

Fig. 2 The bond tension (f) increases exponentially from the periphery to the branching center of a dendritic macromolecule. d – the number of bonds between branch points, p – branching functionality, s – the number of bonds away from the branching center. Adapted with permission from Bacanu A and Rubinstein M, unpublished manuscript

Similar to externally deformed samples, self-strained molecular systems exhibit non-uniform distribution of strains, and hence forces, over the constituting bonds and angles. The strain distribution is determined by molecular architecture and can be modulated upon interaction with the surrounding environment. Analogous to macroscopic constructions (houses, towers, and bridges), the design of strained molecules can be viewed as molecular mechanical engineering, which explores distribution of internal stresses when connecting identical chemical groups into physically distinct structures. The physical distinction results from the effect of bond strain on the electronic structure along with the corresponding opto-electronic properties (color, conductivity, energy conversion). This elicits the idea of using dendrimers as photon-harvesting antennas to channel the absorbed infrared energy from the matrix to the azobenzene core, causing its isomerization [59]. The gradient in bond tension along the dendritic branches (Fig. 2) may be responsible for guiding the intramolecular process of energy transfer. Note also that molecular strain typically involves conformational changes, including contributions of bond length and angle deformations. Frequently, mechanical activation is discussed in terms of bond elongation, and deformation of bond angles is barely considered. However, in fact, changes in bond angles may provide a larger contribution to overall molecular deformation and strain energy. Recently, Boydston et al. [60, 61] reported mechanical activation of bonds orthogonal to an elongated polymer main chain. Similar to microcycles (Sect. 3.1), the so-called "flex activation" has been ascribed to the force-induced increase in bond angles and, hence, strain energy.

As in externally induced deformation, we should distinguish between strain-controlled and stress-controlled molecular systems. For example, deformation induced by a well-defined conformational transition (Fig. 1b, bottom) can be considered as strain-controlled, where the strain is encoded by the new molecular configuration. In contrast, extension of the backbone in molecular bottlebrushes (Fig. 1c, middle) occurs at a constant tensile force controlled by steric repulsion of the densely grafted side chains. In addition to the strain distribution, it is important

to understand the range of possible forces that can emerge in individual macromolecules and span three orders of magnitude ranging from ca. 1 pN to 1 nN. The lower limit corresponds to a soft force required for extension of an ideal polymer chain, which is determined by the change of conformational entropy as $f_{\min} \cong kT\ R/R_0^2$, where $k = 1.38 \times 10^{23}\mathrm{J/K}$ is the Boltzmann's constant, R the end-to-end distance of an extended chain, $R_0^2 \cong Lb$ is a mean square end-to-end distance of an unperturbed coil, L the chain contour length, and b the Kuhn length of the order of 1 nm. For a nearly fully extended chain $R \cong L$, we obtain the lower limit $f_{\min} \cong kT/b \cong 1$ pN. The upper limit can be estimated as change of bond energy upon bond fracture as $f_{\max} \cong E_{\mathrm{dis}}/l_0 \cong 1$ nN, where E_{dis} is the bond dissociation energy of the order of $100\,kT$ and l_0 is the bond length of the order 0.1 nm. Within this broad range (1 pN–1 nN), we may observe dissociation of strong physical bonds (H-bonds) and weak covalent bonds (S–S). It should be noted that the numbers calculated above correspond to nominal lower and upper boundaries which may adopt different values depending on chain extension, persistence length, and bond energy and length.

For externally deformed molecules, we usually consider a change of the free energy before and after force application. A reference state is usually associated with the energy at zero force. As we do not apply any external force and an inherently strained molecule is at equilibrium with its environment, it is necessary to define a reference state for each particular system. Depending on interaction with the environment, chemical bonds/angles can be either extended or compressed. For example, in the next section we show that a diatomic molecule in a gas state is extended with respect to the bond length in the condensed liquid state, whereas the same molecule may get compressed (i.e., bond shortens) when subjected to a geometric confinement. What can we use as a reference state in these systems? Is the compressed bond more reactive than the extended one? What is the reaction coordinate in the absence of an external force vector? What controls the distribution of strained bonds within a macromolecule? Can we create a physically patterned molecular architecture with a programmable distribution of bond strains and energy band gaps? What are the individual contributions of specific bond and angle deformations? All these questions are inspired by *self-strained* molecules and constitute the area of research in *molecular mechanochemistry* – an uncharted territory with new opportunities for mechanocatalysis, organic electronics, and molecular biology.

2 Diatomic Molecules and Polymer Chains

Considering a free diatomic molecule, thermal fluctuations result in either extension or compression of the bond, depending on the packing density and geometric confinement. Weiner et al. have shown that the time-average bond force has two

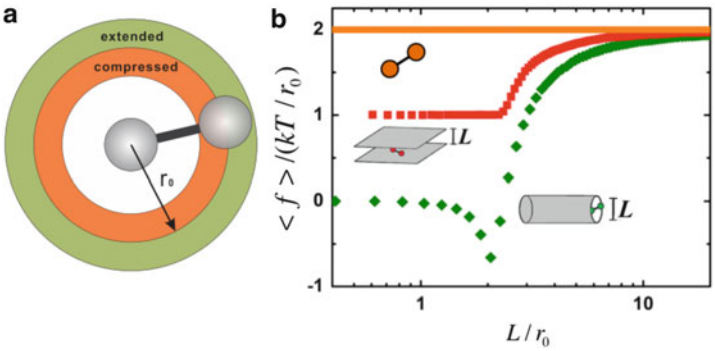

Fig. 3 (**a**) A diatomic molecule in vacuum. Its bond is either stretched or compressed because of thermal fluctuation. (**b**) The change of the average bond tension of a diatomic molecule with the width of a repulsive nanoslit (*red squares*), the diameter of a repulsive nanotube (*green diamonds*), and the average bond tension of a free diatomic molecule in vacuum as a reference (*orange line*). Adapted with permission from Brock J and Rubinstein M, unpublished manuscript

contributions and can be presented as $f = f_c + f_{nc} = \frac{\sum fe^{-E/kT}}{\sum e^{-E/kT}} = (D-1)kT/r_0$, where f_c is the force exerted by the covalent bond potential, f_{nc} arises from the intermolecular (non-covalent) interaction forces projected onto the bond axis, D is the spatial dimension, and r_0 is the average bond length corresponding to zero force [62]. For example, in a 3D gas phase ($D = 3$ and $f_{nc} = 0$), the bond in a diatomic molecule is stretched with a force of $f_c = 2kT/r_0 \sim 100$ pN. This force arising from "nowhere" can be viewed as a centrifugal force of entropic origin which arises in a diatomic molecule when it rotates in a 3D space and, hence, occupies a larger pervaded volume in its stretched state (Fig. 3a). With an increasing packing density, this inherent bond tension decreases and may even change sign to become compressive. Gao and Weiner applied molecular dynamics (MD) calculations to study bond forces in diatomic molecules in the liquid state and showed that the average bond force is negative, i.e., the bond is in a compressed state for most of the time [62].

Additional modulation of the bond strain can be caused by a geometric confinement. If a diatomic molecule is placed in a repulsive nanoslit, the bond tension depends on the slit width. As the width decreases, the diatomic molecule becomes more confined (from a 3D to a 2D space), and the average bond tension decreases from $2kT/r_0$ to kT/r_0 (Fig. 3b). Another interesting case is confining a diatomic molecule in a nanotube. The molecule first gets compressed, resulting in a negative force, and then stretched to an average zero force as tube diameter increases (Brock, Rubinstein, unpublished manuscript). The initial contraction is ascribed to gaining of additional rotational degrees of freedom when the bond shortens inside the tube. The zero-force corresponds to average bond tension in a 1D oscillator in vacuum. It should be noted that the force sign is relative and depends on the choice of a

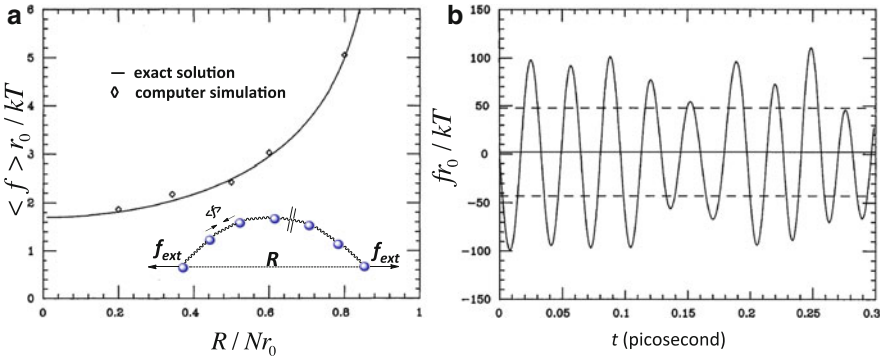

Fig. 4 (**a**) Mean bond force $< f >$ in a freely jointed long-chain molecule with $N = 10$ bonds of equilibrium length r_0 and fixed end-to-end displacement R. (**b**) Typical time history of bond force $f(t)$ as determined by computer simulation with $N = 10$ at room temperature. Mean bond force and its root mean square deviations are shown as *solid and dashed horizontal lines*, respectively. Adapted with permission from [63]

reference state. However, what matters in the self-strained systems is the bond length, which is an absolute and measurable parameter.

If the diatomic molecules are connected to each other to form a polymer chain, we should distinguish between an external force (if any) applied to chain ends and a force at a particular bond within the chain. Because the total strain is distributed over multiple covalent bonds and torsional angles, tension in an individual bond is usually different from the externally applied force [63, 64]. Even for unperturbed polymer coils at zero external force, the average bond force is non-zero [63]. For a single chain at a zero displacement of the end-to-end vector, the bond tension was found as $f_b \cong 2kT/r_0$ and viewed as the centrifugal force acting in a bond connecting two atoms in thermal motion. Even though the average force is not very large on the order of 100 pN, the short-term (0.01 ps) force fluctuations around the mean value can exceed 10 nN [63] (Fig. 4b). The force remains nearly constant for small end-to-end distance (R) and then exponentially increases as R approaches its fully extended contour length $R_{max} \cong Nr_0$ (Fig. 4a). The bond force depends not only on the end-to-end distance of the chain but also on the packing density and geometric constraints. When the packing density and excluded volume interactions between the neighboring chains become significant, the bond force decreases and may even become compressive [64]. Bond compression may also occur in extended polymer chains confined in a narrow channel. In polymer molecules with pendant groups, the bond force in the backbone may also depend on the orientation of the bond relative to the chain force. Tenable evidence for this argument is that mechanochemical activation of mechanophores covalently bonded in polymer backbones and oriented in the tensile direction occurs preferentially [65].

3 Cyclic Molecules

Strain in cyclic molecules has attracted scientists' interest for over a century since the late nineteenth century. In 1885, Adolf von Baeyer proposed the strain theory which successfully explained that three- and four-membered rings would be less stable than five- or six-membered rings because of the deviation of bond angles from the normal tetrahedral values [66]. However, his theory failed when it was applied to larger rings, e.g., seven- to twelve-membered rings where strain is present for a different reason rather than bond angle distortion. The concept of strain has been developed and expanded from von Baeyer's original idea and is now discussed in terms of bond length and bond angle distortions as well as torsional strains and nonbonded interactions, thanks to the development of synthetic methodology and computational modeling. There have been many review articles written about strained molecular cycles. Two reviews by Wiberg [67] and by Liebman and Greenberg [68] deal with strained organic molecules with carbon skeletons. Another two contributions cover small-ring heterocycles by Murray [69] and by Tochtermann and Olsson [70], respectively. Alder's review discusses the strain effects on amine basicities [71]. More reviews can be found in the introduction of an issue dedicated to strained organic compounds [72]. In this account we focus on small rings as well as strained macrocycles from the aspect of *molecular mechanochemistry*.

3.1 Mechanical Activation of Microcycles

Here microcycles refer to three- to five-membered rings and their derivatives. Microcycles can easily be activated by mechanical force and/or other stimuli because of their high strain energies. As mentioned above, four components contribute to the total strain energy: bond length distortion, bond angle distortion, torsional strain, and nonbonded interactions. In microcycles, distortion of bond angles results in significant contribution to the total strain energy. For example, the C–C–C bond angles of cyclopropane and cyclobutane deviate from the natural 109.5° by about 50° and 20°, respectively. As shown in Table 1, the strain energy increases with decreasing cycle size and reaches a maximum value of 26–27 kcal/mol for cyclobutane and cyclopropane. This explains the exceptionally high reactivity of cyclobutane and cyclopropane derivatives which have been employed in ring-opening polymerization [73, 74], electrophilic and nucleophilic additions, etc. [75].

Among cyclic compounds of carbon, cyclopropane and its derivatives exhibit the highest strain energy and, hence, chemical reactivity. The C–H bonds in cyclopropane are shorter, have a higher tensile force constant, and exhibit a stronger ^{13}C-H NMR coupling constant than in propane [76]. These data are in agreement with the thermochemical verification of higher strength of the C–H bonds in

Table 1 The structural features and the strain energy of small cycloalkanes compared to *n*-alkane

	C–C (Å)	C–C–C angle (deg)	Strain energy (kcal/mol)
n-Alkane	1.54	109.5	0
Cyclohexane	1.54	111.4	0
Cyclopentane	1.55	107	6.3
Cyclobutane	1.56	90	26
Cyclopropane	1.50	60	27

cyclopropane than either the primary or secondary C–H bonds in propane [77]. The C–C bonds in cyclopropane [78, 79] are also shorter than in propane [80], which may lead to the illusion that the former C–C bonds are more stable. However, interestingly, the C–C bond dissociation energy in cyclopropane is estimated to be 50 kcal/mol [81], which is significantly lower than that for ordinary C–C bonds (~84 kcal/mol) [82], indicating that the cyclopropane C–C bond is actually weaker, which is attributed to ring strain in cyclopropane. The C–C–C internuclear angle in cyclopropane is 60°, bearing an angle deformation of 49.5° in contrast to the interorbital and internuclear angle of 109.5° in methane, which gives a strain energy of 27.5 kcal/mol [67]. In fact, the density of the bonding electrons is greatest off the C–C connecting line, and so the C–C bond is indeed "bent" [83], with an interorbital angle of ~104° by calculation [84–86].

Craig and co-workers pioneered the use of strained cyclopropane as a pre-activated mechanophore and conducted systematic study of its mechanical activation behavior. One of the implications of these studies for mechanochemistry is to understand the interplay between internally strained molecules and externally applied forces. In a proof-of-concept study, gem-dichlorocyclopropanes (gDCCs) were incorporated into *cis*-polybutadiene chains and underwent ring opening under mechanical activation by sonication [46]. The uniqueness of gem-DCC polymers is that there are abundant mechanophores in a single polymer chain. Atomic force microscopy (AFM)-based single-molecule force spectroscopy (SMFS) revealed a plateau at ~1 nN in the force-separation curve for the extension of a single gem-dibromocyclopropane (*g*DBC) functionalized polymer [87], which was attributed to force-induced ring opening reactions of the cyclopropane moieties (Fig. 5b). Interestingly, the plateau force depends on the structural properties of the backbone [88, 89]. Besides, the same group reported another type of copolymer with high mechanophore content, polyester-acrylate ABA block copolymers with gDCCs in the middle block [90]. The ABA triblock architecture ensures a mechanophore-rich region near the center of the chain facilitating the selective activation near the midpoint by sonication [91–93]. Concurrently, Moore and co-workers designed a new mechanophore based on a gem-dichlorocyclopropanated indene which is able to release hydrochloride under mechanical stress [94].

As an example of application of the *gem*-dihalocyclopropane (*g*DHC) polymers, Craig and co-workers demonstrated that under the acoustic field generated by pulsed ultrasound (20 kHz and 11.9 W/cm^2) *trans gem*-difluorocyclopropane (*g*DFC) is mechanically forced to undergo the thermally forbidden conrotatory

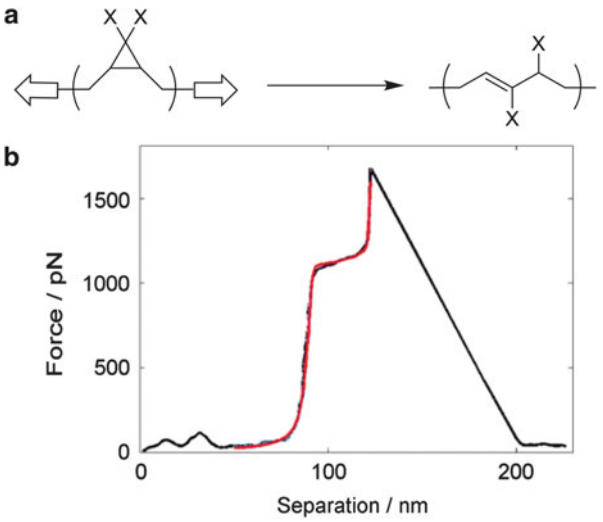

Fig. 5 (**a**) Force induced ring opening of *gem*-dihalocyclopropane (*g*DHC). X=F, Cl, and Br. (**b**) Force-distance curve measured upon extension of gDBC by single molecule AFM at a constant tip withdrawal velocity of 3 μm/s. Adapted with permission from [87]. Copyright 2010 American Chemical Society

ring opening [8], which corroborates the work by Hickenboth et al. showing that mechanical activation could override Woodward–Hoffman orbital symmetry rules in the activation of benzocyclobutene to an *ortho*-quinodimethane intermediate [7]. Mechanical activation of the polymers with *g*DFCs incorporated can also trap a 1,3-diradical which is a transition state in the stress-free electrocyclic isomerization, generated from the ring opening reaction under tension [8, 95]. Even though the lifetime of 1,3-diradical was initially predicted to be of the order of 10^{-13} s, Craig and co-workers have shown that mechanical tension could elongate its lifetime and thus allow the capture of the transition state with a chromophoric radical trap. Its lifetime estimated from the trapping efficiency was at least 10^{-9} s, indicating that the force generated by sonication was able to elongate the lifetime of the diradical by several orders of magnitude.

Incorporation of strained microcycles favors significant dissipation of mechanical energy and may lead to enhancement of toughness and strength of polymer elastomers and gels. Recently, Craig and co-workers reported mechanochemical strengthening of polybutadiene with embedded *g*DBC mechanophores in response to shear forces [96]. The *g*DBC underwent ring-opening reactions induced by shear forces generated from extrusion or sonication, yielding allylic bromides. The allylic bromides were crosslinked in situ by nucleophilic substitution reactions with carboxylates, leading to an increase in bulk modulus or gelation of *g*DBC solution, even though polymer backbone scission also occurred. This work demonstrated potential applications of *g*DHC mechanophores in stress responsive materials. More about *g*DHC mechanophores can be found in a review by the same group [97].

Similarly, primarily because of the high inherent ring strain, the selective cleavage of a cyclobutane bond is facile, which makes cyclobutane and its derivatives promising mechanophores as well [98–101].

3.2 Strained Macrocycles

It was demonstrated by Gaub and co-workers in 2002 that a single polymer chain of azobenzene monomeric units stretched between an AFM tip and a glass slide contracted upon light induced *trans–cis* transition of azobenzene [24]. The restoring force caused by contraction of the polymer was balanced by the elastic force of the bent cantilever. This paradigmatic example shows that configuration transition between *cis*- and *trans*-azobenzene can generate significant restoring force, which has direct implications for the design of stressed molecules.

Several years later, Boulatov and co-workers designed a molecular force probe based on stiff stilbene (1,1'-diindanylidene) [44]. Similar to azobenzene, stilbene also has two stable and structurally distinct isomers that can be accessed via photoisomerization [102]. Instead of being attached to an AFM tip and a glass slide respectively, the C6 and C6′ atoms of *Z*-isomer of the stiff stilbene were bridged with a linker where a functional group of interest could be incorporated to yield a macrocyclic molecule. The relaxed *Z*-isomer was converted to *E*-isomer with a large increase in the C6···C6′ distance upon irradiation at 365 or 375 nm, generating a substantial restoring force within the molecule (Fig. 6a). Such macrocycles can be used as models of reactive sites in stretched polymers. For example, the force-rate correlation of dibromocyclopropane isomerization from macrocycles and SMFS experiments is identical [103, 104]. Yet, it should be pointed out that force distribution on individual bonds within a mechanophore stretched by the macrocycles (strain-controlled system) may be different from that by an external pulling force under a controlled loading rate [105]. In addition, there are several advantages of the macrocyclic force probe. First, it is compatible with a broad range of functional groups, including cyclobutane [44, 106], cyclopropane [103], disulfide [107, 108], sulfonate [109], ester [110], and catalytic ligand [111], which allows investigation into various chemical reactions. Second, the restoring force can be adjusted by varying the length and/or conformational flexibility of the linker, up to hundreds of pico-Newtons (Fig. 6b). Third, compared to microscopic force probes, the restoring force is generated from distortions of the macrocyclic molecules without external stretching forces, and it does not suffer from the lack of product characterization methods. The restoring force can be calculated either by optimization of the macrocycles with the group of interest removed [44], or from the relationship between the ensemble-averaged length of a local coordinate and the constant force [103]. A possible drawback of the macrocycles is that they may not be able to cover the forces in the nano-Newton range.

Successful applications of the macrocyclic force probes have been demonstrated in the kinetic study of mechanochemical reactions, especially multistep reactions. By incorporating an ester group in the stiff stilbene-based macrocycle, Boulatov and co-workers investigated its alkaline hydrolysis as a function of restoring force [110]. It was found that the hydrolysis of ester is insensitive to mechanical force, which is in agreement with MD simulations [112]. This is because the relative

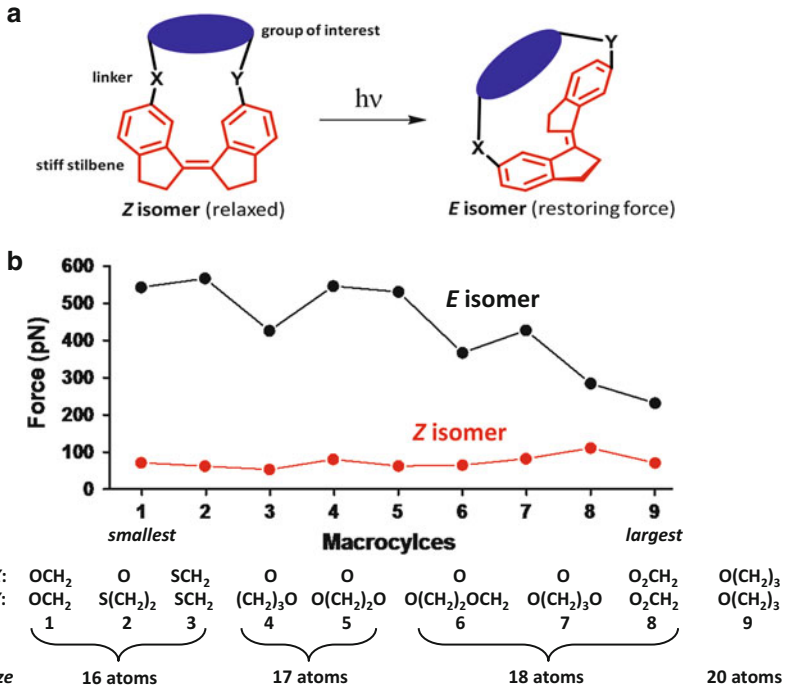

Fig. 6 (**a**) Stiff stilbene-based molecular force probe. Upon UV irradiation at 365 or 375 nm, the relaxed *Z*-isomer switches to strained *E*-isomer, resulting in the restoring force in the bonds of the group of interest. (**b**) Quantum-chemically calculated restoring force along the axis of two end carbons of the macrocyclic fragment obtained by replacing the group of interest with a pair of hydrogen atoms. Adapted with permission from [44]

energy of the rate-determining transition state (one of the two transition states) and therefore the activation free energy are hardly affected by force. More recently, the same group reported the reduction of organic disulfides that were also incorporated in stiff stilbene based macrocycles by phosphines in water [108]. The reaction involves two steps: (1) the reactants go through transition state 1 to yield a thiophosphonium intermediate, which is a force-dependent step; (2) the intermediate proceeds over transition state 2 and gives the products, which is the rate-determining step in the absence of force and depends on pH. The second step is orthogonal to the pulling axis and therefore not affected by force, the energy barrier of the first step decreasing with increasing stretching force applied to the disulfide bond. At restoring forces below a threshold of ~120 pN, the reduction is accelerated without a change in the rate-determining step, and at forces above the threshold, the apparent reduction rate constant becomes independent of the solution acidity, indicating the shift of the rate-determining step from the second to the first step. This fundamental study is of great significance as it provides new insights into the kinetics of mechanochemical reactions.

4 Polymer Knots

Knots have been discovered in both biopolymers (e.g., nucleic acids and proteins) and synthetic polymers [113]. Polymer knots have drawn remarkable interest, partially because of their influence on the structure and mechanical properties of polymers [114]. In fact, the topological constriction of knots can be detrimental to polymer stability. Klein and co-workers conducted molecular dynamics (MD) calculations on knotted polyethylene-like alkane chains [52]. As shown in Fig. 7, the strain energy of the bonds at the entrance is substantially higher, where breakage may therefore occur preferentially, as in a knotted rope [115]. This indicates that the knot significantly weakens the bonds localized at the entrance of the knot. This was confirmed experimentally soon afterwards by Harada and co-workers [116]. In their experiment, both ends of an actin filament were manipulated with optical tweezers to tie a simple open knot, and then the filament was pulled stepwise to tighten the knot; it broke at the knot point within 10 s after the pulling force was raised to ~1 pN. Given the fact that the tensile strength of unknotted straight actin filaments is ~600 pN [117], the knotted filament was greatly weakened by the knot.

In analogy with molecular knots, Saitta and Klein found that physical entanglements of polymers also reduce the tensile strength of individual entangled chains [118]. Bond rupture invariably occurs at the crosspoint under external tensile loading, which is facilitated by bond friction. This suggests that molecular topological constrictions (e.g., knots and entanglements) may serve as a tool towards the design of new classes of mechanophores.

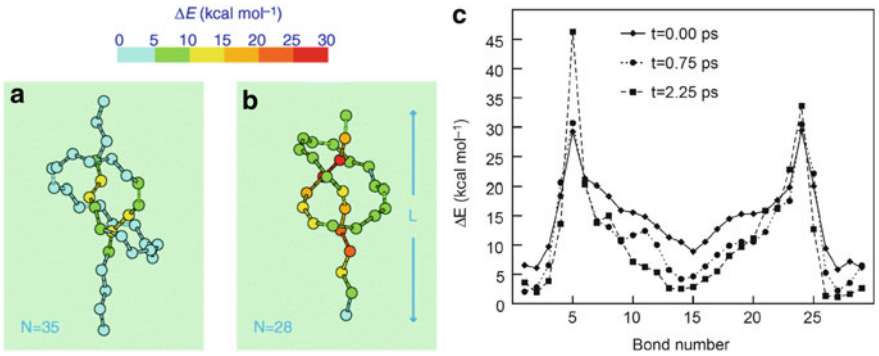

Fig. 7 Tightening the knot within a polymer backbone weakens the bonds localized at the entrance and exit of the knot substantially. Strain energy distributions as shown are taken from constrained classic MD simulations for $C_{35}H_{72}$ (**a**) and $C_{28}H_{58}$ (**b**). (**c**) Relaxation of the strain energy distribution along a $C_{30}H_{62}$ chain containing a trefoil during Car–Parrinello MD energy minimization at $T = 0$ K. Adapted with permission from [52]. Copyright 1999 Nature Publishing Group

5 Highly Branched Macromolecules

In the previous sections, we have discussed inherent strain of relatively small molecules that adopt energetically unfavorable micro-conformations either upon synthesis or because of conformational transition causing direct perturbation of shared electron clouds (covalent bonds). As discussed in Sect. 2, covalent connectivity may cause net tensile force in chemical bonds on the order of 100 pN [63, 64]. Additional strain occurs upon introducing bulky substituents which transmit steric repulsion to particular covalent bonds and angles. For example, the S–S bond in di(2,4,6-tri-*tert*-butylbenzyl) disulfide is strained by ~17 kcal/mol compared to its analogue in the absence of steric hindrance [119], and the length of the C–C bond formed by coupling nanometer-sized, diamond-like, highly rigid hydrocarbon structures known as diamondoids can be up to 1.704 Å [120]. However, in the latter case, the repulsion interactions that cause the elongation of the C–C bond are balanced by the attractive dispersion interactions between the intramolecular H···H contact surfaces, resulting in the stabilization of the ultralong C–C bond [120].

Steric repulsion can be further controlled in large macromolecules through incorporation of dense polymer branches. Even though the steric repulsion between individual chain sections within a polymeric structure is relatively weak (~kT), the architecture allows the focusing of this weak repulsion to a specific section of an individual macromolecule, which results in significant tension amplification. The uneven distribution of bond tension in a molecular architecture is analogous to stress distribution in macroscopic constructions (buildings, bridges, and towers), allowing for effective control of strain distribution in molecular architectures and supramolecular assemblies. Akin to a combination of load-bearing and decorative construction elements in buildings, molecular architecture may also include overstressed bonds which undergo preferential scission. In this section, we show how the bond tension can be focused to a specific bond and amplified to the nano-Newton level.

5.1 Molecular Bottlebrushes

Molecular bottlebrushes are a special type of graft copolymer in which multiple polymer chains are densely grafted to a linear polymer. The main chain is commonly referred to as the backbone and the branches as side chains. Unlike regular comb-like polymers, the distance between neighboring side chains in bottlebrushes is much shorter than the side chain size (e.g., radius of gyration), which results in significant extension of both the backbone and side chains. Synthetically, a variety of approaches has been adopted to allow the preparation of molecular bottlebrushes, including “grafting through” (polymerization of macromonomers), “grafting to” (attachment of the side chains to the backbone), and “grafting from” (grafting the side chains from the backbone) [27, 121]. Within each approach, various

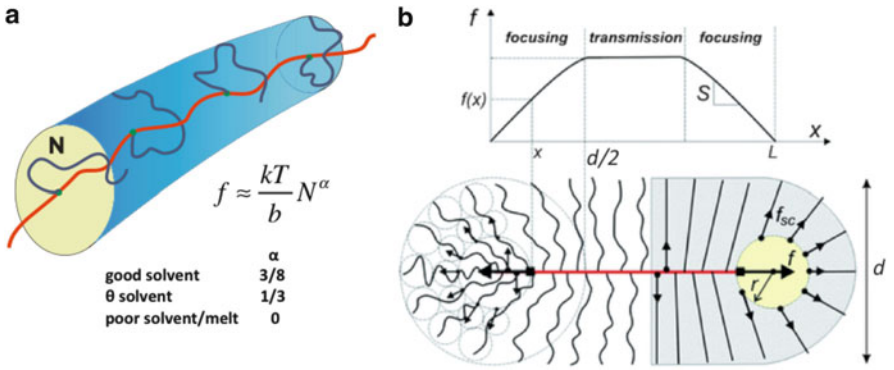

Fig. 8 (**a**) The backbone tension in molecular bottlebrushes depends on side chain length and solvent quality. (**b**) The backbone of an adsorbed bottlebrush is pulled by side chains with a force of f_{sc}, resulting in a linear increase of force along the backbone at the end-cups of the bottlebrush as $f \cong Sx$, where S is the spreading coefficient. In the transmission zone, the force along the backbone is constant $f \cong Sd$

polymerization techniques such as anionic polymerization, ring-opening metathesis polymerization, conventional and controlled radical polymerizations, various coupling reactions ("click chemistry"), and miniemulsion polymerization have been employed. Each of these techniques has its own pros and cons with respect to control of the bottlebrush architecture in terms of dispersity and degree of polymerization (DP) of the side chains, dispersity and DP of the backbone, and grafting density. It remains challenging to prepare bottlebrushes with long backbone (DP > 1,000), long side chains (DP > 100), and high grafting density.

Steric repulsion between the densely grafted side chains causes extension of the backbone. Theoretical studies [122–124] show that the backbone tension increases with grafting density, side chain length, and solvent quality. The backbone tension in dense bottlebrushes with side chains attached to every backbone monomer is on the order of $f_0 N^{3/8}$ in good solvents, $f_0 N^{1/3}$ in θ solvents, and f_0 in poor solvents and melts, where N is the DP of side chains, $f_0 = kT/b \cong 1$ pN is the nominal tension in a fully extended polymer chain, and b is the Kuhn length (Fig. 8a). In solution or melt, the force is small (pico-Newtons); and it can be amplified up to nano-Newtons upon adsorption onto an attractive substrate because the steric repulsion between the side chains is enhanced in the substrate plane [122, 125], as shown in Fig. 8b. There is a simple scaling relation for the force on a substrate: $f \cong S \cdot d$, where S is the spreading coefficient related to the surface energy of the substrate and d is the width of adsorbed bottlebrush molecules.

The amplified tension caused by adsorption of side chains can lead to the scission of covalent bonds in the backbone once it exceeds their strength. We have shown that the C–C bonds in poly(2-hydroxyethyl methacrylate) backbone with long poly(*n*-butyl acrylate) (PBA) side chains ruptured spontaneously upon adsorption onto an aqueous substrate (Fig. 9) [126]. The kinetics of backbone scission was followed by monitoring the average contour length by AFM as a

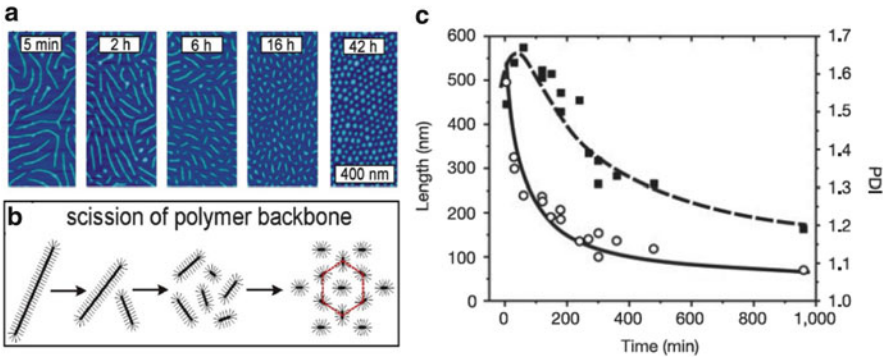

Fig. 9 (**a**) Height AFM micrographs of bottlebrush molecules with long side chains (DP = 140) were measured at different exposure times to the water/propanol (99.8/0.2 w/w) substrate [126]. (**b**) The molecular bottlebrushes get shorter with longer exposure time to the substrate, which is ascribed to spontaneous scission of the backbone. (**c**) The number average contour length decreases with increasing exposure time (*white circles*); the *solid line* is a fit to the experimental data assuming bond scission as a first-order reaction. The experimentally determined polydispersity index PDI initially increases and then decays, which is in agreement with the computer simulation results (*dashed line*)

function of exposure time to the substrate. The backbone scission is extremely sensitive to the substrate surface energy. For example, the scission rate of poly (2-hydroxyethyl methacrylate) backbone in bottlebrushes with PBA side chains with DP of 140 is about six times slower when the surface energy of the substrate decreases from 71.2 to 69.2 mN/m [127]. Interestingly, the surface energy decreases with temperature, which is the reason for the anti-Arrhenius scission of bottlebrush backbones on water/propanol substrate [128, 129].

Unlike scission of polymer chains in elongational flow or upon sonication where bond rupture occurs preferentially near the midpoint of the chain, the bond breaks randomly in the bottlebrush backbone upon adsorption on a liquid substrate. This is attributed to uniform distribution of force along the backbone except for the end-cups of the bottlebrushes (Fig. 8b). However, mechanical activation of specific bonds/groups can still be achieved by three means. First, a relative weak bond compared to C–C bond can be inserted into the bottlebrush backbone. As a proof-of-concept study, we demonstrated selective scission of disulfide bonds (S–S) incorporated into the middle of a bottlebrush backbone although S–C, C–O and C–C bonds remained intact or their scission rate was much slower (Fig. 10a), because the bond dissociation energy of the S–S bond is lower [45]. Even if the force is not large enough to break the S–S bond, it can accelerate the reduction of the S–S bond by dithiothreitol (DTT) [4]. For example, the reduction rate increased by more than 10 times as the backbone tension increased from 0.95 to 1.26 nN. This allows the use of molecular bottlebrushes as tensile machines to activate specific bonds or functional group and therefore to study their mechanochemical reactions. Second, the entire backbone can be made of functional groups of interest. For example, UV–vis emission of molecular bottlebrushes with polythiophene

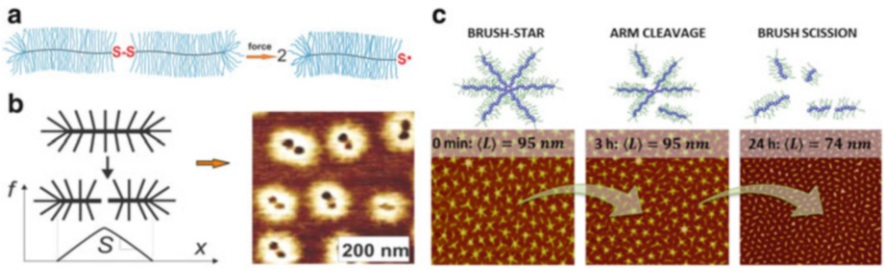

Fig. 10 Site-specific activation. (**a**) Mid-chain scission of molecular bottlebrushes occurs selectively at the disulfide linkage. (**b**) In a short bottlebrush, tension is focused to the middle of the backbone, resulting in its mid-chain scission. (**c**) By focusing bond tension at the branching center, molecular stars with bottlebrush arms undergo sequential scission of covalent bonds upon adsorption onto an aqueous substrate

backbone and PBA side chains initially exhibits redshift and then blueshift with increasing tension because of the increase of conjugation length and the deformation of bond lengths/angles, respectively [130]. Similar redshifts have been observed upon conformational changes in polythiophene backbones of molecular bottlebrushes caused by temperature-induced conformational transition of poly(*N*-isopropylacrylamide) side chains [131, 132] and variations of solvent quality [133]. Third, molecular branched architecture can be tuned to ensure maximum concentration of mechanical tension at a specific chemical bond. For example, star-like [134] and pom-pom structures [125] as well as short bottlebrushes [135] may be used to introduce site-specific activation at the branching center. Figure 10b displays the concentration of tension in the middle of the backbone resulting in its mid-chain scission. In a similar fashion (Fig. 10c), molecular stars with a spoke wheel core and bottlebrush arms exhibit preferential dissociation of the arms followed by the scission of covalent bonds in the bottlebrush backbones [134]. The preferential cleavage of the arms is ascribed to stronger steric repulsion between the bottlebrushes at the branching center.

Not only do the molecular bottlebrushes break upon adsorption to a liquid substrate but also they can break during flow on a solid substrate. In spreading films, extension of macromolecules occurs because of progressive adsorption of chain segments as film pressure reduces along the flow direction [136]. Similar to the case of adsorption to a liquid substrate, steric repulsion between the densely grafted side chains raises the force in the backbone from the 10 pN to the 1 nN level, triggering the scission of bonds during flow on a solid substrate (Fig. 11a). Molecular bottlebrushes with a long polymethacrylate (PMA) backbone of DP = 3600 and PBA side chains of DP = 140 were subject to an abrupt decrease in size within a relatively narrow section of the film during spreading on mica [137]. As shown in Fig. 11b, in an 18-μm-long film, all bottlebrush molecules broke apart within a confined film region of ~1 μm width. The spreading-induced molecular fracture has two distinct features. First, it occurs spontaneously, driven by minimization of the surface free energy, which is accomplished through two concurrent spreading

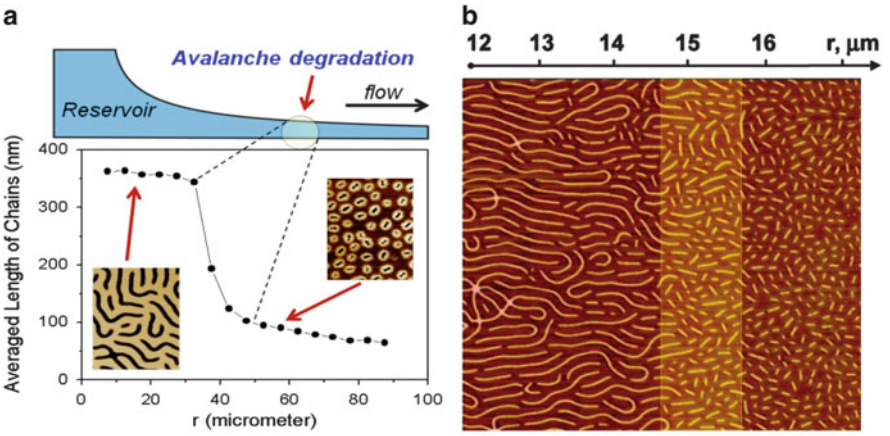

Fig. 11 Avalanche degradation of bottlebrush macromolecules in flow. (**a**) The rupture occurs at a well-defined distance from the drop, where tension reaches ~3 nN and the lifetime of C–C bonds is in the second range. (**b**) AFM height micrographs of molecular bottlebrushes along the spreading direction for the precursor film spreading on mica. The flowing molecular bottlebrushes fracture predominately within a narrow region as highlighted

processes: (1) macroscopic flow of bottlebrush polymer melts and (2) spreading of individual bottlebrushes, which results in bond scission. Second, the intrinsic gradient of the film pressure creates a well-defined loading rate for each individual molecule within the flowing film. The tensile force increases with distance along the flow direction and reaches its maximum at the film edge. This force gradient is the origin of the avalanche-like degradation of flowing molecular bottlebrushes. In addition, at distances farther away from the highlighted degradation region along the flow direction, the degradation process changes its pattern from random to mid-chain scission because of triangular distribution of tension in shorter bottlebrushes [135].

Zheng et al. observed the scission of polymer bottlebrushes with a PMA backbone and block side chains of poly[oligo(ethylene glycol)methacrylate]-*block*-poly[2-(dimethylamino)ethyl methacrylate] (POEGMA-*b*-PDMAEMA) or POEGMA-*block*-poly[2-(methacryloyloxy)ethyl trimethylammoniumiodide] (POEGMA-*b*-PMETAI) into small beads upon spin-coating from aqueous solution on mica or silicon substrates [138]. They attributed the scission of C–C bonds in the backbone to the contraction of POEGMA core upon water evaporation and the Coulombic interactions between the shell (PDMAEMA or PMETAI) and the negatively charged surface. If the energy of the Coulombic interactions is n times as strong as that of a C–C bond, n single C–C bonds in the backbone rupture and the bottlebrush breaks into $n+1$ small beads; however, if the energy of the Coulombic interactions is smaller than that of a C–C bond, the contraction of the POEGMA core leads to the sliding rather than anchoring of the shell and therefore a more compact conformation without scission of the backbone. The scission behavior can

be tuned by controlling the surface properties, varying pH, or adding multivalent counterions in the aqueous solution.

5.2 Dendritic Polymers

Dendrimers are a unique class of branched molecules composed of multiple perfectly branched monomers emanating radially from a central core. Because of their dendritic structures, dendrimers have many interesting properties, such as globular conformations and layered architectures [139]. Here, we draw attention to the concept of the "starburst limit" [140] which describes the crowdedness of dendrimers. If one considers that the number of monomer units in a dendrimers increases exponentially as a function of generation (the number of branching points encountered in the molecular skeleton when tracing a path from the core to the surface), and the sphere accommodating them only increases with the cube of generation, it is apparent that there is a limit for the generation beyond which the dendrimers cannot grow because of lack of space. Because dendrimers are heavily crowded, especially at high generations, substantially large tension up to hundreds of pico-Newtons could be generated in their dendritic skeletons, and the bond tension increases exponentially from the pico-Newton to the nano-Newton level as the bond approaches the core (Rubinstein M, unpublished manuscript). Moreover, branched architectures result in distribution of tension over the constituting chemical bonds. This presents a unique molecular system, where chemically identical bonds exhibit different tensions and hence different physical properties within an individual macromolecule. A molecule's topology can greatly affect the distribution of tension in its bonds, which can in turn affect its physical properties. Rubinstein et al. have shown that the exponential branching of a dendritic architecture causes enhancement of steric repulsion resulting in the corresponding exponential increase of bond tension from its outer surface to its inner core (Fig. 12). This finding emphasizes that even small dendrimers display altered physical properties.

Dendrimers can be used as precursors for the synthesis of the so-called pom-pom macromolecules. A pom-pom macromolecule containing two dendritic cores with z-arms grown from each core connected with a linear spacer can work as an effective molecular tension amplifier. The tension in the brush arms is typically below 1 pN. However, because of steric crowding of the arms, the pom-pom architecture enables amplification of tension from the pico-Newton range in its arms to nano-Newtons in the spacer, even in solution without applying any external force [125], which can be complementary to molecular bottlebrushes which can only achieve nano-Newton tension on substrates. In a good solvent, for a short and fully-stretched spacer, the tension is given by $f_{sp} \cong f_0 z^{3/2}/m$, where $f_0 = kT/b$, z the number of branches, m the number of Kuhn monomers in the spacer, and b the Kuhn length. As shown in Fig. 13, the tension for short spacers ($m \cong \sqrt{z}$) is on the

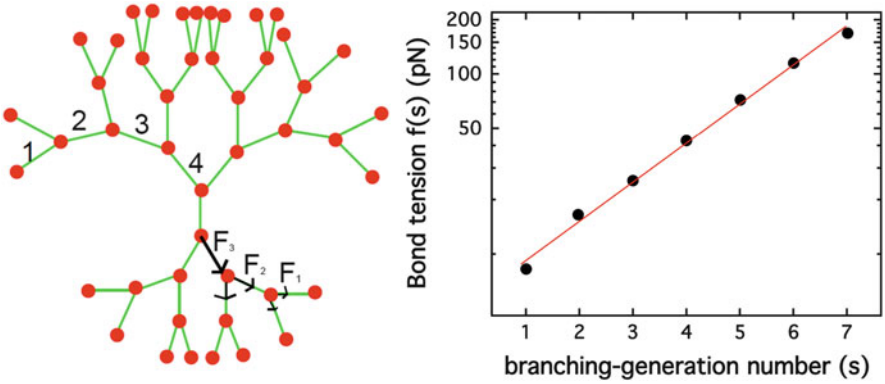

Fig. 12 The bond tension increases exponentially as one goes from the outer shell to the inner region of dendritic macromolecule. Unpublished results by Rubinstein et al.

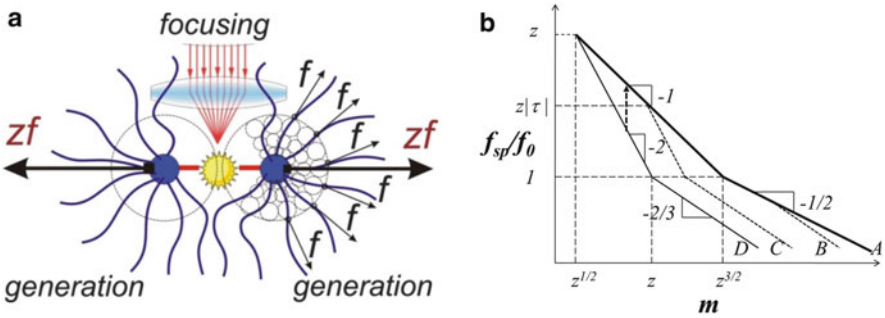

Fig. 13 Tension amplification in a pom-pom macromolecule. (**a**) Architecture of a pom-pom macromolecule including a dense branching core and the corona of $2z$ arms whose conformation is perturbed by linking (pushing) together two z-arm stars, which results in z-fold tension amplification in the linker (spacer). (**b**) Log-log plot of tension f_{sp} in a spacer with m Kuhn segments for pom-pom in different solvents. $-1 < \tau < 1$ indicates solvent quality. *Upper curve* (*A*)–good solvent; *middle curves* (*B*, *C*)–poor solvent; *lower curve* (*D*)–melt condition

order of zf_0. For example, seventh-generation dendrimers with a branching functionality of 3 and $z = 512$ arms induce tension in the spacer of about 512×4 pN ≈ 2 nN, which is close to the strength of covalent bonds.

Using polyelectrolyte arms presents an additional option for tension amplification (Sheiko et al., unpublished results). Polyelectrolyte pom-poms correspond to the so-called osmotic regime, where the majority of the counterions stay inside a pom-pom macromolecule. In this regime, because of the relatively small net charge of the macromolecule, electrostatic interactions between charged monomeric units can be neglected compared to the osmotic pressure of the confined counterions. This osmotic pressure allows for higher tension over a longer range of linker length. This suggests that it is possible to synthesize highly strained pom-poms using a smaller number of arms and longer linkers compared to a neutral pom-pom of the same molecular dimensions.

Although there have been no reports on mechanically induced self-cleavage of dendrimers or pom-poms, Yu et al. reported main-chain scission of polymer "bottlebrushes" with dendronized side chains (fifth generation) in solutions [141]. Similar to the conventional bottlebrushes discussed above, steric repulsion between the dendronized side chains causes strain in the backbone, which may further be enhanced by Coulombic repulsion between the charged functional groups in the dendritic periphery. This strain may facilitate scission of the backbone upon external stimulus (e.g., shear force by stirring), though the mechanism is not fully understood. Another relevant report [142] was about scission of a linker in surface-tethered dendrimers discussed in the next section (Fig. 14).

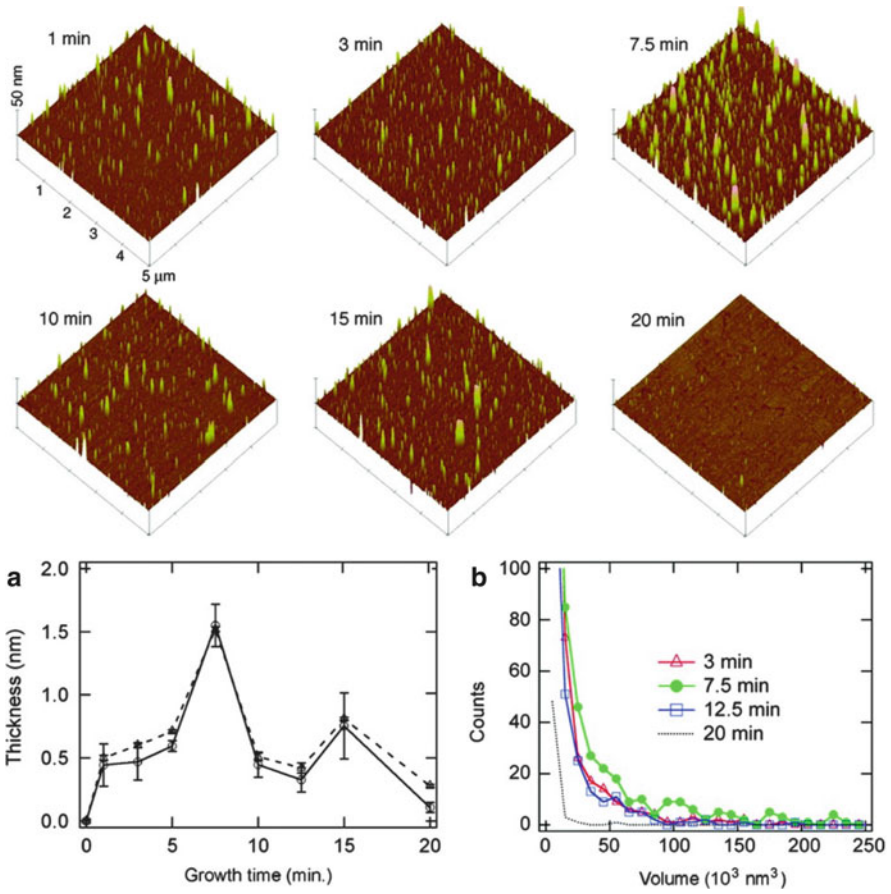

Fig. 14 Tapping-mode AFM height images of HPG on a SAM of 2.6% –S–$(CH_2)_{10}$COOH in a matrix of –S–$(CH_2)_9CH_3$ for different growth times. (**a**) Average thickness of HPG film as a function of growth time from AFM (*circles* and *solid line*) and ellipsometry (*triangles* and *dashed line*). (**b**) Histogram analysis of the size of HPG molecules on surface for different growth times. Reprinted with permission from [142]. Copyright 2007 American Chemical Society

6 Surface-Grafted Polymer Brushes

Polymer brushes are long polymer chains attached by one end to a surface or interface with a high enough density of attachment points so that the chains are crowded and forced to stretch away from the surface or interface, sometimes much farther than the end-to-end distance of an unperturbed chain [143]. They have been extensively studied both theoretically and experimentally for decades and have wide applications in tuning surface properties (e.g., wettability and friction), "smart" surfaces, cell culture, etc. [143–145]. Generally, polymer brushes can be prepared either by physisorption or covalent attachment. Covalently tethered polymer brushes are more stable than physically adsorbed polymer brushes where the interaction (e.g., van der Waals force and hydrogen bonding) between the substrate and the polymers is weak. However, this stability is confronted by chain extension in densely grafted polymer brushes which experience significant steric repulsion and entropy loss caused by chain extension. This entropic tension is on the order of pico-Newtons [122], which is too small to break a covalent bond. However, osmotic stress, electrostatic repulsion, and unfavorable interaction between the polymers and the substrate may result in additional tension, leading to the detachment of polymer chains off the substrate, if it exceeds the strength of a covalent bond. On the other hand, the degradation of the stressed polymer brushes may be accelerated by tension, even if it is not large enough to break a covalent bond.

6.1 Neutral Polymer Brushes

Early studies of the stability of poly(ethylene glycol) (PEG) thin films grafted onto SiO_x surfaces showed that incubation of these films in phosphate buffered saline (PBS) led to a gradual decrease in film thickness, which was attributed to detachment of the PEG chains from the surface caused by oxidative degradation [146, 147]. Although the tension in PEG chains might facilitate the degradation processes, it was neglected and not discussed until Sheiko et al. found that adsorption of molecular bottlebrush side chains onto a substrate can induce spontaneous rupture of covalent bonds in the backbone [126]. Since then, attention has been paid to the effects of tension on the stability of polymer brushes.

Zhu et al. demonstrated that a covalently tethered dendritic macromolecule can spontaneously break away from a solid substrate when the macromolecule/surface interaction is unfavorable, resulting in a negative spreading parameter [142]. Self-assembled monolayer (SAM) of HS-$(CH_2)_{10}$-COOH and HS-$(CH_2)_9$-CH_3 was adsorbed onto Au substrate, and the growth of hyperbranched polyglycidol (HPG) was initiated from $–COO^-$ sites and proceeded via anionic ring-opening polymerization of glycidol. As an HPG molecule grew larger, it formed more hydrogen bonds with the hydrophilic solvent (glycidol) and encountered more unfavorable interactions with the hydrophobic SAM matrix. When the HPG

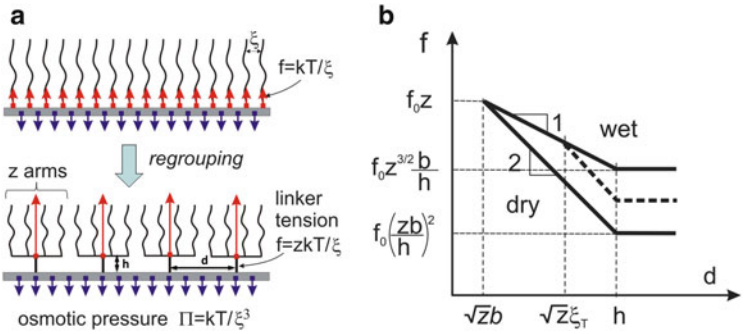

Fig. 15 Tension amplification in tethered macromolecules. (**a**) In polymer brushes, the osmotic pressure (*downward arrows*) is balanced by the tension in the linkers (*upward arrows*). By reconnecting the linear chains of a planar brush in groups of z arms, one gains *z*-fold amplification of the linker tension. (**b**) Tensile force in the linker between the tethered star-like brush and the substrate is presented as a function of the distance between the grafting sites *d* (double-logarithmic plot) for three different solvent regimes: wet (*upper solid line*), dry (*lower solid line*), and poor solvent at the thermal blob size $\xi_T < \xi$ (*dashed line*). The wet regime includes good solvents ($T > \Theta$), theta solvents ($T \cong \Theta$), and moderately poor solvents ($T < \Theta$ and $\xi_T > \xi$). For isolated molecules and loose brushes ($d > h$, $\sigma < 1/h^2$), the force does not depend on the grafting density and is determined by the length of the linker *h*. At higher grafting densities, the tension increases until it reaches the maximum value of $f \cong zf_0$ at a grafting density of $\sigma < 1/(zb^2)$. The poor solvent line (*dashed*) merges with the solvent line when the distance between neighboring arms becomes comparable to the thermal blob size ξ_T at $\alpha \cong 1/\left(z\xi_T^2\right)$

molecule reached a certain critical size, the unfavorable interactions could overcome the strength of a covalent bond, leading to its detachment from the hydrophobic surface at the sacrifice of the covalent bond (Fig. 14). However, it was not known which bond actually broke.

This finding corroborates theoretical studies of tension amplification in planar polymer brushes [148]. The tension amplification occurs because of steric repulsion of multiple branches growing from the same stem (linker). The principle of tension amplification is sketched in Fig. 15a. In a dense planar brush, linear chains are under tension $f_0 \cong kT/\xi$, where ξ-interchain distance. By reconnecting the individual chains in groups of z branches, one obtains z-fold amplification of the tension in the linker as $f \cong zf_0$. At large $z \sim 100$–1,000, the generated tension may exceed the strength of covalent bonds and sever the linker. As shown in Fig. 15b, the tension also depends on the grafting density, linker length, and quality of the surrounding solvent.

The theoretical predictions are consistent with experimental observations by Klok et al., demonstrating that poly(poly(ethylene glycol) methacrylate) (PPEGMA) brushes may detach from glass or silicon substrates at high grafting densities, accompanied by a strong decrease in the receding water contact angle [149]. Surface-initiated atom transfer radical polymerization (SI-ATRP) was used to grow PPEGMA from the initiator sites on the substrate, which allowed precise tailoring of both grafting density by varying the surface density of ATRP initiator

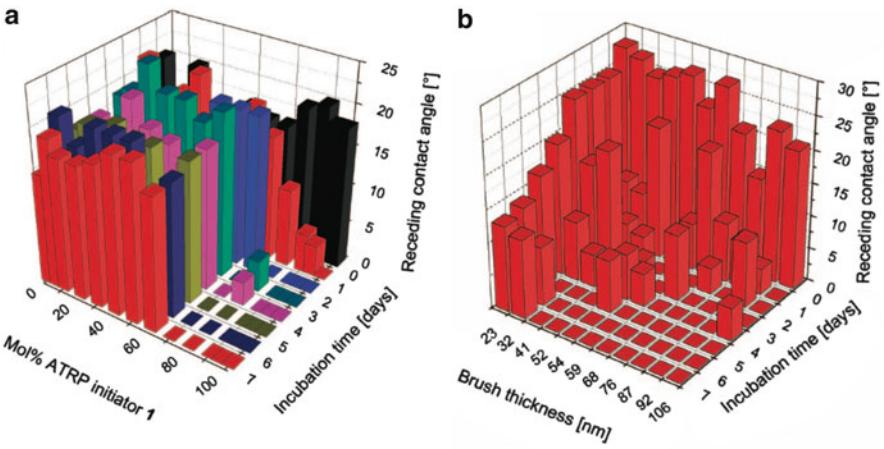

Fig. 16 The stability of PPEGMA functionalized glass substrates indicated by the measured receding water contact angle as a function of mol% ATRP initiator (**a**) and brush thickness (**b**) upon incubation in cell culture medium at 37 °C. Adapted with permission from [149]. Copyright 2008 American Chemical Society

groups with the use of non-ATRP reactive diluent and thickness by controlling the polymerization time. It was found that PPEGMA brushes prepared from substrates with $\geq$70 mol% ATRP initiators deteriorated and lost their stability within 1–2 days, indicated by the sharp decrease of the receding water contact angle in cell culture medium, whereas the PPEGMA brushes prepared from substrates with less than 70 mol% ATRP initiators showed no significant changes in the receding water contact angle in at least a week (Fig. 16a). On the other hand, the stabilities of PPEGMA brushes with different thickness from 23 to 106 nm grown from substrates with 100 mol% ATRP initiators were also studied. It was demonstrated that the decreasing brush thickness retarded the drop in the receding water contact angle (Fig. 16b). These observations were ascribed to the cleavage of Si–O bonds at the brush and substrate interface induced by steric repulsion and osmotic stresses which act on the brushes in cell culture medium. Stretching, steric crowding, and swelling of the PPEGMA brushes were caused by their water solubility. The salt concentration in the brushes could be higher than that in the cell culture medium because of the ability of PEG side chains to bind alkali and alkaline earth metal ions [150], which would result in osmotic stresses in the stretched polymer chains. Both of these factors may induce additional tension along the already stretched polymer brush backbones, which facilitates the hydrolysis of Si–O bonds and detachment of the brushes at high brush densities. This hypothesis was verified by control experiments showing that poly(2-hydroxyethyl methacrylate) (PHEMA) brushes did not reveal any signs of detachment upon incubation in cell culture medium and that all PPEGMA brushes with different thicknesses and densities did not show any noticeable loss of stability upon incubation in pure water over a period of at least 7 days. A follow-up study by the same group showed the stability of the grafted

brushes increases as the spacer length of the initiator increases, which was ascribed to the increase in the hydrophobicity of the anchoring layer [151]. This argument may not be tenable, because the grafting densities of the grafted polymers were not controlled or even discussed in the report. An alternative explanation could be that the tension in the ester bond in the linker (initiator) decreases with increasing spacer length.

A later study by Chen et al. reported that surface-grafted polybutadiene (PBd) and polynorbornene (PNb) brushes suffered acute degradation upon solvent rinsing under ambient conditions, leading to the decrease in film thickness [152]. The degradation was ascribed to the rapid auto-oxidation of allylic carbon-hydrogen bonds, supported by an earlier work by Jennings and co-workers which demonstrated that the loss of PNb films was probably caused by the cleavage of polymer chains at the olefin sites [153] and the control experiment that degradation of PBd film did not occur when solvent rinsing was carried under nitrogen in a glovebox. To compare free polyolefins with surface tethered polyolefins, two commercial PBd samples were dissolved in oxygen-saturated tetrahydrofuran to test their stabilities. No changes in molecular weight were observed by gel permeation chromatography (GPC) after 48 h for both samples, indicating that the degradation of free PBd chains in solution was negligible in comparison with that of surface tethered PBd. The authors concluded that the degradation at the substrate–solvent interface was exacerbated by entropic gain produced by chain scission and the diffusion of degraded segments from high concentration interface to low concentration solution media. Although not mentioned, it is likely that the tension in the surface-grafted polyolefin brushes caused by steric crowding and swelling accelerated the oxidation of allylic carbon–hydrogen bonds and promoted the degradation.

6.2 Charged Polymer Brushes

Charged polymer brushes are also called polyelectrolyte brushes. Theory distinguishes between two classes of polyelectrolyte brushes. One is quenched polyelectrolyte brushes where the grafted chains are strongly dissociating polyelectrolytes of which the degree of charging is fixed and independent of external conditions, e.g., poly(styrenesulfonic acid) (PSSA). The other is called annealed polyelectrolyte brushes where weak polyelectrolytes, e.g., poly(acrylic acid) (PAA), are grafted. Adjustment of the degree of ionization of the weak polyelectrolytes to external conditions (e.g., pH and ionic strength) is needed to achieve equilibrium of the system. Compared to neutral polymer brushes, additional tension can be generated along the grafted chains in polyelectrolyte brushes caused by strong electrostatic repulsion, which may further decrease the stability. The additional amplification of tension produced by charges is discussed in application to the pom-pom architectures with polyelectrolyte arms in Sect. 5, which is also relevant to polyelectrolyte brushes tethered to a flat substrate.

A pioneering study of mechanical tension induced covalent bond breakage in polyelectrolyte brushes was carried out by Ma and co-workers [154]. In their study, random copolymers of oligo (ethylene glycol) methacrylate (OEGMA) and 2-hydroxyethyl methacrylate (HEMA) were grafted from an Au coated quartz crystal microbalance (QCM) chip, and the resulting neutral poly(OEGMA-*r*-HEMA) grafts were then converted to weak polyelectrolytes by reacting with succinic anhydride. The swelling behavior of the polyelectrolyte brushes was monitored by QCM based on its piezoelectric effect that mass loading to a QCM chip causes a decrease in the resonant frequency [155]. No increase in resonant frequency was observed for the polyelectrolyte brushes incubated in Milli-Q water for up to 72 h. However, when Milli-Q water was replaced with PBS (pH 7.4, $[Na^+]$=150 mM), the resonant frequency for the polyelectrolyte brush sample with a dry thickness of 75 nm increased dramatically to a value which was overlapped with an initiator modified QCM chip in PBS, indicating that the polyelectrolyte brush was instantaneously pulled off the Au substrate, whereas the polyelectrolyte brush sample with a dry thickness of 54 nm showed a decrease in resonant frequency caused by further swelling in PBS as weak polyelectrolytes are sensitive to pH and salt concentration [156, 157]. The authors speculated that the Au–S bond was broken accompanied by the detachment of the polyelectrolytes because it was the weakest bond in the tested systems. In fact, the detachment of the polyelectrolyte brushes was only observed for the samples with dry thickness larger than 75 nm (critical dry thickness), which was attributed to pH and/or the ion related swelling of the polyelectrolyte chains which could cause additional tension along the chains (Fig. 17). It was stated that its instability was introduced and stored in the system during the synthesis process, because such bond breaking was not observed for carboxylated poly(OEGMA) or poly(HEMA). A follow-up study by the same group investigated the effects of pH and ionic strength on the swelling behavior of the weak polyelectrolytes, carboxylated poly(OEGMA-*r*-HEMA) [158]. The thickness of the swollen polyelectrolyte brush was sensitive to pH and ionic strength. Once its

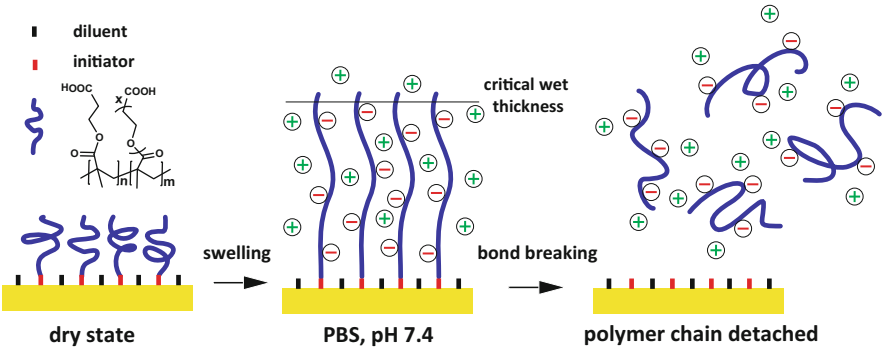

Fig. 17 Swelling induced detachment of carboxylated poly(OEGMA-***r***-HEMA) brush anchored to a QCM chip via Au-S bond. The swelling behavior depends on the ionic strength and pH of the solution. The polyelectrolyte brush detaches from the substrate beyond a critical wet thickness

thickness was beyond a critical value of 255 nm, Au–S bonds would break followed by the detachment of the polyelectrolyte coating in PBS (pH 7.4). By grafting carboxylated poly(OEGMA-*r*-HEMA) on different metal surface (e.g., Pt and Ag), the critical dry thickness for Ag surface was found to be 47 nm, smaller than the 75 nm for Au surface in PBS (pH 7.4, $[Na^+]$=150 mM), whereas no covalent bond-breaking event was observed for the polyelectrolyte brushes grafted from Pt surface with a dry thickness up to 108 nm. The order of the critical dry thickness for the polyelectrolyte brushes grafted from the metal surfaces was in good agreement with the trends of calculated adsorption energies of metal–S bonds. In a more recent paper, the same group reported another interesting discovery: the Au–S bond breakage depends on the film area of grafted poly(OEGMA-*r*-HEMA) [159]. Patterned films with areas smaller than 160 μm^2 underwent partial Au–S bond breakage accompanied by significant morphological changes, buckling out of the pristine smooth surfaces after immersion in PBS for 24 h, in contrast with their macroscale controls in which the films detached from the substrates completely. However, the reason behind this phenomenon remains unknown.

On the other hand, Maekawa and co-workers reported swelling-induced detachment of grafted hydrophilic PSSA, a strong polyelectrolyte, from hydrophobic polymer substrates in aqueous media [160]. PSSA was grafted on crosslinked poly(tetrafluoroethylene) (cPTFE), poly(ethylene-*co*-tetrafluoroethylene) (ETFE), and poly(ether ether ketone) (PEEK) substrates by γ-ray irradiation-initiated radical polymerization followed by further functionalization. Upon swelling in hot water (85 °C), PSSA-grafted fluorinated films (cPTFE and ETFE) with the same grafting degree (51%) showed significant weight loss caused by the detachment of PSSA grafts without decomposition of grafted chains, as confirmed by the fact that the extracted PSSA grafts possessed the same molecular structure during the whole degradation course. These observations suggested that the scission of the grafts must be located at the interface of PSSA grafts and the substrate. However, no obvious weight loss was observed for PSSA grafted PEEK with even higher grafting degree of 56%. The detachment of the PSSA grafts was pronounced in the order of cPTFE > ETFE > PEEK, which agrees with the trends of the differences in solubility parameters between PSSA precursors (18 $(J/cm^3)^{1/2}$) and the substrates (13 $(J/cm^3)^{1/2}$, 14 $(J/cm^3)^{1/2}$, and 21 $(J/cm^3)^{1/2}$ for cPTFE, TEFE, and PEEK, respectively). In addition to entropic tension and electrostatic repulsion, unfavorable interactions between hydrophilic PSSA grafts and hydrophobic substrates resulted in additional tension which was prominent at the interfacial boundary, promoting the detachment of the grafts from the substrates.

Genzer and co-workers studied the effects of weak linkers (e.g., ester bond) on the stability of surface-grafted PDMAEMA (a weak polyelectrolyte) brushes at varying conditions of pH [161]. Two sets of PDMAEMA brushes were prepared by surface-initiated free radical polymerization (SI-FRP) from the so-called BAIN initiator and SI-ATRP from [11-(2-bromo-2-methyl)propionyloxy]-undecyltrichlorosilane (BMPUS) initiator, respectively. BAIN is special compared to

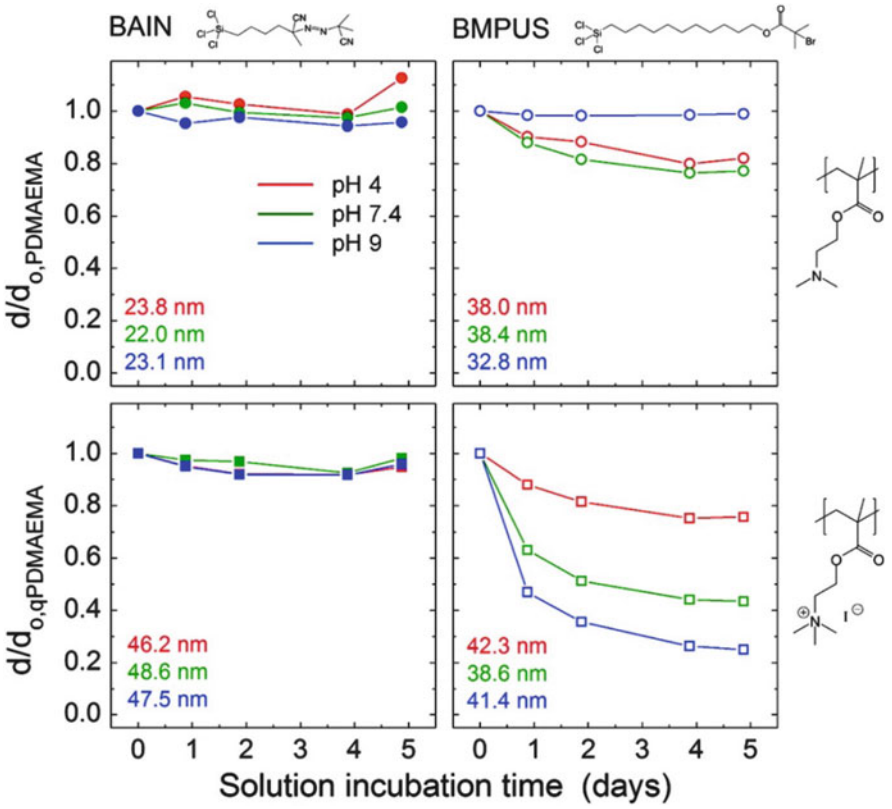

Fig. 18 Relative dry thickness d/d_0 of PDMAEMA brushes (*circles*) and quaternized PDMAEMA brushes (*squares*) formed by SI-FRP from BAIN (*closed symbols*), and by SI-ATRP from BMPUS (*open symbols*), as a function of incubation time in PBS solution of pH 4 (*red*), pH 7.4 (*green*), and pH 9 (*blue*). Initial thicknesses d_0 of the samples are indicated in the *lower left corner* of each pane. Reprinted with permission from [161]. Copyright 2012 American Chemical Society

BMPUS, as it does not contain an ester group. As shown in Fig. 18, the thickness of both PDMAEMA (weak electrolyte) and quaternized PDMAEMA (qPDMAEMA, strong electrolyte) brushes by SI-FRP from BAIN did not change significantly after incubation in PBS solution, regardless of the pH, indicating that the Si–O bonds were stable in these conditions. In contrast, the thickness of PDMAEMA brushes by SI-ATRP from BMPUS remained constant at pH 9, but decreased by ~18% at pH 4 and by ~23% at pH 7.4. The degrafting of brush chains was ascribed to base-catalyzed hydrolysis of ester. The concentration of hydroxide ions increased with pH, resulting in the acceleration of ester hydrolysis, whereas the tension in the brush was reduced because of the decrease in charge fraction as pH increased, leading to the deceleration of hydrolysis. These two counterbalancing effects resulted in maximum degrafting at pH 7.4. This was further supported by the

experimental observation that the degrafting rate of qPDMAEMA brushes increased with increasing pH. This study can be significant as it demonstrated that the ester bond could be more susceptible to mechanically assisted hydrolysis than the Si–O bond.

7 Conclusions

In this account, we have reviewed recent advances in the design and development of inherently stressed/strained molecules and their application in mechanochemistry. Generally, tension is hierarchically developed in chemical bonds starting from diatomic molecules to polymer chains and highly branched macromolecules. The bond tension in a diatomic molecule originates from thermal fluctuation of the bond and entropy gain from stretching, yet it is small and cannot readily activate the bond. Substantially higher tension can be generated because of topological constriction, ring strain, and steric repulsion, which may cause spontaneous bond cleavage, acceleration of chemical reactions, and other mechanochemical changes. Particularly, evolution of tension in polymer knots, cyclic molecules, and highly branched macromolecules is highlighted, which is hoped to shed light on the design of new mechanophores, molecular force probes, or molecular tensile machines. At the end of this review, examples of mechanically assisted degrafting of surface tethered polymer brushes are discussed in detail, because it is a new field with many open questions. The mechanisms of degrafting and selectivity of bond cleavage are not fully understood. All these challenges provide new opportunities in mechanochemistry which can be addressed through rational design of molecular architectures, quantitative molecular-scale experiments, and predictive theories.

Acknowledgements The authors acknowledge financial support from the National Science Foundation (DMR-1122483). YL is grateful to the support from the Army Research Office National Research Council Postdoctoral Research Fellowship.

References

1. Wiggins KM, Brantley JN, Bielawski CW (2012) Polymer mechanochemistry: force enabled transformations. ACS Marco Lett 1:623
2. Bensimon D (1996) Force: a new structural control parameter? Structure 4:885
3. Wiita AP, Ainavarapu SRK, Huang HH, Fernandez JM (2006) Force-dependent chemical kinetics of disulfide bond reduction observed with single-molecule techniques. Proc Natl Acad Sci U S A 103:7222
4. Li Y, Nese A, Lebedeva NV, Davis T, Matyjaszewski K, Sheiko SS (2011) Molecular tensile machines: intrinsic acceleration of disulfide reduction by dithiothreitol. J Am Chem Soc 133:17479
5. Piermattei A, Karthikeyan S, Sijbesma RP (2009) Activating catalysts with mechanical force. Nat Chem 1:133

6. Tennyson AG, Wiggins KM, Bielawski CW (2010) Mechanical activation of catalysts for C–C bond forming and anionic polymerization reactions from a single macromolecular reagent. J Am Chem Soc 132:16631
7. Hickenboth CR, Moore JS, White SR, Sottos NR, Baudry J, Wilson SR (2007) Biasing reaction pathways with mechanical force. Nature 446:423
8. Lenhardt JM, Ong MT, Choe R, Evenhuis CR, Martinez TJ, Craig SL (2010) Trapping a diradical transition state by mechanochemical polymer extension. Science 329:1057
9. Diesendruck CE, Peterson GI, Kulik HJ, Kaitz JA, Mar BD, May PA, White SR, Martínez TJ, Boydston AJ, Moore JS (2014) Mechanically triggered heterolytic unzipping of a low-ceiling-temperature polymer. Nat Chem 6:623
10. Klibanov AM, Samokhin GP, Martinek K, Berezin IV (1976) Enzymatic mechanochemistry: a new approach to studying the mechanism of enzyme action. Biochim Biophys Acta 438:1
11. Alegre-Cebollada J, Perez-Jimenez R, Kosuri P, Fernandez JM (2010) Single-molecule force spectroscopy approach to enzyme catalysis. J Biol Chem 285:18961
12. Camp RJ, Liles M, Beale J, Saeidi N, Flynn BP, Moore E, Murthy SK, Ruberti JW (2011) Molecular mechanochemistry: low force switch slows enzymatic cleavage of human type I collagen monomer. J Am Chem Soc 133:4073
13. Golovin YI, Gribanovskii SL, Klyachko NL, Kabanov AV (2014) Nanomechanical control of the activity of enzymes immobilized on single-domain magnetic nanoparticles. Tech Phys 59:932
14. Visscher K, Schnitzer MJ, Block SM (1999) Single kinesin molecules studied with a molecular force clamp. Nature 400:184
15. Vale RD, Milligan RA (2000) The way things move: looking under the hood of molecular motor proteins. Science 288:88
16. Schnitzer MJ, Visscher K, Block SM (2000) Force production by single kinesin motors. Nat Cell Biol 2:718
17. Bustamante C, Keller D, Oster G (2001) The physics of molecular motors. Acc Chem Res 34:412
18. Carter NJ, Cross RA (2005) Mechanics of the kinesin step. Nature 435:308
19. Kolomeisky AB, Fisher ME (2007) Molecular motors: a theorist's perspective. Annu Rev Phys Chem 58:675
20. Bloom K (2008) Beyond the code: the mechanical properties of DNA as they relate to mitosis. Chromosoma 117:103
21. Stephens AD, Haase J, Vicci L, Taylor RM, Bloom K (2011) Cohesin, condensin, and the intramolecular centromere loop together generate the mitotic chromatin spring. J Cell Biol 193:1167
22. Cross RA, McAinsh A (2014) Prime movers: the mechanochemistry of mitotic kinesins. Nat Rev Mol Cell Bio 15:257
23. Gordon AM, Homsher E, Regnier M (2000) Regulation of contraction in striated muscle. Physiol Rev 80:853
24. Hugel T, Holland NB, Cattani A, Moroder L, Seitz M, Gaub HE (2002) Single-molecule optomechanical cycle. Science 296:1103
25. Lin J, Beratan DN (2004) Tunneling while pulling: the dependence of tunneling current on end-to-end distance in a flexible molecule. J Phys Chem A 108:5655
26. Chang S, He J, Kibel A, Lee M, Sankey O, Zhang P, Lindsay S (2009) Tunnelling readout of hydrogen-bonding-based recognition. Nat Nanotechnol 4:297
27. Lafferentz L, Ample F, Yu H, Hecht S, Joachim C, Grill L (2009) Conductance of a single conjugated polymer as a continuous function of its length. Science 323:1193
28. Quek SY, Kamenetska M, Steigerwald ML, Choi HJ, Louie SG, Hybertsen MS, Neaton JB, Venkataraman L (2009) Mechanically controlled binary conductance switching of a single-molecule junction. Nat Nanotechnol 4:230
29. Parks JJ, Champagne AR, Costi TA, Shum WW, Pasupathy AN, Neuscamman E, Flores-Torres S, Cornaglia PS, Aligia AA, Balseiro CA, Chan GK-L, Abruña HD, Ralph DC (2010)

Mechanical control of spin states in spin-1 molecules and the underscreened Kondo effect. Science 328:1370
30. Chen Y, Spiering AJH, KarthikeyanS PGWM, Meijer EW, Sijbesma RP (2012) Mechanically induced chemiluminescence from polymers incorporating a 1,2-dioxetane unit in the main chain. Nat Chem 4:559
31. Ariga K, Mori T, Hill JP (2012) Mechanical control of nanomaterials and nanosystems. Adv Mater 24:158
32. Caruso MM, Davis DA, Shen Q, Odom SA, Sottos NR, White SR, Moore JS (2009) Mechanically-induced chemical changes in polymeric materials. Chem Rev 109:5755
33. Black AL, Lenhardt JM, Craig SL (2011) From molecular mechanochemistry to stress-responsive materials. J Mater Chem 21:1655
34. Brantley JN, Bailey CB, Wiggins KM, Keatinge-Clay AT, Bielawski CW (2013) Mechanobiochemistry: harnessing biomacromolecules for force-responsive materials. Polym Chem 4:3916
35. Groote R, Jakobs RTM, Sijbesma RP (2013) Mechanocatalysis: forcing latent catalysts into action. Polym Chem 4:4846
36. Ashkin A, Schutze K, Dziedzic JM, Euteneuer U, Schliwa M (1990) Force generation of organelle transport measured in vivo by an infrared laser trap. Nature 348:346
37. Crick FHC, Hughes AFW (1950) The physical properties of cytoplasm: a study by means of the magnetic particle method. Part I. Experimental. Exp Cell Res 1:37
38. Smith S, Finzi L, Bustamante C (1992) Direct mechanical measurements of the elasticity of single DNA molecules by using magnetic beads. Science 258:1122
39. Florin E, Moy V, Gaub H (1994) Adhesion forces between individual ligand-receptor pairs. Science 264:415
40. Grandbois M, Beyer M, Rief M, Clausen-Schaumann H, Gaub HE (1999) How strong is a covalent bond? Science 283:1727
41. Oberhauser AF, Hansma PK, Carrion-Vazquez M, Fernandez JM (2001) Stepwise unfolding of titin under force-clamp atomic force microscopy. Proc Natl Acad Sci U S A 98:468
42. Kishino A, Yanagida T (1988) Force measurements by micromanipulation of a single actin filament by glass needles. Nature 334:74
43. Evans E, Ritchie K, Merkel R (1995) Sensitive force technique to probe molecular adhesion and structural linkages at biological interfaces. Biophys J 68:2580
44. Yang Q-Z, Huang Z, Kucharski TJ, Khvostichenko D, Chen J, Boulatov R (2009) A molecular force probe. Nat Nanotechnol 4:302
45. Park I, Sheiko SS, Nese A, Matyjaszewski K (2009) Molecular tensile testing machines: breaking a specific covalent bond by adsorption-induced tension in brushlike macromolecules. Macromolecules 42:1805
46. Lenhardt JM, Black AL, Craig SL (2009) gem-Dichlorocyclopropanes as abundant and efficient mechanophores in polybutadiene copolymers under mechanical stress. J Am Chem Soc 131:10818
47. Kauzmann W, Eyring H (1940) The viscous flow of large molecules. J Am Chem Soc 62:3113
48. Kramers HA (1940) Brownian motion in a field of force and the diffusion model of chemical reactions. Physica 7:284
49. Zhurkov SN (1965) Int J Fract Mech 1:311
50. Bell G (1978) Models for the specific adhesion of cells to cells. Science 200:618
51. Evans E, Ritchie K (1997) Dynamic strength of molecular adhesion bonds. Biophys J 72:1541
52. Saitta AM, Soper PD, Wasserman E, Klein ML (1999) Influence of a knot on the strength of a polymer strand. Nature 399:46
53. Beyer MK (2000) The mechanical strength of a covalent bond calculated by density functional theory. J Chem Phys 112:7307

54. Hummer G, Szabo A (2003) Kinetics from nonequilibrium single-molecule pulling experiments. Biophys J 85:5
55. Dudko OK, Hummer G, Szabo A (2006) Intrinsic rates and activation free energies from single-molecule pulling experiments. Phys Rev Lett 96:108101
56. Ribas-Arino J, Shiga M, Marx D (2010) Mechanochemical transduction of externally applied forces to mechanophores. J Am Chem Soc 132:10609
57. Ribas-Arino J, Marx D (2012) Covalent mechanochemistry: theoretical concepts and computational tools with applications to molecular nanomechanics. Chem Rev 112:5412
58. Huang Z, Boulatov R (2011) Chemomechanics: chemical kinetics for multiscale phenomena. Chem Soc Rev 40:2359
59. Jiang D-L, Aida T (1997) Photoisomerization in dendrimers by harvesting of low-energy photons. Nature 388:454
60. Larsen MB, Boydston AJ (2013) "Flex-activated" mechanophores: using polymer mechanochemistry to direct bond bending activation. J Am Chem Soc 135:8189
61. Larsen MB, Boydston AJ (2014) Successive mechanochemical activation and small molecule release in an elastomeric material. J Am Chem Soc 136:1276
62. Gao J, Weiner JH (1990) Bond forces and pressure in diatomic liquids. Mol Phys 70:299
63. Weiner JH, Berman DH (1985) Bond forces in long-chain molecules. J Chem Phys 82:548
64. Gao J, Weiner JH (1989) Excluded-volume effects in rubber elasticity. 4. Nonhydrostatic contribution to stress. Macromolecules 22:979
65. Beiermann BA, Kramer SLB, Moore JS, White SR, Sottos NR (2011) Role of mechanophore orientation in mechanochemical reactions. ACS Marco Lett 1:163
66. von Baeyer A (1885) Ber Dtsch Chem Ges 18:2278
67. Wiberg KB (1986) The concept of strain in organic chemistry. Angew Chem Int Ed 25:312
68. Liebman JF, Greenberg A (1976) A survey of strained organic molecules. Chem Rev 76:311
69. Murray RW (1989) Chemistry of dioxiranes. 12. Dioxiranes. Chem Rev 89:1187
70. Tochtermann W, Olsson G (1989) 3-Heteroquadricyclanes in organic synthesis. Chem Rev 89:1203
71. Alder RW (1989) Strain effects on amine basicities. Chem Rev 89:1215
72. Michl J, Gladysz J (1989) Strained organic compounds: introduction. Chem Rev 89:973
73. Moszner N, Zeuner F, Völkel T, Rheinberger V (1999) Synthesis and polymerization of vinylcyclopropanes. Macromol Chem Phys 200:2173
74. Boileau S, Illy N (2011) Activation in anionic polymerization: why phosphazene bases are very exciting promoters. Prog Polym Sci 36:1132
75. Wong HNC, Hon MY, Tse CW, Yip YC, Tanko J, Hudlicky T (1989) Use of cyclopropanes and their derivatives in organic synthesis. Chem Rev 89:165
76. Ferguson LN (1973) Highlights of alicyclic chemistry. Franklin Publishing Co., Palisades
77. Benson SW (1968) Themraochemical kinetics. Wiley, New York
78. Bastiansen O, Fritsch FN, Hedberg K (1964) Least-squares refinement of molecular structures from gaseous electron-diffraction sector-microphotometer data. III. Refinement of cyclopropane. Acta Crystallogr 17:538
79. Jones WJ, Stoicheff BP (1964) High-resolution Raman spectroscopy of gases: XVIII. Pure rotational spectra of cyclopropane and cyclopropane-d6. Can J Phys 42:2259
80. Lide JDR (1960) Microwave spectrum, structure, and dipole moment of propane. J Chem Phys 33:1514
81. Seubold JFH (1953) Carbon-carbon bond dissociation energies in the cycloalkanes. J Chem Phys 21:1616
82. Cottrell TL (1958) The strengths of chemical bonds. Butterworths, London
83. Coulson CA, Moffitt WE (1947) Strain in non-tetrahedral carbon atoms. J Chem Phys 15:151
84. Coulson CA, Moffitt WE (1949) The properties of certain strained hydrocarbons. Philoso Mag Ser 7 40:1
85. Coulson CA, Goodwin TH (1962) Bent bonds in cycloalkanes. J Chem Soc (Resumed) 557:2851

86. Lipscomb WN, Stevens RM, Switkes E, Laws EA (1971) Self-consistent-field studies of the electronic structures of cyclopropane and benzene. J Am Chem Soc 93:2603
87. Wu D, Lenhardt JM, Black AL, Akhremitchev BB, Craig SL (2010) Molecular stress relief through a force-induced irreversible extension in polymer contour length. J Am Chem Soc 132:15936
88. Klukovich HM, Kouznetsova TB, Kean ZS, Lenhardt JM, Craig SL (2012) A backbone lever-arm effect enhances polymer mechanochemistry. Nat Chem 5:110
89. Wang J, Kouznetsova TB, Kean ZS, Fan L, Mar BD, Martínez TJ, Craig SL (2014) A remote stereochemical lever arm effect in polymer mechanochemistry. J Am Chem Soc 136:15162
90. Kean ZS, Ramirez ALB, Craig SL (2012) High mechanophore content polyester-acrylate ABA block copolymers: synthesis and sonochemical activation. J Polym Sci Part A Polym Chem 50:3481
91. Glynn PAR, Van Der Hoff BME, Reilly PM (1972) A general model for prediction of molecular weight distributions of degraded polymers. development and comparison with ultrasonic degradation experiments. J Macromol Sci Part A Chem 6:1653
92. Glynn PAR, van der Hoff BME (1973) Degradation of polystyrene in solution by ultrasonation – a molecular weight distribution study. J Macromol Sci Part A Chem 7:1695
93. Koda S, Mori H, Matsumoto K, Nomura H (1994) Ultrasonic degradation of water-soluble polymers. Polymer 35:30
94. Diesendruck CE, Steinberg BD, Sugai N, Silberstein MN, Sottos NR, White SR, Braun PV, Moore JS (2012) Proton-coupled mechanochemical transduction: a mechanogenerated acid. J Am Chem Soc 134:12446
95. Lenhardt JM, Ogle JW, Ong MT, Choe R, Martinez TJ, Craig SL (2011) Reactive cross-talk between adjacent tension-trapped transition states. J Am Chem Soc 133:3222
96. Ramirez ALB, Kean ZS, Orlicki JA, Champhekar M, Elsakr SM, Krause WE, Craig SL (2013) Mechanochemical strengthening of a synthetic polymer in response to typically destructive shear forces. Nat Chem 5:757
97. Kean ZS, Craig SL (2012) Mechanochemical remodeling of synthetic polymers. Polymer 53:1035
98. Klukovich HM, Kean ZS, Iacono ST, Craig SL (2011) Mechanically induced scission and subsequent thermal remending of perfluorocyclobutane polymers. J Am Chem Soc 133:17882
99. Kryger MJ, Munaretto AM, Moore JS (2011) Structure–mechanochemical activity relationships for cyclobutane mechanophores. J Am Chem Soc 133:18992
100. Kean ZS, Black Ramirez AL, Yan Y, Craig SL (2012) Bicyclo[3.2.0]heptane mechanophores for the non-scissile and photochemically reversible generation of reactive bis-enones. J Am Chem Soc 134:12939
101. Kean ZS, Niu Z, Hewage GB, Rheingold AL, Craig SL (2013) Stress-responsive polymers containing cyclobutane core mechanophores: reactivity and mechanistic insights. J Am Chem Soc 135:13598
102. Waldeck DH (1991) Photoisomerization dynamics of stilbenes. Chem Rev 91:415
103. Akbulatov S, Tian Y, Boulatov R (2012) Force–reactivity property of a single monomer is sufficient to predict the micromechanical behavior of its polymer. J Am Chem Soc 134:7620
104. Lai C, Guo W, Tang X, Zhang G, Pan Q, Pei M (2011) Cross-linking conducting polythiophene with yellow-green light-emitting properties and good thermal stability via free radical polymerization and electropolymerization. Synth Met 161:1886
105. Li W, Edwards SA, Lu L, Kubar T, Patil SP, Grubmüller H, Groenhof G, Gräter F (2013) Force distribution analysis of mechanochemically reactive dimethylcyclobutene. ChemPhysChem 14:2687
106. Huang Z, Yang Q-Z, Khvostichenko D, Kucharski TJ, Chen J, Boulatov R (2009) Method to derive restoring forces of strained molecules from kinetic measurements. J Am Chem Soc 131:1407

107. Kucharski TJ, Huang Z, Yang Q-Z, Tian Y, Rubin NC, Concepcion CD, Boulatov R (2009) Kinetics of thiol/disulfide exchange correlate weakly with the restoring force in the disulfide moiety. Angew Chem Int Ed 48:7040
108. Tian Y, Kucharski TJ, Yang Q-Z, Boulatov R (2013) Model studies of force-dependent kinetics of multi-barrier reactions. Nat Commun 2013:4
109. Kucharski TJ, Yang Q-Z, Tian Y, Boulatov R (2010) Strain-dependent acceleration of a paradigmatic SN2 reaction accurately predicted by the force formalism. J Phys Chem Lett 1:2820
110. Akbulatov S, Tian Y, Kapustin E, Boulatov R (2013) Model studies of the kinetics of ester hydrolysis under stretching force. Angew Chem Int Ed 52:6992
111. Kean ZS, Akbulatov S, Tian Y, Widenhoefer RA, Boulatov R, Craig SL (2014) Photomechanical actuation of ligand geometry in enantioselective catalysis. Angew Chem 126:14736
112. Xia F, Bronowska AK, Cheng S, Gräter F (2011) Base-catalyzed peptide hydrolysis is insensitive to mechanical stress. J Phys Chem B 115:10126
113. Ayme J-F, Beves JE, Campbell CJ, Leigh DA (2013) Template synthesis of molecular knots. Chem Soc Rev 42:1700
114. Bayer RK (1994) Structure transfer from a polymeric melt to the solid state. Part III: influence of knots on structure and mechanical properties of semicrystalline polymers. Colloid Polym Sci 272:910
115. Ashley CW (1993) The ashley book of knots. Doubleday, New York
116. Arai Y, Yasuda R, K-i A, Harada Y, Miyata H, Kinosita K, Itoh H (1999) Tying a molecular knot with optical tweezers. Nature 399:446
117. Tsuda Y, Yasutake H, Ishijima A, Yanagida T (1996) Torsional rigidity of single actin filaments and actin–actin bond breaking force under torsion measured directly by in vitro micromanipulation. Proc Natl Acad Sci USA 93:12937
118. Saitta AM, Klein ML (2000) First-principles study of bond rupture of entangled polymer chains. J Phys Chem B 104:2197
119. Griller D, Barclay LRC, Ingold KU (1975) Kinetic applications of electron paramagnetic resonance spectroscopy. XX. 2,4,6-Tri(tert-butyl)benzyl, -anilino, -phenoxy, and -phenylthiyl radicals. J Am Chem Soc 97:6151
120. Schreiner PR, Chernish LV, Gunchenko PA, Tikhonchuk EY, Hausmann H, Serafin M, Schlecht S, Dahl JEP, Carlson RMK, Fokin AA (2011) Overcoming lability of extremely long alkane carbon-carbon bonds through dispersion forces. Nature 477:308
121. Sheiko SS, Sumerlin BS, Matyjaszewski K (2008) Cylindrical molecular brushes: synthesis, characterization, and properties. Prog Polym Sci 33:759
122. Panyukov S, Zhulina EB, Sheiko SS, Randall GC, Brock J, Rubinstein M (2009) Tension amplification in molecular brushes in solutions and on substrates. J Phys Chem B 113:3750
123. Milchev A, Paturej J, Rostiashvili VG, Vilgis TA (2011) Thermal degradation of adsorbed bottle-brush macromolecules: a molecular dynamics simulation. Macromolecules 44:3981
124. Paturej J, Kuban L, Milchev A, Vilgis TA (2012) Tension enhancement in branched macromolecules upon adhesion on a solid substrate. EPL (Europhys Lett) 97:58003
125. Panyukov SV, Sheiko SS, Rubinstein M (2009) Amplification of tension in branched macromolecules. Phys Rev Lett 102:148301
126. Sheiko SS, Sun FC, Randall A, Shirvanyants D, Rubinstein M, H-i L, Matyjaszewski K (2006) Adsorption-induced scission of carbon-carbon bonds. Nature 440:191
127. Lebedeva NV, Sun FC, H-i L, Matyjaszewski K, Sheiko SS (2008) "Fatal adsorption" of brushlike macromolecules: high sensitivity of C–C bond cleavage rates to substrate surface energy. J Am Chem Soc 130:4228
128. Lebedeva NV, Nese A, Sun FC, Matyjaszewski K, Sheiko SS (2012) Anti-Arrhenius cleavage of covalent bonds in bottlebrush macromolecules on substrate. Proc Natl Acad Sci U S A 109:9276
129. Li Y, Nese A, Matyjaszewski K, Sheiko SS (2013) Molecular tensile machines: anti-Arrhenius cleavage of disulfide bonds. Macromolecules 46:7196

130. Li Y, Nese A, Hu X, Lebedeva NV, LaJoie TW, Burdyńska J, Stefan MC, You W, Yang W, Matyjaszewski K, Sheiko SS (2014) Shifting electronic structure by inherent tension in molecular bottlebrushes with polythiophene backbones. ACS Marco Lett 3:738
131. Balamurugan SS, Bantchev GB, Yang Y, McCarley RL (2005) Highly water-soluble thermally responsive poly(thiophene)-based brushes. Angew Chem Int Ed 44:4872
132. Choi J, Ruiz CR, Nesterov EE (2010) Temperature-induced control of conformation and conjugation length in water-soluble fluorescent polythiophenes. Macromolecules 43:1964
133. Wang M, Zou S, Guerin G, Shen L, Deng K, Jones M, Walker GC, Scholes GD, Winnik MA (2008) A water-soluble pH-responsive molecular brush of poly(N,N-dimethylaminoethyl methacrylate) grafted polythiophene. Macromolecules 41:6993
134. Burdyńska J, Li Y, Aggarwal AV, Höger S, Sheiko SS, Matyjaszewski K (2014) Synthesis and arm dissociation in molecular stars with a spoked wheel core and bottlebrush arms. J Am Chem Soc 136:12762
135. Park I, Nese A, Pietrasik J, Matyjaszewski K, Sheiko SS (2011) Focusing bond tension in bottle-brush macromolecules during spreading. J Mater Chem 21:8448
136. Xu H, Sun FC, Shirvanyants DG, Rubinstein M, Shabratov D, Beers KL, Matyjaszewski K, Sheiko SS (2007) Molecular pressure sensors. Adv Mater 19:2930
137. Park I, Shirvanyants D, Nese A, Matyjaszewski K, Rubinstein M, Sheiko SS (2010) Spontaneous and specific activation of chemical bonds in macromolecular fluids. J Am Chem Soc 132:12487
138. Zheng Z, Müllner M, Ling J, Müller AHE (2013) Surface interactions surpass carbon–carbon bond: understanding and control of the scission behavior of core–shell polymer brushes on surfaces. ACS Nano 7:2284
139. Matthews OA, Shipway AN, Stoddart JF (1998) Dendrimers–branching out from curiosities into new technologies. Prog Polym Sci 23:1
140. de Gennes PG, Hervet H (1983) J Phys Lett 44:351
141. Yu H, Schlüter AD, Zhang B (2012) Main-chain scission of a charged fifth-generation dendronized polymer. Helvetica Chim Acta 95:2399
142. Deng Y, Zhu XY (2007) A nanotumbleweed: breaking away a covalently tethered polymer molecule by noncovalent interactions. J Am Chem Soc 129:7557
143. Milner ST (1991) Polymer brushes. Science 251:905
144. Zhao B, Brittain WJ (2000) Polymer brushes: surface-immobilized macromolecules. Prog Polym Sci 25:677
145. Barbey R, Lavanant L, Paripovic D, Schüwer N, Sugnaux C, Tugulu S, Klok H-A (2009) Polymer brushes via surface-initiated controlled radical polymerization: synthesis, characterization, properties, and applications. Chem Rev 109:5437
146. Branch DW, Wheeler BC, Brewer GJ, Leckband DE (2001) Long-term stability of grafted polyethylene glycol surfaces for use with microstamped substrates in neuronal cell culture. Biomaterials 22:1035
147. Sharma S, Johnson RW, Desai TA (2003) Evaluation of the stability of nonfouling ultrathin poly(ethylene glycol) films for silicon-based microdevices. Langmuir 20:348
148. Sheiko SS, Panyukov S, Rubinstein M (2011) Bond tension in tethered macromolecules. Macromolecules 44:4520
149. Tugulu S, Klok H-A (2008) Stability and nonfouling properties of poly(poly(ethylene glycol) methacrylate) brushes under cell culture conditions. Biomacromolecules 9:906
150. Harris MJ (1992) In: Harris MJ (ed) Poly(ethylene glycol), chemistry, biotechnological and biomedical applications. New York, Plenum
151. Paripovic D, Klok H-A (2011) Improving the stability in aqueous media of polymer brushes grafted from silicon oxide substrates by surface-initiated atom transfer radical polymerization. Macromol Chem Phys 212:950
152. Lerum MFZ, Chen W (2009) Acute degradation of surface-bound unsaturated polyolefins in common solvents under ambient conditions. Langmuir 25:11250

153. Berron BJ, Payne PA, Jennings GK (2008) Sulfonation of surface-initiated polynorbornene films. Ind Eng Chem Res 47:7707
154. Zhang Y, Ja H, Zhu Y, Chen H, Ma H (2011) Directly observed Au-S bond breakage due to swelling of the anchored polyelectrolyte. Chem Commun 47:1190
155. Ward MD, Buttry DA (1990) In situ interfacial mass detection with piezoelectric transducers. Science 249:1000
156. Zhulina EB, Birshtein TM, Borisov OV (1995) Theory of ionizable polymer brushes. Macromolecules 28:1491
157. Biesalski M, Johannsmann D, Ruhe J (2002) Synthesis and swelling behavior of a weak polyacid brush. J Chem Phys 117:4988
158. Zhang Y, Lv Be LZ, Ja H, Zhang S, Chen H, Ma H (2011) Predicting Au-S bond breakage from the swelling behavior of surface tethered polyelectrolytes. Soft Matter 7:11496
159. Be L, Zhou Y, Cha W, Wu Y, Hu J, Li L, Chi L, Ma H (2014) Molecular composition, grafting density and film area affect the swelling-induced Au–S bond breakage. ACS Appl Mater Inter 6:8313
160. Enomoto K, Takahashi S, Iwase T, Yamashita T, Maekawa Y (2011) Degradation manner of polymer grafts chemically attached on thermally stable polymer films: swelling-induced detachment of hydrophilic grafts from hydrophobic polymer substrates in aqueous media. J Mater Chem 21:9343
161. Bain ED, Dawes K, Özçam AE, Hu X, Gorman CB, Šrogl J, Genzer J (2012) Surface-initiated polymerization by means of novel, stable, non-ester-based radical initiator. Macromolecules 45:3802

Top Curr Chem (2015) 369: 37–96
DOI: 10.1007/128_2015_648

Published online: 2 August 2015

Theoretical Approaches for Understanding the Interplay Between Stress and Chemical Reactivity

Gurpaul S. Kochhar, Gavin S. Heverly-Coulson, and Nicholas J. Mosey

Abstract The use of mechanical stresses to induce chemical reactions has attracted significant interest in recent years. Computational modeling can play a significant role in developing a comprehensive understanding of the interplay between stresses and chemical reactivity. In this review, we discuss techniques for simulating chemical reactions occurring under mechanochemical conditions. The methods described are broadly divided into techniques that are appropriate for studying molecular mechanochemistry and those suited to modeling bulk mechanochemistry. In both cases, several different approaches are described and compared. Methods for examining molecular mechanochemistry are based on exploring the force-modified potential energy surface on which a molecule subjected to an external force moves. Meanwhile, it is suggested that condensed phase simulation methods typically used to study tribochemical reactions, i.e., those occurring in sliding contacts, can be adapted to study bulk mechanochemistry.

Keywords Chemical simulation · Mechanochemistry · Modeling · Tribochemistry

Contents

G.S. Kochhar, G.S. Heverly-Coulson, and N.J. Mosey (✉)
Department of Chemistry, Queen's University, 90 Bader Lane, Kingston, ON, Canada, K7L 3N6
e-mail: nicholas.mosey@chem.queensu.ca

Abbreviations

AFM	Atomic force microscopy
AP	Attachment point
CASMP2	Complete active space Møller–Plesset 2nd order perturbation theory
CASSCF	Complete active space self-consistent field
CPMD	Car–Parrinello molecular dynamics
DFT	Density functional theory
EFEI	External force is explicitly included
FF	Force field
FMPES	Force-modified potential energy surface
GSSNEB	Generalized solid-state nudged elastic band
IRC	Intrinsic reaction coordinate
MD	Molecular dynamics
MEP	Minimum energy path
NEB	Nudged elastic band
PES	Potential energy surface
PP	Pulling point
QC	Quantum chemical
QM/MM	Quantum mechanics/molecular mechanics
RI	Registry index
SMD	Steered molecular dynamics
TS	Transition state

1 Introduction

For a chemical reaction to occur, the reacting species generally need to acquire sufficient energy to overcome the associated reaction barrier as the system moves along a direction that converts the reactants into products. The energy required to activate these reactions has been provided conventionally in the form of heat (thermochemistry), light (photochemistry), or an electric potential (electrochemistry). Thermochemistry involves the distribution of thermal energy amongst the different nuclear degrees of freedom in a molecule, which allows reactions to occur while the system remains in a particular electronic state. Photochemistry focuses on using light to promote chemical systems to higher energy electronic states, which generally have potential energy surfaces with different shapes than that of the ground state, and can thus lead to different reactions. Meanwhile, electrochemistry uses an applied potential to shift the electronic energy levels of reacting species to induce processes such as electron transfer.

Recent years have seen the development and application of techniques that allow one to activate chemical processes by acting on parts of a molecule or material with external forces or stresses [1–6]. In this approach, termed mechanochemistry, the forces or stresses acting on a system perform work as the system undergoes changes in structure, such as those that occur during a chemical reaction. The work performed on the system provides energy that can activate chemical reactions, whereas the directional nature of an applied force can be used to guide chemical systems along specific reaction pathways. This approach affects nuclear degrees of freedom, and is thus distinct from photochemical and electrochemical methods. In addition, the directional natures of external forces or stresses render mechanochemistry distinct from thermochemical approaches, where heat is distributed throughout the entire system.

The fact that mechanochemical conditions promote reactions in ways that differ distinctly from thermochemistry, photochemistry, and electrochemistry suggests that mechanochemistry may offer a means of activating reactions that are difficult to achieve through these conventional experimental approaches to induce reactions. This potential has prompted extensive research over the last decade into the ability to subject molecules and materials to external forces and stresses in a controlled manner and to use these conditions to activate chemical reactions [1–6]. The ability to subject molecules and materials to mechanochemical conditions has been made possible through developments in experimental techniques such as atomic force microscopy (AFM) [7–9], optical and magnetic tweezers [10–13], molecular force probes [14, 15], sonication techniques [16–19], and grinding and milling [3, 20–22]. These techniques operate on various length scales, with methods such as AFMs, tweezers, and force probes acting at the molecular level, and sonication, grinding, and milling being applicable to bulk systems. Overall, the application of these techniques has illustrated the potential to guide chemical systems along specific reaction pathways using applied stresses [19, 23], permitted the examination of processes such as the unfolding of proteins and DNA [10, 24–27], and even led to practical applications such as visible stress sensors [6, 28].

A large number of theoretical studies of chemical processes occurring under mechanochemical conditions have been reported to complement experimental efforts, help explain experimental outcomes, and provide new insights into the interplay between applied forces or stresses and chemical reactivity [29–38]. These studies have focused primarily on simulating molecular systems exposed to external forces by treating the system as though it moves on a force-modified potential energy surface that incorporates the work performed on a chemical system as it undergoes structural changes in the presence of an external force. These studies have examined the rupture forces of bonds [32], the reactivities of molecules subjected to tensile stresses and strains [38–41], the effects of strains on pericyclic reactions [14, 29–31, 33, 34, 42–44], the differences between thermochemistry and mechanochemistry [45], and the effects of chain length on the transduction of external forces at atomic levels [46, 47].

Interestingly, despite the longer history of mechanochemical activation of bulk systems in experimental research [2], e.g., through processes such as grinding and

milling, fewer theoretical studies have focused specifically on the mechanochemistry of bulk systems. However, the stress-induced processes involving bulk systems have been modeled extensively in the context of tribology, which is the study of friction, wear, and lubrication [48, 49]. As such, potential exists to apply existing techniques used to study systems such as sliding contacts in the context of the mechanochemical activation of reactions occurring in bulk systems where shear and compressive stresses play key roles in activating reactions.

Herein, we describe the different types of chemical simulation methods that can be used to study mechanochemical reactions at molecular and bulk levels, with the goal of providing basic information regarding these simulation techniques. Section 2 focuses on molecular mechanochemistry and describes models that can be used to predict the energies and properties of systems exposed to applied forces. Section 3 provides an overview of techniques used to study bulk systems that are exposed to compressive and shear stresses. Concluding remarks are provided in Sect. 4.

2 Methods for Simulating Molecular Mechanochemistry

Molecular mechanochemistry involves subjecting molecules to a tensile force of magnitude F that is applied between two regions in the molecule. This is illustrated schematically in Fig. 1 for the application of F between a pair of hydrogen atoms in cyclobutene, which can be used to model the ring-opening of this molecule under mechanochemical conditions. In this figure, F indicates the applied force and R is the distance between the two groups subjected to the force. From an experimental standpoint, the application of F is achieved through the use of single molecule manipulation techniques, e.g., optical or magnetic tweezers, atomic-force microscopes, by subjecting mechanophores embedded within polymers to ultrasound pulses, or by incorporating mechanophores into molecular force probes, or other

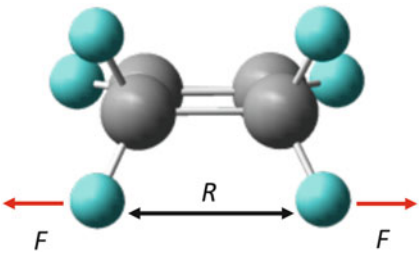

Fig. 1 Application of an external force of magnitude, F, to two hydrogen atoms in cyclobutene which are separated by a distance, R. The general concept of subjecting groups in a molecule to external forces while they undergo changes in separation underpins the methods used to simulate mechanochemical reactions at the molecular level. *Silver and turquoise spheres* indicate carbon and hydrogen atoms, respectively

means. These techniques have been used to study a wide range of processes such as the unfolding of proteins [25–27, 50, 51], ring opening reactions [14, 19, 44, 52], and detaching anchored molecules from surfaces [53, 54]. In general, it is found that the application of F can alter the thermodynamic and kinetic properties of reactions. The ability to affect these aspects of reactions is derived from the effects of F on molecular structures and energies. In particular, the application of F alters molecular geometries, whereas the work performed in the presence of F as a system changes structure during a reaction supplies energy that can be used to promote reactions.

The effect of subjecting molecules to F can be described through the concept of a force-modified potential energy surface (FMPES). If one considers the typical case in which F is applied between two positions in a molecule, the FMPES takes on the form of

$$E_F(\mathbf{q}, F) = E_0(\mathbf{q}) - FR, \tag{1}$$

where $\mathbf{q}$ represents the nuclear coordinates that define the geometry of the molecule, $E_0(\mathbf{q})$ is the potential energy of the system on the zero-F PES, and R is the distance between the atoms or groups that are subjected to F. In the context of simulating reactions involving changes in bonding, it is necessary obtain $E_0(\mathbf{q})$ using quantum chemical (QC) methods, reactive force fields (FFs), or QM/MM methods that can account for the formation and/or dissociation of bonds.

The FMPES is the mechanochemical analogue of the Born–Oppenheimer PES used to study changes in potential energies during reactions with QC calculations, which can then be related to thermodynamic and kinetic quantities, and thus the evaluation of the FMPES is important in the context of understanding the effects of F on reactions. Methods for evaluating and examining the FMPES and making connections to changes in free energy are described in what follows. Section 2.1 describes means of directly evaluating properties of the FMPES. Section 2.2 describes models in which information related to the FMPES is obtained indirectly from features of the zero-F PES.

2.1 *Direct Evaluation of the FMPES*

Access to the FMPES in (1) is central to the computational study of mechanochemical processes. The FMPES is straightforward to evaluate using potential energies obtained through QC or FF calculations, which can provide $E_0(\mathbf{q})$, in conjunction with knowledge of the molecular structure, which provides R. Although a discussion of QC and FF methods is beyond the scope of this review, the suitability of different QC methods for modeling mechanochemical processes involving bond rupture has been examined recently [55]. Several different approaches exist for treating the mechanical work term in (1). The differences between these methods arise from the manner in which F is applied in the

calculations. Despite the differences in the specific details of these techniques, all mechanochemical simulation methods that directly calculate the FMPES employ some form of (1), which is differentiable with respect to the nuclear positions. This allows one to examine the FMPES using procedures that are commonly used in conventional computational studies of chemical systems such as geometry optimizations, frequency calculations, intrinsic reaction coordinate (IRC), or minimum energy pathway (MEP) calculations and molecular dynamics (MD) simulations.

In the context of experiments, subjecting a molecule to F typically involves the mechanical manipulation of groups within that molecule. For example, a polymer subjected to mechanochemical conditions in an AFM experiment may be attached to a surface at one end and the AFM tip at the other. In this context, the polymer corresponds to the molecule being exposed to mechanochemical conditions, and the surface and AFM tip may be thought of as external groups used to impose those conditions. To do this, the distance between the AFM tip and the surface is increased, which in turn subjects the polymer to F. Similar scenarios occur in other experimental approaches to mechanochemistry, where large structural changes in macromolecules are used to apply F to molecules attached to force probes, and the movement of polymers attached to reactive species is used to apply F in sonication experiments, for example.

In the context of simulation, computational expense typically prevents the use of model systems that are exact replicas of those used in experiments. As a result, the model systems used in calculations of mechanochemical processes generally employ truncated or coarse-grained representations of the external groups used to apply F, or even exclude these groups entirely. The limited treatment of the external groups, or even their complete elimination from the calculations, requires the use of approximate schemes for subjecting molecules to F in calculations.

In general, two classes of methods exist for subjecting molecules to F in calculations. In the first class of methods, selected atoms in the simulated system are subjected to forces that are directed toward artificial points that are external to the molecule. These points correspond to the locations at which the external groups used to apply F in experiments would be located. Consider the extension of a surface-bound polymer in an AFM experiment as outlined above. In that case, the polymer, or a small portion thereof, would be simulated explicitly, whereas the surface and AFM tip would be replace by artificial points at appropriate locations around that molecule. Mechanochemical conditions could then be simulated by subjecting the atoms at either end of the polymer to forces directed toward the nearest artificial external point. Methods that employ artificial external points to apply F are described in Sect. 2.1.1.

The second class of methods for modeling mechanochemical conditions applies F between atoms in the system without employing artificial external groups. Once again, consider the AFM experiment described above. The application of F leads to an increase in the distance between the ends of the polymer. The extension of the molecule can be simulated without employing any external groups by fixing the distances between the atoms at the end of the molecule to specific values or by applying F along the vector connecting these atoms to induce a change in distance.

Techniques that apply F by using groups that are internal to the molecule being simulated are described in Sect. 2.1.2.

In addition to considerations regarding the manner in which F is applied, it is also important to note that experimental mechanochemistry is performed somewhere along the spectrum ranging from controlled separation to isotensional conditions. Controlled separation corresponds to fixing the distance, R, between the groups associated with the degree of freedom to which F is applied and measuring the F required to maintain R. Such conditions apply, for example, to force-extension curves obtained in AFM experiments in which the end-to-end distance of a molecule is fixed and the F required to keep the distance fixed is measured. Measuring F for multiple values of R yields a force-extension curve, which can be useful in determining the values of F needed to induce processes such as the unfolding proteins [35, 56, 57] or the rupture of polymers [58, 59]. At the other end of the spectrum, isotensional conditions involve subjecting a molecule to a constant tensile force, F, and allowing the affected degrees of freedom to change as needed to accommodate F. Such conditions have been achieved in AFM experiments of stretched macromolecules [7, 60] and the ultrasonic cleavage of metal-ligand coordination complexes [61–63], for example. Of course, in practice, the need to move between different values of F or R, as well as phenomena such as thermal fluctuations, lead to deviations from strictly controlled separation or isotensional conditions in experiments. Instead, molecules are subjected to mechanochemical conditions in ways that cause F and/or R to change in a time-dependent manner. Capturing the specific mechanochemical conditions experienced by a system is important to ensure a meaningful connection between simulation and experiment. As discussed below, achieving this in calculations requires different treatments of the work term ($-FR$) appearing in (1).

2.1.1 Application of F via Artificial External Groups

Molecular mechanochemistry involves subjecting a molecule to F via groups that are external to it. An explicit treatment of these external groups can be avoided in calculations by devising a model system that includes an explicit representation of the molecule of interest and adding a set of artificial external points, called pulling points (PPs), at locations around the molecule where the external groups would reside in the real system of interest. The PPs are each connected to atoms called attachment points (APs) within the simulated molecule in a manner that allows F to be applied between the PPs and APs.

A model that could be used to study the mechanochemical ring-opening of cyclobutene produced by the application of F between APs and PPs is shown in Fig. 2. In this case, the APs correspond to one of the hydrogen atoms bonded to each of the carbon atoms involved in the scissile bond and the PPs are placed at locations corresponding to the positions at which groups, such as polymers, that would be used to apply F are attached to the ring. In this model, each AP is associated with

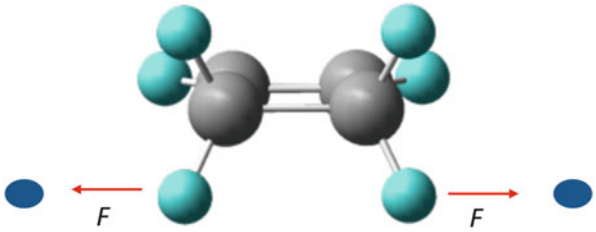

Fig. 2 Application of F in the steered molecular dynamics model. In this case, two hydrogen atoms in cyclobutene are treated as attachment points each attached to one external PP (indicated by *blue circles*). *Silver and turquoise spheres* indicate carbon and hydrogen atoms, respectively

one of the PPs and is subjected to an external force of magnitude F applied along the vector connecting the AP to the PP with which it is associated.

Significant flexibility exists in terms of the manner in which F is applied using models such as that shown in Fig. 2. For example, it is possible to keep the PPs at fixed positions and apply a constant value of F along the vector connecting each PP to its associated AP. Alternatively, the magnitude of F can be obtained through the introduction of an interaction potential for each AP-PP pair. For example, if one employs a harmonic potential for this purpose, the force associated with a given AP-PP pair is $F = -k(r - r^{\mathrm{eq}})$, where k is the stiffness of the potential, r is the distance between the AP and its associated PPs, and r^{eq} is the equilibrium value for this distance. Employing interaction potentials to apply F to the APs is particularly useful if the PPs are moved over time, e.g., to simulate the manner in which the external groups are moved to impose F in experiments, where the changes in the positions of the PPs lead to time-dependent forces of the form $F(t) = -k(r - r^{\mathrm{eq}} + vt)$, where v represents the velocity at which the PP is moved.

Regardless of the specific manner in which the magnitude of F is determined, the external force applied to the system by the PP-AP interactions is given by

$$\mathbf{F}_{\mathrm{ext}} = \sum_{i=1}^{n_{\mathrm{AP}}} F\mathbf{n}_i, \tag{2}$$

where n_{AP} is the number of APs, which is usually 2 when modeling mechano-chemical processes, and $\mathbf{n}_i$ is the unit vector along the direction connecting the ith AP-PP pair. The FMPES arising from the application of F in this manner is then given by

$$E_F(\mathbf{q}, F) = E_0(\mathbf{q}) - \sum_{i=1}^{n_{\mathrm{PP}}} F\left(r_i - r_i^0\right), \tag{3}$$

where $\mathbf{q}$ represents the atomic coordinates in the system, $E_0(\mathbf{q})$ is the energy of the system on the zero-F PES, r_i represents the current distance between the ith AP and its associated PP, and r_i^0 is a reference value for this distance, which can in principle take on any value, with sensible choices being zero or r_i^{eq}.

The application of F through the use of artificial external PPs connected to APs in a simulated molecule is called steered molecular dynamics (SMD) [64–66]. SMD methods are available in some chemical simulation packages, and in cases where such techniques have not been implemented it is straightforward to add the F-dependent terms appearing in the energies and nuclear forces to existing packages to enable simulations on the FMPES. A drawback of the method lies in the fact that the energy in (3) is dependent upon the positions of the PPs, which must be chosen by the person performing the calculation. A sensible choice is to define the positions of the PPs to lie along directions between the APs and atoms that would be present in the devices used to subject the molecule to F.

SMD simulations have a long history, with initial applications focusing primarily on the study of folding and unfolding of proteins [65–69]. It is worth noting that, despite the emphasis on MD simulations in the SMD label, it is also possible to optimize molecular structures, perform frequency calculations, and locate minimum energy pathways (MEPs) on the FMPES given in (3). In recent years, SMD simulations have become increasingly used in the context of simulating mechanochemical reactions in a broader sense. Selected applications using SMD methods in the context of studying molecular mechanochemistry are described in what follows.

Modern interest in molecular mechanochemistry was stimulated in part by experiments demonstrating how subjecting benzocyclobutene moieties with polymeric substituents to F via ultrasound pulses could induce the ring opening of this molecule in a manner that circumvented the Woodward–Hoffman rules [19]. In these experiments, the polymers were bonded to the carbon atoms of the scissile bond in cyclobutene and the conrotatory ring-opening pathway was favored when these polymers were attached in a *trans* arrangement with respect to the plane of the ring, whereas the disrotatory pathway was favored if the polymers were attached in a *cis* orientation.

The F-induced ring-opening of cyclobutene and benzocyclobutene was studied via SMD simulations by Martinez and coworkers [30]. Their simulations employed models such a that shown in Fig. 2, with the hydrogen atoms on the scissile C–C bond acting as APs. APs in *cis* and *trans* arrangements were examined to focus on the experimental conditions that favored the disrotatory and conrotatory pathways, respectively. Each AP was attached to an external PP that remained at a fixed location and a constant F was applied between each PP and its associated AP. The zero-F potential energy, $E(\mathbf{q})$, was evaluated at the CASMP2(4,4)/6-31G** level of theory, which is suitable for describing the underlying changes in electronic structure that occurs along the disrotatory pathway. These models were used to perform MD simulations on the FMPES, with the results indicating that disrotatory ring-opening occurred with *cis* PPs within the simulated period of 1.0 ps for $F > 1.5$ nN. The ability of the system to follow the disrotatory pathway with *cis* PPs was rationalized by evaluating the MEPs along the conrotatory and disrotatory pathways at different F. The results of the calculations showed that the barriers along both reaction pathways were lowered by the application of F; however, that along the disrotatory pathway was more affected by F and thus became kinetically favored as F was increased. Overall, these results were consistent with the results of

the ultrasound experiments, and provided insights into the results of those experiments in terms of the underlying features of the FMPES.

The Martinez group has applied SMD methods in additional studies aimed at understanding the *F*-induced chemistry of mechanophores embedded in polymers [42–44, 58, 70, 71]. For example, SMD simulations have been used in conjunction with constrained distance calculations (see below) to help design and understand the functionality of visible stresses sensors based on polymers bonded to spiropyrans, which undergo a stress-induced conversion to merocyanines along with a change in color [58]. SMD simulations were also used to find how applied stresses induce the opening of strained rings to form cyanoacrylates [44]. Additional studies used SMD simulations and MEP calculations on the FMPES to explain the *F*-induced change in the *cis–trans* product ratios of the ring opening of *gem*-difluorocyclopropanes [42, 43]. Experiments show that the *trans* product of this reaction is favored in the absence of *F*, which is consistent with the relative stabilities of the *cis* and *trans* forms, yet the *cis* product was formed in increasing amounts under the application of ultrasound pulses. The calculations showed that the change in the product ratios was caused by *F*-induced changes in the PES that caused a diradical species corresponding to the TS on the zero-*F* PES to become a minimum on the FMPES, with this species becoming the global minimum at high *F*. The change in the nature of the diradical species introduced a new step along the reaction pathway, with calculations showing that at high *F* the ring opening of both *cis* and *trans* forms of the reactant yielded the diradical structure followed by progression from this species to the *cis* product as *F* is removed. Overall, this work illustrates the ability of SMD calculations to provide insights that can be used to explain experimental observations. In addition, the calculations illustrated that the *F*-induced stabilization of the zero-*F* TS may provide a means of trapping and probing TS structures in experiments.

The manner in which oligorotaxanes unfold in AFM experiments has been examined with SMD simulations by Ratner and coworkers [72, 73]. In their studies, one end of a molecule representing an oligorotaxane was attached to a PP via a stiff harmonic potential to mimic the attachment of this molecule to a surface in AFM experiments. The other end of the molecule was then attached to a PP by another harmonic potential. *F* was applied by moving the latter PP at a constant speed along the direction connecting the terminal atoms of the molecule. $E_0(\mathbf{q})$ was evaluated with FF methods, because bond rupture was not expected to occur, and hence the authors could examine relatively large models over a wide range of pulling speeds. The results demonstrated that pulling speeds on the order of 10^{-3} Å/ps were sufficient to obtain reversible behavior when *F* was applied and then removed. Force-extension isotherms were obtained in the simulations and showed that regions exist in which the molecule is mechanically unstable, which leads to unfolding and results in transitions between high-*F* and low-*F* regimes. The development of these mechanically unstable regions and the transitions between force regimes were found to be related to fluctuations in *F*, which in turn are related to the stiffness of the harmonic potential used to apply *F*. Additional simulations by Vilgis

and coworkers have modeled F-induced polymer chain scission using similar models [74–77].

As noted above, SMD simulations were originally used in the context of examining the mechanisms associated with protein unfolding and this remains an active area of research, with many recent studies focused on the reduction of disulfide bonds, which exhibit a variety of responses to F. For example, Gräter and coworkers have used SMD simulations to account for F-induced changes in the mechanism by which thioredoxin catalyzes the reduction of S–S bonds, where experimental studies showed that the reaction rate decreases with low F before increasing again at higher F [78]. The simulations performed to explore the origins of this behavior employed a variant of SMD termed force probe MD. In this method, the PPs are attached to the APs via harmonic potentials and F is applied by moving the PPs at constant velocities. In this case, standard FFs were used to obtain the zero-F energies of systems representing the active site and relevant model protein residues, and the PPs were attached to C_α atoms of the terminal residues. The results of the simulations showed that applying F caused the disulfide to reorient such that it was aligned to within ~20° of the coordinate along which F was applied. This reorientation requires a large rotation to occur in order for the disulfide bond to become aligned with a third sulfur in the S_N2 TS for this reaction. This rotational motion results in a decrease in the length coordinate upon moving from the reactant to the TS and thus causes a reduction in the rate within increasing F. This study was unable to account for the subsequent increase in the rate at higher F, but it was hypothesized that the reduction in the rate (or underlying increase in the reaction barrier) of the standard S_N2 process with F may render other competing mechanisms for this reaction kinetically favorable at higher F.

The effect of F on the thiol-disulfide exchange was examined further using force probe MD simulations based on QM/MM representations of a system corresponding to a dithiothreitol reducing agent interacting with a truncated model of I27 [79]. The force probe MD simulations were performed in conjunction with transition path sampling methods to examine ensembles of reactive trajectories of the force-modified free energy surface. The results of these simulations demonstrated that low F shifts the TS toward the reactant, thus leading to an increase in the reaction rate. The application of higher F was found to populate TS structures that are unfavorable at lower F, causing the system to follow preferentially an alternate reaction path. Other uses of force probe MD simulations in the context of the mechanochemistry of disulfide bonds have examined the electrochemistry of this reaction [80].

2.1.2 Application of F via Internal Groups

The application of F via external groups, e.g., artificial PPs in SMD simulations or external devices used to manipulate molecules in experiments, leads to changes in the structure of the molecule being subjected to F. If the molecule is subjected to a tensile stress, which is the typical case in molecular mechanochemistry, the

distance between the atoms that interact with the external groups increases relative to the analogous distance in the absence of F. The extension of the molecule can be interpreted in the context of the application of a force along the vector, **R**, connecting the atoms attached to these devices. When an equilibrium structure is reached, the force applied along **R** is equivalent to the restoring force of the molecule at that length; however, the internal and external forces may not be balanced when the system is not at equilibrium. The fact that the external application of F induces changes in the distances and forces between atoms contained entirely within the molecule exposed to F suggests that it is possible to simulate mechanochemical conditions without employing artificial external PPs to apply F.

Simulations of mechanochemical conditions that apply F using groups contained in the molecule of interest are discussed in what follows. The section "Application of F Through Constrained Geometries" discusses techniques in which the molecular geometry is constrained to mimic the application of F. The section "Application of F Between Atoms" describes an approach termed external force is explicitly included (EFEI) in which a constant F is applied along the vector connecting a selected pair of atoms in the molecule. Constrained geometry and EFEI calculations employ different controlled variables, i.e., distances and forces, respectively, to subject the system to F and thus model different experimental conditions. These differences and their potential impacts on the results of calculations are discussed in section "Comparison of Internal Group Models".

Application of F Through Constrained Geometries

The application of F to a specific pair of atoms in a molecule can be modeled by constraining the distance between these atoms, R, to some specified value, R_0, at the same time allowing the system to move along the remaining $3N-7$ nuclear degrees of freedom using methods such as geometry optimizations or MD simulations. The satisfaction of the constraint $R{=}R_0$ is equivalent to subjecting the system to an external force, F, that is equivalent in magnitude, but opposite in direction, to the internal force, $F_{\text{int}} = \partial E_0(\mathbf{q})/\partial R$, acting along the vector connecting the constrained pair of atoms. Note that F_{int} is dependent upon the positions of the nuclei along the $3N-7$ unconstrained coordinates in addition to the value of the constrained distance, R_0. This leads to the definition of the FMPES as

$$E_F\left(\mathbf{q}^*; R_0\right) = E_0\left(\mathbf{q}^*; R_0\right) + F_{\text{int}} R_0, \tag{4}$$

where **q*** represents the $3N-7$ degrees of freedom that are not constrained, R_0 is a parameter corresponding to the value of the constrained distance, and E_0 is the energy of the system with the set of $3N-6$ atomic coordinates $\{\mathbf{q}^*,R_0\}$ on the zero-F PES.

The use of geometric constraints has the advantage that such constraints are used in many types of QC simulations unrelated to mechanochemistry. For example,

constrained distances (or other degrees of freedom) are used extensively in applications such as exploring the features of the zero-F PES or evaluating changes in free energies during MD simulations [81]. As a result, many simulation software packages have the ability to constrain the distances between atoms, which permits the use of geometric constraints without any modification of those codes. Moreover, the application of F between specific pairs of atoms removes any subjectivity associated with the choice of the locations and velocities of PPs in SMD simulations.

Constrained distance methods are most commonly used in conjunction with geometry optimizations or MD simulations. In the former case, the unconstrained atoms in the system relax such that the system adopts a structure that is a local energy minimum on an FMPES defined by the $3N-7$ unconstrained degrees of freedom with the fixed value of $R{=}R_0$. In the latter case, the system samples regions of this $3N-7$ dimensional FMPES around this local minimum. Because R_0 is typically associated with an interatomic separation which changes significantly during the reaction of interest, it is common practice to study the FMPESs at different values of R_0 via relaxed PES scans or by changing R_0 linearly in time to simulate the extension of a molecule during MD simulations.

Constrained geometries have been used extensively in the context of mechanochemistry, with applications including studies of bond rupture [82–86], reactivity of disulfide bonds [87], unfolding of supramolecular polymers [88], mechanochemical synthesis of phenyl cations [89], extraction of gold nanowires [90], evaluation of restoring forces in force probes [14, 91], and calculation of free energy barriers [92–98]. Examples of selected applications are described below.

Frank and coworkers have employed a constrained distance method in conjunction with Car–Parrinello MD (CPMD) simulations [99] to examine a variety of mechanochemical processes [33, 39–41, 100, 101]. During these simulations, F is applied by increasing the distance between a pair of atoms at a constant velocity. They have used this approach to explore the changes in electronic structure that occur when solvated polymers are stretched to the point of rupture [41]. Their studies showed that bond rupture occurred through a heterolytic process involving solvent molecules. Interestingly, their simulations showed that the weakest bond does not necessarily correspond to the site of bond rupture. Rather, the bond that is made most accessible to attack by solvent via F-induced changes in structure most frequently corresponds to the site at which the polymer dissociates.

CPMD simulations in which F was applied by increasing the separation of a pair of atoms at a constant velocity in conjunction with detailed analyses of the electronic structure have also been used to study the dissociation of disulfide bonds in the presence of reducing agents [100]. Those simulations showed that this reaction does not necessarily involve electron transfer, as is common for redox processes, but rather can occur through heterolytic dissociation of the S–S bond followed by proton transfer. The mechanisms available for the F-induced reduction of the S–S bond in the presence of various nucleophiles has also been examined [101], with results illustrating that a wide range of mechanisms exist in addition to the S_N2 mechanism favored at zero F. The existence of multiple mechanisms, and

the change in the kinetically preferred mechanism with F, was suggested to be the origin of the F-dependence of rates of disulfide reduction observed in experiments.

Boulatov and coworkers have employed constrained geometry calculations of reactive sites coupled to a weak harmonic constraining potential [7] that represents the external device used to evaluate free energy barriers to reactions [92–98]. In this approach, constrained geometry optimizations are used to obtain reactant and TS structures, energies, and internal forces, and the effect of the external system is subsequently included via the compliance and length of the external harmonic potential. The potential energies of the system comprising the reactive site and constraining potential were augmented with standard thermochemical corrections and conformational averaging to yield free energy barriers, which are of greater relevance to experiments than potential energies. In addition, these constrained calculations were used to examine the F-dependence of the barrier upon the length coordinate used in the calculations. It was found that the F-dependence can be described in terms of a conveniently chosen local coordinate, e.g., the distance between groups within the reactive site, instead of using a length coordinate associated with the vector connecting the ends of groups such as polymers that are used to apply F in experiments, which may not be accurately represented in the truncated model systems.

Although constrained distance methods employ the distance R_0 as a controlled variable, they can be used to model conditions in which F is constant. To do this, it is necessary to vary R_0 to locate different structures on the FMPES where the internal force, F_{int}, associated with R is equivalent. If pairs of these structures correspond to species that are relevant for a given reaction, e.g., the reactants, products, or TS, the differences in their energies on the FMPES correspond to reaction energies or barriers under constant F conditions. As discussed in what follows, this approach has been used to examine phenomena such as F-induced changes in proton affinity [38] and reaction barriers [83]. Unfortunately, such calculations can be difficult because it is necessary to locate pairs of structures that have the same values of F_{int}, which typically involves performing scans over large regions of the FMPES.

Beyer provided an early example of this approach by using constrained distance calculations to study the F-dependence of the proton affinity of dimethyl ether [38]. In these calculations, a hydrogen atom on each of the methyl groups was used as a PP and the distance between the PPs was constrained to a discrete set of values to one-dimensional relaxed scans of the zero-F PES for the protonated and unprotonated forms of the molecule. These energies were then fitted to fourth-order polynomials to yield functions that could be differentiated analytically to locate PP separations at which the internal force associated with the constrained distance was equal in the reactants and products. These data were used to evaluate the relative energies of the protonated and unprotonated forms of the molecule according to (4), with results showing that the proton affinity increased steadily as F increased. The authors attributed the increase in proton affinity to the lower strain energy of the protonated relative to that of the unprotonated form. This difference

was attributed to the fact that the protonated is less stiff than the unprotonated form of the molecule, and thus extended to a greater extent through the application of F.

Uggerud and coworkers have used a similar approach to evaluating F-dependent barriers to chemical reactions. For example, one-dimensional projections of the FMPES were obtained by relaxed PES scans in which the distances between PPs in the reactants and TS structures associated with the ring opening and decomposition of substituted triazoles [83] were varied over a wide range of values. The calculations showed that the kinetically preferred mechanism changed with increasing F, with ring opening preferred at low F and C–C bond dissociation becoming preferred as F was increased. The same group has also used constrained distance calculations to assess the factors that determine which bond in a polymer breaks in response to applied F [82]. The results of that work showed that the weakest bond in the system does not necessarily correspond to the rupture site, which is consistent with the work of Frank mentioned above, but rather the bond that dissociates is dependent on bond strength, bond stiffness, and the orientation of the bond with respect to the direction along which F is applied.

The approaches to constraining geometries described above all employ procedures in which a single interatomic distance is fixed to a value, which may be changed to scan the PES or induce reactions in MD simulations. Boulatov and coworkers have employed an alternative approach to constraining geometries to evaluate the restoring forces of molecules in molecular force probes [14, 91]. The force probes used in their experiments corresponded to macrocycles consisting of a cyclobutene moiety attached to a *cis* stilbene through linkers of different lengths. F was applied by photoisomerization of the stilbene, which led to the ring opening of the cyclobutene moiety. It was found that the rate of ring opening was F-dependent, with shorter linkers leading to greater accelerations. The F applied during the photoisomerization process was calculated by first optimizing the reactant and TS structures for the ring opening process using full models of each macrocycle. The cyclobutene moieties in the reactant and TS for each macrocycle were then excised from these models, the resulting dangling bonds were capped appropriately, and the forces on all atoms in these truncated models were evaluated. The forces acting along different length coordinates were evaluated by vector addition of the atomic forces, and were associated with the forces exerted by the stilbene component on the cyclobutene moiety in the full models of the macrocycle. A comparison of the calculated restoring forces with the rates obtained in the experiments showed that the F-dependence of the rates could be described adequately by a single-coordinate model in which F was applied between groups directly bonded to the scissile bond of cyclobutene.

Application of F Between Atoms

Modeling isotensional experimental conditions involves subjecting atoms to a constant external force. One means of achieving this is by treating specific pairs of atoms in a molecule as PPs and applying an external force, F, along the vector, $\mathbf{R}$,

connecting these atoms. This approach is known as the external force is explicitly included (EFEI) model [31]. The application of the F along this direction leads to the FMPES:

$$E_F(\mathbf{q};F) = E_0(\mathbf{q}) - FR(\mathbf{q}), \tag{5}$$

where $\mathbf{q}$ represents the nuclear degrees of freedom, which either include R explicitly as an internal coordinate or can be used to calculate R as the distance between the atoms corresponding to the PPs, E_0 is the energy of the structure on the zero-F PES, and R is the distance between the atoms used as PPs. Equation (5) is differentiable with respect to the nuclear positions, which allows procedures such as geometry optimizations, frequency calculations, IRC calculations, and MD simulations to be performed directly on the FMPES. These abilities allow one to examine the F-dependence of molecular structures and energies by changing the value of F used in the calculation. For example, in the case of studying F-dependent reaction kinetics, one can locate reactant and TS structures on the FMPES defined by (5) at different values of F to assess how reactions barriers depend on F. In addition, MD simulations can be performed at different constant values of F or with time-dependent values of F to gain insight into the F-dependent behavior of chemical systems.

Unlike the holonomic constraints used to constrain geometries, the EFEI approach is not implemented in the distributed versions of any software package to our knowledge. However, the modifications to such codes needed to implement the definition of the energy in (5) along with the associated additions to the first and second derivatives of the potential energy with respect to nuclear positions are straightforward to add to existing simulation software. The use of (5) requires the definition of which atoms act as PPs, yet eliminates the need to choose directions along which F is applied. In fact, by applying F along the vector connecting two atoms in the system, one ensures that no net external force is added to the molecule. Despite these benefits, the application of F along the vector connecting two specific atoms in a molecule is clearly an approximation to the manner in which mechanochemistry is achieved under isotensional conditions, because the devices used to subject the molecule to F are not incorporated into the model in any way. EFEI calculations have been used to model processes such as the rupture of covalent bonds in pericyclic reactions [29, 34, 47], cyclizations [102], and the design of optical force probes [103]. Selected studies are described in what follows.

Marx and coworkers have used EFEI methods to examine the ring opening of cyclobutene, and substituted variants thereof [31, 34]. As discussed in greater detail in the section "Comparison of Internal Group Models," these simulations showed that F can alter the barrier to this reaction in a way that circumvents the Woodward–Hoffman rules. In addition, they used EFEI calculations to examine the transmission of F via oligomers bonded to the carbon atoms in the scissile bond of cyclobutene [46, 47]. The factors that affect the transmission of F through these chains is of fundamental importance in mechanochemistry because oligomers are used for this purpose in many experimental techniques for subjecting molecules to F. They

showed that the applied force, F_{max}, at which the reaction occurs without additional thermal activation, i.e., the value of F at which the reaction is barrierless on the FMPES, is dependent on the chain length, and that alternating between even and odd numbers of units in the oligomers can drastically alter F_{max} for short chains. It was also found that F_{max} depends on the angle between the chain and the reactive bonds, the manner in which this angle changes in response to F, as well as the stiffness of the degrees of freedom within the chain. All these factors can be controlled experimentally, and thus this study provides insights that can be used to rationally design groups for applying F in experiments.

Uggerud and coworkers used EFEI-based MD simulations in conjunction with DFT calculations and models consisting of a chain of Morse potentials to study the basic features of mechanochemical processes under dynamic conditions [104]. The results of this study showed that the simple model consisting of Morse potentials is adequate for describing the F-dependent dynamics of polymers, which may reduce the computational costs of simulations of mechanochemical processes. In addition, the study demonstrated significant differences between the results of simulations performed with F held fixed and with F applied suddenly. In particular, sudden-F approaches preferentially led to bond rupture in the central portion of the polymer, whereas fixed-F simulations preferentially led to the rupture of terminal bonds. These results illustrate that care must be taken in terms of simulating F-induce bond rupture processes, with a particular need to ensure that the manner in which F is applied mimics that found in experiments.

Comparison of Internal Group Models

The methods employing constrained geometries implicitly apply F, whereas the SMD and EFEI methods model the application of F explicitly. As such, one may anticipate that simulations using these methods would yield different results. In what follows, we compare how the outcomes of calculations can be affected by the manner in which F is applied in the context of geometry optimizations, and MD simulations.

Geometry optimizations performed on the EFEI FMPES obtained with a given F yield stationary points in which the length associated with the coordinate $\mathbf{R}$ adopts a value, R_{opt}, at which the internal force along this degree of freedom, F_{int}, equals F. Meanwhile, the forces acting along all other degrees of freedom are zero. The energies of these stationary points are identical to those obtained through constrained geometry optimizations in which R_0 is fixed to R_{opt}. As such, constrained geometry optimizations and EFEI calculations yield identical values of quantities such as reaction energies or activation energies, which are based on the relative energies of stationary points. This equivalence allows either method to be used for the purposes of exploring thermodynamics and kinetics on the basis of comparing the energies of stationary points on the FMPES.

Meanwhile, many computational studies of reactions occurring under mechanochemical conditions have employed MD simulations. These simulations can

provide detailed atomic-level information regarding the changes in structure that occur during reactions, and are thus useful in elucidating reaction mechanisms. Such insights can be particularly valuable in the context of mechanochemistry, where the reaction mechanism followed by the system can be dependent on F. The identification of such mechanisms is important in the context of ensuring that the relevant reaction steps are examined in static calculations, i.e., geometry optimizations, which generally require a priori knowledge of the reaction mechanism to locate any intermediate and TS structures along the reaction pathway.

MD simulations of mechanochemical processes have been reported in which either F is treated as a controlled parameter or an interatomic distance is constrained to mimic the application of F. In cases where F is applied explicitly, the system can move along all the $3N-6$ nuclear degrees of freedom to progress from reactants to products on the FMPES. In some cases, these simulations also increase F over time to mimic AFM experiments, for example, or to promote the occurrence of reactions on the timescales accessible in MD simulations. Meanwhile, constraining a distance to a particular value of R_0 only allows the system to move along the remaining $3N-7$ nuclear degrees of freedom. Assuming the constrained distance is related to the reaction of interest, fixing it to one value precludes the occurrence of this reaction during the simulation. To overcome this limitation, it is common practice to change the value of R_0 over time at a predefined rate, v, from some initial value, $R_0(0)$, i.e., $R_0 = R_0(0) + vt$ [33, 39–41, 90, 100, 101]. Changing R_0 in this manner causes the system to sample the series of FMPESs defined by (4) with the different values of R_0 encountered in the simulation. This approach is computationally convenient because it employs thermodynamic integration techniques available in most MD simulation packages. However, changing R_0 over time causes the constraint to mimic the application of external forces which change dramatically during the course of the reaction. For R_0 below the value of the constrained distance in the TS, the constraint mimics a tensile force, whereas the constraint mimics a compressive force as the system moves from the TS to the product. Such changes in F do not correspond to the conditions imposed in experiments and differ significantly from those modeled in simulations where F is explicitly applied.

The differences in the outcomes obtained in MD simulations in which F is applied explicitly or implicitly through the application of a time-dependent distance constraint are evident from studies of the ring-opening of cyclobutene along conrotatory and disrotatory pathways [29–31, 33, 34]. As described above, this reaction has been examined extensively in light of experiments illustrating that mechanochemical conditions can be used to alter the major product of the ring-opening reaction by biasing the system along either of the conrotatory or disrotatory directions irrespective of the Woodward–Hoffmann rules.

MD simulations in which F was applied explicitly yield results consistent with these experiments [29–31, 34]. For instance, an SMD study [30], in which 20 trajectories of cyclobutene were subjected to F using the hydrogen atoms on the carbon atoms of the scissile as APs, showed that the conrotatory pathway was consistently followed if the APs were in a *trans* configuration, whereas the

disrotatory pathway was consistently followed if the APs were in a *cis* configuration. These results were rationalized in terms of the underlying energetics, which showed that the application of F using *cis* or *trans* APs preferentially reduced the barriers along the disrotatory and conrotatory pathways, respectively. Analogous results have been obtained in static calculations and MD simulations using the EFEI approach [29, 31, 34].

The mechanochemical ring opening of cyclobutene was also investigated using a time-dependent distance constraint to mimic the application of F during MD simulations [33]. In those simulations, the constraint was applied between hydrogen atoms bonded to the carbon atoms in the scissile bond of cyclobutene that were in a *cis* arrangement with respect to the ring in an attempt to induce disrotatory opening. The target separation of these atoms was then increased at a rate of 2.0 Å/ps during the simulation to mimic the application of an external force. A total of 20 independent simulations were performed using DFT methods. The results of the MD simulations showed that the conrotatory product was formed for all 20 trajectories, which is inconsistent with the results of the sonication experiments [19], SMD simulations [30], and EFEI calculations [29, 31, 34].

The discrepancy between the results of simulations of cyclobutene subjected to constrained distance and isometric conditions motivated us to explore the differences between the methods in greater detail. To accomplish this, we performed MD simulations for the ring opening of cyclobutene using a constrained distance or EFEI methods to apply F implicitly or explicitly, respectively. The outcomes of the simulations were also analyzed through relaxed potential energy surface scans. In these calculations, the QC energy was evaluated at the CASSCF(4,4)/6-31G(d,p) level of theory. The MD simulations were performed with a version of the GAMESS-US software package that we modified to perform MD simulations with time-dependent distance constraints or the explicit application of F through the EFEI method [105], whereas the PES scans were performed with Gaussian09 [106].

The MD simulations of cyclobutene that employed a constrained distance were performed by increasing the distance between a pair of hydrogen atoms in a *cis* configuration at rates of 0.5, 1.5, 2.5, and 5.0 Å/ps. Five independent trajectories were evaluated at each pulling rate. All AIMD simulations showed that ring opening of cyclobutene occurred exclusively through the conrotatory pathway, which is in agreement with the previous study using similar methods [33], but is inconsistent with EFEI calculations [29, 31, 34], previous SMD simulations [30], and experiments performed under mechanochemical conditions [19]. Structures observed during the simulation performed with a pulling rate of 0.5 Å/ps are shown in Fig. 3 to illustrate the conrotatory ring opening process. At $t = 0.0$ ps, the system is in the form of cyclobutene. The carbon–carbon scissile bond ruptures at $t = 2.8$ ps. At this point, the orientation of both methylene groups is consistent with the opening along the disrotatory pathway. At around $t = 3.0$ ps, however, one of the methylene groups rotates such that system starts to follow a conrotatory pathway.

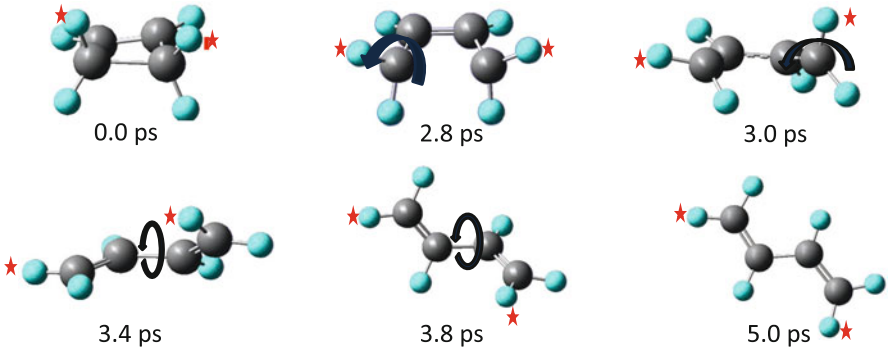

Fig. 3 Structures for the ring opening of cyclobutene during an MD simulation at a pulling rate of 0.5 Å/ps. Hydrogen atoms in a *cis* configuration were selected as the PPs and are indicated with *red stars*. The motion of the system is indicated using *dark blue arrows*. *Silver and turquoise spheres* indicate carbon and hydrogen atoms, respectively

As the system progresses along the conrotatory pathway, rotation occurs about the central carbon–carbon bond, leading to the formation of *trans*-1,3-butadiene.

To illustrate further that the system followed the conrotatory pathway, the changes in the length of the carbon–carbon scissile bond and the torsions associated with the conrotatory and disrotatory motions were monitored during the simulations. These quantities are shown in Fig. 4, along with definitions of the conrotatory and disrotatory simulations, for a simulation performed with a pulling rate of 0.5 Å/ps. The data show that the length of the carbon–carbon scissile bond increases slowly at the beginning of the simulation, and then increases rapidly at approximately 3.0 ps, because of bond rupture. Prior to the point of bond rupture, the conrotatory angle fluctuates around zero and the disrotatory angle increases steadily. At the point of bond rupture, however, the conrotatory angle increases sharply and the disrotatory angle decreases to approximately zero. The changes in angles indicate that the ring opening of cyclobutene proceeds toward the disrotatory product at the initial stages of the simulation until the rupture of the carbon–carbon scissile bond. After this point, the system progresses along the conrotatory pathway. Although it may be possible for the system to follow the disrotatory pathway if higher extension rates were used, progression along the conrotatory pathway was observed in all simulations performed with constrained distances, even when the extension rate was ten times faster than that used to generate the data in Fig. 4.

An analogous set of MD simulations were performed on the EFEI FMPES applying F to the same hydrogen atoms that were used to define the constrained distance in the MD simulations discussed above. Five independent trajectories were calculated at six different values of F ranging from 2,500 to 3,000 pN in 100 pN intervals. All the simulations showed that ring opening of cyclobutene proceeds exclusively through the disrotatory pathway, which is inconsistent with the simulations that employed distance constraints, yet is consistent with the sonication experiments [19], in which the major product formed resulted from the disrotatory

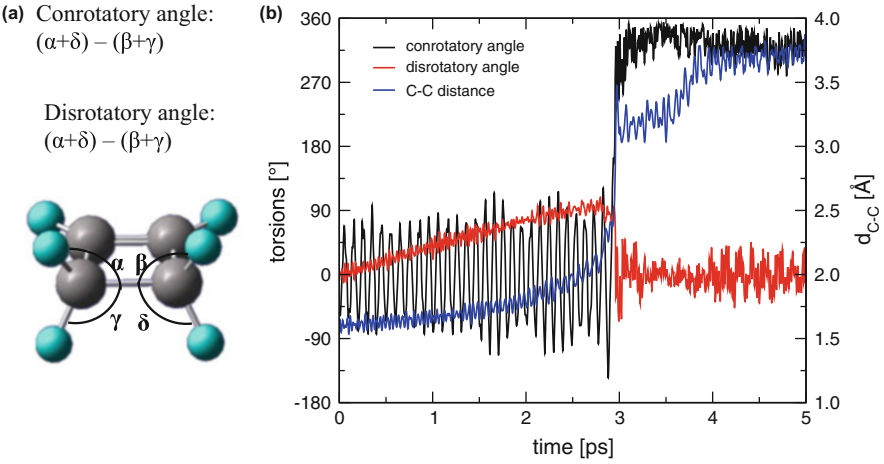

Fig. 4 (**a**) Schematic representation of the angles defining the ring opening of cyclobutene along conrotatory and disrotatory pathways. Changes in either angle toward 360° indicate that the associated ring-opening pathway (i.e., conrotatory or disrotatory) is followed. (**b**) Length of carbon–carbon scissile bond distance, $d_{C–C}$, conrotatory angle, and disrotatory angle during an MD simulation of the ring opening of cyclobutene under mechanochemical conditions imposed by increasing the distance between the *cis*-PPs at a pulling rate of 0.5 Å/ps

pathway. Structures observed during the MD simulation at $F = 2900$ pN are shown in Fig. 5. The structure at 0.1 ps shows that the carbon–carbon scissile bond is quite extended and the methylene groups are rotated in a manner consistent with motion along the disrotatory pathway. This deformation of the structure is because of the application of F. The scissile bond ruptured at approximately 1.6 ps, with the methylene groups moving in a manner that yields the disrotatory product. Rotation about the central carbon–carbon bond followed. Ultimately, this series of processes yields *trans*-1,3-butadiene along a disrotatory pathway.

To illustrate the formation of the disrotatory product in the EFEI-based MD simulations, the changes in the carbon–carbon scissile bond distance and conrotatory and disrotatory angle were monitored over time. These quantities are shown in Fig. 6. At the beginning of the MD simulation, the carbon–carbon scissile bond distance fluctuated around the equilibrium bond length until increasing rapidly around when this bond ruptured at approximately 1.5 ps. The conrotatory and disrotatory angles fluctuate around 0 and 100°, respectively at the beginning of the simulation. At approximately 1.6 ps, the disrotatory angle increased sharply and the conrotatory angle dropped to approximately 0°. The analysis of the angles indicates that the disrotatory angle dominates the behavior of the system throughout the MD simulation. The results obtained for the carbon–carbon scissile bond length as well as the conrotatory and disrotatory angles were observed for the MD simulations at the other values of F.

Portions of the FMPESs obtained with F applied either explicitly through the EFEI method or implicitly via distance constraints were examined to gain insights

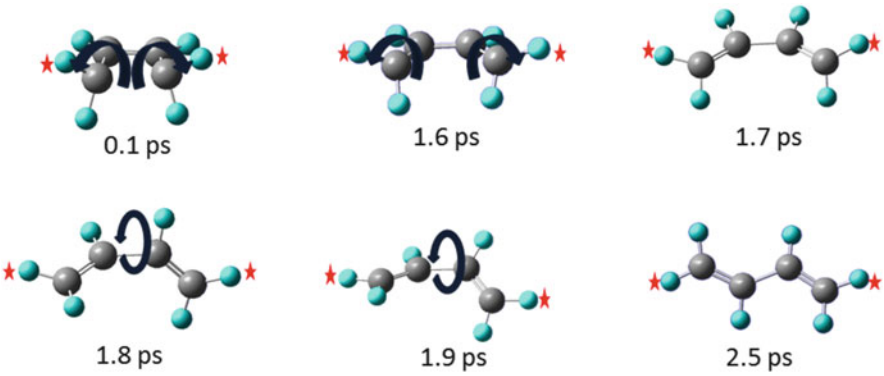

Fig. 5 Snapshots taken during an MD simulation for the ring opening of cyclobutene at $F = 2900$ pN. *cis*-PPs were used in the simulation and are indicated with *red stars*. As the reaction progresses, both methylene groups rotate in opposite directions to yield the *cis* disrotatory product observed at around 1.8 ps. Rotation around the carbon–carbon single bond leads to the formation of the *trans* disrotatory product at 2.5 ps. The motion of the system is indicated using *dark blue arrows*. *Silver and turquoise spheres* indicate carbon and hydrogen atoms, respectively

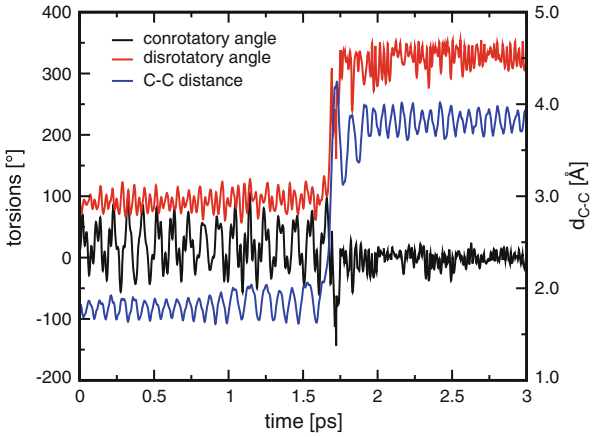

Fig. 6 Length of the carbon–carbon scissile bond, $d_{C\text{–}C}$, conrotatory angle, and disrotatory angle during an MD simulation of the ring opening of cyclobutene under EFEI mechanochemical conditions using *cis*-PPs at $F = 2{,}900$ pN

into the origins of the differences in the results of the MD simulations performed with these two approaches. To do this, a series of relaxed PES scans were performed at the CASSCF(4,4)/6-31G(d,p) level of theory. The scanned coordinates corresponded to the H-H distance associated with the PPs used in the MD simulations and the torsions associated with the movement of the methylene groups along conrotatory or disrotatory directions. Specifically, conrotatory movement was examined by fixing the dihedrals α and δ in Fig. 4a equal to each other, whereas

the disrotatory surface was examined by setting the dihedrals α and β equal to each other. Overall, this corresponds to performing a series of geometry optimizations in which one distance (R_0) and two dihedrals were constrained, at the same time allowing the remaining degrees of freedom to relax. The BO energies of these constrained structures were obtained through these optimizations. The internal forces acting along the direction between the hydrogen atoms used as PPs in the MD simulations were then used in conjunction with the distance between these atoms for each scanned structure to construct the slices of the constrained-distance FMPESs associated with varying the dihedral angles associated with conrotatory or disrotatory ring-opening at different values of R_0. Similarly, a constant external force, F, was multiplied by the PP separation for each structure to construct the EFEI FMPESs at different values of F.

The set of slices of the constrained-distance FMPESs associated with conrotatory and disrotatory movement of the methylene groups in cyclobutene are shown in Fig. 7a, b, respectively. The label 'PP separation' corresponds to the parameter, R_0, that was varied in the MD simulations that applied F via constrained distances. The torsions associated with the minimum energy structure for each value of R_0 sheds light on the sequence of structures that the system follows preferentially during MD simulations in which R_0 is increased in a time-dependent manner. The minimum energy paths (MEPs) associated with this series of structures are indicated as solid black lines on the surfaces in Fig. 7a, b.

The MEP on the conrotatory surface shows that the system follows a path connecting the reactants and products in which the PP separation increases to 3.4 Å without any large change in the torsions associated with the methylene groups. Increasing the PP separation from 3.4 Å to 4.2 Å results in the torsions increasing from 120° to 180° to follow a pathway corresponding to the conrotatory ring opening to yield a structure similar to the optimized structure of *cis*-1,3-butadiene on the BO PES. As the PP distance increases further, the system progresses past minima corresponding to the *cis* and *trans* forms of 1,3-butadiene.

The minimum energy pathway on the disrotatory surface does not connect cyclobutene with the 1,3-butadiene. Instead, increasing the PP separation from 3.0 Å to 3.7 Å increases the torsions to 150°. These angles then drop to 120° when the carbon–carbon scissile bond ruptures at a distance of 4.3 Å, which is consistent with the results of the MD simulations. In the structure where the constrained torsions reach 120°, all four values of α, β, γ, and δ are 120°. As such, the system can move from this point toward either the conrotatory or disrotatory products. The data indicate that the lowest energy path from this structure toward larger PP separations on the disrotatory surface does not lead to the 1,3-butadiene product. Instead, once the torsions reach 120°, it is energetically favorable for the system to move to the conrotatory surface (Fig. 7b), with the torsions increasing in a manner that involves both methylene groups rotating in the same direction. This pathway is designated by the dashed line on the conrotatory FMPES, which is a continuation of the solid black line on the disrotatory PES. These features of the conrotatory and disrotatory surfaces obtained through

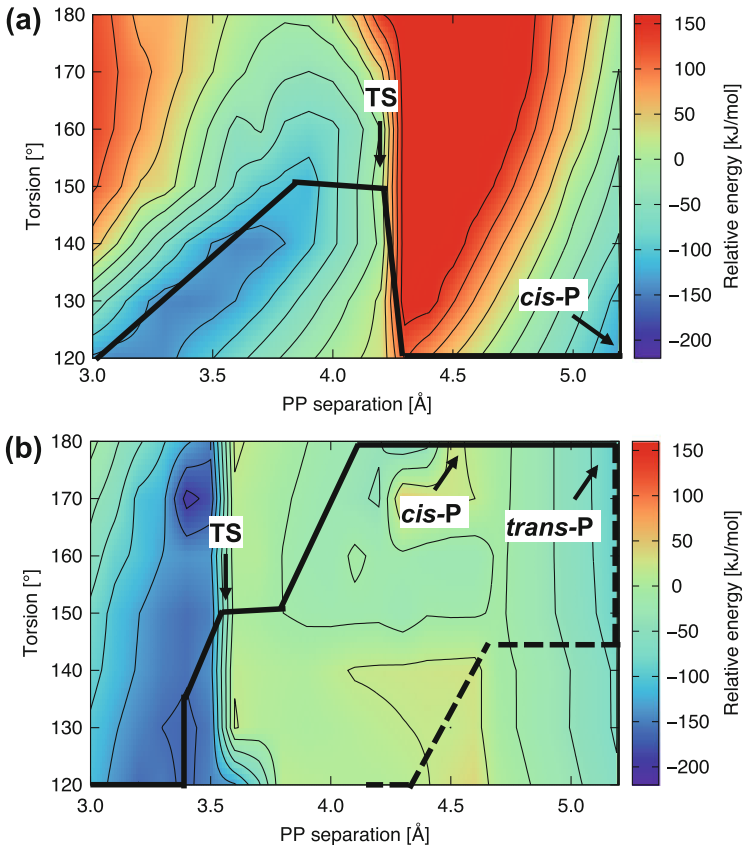

Fig. 7 Portions of the FMPESs associated with rotating methylene groups of cyclobutene at different PP separations under constrained distance conditions for (**a**) the disrotatory pathway and (**b**) the conrotatory pathway. The energies on the surfaces are plotted relative to that of the structures on the disrotatory surface with a PP separation of 3.0 Å and torsion of 180°. *Solid lines* indicate the MEP on each surface. The *dashed line* indicates the path the system follows upon moving from the disrotatory to conrotatory surface after the dissociation of the scissile bond. Locations of transition states and products are indicated as 'TS' and 'P,' respectively

calculations employing constrained distances account for the fact that only conrotatory products were observed during the MD simulations.

The portion of the EFEI FMPES calculated with $F = 1{,}500$ pN is shown in Fig. 8. The data show that the structures corresponding to conrotatory and disrotatory products are minima on their respective surfaces. MEPs connecting the reactants with these products could be identified on each surface, and are indicated by the solid lines. The changes in structure that occur along these MEPs are consistent with those observed during the MD simulations performed under EFEI conditions.

Overall, the results of these calculations illustrate that MD simulations in which F is applied explicitly can provide different results than those in which F is applied

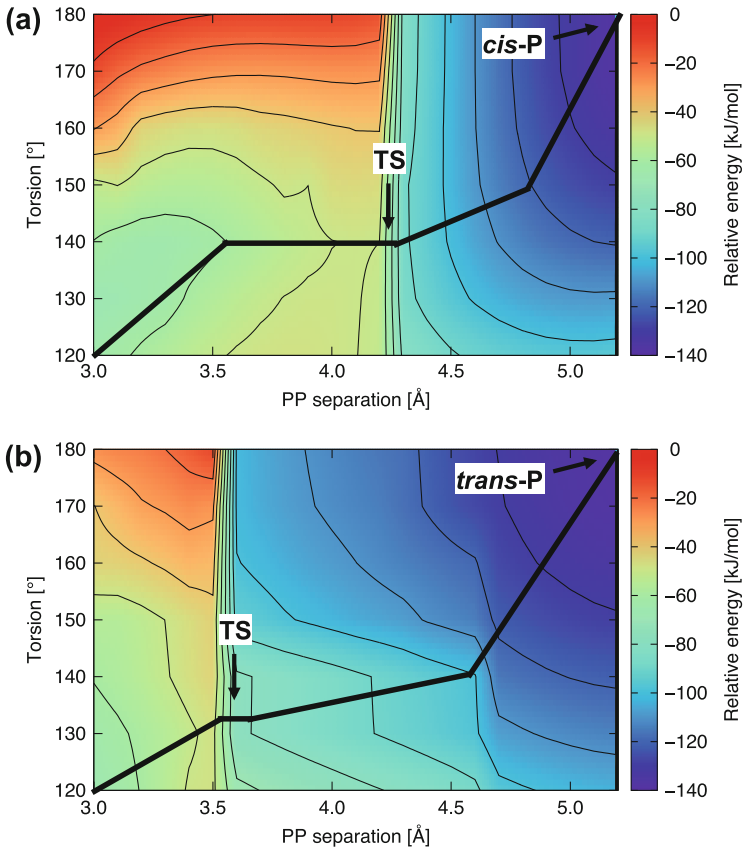

Fig. 8 Portion of the FMPES associated with rotating methylene groups of cyclobutene at different PP separations under EFEI mechanochemical conditions at $F = 1{,}500$ pN for (**a**) the disrotatory pathway and (**b**) the conrotatory pathway. The energies on the surfaces are plotted relative to that of the structures on the disrotatory surface with a PP separation of 3.0 Å and torsion of 180°. *Solid lines* indicate the MEP on each surface. Locations of transition states and products are indicated as 'TS' and 'P,' respectively

by varying R_0 over time. In the case of the former, a constant F is applied and the system is allowed to move on a single FMPES along all $3N-6$ degrees of freedom to follow the MEP connecting reactants to products. In the case of the latter, the system can move along $3N-7$ degrees of freedom to sample a series of FMPESs defined by the values of R_0 spanned during the simulation. These differences are evident from an examination of the MEPs in Figs. 7 and 8, as well as the differences in the outcomes of the MD simulations described above. The ring-opening of cyclobutene is likely to be an extreme example of these artifacts because the product formed during the reaction depends on the rupture of a C–C bond and rotation of two methylene groups. The rupture of the scissile bond and rotation along the disrotatory pathway are both favored in simulations where F is applied

explicitly in a tensile manner because both of these processes increase the separation of the PPs. Meanwhile, increasing R_0 from its equilibrium value in cyclobutene imposes a tensile F that favors the rupture of the C–C bond, but increasing R_0 from the point at which bond scission occurs leads to the application of a compressive F that disfavors rotation of the methylene groups along the disrotatory path. In other cases where the reaction is dominated by the change in a given interatomic distance, e.g., the dissociation of strained polymers via the rupture of an individual bond or the dissociation of S–S bonds in proteins, the differences between MD simulations in which F is applied explicitly and those in which F is applied via time-dependent distance constraints may be less significant. Nonetheless, one should be aware of these differences when selecting an approach for imposing F in MD simulations of mechanochemical processes.

2.2 Indirect Evaluation of the FMPES

A qualitative understanding of the manner in which F alters the PES can be useful in developing strategies for the mechanochemical activation of reactions and for understanding the outcomes of experiments performed under mechanochemical conditions. For example, understanding how F affects the relative energies of reactant and TS species, as well as the structures of those species, can aid in the selection of groups that are subjected to F in order to activate reactions under mechanochemical conditions. Such information can be obtained by locating the structures of these species on the FMPESs associated with different values of F through calculations performed directly on the FMPES using the methods describe above. However, such calculations must be performed at each value of F and can thus be quite laborious. Instead, useful insights regarding the relationships between F and the activation of reactions can be obtained by using knowledge of the zero-F PES to predict indirectly features of the FMPES. Kauzmann and Eyring developed one of the first 'indirect' models to describe the reactivity of chemical systems on the FMPES [107]. That model involved extending transition state theory to incorporate the effect of F on the activation energy, $\Delta E^{\ddagger}$, with $\Delta E^{\ddagger}$ being reduced from its zero-F value in a manner that depends linearly on F. This model was found to account for the increased rate of homolytic bond cleavage of polymers with mechanical force. More recently, additional methods for indirectly predicting the features of the FMPES on the basis of knowledge of the zero-F PES have been reported. These techniques are discussed in what follows.

2.2.1 Bell's Model

Bell developed a theoretical framework to predict the effects of F on the adhesion between cell surfaces [108]. In Bell's model, it is assumed that applying F does not affect the structures of reactants, TS, and products of a reaction, but rather the sole

effect of F is to perform work on the system as it moves between these species during the course of a reaction. In the context of reaction kinetics, the work performed on the system occurs as a result of a change in the separation of groups subjected to F as the system moves from the reactants to the TS. Within the assumption that F does not affect the reactant and TS structures, it is possible to determine this change in separation, $\Delta R(0)$, using knowledge of these structures on the zero-F PES, and it follows that the barrier on the FMPES can be approximated as

$$\Delta E^{\ddagger}(F) = \Delta E^{\ddagger}(0) - F\Delta R(0), \tag{6}$$

where $\Delta E^{\ddagger}(0)$ is the barrier on the zero-F PES.

The simplicity of Bell's model is useful in the context of chemical simulation because its use only requires the evaluation of reactant and TS structures on the zero-F PES, yet provides the ability to predict properties on the FMPES. Of course, the assumption that the reactant and TS structures are invariant to F is only reliable (even qualitatively) for low values of F, which limits the range of F over which Bell's model can provide reliable predictions regarding the relationships between reaction barriers and F. Nonetheless, the simplicity of Bell's model combined with its ability to provide a qualitatively accurate description of the relationship between reaction barriers and F has led to its application in many practical contexts. For instance, Bell's model has been used extensively to study the mechanochemical response of several biological systems such as the rupture of disulfide bonds in proteins [109], the distortion of extracellular matrices in cells and tissues [110], and the force generation in actin-binding protein motors [111].

2.2.2 Tilted Potential Energy Profile Model

The assumption that the reactant and TS structures are invariant to F is a key limitation of Bell's model. The movement of these structures produced by the application of F is addressed in a limited manner by the tilted potential energy profile model [112]. In this model, it is assumed that F is aligned exactly with the zero-F reaction coordinate. The application of F then shifts the energies of all structures along this coordinate by $-FR$, where R is the distance between the atoms subjected to F at each point along the reaction coordinate. This modification of the energies along the reaction coordinate is illustrated schematically in Fig. 9. As shown in that figure, the modification of the energies has the effect of allowing the reactant and TS structures to move to new locations along the reaction coordinate. In particular, if F is positive and R increases along the reaction coordinate, the reactant and TS structures move closer to one another and the activation energy is reduced, which is consistent with the Hammond postulate. However, by restricting structural changes to occur only along the zero-F reaction coordinate, the tilted potential energy profile model fails to account for anti-Hammond effects, which can influence the activation energy and even cause the system to follow alternate

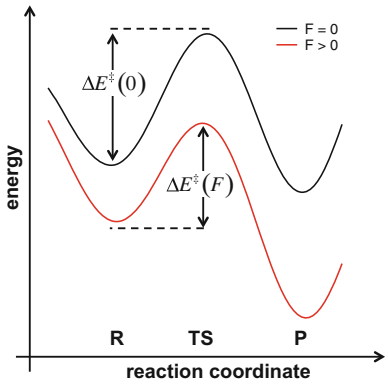

Fig. 9 A general schematic showing the effect of F on the PES on which a molecule moves as described in the tilted potential energy profile model. The *black curve* illustrates the change in energy along the reaction coordinate in the absence of an external force. The labels R, TS, and P indicate the positions of the zero-F reactants, transition state, and products along this reaction coordinate, respectively. The *red curve* is obtained by adding $-FR$ to the zero-F energies. The addition of this work term lowers the barrier relative to its value in the absence of applied F. The application of F also shifts the locations of R, TS, and P from their zero-F positions, but otherwise this model assumes the series structures comprising the reaction coordinate in the absence and presence of F are identical

reaction pathways. The tilted potential energy profile model can also be relatively demanding from a computational standpoint, because the energies of multiple structures along the zero-F reaction coordinate must be evaluated to use it. This model has been applied to study the effect of F on the kinetics of several biochemical processes [112–114].

2.2.3 Extended Bell's Model

Bell's model provides a qualitatively correct description of the effect of F on reaction barriers. However, the assumption that the reactant and TS structures are unaffected by the application of F restricts the range of F over which Bell's model applies. The F-induced movements of the reactant and TS structures along the zero-F reaction coordinate are captured partially by the tilted potential energy profile model; however, in general, the application of F can induce changes in the reactant and TS structures that are orthogonal to the zero-F reaction coordinate. Such changes in structure, and the consequent effects on reaction barriers, can be captured by expanding the FMPES as a Taylor series with respect to the nuclear positions [37, 97, 115].

A second-order expansion of the FMPES at a stationary point on the zero-F PES yields

$$E_F(\mathbf{q}_0 + \delta\mathbf{q}; F) = E_0(\mathbf{q}_0) + \frac{1}{2}\delta\mathbf{q}^T\mathbf{H}_{\text{int}}\delta\mathbf{q} - F(R_0 + \delta R), \tag{7}$$

where $\mathbf{q}_0$ represents the nuclear coordinates corresponding to a stationary point on the zero-F PES, $\delta\mathbf{q}$ represents the changes in these coordinates upon the application of F, R_0 is the distance between the atoms subjected to F when F is not applied, and δR is the change in R produced by the application of F. All first derivatives of $E(\mathbf{q})$ with respect to nuclear coordinates are zero and are therefore not included in (7). The second derivatives of E_0 with respect to nuclear coordinates are grouped into the term $\mathbf{H}_{\text{int}}$, which is the Hessian in terms of internal coordinates. The distance between atoms that are subjected to F, termed R, represents one of the internal coordinates used to construct $\mathbf{H}_{\text{int}}$.

The change in the structure of a stationary point upon moving from the zero-F PES to the FMPES can be quantified as

$$\delta\mathbf{q} = \mathbf{C}\mathbf{F}, \tag{8}$$

where $\mathbf{C} = \mathbf{H}_{\text{int}}^{-1}$ is the compliance matrix and $\mathbf{F}$ is a vector whose components are all zero except for that associated with internal coordinate $\mathbf{R}$, which has a magnitude of F. Substituting (8) into (7) and noting that F is the only non-zero component of $\mathbf{F}$ yields

$$E_F(\mathbf{q}_0 + \delta\mathbf{q}; F) = E_0(\mathbf{q}_0) - FR_0 - \frac{F^2}{2}C_{RR}, \tag{9}$$

where C_{RR} is a compliance term that accounts for the relationship between δR and F while taking into account the relaxation along all other internal coordinates. Equation (9) can be applied to reactant and TS geometries to estimate the reaction barrier on the FMPES as

$$\Delta E^{\ddagger}(F) = \Delta E^{\ddagger}(0) - F\Delta R_0 - \frac{F^2}{2}\Delta C_{RR}, \tag{10}$$

where $\Delta R_0 = R_0^{TS} - R_0^r$ is the change in R as the system progresses from the reactant to the TS and $\Delta C_{RR} = C_{RR}^{TS} - C_{RR}^r$ is the change in compliance matrix element along the direction R between the TS and the reactant. The first two terms in (10) are equivalent to Bell's model – see (6) – whereas the last term incorporates changes in energy that arise from F-induced changes in the structures of the reactants and TS.

The extended Bell's model outlined in (10) provides an estimate of the reaction barrier on the FMPES without performing a large number of quantum chemical calculations. The terms in this model can provide information in the selection of the atoms that are subjected to F to achieve a desired mechanochemical response. For instance, this model indicates that lowering the barriers on the FMPES, and hence activating reactions, can be achieved by selecting pairs of atoms whose separations increase upon moving from the reactant to TS and/or for which the TS is more

compliant than the reactant $\left(C_{RR}^{TS} > C_{RR}^{r}\right)$. This model has been used to describe the effect of applied force on the rupture of bonds in pericyclic reactions [37] and the influence of anti-Hammond effects on barriers [116], and to explore how the regiochemistry of polymers attached to mechanophores can affect F-dependent changes in reaction rates. [117].

One of the main limitations of this model is that the barrier on the FMPES is predicted using structures, energies, and Hessians obtained with zero-F reactant and TS structures. As such, the predictions made with (10) become increasingly unreliable as F is increased. It may be possible to improve the abilities of extended Bell's models to predict accurately the structures of reactant and TS structures, as well as barriers, at higher F by increasing the order to which the zero-F energy is expanded with respect to changes in structure; however, no proof showing that this Taylor series expansion converges exists to our knowledge. Regardless, calculating the higher order derivatives of the zero-F energy with respect to the nuclear positions is generally computationally intractable.

An extended version of Bell's model that is applicable to a wider range of F than that in (10) has been reported by Makarov and coworkers [36]. Their model straddles the line between indirect and direct evaluation of the FMPES by using Hessians obtained at non-zero F to propagate numerically the reactant and TS structures over a range of F. This approach involves representing the structure of a stationary point on the FMPES as

$$\Delta E^{\ddagger}(F) = \Delta E^{\ddagger}(0) - \int_0^F \left[\mathbf{q}_{TS}\left(F'\right) - \mathbf{q}_R\left(F'\right)\right]\mathbf{l}dF', \tag{11}$$

where $\mathbf{l}$ is a vector indicating the direction along which F is applied. The structures obtained at different values of F can then be used to find reaction barriers at higher F:

$$\Delta E^{\ddagger}(F) = \Delta E^{\ddagger}(0) - \int_0^F \left[\mathbf{q}_{TS}\left(F'\right) - \mathbf{q}_R\left(F'\right)\right]\mathbf{l}dF', \tag{12}$$

where $\mathbf{q}_{TS}$ and $\mathbf{q}_R$ are the structures of the TS and reactant, respectively, at F. Although this approach overcomes the limited abilities of (10) at higher F, its use imposes additional computational demands because a Hessian must be generated for the reactant and TS at each F considered. The additional information obtained by generating Hessians at higher F makes it possible to identify and characterize F-induced instabilities in reactant and TS structures in terms of F-induced changes to the eigenvalues of the Hessian. However, the F-induced changes in the reactant and TS structures arising from these instabilities can also be determined from geometry optimizations of these structures on the FMPES at a comparable or even lower computational cost than that associated with performing multiple calculations of the Hessian.

The models described above aim to obtain approximate details regarding the FMPES using information from the zero-F PES. However, chemical processes are governed by free energies. Boulatov and coworkers have explored the ability to access free energy barriers using truncated Taylor series expansions [97, 118]. The contribution of the potential energy is obtained by treating the system as reactive site coupled to an external harmonic constraining potential as discussed in the section "Application of F through Constrained Geometries," which incorporates the effects of polymers used to subject the reactive site to F without employing an explicit treatment of those polymers. The constraining potential has a compliance, C^{c}, and equilibrium length, R^{c}, which are incorporated into the potential energy to yield. Incorporation of the vibrational partition functions, Z, which are dependent upon C^{c}, yields the free energy barrier for the dominant reactant conformer as

$$\Delta G^{\ddagger}(C^{c},F) = \Delta G^{\ddagger}(\infty,0) + \left(F\Delta R_0 + \frac{F^2(\Delta C_{RR})}{2}\right)\left(\frac{C^{c}+C^{r}_{RR}}{C^{c}+C^{TS}_{RR}}\right) + \frac{\Delta R_0^2}{C^2+C^{T}_{RR}} - k_B T \ln\left(\frac{Z^0}{Z^c}\right)^{\ddagger}\left(\frac{Z^c}{Z^0}\right)^{r} \tag{13}$$

where terms with a superscript 'c' refer to quantities that incorporate the compliance of the confining potential. Equation (13) reduces to (10) in the limit that $C^c \rightarrow \infty$ and $R^c \rightarrow \infty$.

Equation (13) is intended to describe the free energy barrier of a reactive site embedded in a polymer, where ΔR should correspond to the distance between the PPs in the experimental system where F is applied two polymers that are grafted onto a reactive site. Computational limitations prevent the use of model systems that accurately include polymers of sufficient length to ensure that (13) reliably reproduces experimental conditions. To overcome this limitation, Boulatov and coworkers employed the previously demonstrated relationship between the F applied along a conveniently defined local coordinate that applied between the PPs to cast (13) in a form amenable to use to quantities obtained through QC calculations of small model systems in the limit that $C^c \rightarrow \infty$ and $R^c \rightarrow \infty$:

$$\Delta G^{\ddagger}(C^{c},F_l) = \Delta G^{\ddagger}(\infty,0) + \left(F_l \Delta R_0^{l} + \frac{F_l^2(\Delta C_{ll})}{2}\right), \tag{14}$$

where the forces, separations, and compliances correspond to those associated with the local coordinate, l, as opposed to the coordinate connecting the ends of the polymers used in experiments. Equation (14) is compatible with QC calculations of small model systems, where the necessary distances and compliances can be obtained using a local mechanochemical reaction coordinate that is relevant to the reaction being studied, e.g., a bond length that changes during a reactions. The comparison of this model with Bell's model and a full statistical mechanical

treatment of reaction kinetics has shown that it is suitable for describing mechanochemical processes over the range of F encountered in experiments [118].

2.2.4 Comparison of Indirect Models for Predicting the FMPES

The conceptual models outlined above all describe the effects of F on reaction barriers to different levels of approximation. The abilities of these models can be assessed by comparing the predicted barriers to those obtained from QC calculations of the barriers on the FMPES. Such a comparison is provided in Fig. 10, which compares the barriers obtained with different conceptual methods for the ring-opening of 1,3-cyclohexadiene with F applied to the atoms indicated with asterisks in Fig. 10a. QC structures, energies, and frequencies of the reactant and TS

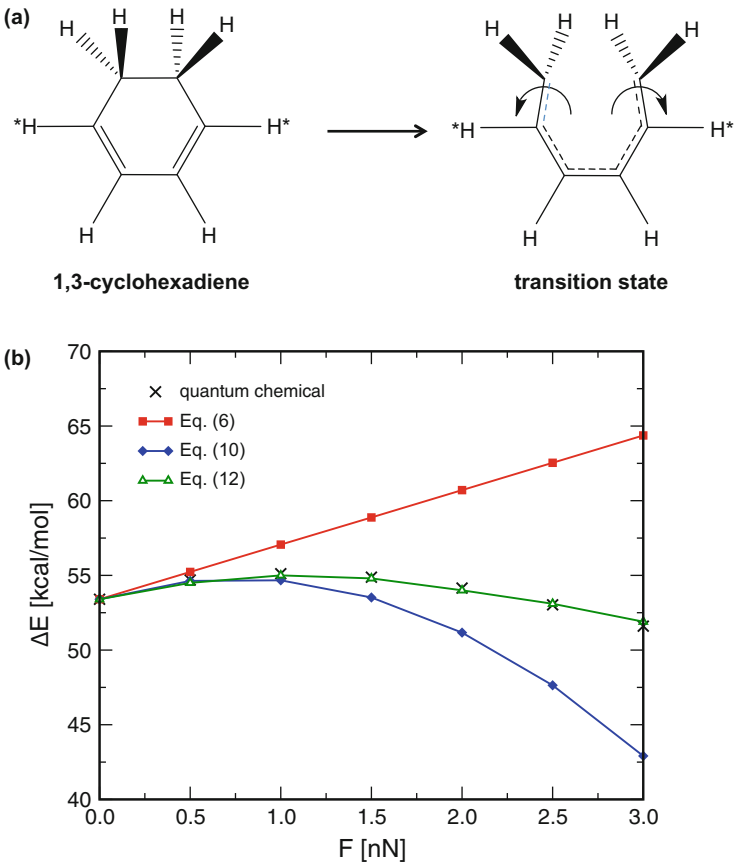

Fig. 10 (**a**) Reaction scheme for the ring opening of cyclohexadiene along the disrotatory (allowed) pathway. The atoms indicated with *asterisks* were used to apply F. (**b**) Reaction barriers as a function of F applied at the CASSCF(6,6)/6-31G(d,p) level and using (6), (10), and (12)

for this reaction were calculated at different F using CASSCF(6,6)/6-31G(d,p) methods. These data were then used to predict the barriers at different F using (6), (10), and (12). The comparison of the reaction barriers obtained with these different methods is given in Fig. 10b.

The results demonstrated that the agreement between the models and the QC values increases with the amount of information incorporated into the models. For instance, Bell's model – see (6) – captures the increase in $\Delta E^{\ddagger}$ at low F, but fails to describe the reduction in $\Delta E^{\ddagger}$ at higher F. This is clearly a result of using a linear model to describe the F-induced changes in $\Delta E^{\ddagger}$. The extended Bell's model based on zero-F data – see (10) – qualitatively captures the changes in $\Delta E^{\ddagger}$, with this quantity increasing at low F and decreasing at high F. However, the quantitative agreement between the barriers predicted with those model and the QC barriers becomes increasing poor as F is increased. Meanwhile, the barriers predicted using an extended Bell's model with F-dependent parameters – see (12) – agrees well with the QC barriers over the entire range of F considered. In general, the agreement between the conceptual models and the QC barriers varies with the nature of the reaction and the atoms used to apply F. However, the relative agreement between the results obtained with the conceptual models and the QC data illustrated in this example are qualitatively consistent with what one would expect.

Although the agreement between the barriers predicted with these models and the QC data improves as (6) < (10) < (12), the computational requirements associated with these methods trend in the opposite direction. Specifically, Bell's model can be directly used if the zero-F structures and energies of the reactants and TS are known. The extended Bell's model given by (10) requires information regarding the zero-F compliance matrices of the reactant and TS. The Hessians associated with these structures are generally available after QC optimizations of these structures (assuming one has confirmed the natures of these stationary points via frequency calculations); however, a small amount of additional effort is needed to transform the Hessians to the coordinate systems associated with a set of internal coordinates that explicitly contain R. The use of (12) has significantly greater computational requirements because the Hessian must be evaluated at each F. This can become particularly costly if one is examining the dependence of the reaction barriers upon the different pairs of atoms used to apply F because a series of Hessian calculations would be required for each pair of atoms considered.

3 Methods for Simulating Bulk Mechanochemistry

The methods discussed in Sect. 3 are suited to modeling mechanochemical experiments in which individual molecules are subjected to tensile stresses applied between regions in those molecules. However, a large branch of mechanochemical experiments employ techniques such as milling and grinding in which shear and/or compressive stresses applied at the macroscopic levels induce reactions. Methods that focus on the action of tensile stresses at the molecular level, such as those

described in Sect. 3, are not well-suited to modeling the shear conditions relevant for this type of mechanochemical activation. For instance, separating two regions of an individual molecule via a one-dimensional PES scan, SMD, or EFEI methods in an effort to mimic shear at the level of an individual molecule induces rotation as opposed to shear. In addition, shear and compressive stresses are typically transmitted via intermolecular interactions, and thus single molecule representations are not appropriate for modeling mechanochemical processes induced by shear and/or compression.

Invoking mechanochemical reactions via the application of shear and/or compressive stresses is similar to the field of tribochemistry, which involves studying reactions that are induced by the conditions experienced when surfaces slide past one another [119]. These conditions include stresses that reach the theoretical yield strengths of the materials in contact (which can reach several GPa) and local temperatures that reach the melting points of these materials (which can reach hundreds or even thousands of Kelvin depending on the materials). The high temperatures achieved can induce thermochemical processes, whereas the extreme stresses experienced in sliding contacts can promote mechanochemical reactions. As such, mechanochemical processes induced via shear and compression can be thought of as a subset of tribochemical reactions [120], and simulation techniques that are suitable for studying tribochemical processes can also be used to model these types of mechanochemical reactions. Despite this potential, far fewer simulations of these 'bulk' mechanochemical processes have been reported than their molecular counterparts, and thus the application of methods used in tribochemistry to study mechanochemical processes represents a relatively open avenue for further research.

To account for conditions of shear and compression, tribochemical simulations employ models that are sufficiently large to account for the interactions between molecules and, potentially, surfaces that impose and transmit these stresses. Such models often include surfaces that can be moved relative to one another to induce stresses and/or place the system in a simulation cell that can be deformed to impose stresses and strains. Schematics of such models are given in Fig. 11. Figure 11a shows a system containing two slabs that are separated by material that is to be sheared. This is achieved by moving the upper slab related to the bottom slab. Figure 11b shows a system in which an interface has been placed in a simulation cell. Compression can be invoked by subjecting the cell to stresses or strains perpendicular to the interface, whereas shear can be achieved by applying stresses or strains parallel to the interface.

In what follows, we describe how models such as those in Fig. 11 can be used to study stress-activated processes. As indicated above, these techniques have been used primarily to investigate tribochemical reactions; however, these techniques should be transferrable to studies of mechanochemical reactions. Section 3.1 focuses on describing techniques that allow tribochemical reactions to be modeled with static calculations such as geometry optimizations, potential energy surface scans, and minimum energy path calculations. Section 3.2 focuses on using MD

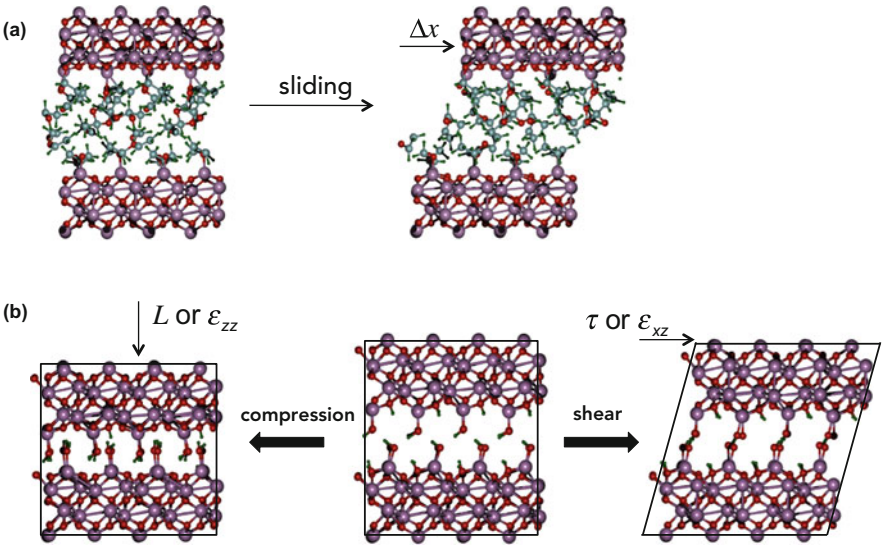

Fig. 11 (**a**) Two slabs of alumina separated by a collection of aldehydes. Shear stress is imposed by moving the upper slab a distance, Δx, relative to the lower slab. (**b**) A hydroxylated alumina interface contained within a simulation cell. Compression can be achieved by subjecting the system to a stress (L) or strain (ε_{zz}) perpendicular to the interface. Shear can be achieved by applying a shear stress (τ) or a shear strain (ε_{xz}) parallel to the interface

simulations to examine the chemical behavior of systems that are exposed to compressive and/or shear stresses.

3.1 Static Simulation Methods

Static calculation methods include techniques such as single point energy calculations and geometry optimizations, which can be used to examine features of the PES without actually simulating the dynamics of the system. The use of static simulation methods to study the changes in energy and structure that occur during tribochemical processes has a long history [48, 49]. These methods have been used to optimize the reactants and products of tribochemical reactions, to examine the PES associated with the movement of surfaces relative to one another, and to identify the MEPs connecting the reactants and products of tribochemical reactions. The calculations provide insight into the changes in energies and stresses associated with these reactions, which are then used to predict properties such as friction forces and friction coefficients. Methods for mapping PESs are described in Sect. 3.1.1 and techniques for locating the MEPs of sheared systems are described in Sect. 3.1.2. In the context of mechanochemistry, these types of calculations may

be useful for determining the structural transformations that occur during reactions and in evaluating the stresses to which molecules in contact are exposed.

3.1.1 Mapping Potential Energy Surfaces

As noted above, static computational models do not attempt to simulate the dynamics associated with chemical reactions. However, by performing a series of static calculations on systems whose structural features vary in a systematic manner, one can develop an understanding of the changes in structure and energetics that occur during a reaction. In the context of tribochemistry, such calculations are often used to map out the two-dimensional PES associated with the movement of one surface relative to another using models of the form shown in Fig. 11, which may or may not contain material between the slabs depending on the particular application. The construction of the PES is achieved by moving the upper surface relative to the bottom one over a series of fixed increments and evaluating the energies of each structure. The changes in energy on the resultant PES can be used to identify low energy pathways along this surface, which should correspond to the preferred directions for slip and shear, and can also be used to estimate the energetic barriers associated with slip along these directions. An example of a PES constructed via this approach and the consequent estimation of slip barriers along competing directions is shown in Fig. 12. The usefulness of the information gained from these PES scans is dependent upon how closely the changes in structure permitted during the simulations, e.g. relaxation of atomic coordinates and/or components of the lattice vectors orthogonal to the cell deformation, represent those which would occur if the system was simply allowed to evolve naturally.

Mapping the PES using a set of static calculations, as opposed to exploring the reaction via dynamic methods, is advantageous from the standpoint of computational requirements. The overall computational cost can easily be moderated by selecting the density of the points in the scan. A low density of grid points can be used to obtain a coarse description of the shape of the PES and then a set of calculations using a higher density of grid points can be used to gain a refined representation of the PES along important directions such as slip pathways. This approach also has built-in parallelism. Because the points of the surface are decoupled, calculations of individual points be can be performed independently of one other and the limit of parallelism is effectively nonexistent.

An early example of fully mapping a PES between two materials was reported by Smith et al. in 1998 [122]. In that study, they use the ACRES method [123], a parallelizable grid-based method for calculating DFT energies, to calculate the PES associated with movement along the interface between molybdenum trioxide (MoO_3) and molybdenum disulfide (MoS_2). To do this, they built slabs of each material, brought the slabs into contact to form an interface that spanned the x–y plane, and then minimized the energy of the system with respect to the interfacial separation at 16 lateral positions in the x–y plane. Because of computational costs, only the interfacial distance was varied at each point on the PES while the atomic

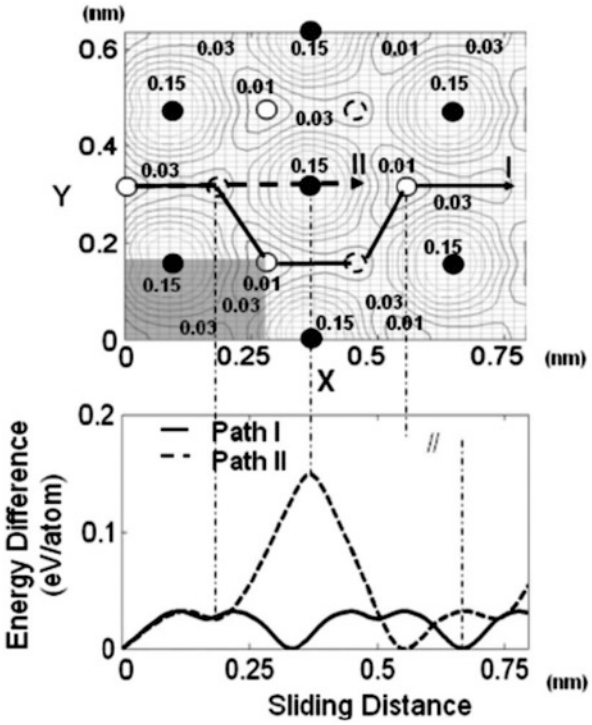

Fig. 12 *Upper panel*: A two-dimensional PES constructed by moving one slabs of MoS_2 relative to another along the *x* and *y* directions. Possible slip paths on the surface are shown with the *solid and dashed lines*. *Numbers* indicate energies in eV/atom relative to the energy of the optimized structure of MoS_2 at various positions on the surface. *Lower panel*: Changes in energy along the paths designated I and II in the *upper panel* as a function of sliding distance. Figure reprinted with permission from Liang et al. [121]. Copyright (2008) by the American Physical Society

positions were held fixed. The PES obtained through these calculations led to the identification of a clearly preferred slip pathway along the interface, which corresponded to a groove on the MoS_2 surface into which the oxygen atoms at the surface of the MoO_3 slab fit. Because the interfacial distance was relaxed, it provided some information regarding the manner in which the surfaces interact at various lateral positions as well. It was found that orienting the surfaces in relative positions that caused the oxygen atoms in the MoO_3 surface to move out of the groove in the MoS_2 surface led to an interfacial separation that was 0.5 Å greater than the minimum energy interfacial separation for this system. Meanwhile, moving along the grooves showed that the interfacial separation varied by only 0.01 Å.

Phillpot et al. [121] expanded on the work of Smith and coworkers by evaluating the PESs of MoO_3/MoO_3, MoS_2/MoS_2, and MoO_3/MoS_2 interfaces using model systems contained in periodically-repeated simulation cells in conjunction with plane-wave DFT calculations. In the approach used in their study, the entire simulation cell was first optimized to ensure the system was at a minimum configuration before scanning the PES. This optimization was performed by allowing the atoms in the system to relax while keeping the lattice vectors defining the simulation cell fixed. An external load was then applied by compressing the system in the direction perpendicular to the interface, fixing the top and bottom atomic layers, and allowing the remaining atoms to relax. This procedure was continued until the magnitude of

the system's internal stress along the compressed direction was equal to the desired normal load. The application of a load in this context can be useful to determine the load-dependence of properties such as shear strengths and slip barriers. After the target load was reached, the PES was mapped by rigidly moving the top half of the system in the *x*–*y* plane, relaxing the atoms at each point, and comparing the energy to that of the untranslated system. When moving the system in this manner, it is important to tilt the **c** lattice vector according the Lees–Edwards boundary conditions [124] to avoid introducing a second slip plane at the periodic boundary of the cell.

The PES scans of the MoO_3/MoO_3, MoS_2/MoS_2, and MoO_3/MoS_2 interfaces led to the conclusion that sliding MoO_3 on MoO_3 has the highest slip energy barrier and consequently requires the largest force to induce slip. Meanwhile, the mixed MoO_3/MoS_2 interface required a force that was approximately an order of magnitude lower to pass over its slip barrier. This methodology, or variations of it, has become a standard approach to constructing the PESs associated with tribochemical reactions and has been used to study hydrogenated [125, 126] and fluorinated-diamond surfaces [126], graphene oxide [127], graphane and fluorographane [128], and graphene/boron nitride [129], among other systems.

In 2013, Hod proposed a method for predicting slip paths in materials called the registry index (RI) [130], which has lower computational demands than PES scans. This method is based on the concept that the highest energy inter-surface stacking mode is generally the one with the most overlapping atoms between the two surfaces (e.g., in graphite, the highest energy configuration has the carbon atoms in adjacent sheets directly on top of each other, although the lowest energy configuration minimizes this overlap). To calculate the RI, each atomic center is assigned a circle of given radius and the projected overlap between the circles in two adjacent layers, designated the S_{CC}, is calculated. This value has a maximum at the highest energy stacking mode and a minimum at the lowest energy mode. The RI is then evaluated as

$$\mathrm{RI} = \frac{S_{CC} - S_{CC}^{\min}}{S_{CC}^{\max} - S_{CC}^{\min}}, \tag{15}$$

which is bound to values between zero and one. In essence, RI is a measure of the extent of electron cloud overlap between two layers, which is one of the primary contributors to the sliding energy landscape in materials. Hod has shown the usefulness of RI in studying graphite, hexagonal boron nitride, MoS_2, graphene/boron nitride, and multi-walled boron nitride nanotubes [129, 130].

3.1.2 PES Scans Along the Slip Path

Mapping the two-dimensional PES associated with sliding one surface past another can be computationally demanding, with the number of energy calculations

increasing quadratically with the number of points considered along each direction. The computational requirements can be reduced considerably in cases where the slip path is known, where it is possible to perform a one-dimensional scan over a series of points along this path. This can be done in a manner similar to that described above, but only stepping along the slip path. Alternatively, optimization schemes, such as the nudged elastic band method, can be used to calculate the minimum energy path that aligns to a particular slip path. Such methods are described below.

One of the earliest reported examples of using one-dimensional scans to study atomic-scale friction with quantum chemical methods was published in 1990 by Zhong and Tománek [131], where they modeled a layer of palladium on graphite. To determine the friction behavior of this system, a one-dimensional PES scan was obtained using DFT by moving the palladium atoms along a specific direction on the graphite surface. The friction force was calculated by differentiating the potential energy with respect to the sliding distance. It was found that friction coefficient was low (on the order of 10^{-2}) for small loads and increased for larger loads, in agreement with previous AFM experiments.

The Pakkanen group has reported a series of studies in which they examined the friction behavior of a variety of materials with known slip paths. For these studies, they developed small models of the material of interest, typically only including a few atomic layers. For example, they modeled hydrogen-terminated diamond surfaces using a $C_{13}H_{22}$ fully saturated tricyclic model [132]. They placed two of these systems in contact and calculated the energy at various points along the sliding path with a load applied normal to the sliding direction. These methods have been employed by the Pakkanen group to study interactions with hydrogen- [132], methyl- [133], and fluoro-terminated [134] diamond surfaces, other hydrocarbons [135], graphene sheets [136], boron nitride [137], and boron nitride on ice [138]. Others have studied the slip behavior of materials using a similar methodology to that used by the Pakkanen group, but using larger model systems. Using periodically repeating models of 22 metals and ceramics, Ogata et al. calculated the shear strain-stress relationships of these materials to determine the maximum strain a crystal can withstand [139]. Mosey, Liao, and Carter used one-dimensional PES scans to predict the shear strengths of materials such as iron oxides and chromia [140–142].

3.1.3 Optimization to a Minimum Energy Path

PES scans over a discrete set of points provide insights into the changes in energy and structure that occur during a slip process. However, it is unlikely that a given point on a scanned PES corresponds exactly to the transition state for a reaction or slip process. This uncertainty in the position of the transition state introduces errors in calculated reaction barriers. In addition, the slip path itself may not correspond to the series of structures along the grid used to construct the PES. To gain a more accurate description of the reaction process, it is useful to evaluate the series of

structures, including the transition state, corresponding to the MEP the system follows as it moves from reactants to products. In calculations of molecular systems, this is often achieved through the evaluation of the IRC, which starts from a known transition state structure and constructs the MEP by following the steepest descent trajectory from the TS to the reactant and product structures it connects. It is not straightforward to optimize TS structures for condensed phase systems such as those used in tribochemical studies without first optimizing the MEP. As such, one cannot readily employ the IRC procedure used to study reactions involving molecular systems. Instead, MEPs for reactions occurring in the condensed phase are obtained by starting from the reactant and product structures and locating the MEP that connects these structures. An approach for locating MEPs for shear-induced transformations is described in what follows. This method is based on the nudged elastic band (NEB) method, which has been used to study condensed phase reactions in which the simulation cell remains fixed.

The NEB method [143–145] is part of a family of path minimization techniques known as chain-of-states methods. In these methods, two positions on a PES are connected by a series of images that trace a path on the surface. After the initial path is generated, various optimization techniques can be used to minimize the path to an MEP on the PES. The features of this process are outlined schematically in Fig. 13. In one chain-of-states approach, called the elastic band method, the images are connected by springs and the path is optimized by minimizing the force experienced by each image as the sum of the true force and the spring force. The true force

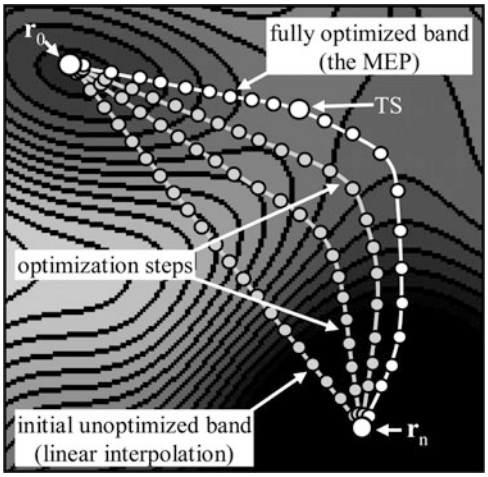

Fig. 13 Optimization to the MEP via the chain-of-states methods. The contour plot designates a PES. The *circles* indicate images along a path on this surface that are moved to obtain the MEP. The initial path is consistent with series of structures changed linearly to connect the reactants and products. The forces acting on each image are used in conjunction with optimization techniques to convert the initial path into the MEP connecting the reactant and product structures. Figure reprinted with permission from Caspersen and Carter [146]. Copyright (2005) National Academy of Sciences, USA

on an image i, which has coordinates $\mathbf{r}_i$, is given by $F_i^{\nabla} = -\nabla E_0(\mathbf{r_i})$ and pulls the intermediate images toward the ends of the path. Meanwhile, the spring force is given by $\mathbf{F}_i^s = -\nabla E_s(\mathbf{r}_i)$ where the spring energy, E_s, is given by $E_s = k_s\left[(\mathbf{r}_{i+1} - \mathbf{r}_i)^2 + (\mathbf{r}_i - \mathbf{r}_{i-1})^2\right]$ and k_s is a spring constant.

The elastic band method does not normally find the correct MEP because of two main issues: image sagging and corner cutting. Image sagging arises when the chosen spring constant is too low and results in the images "sliding" down the path toward the reactant and product. Corner cutting arises from the opposite problem, when the spring constant is too high and the path cannot relax enough to minimize to a curved MEP and cuts the corner, frequently giving an energy barrier that is too high. In practice, it is not possible to choose a spring constant that prevents both issues.

The NEB method recognized that the issues with the elastic band technique arose from specific components of the force. The issues with corner cutting arise from components of the force perpendicular to the path, which tend to pull images away from the path. Image sagging can be attributed to components of the true force parallel to the path; the spacing between images becomes uneven to balance out the net force. The simple solution to these issues is to minimize the elastic band with these force components projected out. The NEB force is

$$\mathbf{F}_i^{\mathrm{NEB}} = \mathbf{F}_i^{\nabla\perp} + \mathbf{F}_i^{s||}, \tag{16}$$

where $\mathbf{F}_i^{\nabla\perp} = \mathbf{F}_i^{\nabla} - \left(\mathbf{F}_i^{\nabla} \cdot \hat{\boldsymbol{\tau}}_i\right)\hat{\boldsymbol{\tau}}_i$ is the true force perpendicular to the path and $\mathbf{F}_i^{s||} = k(|\mathbf{r}_{i+1} - \mathbf{r}_i| - |\mathbf{r}_i - \mathbf{r}_{i-1}|)\hat{\boldsymbol{\tau}}_i$ is the spring force parallel to the path, where $\hat{\boldsymbol{\tau}}_i$ is the unit-tangent to the path and $\mathbf{r}_i$ are the Cartesian positions of the atoms in image i. A later modification to the standard NEB, called climbing image NEB [147], allows the highest energy point along the MEP to move along the path to locate the transition state. The force on the climbing image, $\mathbf{F}_i^{CI} = \mathbf{F}_i^{\nabla} - 2\left(\mathbf{F}_i^{\nabla} \cdot \hat{\boldsymbol{\tau}}_i\right)\hat{\boldsymbol{\tau}}_i$, does not include spring forces and points up $\hat{\boldsymbol{\tau}}_i$ toward the direction in which the energy is increasing. The forces acting on the images in this approach are illustrated in Fig. 14.

The NEB method is particularly attractive for optimizing the MEP of a variety of chemical processes for a number of reasons, including (1) it is computationally inexpensive, only requiring evaluation of the potential energy and first derivative of the energy with respect to coordinates, (2) it provides a robust, but flexible convergence to an MEP, and (3) it is inherently parallelizable, making it particularly appealing for modern, highly parallel computer resources.

Unfortunately, as originally presented, the NEB method cannot be used to study mechanochemistry in the bulk, as there is no way to allow the simulation cell to change in response to shear or compression. Trinkle et al. [149, 150] proposed a method that employs the NEB method to optimize the MEP for the atomic coordinates and relaxes the cell vectors using Parrinello–Rahman molecular dynamics

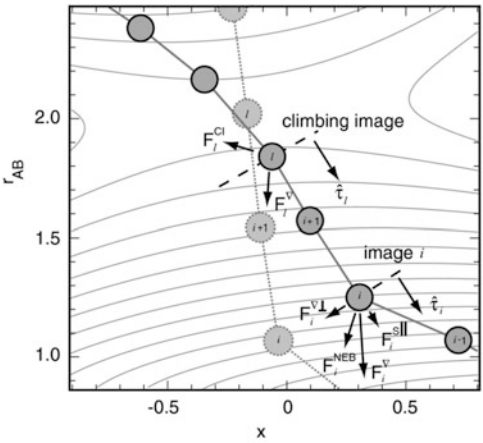

Fig. 14 NEB force projections for a typical image *i* and a climbing image *l*. Reprinted with permission from Sheppard et al. [148]. Copyright 2012, AIP Publishing LLC

techniques [151]. Caspersen and Carter proposed a method that extends the Born–Oppenheimer approximation to assume that the motion of the nuclei is decoupled from the motion of the lattice vectors. They used this concept to relax the nuclear coordinates to a zero force state, and then used the NEB formalism to optimize the cell vectors. These methods ultimately suffer from the same issues that the climbing image NEB was introduced to overcome. Additionally, the motions of the atomic and cell degrees of freedom are not fully decoupled and it has been shown that if these are not coupled properly it can lead to non-physical MEPs [152].

The generalized solid-state NEB (GSSNEB) [148] was developed recently to overcome these problems. This method uses the NEB formalism to optimize simultaneously the atomic coordinates and the simulation cell to the MEP. In the GSSNEB method the strains and stresses associated with the simulations cell are used as analogues of atomic positions and forces. These quantities are incorporated into the calculation by concatenating the strain associated with the cell of a particular image to the changes in atomic positions:

$$\Delta\mathbb{R} = \{J\boldsymbol{\varepsilon}, \Delta\mathbf{r}\}, \tag{17}$$

and the stress, $\boldsymbol{\sigma}$, on an image is similarly concatenated to forces on the atoms:

$$\mathbb{F} = \left\{-\frac{\Omega\boldsymbol{\sigma}}{J}, \mathbf{F}\right\}, \tag{18}$$

where $J = \Omega^{1/3}N^{1/6}$ is a Jacobian introduced to ensure that the stresses and strains have the same units and scale as the forces and positions, respectively, Ω is the volume of the simulation cell, and N is the number of atoms. This method has been used primarily to study phase transitions [148, 153–156] and adsorption/desorption processes [157–159].

3.2 Dynamic Methods

The static methods described above can be used to provide information regarding the changes in structures, energetics, and forces associated with reactions induced through shear and/or compression. However, computational demands typically limit PES scans to examining two dimensions at most, and hence such scans may miss important details of reaction mechanisms that occur along directions that are not scanned. The evaluation of the MEP with techniques such as the GSSNEB approach accounts for the motion of the system along all degrees of freedom as a reaction occurs; however, this method requires a priori knowledge of the reactants and products, and is thus only useful in cases where the reaction to be examined is already known.

MD simulations allow systems to move naturally on the PES and can thus be used to explore known reactions as well as identify new reactions. In order to simulate chemical reactions, i.e., processes involving changes in bonding, it is generally necessary to employ a potential derived from quantum chemical (QC) methods or reactive force fields. These techniques have been used extensively in the context of simulating tribochemical reactions [48, 49]. For instance, Harrison et al. performed a series of studies modeling hydrogen-passivated diamond interfaces using constant strain simulations. In an initial report, they studied the friction behavior of atomically smooth interfaces under various loads and shear rates [160]. Later, they modeled rough interfaces by introducing short alkyl chains to the surface in place of hydrogen atoms [161, 162]. More recently, Harrison used another atomically smooth hydrogen-passivated diamond surface as a model for atomic force microscope tips with different geometries [163]. Luo and coworkers have also used reactive FFs to examine tribochemical processes related to lubrication [164]. Our group has used constant strain conditions to model the friction behavior of hydroxylated alumina surfaces [165, 166] and aldehydes bound to these surfaces [167], as well as aldehydes compressed between these surfaces [168].

As noted above, shear- and compression-induced mechanochemical reactions form a subset of tribochemical reactions, and hence the MD simulation techniques used to study tribochemical processes can be applied to mechanochemical conditions. These techniques involve the introduction of slabs representing surfaces that can be moved relative to one another or placing the system in a simulation cell that is subjected to stresses and/or strains. Techniques for studying stress-induced reactions with MD simulations are described in what follows. Inducing shear stresses by moving surface slabs relative to one another are described in Sect. 3.2.1. The application of shear by subjecting the simulation cell to time-dependent strains is described in Sect. 3.2.2 and the direct application of external stresses to the simulation cell is discussed in Sect. 3.2.3. A comparison of results obtained by subjecting simulations cells to strains and stresses is given in Sect. 4.

In the discussion that follows, we are only looking at ways to impose shear strains and stresses on a simulation cell during molecular dynamics simulations, because this is specifically relevant to mechanochemistry. However, in any MD

simulation, it is important to consider the temperature. The energy introduced via the stress or strains used to induce a mechanochemical reaction are released by the system after the reaction occurs. The release of this energy can lead to large increases in the temperature of the system, which accumulate if not dissipated. Dissipation can be achieved through the use of thermostats; however, the thermostat needs to be applied carefully to ensure the energy is removed from the system in a manner that is consistent with the non-equilibrium nature of these simulations [49].

3.2.1 Relative Movement of Slabs

The PES scans described in Sect. 3.1 involved moving slabs representing surfaces relative to one another to mimic shear and/or compression. Although that section focused on static calculations, this approach can also be used in conjunction with MD simulation methods. In this approach, one constructs a system composed of two slabs that are to be moved relative to one another, which are potentially separated by molecular species that are to be subjected to stresses. A typical example would place lubricant molecules between two surfaces to study lubrication, but this approach can be used in the context of studying other stress-induced processes as well.

Once the system is constructed, stresses are imposed by fixing and/or moving some of the atoms in the system at well-defined positions or velocities. For example, to impose a constant load, L, normal to an interface spanning the x–y plane, the outermost atoms in the slabs representing the interface can be fixed at positions that cause the forces acting along the z direction to equal L. Likewise, shear strains and stresses can be imposed by fixing some of the atoms in the lower slab while moving the atoms in the upper slab along a particular direction. This can be achieved by moving the atoms according to a predetermined velocity profile, e.g., the atoms in the upper slab are moved at a constant velocity, or by attaching some of the atoms in the upper slab to a spring which is moved at a constant velocity and applies forces to the atoms in the upper slab that cause them to move along the slip direction [48, 49]. In both cases, only the uppermost layer or few layers of atoms in the upper slab is/are moved in a predefined manner or is/are affected by the external spring. In this manner, the uppermost layer(s) of atoms act as an external driving force that subjects the interior atoms to stresses without causing the interior atoms to undergo artificial dynamics. The forces acting on the atoms in the system can be monitored to assess the stresses that are experienced by the system and the changes in structure and bonding that occur as a result of these stresses can be observed.

An example of a system consisting of two slabs separated by a fluid is shown in Fig. 15. In this case, a subset of the atoms in the bottom slab is fixed at their equilibrium positions. The atoms in the uppermost portion of the upper slab are fixed in a structure consistent with the equilibrium structure of the material forming the slab to yield a rigid unit. However, unlike the rigid portion of the bottom layer,

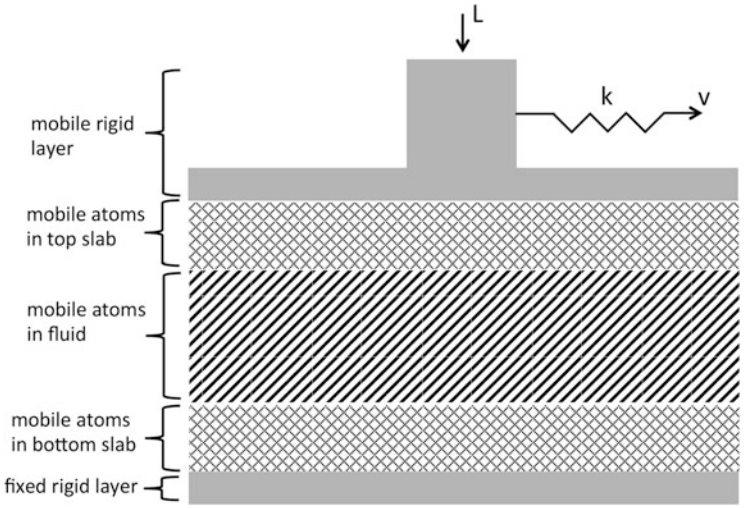

Fig. 15 Schematic of a layered system used to study shear-induced reactions. The system consists of two slabs separated by a fluid. The atoms in the lower portion of the bottom slab, designated 'fixed rigid layer,' are fixed at their equilibrium positions within the material forming the slab. The atoms in the uppermost portion of upper slab, designated 'mobile rigid layer,' are also fixed at relative positions consistent with the equilibrium structure of the material forming the slab. This yields a rigid structure that is moved to subject the rest of the system to shear forces. In this example, this mobile rigid unit is subjected to a compressive load, L, and is attached to a harmonic spring with a force constant, k, with an end that is moved at a constant velocity, v. The change in the length of the spring exerts a force on the mobile rigid unit, which causes it to move. The mobile atoms in *the upper and lower slabs*, as well as those in the fluid, experience a shear force produced by the relative movements of the rigid layers. Shear can also be imposed with similar systems by moving the mobile rigid layer at a constant velocity instead of pulling it with a spring

this portion of the upper layer is subjected to a compressive load, L, and moved laterally by connecting it to a spring with a force constant k that is moved at a constant velocity, v. As the length of the spring changes, the rigid portion of the upper slab is subjected to force that causes it to move as a single unit. The remaining atoms in the system, i.e., those designated the mobile portions of the upper and lower slabs, as well as the fluid, interact with the atoms in the rigid portions of the upper and lower slabs. As such, the relative movement of these rigid regions imposes a shear stress on the interior portion of the system, which can drive reactions.

Techniques in which shear is simulated in MD simulations by moving slabs relative to one another are commonly used in conjunction with force fields. Meanwhile, imposing shear via the relative movement of slabs is not used as commonly in conjunction with QC calculations, particularly planewave DFT calculations, because of the use of periodic simulation cells. If the system consisting of two slabs, and possibly additional molecules between these slabs, is placed in such a cell, the upper portion of the upper slab interacts with the periodic image of the

bottom portion of the bottom slab (and vice versa). If the upper slab is moved along some direction while the bottom slab and the simulation cell itself is held fixed, the interaction between the upper slab and the periodic image of the lower slab introduces an additional interface along which slip occurs. One way to minimize the effects of this additional interface is to use simulation cells that contain large amounts of vacuum space between periodic images along the direction normal to the slabs. Unfortunately, this approach leads to a large increase in the volume of the simulation cell, which in turn increases the number of planewave basis functions needed in the calculation to the point at which computational expense renders these calculations intractable. An alternative approach is to deform the simulation cell in a manner consistent with the motion of the atoms in the slabs to ensure that slip does not occur along the interface between the periodic images. This is most easily achieved by deforming the simulation cell along the desired slip direction and allowing the atoms inside the cell to respond to this deformation, as opposed to moving the atoms directly to impose shear stresses and strains. Techniques for deforming the simulation cell are described in the next section.

3.2.2 Deforming the Simulation Cell

One common approach to compressing and/or shearing systems contained in periodic simulation cells involves deforming the simulation cell itself as indicated in Fig. 11b. Consider a simulation cell defined by the lattice vectors, **a**, **b**, and **c**, where **a** and **b** span the x–y plane. The cell contains a system with two slabs spanning the **a**–**b** plane, which are separated by some material that is to be subjected to compressive and/or shear stresses. In order to impose compressive stresses, one could reduce the z component of the **c** lattice vector at a fixed rate to apply a compressive strain. Similarly, shear can be imposed by moving the x and/or y components of the **c** vector at specific rates along specific directions.

In order for this approach to be effective, it is necessary to ensure that the compressive and/or shear strains to which the simulation cell is subjected are transmitted to the atoms within the cell. Indeed, it is possible in principle to deform the cell in arbitrary ways without altering the positions of the atoms at all and still obtain a perfectly suitable periodically repeated system. To ensure the atoms in the cell move in conjunction with the lattice vectors, it is common practice to represent the atomic positions in fractional coordinates. This approach also ensures that the Lees–Edwards boundary conditions [124] are satisfied to ensure that artificial slip planes are not introduced at the interface between each periodically repeated cell.

The deformation of the cell and its contents leads to changes in the internal stress tensor associated with the system. The internal stresses are in balance with the theoretical external stresses required to induce that deformation of the cell. As such, the internal stresses of the system can be used to ascertain the external stresses experienced by the system, and by correlating these stresses with processes that occur within the system, one can determine the stresses required to induce those processes. This is commonly used, for instance, to determine the stresses needed to

induce slip events, which are directly related to friction forces or the strengths of materials. However, this approach could be used to evaluate the stresses required to promote mechanochemical reactions.

Inducing stresses via deformation of the simulation cell is a conceptually simple approach. However, a few details require careful consideration when using this approach. First, one must consider the rate at which the lattice vectors are deformed. This is ultimately determined by the computational requirements of the simulation method being used. In the case of QC-based MD simulations it is only possible to simulate sub-nanosecond timescales and thus it is often necessary to deform the cell vectors at rates of approximately 1 Å/ps (100 m/s) to induce sufficiently large strains to observe reactions in the accessible timescales. The deformation rates may be decreased by two or three orders of magnitude if the simulations are performed using force fields instead of QC methods, but most force fields are unable to describe changes in bonding, and thus this approach may not be well-suited to studying mechanochemical reactions.

In addition to the rate of cell deformation, the manner in which the cell is deformed also requires consideration. It is common practice to deform the cell linearly, although that may not represent the manner in which a system would move during a stress-induced process. For instance, a system undergoing slip moves very slowly when near its equilibrium configuration and subjected to small shear stresses, whereas it moves quite rapidly during the slip process itself. A linear cell deformation causes the system to move at the same velocities during these two events; effectively, the system moves too fast near the equilibrium state and too slow during slip. This issue is difficult to overcome when using cell deformation to impose stresses unless some a priori information exists regarding the manner in which the cell should be deformed.

An additional aspect that must be considered when deforming the cell in conjunction with planewave DFT calculations stems from the fact that the basis set is dependent upon the size and shape of the cell. In principle, one should regenerate a new set of basis functions every time the cell is changed, although that is neither efficient nor convenient from a computational standpoint. An alternative approach would be to employ a constant set of basis functions throughout the simulation. Unfortunately, the quality of the basis set varies with the deformation of the cell, and thus the results of simulations performed with this approach would only be reliable if very large basis sets were used. A solution to this issue is found in the constant kinetic energy cutoff approach of Bernasconi et al. [169] in which a single set of planewave basis functions is used throughout the simulation while the kinetic energies of those planewaves are adjusted with each change in the size and shape of the simulation cell to ensure the quality of the basis set remains constant throughout the entire simulation.

3.2.3 Subjecting the Simulation Cell to External Stresses

MD simulations in which the cell is deformed treat the changes in the cell vectors as a controlled variable and allow the system to respond to the deformation by exerting a stress on the cell, which can then be correlated with the occurrence of reactive events observed during the simulation. An alternative approach involves subjecting the system to an external stress as indicated in Fig. 11b and allowing shape and size of the simulation cell to respond to this external stress. Once again, events occurring within the cell can be correlated with the external stress, which allows one to determine the stresses required to activate the events.

To allow the simulation cell to respond to an external stress, it is necessary to treat the lattice vectors defining the simulation cell as dynamic variables. This is achieved by assigning a fictitious mass, W, to the lattice vectors and allowing them to move according to Newton's equations of motion using an extended Lagrangian. There are several formulations of this extended Lagrangian approach [151, 170–172], with the Parrinello–Rahman formulation [151] being used most commonly. The extended Lagrangian used in this formulation is

$$L = \frac{1}{2}\sum_{i=1}^{N} m_i \dot{\mathbf{s}}_i \mathbf{G} \dot{\mathbf{s}}_i - V(\mathbf{r}) + \frac{1}{2} W \mathrm{Tr}\left(\dot{\mathbf{h}}^T \dot{\mathbf{h}}\right) - p\Omega, \tag{19}$$

where i runs over all atoms, $\mathbf{h}$ is a matrix containing each lattice vectors as columns, the metric tensor defined as $\mathbf{G} = \mathbf{h}^T\mathbf{h}$, $\mathbf{r}$ represents the Cartesian coordinates of the atoms, and $\mathbf{s}$ represents the atomic positions represented as fractional coordinates of the lattice vectors ($\mathbf{r}_i = \mathbf{h}\mathbf{s}_i$), $V(\mathbf{r})$ is the potential energy, p is the external pressure, and Ω is the volume of the simulation cell. Although devised to study systems at a target external pressure, p, the Parrinello–Rahman method can be used to examine systems that are subjected to pressures that vary over time. This is achieved simply by changing the value of p in a predetermined manner. This approach has been used, for example, to study pressure-induced reactions related to polymerization and lubrication [173–178].

Adjusting p in (19) imposes an isotropic hydrostatic pressure on the system. However, in the context of mechanochemistry it would be more useful to examine shear and compressive stresses. This can be achieved by generalizing the Lagrangian in (19) to allow the system to maintain a target stress tensor, $\mathbf{S}$, as opposed to a pressure. The form of the generalized Lagrangian is

$$L = \frac{1}{2}\sum_{i=1}^{N} m_i \dot{\mathbf{s}}_i \mathbf{G} \dot{\mathbf{s}}_i - V(\mathbf{r}) + \frac{1}{2} W \mathrm{Tr}\left(\dot{\mathbf{h}}^T \dot{\mathbf{h}}\right) - p\Omega - \frac{1}{2} Tr(\boldsymbol{\Sigma}\mathbf{G}), \tag{20}$$

where $\Sigma = \mathbf{h}_0^{-1}(\mathbf{S} - p\mathbf{I})\mathbf{h}_0^{T-1}\Omega_0$, $\mathbf{h}_0$ is a reference matrix that is required to define strains, and Ω_0 is the volume of that reference cell. For a given cell, $\mathbf{h}$, the components of the strain tensor are defined as

$$\boldsymbol{\varepsilon} = \frac{1}{2}\left(\mathbf{h}_0^{T-1}\mathbf{h}^T\mathbf{h}\mathbf{h}_0^{-1} - 1\right), \tag{21}$$

and it follows that the elastic energy is given by

$$V_{el} = p(\Omega - \Omega_0) + \Omega_0 \mathrm{Tr}(\mathbf{S} - p\mathbf{I})\boldsymbol{\varepsilon}. \tag{22}$$

By analogy to the constant pressure formulation of the Parrinello–Rahman method, this extended Lagrangian can be used in conjunction with varying external stresses by changing the components of **S** in a proscribed manner during the simulation. In addition, this approach can be combined with methods that deform the simulation cell to impose shear strains. Indeed, our group has used this approach extensively to study various processes related to friction and tribochemistry, with the Parrinello–Rahman method being used to maintain a constant normal load, and cell deformations being used to impose shear strains [165–168].

Subjecting systems directly to external stresses, as opposed to strains, is advantageous in terms of determining the stress at which a reaction occurs. For instance, if the time at which a reaction occurs during the simulation is known along with the manner in which the external stress is varied over time, it is quite straightforward to determine the external stresses associated with reactive events. By contrast, subjecting the system to proscribed shear strains requires one to determine the stress required to activate a reaction from the internal stress tensor, which tends to oscillate during simulations, leading to errors in the estimated shear stresses.

The application of external stresses allows the size and shape of the simulation cell to change as needed to accommodate the applied stress, which overcomes the linear deformation of the simulation cell that was a drawback associated with applying linearly increasing strains. For instance, a linearly increasing shear strain causes the system to move at a constant speed along a particular direction. Meanwhile, allowing the system to move in response to a linearly increasing shear stress allows the system to navigate better the lowest energy path on the PES and move at different rates during various stages of the shear/slip process.

The method has the disadvantage that the applied stress continues linearly even after slip has been achieved (assuming the stress was being varied in a linear manner). As such, there is a significant imbalance between the external and internal stresses once the system moves to a new local minimum on the PES after slip occurs. One must also be careful in determining the manner in which shear is imposed. Generally, this is achieved by increasing the external stress linearly along the slip direction, although other means of varying the external stress may be needed to represent different types of experimental conditions. In addition, consideration must be made with respect to the rate at which stresses are varied. In general, this is limited by the timescales accessible in the MD simulations. If QC-based methods are used, it may be necessary to change the stresses at rates of 1–10 GPa/ps, whereas rates two to three orders of magnitude slower may be possible if force fields are used. Finally, one must still employ an approach such as that of Bernasconi et al. [169] to maintain a consistent quality of basis set when changing

the shape and/or size of the simulation cell via external stresses when the MD simulations are performed with planewave DFT.

3.2.4 Comparison of Dynamic Methods Involving Deformation of the Simulation Cell

As discussed above, shear-induced processes can be examined with MD simulations by deforming simulation cells in either of two ways. In the first case, one applies a strain along the slip directions, which increases the system's internal stress until a reaction occurs. In the second case, the system is exposed to an external shear stress and the simulation cells change in order to accommodate this stress. These two methods are similar to the constrained distance and EFEI methods described above in the sense that one method involves controlling changes in structure whereas the other involves controlling changes in forces. As such, one may anticipate differences in the outcomes of simulations performed in which the cells are deformed via strains or stresses. To provide some insight into the results obtained with these two different approaches, AIMD simulations were performed in which bulk alumina (Al_2O_3) was sheared along the $[21\bar{3}0]/(0001)$ direction and plane according to these protocols until slip occurred using a version of the Quantum-Espresso simulation package that was modified to apply stresses and strains that varied over time [179]. The calculations were performed using planewave DFT with the PBE exchange-correlation functional [180], valence electrons expanded to a kinetic energy cutoff of 80 Ry, and core electrons represented by norm-conserving pseudopotentials [181]. The results of these simulations are summarized in Fig. 16, which shows how the stresses and cell change during these simulations.

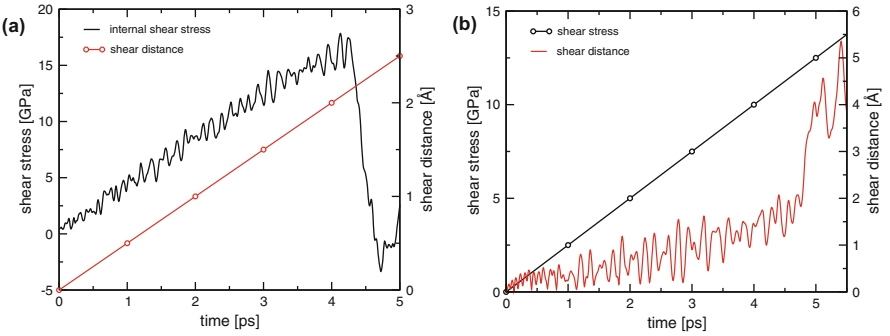

Fig. 16 Shear stress and shear distance vs time for AIMD simulations of bulk alumina shear to induce slip along the $[21\bar{3}0]/(0001)$ direction and plane (**a**) moving the *x* and *y* components of the **c** vector along the slip direction at a rate of 0.5 Å/ps or (**b**) by increasing the external stress applied along the slip direction at a rate of 2.5 GPa/ps

The data in Fig. 16a were obtained using a procedure in which the x and y components of the **c** vector of bulk alumina were varied to move the uppermost portion of the simulation cell along the slip direction at a rate of 0.5 Å/ps. The data in this figure illustrated that the internal stress of the system increases in a relatively linear manner until dropping rapidly at a time of ~4.2 ps. The drop in the internal stress is consistent with the occurrence of a slip event and shear stress reached when slip occurred corresponds to the shear strength of the system, which is in the range of 15–17 GPa according to the data in this figure. The distance the cell is moved along the slip direction is also shown as a function of time. As illustrated in the figure, this distance increases linearly at the proscribed rate of 0.5 Å/ps during all portions of the simulation. As discussed above, this is problematic as the system should likely move at different rates during the shear/slip process, with the system moving slowly during the shearing phase and rapidly during slip as it moves past the slip barrier to the next energy minimum along the slip direction.

The data in Fig. 16b were obtained by subjecting the simulation cell to an external stress that increased at a rate of 2.5 GPa/ps. The data in the figure illustrate how far the end of the **c** lattice vector has moved from its equilibrium position over time in order to accommodate the applied stress. It should be noted that this movement is not restricted to occur exactly along the slip direction, as is required in the fixed strain calculations, but rather the motion of the **c** vector is unrestricted. The data show that the shear distance increases in a relatively linear manner at a rate of ~0.4 Å/ps until a time of ~4.8 ps is reached at which point the shear distance increases rapidly. This rapid increase is correlated with the slip event, and the change in the rate at which the shear distance increases illustrates that the system should move at different rates in the shear and slip phases. The data in the figure also show that the external shear stress increases linearly during the simulation and the external stress at the point where slip occurs corresponds to the shear strength, which in this case is ~12.5 GPa. The applied stress continues to increase after slip occurs, which results in an increase in the rate at which the shear distance increases which is not consistent with the system moving into an energy minimum along the slip direction.

Overall, the data in Fig. 16 illustrate the ways these two different approaches to changing the simulation cell can be used to determine the shear stresses associated with reactive events, which in this case correspond to slip events. In both cases it is straightforward to determine the points at which slip events occur. The use of applied strains has the advantage in terms of selecting the rate at which the strain changes, because this quantity can be related to the velocity of sliding surfaces. Meanwhile, it is more difficult to define the rate at which the shear stress is increased in a meaningful manner. The values of the shear strengths obtained in the simulations performed with these methods differ by several GPa. This can be related partially to the restricted movement of the cell associated with applied strains, which limits the ability of the system to accommodate applied loads. Both methods have deficiencies in the manner in which the cell is deformed after

slip occurs; however, it may be possible to address these issues by reducing the rates at which shear stresses or strains are applied after a slip event occurs.

4 Concluding Remarks

In this review, we have described techniques that can be used to simulate chemical reactions in molecular and bulk systems that occur under mechanochemical conditions. Techniques for modeling molecular mechanochemistry focus on incorporating into the PES the work performed on a molecule that is subjected to an external force applied between two regions in the molecule. These techniques have been used extensively and are well developed, with models existing that are appropriate for qualitative predictions and interpretations, as well as for modeling isometric and isotensional conditions. The discussion of methods for simulating bulk mechanochemical processes focused on techniques that have been used to study tribochemical processes. These techniques focus on studying systems that are subjected to compressive and shear stresses, and are transferable to mechanochemistry. Interestingly, bulk mechanochemical processes have not been studied with simulations nearly as extensively as their molecular counterparts. As such, the application of techniques used to study tribochemical processes to the specific area of bulk mechanochemistry may be a promising avenue for future research.

Acknowledgements Financial support from the Natural Sciences and Engineering Research Council of Canada's Discovery Grant Program is acknowledged. GSK is grateful for support from the Ontario Graduate Scholarship program.

References

1. Ribas-Arino J, Marx D (2012) Covalent mechanochemistry: theoretical concepts and computational tools with applications to molecular nanomechanics. Chem Rev 112:5412–5487
2. Beyer MK, Clausen-Schaumann H (2005) Mechanochemistry: the mechanical activation of covalent bonds. Chem Rev 105:2921–2948
3. James SL, Adams CJ, Bolm C et al (2012) Mechanochemistry: opportunities for new and cleaner synthesis. Chem Soc Rev 41(1):413–447
4. Rosen BM, Percec V (2007) Mechanochemistry: a reaction to stress. Nature 446:381–382
5. Seidel CAM, Kühnemuth R (2014) Mechanochemistry: molecules under pressure. Nat Nanotechnol 9:164–165
6. Black AL, Lenhardt JM, Craig SL (2011) From molecular mechanochemistry to stress-responsive materials. J Mater Chem 21:1655–1663
7. Kreuzer HJ, Payne SH, Livadaru L (2001) Stretching a macromolecule in an atomic force microscope: statistical mechanical analysis. Biophys J 80:2505–2514
8. Kersey FR, Yount WC, Craig SL, Carolina N (2006) Single-molecule force spectroscopy of bimolecular reactions: system homology in the mechanical activation of ligand substitution reactions. J Am Chem Soc 128:3886–3887

9. Duwez A-S, Cuenot S, Jérôme C, Gabriel S, Jérôme R, Rapino S, Zerbetto F (2006) Mechanochemistry: targeted delivery of single molecules. Nat Nanotechnol 1:122–125
10. Wang MD, Yin H, Landick R, Gelles J, Block SM (1997) Stretching DNA with optical tweezers. Biophys J 72:1335–1346
11. Ashkin A, Dziedzic JM, Bjorkholm JE, Chu S (1986) Observation of a single-beam gradient force optical trap for dielectric particles. Opt Lett 11:288–290
12. Moffitt JR, Chemla YR, Smith SB, Bustamante C (2008) Recent advances in optical tweezers. Annu Rev Biochem 77:205–228
13. Grier DG (2003) A revolution in optical manipulation. Nature 424:810–816
14. Yang Q-Z, Huang Z, Kucharski TJ, Khvostichenko D, Chen J, Boulatov R (2009) A molecular force probe. Nat Nanotechnol 4:302–306
15. Lundbæk JA, Collingwood SA (2010) Lipid bilayer regulation of membrane protein function: gramicidin channels as molecular force probes. J R Soc Interface 7:373–395
16. Suslick KS (2004) Sonochemistry. Compr Coord Chem II 1:731–739
17. Basedow AM, Ebert KH (1977) Ultrasonic degradation of polymers in solution. Adv Polym Sci 22:83–148
18. Thompson LH, Doraiswamy LK (1999) Sonochemistry: science and engineering. Ind Eng Chem Res 38:1215–1249
19. Hickenboth CR, Moore JS, White SR, Sottos NR, Baudry J, Wilson SR (2007) Biasing reaction pathways with mechanical force. Nature 446:423–427
20. James SL, Friščić T (2013) Mechanochemistry. Chem Soc Rev 42:7494–7496
21. Friščić T, Halasz I, Beldon PJ, Belenguer AM, Adams F, Kimber SAJ, Honkimäki V, Dinnebier RE (2013) Real-time and in situ monitoring of mechanochemical milling reactions. Nat Chem 5:66–73
22. Christinat N, To J, Schu C, Scopelliti R, Severin K (2009) Synthesis of molecular nanostructures by multicomponent condensation reactions in a ball mill. J Am Chem Soc 131:3154–3155
23. Cravotto G, Cintas P (2010) Reconfiguration of stereoisomers under sonomechanical activation. Angew Chem Int Ed Engl 49:6028–6030
24. Lu H, Isralewitz B, Krammer A, Vogel V, Schulten K (1998) Unfolding of titin immunoglobulin domains by steered molecular dynamics simulation. Biophys J 75:662–671
25. Oberhauser AF, Hansma PK, Carrion-Vazquez M, Fernandez JM (2001) Stepwise unfolding of titin under force-clamp atomic force microscopy. Proc Natl Acad Sci 98:468–472
26. Fowler SB, Best RB, Toca Herrera JL, Rutherford TJ, Steward A, Paci E, Karplus M, Clarke J (2002) Mechanical unfolding of a Titin Ig domain: structure of unfolding intermediate revealed by combining AFM, molecular dynamics simulations, NMR and protein engineering. J Mol Biol 322:841–849
27. Rief M, Gautel M, Oesterhelt F, Fernandez JM, Gaub E, Gaub HE (1997) Reversible unfolding of individual Titin immunoglobulin domains by AFM. Science 276:1109–1112
28. Weder C (2009) Polymers react to stress. Nature 459:45–46
29. Kochhar GS, Bailey A, Mosey NJ (2010) Competition between orbitals and stress in mechanochemistry. Angew Chem Int Ed Engl 49:7452–7455
30. Ong MT, Leiding J, Tao H, Virshup AM, Martinez TJ (2009) First principles dynamics and minimum energy pathways for mechanochemical ring opening of cyclobutene. J Am Chem Soc 131:6377–6379
31. Ribas-Arino J, Shiga M, Marx D (2009) Understanding covalent mechanochemistry. Angew Chem Int Ed Engl 48:4190–4193
32. Beyer MK (2000) The mechanical strength of a covalent bond calculated by density functional theory. J Chem Phys 112:7307–7312
33. Friedrichs J, Lüssmann M, Frank I (2010) Conservation of orbital symmetry can be circumvented in mechanically induced reactions. Chemphyschem 11:3339–3342
34. Ribas-Arino J, Shiga M, Marx D (2009) Unravelling the mechanism of force-induced ring-opening of benzocyclobutenes. Chem Eur J 15:13331–13335

35. Makarov DE, Wang Z, Thompson JB, Hansma HG (2002) On the interpretation of force extension curves of single protein molecules. J Chem Phys 116:7760–7765
36. Konda SSM, Avdoshenko SM, Makarov DE (2014) Exploring the topography of the stress-modified energy landscapes of mechanosensitive molecules. J Chem Phys 140:104114
37. Bailey A, Mosey NJ (2012) Prediction of reaction barriers and force-induced instabilities under mechanochemical conditions with an approximate model: a case study of the ring opening of 1,3-cyclohexadiene. J Chem Phys 136:044102
38. Beyer MK (2003) Coupling of mechanical and chemical energy: proton affinity as a function of external force. Angew Chem Int Ed Engl 42:4913–4915
39. Lupton EM, Achenbach F, Weis J, Bräuchle C, Frank I (2006) Modified chemistry of siloxanes under tensile stress: interaction with environment. J Phys Chem B 110: 14557–14563
40. Lupton EM, Nonnenberg C, Frank I, Achenbach F, Weis J, Bräuchle C (2005) Stretching siloxanes: an ab initio molecular dynamics study. Chem Phys Lett 414:132–137
41. Aktah D, Frank I (2002) Breaking bonds by mechanical stress: when do electrons decide for the other side? J Am Chem Soc 124:3402–3406
42. Lenhardt JM, Ong MT, Choe R, Evenhuis CR, Martinez TJ, Craig SL (2010) Trapping a diradical transition state by mechanochemical polymer extension. Science 329:1057–1060
43. Lenhardt JM, Ogle JW, Ong MT, Choe R, Martinez TJ, Craig SL (2011) Reactive cross-talk between adjacent tension-trapped transition states. J Am Chem Soc 133:3222–3225
44. Kryger MJ, Ong MT, Odom SA, Sottos NR, White SR, Martinez TJ, Moore JS (2010) Masked cyanoacrylates unveiled by mechanical force. J Am Chem Soc 132:4558–4559
45. Konôpka M, Turanský R, Reichert J, Fuchs H, Marx D, Štich I (2008) Mechanochemistry and thermochemistry are different: stress-induced strengthening of chemical bonds. Phys Rev Lett 100:115503
46. Dopieralski P, Anjukandi P, Rückert M, Shiga M, Ribas-Arino J, Marx D (2011) On the role of polymer chains in transducing external mechanical forces to benzocyclobutene mechanophores. J Mater Chem 21:8309–8316
47. Ribas-arino J, Shiga M, Marx D (2010) Mechanochemical transduction of externally applied forces to mechanophores. J Am Chem Soc 132:10609–10614
48. Harrison JA, Gao G, Schall JD, Knippenberg MT, Mikulski PT (2008) Friction between solids. Philos Trans R Socient A 366:1469–1495
49. Mosey NJ, Muser M (2007) Atomistic modeling of friction. In: Lipkowitz KB, Larter R, Cundari TR (eds) Reviews in computational chemistry, 25th ed. Wiley-VCH, New York, pp 67–124
50. Schlierf M, Li H, Fernandez JM (2004) The unfolding kinetics of ubiquitin captured with single-molecule force-clamp techniques. Proc Natl Acad Sci USA 101:7299–7304
51. Fernandez JM, Li H (2004) Force-clamp spectroscopy monitors the folding trajectory of a single protein. Science 303:1674–1678
52. Potisek SL, Davis DA, Sottos NR, White SR, Moore JS (2007) Mechanophore-linked addition polymers. J Am Chem Soc 129:13808–13809
53. Grandbois M, Beyer M, Rief M, Clausen-Schaumann H, Gaub HE (1999) How strong is a covalent bond? Science 283:1727–1730
54. Freitas A, Sharma M (2001) Detachment of particles from surfaces: an AFM study. J Colloid Interface Sci 233:73–82
55. Iozzi MF, Helgaker T, Uggerud E (2009) Assessment of theoretical methods for the determination of the mechanochemical strength of covalent bonds. Mol Phys 107:2537–2546
56. Su T, Purohit PK (2009) Mechanics of forced unfolding of proteins. Acta Biomater 5:1855–1863
57. Ikai A, Alimujiang Y (2001) Force–extension curves of dimerized polyglutamic acid. Appl Phys A 120:117–120
58. Davis DA, Hamilton A, Yang J et al (2009) Force-induced activation of covalent bonds in mechanoresponsive polymeric materials. Nature 459:68–72

59. Zemanová M, Bleha T (2005) Isometric and isotensional force-length profiles in polymethylene chains. Macromol Theory Simulations 14:596–604
60. Keller D, Swigon D, Bustamante C (2003) Relating single-molecule measurements to thermodynamics. Biophys J 84:733–738
61. Paulusse JMJ, Sijbesma RP (2004) Reversible mechanochemistry of a Pd(II) coordination polymer. Angew Chem Int Ed Engl 43:4460–4462
62. Karthikeyan S, Potisek SL, Piermattei A, Sijbesma RP (2008) Highly efficient mechanochemical scission of silver-carbene coordination polymers. J Am Chem Soc 130: 14968–14969
63. Piermattei A, Karthikeyan S, Sijbesma RP (2009) Activating catalysts with mechanical force. Nat Chem 1:133–137
64. Izailev S, Stepaniants S et al (1999) Steered molecular dynamics. In: Deuflhard P, Hermans J, Leimkuhler B, Mark AE, Reich S, Skeel RD (eds) Computational molecular dynamics: challenges, methods, ideas, vol 4. Springer, New York, pp 39–65
65. Izrailev S, Stepaniants S, Balsera M, Oono Y, Schulten K (1997) Molecular dynamics study of unbinding of the avidin-biotin complex. Biophys J 72:1568–1581
66. Grubmuiller H, Heymann B, Tavan P (1996) Ligand binding: molecular mechanics calculation of the streptavidin-biotin rupture force. Science 271:997–999
67. Isralewitz B, Baudry J, Gullingsrud J, Kosztin D, Schulten K (2001) Steered molecular dynamics investigations of protein function. J Mol Graph Model 19:13–25
68. Isralewitz B, Gao M, Schulten K (2001) Steered molecular dynamics and mechanical functions of proteins. Curr Opin Struct Biol 11:224–230
69. Stepaniants S, Izrailev S, Schulten K (1997) Extraction of lipids from phospholipid membranes by steered molecular dynamics. J Mol Model 3:473–475
70. Silberstein MN, Cremar LD, Beiermann BA, Kramer SB, Martinez TJ, White SR, Sottos NR (2014) Modeling mechanophore activation within a viscous rubbery network. J Mech Phys Solids 63:141–153
71. Diesendruck CE, Peterson GI, Kulik HJ, Kaitz JA, Mar BD, May PA, White SR, Martínez TJ, Boydston AJ, Moore JS (2014) Mechanically triggered heterolytic unzipping of a low-ceiling-temperature polymer. Nat Chem 6:623–628
72. Franco I, George CB, Solomon GC, Schatz GC, Ratner MA (2011) Mechanically activated molecular switch through single-molecule pulling. J Am Chem Soc 133:2242–2249
73. Franco I, Schatz GC, Ratner MA (2009) Single-molecule pulling and the folding of donor-acceptor oligorotaxanes: phenomenology and interpretation. J Chem Phys 131:124902
74. Paturej J, Kuban L, Milchev A, Vilgis TA (2012) Tension enhancement in branched macromolecules upon adhesion on a solid substrate. Europhys Lett 97:58003
75. Ghosh A, Dimitrov DI, Rostiashvili VG, Milchev A, Vilgis TA (2010) Thermal breakage and self-healing of a polymer chain under tensile stress. J Chem Phys 132:204902
76. Paturej J, Milchev A, Rostiashvili VG, Vilgis TA (2011) Polymer chain scission at constant tension – an example of force-induced collective behaviour. Europhys Lett 94:48003
77. Paturej J, Dubbeldam JLA, Rostiashvili VG, Milchev A, Vilgis TA (2014) Force spectroscopy of polymer desorption: theory and molecular dynamics simulation. Soft Matter 10: 2785–2799
78. Wiita AP, Perez-Jimenez R, Walther KA, Gräter F, Berne BJ, Holmgren A, Sanchez-Ruiz JM, Fernandez JM (2007) Probing the chemistry of thioredoxin catalysis with force. Nature 450:124–127
79. Li W, Gräter F (2010) Atomistic evidence of how force dynamically regulates thiol/disulfide exchange. J Am Chem Soc 132:16790–16795
80. Baldus IB, Gräter F (2012) Mechanical force can fine-tune redox potentials of disulfide bonds. Biophys J 102:622–629
81. Ryckaert J-P, Ciccotti G, Berendsen HJ (1977) Numerical integration of the Cartesian equations of motion of a system with constraints: molecular dynamics of n-alkanes. J Comput Phys 23:327–341

82. Smalø HS, Uggerud E (2013) Breaking covalent bonds using mechanical force, which bond breaks? Mol Phys 111:1563–1573
83. Smalø HS, Uggerud E (2012) Ring opening vs. direct bond scission of the chain in polymeric triazoles under the influence of an external force. Chem Comm 48:10443–10445
84. Kryger MJ, Munaretto AM, Moore S (2011) Structure-mechanochemical activity relationships for cyclobutane mechanophores. J Am Chem Soc 133:18992–18998
85. Lourderaj U, McAfee JL, Hase WL (2008) Potential energy surface and unimolecular dynamics of stretched n-butane. J Chem Phys 129:094701
86. Schmidt SW, Beyer MK, Clausen-Schaumann H (2008) Dynamic strength of the silicon-carbon bond observed over three decades of force-loading rates. J Am Chem Soc 130: 3664–3668
87. Iozzi MF, Helgaker T, Uggerud E (2011) Influence of external force on properties and reactivity of disulfide bonds. J Phys Chem A 115:2308–3215
88. Groote R, Szyja M, Pidko EA, Hensen EJM, Sijbesma RP (2011) Unfolding and mechanochemical scission of supramolecular polymers containing a metal-ligand coordination bond. Macromolecules 44:9187–9195
89. Shiraki T, Diesendruck CE, Moore JS (2014) The mechanochemical production of phenyl cations through heterolytic bond scission. Faraday Discuss. doi:10.1039/C4FD00027G
90. Krüger D, Rousseau R, Fuchs H, Marx D (2003) Towards "mechanochemistry": mechanically induced isomerizations of thiolate-gold clusters. Angew Chem Int Ed Engl 42: 2251–2253
91. Huang Z, Yang Q, Khvostichenko D, Kucharski TJ, Chen J, Boulatov R (2009) Method to derive restoring forces of strained molecules from kinetic measurements. J Am Chem Soc 131:1407–1409
92. Kucharski TJ, Yang Q-Z, Tian Y, Boulatov R (2010) Strain-dependent acceleration of a paradigmatic S_N2 reaction accurately predicted by the force formalism. J Phys Chem Lett 1:2820–2825
93. Kucharski TJ, Huang Z, Yang Q-Z, Tian Y, Rubin NC, Concepcion CD, Boulatov R (2009) Kinetics of thiol/disulfide exchange correlate weakly with the restoring force in the disulfide moiety. Angew Chemie 121:7174–7177
94. Akbulatov S, Tian Y, Kapustin E, Boulatov R (2013) Model studies of the kinetics of ester hydrolysis under stretching force. Angew Chem Int Ed Engl 52:6992–6995
95. Akbulatov S, Tian Y, Boulatov R (2012) Force−reactivity property of a single monomer is sufficient to predict the micromechanical behavior of its polymer. J Am Chem Soc 134: 7620–7623
96. Tian Y, Kucharski TJ, Yang Q-Z, Boulatov R (2013) Model studies of force-dependent kinetics of multi-barrier reactions. Nat Commun 4:2538
97. Kucharski TJ, Boulatov R (2011) The physical chemistry of mechanoresponsive polymers. J Mater Chem 21:8237–8255
98. Hermes M, Boulatov R (2011) The entropic and enthalpic contributions to force-dependent dissociation kinetics of the pyrophosphate bond. J Am Chem Soc 133(50):20044–20047
99. Car R, Parrinello M (1985) Unified approach for molecular dynamics and density-functional theory. Phys Rev Lett 55:2471–2474
100. Hofbauer F, Frank I (2010) Disulfide bond cleavage: a redox reaction without electron transfer. Chem Eur J 16:5097–5101
101. Hofbauer F, Frank I (2012) CPMD simulation of a bimolecular chemical reaction: nucleophilic attack of a disulfide bond under mechanical stress. Chem Eur J 18:16332–16338
102. Krupička M, Sander W, Marx D (2014) Mechanical manipulation of chemical reactions: reactivity switching of Bergman cyclizations. J Phys Chem Lett 5:905–909
103. Stauch T, Dreuw A (2014) Force-spectrum relations for molecular optical force probes. Angew Chem Int Ed Engl 53:2759–2761
104. Smalø HS, Rybkin VV, Klopper W, Helgaker T, Uggerud E (2014) Mechanochemistry: the effect of dynamics. J Phys Chem A 118:7683–7694

105. Schmidt M, Baldridge K (1993) General atomic and molecular electronic structure system. J Comput Chem 14:1347–1363
106. Frisch MJ, Trucks GW, Schlegel HB, Scuseria GE, Robb MA, Cheeseman JR, Scalmani G, Barone V, Mennucci B, Petersson GA, Nakatsuji H, Caricato M, Li X, Hratchian HP, Izmaylov AF, Bloino J, Zheng G, Sonnenberg JL, Hada M, Ehara M, Toyota K, Fukuda R, Hasegawa J, Ishida M, Nakajima T, Honda Y, Kitao O, Nakai H, Vreven T, Montgomery JA Jr, Peralta JE, Ogliaro F, Bearpark M, Heyd JJ, Brothers E, Kudin KN, Staroverov VN, Keith T, Kobayashi R, Normand J, Raghavachari K, Rendell A, Burant JC, Iyengar SS, Tomasi J, Cossi M, Rega N, Millam JM, Klene M, Knox JE, Cross JB, Bakken V, Adamo C, Jaramillo J, Gomperts R, Stratmann RE, Yazyev O, Austin AJ, Cammi R, Pomelli C, Ochterski JW, Martin RL, Morokuma K, Zakrzewski VG, Voth GA, Salvador P, Dannenberg JJ, Dapprich S, Daniels AD, Farkas O, Foresman JB, Ortiz JV, Cioslowski J, Fox DJ (2009) Gaussian 09, revision D.01. Gaussian, Wallingford
107. Kauzmann W, Eyring H (1940) The viscous flow of large molecules. J Am Chem Soc 62: 3113–3125
108. Bell G (1978) Models for the specific adhesion of cells to cells. Science 200:618–627
109. Dopieralski P, Ribas-Arino J, Anjukandi P, Krupicka M, Kiss J, Marx D (2013) The Janus-faced role of external forces in mechanochemical disulfide bond cleavage. Nat Chem 5: 685–691
110. Lele TP, Thodeti CK, Ingber DE (2006) Force meets chemistry: analysis of mechanochemical conversion in focal adhesions using fluorescence recovery after photobleaching. J Cell Biochem 97:1175–1183
111. Greenberg MJ, Moore JR (2010) The molecular basis of frictional loads in the in vitro motility assay with applications to the study of the loaded mechanochemistry of molecular motors. Cytoskeleton 67:273–285
112. Bustamante C, Chemla YR, Forde NR, Izhaky D (2004) Mechanical processes in biochemistry. Annu Rev Biochem 73:705–748
113. Evans E, Ritchie K (1997) Dynamic strength of molecular adhesion bonds. Biophys J 72(4): 1541–1555
114. Evans E (2001) Probing the relation between force-lifetime and chemistry. Annu Rev Biophys Biomol Struct 30:105–128
115. Konda SSM, Brantley JN, Bielawski CW, Makarov DE (2011) Chemical reactions modulated by mechanical stress: extended Bell theory. J Chem Phys 135:164103
116. Konda SSM, Brantley JN, Varghese BT, Wiggins KM, Bielawski CW, Makarov DE (2013) Molecular catch bonds and the anti-Hammond effect in polymer mechanochemistry. J Am Chem Soc 135:12722–12729
117. Brantley JN, Konda SSM, Makarov DE, Bielawski CW (2012) Regiochemical effects on molecular stability: a mechanochemical evaluation of 1,4- and 1,5-disubstituted triazoles. J Am Chem Soc 134:9882–9885
118. Tian Y, Boulatov R (2013) Comparison of the predictive performance of the Bell-Evans, Taylor-expansion and statistical-mechanics models of mechanochemistry. Chem Comm 49: 4187–4189
119. Hsu SM, Zhang J, Yin Z (2002) The nature and origin of tribochemistry. Tribol Lett 13: 131–139
120. Kajdas C (2013) General approach to mechanochemistry and its relations to tribochemistry. In: Pihtili H (ed) Tribology in engineering. InTech, pp 209–240
121. Liang T, Sawyer WG, Perry SS, Sinnott SB, Phillpot SR (2008) First-principles determination of static potential energy surfaces for atomic friction in MoS_2 and MoO_3. Phys Rev B 77: 104105
122. Smith GS, Modine NA, Waghmare UV, Kaxiras E (1998) First-principles study of static nanoscale friction between MoO_3. J Comput Mater Des 5:61–71
123. Modine NA, Zumbach G, Kaxiras E (1997) Adaptive-coordinate real-space electronic structure calculations for atoms, molecules, and solids. Phys Rev B 55:10289

124. Lees AW, Edwards SF (1972) The computer study of transport processes under extreme conditions. J Phys C Solid State Phys 5:1921–1929
125. Zilibotti G, Righi MC (2011) Ab initio calculation of the adhesion and ideal shear strength of planar diamond interfaces with different atomic structure and hydrogen coverage. Langmuir 27:6862–6867
126. Wang J, Want F, Li J, Sun Q, Yuan P, Jia Y (2013) Comparative study of friction properties for hydrogen- and fluorine-modified diamond surfaces: a first-principles investigation. Surf Sci 608:74–79
127. Wang L-F, Ma T-B, Hu Y-Z, Wang H (2012) Atomic-scale friction in graphene oxide: an interfacial interaction perspective from first-principles calculations. Phys Rev B 86:125436
128. Wang L-F, Ma T-B, Hu Y-Z, Wang H, Shao T-M (2013) Ab initio study of the friction mechanism of fluorographene and graphane. J Phys Chem C 117:12520–12525
129. Leven I, Krepel D, Shemesh O, Hod O (2013) Robust superlubricity in graphene/h-BN heterojunctions. J Phys Chem Lett 4:115–120
130. Hod O (2013) The registry index: a quantitative measure of materials' interfacial commensurability. ChemPhysChem 14:2376–2391
131. Zhong W, Tománek D (1990) First-principles theory of atomic-scale friction. Phys Rev Lett 64:3054–3057
132. Neitola R, Pakkanen TA (2001) Ab initio studies on the atomic-scale origin of friction between diamond (111) surfaces. J Phys Chem B 105:1338–1343
133. Koskilinna JO, Linnolahti M, Pakkanen TA (2005) Tribochemical reactions between methylated diamond (111) surfaces: a theoretical study. Tribol Lett 20:157–161
134. Neitola R, Pakkanen TA (2006) Ab initio studies on nanoscale friction between fluorinated diamond surfaces: effect of model size and level of theory. J Phys Chem B 110:16660–16665
135. Neitola R, Pakkanen TA (2004) Ab initio studies on the atomic-scale origin of friction between hydrocarbon layers. Chem Phys 299:47–56
136. Neitola R, Ruuska H, Pakkanen TA (2005) Ab initio studies on nanoscale friction between graphite layers: effect of model size and level of theory. J Phys Chem B 109:10348–10354
137. Koskilinna JO, Linnolahti M, Pakkanen TA (2007) Friction paths for cubic boron nitride: an ab initio study. Tribol Lett 27:145–154
138. Koskilinna JO, Linnolahti M, Pakkanen TA (2008) Friction and a tribochemical reaction between ice and hexagonal boron nitride: a theoretical study. Tribol Lett 29:163–167
139. Ogata S, Li J, Hirosaki N, Shibutani Y, Yip S (2004) Ideal shear strain of metals and ceramics. Phys Rev B 70:104104
140. Liao P, Carter EA (2010) Ab initio density functional theory+U predictions of the shear response of iron oxides. Acta Mater 58:5912–5925
141. Mosey NJ, Liao P, Carter EA (2008) Rotationally invariant ab initio evaluation of Coulomb and exchange parameters for DFT+U calculations. J Chem Phys 129:014103
142. Mosey NJ, Carter EA (2009) Shear strength of chromia across multiple length scales: An LDA+U study. Acta Mater 57:2933–2943
143. Mills G, Jónsson H (1994) Quantum and thermal effects in H_2 dissociative adsorption: evaluation of free energy barriers in multidimensional quantum systems. Phys Rev Lett 72: 1124–1127
144. Mills G, Jónsson H, Schenter G (1995) Reversible work transition state theory: application to dissociative adsorption of hydrogen. Surf Sci 324:305–337
145. Jónsson H, Mills G, Jacobsen KW (1998) Nudged elastic band method for finding minimum energy paths of transitions. In: Berne BJ, Ciccotti G, Coker DF (eds) Class Quantum Dyn Condens Phase Simulations. World Scientific, Singapore, pp 385–404
146. Caspersen KJ, Carter EA (2005) Finding transition states for crystalline solid-solid phase transformations. Proc Natl Acad Sci 102:6738–6743
147. Henkelman G, Uberuaga BP, Jónsson H (2000) A climbing image nudged elastic band method for finding saddle points and minimum energy paths. J Chem Phys 113:9901–9904

148. Sheppard D, Xiao P, Chemelewski W, Johnson DD, Henkelman G (2012) A generalized solid-state nudged elastic band method. J Chem Phys 136:074103
149. Trinkle D, Hennig R, Srinivasan S, Hatch D, Jones M, Stokes H, Albers R, Wilkins J (2003) New mechanism for the α to ω martensitic transformation in pure titanium. Phys Rev Lett 91:025701
150. Hennig RG, Trinkle DR, Bouchet J, Srinivasan SG, Albers RC, Wilkins JW (2005) Impurities block the α to ω martensitic transformation in titanium. Nat Mater 4:129–133
151. Parrinello M, Rahman A (1981) Polymorphic transitions in single crystals: a new molecular dynamics method. J Appl Phys 52:7182–7190
152. Liu J, Johnson D (2009) bcc-to-hcp transformation pathways for iron versus hydrostatic pressure: coupled shuffle and shear modes. Phys Rev B 79:134113
153. Xiao P, Henkelman G (2012) Communication: from graphite to diamond: reaction pathways of the phase transition. J Chem Phys 137:101101
154. Vu NH, Le HV, Cao TM, Pham VV, Le HM, Nguyen-Manh D (2012) Anatase-rutile phase transformation of titanium dioxide bulk material: a DFT + U approach. J Phys Condens Matter 24:405501
155. Dong X, Zhou X-F, Qian G-R, Zhao Z, Tian Y, Wang H-T (2013) An ab initio study on the transition paths from graphite to diamond under pressure. J Phys Condens Matter 25:145402
156. Xiao P, Cheng J-G, Zhou J-S, Goodenough JB, Henkelman G (2013) Mechanism of the $CaIrO_3$ post-perovskite phase transition under pressure. Phys Rev B 88:144102
157. Dai Y, Ni S, Li Z, Yang J (2013) Diffusion and desorption of oxygen atoms on graphene. J Phys Condens Matter 25:405301
158. Briquet LGV, Wirtz T, Philipp P (2013) First principles investigation of Ti adsorption and migration on Si(100) surfaces. J Appl Phys 114:243505
159. Jennings PC, Aleksandrov HA, Neyman KM, Johnston RL (2014) A DFT study of oxygen dissociation on platinum based nanoparticles. Nanoscale 6:1153–1165
160. Harrison JA, White CT, Colton RJ, Brenner DW (1992) Molecular-dynamics simulation of atomic-scale friction of diamond surfaces. Phys Rev B 46:9700–9708
161. Harrison JA, Colton RJ, White CT, Brenner DW (1993) Effect of atomic-scale surface roughness on friction: a molecular dynamics study of diamond surfaces. Wear 168:127–133
162. Harrison JA, White CT, Colton RJ, Brenner DW (1995) Investigation of the atomic-scale friction and energy dissipation in diamond using molecular dynamics. Thin Solid Films 260:205–211
163. Gao G, Cannara RJ, Carpick RW, Harrison JA (2007) Atomic-scale friction on diamond: a comparison of different sliding directions on (001) and (111) surfaces using MD and AFM. Langmuir 23:5394–5405
164. Yue D-C, Ma T-B, Hu Y-Z, Yeon J, van Duin ACT, Wang H, Luo J (2013) Tribochemistry of phosphoric acid sheared between quartz surfaces: a reactive molecular dynamics study. J Phys Chem C 117:25604–25614
165. Carkner CJ, Mosey NJ (2010) Slip mechanisms of hydroxylated α-Al_2O_3 (0001)/(0001) interfaces: a first-principles molecular dynamics study. J Phys Chem C 114:17709–17719
166. Carkner CJ, Haw SM, Mosey NJ (2010) Effect of adhesive interactions on static friction at the atomic scale. Phys Rev Lett 105:056102
167. Haw SM, Mosey NJ (2012) Tribochemistry of aldehydes sheared between (0001) surfaces of α-alumina from first-principles molecular dynamics. J Phys Chem C 116:2132–2145
168. Haw SM, Mosey NJ (2011) Chemical response of aldehydes to compression between (0001) surfaces of α-alumina. J Chem Phys 134:014702
169. Bernasconi M, Chiarotti GL, Focher P, Scandolo S, Tosatti E, Parrinello M (1995) First-principle-constant pressure molecular dynamics. J Phys Chem Solids 56:501–505
170. Wentzcovitch R (1991) Invariant molecular-dynamics approach to structural phase transitions. Phys Rev B 44:2358–2361
171. Berendsen HJC, Postma JPM, van Gunsteren WF, DiNola A, Haak JR (1984) Molecular dynamics with coupling to an external bath. J Chem Phys 81:3684

172. Andersen HC (1980) Molecular dynamics simulations at constant pressure and/or temperature. J Chem Phys 72:2384–2393
173. Serra S (1999) Pressure-induced solid carbonates from molecular CO_2 by computer simulation. Science 284:788–790
174. Mugnai M, Pagliai M, Cardini G, Schettino V (2008) Mechanism of the ethylene polymerization at very high pressure. J Chem Theory Comput 4:646–651
175. Bernasconi M, Chiarotti G, Focher P, Parrinello M, Tosatti E (1997) Solid-state polymerization of acetylene under pressure: ab initio simulation. Phys Rev Lett 78:2008–2011
176. Schettino V, Bini R (2007) Constraining molecules at the closest approach: chemistry at high pressure. Chem Soc Rev 36:869–880
177. Mosey N, Woo T, Müser M (2005) Energy dissipation via quantum chemical hysteresis during high-pressure compression: a first-principles molecular dynamics study of phosphates. Phys Rev B 72:054124
178. Mosey NJ, Müser MH, Woo TK (2005) Molecular mechanisms for the functionality of lubricant additives. Science 307:1612–1615
179. Giannozzi P, Baroni S, Bonini N et al (2009) QUANTUM ESPRESSO: a modular and open-source software project for quantum simulations of materials. J Phys Condens Matter 21: 395502
180. Perdew JP, Burke K, Ernzerhof M (1996) Generalized gradient approximation made simple. Phys Rev Lett 77:3865–3868
181. Troullier N, Martins JL (1991) Efficient pseudopotentials for plane-wave calculations. Phys Rev B 43:1993–2006

Top Curr Chem (2015) 369: 97–134
DOI: 10.1007/128_2015_628

Published online: 10 April 2015

Supramolecular Chemistry and Mechanochemistry of Macromolecules: Recent Advances by Single-Molecule Force Spectroscopy

Bo Cheng and Shuxun Cui

Abstract Atomic force spectroscopy (AFM)-based single-molecule force spectroscopy (SMFS) was invented in the 1990s. Since then, SMFS has been developed into a powerful tool to study the inter- and intra-molecular interactions of macromolecules. Using SMFS, a number of problems in the field of supramolecular chemistry and mechanochemistry have been studied at the single-molecule level, which are not accessible by traditional ensemble characterization methods. In this review, the principles of SMFS are introduced, followed by the discussion of several problems of contemporary interest at the interface of supramolecular chemistry and mechanochemistry of macromolecules, including single-chain elasticity of macromolecules, interactions between water and macromolecules, interactions between macromolecules and solid surface, and the interactions in supramolecular polymers.

Keywords AFM · Desorption · Inherent elasticity · Macromolecules · Mechanochemistry · Molecular motor · Non-covalent interactions · Polymer models · QM calculations · Single-molecule elasticity · SMFS · Supramolecular chemistry · Supramolecular polymer · Water rearrangement

Contents

B. Cheng and S. Cui (✉)
Key Lab of Advanced Technologies of Materials, Ministry of Education of China, Southwest Jiaotong University, Chengdu 610031, China
e-mail: cuishuxun@swjtu.edu.cn

Abbreviations

AFM	Atomic force spectroscopy
AMIMCl	Allyl-3-methylimidazolium chloride
bisUPy	Bis(2-ureido-4[1*H*]-pyrimidinone)
CB[8]	Cucurbit[8]uril
DEBenzene	Diethylbenzene
DP	Degree of polymerization
dsDNA	Double-stranded DNA
FJC	Freely jointed chain
Force curve	Force-extension curve
FRC	Freely rotating chain
Gua	Guanidine chloride
HSCT	Host-stabilized charge transfer
IL	Ionic liquid
LbL	Layer-by-layer
MD	Molecular dynamics
M-FJC	Modified FJC
NIPAM	*N*-Isopropylacrylamide
nN	NanoNewtons
P4VP	Poly(4-vinyl pyridine)
PAAM	Polyacrylamide
PAMPS	Poly(2-acrylamido-2-methyl propane sulfonic acid)
PBS	Phosphate buffered saline
PDEAM	Poly(*N*,*N*-diethylacrylamide)

PEG	Polyethylene glycol
PFS	Poly(ferrocenylsilane)
pN	PicoNewtons
PNIPAM	Poly(*N*-isopropylacrylamide)
PS	Polystyrene
PVA	Poly(vinyl alcohol)
RT	Room temperature
SMFS	Single-molecule force spectroscopy
ssDNA	Single-stranded DNA
UAT	Urea-aminotriazine
WLC	Worm-like chain
β-CD	β-Cyclodextrin
$\chi_{methanol}$	Methanol molar fraction

1 Introduction

Since 1987, supramolecular chemistry has developed into a major field [1]. New structures with novel properties have been created from existing molecules via non-covalent interactions, including hydrophobic interactions, electrostatic forces, H-bonding, van der Waals forces, etc. At the very beginning, supramolecular chemistry dealt with small molecules such as crown ethers and cryptands. Later, non-covalent interactions were applied to the field of macromolecules, yielding an important concept of a supramolecular polymer [2]. Connected by non-covalent interactions, the dynamic supramolecular polymer fused the two fields of small organic molecules and macromolecules. The principle of supramolecular chemistry is central not only to chemical sciences but also to life and material sciences [3–7].

Mechanochemistry has recently emerged as an important field. Mechanical force has a fundamental role in biological processes and material applications. For a bulk material, the elastic modulus and other mechanical properties can easily be measured with universal testing machines. However, the output force of a molecular motor cannot be obtained by bulk measurements. Biomacromolecules often work in self-assemblies of only one or several molecules. The mechanical properties at the single-molecule level are key parameters for these systems. When using bulk/ensemble methods, only average properties can be deduced from the experimental results. In order to measure the mechanical properties of biomacromolecules directly, several single-molecule manipulation techniques were invented in the 1990s, such as optical tweezers, magnetic tweezers, and atomic force spectroscopy (AFM) based single-molecule force spectroscopy (SMFS) [8–10].

A number of important problems in supramolecular chemistry and mechanochemistry on the single-molecule level, such as the strength of the covalent bond and of intermolecular interactions, and the elasticity of an isolated polymer chain, cannot be addressed by bulk measurements. By solving these problems during the

last two decades, AFM-SMFS has become widely accepted as a powerful tool to study inter- and intra-molecular interactions of macromolecules [11–24]. Many reviews on AFM-SMFS have been published, discussing the instrumentation, the applications to the problems of biological and synthetic macromolecules. In this review, we focus on recent advances by AFM-SMFS in the fields of supramolecular chemistry and mechanochemistry. First, the principles of SMFS are briefly introduced. Then, single-chain elasticity of macromolecules and the theoretical models, which form the foundation of our understanding of many aspects of micromechanical behavior of macromolecules, are discussed. Later, the application of SMFS to understand the interactions between macromolecules and surroundings (i.e., water and solid surfaces) is reviewed. Finally, the binding interactions in supramolecular polymers and synthetic molecular machines are discussed.

2 Basic Principles of AFM-SMFS

AFM was invented in 1986 by the Nobel Laureate Gerd Binnig and his colleagues as a tool for the imaging of surfaces with high resolution [25]. Because of the high resolution of force sensing, AFM can also be utilized to detect inter- and intramolecular interactions in surface-immobilized systems. This feature is the origin of AFM-SMFS. In brief, the principle of SMFS is to manipulate a macromolecule that bridges an AFM tip and a solid support (also called substrate). During the manipulation of the molecule bridge, a cantilever deflection-piezopath curve is recorded and later converted into a force-molecule extension curve (in brief, force curve). A schematic drawing of the SMFS setup and the principles of its operation are shown in Fig. 1 [11, 12, 26, 27].

The molecular bridge can be formed by various methods, which can be classified into two types: physisorption and chemisorption. Physisorption is a simple method, in which molecules are first adsorbed onto the substrate and then the tip captures one or more molecules from the substrate when a compressive force of up to several nanoNewtons (nN) is applied for several seconds [10, 13, 28]. According to many studies, such compressive force is sufficient to facilitate a strong non-specific adsorption between the AFM tip and the target molecule [12, 29–32]. The other strategy to form a macromolecular bridge between the tip and the substrate is to bind the molecule to the surfaces covalently. The terminal groups of the target molecule and the tip (and/or the substrate) are modified with chemically reactive groups, which can form a bond (covalent, coordination, or other intermolecular interactions with similar strength) upon contact at room temperature [33–35]. For both strategies, the interaction between the tip and the target molecule should be stronger than the non-covalent interactions to be measured. In an ideal case, the force resolution of a SMFS is about 10 picoNewtons (pN), which is high enough for detecting the intermolecular interactions involved in the supramolecular self-assembly.

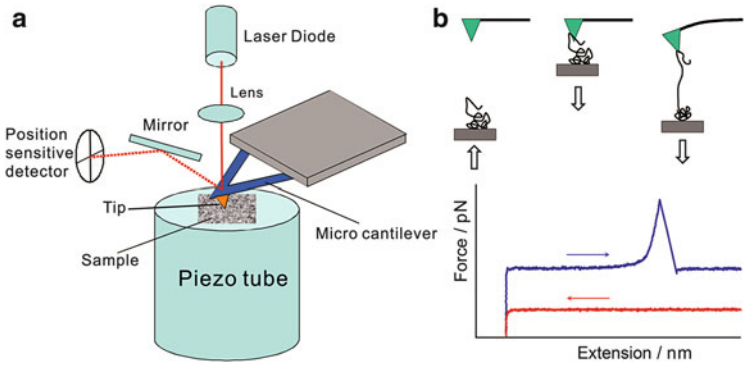

Fig. 1 (**a**) Schematic of AFM-based SMFS. (**b**) Schematic of pulling a single polymer chain and the corresponding force curve obtained by SMFS

Typically, force-extension curves are measured in a liquid to prevent interference from the capillary force at surfaces. This condition makes force measurements relevant to supramolecular systems, because self-assembly is usually performed in a liquid medium [36]. Aqueous solutions, organic solvents, and mixture of them have been used as the liquid environment for force measurements. The following sections illustrate some typical applications of SMFS on the study of supramolecular chemistry and mechanochemistry of macromolecules.

3 Inherent Single-Chain Elasticity of Macromolecules

In the past 20 years, with the development of single-molecule experimental methods [10, 37–39], the behavior of many macromolecules during stretching has been investigated at the single-chain level [9, 10, 26, 27, 40]. The stretching elasticity of a single polymer chain has been found to depend on several factors, including the structure of the side chains, the solvent and any solutes (such as a denaturant and/or a salt), and the temperature [13, 14, 29, 41]. Molecular understanding of this body of empirical data must start with quantifying the inherent elasticity of the polymer chain, i.e., the micromechanical behavior of an ideal polymer chain without long range interactions and specific interactions with the solvent. A practical condition is a nonpolar organic solvent, in which the interactions between the solvent molecules and the polymer chains are limited to van der Waals forces, which can be ignored in SMFS studies. In recent years, Cui et al. utilized SMFS to investigate the inherent single-chain elasticity of a series of macromolecules [42, 43].

3.1 Three Polymer Models that Combine Elasticity from Quantum Mechanical Calculations

With the development of experimental tools to study single-chain mechanics of polymers, theoretical models have become increasingly important in understanding the measured single-chain stretching behavior of macromolecules. Generally, because of the large number of degrees of freedom, the single-chain stretching behavior has to be treated using the approaches of statistical mechanics, by replacing the atomistic description of the chain structure with simplified models [44]. The three models most commonly used to describe single polymer chains, all based on the seminal work of Flory and others, are the freely jointed chain (FJC) model, the freely rotating chain (FRC) model, and the worm-like chain (WLC) model, mathematically represented by (1–3) below:

$$R = L[\mathrm{F}] \cdot \{\coth[(F \cdot l_k)/(k_B \cdot T)] - (k_B \cdot T)/(F \cdot l_k)\}, \tag{1}$$

$$R = L[\mathrm{F}] \cdot [1 - k_B T/(2F \cdot l_b)], \tag{2}$$

$$F\frac{l_p}{k_B T} = \frac{R}{L[\mathrm{F}]} + \frac{1}{4(1 - R/L[\mathrm{F}])^2} - \frac{1}{4}. \tag{3}$$

In these equations, F is the external stretching force acting across the termini of the chain, R the end-to-end distance of a polymer chain under F, $L[\mathrm{F}]$ the F dependent contour length of the polymer chain, k_B the Boltzmann constant, T the absolute temperature, and l_k, l_p, and l_b denote the Kuhn length, persistence length, and rotating unit length of the polymer chain, respectively. $L[\mathrm{F}]$ and l_k (or l_p or l_b) are two free parameters for model fitting.

With the advancement of SMFS, the validity of these models has been demonstrated. The WLC model was successfully applied to describe the measured single-molecule elasticity of a double stranded DNA, proteins, and other polymers [45, 46]. The FJC model was exploited to fit the single-chain elasticity of many kinds of polymers, such as amylose and cellulose [26, 27, 29]. However, these models assume that polymer chains have only entropic elasticity, i.e., the contour length of a polymer chain is inextensible, although contour length is extensible by the deformation of bond angles and bond lengths. Enthalpic elasticity is integrated into these models by means of force-dependent contour length, $L[\mathrm{F}]$:

$$L[\mathrm{F}] = L_0 \cdot (1 + F/K_0), \tag{4}$$

where K_0 is the linear elasticity of the single polymer chain, and L_0 the contour length of free polymer. Together with K_0, there are three free fitting parameters for each of the above-mentioned models. In practice, these free fitting parameters are determined by the trial and error method. In general, the fitted parameter l_k (or l_p or l_b) has no close relationship with the molecular chain structure of the polymer.

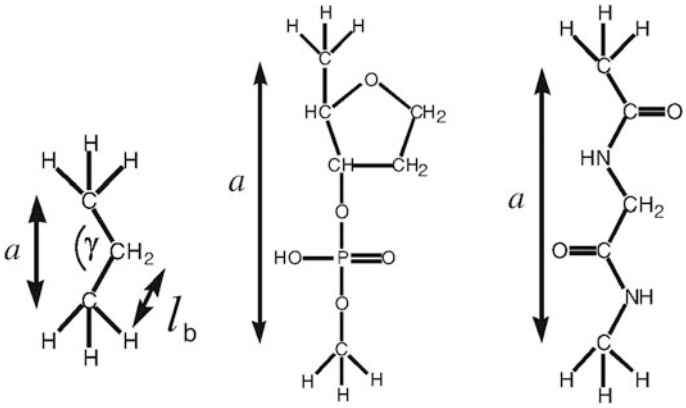

Fig. 2 Schematic of one unit of three kinds of polymers (propane, DNA, and a di-peptide) used in the MP2 calculations. Figure reproduced with permission from [47]

In 2005, Hugel et al. reported the enthalpic elasticity with high-accuracy of a monomer of three kinds of polymers (Fig. 2), which was calculated at the MP2 level of theory [47]. The modulus of the monomer was nonlinear and can be expressed in a polynomial expansion:

$$F = \sum_{n=1}^{\infty} \gamma_n (a[\mathrm{F}]/a_0 - 1)^n, \tag{5}$$

where a_0 and $a[\mathrm{F}]$ are the length of the monomer at zero force and force F, respectively, and γ_n is the nth polynomial coefficient.

Because changes of bond angles and bond lengths are already included in the calculations on one repeating unit, (5) can be rewritten for the whole polymer chain (fitting results support this assumption; see Sect. 3.2):

$$F = \sum_{n=1}^{\infty} \gamma_n (L[\mathrm{F}]/L_0 - 1)^n. \tag{6}$$

To simplify the calculations involved in the original models, L_0 is introduced into the models as follows:

$$R/L_0 = (L[\mathrm{F}]/L_0) \cdot \{\coth[(F \cdot l_k)/(k_B \cdot T)] - (k_B \cdot T)/(F \cdot l_k)\}, \tag{7}$$

$$R/L_0 = (L[\mathrm{F}]/L_0) \cdot [1 - k_B T/(2F \cdot l_b)], \tag{8}$$

$$F\frac{l_p}{k_B T} = \frac{R/L_0}{L[\mathrm{F}]/L_0} + \frac{1}{4(1 - (R/L_0)/(L[\mathrm{F}]/L_0))^2} - \frac{1}{4}. \tag{9}$$

If $L[\mathrm{F}]/L_0$ is known, the corresponding F can be calculated by (6). Because (7)–(9) incorporate quantum mechanical (QM) results, the respective models are called

Scheme 1 Primary structures of three polymers with C–C backbone. Figure reproduced with permission from [43]

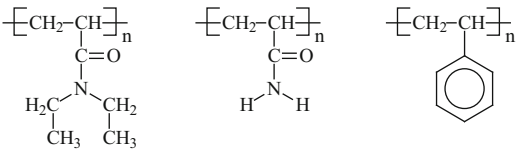

QM-FJC, QM-FRC, and QM-WLC, each with only one free-fit parameter (l_k, l_b, and l_p, respectively) [48].

3.2 Macromolecules with a Carbon–Carbon (C–C)Backbone

To test these new models, Cui et al. investigated the single-chain mechanics of a series of polymers with the C–C backbone (poly(*N*,*N*-diethylacrylamide) (PDEAM), polyacrylamide (PAAm), and polystyrene (PS); Scheme 1) in nonpolar solvents by SMFS [43]. To compare SMFS-behavior of polydisperse polymers with varying contour length, the extension measured in individual experiments is divided by the strain-free contour length to yield normalized extension (see below for detail), which is plotted against applied force. The normalized force curves of these polymers measured in octane were superimposable over the entire force regime; see Fig. 3. The only marked difference is the beginning part of the force curves, which originates from the strong or weak adhesion force between the AFM tip and the sample surface. It can be concluded that the inherent elasticity of a polymer chain with C–C backbone did not depend on the side chains, at least if they were moderately sized. This result is very different from those observed from the bulk measurements; for instance, the sizes of the side chains have a marked influence on the temperature of glass transition, Tg (http://en.wikipedia.org/wiki/Glass_transition).

The experimental force curves of these C–C backbone-based polymers were fitted to QM-FRC model using the coefficients of Hugel et al. [47]:

$$F = \sum_{n=1}^{3} \gamma_n (L[\mathrm{F}]/L_0 - 1)^n \gamma_1 = 28.7\ \mathrm{nN},\ \gamma_2 = -42.0\ \mathrm{nN},\ \gamma_3 = 16.9\ \mathrm{nN}, \quad (10)$$

where γ_1 is the linear elasticity of the repeating unit, and the other two coefficients γ_2 and γ_3 are nonlinear corrections. It should be noted that the modulus coefficients have a dimension of force, which is different from the bulk materials (force/area). The area of the cross section of the single-chain is omitted because it is a variable depending on the position of the chain.

During stretching of a single polymer chain, its $L[\mathrm{F}]/L_0$ increases from 1.0 as F increases until the polymer bridge ruptures, i.e., $L[\mathrm{F}]/L_0$ is a monotonically

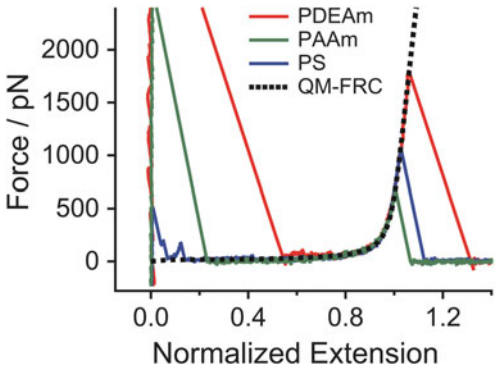

Fig. 3 Comparison of measured normalized force curves of poly(*N*,*N*-diethylacrylamide) (PDEAm), polyacrylamide (PAAm), and polystyrene (PS) obtained in octane and the QM-FRC fitting curve. Figure reproduced with permission from [43]

increasing function of F and vice versa. Assuming the upper limit for F is 2,000 pN [8], the upper limit for $L[\mathrm{F}]/L_0$ is about 1.07 according to (10). For any given value of $L[\mathrm{F}]/L_0$, F is calculated by (10). Any pair of values for $L[\mathrm{F}]/L_0$ and F are then converted to the corresponding normalized extension of polymer, R/L_0, according to (7)–(9). In this way, the whole QM-based fitting curve can be generated when $L[\mathrm{F}]/L_0$ is increased from 1.0 to 1.07.

The force curves in Fig. 3 were best reproduced with the QM-FRC model (8) with $l_b = 0.154$ nm [43], which is identical to the C–C bond length. With a single C–C bond as the rotating unit and the chain elasticity deduced from QM calculations, the QM-FRC model has been developed into a parameter free and structure relevant single-chain model, which can quantitatively describe polymers with C–C backbone. Although there are some exceptions when the side chain is large (e.g., dendrimer or long graft chain) [43], this work provides a general result for the inherent elasticity of single neutral polymer chains with C–C backbones. These fitting results confirmed that the QM-FRC model is very successful in describing the micromechanics of these flexible polymers.

3.3 Natural Cellulose

Cellulose is a widely distributed polysaccharide in nature, and is polymerized glucose. It is the most important substance in plants, where it serves as the basic building material of cell walls [49, 50]. Interestingly, the Young's modulus of a perfect cellulose crystal may be as high as that of steel, which is much higher than that of most polymer materials [51, 52]. A single cellulose chain is generally expected to be rigid [49]. Single-molecule measurements of natural cellulose (NC) are complicated by its poor solubility in common solvents. NC is soluble in several ionic liquids (IL) [53], which allowed Cui et al. recently to investigate the single-chain elasticity of NC by SMFS (Fig. 4). To obtain the inherent elasticity of NC, they measured the single-chain force curve of an NC sample prepared from an IL (1-allyl-3-methylimidazolium chloride, AMIMCl) [54] solution [42] and fitted it

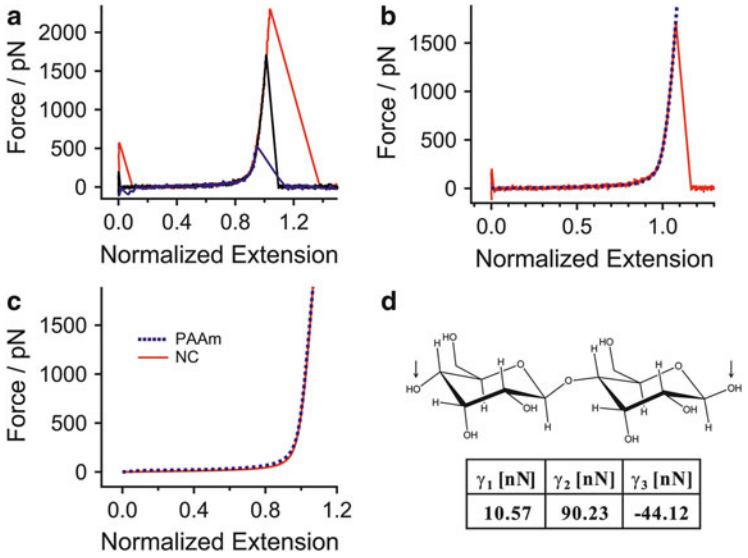

Fig. 4 (**a**) Normalized force curves of NC obtained in octane. (**b**) Comparison of a force curve of NC obtained in octane and the QM-FJC fitting curve. (**c**) Comparison of force curves of PAAm and NC obtained in octane. (**d**) Molecular structure of the dimer (cellobiose) used in QM calculations and the QM results. The *arrows* indicate the atoms defining the constrained distance. Figure reproduced with permission from [42]

to the QM-FJC model [47, 48], using the following three parameters derived by QM calculations on a glucose dimer:

$$F = \sum_{n=1}^{3} \gamma_n (L[F]/L_0 - 1)^n \gamma_1 = 10.57 \text{ nN}, \gamma_2 = 90.23 \text{ nN}, \text{ and } \gamma_3 = -44.12 \text{ nN}. \quad (11)$$

Interestingly, the experimental force curve could be fitted well to the QM-FJC model (with $l_k = 0.514$ nm) but not to the QM-WLC alternative. In other words, the NC chain seemed flexible at the single-molecule level, which was also confirmed by the similarity of the normalized force curves of NC and PAAM, with free rotation around the C–C bonds of the backbone. This finding contradicts the traditional view of NC as a rigid polymer [49], which probably reflects the rigidifying effect of extensive H bonding between NC chains in its crystals [55], on which all previous mechanical measurements had been done. The QM-FJC model fitting results revealed that the length of a pyranose ring of NC equaled the length of a Kuhn segment (l_k) in the model [56]. This result means that cellulose on the single chain scale is rather flexible, which is surprising because cellobiose (consisting of two pyranose rings) has been recognized to be the repeat unit of cellulose for a long time. With the fine flexibility, each of the pyranose rings can find its best binding

site on the crystal surface, which perfectly lowers the energy of the self-assembled structures. This may explain why NC became the basic building material of plants during plant evolution.

4 Interactions Between Water and Macromolecules

Water can be regarded as the most important substance for life on Earth. It is the most widely used solvent of biomolecules. However, it is also a very complicated solvent. With H-bonding donor and acceptor sites, this polar solvent strongly influences the properties of solutes. It is interesting that water forms supramolecular structures with many kinds of macromolecules, including DNA, proteins, and many synthetic polymers [26, 29, 32, 41, 57, 58]. Several typical water–macromolecule assemblies have been investigated by SMFS.

4.1 PEG

Polyethylene glycol (PEG) is a water soluble polymer with many applications from industrial manufacturing to medicine [59]. PEG is prepared by polymerization of ethylene oxide, and is commercially available. The molecular weight of PEG can be up to several megadaltons (MDa), corresponding to the contour length of up to several microns. Gaub and co-workers studied the single-molecule mechanics of PEG in water and hexadecane [26], and found that the force curves obtained in the two environments were superimposable in the low-force regime, which reflected the entropic elasticity of an ideal polymer; and in the very high force regime, which is dominated by the enthalpic elasticity. However, in the middle force regime, the behavior of PEG in the two solvents was very different; see Fig. 5a. The phenomenon was attributed to the formation of solvent-induced supramolecular structures. In hexadecane, upon stretching the PEG molecule behaved as an ideal polymer chain with pure entropic elasticity, which was confirmed by the subsequent fitting result to the modified FJC (M-FJC) model [44]. In water, however, PEG adopted the *trans-trans-gauche* state (helical conformation) [60]. Two adjacent oxygen atoms of PEG formed H-bonds to a water molecule, establishing a water-bridged supramolecular structure which stabilized the helical state (Fig. 5b). Above a threshold force, the helical state changed into the all *trans* state [8, 61], where the adjacent oxygen atoms were separated by a longer distance than is required to maintain the water bridge. Therefore, the difference between force curves obtained in the two solvents was attributed to the free energy cost of breaking the water bridge, which was calculated to be about $3\,k_B$T/monomer.

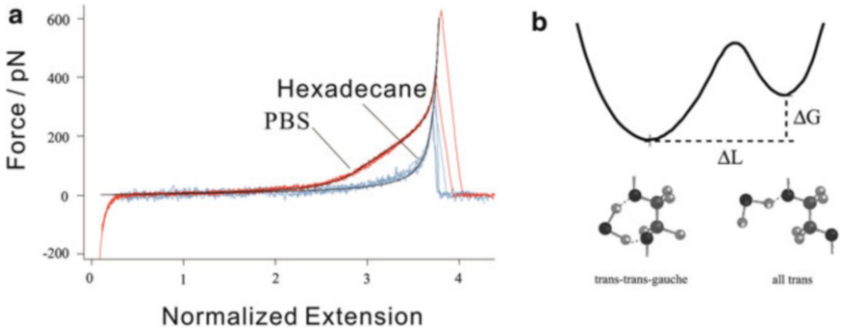

Fig. 5 (**a**) Force curves of polyethylene glycol (PEG) measured in aqueous solution (*red*) and hexadecane (*blue*) along with smoothed curves (*black lines*). (**b**) Schematic of conformation transition from the helical state to all *trans* state. Figure reproduced with permission from [26]

4.2 PAAm and PVA

Besides PEG, other water soluble polymers, such as poly(vinyl alcohol) (PVA) [41] and polyacrylamide (PAAm) [29], can also form water-mediated supramolecular structures in aqueous solution. SMFS results indicated that the force curves of PVA and PAAm measured in water could not be fitted well to the WLC model (for PVA) or the M-FJC model (for PAAm). However, the force curves in aqueous 8 M urea solution (urea is generally considered to break H-bonds) were remarkably distinct from those measured in water and fitted well to the WLC model and M-FJC model for PVA and PAAm, respectively. This fact demonstrated the existence of H-bonded supramolecular structures in PVA and PAAM in water, which were destroyed in 8 M urea.

4.3 DNA

DNA, with its special double helix structure, is a typical supramolecular system, and it plays the central role in the transcription, expression, and conservation of genetic information [62]. The biological function of DNA is closely related to the stability and the integrality of the double strands [63], and the mechanical stability of double-stranded DNA (dsDNA) strongly depends on the ambient conditions. Recently, Cui et al. investigated the important role of water in determining or stabilizing the supramolecular structure of DNA by SMFS [31, 32].

An advantage of SMFS is that the polymer sample can be measured in different environments. Such measurements suggest that the double-stranded DNA is thermodynamically unstable in at least some non-aqueous media. To screen the effects of water on the structure of DNA, Cui et al. performed the SMFS experiments on dsDNA in diethylbenzene (DEB, a poor solvent for DNA) [64]. The force curves obtained in DEB were very different from those obtained in water in that they

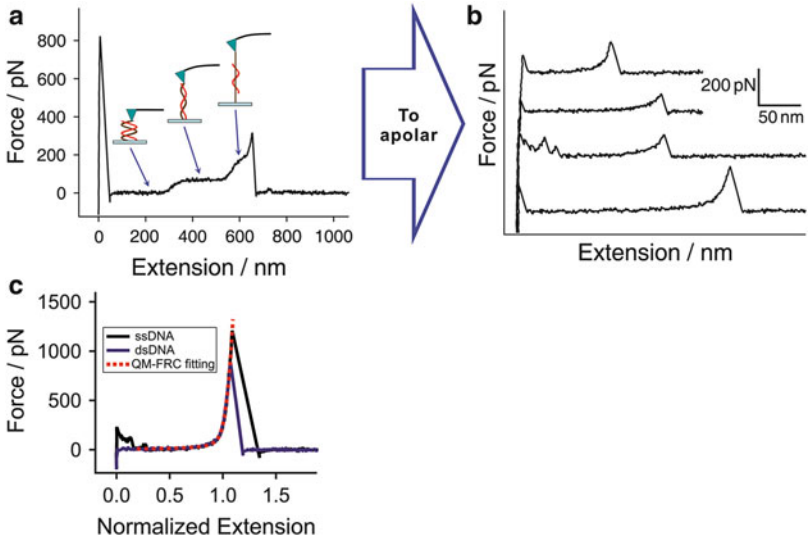

Fig. 6 (**a**) Typical "B-S" force curve of dsDNA. (**b**) Force curves of dsDNA obtained in a poor solvent, DEB. (**c**) Comparison of forces curve measured on dsDNA and ssDNA in poor solvent and fitting curve to the QM-FRC model. Figure reproduced with permission from [32]

lacked the characteristic "B-S" transition plateau [38–40, 46] (Fig. 6b). A similar result was observed in another poor solvent for DNA, 1-propanol, which does not form aromatic stacking interactions with DNA. The force curves of dsDNA measured in poor solvents (DBE and 1-propanol) were similar to those of an unstructured polymer chain. These facts implied that dsDNA was already denatured into single-stranded DNA (ssDNA). To confirm this, Cui et al. utilized a theoretical single-chain elasticity (calculated at the MP2 level) of ssDNA to fit the force curve of dsDNA in organic solvents.

In order to find the most appropriate model to describe the single-chain elasticity of dsDNA in poor solvents, the force curves were fitted to three QM models [48]. Fitting results suggested that $l_k = 0.59$ nm for QM-FJC model and $l_b = 0.295$ nm for QM-FRC model (Fig. 7a, b). Because the length of a repeating unit of ssDNA is 0.59 nm, QM-FJC is a structure relevant model [31, 32]. The inability to fit the experimental data to the QM-WLC model (Fig. 7d) suggested that the rigid dsDNA chain in water became flexible when stretched in a poor solvent. Thus, dsDNA was concluded to have already denatured into two ssDNA strands when it was pulled into the poor solvents. Fitting results also indicated that the QM-FJC and QM-FRC models become identical at force >25 pN (Fig. 7c). Because $l_k = 2l_b$, this result can be explained by viewing one repeating unit of ssDNA as composed of two rotating units, i.e., the sugar ring and the phosphate group.

As further corroboration of the dsDNA denaturation in poor solvents, force measurements were performed in a denaturing environment, an aqueous solution

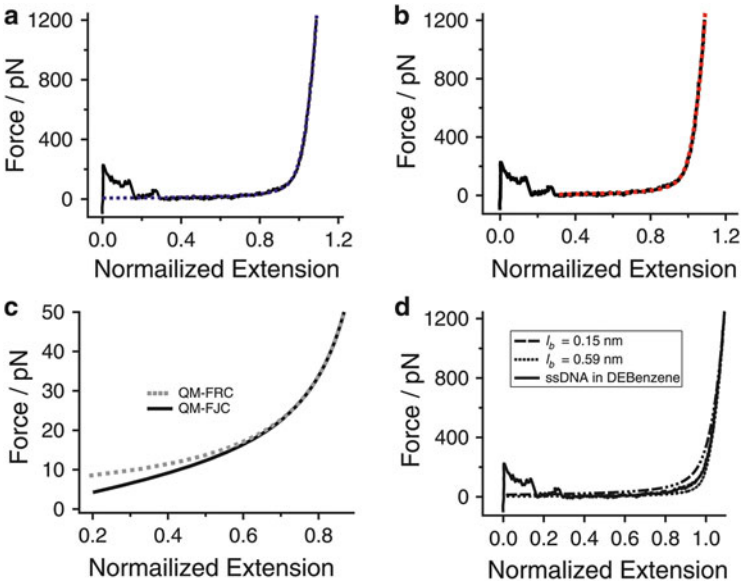

Fig. 7 Experimental force curves fitted to the QM-FRC (**a**) and the QM-FJC (**b**) models. Low-force regime of the two fits is compared in (**c**). QM-WLC fitting results (**d**) of ssDNA with various l_b values from 0.3 nm (*left*) to 10 nm (*right*). Figure reproduced with permission from [48]

of guanidine chloride (Gua), which is a typical denaturant of dsDNA. The force curves obtained in this case were identical to those measured in DEB. The perfect superposition of normalized force curves measured on dsDNA and ssDNA in DEB undoubtedly demonstrates that dsDNA is denatured into ssDNA upon pulling it in a poor solvent.

Molecular dynamics (MD) simulations were carried out to observe the details of the denaturation of dsDNA [65]. It was observed dsDNA unwind spontaneously when put into the apolar solvent directly, which may explain why dsDNA are denatured in both DEB (water immiscible) and propanol (water miscible). The main reason should be the absence of hydrophobic force in non-aqueous media [66], which contributes greatly to the stability of dsDNA in aqueous media. The thermal disturbance at room temperature could be strong enough to destroy the supramolecular structure of dsDNA when hydrophobic force is absent.

The single-chain mechanics of ssDNA in an aqueous environment was also measured, and then the force curves obtained in solution of phosphate buffered saline (PBS) and DEB were normalized and compared (Fig. 8a). It was found that there was a clear difference in the middle force regime, but no deviation in the low and high force regimes [31].

By excluding the effects of salt and poor solvent types, the deviation was attributed to the water rearrangement upon elongation [26]. At the free state ($F = 0$), there is more bound water around ssDNA. Upon elongation, the distances between the H-bond donors and acceptors of ssDNA are increased, which caused a

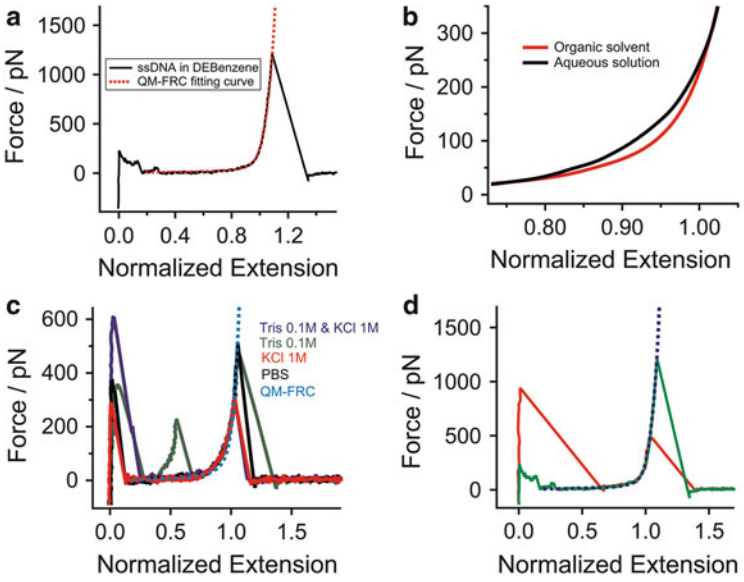

Fig. 8 (**a**) Comparison of the force curve of ssDNA obtained in DEB and the QM-FRC fitting curve. (**b**) Comparison between the smoothed force curve of ssDNA obtained in aqueous solution and in DEB. (**c**) Comparison between the force curves of ssDNA obtained in various aqueous media and QM-FRC fitting curve. (**d**) Comparison between the force curves obtained in aqueous guanidine chloride and DEB. Figure reproduced with permission from [31]

water rearrangement. Thus, an addition energy ($0.58\,k_BT$/unit) is needed for the water rearrangement, which is reflected by the deviation between the force curves obtained in water and organic solvent. Comparing with other water soluble polymers [26, 30], one can find that the ssDNA system consumes the lowest energy for the water rearrangement. It was speculated that the weak competition influence of water may be an important factor for DNA to form a stable double helix in water.

In fact, the water rearrangement around the ssDNA chain can be expressed in another form, i.e., it can be regarded as a partial dehydration process:

$$\text{ssDNA} \cdot x\,\text{H}_2\text{O} \rightleftharpoons \text{ssDNA} \cdot z\,\text{H}_2\text{O} + (x - z)\,\text{H}_2\text{O}. \tag{12}$$

The self-organization from ssDNA to dsDNA is an important process for life. This process can be formularized below, where ssDNA′ denotes the complimentary chain of ssDNA:

$$\text{ssDNA} + \text{ssDNA}' \rightleftharpoons \text{dsDNA}. \tag{13}$$

However, the formula is incomplete, because the bound water around dsDNA and ssDNA chains is not considered [67]. It is known that both ssDNA and dsDNA chains are hydrated in the aqueous solution. Because the bases are hidden in the duplex, one dsDNA chain has less binding sites with water than that of the sum of

the two corresponding ssDNA chains [68]. Therefore, before the self-organization from ssDNA to dsDNA, a partial dehydration process of ssDNA should occur. Thus, (13) should be modified into a more rigorous form as follows:

$$\text{ssDNA} \cdot x\text{H}_2\text{O} \; + \; \text{ssDNA}' \cdot x\text{H}_2\text{O} \rightleftharpoons \text{dsDNA} \cdot y\text{H}_2\text{O} \; + \; (2x - y)\,\text{H}_2\text{O}. \quad (14)$$

For the reaction, a typical value for the free energy change (ΔG_{14}) measured by differential scanning calorimetry (DSC) is -4.3 kJ/(mol · residue) [69]. In this process, the formation of dsDNA can be separated into two steps, including the partial dehydration and the supramolecular self-assembly, as described by the following two equations:

$$\text{ssDNA} \cdot x\,\text{H}_2\text{O} \rightleftharpoons \text{ssDNA} \cdot y/2\,\text{H}_2\text{O} \; + \; (x - y/2)\,\text{H}_2\text{O}, \quad (15)$$

$$\text{ssDNA} \cdot y/2\,\text{H}_2\text{O} \; + \; \text{ssDNA}' \cdot y/2\,\text{H}_2\text{O} \rightleftharpoons \text{dsDNA} \cdot y\text{H}_2\text{O}. \quad (16)$$

In the two steps, all the water rearrangement is completed in (15), and all the assembly occurs in (16), which are a non-spontaneous ($\Delta G_{15} > 0$) and a spontaneous process ($\Delta G_{16} < 0$), respectively. However, for the total process, which is a favorable reaction with the physiological conditions, the free energy change ($\Delta G_{14} = \Delta G_{15} + \Delta G_{16}$) is negative. Thus, the free energy necessary to remove partially the hydration shell of ssDNA must be compensated by the free energy of the formation of the dsDNA (that is, $\Delta G_{15} < \Delta G_{16}$). However, neither ΔG_{15} or ΔG_{16} is readily available in references or a value which can be easily measured.

It can be seen that the process of partial dehydration in (15) is very similar to the process of the loss of bound water in (12). Then, it is expected that the free energy changes of (12) and (15) are very close; $\Delta G_{12} \approx \Delta G_{15} \approx 1.4$ kJ/(mol · residue). Thus, one can calculate that ΔG_{15} is about -7.1 kJ/(mol · base), which is not far from zero. Based on these calculations, it is found that the value of ΔG_{15} is vital to the process of (14). If ΔG_{15} is a much larger value (e.g., >3.6), the whole process of DNA organization is not be favorable, because ΔG_{14} would be a positive value. Although the water rearrangement upon stretching also occurs in other macromolecule/water systems, such as the poly(*N*-vinyl-2-pyrrolidone)/water system (13.0 kJ mol^{-1} unit)[30] or the PEG/water system (7.2 kJ mol^{-1} unit) [26], it is found that the dsDNA system involves the lowest energy among them.

As discussed above, water plays a key role in the self-assembly process of dsDNA (see Scheme 2). On the one hand, it is the weak disturbance of water molecules that ensures the stability of the dsDNA in aqueous solution. On the other, by shaving off the water molecules, dsDNA can be destabilized and tends to unwind. Another factor is that there are many kinds of water soluble macromolecules, but few can form a stable supramolecular structure in water. This may imply that DNA is somewhat special in the molecular structure.

In fact, the specific structure of DNA is not occasional, it is more likely to be the final result of natural selection. Cui conceived a possible route for the prebiotic evolution as follows.

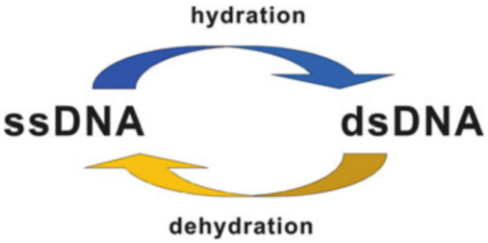

Scheme 2 Hydration/dehydration processes regulate the supramolecular structures of DNA. Figure reproduced with permission from [57]

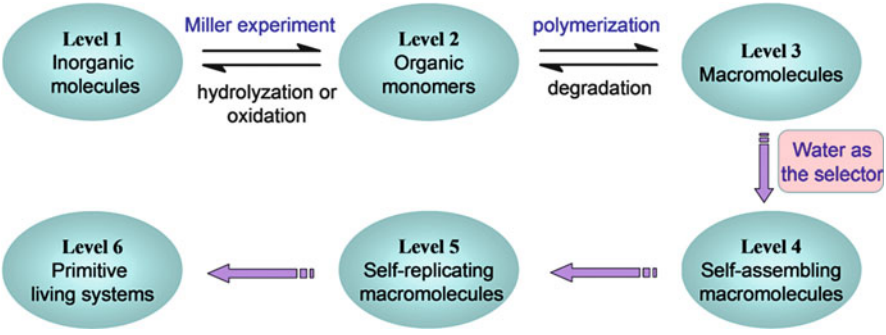

Scheme 3 Possible evolution route from inorganic molecules to the primitive living systems. Figure reproduced with permission from [57]

Because of the complexity involved, the whole prebiotic chemical evolution is fractionized into six levels; see Scheme 3. First, the primitive Earth is an inorganic world, in which there are gas mixtures, water, and so on (Level 1). The inorganic compounds may be converted into organic monomers by the Miller experiment [70] and other possible routes (Level 2). After that, many macromolecules can be generated by polymerization reactions (Level 3). For the three levels, these reactions are in a dynamic equilibrium because of the reversibility. To prevent the degradation into monomers, these macromolecules must form a stable supramolecular structure in the aqueous solution (Level 4). However, water is a strong solvent, which usually has remarkable impact on the solute molecules. With the interference from water, only a few macromolecules can form stable supramolecular structures in water. As a result of long-term chemical evolution [71], the primary structure of dsDNA has been selected in a Darwinian fashion to adapt to the water environment. In further evolution, combined with the function of self-replication (Level 5), it is expected that the primitive life would emerge (Level 6).

During the whole chemical evolution, water is the most important substance. As a reactant in the Miller experiment and the only solvent in Level 2, water directly participated in the early prebiotic chemical evolution. In addition, as a "selector" from Level 3 to Level 4, most of the macromolecules in Level 3 were screened out by the water environment. Water is the primary environment of terrestrial life,

which supports life and, at the same time, restricts the form of life. It is therefore water that defines and shapes life. It is believed that this notion casts a new light on the origin of life

4.4 Hyaluronan

Hyaluronan (also called hyaluronic acid, HA) is a linear polysaccharide widely present in the extracellular matrix [72]. Because of direct communication with proteins and cells present in tissues, HA is an important molecule in the regulation of many cellular and biological processes. Hydration is believed to be one of the key factors influencing its functions. In 2007, Vancso et al. reported the single chain behavior of HA in different conditions. In aqueous media, HA showed marked deviation between the single-chain force curves obtained at different temperatures. The force curves obtained at 46°C can be described well by the m-FJC model. For those obtained at 29°C, only the high force regime (>700 pN) can be fitted by the model. This deviation was at various temperatures. After normalization, these two kinds of force curves can be superposed well in the high force regime. The deviation between the two kinds of force curves was attributed to the superstructure of HA in aqueous media at lower temperature, i.e., a local structure involving a H-bonded network along the polymeric chain, with H-bonds between the polar groups of HA and possibly water and water-mediated intramolecular bonds. This hypothesis is reasonable, because it was reported that the superstructure becomes increasingly destabilized when the temperature is raised to 46°C [73]. This conclusion was further supported by the result obtained in DMSO (an effective breaker of H-bonds), in which the force curve was similar to that obtained in aqueous media at 46°C.

4.5 PNIPAM

Since Pelton and Chibante reported the synthesis of the first temperature-sensitive microgel from *N*-isopropylacrylamide (NIPAM) and crosslinker in 1986 [74], responsive microgels have attracted numerous attempts to explore their potential application in many fields, such as sensing and drug delivery [75]. Now the most extensively studied responsive microgels are prepared with poly(*N*-isopropylacrylamide) (PNIPAM) [2]. It is well known that the phase transition temperature of PNIPAM is about 32°C [76]. When $T < \text{LCST}$, the PNIPAM chain is soluble in water as a random coil. When $T \sim \text{LCST}$, the subtle balance between PNIPAM and water is broken and phase transition occurs [77]. However, the single-molecule level mechanism of the phase transition of PNIPAM had not been proposed until very recently.

Since 2012, Cui et al. have carried out a series of studies to try to understand further the mechanism by means of SMFS at the single-molecule level

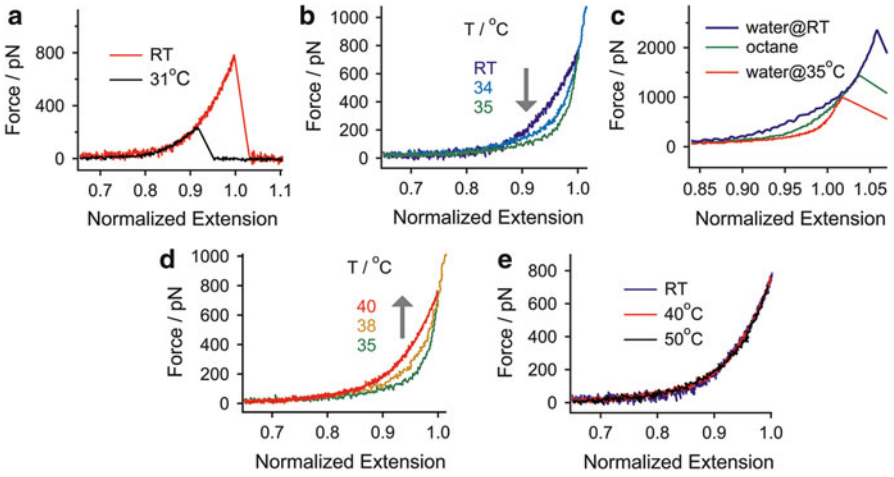

Fig. 9 Comparisons of force curves of PNIPAM obtained in water at different temperatures and in octane at RT. Figure reproduced with permission from [78]

[78–80]. One of the key features of PNIPAM is that the single-chain conformation in aqueous solution can be tuned easily by changing the temperature around its LCST [81–84]. When the temperature is below its LCST, it is a random coil state. However, the conformation of a single PNIPAM chain is changed from coil to globule state spontaneously if the temperature rises above its LCST. The single-chain elasticity of PNIPAM at different temperatures in water has been measured; see Fig. 9. When the temperature was below LCST, there was no difference in the whole force regime among the normalized force curves obtained at different temperatures. Above LCST, an obvious deviation in the middle force range can be found with increase of temperature. Interestingly, $T = 35°C$ was a turning point of the whole variation; when T ranged from 31 to 35°C, the middle parts of the force curves dropped gradually, whereas from 35 to 40°C, the middle parts rose gradually.

When PNIPAM was dissolved in water, both the hydrophilic group and the hydrophobic group of the PNIPAM chain were hydrated in water [85–87]. It was expected that there were many fewer bound water molecules in the fully stretched state than that in the free coil state because of the limitation in chain conformation [8]. Thus, the hydrated PNIPAM chain would lose bound water gradually during the force extension process. Then the bound water molecules around the PNIPAM chain were forced to undergo rearrangement upon stretching. During the elongation, the water rearrangement would consume additional energy over and above that needed for the inherent elasticity of the chain. This energy cost for the water rearrangement upon stretching was reflected by the deviation between the force curves obtained in organic solvents and in water at room temperature (RT). The deviation was calculated to be about 2.1 k_BT/unit.

However, it could be seen that the middle part of the force curve in water at 35°C was even lower than that in organic solvents, which could be explained by two factors. First, water was a poor solvent for PNIPAM at 35°C, and the amount of bound water around the PNIPAM chain was considerably reduced in this condition compared to the case at RT [85–87]. Thus, compared to the case in water at RT, the energy needed for the water rearrangement upon stretching PNIPAM chain was greatly reduced in water at 35°C. This factor may roughly correspond to the energy difference between water at RT and organic solvents.

According to Boltzmann's entropy formula ($S = k_B \ln \Omega$), the entropy of a polymer chain approaches zero when the chain is highly stretched by an external stretching force. That is, the entropies of the final state are the same ($S \approx 0$) in the two conditions. However, it is known that the conformation of PNIPAM in water at 35°C is much more compact than that in water at RT, i.e., the initial entropy of PNIPAM at 35°C is much less than that at RT. Thus, the energy cost of a compact conformation would be less than that of a coil conformation. This factor may roughly correspond to the energy difference between water at 35°C and organic solvents.

When the temperature was increased from 35 to 40°C, the middle parts of the force curves began to rise gradually, which may be attributed to the formation of intrachain H-bonds [81]. This assumption could be well supported by the work of Peiyi Wu's group [87], who proposed that the formation of H-bonds between the amide groups was the final step in the multistep conformational change. In the free state, the globule conformation of the PNIPAM chain ($T >$ LCST) could be stabilized by the formation of intrachain H-bonds. However, under tension it was expected that the elongation of the chain would lead to breakage of the intrachain H-bonds. Because the H-bonds between PNIPAM and water were greatly depleted at $T >$ LCST, it was anticipated that new H-bonds would be unlikely to be formed between PNIPAM and water upon the breakage of the intrachain H-bonds. Therefore, there was almost no energy compensation from the formation of H-bonds with water. Thus, the deviation between the force curves obtained at $T > 35$ and 35°C was mainly contributed by the intrachain H-bonds of PNIPAM. This change of single-chain mechanics from 35°C to 40°C can be used to realize the thermal-mechanical energy conversion at the single-molecule level. That is, the single PNIPAM chain can convert the thermal energy to mechanical work in the range of 35–40°C (see Fig. 10). Thus, this study provided a theoretical basis for the design of nano-devices, namely molecular heat engines, for thermal-mechanical energy conversion [88].

Besides temperature, the variation of the solvent composition can also induce the phase transition of PNIPAM, which is often called cononsolvency [89]. PNIPAM in the mixed solvent of water and methanol is the most studied cononsolvency system. The PNIPAM chain acts as a random coil in pure water or pure methanol, whereas it exists as a globule in a range of concentrations in the water/methanol mixed solvents. As the methanol molar fraction (χ_{methanol}) increases from 0% to 35%, the LCST of PNIPAM in the water/methanol mixed solvent is decreased from 32°C to 7.5°C Then from 35% to 45%, a sharp increase follows [90]. Therefore, an

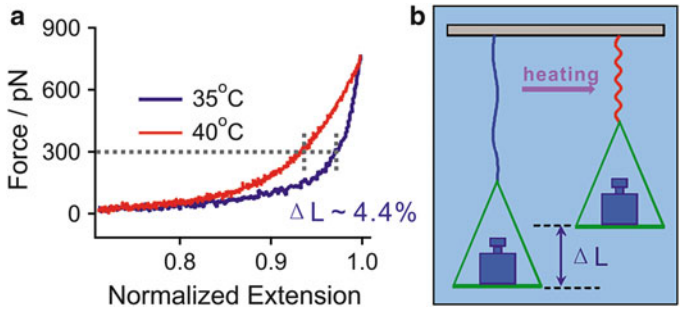

Fig. 10 (**a**) Force curves of PNIPAM obtained at 35°C and 40°C in water. (**b**) Novel synthetic molecular heat engine can be proposed according to the variation of the single PNIPAM chain mechanics between 35°C and 40°C. Figure reproduced with permission from [78]

interesting coil-to-globule-to-coil transition of PNIPAM takes place in the water/methanol mixed solvent with gradual increase of $\chi_{methanol}$ at RT [84, 89, 91, 92]. To gain a better understanding, Cui et al. used the SMFS method to investigate the single-chain mechanics of PNIPAM in the water/methanol mixed solvent at RT [79] (Fig. 11). It was found that the mechanical properties of the PNIPAM chain were greatly dependent on $\chi_{methanol}$ of the mixed solvents. From 0% to 10% there was no obvious difference between the obtained force curve. The complexes of methanol and water were formed and dispersed well in the mixed solvents. Therefore, the complexes had almost no influence on the PNIPAM chains because of the low density. Further increased from 10% to 51%, all the force curves obtained in different $\chi_{methanol}$ were superposed very well after normalization in the high and low force regimes, but, in the middle regime, remarkable deviation can be observed with the increase of $\chi_{methanol}$. As with the temperature-dependent transition, there was also a turning point at $\chi_{methanol}$ 16 %, which was found by Swanson et al. in another study [93]. When $\chi_{methanol}$ gradually increased from 10% to 16%, more and more water–methanol complexes were formed and, at the same time, the bound water molecules of the PNIPAM chain became fewer and fewer. Then the dehydrated PNIPAM chain is unstable and the conformation of the polymer chain changes from the coil state to the collapsed state. Because the rearrangement of bound water consumes additional energy upon stretching, the fewer water molecule bound collapsed state was expected to cost less energy. That is why the middle part of the force curve obtained at $\chi_{methanol} = 16\%$ was lower than that at 10%. However, as $\chi_{methanol}$ further increased up to 18%, the water–methanol complexes continued to be formed. Because of the continuous dehydration of PNIPAM, intrachain C=O...H–N H-bonds were formed [81]. Thus, during chain elongation, the additional energy would be consumed to break the intrachain H-bonds, which was reflected by the deviation of force curves. It should be noted that the energy cost to stretch the PNIPAM chain at $\chi_{methanol} = 18\%$ was lower than that in water at 40°C. This is because the qualities of the intrachain H-bonds formed at $\chi_{methanol} = 18\%$ were lower than in water at $T = 40$°C [89]. That is, the methanol-

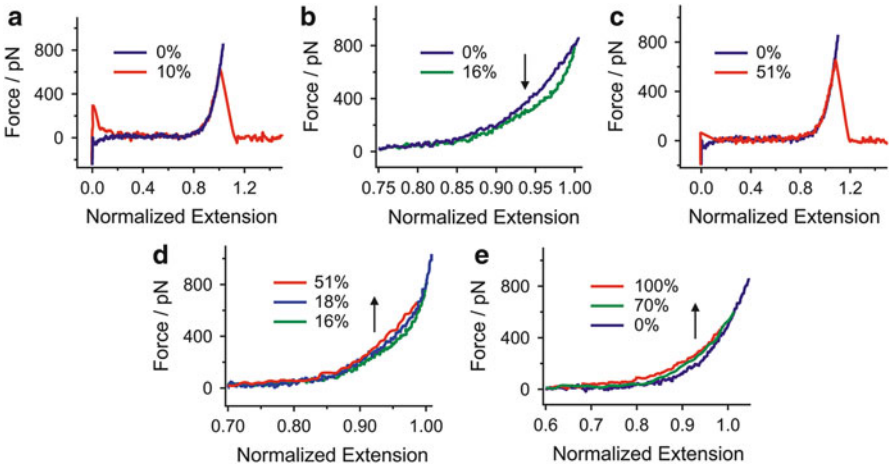

Fig. 11 Comparisons of force curves of PNIPAM obtained in different water/methanol mixed solvents. Figure reproduced with permission from [79]

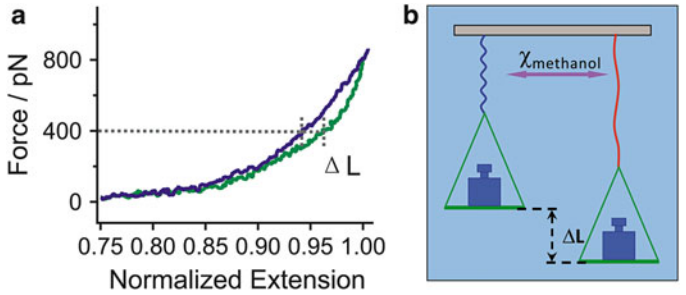

Fig. 12 (**a**) Force curves of PNIPAM obtained in 0% and 16% of methanol/water mixed solvent. (**b**) Potential design of a molecular motor for chemical–mechanical energy conversion. Figure reproduced with permission from [79]

induced collapsed state of PNIPAM chain was less compact than that induced by thermal at $T = 40°C$. With an increase of methanol from 18% to <50%, the solvent quality was still worse than that of water at RT. At $\chi_{methanol} = 51\%$, the force curves superposed very well with those obtained in water at RT, which indicated that the conformations of the PNIPAM chain in the mixed solvent of $\chi_{methanol} = 51\%$ were similar to those in water at RT. Therefore, the solvent quality of the mixed solvent of $51\% < \chi_{methanol} < 100\%$ was better than that of water for PNIPAM. In addition, based on the results obtained at $\chi_{methanol} = 16\%$ and pure water, it was possible to convert the chemical energy to the mechanical energy at RT; see Fig. 12. Therefore, the current work cast new light on the design of nano-devices with a function of chemical–mechanical energy conversion.

PDEAM is one of the polymers most similar to PNIPAM, which also has a coil-to-globule transition in aqueous solution above its LCST (~30°C) [94] (Scheme 4).

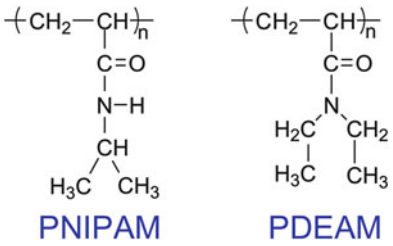

Scheme 4 Structures of PNIPAM and PDEAM. Figure reproduced with permission from [80]

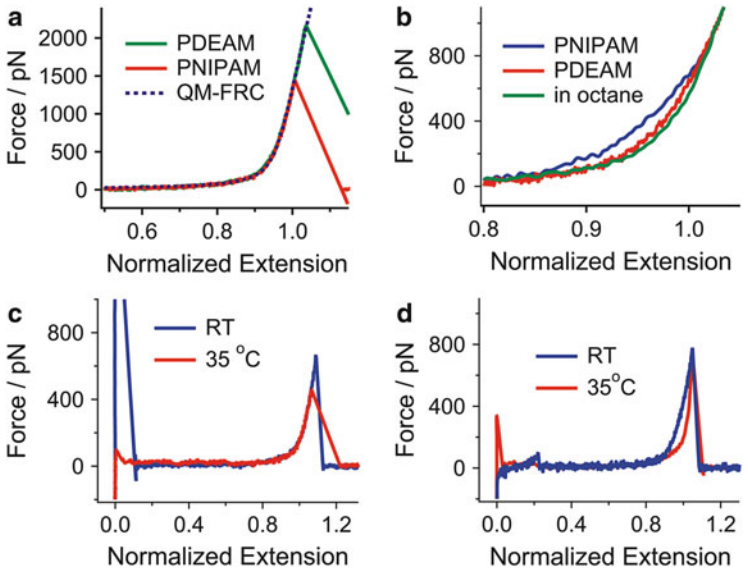

Fig. 13 (**a**) Comparison among the QM-FRC fitting curves and force curves of PNIPAM and PDEAM obtained in octane. (**b**) Comparison among the force curves of PNIPAM and PDEAM obtained in water and that obtained in octane. (**c**) Comparison of force curves of PDEAM at RT and 35°C. (**d**) Comparison of force curves of PNIPAM at RT and 35°C. Figure reproduced with permission from [80]

To understand PNIPAM better, Cui et al. measured the single-molecule mechanical properties of PDEAM, and investigated the coil-to-globule transition and the hydration of a single PDEAM chain [80]. The normalized force curves of the two polymers obtained in nonpolar organic solvents, in which the inherent elasticity of individual polymer chain was reflected, superposed very well in the entire force curve. It was expected that, in most cases, the inherent elasticity of a polymer chain was only related to the backbone but was independent of the side groups (Fig. 13a). However, it was shown that the behaviors of the two polymers in water at RT were very different in the SMFS results; see Fig. 13b–d. During the chain elongation at RT, the additional energy consumed for the water rearrangement showed a large

difference (~5.19 ± 0.10 kJ/mol for PNIPAM and ~1.13 ± 0.10 kJ/mol for PDEAM), which was attributed to the different polymer side groups [94]. The key point was that, on the N atom of the side groups of the two polymers, there are an H atom and a hydrophobic isopropyl group for PNIPAM, but for PDEAM there are only two hydrophobic ethyl groups. Because the PNIPAM chain contains both H-bond donor and acceptor, it was more hydrated in water than the PDEAM chain, which only contains acceptor. Therefore, more energy would be consumed for PNIPAM upon elongation.

When the temperature was above its LCST, the single-chain elasticity of PDEAM was not dependent on the temperature, remarkably different to PNIPAM. This may indicate that the variation of the mechanical properties of PDEAM chain during the phase transition is too small to be distinguished (beyond the force resolution of AFM). The significant different temperature-dependence of the two polymers can be explained by two factors: conformation and hydration. First, the globule conformation of PNIPAM was more compact than that of PDEAM at $T >$ LCST. Second, the formation of the intrachain H-bonds of PDEAM was not possible because of the absence of the H-bonds donors in the chain. As a result, with increase of temperature the amount of water molecules dehydrated from the polymer chain of PNIPAM was more than that of PDEAM. That is, the PNIPAM consumes more energy upon stretching [95]. By SMFS, the minor change in structure of the polymer chain was clearly distinguished.

5 Interactions Between Macromolecules and Solid Surface

Great progress has been made recently in the preparation and characterization of organic and polymeric ultra-thin multilayer films. Particularly, the layer-by-layer (LbL) assembly technique, which can be traced back to the pioneering work of Iler in 1966, has been developed very rapidly and has produced promising results [96–99]. The growing interest in LbL assembly is because of the unusual properties of the resulting nanostructured materials and their anticipated applications in the fields of advanced devices and sensors. To date, many delicate methods have been well established to fabricate layered assemblies with tailored architectures. These methods are mainly based on either one or in most cases several combined intermolecular interactions, such as electrostatic forces, H-bonding, and van der Waals interactions. Although the assembly methods are well established, there are still many problems to be addressed, above all the strength of the driving force in LbL assembly. Unfortunately, the strength at the single-molecule level cannot be directly measured by traditional methods. Since the early 2000s, Zhang and coworkers have combined the LbL construction technique and SMFS to investigate directly the strength of the driving force in LbL assembly by detaching the target polymer chain from a substrate [100–103].

5.1 Desorption of Polyelectrolytes from Solid Surface

Utilizing the electrostatic interactions as the driving force, various polyelectrolytes are often used as building blocks in LbL assembly. To initiate the target first layer assembly, the substrate is usually treated to bear charge. For instance, the unmodified clean quartz substrate is nearly neutral in charge. However, a chemical modification by amino groups results in a positively charged surface when immersed into neutral or acidic aqueous solutions [101, 103]. A widely used polyanion, poly(2-acrylamido-2-methyl propane sulfonic acid) (PAMPS), can be adsorbed onto the oppositely charged amino-modified quartz. The strength of the driving force for this case has been measured by SMFS in aqueous environment [103]. The typical force curve of the desorption of single chain of PAMPS from the amino-modified quartz is shown in Fig. 14. The sharp peak in the initial stage of each force curve corresponds to the strong adhesion force between the bare tip and the uncovered regions of the substrate. For the case that one polymer chain is captured by the tip, only a little of the apex surface area is affected and the strong interaction between the tip and substrate is retained. Subsequently followed by a long plateau, the force drops to zero, indicating a rupture of the polymer bridge. The distance from the initial stage to the end of plateau is about 230 nm, giving an apparent contour length of the polymer chain being stretched (see Fig. 14). The applied force remains constant over the whole range of the plateau, which indicates that no remarkable elastic elongation occurs on the polymer chain being stretched. Because of the repulsion between monomers, the strongly charged polyelectrolyte chain assumes an extended conformation in solution [104], which facilitates an adsorption of single chains in a train-like conformation on the surface with opposite charge. When the long adsorbed train is attached, the AFM tip retraction progressively unzips the sequence of its binding sites with the surface and the force should

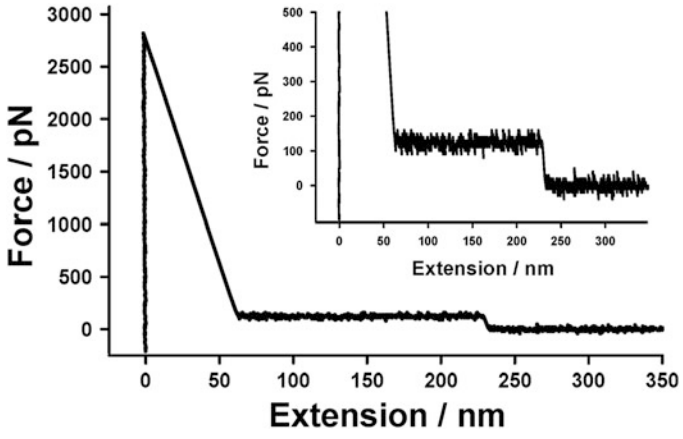

Fig. 14 Typical force curve of PAMPS that shows a long plateau with height of ~120 pN. Figure reproduced with permission from [103]

remain constant, resulting in a long plateau in the force curve [101, 105]. The desorption force of the single PAMPS chain from the substrate, indicated by the height of the long plateau, remains ~120 pN along the desorption (unzipping) process (see more clearly from the inset of Fig. 14). The loading rate-independent result implies that the lifetime of the bond between the PAMPS chain and the substrate is much shorter than the time scale in our experiments (0.1–1 ms), and the desorption process is carried out in an quasi-equilibrium state. Thus, the adhesion force between PAMPS chain and the substrate is equal to the desorption force obtained.

5.2 Desorption of Neutral Polymers from Solid Surface

In many studies, poly(4-vinyl pyridine) (P4VP) was deposited as the first layer on the substrate, such as the amino group modified quartz. It was assumed that the main driving force is H-bonding [106–108]. By utilizing the SMFS method, Zhang et al. exploited the same system to investigate the strength of the driving force of the first P4VP layer in LbL assembly [100]. Each peak in the force curve after the initial large peak corresponds to the detachment of a polymer segment from the substrate. Several peaks appear in each curve, producing an overall sawtooth pattern. The sawtooth pattern in the force curves has been attributed to the detachment of polymer loops from the substrate in series.

Statistical analysis revealed that the most probable desorption force is ~180 pN. Besides, the desorption force distribution showed that the integer multiples of 180 pN are also frequently observed. This result suggests that the value of 180 pN is an elementary force quantum, which can be attributed to the desorption of a single anchor point of P4VP from the substrate. When the substrate is changed to hydroxyl group-modified quartz, the most probable desorption force shifts to higher values. This result confirms that the signals observed in the force curve correspond to the desorption of P4VP from the substrate, not from the AFM tip. Further experiments shows that the desorption force of a single anchor point is independent of the loading rate, implying that the measurement is carried out in a quasi-equilibrium condition. In other words, the adsorption force between P4VP and the substrate is equal to the measured desorption force. It should be noted that the adsorption force of a single anchor point of P4VP is much stronger than a single H-bond [14, 109], which may suggest that, besides the H-bonding, other interactions (such as the solvophobic interactions) contribute to the driving force of the LbL assembly [110].

It is generally accepted that hydrophobic forces play a central role in the self-assembly carried out in aqueous medium, especially when large building blocks are involved. Yet, a quantitative understanding of this role has been elusive [111]. Again, SMFS is more powerful than traditional methods in this case, which was demonstrated by the work of Zhang et al. in 2003 [102]. To measure

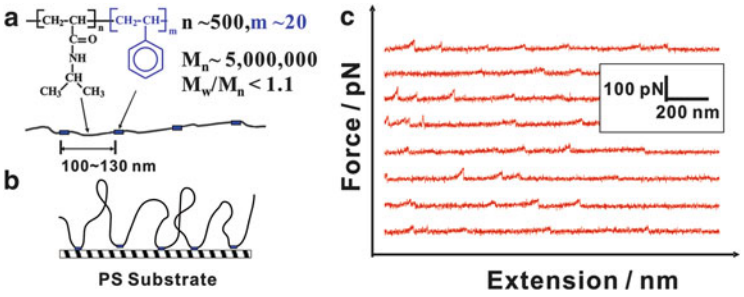

Fig. 15 (**a**) Molecular structure of PNIPAM-seg-PS. (**b**) Schematic of the adsorbed conformation of PNIPAM-seg-PS on PS substrate. (**c**) Typical force curves obtained in DI water. Figure reproduced with permission from [102]

the hydrophobic forces per monomer unit, they prepared a segmented copolymer called PNIPAM-seg-PS, in which short hydrophobic PS segments were more uniformly inserted into a linear PNIPAM hydrophilic backbone [112]. The structure and composition of such a copolymer chain is schematically shown in Fig. 15a. It is reasonable to expect that the adsorption of insoluble short hydrophobic PS segments onto the hydrophobic PS substrate result in many PNIPAM "loops". Figure 15c shows that the force curves exhibit a similar characteristic, namely, a sawtooth pattern. To find why such a pattern exists and how it is related to the chain structure, the distance between each two adjacent peaks in the force curves was analyzed statistically. The Gaussian fitting of the histogram led to an average distance of ~114 nm, which is very close to the average length of the "repeat unit" (one long PNIPAM segment plus one short PS segment, ~100–130 nm in length) in the copolymer chain. These results suggest that the copolymer chain forms loops with a similar size on the PS substrate. Therefore, the sawtooth pattern corresponds to the detachment of the adsorbed PS segments in a single chain from the PS substrate. It was found that for a given stretching velocity ($V_{\text{stretch}} = 4{,}600$ nm/s) the desorption force essentially follows a Gaussian distribution and the most probable desorption force (F_{MPD}) is ~41 pN. An interesting observation is that FMPD increases with increasing V_{stretch}. The linear dependence of FMPD on $\log(V_{\text{stretch}})$ indicates that the adsorption and desorption of the PS segments on the PS substrate is a dynamic process. Because each PS segment contains 20 monomer units on average, it is estimated that the desorption force per PS monomer unit from the PS substrate in water is in the range of 1.3–2.1 pN, depending on the imposed stretching velocity. Compared with previous achievements using different methods [66, 113], this study provides, for the first time, a more direct determination because of its single chain manipulation.

6 SMFS Studies on the Interactions Involved in Supramolecular Polymers

In recent years, the development of supramolecular chemistry is usually related to the finding of new acceptors, including cyclodextrins [114], calixarenes [115], cucurbiturils [116], and pillararenes [117], which have frequently been used in the supramolecular systems. Since the concept of "supramolecular polymer" was proposed [2], the interest of supramolecular chemistry has been extended from the host–guest recognition interactions to the discovery of polymerization methods and functional materials with different applications, which include stimuli responsiveness, self-healing, and environmental adaptation [3, 118–120]. With the development of a series of supramolecular polymerization methods, a variety of novel supramolecular polymers are prepared with various non-covalently interactions [121], including host–guest, metal–ligand, H-bonding, π–π, and charge-transfer interactions.

6.1 Host–Guest Interactions

Molecular recognition is the specific binding of a guest molecule to a complementary host molecule to form a host–guest complex [36]. This concept was proposed in the very early stages during the developing of supramolecular chemistry. There are many examples utilizing host–guest interactions to construct supramolecular systems. Among others, the β-cyclodextrin (β-CD), a cyclic oligosaccharide consisting of seven glucose units linked via α-1-4 glycosidic bonds, is a commonly used host molecule, and various molecules (e.g., ferrocene) can be bound in the cavity as guest, mainly via hydrophobic forces [122, 123]. SMFS has been utilized to investigate this important supramolecular system at the single-molecule level [124–128].

The strategy of the experiment involves two steps. The first step is to chemically modify the AFM tip and substrate with host and guest molecules, respectively. The second step is to enable the formation of host–guest complex by bringing together the two surfaces, and rupturing the complex by separating them (see Fig. 16). During the latter step, the force curve is recorded, which provides extensive information on the system. One useful piece of information which can be extracted from the force curve is the rupture force of the host–guest complex. In an ideal case, an individual rupture event is observed in one force curve. However, multiple rupture events can occur simultaneously, which is actually the usual case. Therefore, a statistical analysis on plenty of similar force curves is necessary. Such analysis has shown that the observed rupture forces are integer multiples of one fundamental force quantum of 55 ± 10 pN, which is attributed to the rupture of an individual ferrocene–CD complexes in aqueous medium [124]. Further investigation of ferrocene–CD complexes showed that this force quantum is independent of

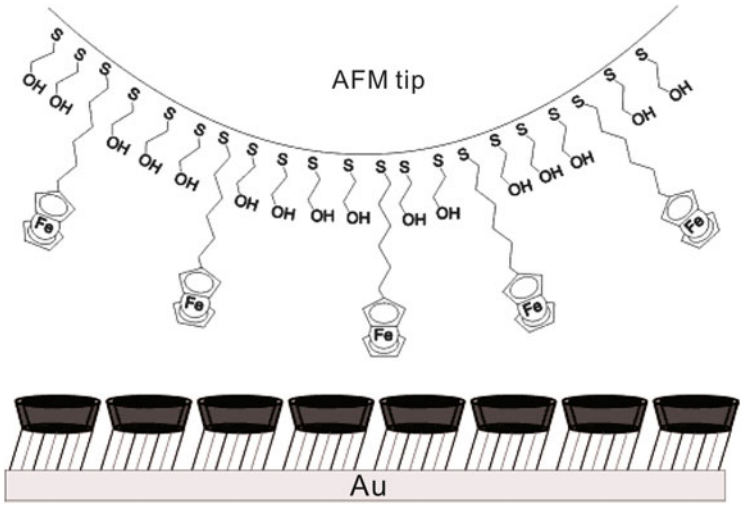

Fig. 16 Schematic representation (not to scale) of SMFS of ferrocene guest immobilized in a hydroxyl terminated SAM on an AFM tip and a SAM of CD on Au(111). Figure reproduced with permission from [124]

the spacer length, and independent of the unloading rate [125]. These results indicate that the host–guest complex rupture forces were probed under conditions of thermodynamic equilibrium. This is different from the previously studied biological systems, which are dependent of the unloading rate [129–131].

Besides ferrocene, other molecules with similar shape, such as adamantane and benzene, can be guest molecules in the β-CD host. Systematic studies of SMFS found similar results. The analysis of the histograms revealed periodic distributions of forces with loading-rate independent maxima at integer multiples of a certain force quantum characteristic of each guest. For instance, the observed force quanta were 39 ± 15 pN for benzene and 102 ± 15 pN for adamantane, respectively. The force values followed the same trend as the free binding energy ΔG measured for model guest compounds in solution or on β-CD monolayers, as determined by microcalorimetry and surface plasmon resonance measurements, respectively [126].

6.2 Metal–Ligand Interactions

Metal–ligand interactions are often used to fabricate supramolecular systems with regular shapes, e.g., double helicates, racks, grids, and linear rods [36]. These systems are well understood with respect to their behaviors in the solid state as well as on surfaces. However, little was known about the binding force of the supramolecular complexes. Several systems on the topic of metallo-supramolecules

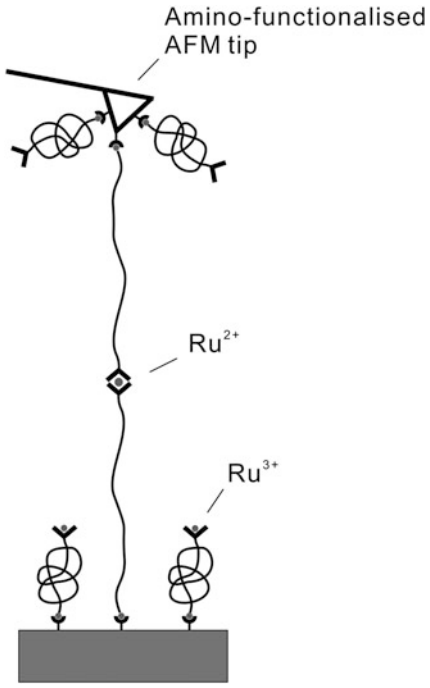

Fig. 17 Schematic of the SMFS experiment. Figure reproduced with permission from [33]

have been studied by SMFS [33, 132]. For such purpose, the researchers chemically modified the substrate with a layer of terpyridine Ru(II) mono-complexes, as shown in Fig. 17. The tip was chemically modified with a layer of non-complexed terpyridine ligand. By bringing together the tip and the substrate, the direct proximity of the free ligand and the mono-complex allow the formation of bisterpyridine complexes. By retracting the tip from the substrate, the complex is stretched till rupture, where the rupture force corresponds to the binding force of the bisterpyridine Ru(II) complexes. Statistical analysis of the rupture force shows that, at a given velocity of 118 nm/s, the histogram exhibits one pronounced peak at 95 pN followed by weaker peaks at 171 and 253 pN. The weaker peaks were attributed to the simultaneous rupture of two or three parallel complexes, respectively. This hypothesis was supported by elasticity model fitting and Monte Carlo simulations [33].

6.3 H-Bonding

Supramolecular polymers [2, 133] (also called reversible polymers) are comprised of bifunctional monomeric units that are reversibly aggregated through relatively strong non-covalent interactions. For instance, the self-complementary and recognition of the quadruple H-bonded bis(2-ureido-4[1*H*]-pyrimidinone) (bisUPy) can

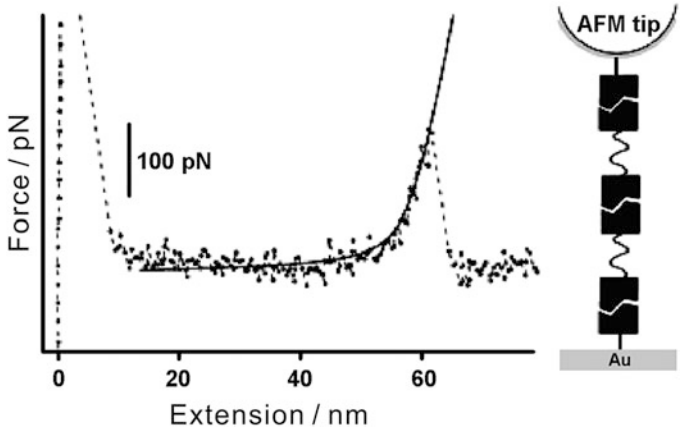

Fig. 18 Schematic of the SMFS experiment and typical force curve obtained in a hexadecane. Figure reproduced with permission from [134]

form rather stable supramolecular polymers. By utilizing SMFS, Zou et al. measured the strength of the driving force of the self-assembly between the monomers (Fig. 18) [134, 135].

As shown in Fig. 18, the apex of the peak of the force curve corresponds to the rupture of the supramolecular polymer upon stretching, from which the "degree of polymerization" (DP) can be estimated to be 2–15. At 301 K and a loading rate of 35 nN/s, the rupture force of the supramolecular polymer upon stretching, which is indicated by the apex of the peak, is 172 ± 23 pN. For the pure dimmers, the rupture force is 180 ± 21 pN [134]. The rupture forces decrease with increasing lengths of the stretched supramolecular polymer chains. This observation is in agreement with the theory developed by Evans et al. [136, 137], who predicted a decrease in the magnitude of the single-complex rupture force with increasing spacer length [138].

By contrast, for measurements carried out in situ at 330 K, no loading-rate dependence was observed for rates between 5 and 200 nN/s. This observation indicates that the corresponding experiment was carried out under quasi-equilibrium conditions. These data obtained at 330 K are equivalent to those obtained at 301 K, but at a lower loading rate [135, 139].

To obtain the thermal force and dimer equilibrium constant K_{eq} using the Evans model, the most probable rupture force between the binding motifs is usually measured for various loading rate. By utilizing the theory of Evans and Williams, Vancso et al. found that those parameters can be obtained even with one data set at a single loading rate. The value of the dimer equilibrium constant obtained for UPy–UPy dimers in hexadecane agrees very well with the value of $K_{eq} \sim 1 \times 109\ M^{-1}$ predicted by previous studies with bulk measurements [140].

More recently, the binding force of another self-complementary quadruple H-bonding motif, urea-aminotriazine (UAT), was investigated by SMFS [141, 142]. By measuring the rupture force between UAT at various loading rates, the

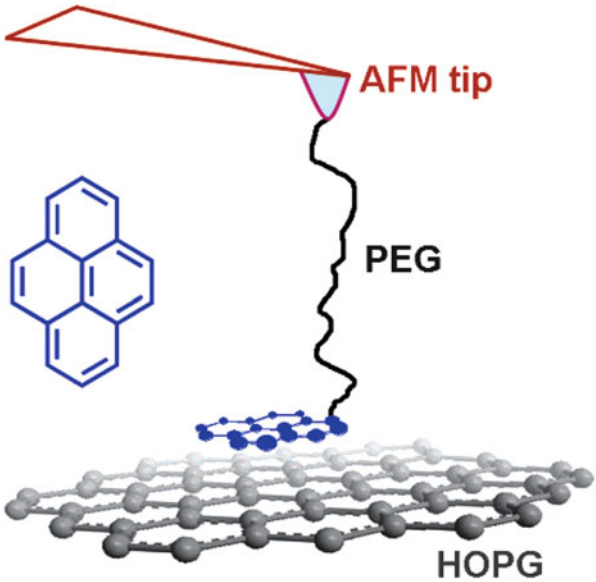

Fig. 19 Schematic setup for measuring the π–π interaction between pyrene and graphite in aqueous medium by SMFS. Figure reproduced with permission from [144]

bond lifetime at zero force, $t_{off}(0)$, can be estimated to be 100 ± 80 ms. This SMFS result is nearly three times higher than that estimated from the data of bulk measurements. This marked discrepancy shows that the complex is much more stable than predicted on the basis of the simple model, in which the stabilization effect of the planarized molecular geometry is not covered. These studies demonstrated that SMFS is an indispensable supplement to the characterization methods.

6.4 π–π Interactions

The π–π interactions (aromatic interactions) are ubiquitous and important in diverse phenomena, including stabilizing DNA and protein structures, packing aromatic molecules in crystals, and binding guest moieties to host systems. It has been suggested that π-π interactions consist of electrostatic, hydrophobic, and van der Waals forces [143]. By modifying the AFM tip with a pyrene tailored polymer chain, Zhang et al. successfully detected the desorption force of a single pyrene unit from a graphite surface (see Fig. 19) [144]. Interestingly, the measured force, 55 ± 16 pN, is independent of the loading rate, implying that the measurement is carried out under quasi-equilibrium conditions. In other words, the adsorption force between the pyrene unit and the graphite surface is equal to the desorption force obtained.

6.5 *Host-Stabilized Charge Transfer Interactions*

Host-stabilized charge transfer interaction (HSCT) is a concept that was proposed by Kim et al. in which donor and acceptor are both encapsulated in the cavity of the host cucurbit[8]uril (CB[8]) [145, 146]. Because of the short distance between the donor and the acceptor, the CT interaction is remarkably enhanced. However, attempts to obtain supramolecular polymers with a high degree of polymerization utilizing only single HSCT interactions have failed for the following reasons: (1) the strength of single HSCT interactions was not sufficient and (2) single HSCT interactions do not have high orientation selectivity, thus leading to the formation of cyclic species and suppressing the formation of polymeric species.

Recently, Zhang et al. have developed a new idea of utilizing multiple HSCT interactions for fabricating supramolecular polymers [121, 128]. By using a carefully designed multifunctional monomer, the cyclization is successfully suppressed, leading to the formation of supramolecular polymers. SMFS results revealed that the rupture force of the supramolecular polymer can be nearly 200 pN, indicating that the binding force within the supramolecular polymer is rather strong. The contour length measured by SMFS can reach as high as 600 nm, implying that the supramolecular polymer has a high degree of polymerization.

7 SMFS Studies on Synthetic Molecular Machines and Analog Systems

To mimic the fantastic biomolecules that can generate directional forces, people have attempted to design and synthesize a number of molecular machines during the last two decades. Because molecular machines usually work at the single-molecule level, SMFS is an ideal method to investigate those systems. We would like to provide four examples of SMFS studies of the synthetic molecular machines in this section.

Azobenzene is a light-sensitive molecule. Under irradiation by UV light of 365 nm, the azobenzene in *trans* configuration is converted to *cis* isomer, and under irradiation by light of 420 nm, an inverse process takes place. A change of end-to-end distance is expected with these transitions, i.e., the molecule is shortened upon transition from *trans* to *cis* and vice versa. By utilizing a polymer containing azobenzene groups in the backbone, Gaub et al. first realized the conversion from light energy to mechanical work at the single-molecule level [147, 148]. To minimize the negative effects to the AFM cantilever, the evanescent wave from total internal reflection was used. A shortening of ~3 % of the polymer chain was observed from the saturated *trans-azo* state to the saturated *cis-azo* state. The efficiency of converting optical energy to mechanical work was up to 10 %.

In 2007, Vancso and coworkers realized the closed-cycle conversion from electric energy to mechanical work at the single-molecule level [149]. The

electrochemically responsive polymer, poly(ferrocenylsilane) (PFS), was covalently attached to a gold electrode. Using SMFS it was found that the PFS chain shrank when the oxidized state was converted into the neutral state. The shrinkage against an external load can be used to design a molecular device. A maximum conversion efficiency of 26% was obtained in the single molecule experiments.

Rotaxanes are paradigm synthetic molecular machine systems which enable controlled large-amplitude movement and positioning of one mechanically interlocked component with respect to another. Differing from the previously studied biological/synthetic molecular machines, a rotaxane is a small molecule (less than 5 nm long). Recently, Leigh and his coworkers investigated an elegant system with rotaxanes by SMFS [150, 151]. In a rotaxane, the molecular ring is threaded onto a molecular axle. There are two H-bond binding site in the axle, but with different affinities to the motif in the ring. A peak of ~30 pN can be found upon elongation of the PEO chain, which is linked to the ring of rotaxane. This peak can be observed upon elongation or relaxation, which indicates that the process is reversible. Confirmed by control experiments, the peak is attributed to the process of breaking/forming of the H-bonding between the two motifs in the molecule ring and axle of the rotaxane, respectively. In the relaxation process, the macrocycle travels back from the weak binding site to the strong one and it is able to generate a force against the external load of 30 pN, similar to those generated by biological machines. The mechanical work produced by this sub-molecular motion is ~6 kcal mol^{-1}. This work demonstrates that AFM-SMFS can be used to investigate the mechanochemical behavior of a molecule less than 5 nm in size.

During the past 20 years, proteins and synthetic polymers have been investigated by SMFS, which has aided in the understanding of their nanomechanical properties. However, it remains a challenge to correlate directly the bulk mechanical performance to the nanomechanical properties of individual constituent macromolecules. Guan et al. recently made major progress towards this goal [152–154]. They synthesized a biomimetic modular polymer with two UPy (see also Sect. 6.3) motifs in each module. By stretching/relaxing, the UPy motifs in single modular polymer chain can be unfolded/refolded, resulting in a sawtooth pattern in the force curve, which resembles that of a modular protein, titin. By increasing the stretching velocity, an increase of the rupture force of the UPy motifs can be observed, through which the parameters of the single-molecule energy landscape can be derived. When the mechanical properties of bulk material from the same polymer were compared with those at the single-molecule level, Guan et al. found direct correlations between these two block of data: the high rupture force and quantitative passive re-folding observed at the single-molecule level can be associated with the large energy dissipation during plastic deformation, as well as the slow but complete recovery of strength, strain, and toughness observed during the course of the load relaxation recovery cycle in the bulk experiment. These results illustrated the potential for SMFS to serve as a guide for future rational design of advanced multifunctional materials.

8 Summary and Perspective

During the last two decades, the supramolecular chemistry and mechanochemistry of macromolecules have been developed greatly. The SMFS method provided an effective way to access the macromolecules at the single-chain level. With the single-molecule mechanics results, the classic polymer chain theory of Flory has been verified for the first time. The bound water of macromolecules and the rearrangement upon elongation have been investigated, showing that the energies associated with the bound water is very important to the self-assembly of biomacromolecules. For supramolecular polymers, the binding force between the moieties has been measured directly. With the great effort of researchers, a clearer image of macromolecules system has been revealed at the molecular level.

However, there are still some challenges in this field. Here are two examples. (1) The database of single-chain elasticity of macromolecules is not yet complete. As with the periodic table of elements, a complete database of macromolecules would certainly be helpful for the development of science and engineering. (2) The noise level of SMFS is still too high. A typical noise of 5–10 pN conceals some important data. However, it is greatly anticipated that, in the future, SMFS can contribute further to the development of supramolecular chemistry and mechanochemistry of macromolecules.

Acknowledgements This work was supported by the Natural Science Foundation of China (21222401, 21074102), the program for New Century Excellent Talents in University (NCET-11-0708), and the Fundamental Research Funds for the Central Universities (SWJTU11ZT05, SWJTU12CX001).

References

1. Lehn J-M (1985) Science 227:849
2. Brunsveld L, Folmer BJB, Meijer EW, Sijbesma RP (2001) Chem Rev 101:4071
3. Lehn J-M (2013) Angew Chem Int Ed 52:2836
4. Lehn J-M (2007) Chem Soc Rev 36:151
5. Lehn JM (2002) Proc Natl Acad Sci U S A 99:4763
6. Lehn JM (2002) Polym Int 51:825
7. Gulik-Krzywicki T, Fouquey C, Lehn J (1993) Proc Natl Acad Sci U S A 90:163
8. Grandbois M, Beyer M, Rief M, Clausen-Schaumann H, Gaub HE (1999) Science 283:1727
9. Rief M, Oesterhelt F, Heymann B, Gaub HE (1997) Science (Washington D.C.) 275:1295
10. Rief M, Gautel M, Oesterhelt F, Fernandez JM, Gaub HE (1997) Science 276:1109
11. Hugel T, Seitz M (2001) Macromol. Rapid Commun 22:989
12. Janshoff A, Neitzert M, Oberdorfer Y, Fuchs H (2000) Angew Chem Int Ed 39:3212
13. Clausen-Schaumann H, Rief M, Tolksdorf C, Gaub HE (2000) Biophys J 78:1997
14. Rief M, Clausen-Schaumann H, Gaub HE (1999) Nat Struct Mol Biol 6:346
15. Marszalek PE, Lu H, Li HB, Carrion-Vazquez M, Oberhauser AF, Schulten K, Fernandez JM (1999) Nature 402:100
16. Li YR, Qin M, Li Y, Cao Y, Wang W (2014) Langmuir 30:4358
17. Fuhrmann A, Getfert S, Fu Q, Reimann P, Lindsay S, Ros R (2012) Biophys J 102:2381

18. Friddle RW, Noy A, De Yoreo JJ (2012) Proc Natl Acad Sci U S A 109:13573
19. Jiang ZH, Zhang YH, Yu Y, Wang ZQ, Zhang X, Duan XR, Wang S (2010) Langmuir 26:13773
20. Song B, Schönherr H (2012) Supramolecular chemistry. Wiley, Ltd
21. Schroeder T, Walhorn V, Mattay J, Anselmetti D (2012) Analytical Methods in Supramolecular Chemistry. Volume 1&2, Second Edition: 559 Wiley Online Library
22. Neuman KC, Nagy A (2008) Nat Methods 5:491
23. Liu K, Song Y, Feng W, Liu N, Zhang W, Zhang X (2011) J Am Chem Soc 133:3226
24. Liu N, Peng B, Lin Y, Su Z, Niu Z, Wang Q, Zhang W, Li H, Shen J (2010) J Am Chem Soc 132:11036
25. Binnig G, Quate CF, Gerber C (1986) Phys Rev Lett 56:930
26. Oesterhelt F, Rief M, Gaub HE (1999) New J Phys 1:6.1
27. Zhang W, Zhang X (2003) Prog Polym Sci 28:1271
28. Marszalek PE, Oberhauser AF, Pang Y, Fernandez JM (1998) Nature 396:661
29. Zhang WK, Zou S, Wang C, Zhang X (2000) J Phys Chem B 104:10258
30. Liu C, Cui S, Wang Z, Zhang X (2005) J Phys Chem B 109:14807
31. Cui S, Albrecht C, Kühner F, Gaub HE (2006) J Am Chem Soc 128:6636
32. Cui S, Yu J, Kuehner F, Schulten K, Gaub HE (2007) J Am Chem Soc 129:14710
33. Kudera M, Eschbaumer C, Gaub HE, Schubert US (2003) Adv Func Mater 13:615
34. Kuehner F, Erdmann M, Sonnenberg L, Serr A, Morfill J, Gaub HE (2006) Langmuir 22:11180
35. Sonnenberg L, Luo Y, Schlaad H, Seitz M, Coelfen H, Gaub HE (2007) J Am Chem Soc 129:15364
36. Lehn J-M (1995) Supramolecular chemistry: concepts and perspectives. VCH, Weinheim
37. Kellermayer MSZ, Smith SB, Granzier HL, Bustamante C (1997) Science 276:1112
38. Bustamante C, Marko JF, Siggia ED, Smith S (1994) Science (Washington, D.C.) 265:1599
39. Smith SB, Finzi L, Bustamante C (1992) Science 258:1122
40. Smith SB, Cui Y, Bustamante C (1996) Science 271:795
41. Li HB, Zhang WK, Xu WQ, Zhang X (2000) Macromolecules 33:465
42. Bao Y, Qian HJ, Lu ZY, Cui SX (2014) Nanoscale 6:13421
43. Wang K, Pang X, Cui S (2013) Langmuir 29:4315
44. Flory P, Volkenstein M (1969) Statistical mechanics of chain molecules. Wiley Online Library
45. Tskhovrebova L, Trinick J, Sleep JA, Simmons RM (1997) Nature 387:308
46. Marko JF, Siggia ED (1995) Macromolecules 28:8759
47. Hugel T, Rief M, Seitz M, Gaub HE, Netz RR (2005) Phys Rev Lett 94:048301
48. Cui S, Yu Y, Lin Z (2009) Polymer 50:930
49. Klemm D, Heublein B, Fink HP, Bohn A (2005) Angew Chem Int Ed 44:3358
50. Wan Z, Li L, Cui S (2008) Biopolymers 89:1170
51. Azizi Samir MAS, Alloin F, Dufresne A (2005) Biomacromolecules 6:612
52. Sakurada I, Nukushina Y, Ito T (1962) J Polym Sci Pol Chem 57:651
53. Wang H, Gurau G, Rogers RD (2012) Chem Soc Rev 41:1519
54. Zhang H, Wu J, Zhang J, He J (2005) Macromolecules 38:8272
55. Eichhorn S, Young R (2001) Cellulose 8:197
56. French AD, Johnson GP (2009) Cellulose 16:959
57. Cui S (2010) Phys Chem Chem Phys 12:10147
58. Tanford C (1970) Adv Prot Chem 24:195
59. Bergstrom K, Holmberg K, Safranj A, Hoffman AS, Edgell MJ, Kozlowski A, Hovanes BA, Harris JM (1992) J Biomed Mater Res 26:779
60. Mandelkern L (1990) Acc Chem Res 23:380
61. Begum R, Matsuura H (1997) J Am Chem Soc 93:3839
62. Watson JD, Crick FH (1953) Nature 171:737
63. Kool ET, Morales JC, Guckian KM (2000) Angew Chem Int Ed 39:990

64. Tanaka K, Okahata Y (1996) J Am Chem Soc 118:10679
65. Brooks BR, Bruccoleri RE, Olafson BD, States DJ, Swaminathan S, Karplus M (1983) J Comput Chem 4:187
66. Pashley RM, McGuiggan PM, Ninham BW, Evans DF (1985) Science 229:1088
67. Ball P (2008) Nature 452:291
68. Brovchenko I, Krukau A, Oleinikova A, Mazur AK (2008) J Am Chem Soc 130:121
69. Breslauer KJ, Frank R, Blöcker H, Marky LA (1986) Proc Natl Acad Sci U S A 83:3746
70. Miller SL (1953) Science 117:528
71. Knight RD, Landweber LF (2000) Cell 101:569
72. Giannotti MI, Rinaudo M, Vancso GJ (2007) Biomacromolecules 8:2648
73. Haxaire K, Buhler E, Milas M, Perez S, Rinaudo M (2002) Hyaluronan, vol 1. Woodhead Publishing Ltd., Cambridge, p. 37
74. Pelton R, Chibante P (1986) Colloids Surf 20:247
75. Meyer DE, Shin B, Kong G, Dewhirst M, Chilkoti A (2001) J Control Release 74:213
76. Schild H (1992) Prog Polym Sci 17:163
77. Lessard D, Ousalem M, Zhu X, Eisenberg A, Carreau P (2003) J Polym Sci Pol Phys 41:1627
78. Cui S, Pang X, Zhang S, Yu Y, Ma H, Zhang X (2012) Langmuir 28:5151
79. Pang X, Wang K, Cui S (2013) Polymer 54:3737
80. Pang X, Cui S (2013) Langmuir 29:12176
81. Wang X, Qiu X, Wu C (1998) Macromolecules 31:2972
82. Okada Y, Tanaka F (2005) Macromolecules 38:4465
83. Cheng H, Shen L, Wu C (2006) Macromolecules 39:2325
84. Tanaka F, Koga T, Winnik FM (2008) Phys Rev Lett 101:028302
85. Ono Y, Shikata T (2006) J Am Chem Soc 128:10030
86. Cho EC, Lee J, Cho K (2003) Macromolecules 36:9929
87. Sun B, Lin Y, Wu P, Siesler HW (2008) Macromolecules 41:1512
88. Kay ER, Leigh DA, Zerbetto F (2007) Angew Chem Int Ed 46:72
89. Zhang G, Wu C (2001) Phys Rev Lett 86:822
90. Winnik FM, Ringsdorf H, Venzmer J (1990) Macromolecules 23:2415
91. Tanaka F, Koga T, Kojima H, Winnik FM (2009) Macromolecules 42:1321
92. Katsumoto Y, Tanaka T, Ihara K, Koyama M, Ozaki Y (2007) J Phys Chem B 111:12730
93. Chee CK, Hunt BJ, Rimmer S, Soutar I, Swanson L (2011) Soft Matter 7:1176
94. Idziak I, Avoce D, Lessard D, Gravel D, Zhu X (1999) Macromolecules 32:1260
95. Maeda Y, Nakamura T, Ikeda I (2001) Macromolecules 34:1391
96. Iler RK (1966) J Colloid Interface Sci 21:569
97. Decher G, Hong JD (1991) Makromol Chem Macromol Symp 46:321
98. Decher G (1997) Science 277:1232
99. Zhang X, Chen H, Zhang H (2007) Chem Commun 1395
100. Zhang W, Cui S, Fu Y, Zhang X (2002) J Phys Chem B 106:12705
101. Cui S, Liu C, Zhang X (2003) Nano Lett 3:245
102. Cui SX, Liu CJ, Zhang WK, Zhang X, Wu C (2003) Macromolecules 36:3779
103. Cui S, Liu C, Wang Z, Zhang X, Strandman S, Tenhu H (2004) Macromolecules 37:946
104. Netz R, Joanny J (1999) Macromolecules 32:9013
105. Conti M, Bustanji Y, Falini G, Ferruti P, Stefoni S, Samori B (2001) ChemPhysChem 10:610
106. Wang LY, Wang ZQ, Zhang X, Shen JC (1997) Macromol. Rapid Commun 18:509
107. Wang L, Cui S, Zhang X, Jiang M, Chi L, Fuchs H (2000) Langmuir 16:10490
108. Fu Y, Bai SL, Cui SX, Qiu DL, Wang ZQ, Zhang X (2002) Macromolecules 35:9451
109. Han T, Williams JM, Beebe TP (1995) Anal Chim Acta 307:365
110. Ray A (1971) Nature 231:313
111. Lum K, Chandler D, Weeks JD (1999) J Phys Chem B 103:4570
112. Zhang G, Wu C (2003) Phys Rev Lett 90:035506
113. Zhao X, Zhao W, Zheng X, Rafailovich M, Sokolov J, Schwarz S, Pudensi M, Russell T, Kumar S, Fetters L (1992) Phys Rev Lett 69:776

114. Harada A, Hashidzume A, Yamaguchi H, Takashima Y (2009) Chem Rev 109:5974
115. Botana E, Da Silva E, Benet-Buchholz J, Ballester P, de Mendoza J (2007) Angew Chem Int Ed 46:198
116. Bhasikuttan AC, Pal H, Mohanty J (2011) Chem Commun (Camb) 47:9959
117. Xue M, Yang Y, Chi X, Zhang Z, Huang F (2012) Acc Chem Res 45:1294
118. Dong S, Zheng B, Wang F, Huang F (2014) Acc Chem Res 47:1982
119. Huang Z, Yang L, Liu Y, Wang Z, Scherman OA, Zhang X (2014) Angew Chem Int Ed 53:5351
120. Yan X, Wang F, Zheng B, Huang F (2012) Chem Soc Rev 41:6042
121. Liu YL, Liu K, Wang ZQ, Zhang X (2011) Chem Eur J 17:9930
122. Wenz G (1994) Angew Chem Int Ed 33:803
123. Rekharsky MV, Inoue Y (1998) Chem Rev 98:1875
124. Schoenherr H, Beulen MWJ, Buegler J, Huskens J, van Veggel FC, Reinhoudt DN, Vancso GJ (2000) J Am Chem Soc 122:4963
125. Zapotoczny S, Auletta T, Jong MRD, Schoenherr H, Huskens J, van Veggel FC, Reinhoudt DN, Vancso GJ (2002) Langmuir 18:6988
126. Auletta T, de Jong MR, Mulder A, van Veggel FC, Huskens J, Reinhoudt DN, Zou S, Zapotoczny S, Schoenherr H, Vancso GJ, Kuipers L (2004) J Am Chem Soc 126:1577
127. Kado S, Kimura K (2003) J Am Chem Soc 125:4560
128. Liu Y, Wang Z, Zhang X (2012) Chem Soc Rev 41:5922
129. Kienberger F, Kada G, Gruber HJ, Pastushenko VP, Riener C, Trieb M, Knaus H-G, Schindler H, Hinterdorfer P (2000) Single Mol 1:59
130. Merkel R, Nassoy P, Leung A, Ritchie K, Evans E (1999) Nature 397:50
131. Evans EA, Calderwood DA (2007) Science 316:1148
132. Kersey FR, Yount WC, Craig SL (2006) J Am Chem Soc 128:3886
133. Lehn JM (1993) Makromol. Chem. Macromol Symp 69:1
134. Zou S, Schoenherr H, Vancso GJ (2005) Angew Chem Int Ed 44:956
135. Zou S, Schoenherr H, Vancso GJ (2005) J Am Chem Soc 127:11230
136. Evans E, Ritchie K, Merkel R (1995) Biophys J 68:2580
137. Evans E, Ritchie K (1997) Biophys J 72:1541
138. Evans E (2001) Annu Rev Biophys Biomol Struct 30:105
139. Vancso GJ (2007) Angew Chem Int Ed 46:3794
140. Embrechts A, Schonherr H, Vancso GJ (2008) J Phys Chem B 112:7359
141. Embrechts A, Schonherr H, Vancso GJ (2012) J Phys Chem B 116:565
142. Embrechts A, Velders AH, Schonherr H, Vancso GJ (2011) Langmuir 27:14272
143. Hoeben FJM, Jonkheijm P, Meijer EW, Schenning AP (2005) Chem Rev 105:1491
144. Zhang Y, Liu C, Shi W, Wang Z, Dai L, Zhang X (2007) Langmuir 23:7911
145. Ko YH, Kim E, Hwang I, Kim K (2007) Chem Commun 1305
146. Ko YH, Kim K, Kang JK, Chun H, Lee JW, Sakamoto S, Yamaguchi K, Fettinger JC, Kim K (2004) J Am Chem Soc 126:1932
147. Holland NB, Hugel T, Neuert G, Cattani-Scholz A, Renner C, Oesterhelt D, Moroder L, Seitz M, Gaub HE (2003) Macromolecules 36:2015
148. Hugel T, Holland NB, Cattani A, Moroder L, Seitz M, Gaub HE (2002) Science 296:1103
149. Shi WQ, Giannotti MI, Zhang X, Hempenius MA, Sconherr H, Vancso GJ (2007) Angew Chem Int Ed 46:8400
150. Van Quaethem A, Lussis P, Leigh DA, Duwez AS, Fustin CA (2014) Chem Sci 5:1449
151. Lussis P, Svaldo-Lanero T, Bertocco A, Fustin CA, Leigh DA, Duwez AS (2011) Nat Nanotechnol 6:553
152. Roland JT, Guan Z (2004) J Am Chem Soc 126:14328
153. Chung J, Kushner AM, Weisman AC, Guan ZB (2014) Nat Mater 13:1055
154. Kushner AM, Gabuchian V, Johnson EG, Guan ZB (2007) J Am Chem Soc 129:14110

Top Curr Chem (2015) 369: 135–208
DOI: 10.1007/128_2014_617

Published online: 20 March 2015

Mechanochemistry of Topological Complex Polymer Systems

Huan Zhang, Yangju Lin, Yuanze Xu, and Wengui Weng

Abstract Although existing since the concept of macromolecules, polymer mechanochemistry is a burgeoning field which attracts great scientific interest in its ability to bias conventional reaction pathways and its potential to fabricate mechanoresponsive materials. We review here the effect of topology on the mechanical degradation of polymer chains and the activation of mechanophores in polymer backbones. The chapter focuses on both experimental and theoretical work carried out in the past 70 years. After a general introduction (Sect. 1), where the concept, the history, and the application of polymer mechanochemistry are briefly described, flow fields to study polymer mechanochemistry are discussed (Sect. 2), results of mechanochemistry study are presented for linear polymers (Sect. 3), cyclic polymers (Sect. 4), graft polymers (Sect. 5), star-shaped polymers (Sect. 6), hyperbranched polymers and dendrimers (Sect. 7), and systems with dynamic topology (Sect. 8). Here we focus on (1) experimental results involving the topological effect on the coil-to-stretch transition and the fracture of the polymer chains, (2) the underlying mechanisms and the key factor that determines the mechanical stability of the macromolecules, (3) theoretical models that relate to the experimental observations, and (4) rational design of mechanophores in complex topology to achieve multiple activations according to the existing results observed in chain degradation.

Keywords Bead-rod model · Complex topology · Mechanical degradation · Mechanophore · Polymer mechanochemistry

H. Zhang, Y. Lin, Y. Xu, and W. Weng (✉)
Department of Chemistry, College of Chemistry and Chemical Engineering, Xiamen University, Xiamen, Fujian 361005, P. R. China
e-mail: wgweng@xmu.edu.cn

Contents

Symbols

$\dot{\varepsilon}$	Strain rate
$\dot{\varepsilon}_A$	Critical strain rate for mechanophore activation
$\dot{\varepsilon}_C$	Critical strain rate for CST
$\dot{\varepsilon}_F$	Critical strain rate for chain scission
$[\eta]$	Intrinsic viscosity
$\Delta E^*(0)$	Activation energy at rest (zero force)

$\Delta E^*(F)$	Activation energy of a reaction as a function of external force
ΔP_A	Pressure drop with the drag reduction agent
ΔP_S	Pressure drop with pure solvent
$\Delta\zeta$	Distance from reactant to transition-state configuration along the reaction coordinate ζ
ζ	Reaction coordinate
η_{Base}	Kinematic viscosity of the base oil
η_{Fresh}	Kinematic viscosity of the fresh unsheared lubricant
η_s	Dynamic viscosity of the fluid
η_{Shear}	Kinematic viscosity of the sheared lubricant
ν	Flory exponent
ξ	Hydrodynamic drag coefficient
ξ_g	Hydrodynamic drag coefficient of grafted chains
ρ_s	Density of the solvent
σ_F	Critical force to break a bond
σ_i	Cumulative hydrodynamic drag force on each bead
σ_{mid}	Maximum hydrodynamic drag force at the midpoint of a *linear* chain
σ_{mid_g}	Additional hydrodynamic drag force from side chain
σ_{mid_graft}	Maximum hydrodynamic drag force at the midpoint of a backbone for grating polymers
τ_0	Longest relaxation time of a polymer chain
a	Radius of the beads
b	Length of chain segment
b_g	Distance between neighboring side chains
c	Size of the bead in the side chain
d	Hydraulic diameter of the pipe
DB	Degree of branching
De	Deborah number
DRE	Drag reduction efficiency
f	Hydrodynamic drag force on a bead
F	External force exerts on a chemical reaction
f_{arm}	Number of arms in a star-shaped molecule
k	Rate constant
k_0	Rate constant at zero force
k_B	Boltzmann constant
M	Total molecular weight of a chain
M_{arm}	Molecular weight of an arm in a star-shape molecule
M_{lim}	Limiting molecular weight of a linear polymer chain to observe mechanical degradation
M_{span}	Molecular weight of a spanning path in a nonlinear macromolecule
M_w	Weight averaged molecular weight
N	Total number of repeating units of a macromolecule
N_{arm}	Number of repeating units of an arm
N_L	Number of repeating unit of the *linear* backbone for grafting chain

N_{lad}	Maximum number of repeating unit permissible of a linear macromolecule in a ladder-like polymer
N_{lin}	Maximum number of repeating unit permissible of a linear macromolecule in isolated conformations
N_{span}	Number of repeating units along the spanning path
p	Number of side chains in bead-rod model
R	End-to-end distance of a polymer coil
R_{arm}	End-to-end distance of the arm
Re	Reynolds number
R_G	Radius of gyration for a polymer coil
R_H	Hydrodynamic radius of a polymer coil
S_1	Shielding factor of the linear backbone
S_2	Shielding factor of the grafting chain
T	Kelvin temperature
V	Mean velocity of the fluid
v_i	Velocity of a bead
Wi	Wiener index

Abbreviations

cPPA	Cyclic poly(*o*-phthalaldehyde)
CST	Coil-to-stretch transition
FTF	Fast-transient-flow
MC	Merocyanine
PAA	Poly(acrylic acid)
PAM	Poly(acrylamide)
PB	Polybutadiene
PDMS	Poly(dimethylsiloxanes)
PE	Polyethylene
PEA	Poly(ethyl acrylate)
PEO	Polyethylene oxide
PiBA	Poly(*iso*-butyl acrylate)
PMA	Poly(methyl acrylate)
PMMA	Poly(methyl methacrylate)
PnBA	Poly(*n*-butyl acrylate)
PS	Polystyrene
PtBA	Poly (*tert*-butyl acrylate)
QSSF	Quasi-static-state-flow
SP	Spiropyran

1 Introduction

1.1 Mechanochemistry

Mechanochemistry is a branch of chemistry which is concerned with chemical and physicochemical changes of substances of all states of aggregation due to the influence of mechanical energy.

The term "mechanochemistry" was first coined by Ostwald (Nobel Prize, 1909) in his books [1, 2]. This definition underlines the mutual transformation of the mechanical and chemical energy and is well accepted by modern researchers. In retrospect, our ancestors had already exploited mechanochemical phenomena for survival since time immemorial, making fire by drilling wood. The first document related to mechanochemical reaction dates back to about 315 B.C. Theophrastus of Eresus, Aristotle's student and successor, wrote a booklet entitled "On Stones." A reference in this book described the reduction of cinnabar to mercury by grinding in a copper mortar with a copper pestle [3]. In the nineteenth century, scientists started the fundamental work in this area. They exploited the influence of mechanical energy on the properties of solid substances by grinding or sliding. Faraday reported the reaction of silver chloride by grinding with zinc, tin, iron, and copper in 1820 [4]. M. Carey Lea systematically studied the decomposition of silver chloride, mercurous chloride, and sodium tetrachloroaurate(III). He also – for the first time – demonstrated the parallelism between the action of electricity, heat, light, and mechanical force on the silver halides [5–10]. From the beginning of the last century, research in mechanochemistry has been rapidly intensifying. Mechanochemical reactions are discovered in fluids, suspensions, colloids, polymers, nanoparticles, and biomolecules [11–14]. New methods and instruments for inputting mechanical energy into the substances are also being developed.

Nowadays, mechanochemistry is a truly interdisciplinary subject which involves mineralogy, inorganic and organic synthesis, tribology, polymer science, and biochemistry. Mechanochemical questions are mutable and emerge in different contexts. In mineralogy, mechanochemistry refers to the mechanochemical processing for the extraction of elements from raw minerals [14]. In biological sciences, mechanochemistry can refer to either the mechanisms by which cells convert mechanical stimuli into chemical activity (mechanotransduction) for physiological functions or the production of mechanical energy by chemical reactions (chemo-mechanics) such as molecular motors or muscle contraction [3]. In macromolecular science, mechanochemistry classically refers to mechanical degradation of polymers via the scission of covalent bonds. However, in the last decade, polymer mechanochemistry has been enlarged with the use of the polymer scaffold for mechanical activation of mechanophores [15].

1.2 Polymer Mechanochemistry

1.2.1 Historical Perspective

Polymer mechanochemistry arose as early as the concept of macromolecules. Indeed, the first reports on flow-induced degradation of polymer were given by Staudinger (Nobel Prize, 1953) [16–18], one of the trailblazers of macromolecular science. The increasing demands for polymeric products from the middle of the last century called for the study of their behavior under mechanical processing. Early work suggested that the depolymerization of chains during ball-milling, drilling, slicing, or sawing can advance by homolytic cleavage (producing two free macroradicals [11, 19]), heterolytic cleavage (two macromolecular ions with opposite charges), or intramolecular disproportionation (two stable macromolecular fragments) [20].

Mechanical degradation of polymers in solution was also implemented. The coil-like characteristics of macromolecules give them unique dynamics in the flow field compared to small molecules. In the 1940s, Kuhn and Frenkel performed experiments in simple shear flow [21, 22]. They believed a simple shear flow with velocity gradient transverse to the flow direction was sufficient to degrade polymer chains. The mechanical stability of macromolecules in solution is thus referred to as "shear stability." However, theoretical work in the early 1960s showed that only elongational flow with velocity gradient parallel to flow direction can extend the coil [23–25]. In this review, we retain the historical term "shear stability" but the reader should be aware of its meaning. After de Gennes' (Nobel Prize, 1991) prediction of the coil-to-stretch transition (CST, Fig. 1) of polymer chains in 1974 [26], experimental progress accelerated. This work revealed a minimum molecular weight M_{lim} required for chain cleavage [20]. Odell and Keller's elegantly designed flow experiments [27, 28] demonstrated the connection between CST and the most basic properties of the polymer chain. Their outstanding work led the subject into the modern era with quantitative studies [15].

In the last decade, researchers have taken advantage of the molecular strain generated during CST to trigger the chemical reaction of certain organic molecules (called *mechanophore*). Moore, Craig, and their co-workers reported breakthroughs in this avenue. Examples include the use of mechanical force to unveil prohibited reaction pathways [29] or to prolong the lifetime of the diradical intermediate [30]. Boulatov demonstrated the role of molecular restoring force, not strain energy, in controlling the reaction barriers in stretched macromolecules [31]. This groundbreaking research has given impetus to the development of mechanoresponsive materials and has marked the beginning of a new epoch in polymer mechanochemistry.

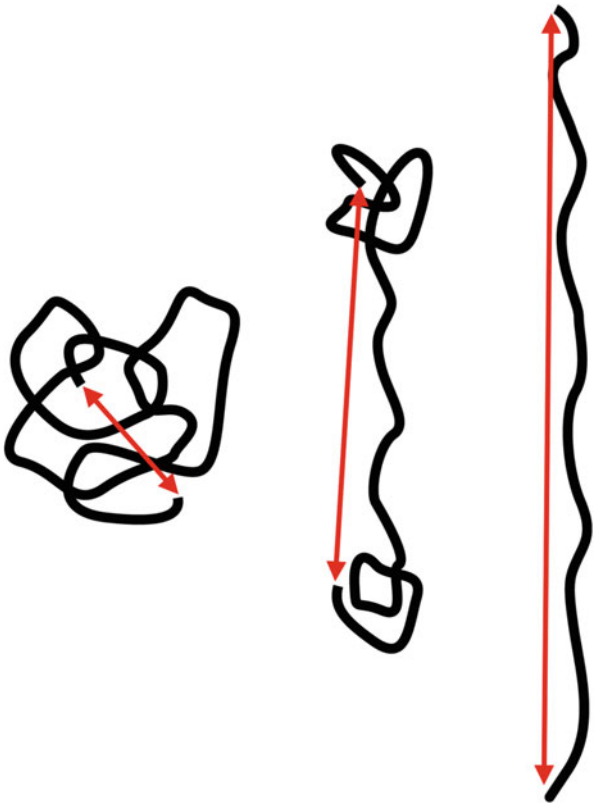

Fig. 1 Coil-to-stretch transition (CST) of a polymer chain. The flow direction is vertical. The *red arrows* highlight the end-to-end distance R of the chain

1.2.2 Mechanophores and Mechanoresponsive Polymers

A mechanophore (blue in Fig. 2a) is a strategically designed chemical entity which responds to mechanical force in a predictable and useful manner (Fig. 2d–f). The polymer strand here acts as an actuator to transmit macroscopic force to the target. For a fully extended polymer chain, the maximum tension force is at the middle point of the chain contour. So the mechanophore should be incorporated into the middle of the chain with its active bond along the chain contour (Fig. 2a) [15, 29, 32]. Examples of mechanochemical reactions include homolytic scission of weak bonds (diazo [33]), electrocyclic ring-opening (benzocyclobutenes [29], spiropyrans [32, 34–45], *gem*-dichlorocyclopropanes [46–49], *gem*-difluorocyclopropanes [30, 50], and epoxide [51]), cycloreversion reactions (cyclobutane derivatives [52–56], Diels-Alder adducts [57, 58], 1,3-dipolar adducts [59, 60], and 1,2-dioxetanes [61]), dative bond scission [62–64], and flex-activated reactions [34, 65, 66], as recently reviewed by Bielawski [67].

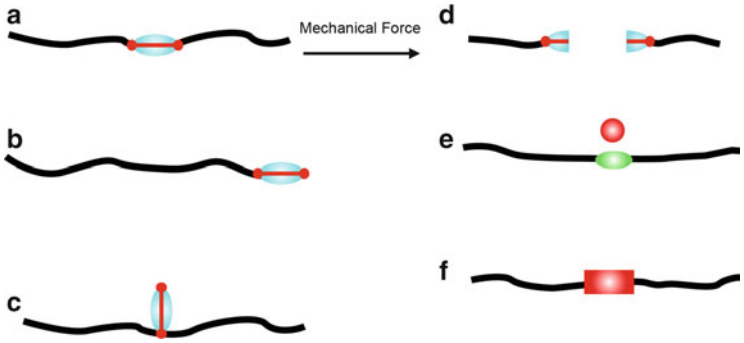

Fig. 2 Schematics of a mechanophore embedded in a polymer chain [15]. (**a**) The mechanophore is in the middle of the chain. (**b**) Control polymer having a mechanophore at the chain terminus or (**c**) as a pendent group. The *red stick* in the mechanophore represents the active bond. Possible responses to force for a mechanophore in the middle of the chain: (**d**) selective scission; (**e**) release of small molecule; (**f**) isomerization

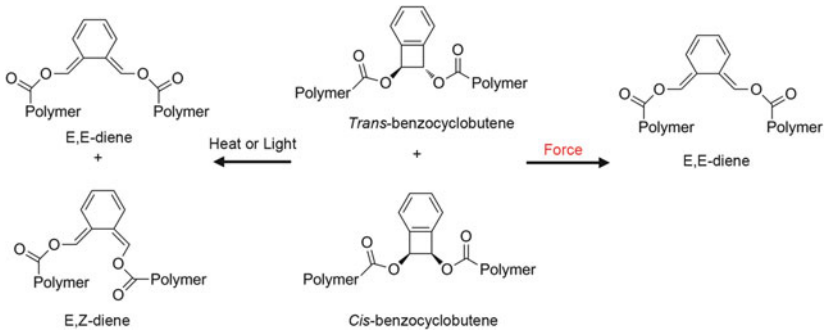

Fig. 3 Force mediated electronic ring-opening of benzocyclobutene moieties avoiding orbital symmetry rules [29]

Mechanical force has the unique ability to impel molecules to react through specific pathways to avoid side reactions and unmask transformations to completely new outcomes. Moore highlighted a salient example of using mechanical force to circumvent thermal and photochemical limitations [29]. It is well known that pericyclic reactions are governed by orbital symmetry theory (the Woodward-Hoffmann rules [68]). As a result, the electrocyclic ring-opening of the mixture of *cis*- and *trans*-benzocyclobutenes gives a mixture of E,E- and E,Z-diene isomers under thermal or photo stimuli. Unexpectedly, the same reaction under mechanical stimulus yields only E,E-diene. Most importantly, the reaction yielding single isomer (E,E-diene) is only accessible via mechanical force (Fig. 3). This milestone

work highlights the new concept of using polymer mechanochemistry to drive the synthesis of small molecules that are otherwise inaccessible [69].

The rational design of mechanophores and polymer scaffolds offers a new avenue towards intelligent polymers which respond to mechanical force in incredible ways [70]. Imagine the following situations. A polymer can send a warning signal by changing its color on deformation [32]. Close to mechanical failure, the force breaks the purposely designed bonds to relieve the local stress by releasing "hidden length" (molecular stress relief) [53, 54, 71] and/or to redistribute the local force by interchain cross-linking (self-strengthening) [72]. Once the chain breaks, it sends a second signal [61] and the outcomes (radicals or other small molecules) can catalyze latent chemical reactions [49, 73, 74]. Even if the material fails, there remains an opportunity to self-heal with the formation of new covalent bonds in mechanophores [75–77]. Mechanophores can also be used in material studies to investigate the structure–property relationship and the fracture mechanism [78]. Other prospects for mechanophores in polymer science have been well reviewed by Craig [70].

1.2.3 Application of Polymer Mechanochemistry

Polymer mechanochemistry has wide-ranging relevance to diverse applications. It is an essential aspect of polymer-processing such as rubber mastication [79, 80], coating, injection molding, rolling, calandering, extrusion, spinning, and fiber drawing. In fluid transportation the addition of small amounts of polymers can drastically reduce the drag, i.e., drag reduction, in turbulence flow. Shear stability is regarded as a critical standard to choose polymer additives for drag reduction applications [81]. In biochemistry, fluidic shear forces can impair the structures of protein molecules, leading to denaturing and loss of biological functions [82]. The mechanical stability of biopolymers or natural polymers is also important in biomedical applications [83–85] and the food-processing industry [86–88]. Sometimes, chain scission under flow is desirable. Flow-induced chain scission is used as a route to produce monodispersed high molar mass polymers in industry [89]. In genome sequencing and biopolymer science, the scission of genomic DNA into short fragments with random break points in the flow field is a critical preparatory technique [90–93]. In applications where the fracture of macromolecules is undesired, the linear chain structure has inherent limitations to resist scission. Generally, this is because the linear chains have larger hydrodynamic volume and experience larger hydrodynamic force than chains with complex topology having the same molecular weight. For this reason, researchers turned to explore the effect of chain architecture.

1.3 Polymers of Different Topologies

Thanks to the rapid development of efficient synthetic strategies, scientists can now create macromolecules with well-defined architectures and examine their behavior. Examples of polymer architectures are shown in Fig. 4.

A cyclic (ring) chain (Fig. 4b) has no chain termini compared with a linear chain (two termini). Ring polymers are synthesized by ring-closure reactions or ring-expansion polymerizations [94]. They manifest unique diffusion behavior and intrachain interactions.

A graft polymer chain (Fig. 4c) has a linear backbone and randomly distributed side chains. The side chains (which can be very long) are structurally distinct from the main chain but can be homopolymers or copolymers. A well-known example of a graft polymer is high-impact polystyrene (HIPS), where polybutadiene (PB) side chains are grafted to the PS backbone.

A star-shaped polymer chain (Fig. 4d) is a structure consisting of three or more linear arms connected to a central core. Star polymers more closely resemble a hard sphere with more compacted structure, higher degrees of segmental density and dynamic entanglement, compared to their linear counterparts of the same molecular weight [95].

Hyperbranched polymers and dendrimers belong to the same group of polymers with densely branched structures and a large number of ends (Fig. 4e, f).

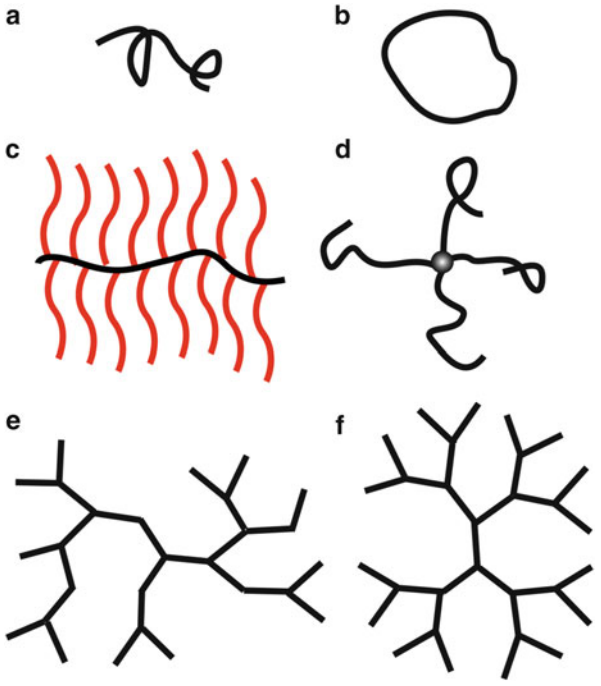

Fig. 4 Polymer architectures: (**a**) linear polymers, (**b**) ring polymers, (**c–f**) branched polymers: (**c**) graft polymers, (**d**) star-shaped polymers, (**e**) hyperbranched polymers, and (**f**) dendrimers

Dendrimers branch perfectly with star-like topologies whereas hyperbranched polymers have imperfectly branched structures. Dendritic polymers have numerous sites per molecule to couple to active species, making them ideal carriers for drug molecules or biomacromolecules [96].

Compared with linear cousins having the same molecular weight, chains with complex topology are usually more compact. The smaller size causes the chains to experience less mechanical force. On the other hand, extremely compact structure increases the repulsive interactions between chain segments, which leads to additional tension in the chains. The mechanical stability of the whole macromolecules is the balance of the two effects.

1.4 Aim of the Current Review

This review is organized on the basis of polymer architecture and highlights its effect on polymer mechanochemistry. The topic is restricted mostly to CST, chain degradation, and activation of mechanophores in *dilute solution* because more experimental and theoretical literature is available than that relating to the solid state. Solution or solid phenomena in which no CST or mechanochemical reaction occurs are therefore excluded.

To make this review self-contained and to provide a foundation for further discussion, we have included the experimental methods and theoretical models of mechanical degradation for linear chains in the second and third sections, respectively. From the fourth to seventh sections, the mechanochemistry of cyclic polymers, graft polymers, star-shaped polymers (star-shaped polymers), dendrimers, and hyperbranched polymers is summarized. In the eighth section, we survey the mechanochemistry of supramolecular aggregates and knotted polymers, where the topology constraints are temporal. We hope our overview can serve as a guideline for the future work in the field of polymer mechanochemistry.

2 Flow Field to Study Polymer Mechanochemistry

Mechanical degradation of polymers has been studied for more than 70 years in several flow fields encompassing strong elongation components. In certain flow fields the streamlines are symmetric with a stagnation point. In the vicinity of the stagnation point, the dwell time of the fluid element is longer than the timescale for coil extension. Such flow is referred to as “quasi-steady-state-flow” (QSSF). In most other cases the dwell time is shorter than the coil extension time and the flow is referred to as “fast-transient-flow” (FTF).

In practice, the geometry of the flow apparatus critically affects the degradation result in the following ways:

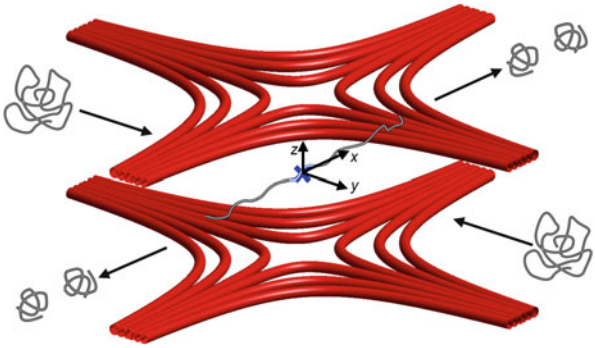

Fig. 5 Schematic diagram of planar elongational flow using cross-slot. Streamlines are marked *red* and the stagnation point is marked as "X." The velocity in the z direction is zero

1. The wall inherently introduces shear deformation containing a rotation component to the deformation gradient, whereas a pure elongational flow field exists only in a small region.
2. The distance between two fluid points in a pure elongational flow with constant stretch rate increases exponentially with time. Nevertheless, the distance cannot develop infinitely because of the experimental geometry, which limits the maximum strain that can impose on the polymer chain.

2.1 Quasi-Steady-State-Flow

A planar elongational flow field is a typical QSSF. It can be generated in a cross-slot device and was widely used by Odell and Keller [27, 28, 97–102]. As shown in Fig. 5, the polymer solutions are pumped into two opposed channels ($+y$ and $-y$ directions) and sucked out of two orthogonally opposed channels ($+x$ and $-x$ directions). The streamlines are symmetrical and have a stagnation point in the center (marked "X"). The velocity of the inlet streams approaches zero at the stagnation point and increases along the outlet directions [103]. Polymer coil trapped at the stagnation point undergoes CST and breaks into pieces. The strain rate at the stagnation point can be controlled by the velocity of the inlet streams and the geometry. Another device that can create QSSF is the Taylor four-roll mill. The mill can produce the entire spectrum of linear flow near the mill center [104]. The rotating speed of the mills controls the strain rate at the stagnation point.

2.2 Fast-Transient-Flow

2.2.1 Contraction Flow

The flow through a contraction channel (e.g., decrease in pipe diameter) results in a sudden increase in the velocity and the strain rate without a stagnation point.

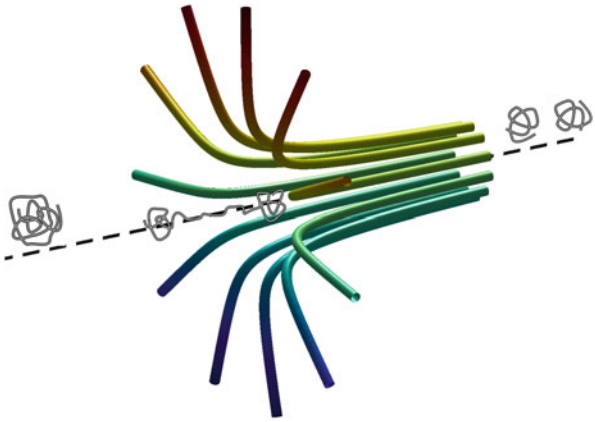

Fig. 6 Contraction flow field. The flow direction is along the *dashed line*

The streamlines of a converging flow field is shown in Fig. 6. In the contraction flow, the polymer coil may not have sufficient time to extend fully. The jet may reach very high speed to create contract flow. This technique was widely studied by Nguyen and Kausch [105–113].

2.2.2 Turbulent Flow

In pipe flow, the Reynolds number Re, see (1), determines the flow patterns:

$$Re = \frac{\rho_s V d}{\eta_s} \tag{1}$$

where V is the mean velocity of the fluid, d is the hydraulic diameter of the pipe, ρ_s is the density of the fluid, and η_s is the dynamic viscosity of the fluid.

Turbulent flow occurs at high values of Re (>2,300). Unlike other flow fields, it is chaotic. Researchers have been interested in the interplay between polymer chains and turbulent flow for a long time [114, 115]. Experiments confirmed that polymer additives not only change the existing turbulent structures but also produce flow structures not found in a pure solvent [116]. de Gennes [117] and Tabor [118] believed the coil experiences both high elongational and shear stress near a microvotex in turbulent flow (Fig. 7).

In the preceding flow fields, strain rates on the order of 10^3 to 10^6 s^{-1} are achievable, and the corresponding limiting molecular weight M_{lim} for chain scission is on the order of 10^6 Da [15]. The extremely high molecular weight is a synthetic challenge, even with more advanced polymerization techniques.

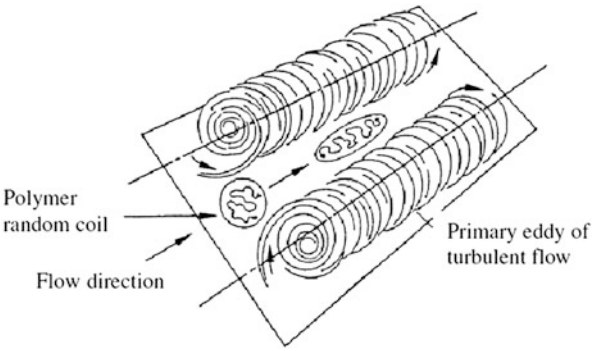

Fig. 7 Schematic representation of the elongational flow between the counter-rotating eddy pairs in turbulent flow. (Reprinted with permission from Kulicke et al. [115], Copyright 1989 Springer)

2.2.3 Ultrasonic Irradiation

Ultrasonic irradiation is a fundamentally different technique from flow fields and used predominantly for studying mechanophores [119, 120]. The main advantages of using this method over an elongational flow field are the high strain rates it can produce and the simplicity of the apparatus. Nguyen and co-workers [113] have suggested that the strain rate in the acoustic field can reach up to 10^7 s^{-1}. The corresponding M_{lim} for chain scission or mechanophore activation is drastically reduced to 10^4 to 10^5 Da, which is synthetically readily attainable.

Chain scission in an acoustic field in solution has been studied over many decades [20, 110, 113, 121–124]. The accepted mechanism involves the nucleation, growth, and collapse of cavities, and CST of the polymer chain. When a high-energy acoustic field is applied to a solution, the local pressure vibrates. If the ultrasonic pressure amplitude exceeds the average pressure in the liquid, the pressure drops below zero (negative pressure). When the applied negative pressure overcomes the cohesive forces of the fluid element, cavitation occurs and dissolved gases escape into cavities. The bubbles are then dilated and contracted by the acoustic field and violently collapse at a certain point. An elongational flow field is thus created, and the strain rate depends both on the time from the onset of the bubble collapse (the instantaneous radius of the imploding void) and on the distance to the bubble. A polymer coil near the collapsing bubble experiences solvodynamic force, undergoes CST, and eventually breaks (Fig. 8).

Compared with flow fields, ultrasound irradiation creates both solvodynamic and thermal effects. The latter may contribute to polymer degradation and mechanophore activation. Although, ideally, hot spots are quenched faster than the diffusion time of the polymer chain (less than 1 μs [110]), an effort to preclude thermal effects should be implemented in the experiment.

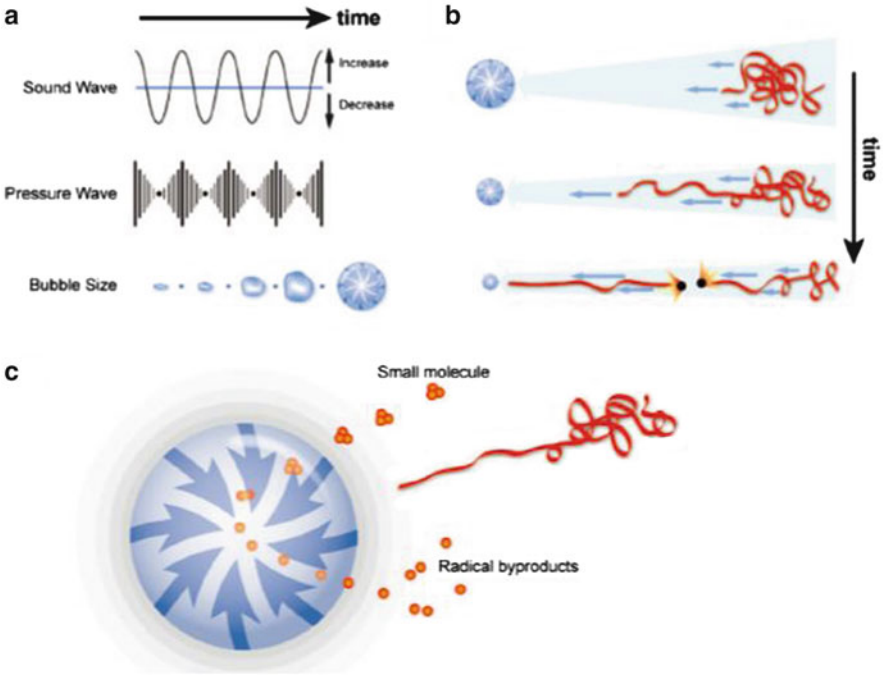

Fig. 8 Mechanism for ultrasound-induced polymer chain scission: (**a**) gradual bubble formation results from pressure variations induced by the acoustic field; (**b**) rapid bubble collapse generates solvodynamic shear; (**c**) small molecules pyrolyze to form radical byproducts upon bubble collapse, while polymer chains do not undergo pyrolytic cleavage because they do not penetrate the bubble interface. (Adopted with permission from Caruso et al. [15], Copyright 2009 American Chemical Society)

3 Mechanochemistry of Linear Polymers

3.1 CST, Chain Scission, and Activation of Mechanophores

At rest, the conformation of a flexible chain in dilute solution looks like a coil with spherical symmetry in the long-term. However, its instantaneous shape is asymmetric [125], which means the chain rotates along a streamline of a flow field with velocity gradient. The hydrodynamic drag force from the friction between the chain segments and the solvent molecules can deform the coil from its equilibrium shape. On the other hand, the conformation of the polymer chain is variable and changing all the time because of thermal fluctuation (Brownian motion of the solvent). So the shape of the chain in the flow field depends on how quickly the solvodynamic force deforms the chain and how slow the whole chain relaxes. This evolves two timescales.

The first timescale is related to the flow field and proportional to the reciprocal of strain rate ($1/\dot{\varepsilon}$). The second timescale is the longest relaxation time of the polymer

τ_0, which is the time for the end-to-end vector to relax fully; to scales with molecular weight M [125]:

$$\begin{array}{l} \tau_0 \propto M^2 \quad \text{(no hydrodynamic interactions, Rouse Model)} \\ \tau_0 \propto M^{3\nu} \quad \text{(hydrodynamic interactions, Zimm Model)} \end{array} \tag{2}$$

where ν is the Flory exponent and is 0.5 in theta solvent but 3/5 in good solvent . In the theta solvent, polymer coils act as ideal chains, assuming their random walk coil dimensions exactly. In good solvent, interactions between polymer segments and solvent molecules are energetically favorable and cause polymer coils to expand. The different scaling exponents in (2) are caused by the hydrodynamic interactions which account for the effect of the disturbance of the chain segments on the flow field. For polydispersed samples, M should be replaced with weight averaged molecular weight M_w.

The two timescales define a dimensionless number, known as the Deborah number (De) [126]:

$$De = \tau_0 \dot{\varepsilon} \tag{3}$$

For $\dot{\varepsilon}$ smaller than a critical value $\dot{\varepsilon}_C$, the chain remains in a "coiled" state. As $\dot{\varepsilon} > \dot{\varepsilon}_C$, the chain drastically extends as shown by a steeper increase in the flow-induced birefringence (Fig. 9). At the onset of CST, the corresponding critical De_C fulfills [26]:

$$De_C = \tau_0 \dot{\varepsilon}_C \approx 0.5 \tag{4}$$

From (4) we obtain the dependence of $\dot{\varepsilon}_C$ on M_w [127]:

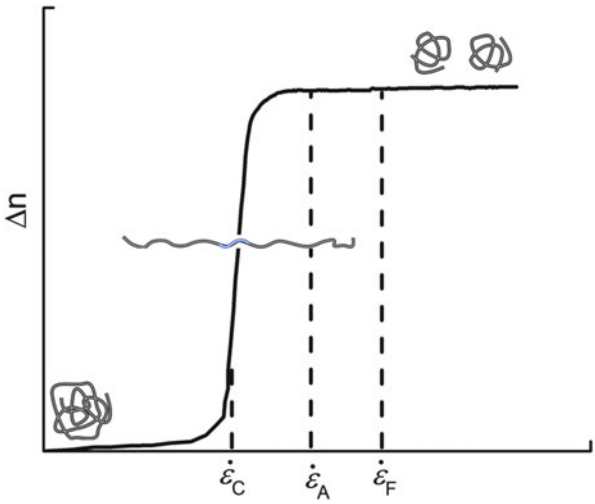

Fig. 9 Schematic drawing of flow-induced birefringence as a function of strain rate during CST and chain scission. (Adopted with permission from Odell and Keller [28]. Copyright 1986 John Wiley & Sons)

$$\dot{\varepsilon}_C \approx \frac{0.5}{\tau_0} \propto M_w^{-2} \text{ (Rouse Model)} \tag{5}$$

$$\dot{\varepsilon}_C \approx \frac{0.5}{\tau_0} \propto M_w^{-3\nu} \text{ (Zimm Model)} \tag{6}$$

From (5) and (6), the shorter of the polymer chains, the higher value of $\dot{\varepsilon}_C$ is required to observe CST. As $\dot{\varepsilon}$ exceeds a second critical value $\dot{\varepsilon}_F$, the hydrodynamic force is sufficient to overcome the binding strength of the covalent bonds (~7 nN, depending on timescale [128]) and the chain scission occurs. The force required to activate the mechanophore may be weaker or close to that to break the covalent bond. The related critical strain rate $\dot{\varepsilon}_A$ is above $\dot{\varepsilon}_C$ and close to $\dot{\varepsilon}_F$ (Fig. 9). Below M_{lim}, CST, activation of mechanophore, and chain scission cannot be observed for the given experimental setup (maximum strain rate attainable).

3.2 Summary of Experimental Results

From the early 1970s, elegantly designed experiments were conducted to study CST and chain scission. Results from both QSSF and FTF are briefly summarized in the following:

3.2.1 General Features

1. In QSSF [27, 28, 97–102, 129], FTF [89, 105–113], and turbulent flow [114, 130], polymer chains are broken at the midpoint along the backbone. Similar results are observed in activation of mechanophores under ultrasonic irradiation, where the mechanochemical transduction is only effective at the midpoint of the chain (Fig. 2a) [15, 67, 119, 120].
2. In QSSF, the degradation yield is very small (~0.4% per pass) [129]. The low yield is consistent with the small proportion of polymer chains trapped at the stagnation point. In FTF, the degradation yield approaches almost 90% for a single pass [106, 110].

3.2.2 Effect of Molecular Weight

In QSSF above $\dot{\varepsilon}_C$, the polymer chain trapped at a stagnation point has enough time to be fully extended and broken when $\dot{\varepsilon} > \dot{\varepsilon}_F$. Both experimental results (Fig. 10, dashed line) and theoretical simulations predict the following scaling law [27, 28, 97, 127, 131]:

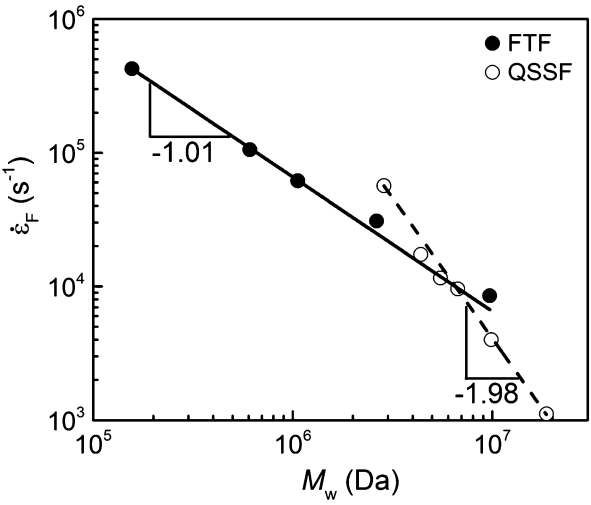

Fig. 10 Dependence of $\dot{\varepsilon}_F$ on M_w for the polystyrene in decalin: FTF (*solid line*); QSSF (*dashed line*). FTF data were taken from Nguyen and Kausch [106]. Copyright 1988 Elsevier. QSSF data were taken from Kellerand Odell [27]. Copyright 1985 Springer

$$\dot{\varepsilon}_F \propto M_w^{-2} \tag{7}$$

For extremely high molecular weight polymers ($>10^6$ Da) with hydrodynamic interactions, (6) and (7) lead to $\dot{\varepsilon}_F \sim \dot{\varepsilon}_C$. An interesting conclusion is that the chain may break before the complete extension in QSSF [27].

However, in FTF the short dwell time in a high $\dot{\varepsilon}$ region prevents the chain from achieving full elongation. Nevertheless, the chain can still be degraded and $\dot{\varepsilon}_F$ scales linearly with M_w (Fig. 10, solid line) [106, 108, 131–134]:

$$\dot{\varepsilon}_F \propto M_w^{-1} \tag{8}$$

As shown in Fig. 10, there is a crossover point for QSSF (dashed line) and FTF (solid line). For M_w below the crossover point, $\dot{\varepsilon}_F$ in FTF is smaller than in QSSF. However, the calculated frictional force in FTF is orders of magnitude less than the breaking strength of the covalent bond. In QSSF, the hydrodynamic drag force corresponds well to the bond strength [129, 135].

3.2.3 Effect of Inertia

The demarcation line between (7) and (8) is not absolute, even in the same flow apparatus. Islam and co-workers studied the effect of inertia [136], as characterized by Re (1), on the scission of polyethylene oxide (PEO) in cross-slot devices. As shown in Fig. 11, in a 50:50 aqueous glycerol mixture ($70 < Re < 940$, open circles), $\dot{\varepsilon}_F \propto M_w^{-1.93\pm0.05}$ but in pure water ($910 < Re < 6{,}600$, open triangles), $\dot{\varepsilon}_F \propto M_w^{-1.04\pm0.07}$.

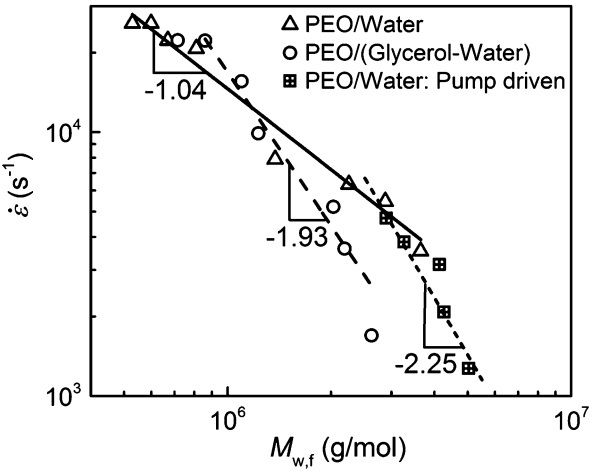

Fig. 11 Imposed strain rates plotted against critical molecular weight for chain fracture for PEO. The *triangles* are for experiments with aqueous PEO solutions performed using the pressure driven flow apparatus and the *squares* are from experiments carried out in the pump driven flow loop. The *circles* are for the viscous solvent (water/glycerol: 50/50; $\eta_s = 6.4$ cP) passed through the flow cell in a pressure-driven configuration. (Reprinted with permission from Islam et al. [136]. Copyright 2004 American Chemical Society)

3.2.4 Effect of Temperature

For a thermal activation process, increasing temperature increases the rate constant. At a high temperature the thermal energy is sufficient to overcome the potential energy barrier for chain dissociation. Odell and Keller [129] investigated the effect of temperature T on chain scission of polystyrene (Fig. 12). After correcting T for decreasing viscosity, both $\dot{\varepsilon}_F$ and $\dot{\varepsilon}_C$ were found to decrease with increasing T. In other words, less mechanical energy is required to assist thermal energy to overcome the potential energy barrier of the scission reaction. The difference between $\dot{\varepsilon}_F$ and $\dot{\varepsilon}_C$ also narrows as the temperature increases. However, Nguyen and Kausch discovered little influence of temperature on the scission yield of PS in dioxane and decalin in FTF [105]. They ascribed the effect to the short dwell time of the chain in the flow field.

In ultrasonic degradation, changing the temperature inevitably affects η_s, the vapor pressure of the solvent, and thus the dynamics of cavity collapse. Experimentally, the chain scission rate decreases with increasing temperature [137–139].

3.2.5 Effect of Solvent

τ_0 of a polymer chain in solution scales linearly with η_s ($\tau_0 \propto \eta_s$) as predicted by Rouse or Zimm model. According to (4), $\dot{\varepsilon}_C$ should scale inversely with η_s. Chain scission is expected to occur at a lower $\dot{\varepsilon}_F$ in a more viscous solvent (9):

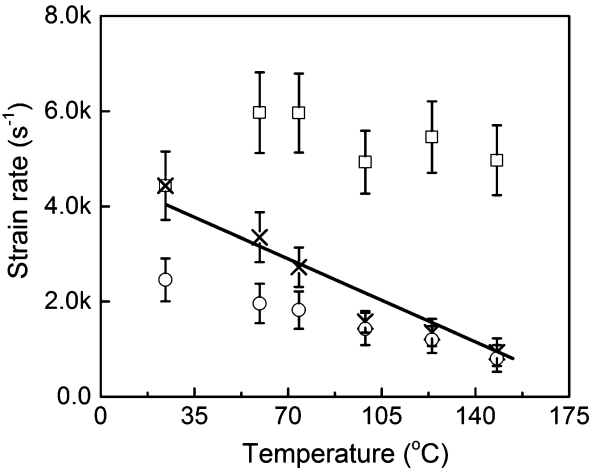

Fig. 12 Critical strain rate for chain scission ($\dot{\varepsilon}_F$) as a function of temperature, uncorrected (*open squares*) and corrected (x) for solvent viscosity. Also shown is the variation of critical strain rate for the coil-stretch transition ($\dot{\varepsilon}_C$) as a function of temperature (*open circles*). The *continuous line* is the "best fit" for the thermally activated barrier to scission model (see Sect. 3.3.3). Reprinted with permission from Odell et al. [129]. Copyright 1990 American Chemical Society

$$\dot{\varepsilon}_F \propto \eta_S^{-1} \tag{9}$$

Equation (9) is in good agreement with experimental observations in QSSF [129] and consistent with the asymptotic behavior of a Rouse chain in elongational flow. However, in FTF $\dot{\varepsilon}_F$ was found relatively insensitive to η_s with an exponent of -0.25 (Fig. 13) [108]:

$$\dot{\varepsilon}_F \propto \eta_S^{-0.25} \tag{10}$$

The weaker dependence is completely unexpected and contradicts the common view that hydrodynamic friction force drives CST and chain fracture. Nguyen and Kausch [108] ascribed (10) to the intramolecular friction (so-called "internal viscosity") between chain segments in the coiled part in FTF. Unlike η_s, the internal viscosity depends on strain rate and could reach much higher values than η_s.

3.2.6 Effect of Polymer Concentration

Increasing polymer concentration affects chain scission in several ways, as it increases the bulk viscoelasticity, the stress transmission efficiency, τ_0, and the hydrodynamic screening. The hydrodynamic screening means the hydrodynamic interactions become negligible between chain segments whose spatial distance apart is larger than a certain value (termed hydrodynamic screen length). In both

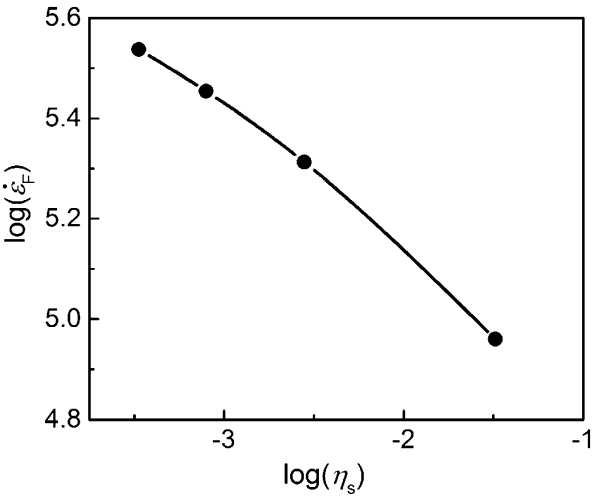

Fig. 13 Dependence of the critical strain rate for chain scission ($\dot{\varepsilon}_F$) on solvent viscosity. (Reprinted with permission from Nguyen and Kausch [108]. Copyright 1990 American Chemical Society)

QSSF and FTF, the change in the stress transmission efficiency seems to dominate [101]. Although midpoint scission is observed at different concentrations, the polydispersity of the product increases with increasing polymer concentration [99]. Because of the increasing number of entanglements in the system, more randomized scission is expected.

In ultrasonic irradiation, the scission rate decreases as polymer concentration increases [140–143], which is primarily ascribed to the suppression of the cavitation process caused by the high solution viscosity.

3.3 Theoretical Consideration

3.3.1 Bead-Rod Model

Odell and Keller first proposed a bead-rod model to explain the degradation of an isolated polymer chain in QSSF [27, 28]. This is also the *basis* for further discussing the effect of chain topology in the following sections. The key assumptions are:

1. The polymer chain is completely extended and considered as a rod with beads inlaid in it (Fig. 14)
2. The polymer chain undergoes fracture if the maximum force along the contour exceeds a critical value, σ_F (the critical-stress-to-fracture theory)

Shown in Fig. 14 is a chain with $N = 2m + 1$ beads in the completely stretched conformation. Each bead experiences a hydrodynamic drag force $f_i = \xi v_i = i\xi\dot{\varepsilon}b$, where v_i is the velocity for given bead i relative to solvent, ξ is the hydrodynamic drag coefficient, and b is the length of chain segment.

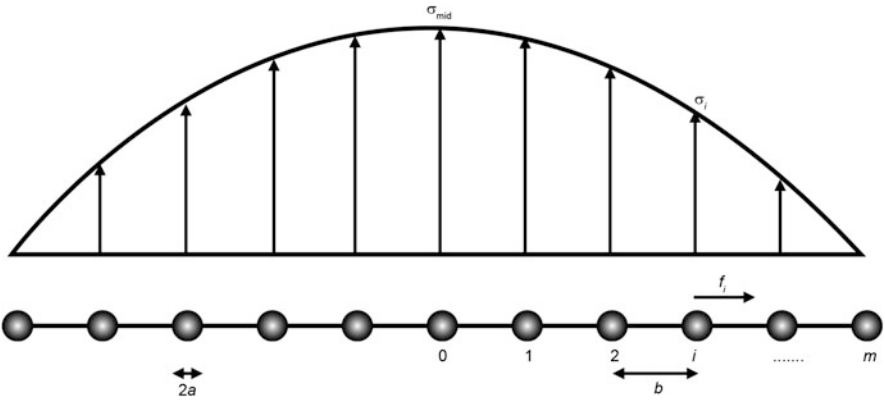

Fig. 14 Parabolic distribution of tensile force along a fully extended chain (bead-rod model)

To calculate the total force on the *i*th bead, f_i should add up along the chain from the terminal ($i = m$) to the *i*th segment:

$$\sigma_i = \sum_{i=m}^{i} f_i = \xi \dot{\varepsilon} b \sum_{i=m}^{i} i \approx \frac{1}{2} \xi \dot{\varepsilon} b \left(m^2 - i^2\right) \tag{11}$$

$$\sigma_{\text{mid}} = \frac{1}{2} \xi \dot{\varepsilon} b m^2 \tag{12}$$

Equation (11) indicates that the drag force along a bead-rod chain has a parabolic distribution with the maximum force at the midpoint (12). Substituting Stoke's law into (12) yields the full expression of σ_{mid}:

$$\sigma_{\text{mid}} = \frac{3}{4} S_1 \pi \dot{\varepsilon} a b \eta_s N^2 \tag{13}$$

where a is the radius of the beads and S_1 is the "shielding factor" which accounts for hydrodynamic interactions between beads. In the fully extended conformation, S_1 is often set equal to 1.

According to the critical-stress-to-fracture theory (assumption **2**), the chain is fractured at $\sigma_{\text{mid}} \approx \sigma_{\text{F}}$. The scaling of the critical fracture strain rate $\dot{\varepsilon}_{\text{F}}$ on η_s and M_w can be derived from (13) as

$$\dot{\varepsilon}_{\text{F}} = \left(\frac{3}{4} S_1 \pi a b \sigma_{\text{F}}\right)^{-1} \eta_s^{-1} N^{-2} \propto \eta_s^{-1} M_w^{-2} \tag{14}$$

Equation (14) perfectly explains the degradation behavior ((7) and (9)) of polymer chains in QSSF observed by Odell and Keller [27, 28, 97–99, 101, 102, 129]. Moreover, the fracture force obtained from (13) corresponds to the strength of C–C bond calculated using Morse potential [27, 28, 129]. Additionally, the above equation is

applicable to the activation of mechanophores and the critical strain rate to activation mechanophore $\dot{\varepsilon}_A$ may have an expression similar to $\dot{\varepsilon}_F$.

3.3.2 "Yo–Yo" Model and Molecular Individualism

Although the bead-rod model is successful in QSSF, it fails to explain the scaling laws in FTF ((8) and (10)). One reason is the validity of assumption **1**. In FTF, the short dwell time precludes the chain from fully elongating. Ryskin proposed a "yo–yo" model to explain the chain dynamics in FTF. Unlike the bead-rod model, the chain is supposed to have a dumbbell conformation where two unraveling coiled ends are connected by a stretched rod in the center (dumbbell shape in Fig. 15). As $\dot{\varepsilon} > \dot{\varepsilon}_C$, the center stick grows in length at the cost of the two coiled parts. Ryskin estimated the length of highly extended portion to be comparable to the equilibrium dimensions of the polymer at rest. Therefore the term relating to the dimension of

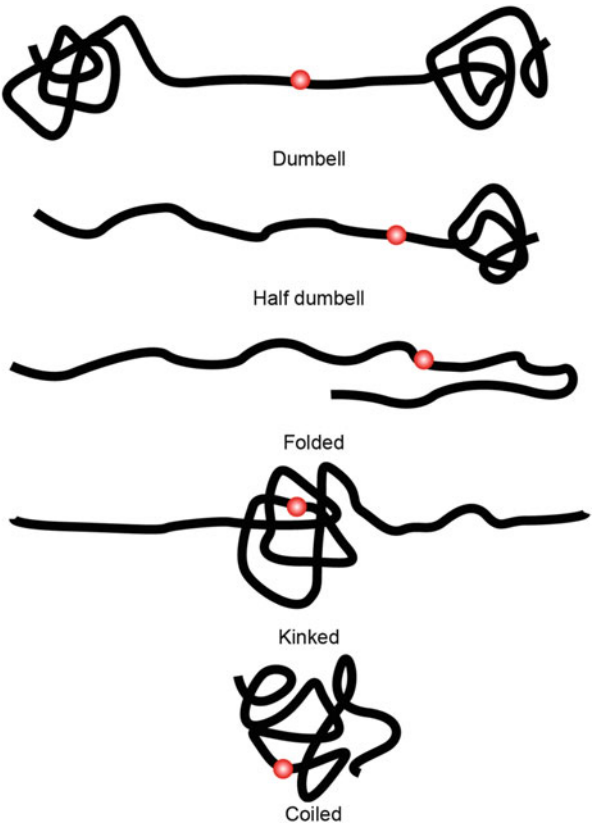

Fig. 15 Schematics of different possible polymer conformations during the act of stretching [144, 145]. The *red dots* represent the midpoint along the chain contour

the chain in (14) (i.e., "N^2") should be replaced by $<R^2>$, the end-to-end distance of the chain:

$$\dot{\varepsilon}_F \propto < R^2 >^{-1} \propto M_w^{-2v} \tag{15}$$

Equation (15) predicts a scaling exponent close to experimental observations (8).

Some researchers also speculate that the primary factor governing chain scission in FTF is not the frictional force at break (critical-stress-to-fracture theory, assumption **2**) but the elastic energy stored in the deformed molecule [110]. A few experimental results seem to support the argument [146, 147].

Recently, Chu and Smith directly observed the chain conformations during CST using cross-slot geometry [144, 145, 148]. They chose fluorescently labeled DNA molecules to eliminate the disturbance from chain polydispersity. Even in homogenous elongational flow, polymer chains with the same lengths and which are subjected to the same dwell time display completely different conformations (coiled, dumbbell, kinked, half dumbbell, or folded shapes; Fig. 15). Among the various shapes, the folded shape unravels more slowly than the others (except the coiled shape) and its proportion in all conformations observed in the flow field increases by up to 40% as *De* increases.

Their outstanding work revealed the most far-reaching aspect of CST, that is, molecular individualism, as highlighted by de Gennes [149]. A flexible chain at rest changes its conformation because of Brownian motion. The average coil shape is sufficient to describe many properties. However, the conformation and the unraveling rate of an individual polymer chain during CST critically depend on the initial conformation of the coil as it enters the flow field. A knotted coil may keep its shape upon stretching. Nevertheless, a coil with both of its ends on the same side of the center of mass with respect to a plane perpendicular to the stretching axis may develop into a folded shape. We believe that not only CST but also the related chain degradation may be "molecular individualistic." The conformation-dependent nature suggests that any theories based on single conformation of the chain (bead-rod model and "yo–yo" model) and any technique based on the statistics of chain ensemble have inherent disadvantages.

It is also unclear which conformations can give selective midpoint scission. The coiled part is obviously more mobile and deformable than the extended part. The position of the maximum tension force thus unlikely doesn't coincide with the middle point of the chain for nonsymmetrical conformations appearing as a half-dumbbell and folded shapes. It is puzzling why the chain breaks precisely at the midpoint of the chain (red dots in Fig. 15) observed in both QSSF and FTF.

3.3.3 Kinetics of Chain Scission and Activation of Mechanophores

The effect of external forces on the rate constant of a chemical reaction was first studied by Kauzmann and Eyring [150, 151], within the context of transition state theory. The same basic hypothesis was used by Zhurkov [152, 153] to study the

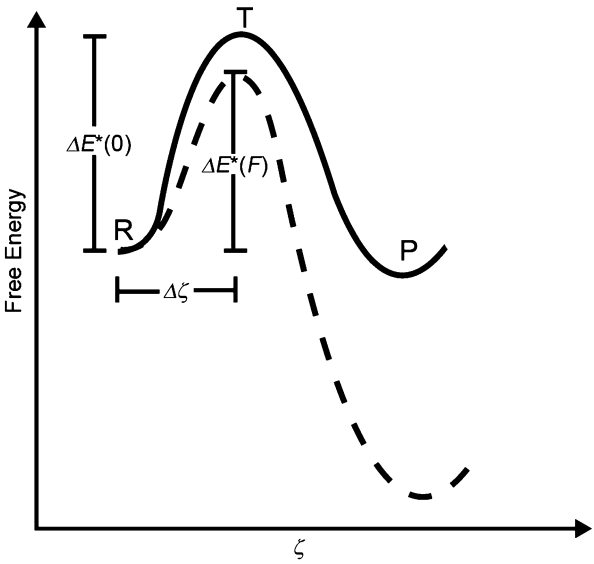

Fig. 16 Schematic drawing of the potential energy landscape as a function of reaction coordinate ζ with (*dashed line*) and without (*solid line*) external force F. R reactant, T transition state, P product

lifetime of materials under tensile stress. Later Bell [154] postulated that the same equation could be employed for bond dissociation in biomolecular processes. In this Eyring–Bell–Evans model, the external force merely exerts work on the reacting polymer to lower the energy barrier (Fig. 16). The key assumption is that the external force does not affect the potential energy landscape of the reaction. The activation energy of a reaction $\Delta E^*(F)$ under a constant external force F can be then expressed by

$$\Delta E^*(F) = \Delta E^*(0) - F\Delta\zeta \tag{16}$$

where $\Delta E^*(0)$ is the activation energy at zero force and $\Delta\zeta$ is the distance from reactant to transition-state configuration along the reaction coordinate ζ, which, according to the assumption, is independent of F for a given reaction. The expression of the rate constant $k(F)$ takes the form

$$\begin{aligned} k(F) &= A\exp\left[-\Delta E^*(0)/k_\mathrm{B}T\right]\exp(F\Delta\zeta/k_\mathrm{B}T) \\ &= k_0\exp(F\Delta\zeta/k_\mathrm{B}T) \end{aligned} \tag{17}$$

where A is the preexponential factor, k_0 is the rate constant at zero force, and k_B is the Boltzmann constant. Later the Eyring-Bell-Evans model was improved to the tilted potential energy surface model, accounting for the effect of F on the potential energy landscape of the reaction. In that case, $\Delta\zeta$ is a function of F.

Odell and Keller [97] developed a thermally activated barrier to scission (TABS) model. They incorporated the expression of F ((11), bead-rod model) into (17) and accounted for the nonuniform distribution of tension along the contours of the

polymer. The TABS model predicts that the degradation rate $k(\dot{\varepsilon})$ grows exponentially as a function of $\dot{\varepsilon}$:

$$k(\dot{\varepsilon}) = C_1 \exp(C_2 \dot{\varepsilon}) \tag{18}$$

where C_1 and C_2 are constants for given experiment setup. Experimental results correlate well with (18) [129, 147, 153].

The Eyring–Bell–Evans model, the titled potential energy surface model, and the thermally activated barrier to scission model are essentially one-dimensional phenomenological models. However, most chemical reactions, including activation of mechanophores, involved in the complicated rearrangement of atoms and bonds, are multidimensional in nature. The preceding models fail to consider the distortion of the multidimensional energy landscape [128]. Quantum-chemical calculations can provide more details to interpret the results in chain degradation and activation of mechanophores [12, 15, 30, 50, 57, 155–157].

Recently, Boulatov developed a chemomechanical kinetic model derived by modeling the reactant and transition states as a series of intersecting harmonic energy wells containing individual conformers [158]. By identifying a local reaction coordinate and estimating its chemomechanical coupling coefficient from quantum-chemical calculation, the profile of activation energy perfectly matches those from explicit quantum-chemical computations [31, 159]. The *k–F* relationship derived from his model is validated by experimental observations [160–163].

4 Mechanochemistry of Cyclic Polymers

4.1 Cyclic Polymers

Unlike linear chains, cyclic chains have no end-groups. In bulk conditions a linear chain diffuses through reptation by moving the chain ends to new positions but the cyclic chain moves with an amoeba-like motion [164]. Cyclic polymers also have more compact conformations than their linear counterparts [165]. For a cyclic chain and a linear chain having the same M, the following equations are predicted by theory [166]:

$$\frac{R_{\mathrm{G,L}}^2}{R_{\mathrm{G,C}}^2} = 2 \tag{19}$$

$$\frac{R_{\mathrm{H,L}}^2}{R_{\mathrm{H,C}}^2} = \left(\frac{3\pi}{8}\right)^2 \tag{20}$$

where R_{G} and R_{H} are the radius of gyration and the hydrodynamic radius, respectively. The subscripts L and C denote linear chain and cyclic chain, respectively.

Equations (19) and (20) are valid in theta solvent. The more compact structure and the lack of chain ends result in different chemical and physical properties of cyclic polymers, including lower translational friction coefficients, higher glass transition temperatures [167], faster crystallization [168], higher refractive index [169], higher density [170], higher critical solution temperature [167], and lower intrinsic viscosity [167, 171, 172].

Despite this progress, high quality experimental data on microscopic structure, dynamics in dilute and concentrated solutions, and mechanochemistry of cyclic polymers are rare. The main deficiency is caused by the presence of linear contaminants in the samples [173, 174].

4.2 CST of Cyclic Polymers

The dynamics of cyclic chains have been studied mainly by computer simulation [175–177]. Cifre and co-workers consider the CST of cyclic polymer solution in QSSF using Brownian dynamics simulation techniques [178]. In Fig. 17a, $< R_G^2 >$ for a ring chain with $N = 25$ beads suddenly increases as $\dot{\varepsilon} > \dot{\varepsilon}_C$. They further exploited the dependence of $\dot{\varepsilon}_C$ on the N and hydrodynamic interactions (Fig. 17b). In both theta solvent and good solvent, $\dot{\varepsilon}_C$ satisfies

$$\dot{\varepsilon}_C = AN^{-2.00\pm0.05} \text{ (no hydrodynamic interactions, Rouse Model)} \tag{21}$$

$$\dot{\varepsilon}_C = AN^{-1.55\pm0.01} \text{ (hydrodynamic interactions, Zimm Model)} \tag{22}$$

Compared to (5) and (6), the exponents of the power laws in (21) and (22) is unaltered in the cyclic chains, varying only in the pre-exponent A. The authors then estimated A for both linear and cyclic topologies, and found that CST of cyclic polymer occurs at a much higher value of $\dot{\varepsilon}_C$:

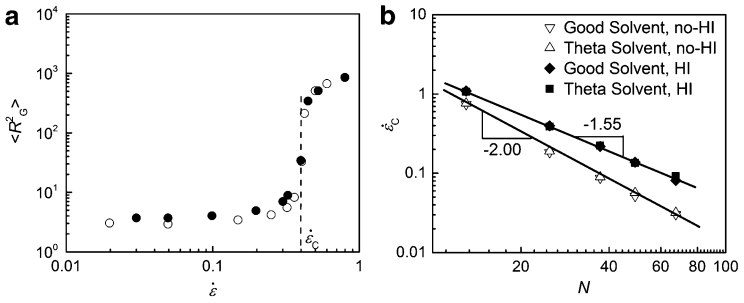

Fig. 17 (**a**) Evolution of the mean squared radius of gyrations $< R_G^2 >$ with strain rate $\dot{\varepsilon}$ for a ring with $N = 25$ beads. (**b**) Dependence of the critical elongational rate on ring size N. All the possible interactions: with or without hydrodynamic interaction, and theta and good solvent conditions are considered. (Adopted with permission from Cifre et al. [178]. Copyright 2005 Elsevier)

$$\frac{A_C}{A_L} \approx 4.1 \tag{23}$$

where A_C and A_L are the pre-exponents for cyclic and linear polymers, respectively. Their simulation work suggests that cyclic polymers are more resistant to extension and scission than their linear counterparts.

4.3 *Mechanical Activation of Mechanophores in Cyclic Polymers*

So far, activation of mechanophores in the cyclic chain has not been reported. One important issue is the location of the mechanophore in the cyclic polymer. If only one mechanophore is incorporated into a ring chain (Fig. 18a), it is unlikely to experience the maximum hydrodynamic force (red dots) because the ring has no definitive midpoint in the flow field. Even if the ring chain breaks, the position of the mechanophore is unlikely to locate just at the midpoint of the linear product. To improve the chance of activation, it is better to have multiple mechanophores incorporated into the cyclic chain, such as random, alternative, or block cyclic copolymers. For example, in Fig. 18b the mechanophores are randomly dispersed into a cyclic macromolecule to increase the activation probability. If the cyclic chain breaks, the mechanophores still have the chance to be located near the midpoint of the linear chain. The linear fragment then undergoes CST and activates the mechanophores.

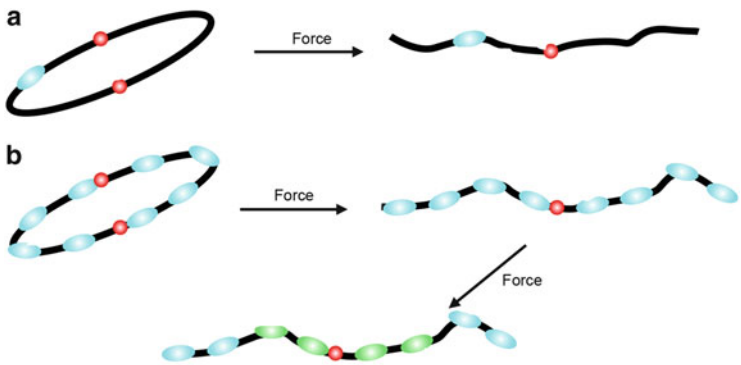

Fig. 18 Activation of mechanophore in cyclic polymers. (**a**) A mechanophore is incorporated into a ring chain. (**b**) The mechanophores form a block of the ring chain. *Red dots* represent probable positions of maximum hydrodynamic drag force. *Blue* and *green ovals* denotes mechanophores

4.4 Mechanochemical Degradation of Cyclic Polymers

Moore and co-workers recently reported mechanically triggered heterolytic unzipping of a cyclic polymer [179]. They prepared cyclic poly(*o*-phthalaldehyde) (cPPA, Fig. 19a) by cationic polymerization. As a reference, they synthesized linear PMA of comparable molecular weight. The scission of the two polymers was studied in an acoustic field. At given sonication time, cPPA degraded faster than PMA. At a first glance, the result is the opposite of Cifre's simulation. The integrated refractive index signal – which is proportional to the concentration of the polymer – drops to 30% of its original value for cPPA but remains nearly constant for the control PMA (Fig. 19b). It suggests a possible depolymerization process in cPPA under sonication. Moore's simulation later confirmed that the faster degradation of cPPA is caused by a mechanically triggered depolymerization. They applied steering forces to the carbon atoms of the terminal methyl groups in a linear and truncated model of the polymer with four monomer units. As shown in Fig. 19c, at a force of 3.5 nN a central C–O bond is first fractured, followed by a sequential monomer rearrangement. Eventually, the whole chain is depolymerized

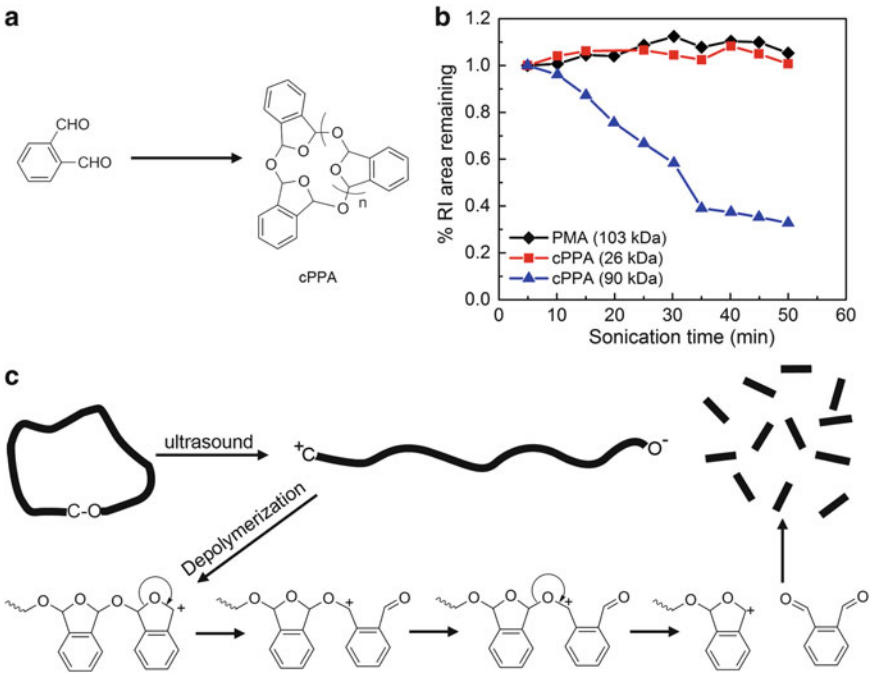

Fig. 19 (**a**) Chemical structure of cPPA. (**b**) Integrated refractive index signal as a function of sonication time. It should be noted that cPPA with molecular weight below a threshold value shows no degradation at all. Therefore the process is indeed mechanically triggered. (Adopted with permission from Diesendruck et al. [179]. Copyright 2014 Nature Publishing Group.) (**c**) Depolymerization process of cPP from ab initio steered molecular dynamics calculations

into monomers. In the control PMA, such depolymerization mechanism is absent. Ultrasonic degradation of a linear PPA of the same M_w as cPPA was not been performed. It is worth noting that, although cPPA is able to depolymerize under mechanical force, whether or not the ether bond connecting the two benzofuran motifs in the chain can be regarded as a mechanophore remains uncertain. It is not clear whether the initial bond disassociation event is a result of a random cleavage of a force-independent or a mechanical sensitive activation event.

Collectively, mechanochemistry of cyclic polymers has been little studied and many questions remain unanswered. What are the conformations above CST for a ring chain? What if the ring has a knot? If a linear chain threads through a ring chain, what happens to CST? Is it possible to cleave a site-specific bond in a ring by flow field? What is the best strategy to incorporate mechanophores into cyclic polymers? These questions impose great challenges on both polymer synthesis and polymer physics.

5 Mechanochemistry of Graft Polymers

5.1 Polymer Shear Stability in Drag Reduction

The study of graft polymers in the flow field is motivated by the searching of polymer additives with high shear stability for use as drag reduction agents. Here we first give a brief introduction to drag reduction. Drag reduction refers to the drastic reduction of drag in turbulent flow below that for the pure solvent by the addition of a small amount of drag reduction agents (less than 100 ppm). These substances include polymers [180–182], surfactants [183], insoluble particles such as grains or fibers [116], or their mixture [184–187]. So far, polymers are the most widely studied and most widely employed in drag reduction applications [188]. The drag reduction efficiency (*DRE*) for pipe flow of incompressible fluid is defined as [184]

$$\mathrm{DRE} = \frac{\Delta P_A - \Delta P_S}{\Delta P_S} \times 100\% \tag{24}$$

where ΔP_A and ΔP_S are the pressure drop with the drag reduction agent and with pure solvent under the same conditions, respectively.

A typical curve of *DRE* as a function of the time or the number of passes is shown in Fig. 20. At the beginning, polymer chains reduce the flow resistance of the solution significantly (high *DRE* value). However, as the same fluid passes the pipe repeatedly, the value of *DRE* drops because of chain scission in the turbulent flow. The underlying mechanisms are not fully understood and are still under intense debate. Phenomenologically, the longer the chain, the better *DRE* but also the faster the chain breaks [116, 189]. The scission rate increases monotonically as the degree

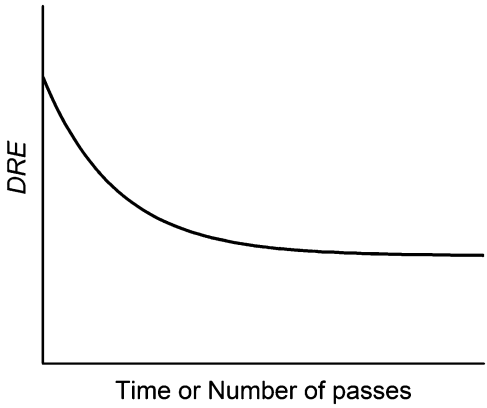

Fig. 20 Schematic illustration of *DRE* as a function of time or the number of passes

of turbulence increases. Hence, the shear stability is regarded as critical as *DRE* for a drag reduction additive [116].

5.2 Shear Stability of Graft Polymers in Drag Reduction

Because of the huge economic benefits of drag reduction in applications such as oil transportation, flood water disposal, and fire-fighting, researchers have been trying to develop polymers with complex topology, which are expected to retain *DRE* while attaining much longer durability under flow. Significant effort has been directed since the 1960s to understanding the shear stability of graft polymers in drag reduction. However, contradictory results were reported.

In 1974, Kim and co-workers synthesized a high molecular weight, branched poly(acrylamide) (PAM) [190]. The drag reduction experiments were performed in a capillary flow system. At $Re = 5{,}730$, branched PAM showed a drop of *DRE* from 60% to 50% with increasing number of passes, but it was more shear stable than linear PAM (from 60% to below 35%). The authors attributed the improved shear stability of branched PAM to the scission of the side chains in preference to the cleavage of the backbone. However, the comparison is not based on the same molecular weight but on the same percentage drag reduction per parts per million. Gryte and co-workers [191] prepared poly(acrylic acid) (PAA) grafted PEO. They irradiated PEO aqueous solutions in the presence of AA under gamma ray. The mole percent of AA varied from 28% to 75%. At $Re = 75{,}000$ they found no difference in *DRE* between ungrafted and grafted PEOs within experimental errors (Fig. 21).

Polysaccharides, along with guar gum and xanthan gum, comprise an important class of drag reduction additives (Fig. 22a) [194]. They are fairly shear stable but not as effective as PEO and PAM. So grafting synthetic polymers onto the backbone of polysaccharides was popular in the late 1980s. Singh and co-workers

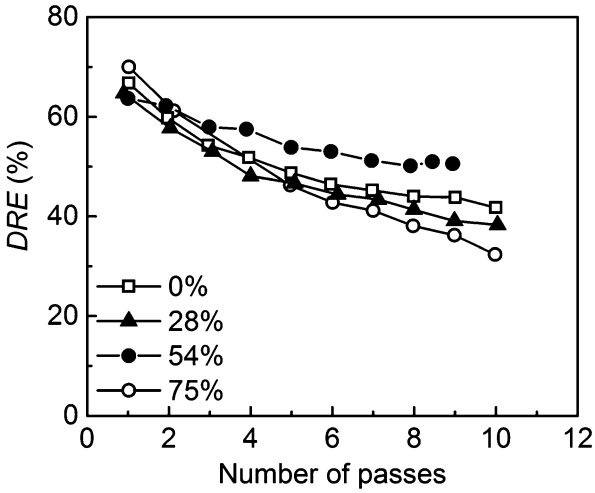

Fig. 21 Degradation behavior of the 50 ppm solutions of PAA-grafted and ungrafted PEO in turbulent flow at Reynolds number $Re = 75{,}000$. The *number in the legend* indicates the molar percent of AA in PAA-grafted PEO. (Adopted with permission from Gryte et al. [191]. Copyright 1980 John Wiley & Sons)

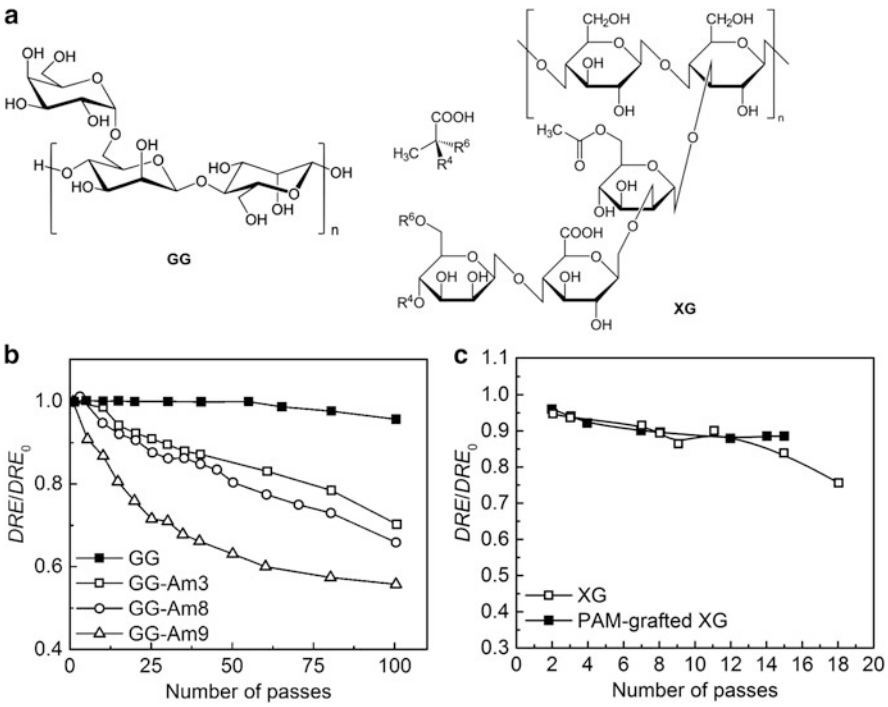

Fig. 22 (**a**) Chemical structures of guar gum and xanthan gum. (**b**) Reduced drag reduction efficiency (DRE/DRE_0) as a function of number of passes for guar gum and acrylamide-grafted guar gum with different PAM length (legend). It should be noted that the grafted guar gum is less shear stable than the ungrafted guar gum. (Adopted with permission from Deshmukh and Singh [192]. Copyright 1987 John Wiley & Sons.) (**c**) DRE/DRE_0 as a function of number of passes for xanthan gum and acrylamide-grafted xanthan gum. (Adopted with permission from Ungeheuer et al. [193]. Copyright 1989 John Wiley & Sons)

prepared PAM-grafted xanthan gum [195] and guar gum [196] using a ceric ion/nitric acid redox initiator. They claimed greater shear stability in drag reduction for the grafted polysaccharides and interpreted their data by Kim's concept of "preferential scission of side chains." Later, they synthesized two series of grafting guar gums [192, 193]. In the first series, the ratio of guar gum and acrylamide was fixed (1:10 w/w) but the average number of grafting sites per guar gum molecule was varied (by the ratio of concentration of ceric ion to guar gum). In the second series, the average grafting site per guar gum molecule was fixed, but the length of the side chain was varied. Nevertheless, PAM-grafted Guar gum showed a notable decrease in *DRE* caused by chain scission, whereas the *DRE* of ungrafted guar gum persisted under the same conditions (Fig. 22b). They also found the shear stabilities of grafted (by PAM) and ungrafted xanthan gum to be similar as shown in Fig. 22c. Other researchers, such as Hoyt, noticed that branched polysaccharides even lost the ability to reduce drag [194].

5.3 *Effect of Side Groups in Ultrasonic Degradation*

Malhotra studied the effect of alkyl substituent on the ultrasonic degradation of poly (alkyl methacrylate) [197]. He prepared poly(isopropyl methacrylate) and poly (octadecyl methacrylate) of identical contour length (Fig. 23a). In an acoustic field, he failed to see any dependence of the rate constant on the size of side groups. Recently, May revisited the effect of side group using a spiropyran

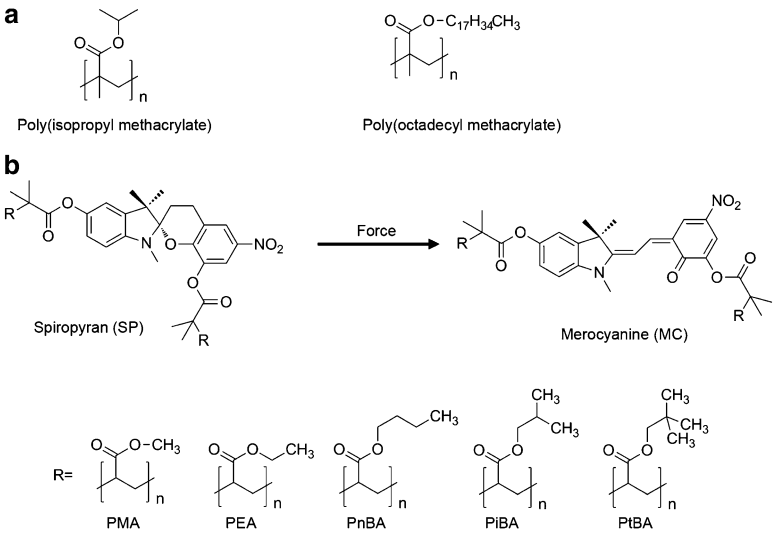

Fig. 23 (**a**) Effect of side groups in ultrasonic degradation. Chemical structure of poly(alkyl methacrylate) [197]. (**b**) Activation of SP to MC by mechanical force and the effect of side groups on the mechanical activation of SP [198]

(SP) mechanophore [198]. As shown in Fig. 23b, colorless SP can undergo a force-induced electrocyclic ring-opening reaction to the purple merocyanine (MC) isomer. Because of this mechanochromic reaction, SP has been incorporated into several polymers [32, 34–45, 199]. May embedded SP into the center of PMA, poly(ethyl acrylate) (PEA), poly(*n*-butyl acrylate) (PnBA), poly(*iso*-butyl acrylate) (PiBA), and poly (*tert*-butyl acrylate) (PtBA). The activation of SP was monitored by in situ UV–Vis spectroscopy. Again, the reaction constant depends only on the backbone length, not on the molecular weight, a result reminiscent of Malhotra's work. It is reasonable that any influence of the side groups on mechanochemistry could be undetectable because the force needed to generate the color is very small.

5.4 Adsorption-Induced Chain Scission of Graft Polymers

Recently, Sheiko and co-workers prepared a series of brushlike macromolecules (comb polymers) [200–208]. They synthesized PnBA side chains and densely grafted them onto the backbone of PMA or poly(2-hydroxyethyl methacrylate) (PHEMA) (Fig. 24a). Because of the high grafting density, the side chains repelled each other and stretched the backbone to extended conformations. If the side chain is long enough, the tension accumulated along the backbone is sufficient to cleave C–C bonds. In their experiments, brush molecules were adsorbed from a dilute solution on the liquid–liquid surface with varying surface tension. They observed C–C cleavage in the midpoint of PHEMA with long PnBA side chains (140 repeating units) (Fig. 24b). However, molecules having the same PHEMA backbone but a slightly shorter side chain (130 repeating units) are almost intact at the same water/

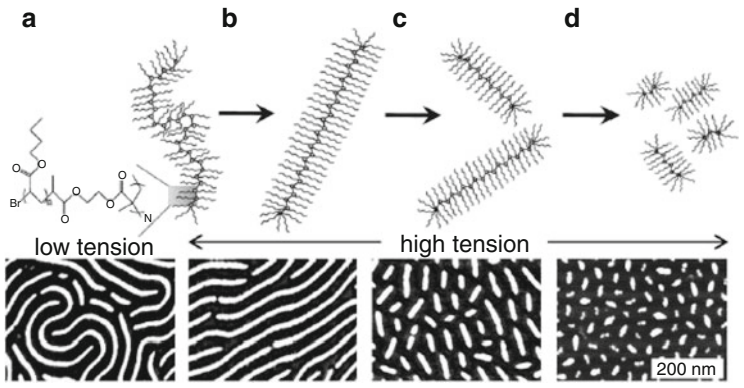

Fig. 24 Significant tension of the order of several nano-Newtons is developed in the polyacrylate backbone of molecular bottlebrushes caused by steric repulsion between the densely grafted PnBA side chains (**a**). This intramolecular tension leads to nearly full extension of the backbone (**b**) and then scission of its C–C bonds (**c**, **d**). (Adopted with permission from Lebedeva et al. [202]. Copyright 2012 National Academy of Sciences)

propanol surface (surface tension = 69 mN m^{-1}). The authors also incorporated disulfide (S–S) bonds in the middle of brush molecules. The bond scission rate upon adsorption is much faster than those with a C–C bond or C–S bond in the middle of the backbone. Based on the similar consideration, we suppose these densely grafted comb polymers are more susceptible than their ungrafted cousins in the flow field.

5.5 *Fracture of an Ideal Graft Macromolecule*

Agarwal and Mashelkar first analyzed contradictory reports from Kim [190], Gryte [191], and Singh [192, 193], and proposed a simple mechanistic model [209]. In stark contrast to the concept of "preferential scission of side chains," their model reveals decreased shear stability by grafting side chains. They extended Odell and Keller's bead-rod model [27]. The backbone was modeled as a fully extended rod with $N_L = 2m + 1$ beads (Fig. 25). p grafted bead-spring chains having g beads with

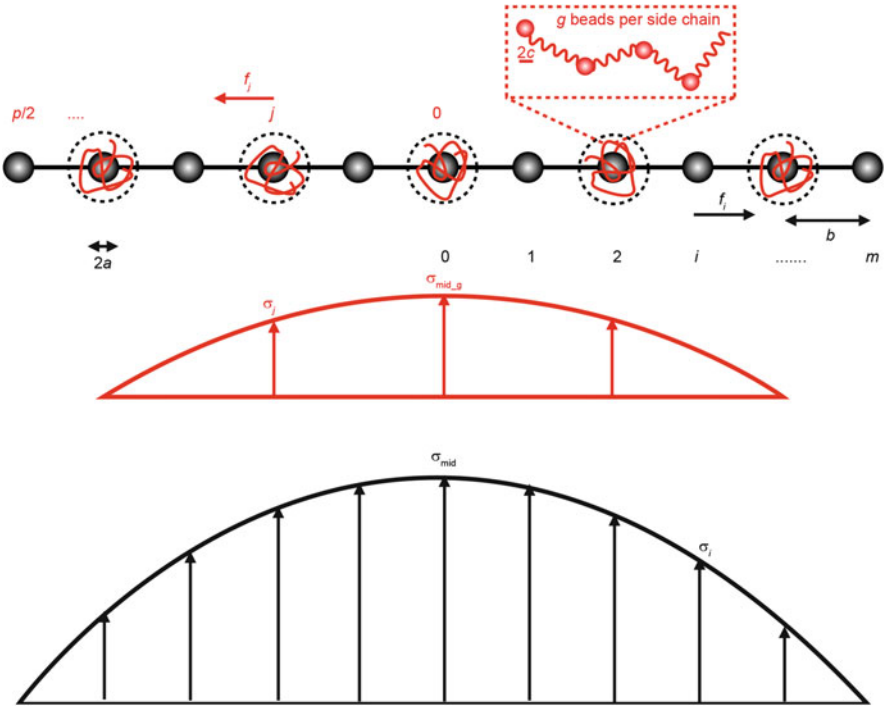

Fig. 25 Agarwal and Mashelkar's modified bead-rod model for grafted chain in elongational flow [209]. The backbone has p uniformly distributed side chains. Each side chain is modeled as a random coil and has g beads with bead size $2c$. The hydrodynamic force exerted on the coils adds additional force to the backbone so the force along the linear backbone consists of two part: σ_{mid_g} from the side chains and σ_{mid} from the beads in the backbone

bead size c are uniformly distributed along the rod. Other parameters are the same as those in Sect. 3.3.1 and Fig. 14. The grafted chains are small and can be approximated to a random coil, and they do not interfere with each other in the flow field. Similar to the deduction in the bead-rod model, the jth ($j = 1, 2, \ldots, p$) coil experiences a hydrodynamic drag force, $f_j = \xi_g v_j = j\xi_g \dot{\varepsilon} b_g$, where $b_g = N_L b/p$ is the space between adjacent coils and $\xi_g = 6\pi\eta_s c g^{0.5}$ is the friction factor of the grafted chain. f_j imparts additional tension in the center of the rod. Similar to (13), this additional tension force can be expressed by

$$\sigma_{mid\_g} = \frac{3}{4} S_2 \pi \dot{\varepsilon} c b_g \eta_s g^{0.5} p^2 \tag{25}$$

where S_2 accounts for the shielding effect between the grafted beads and should be smaller than 1. The total tension in the midpoint of the rod is

$$\begin{aligned} \sigma_{mid\_graft} &= \sigma_{mid} + \sigma_{mid\_g} = \frac{3}{4} S_1 \pi \dot{\varepsilon} a b \eta_s N_L^2 + \frac{3}{4} S_2 \pi \dot{\varepsilon} c b_g \eta_s g^{0.5} p^2 \\ &= \sigma_{mid} \left(1 + \frac{S_2 c}{S_1 a} \frac{p}{N_L} g^{0.5} \right) \end{aligned} \tag{26}$$

For ungrafted chain or short side groups, $p \approx 0$, (26) reduces to (13). This may explain why side groups have a minor effect on scission in acoustic fields [197, 198].

For fixed linear backbone (N_L), (26) suggests grafting side chains reduces its shear stability. The more grafting sites (p) there are and the longer the side chains (g), the higher tendency to degrade. In one of Singh's work [192], he fixed the total acrylamide weight but varied p and g, i.e., $N_g = pg$ was constant. Inserting $N_g = pg$ into (26) yields $\sigma_{mid\_graft} = \sigma_{mid}\,(1 + S_2/S_1 c/a N_g/N_L g^{-0.5})$. It predicts a reduction of shear stability with shortening the side chain, which is consistent with Singh's experimental data [192].

If the side chain is long and densely grafted (comb polymers), the repulsive interactions between the side chains stretch the backbone. A new term accounting for this effect should appear on the right side of (26), further increasing the susceptibility of the polymer to scission. Moreover, the random coil assumption of the side chain in Agarwal and Mashelkar's model becomes increasingly improbable as the grafting density increases. In that instance, the *DRE* of polymers seems to depend not on the total molecular weight but on the maximum spanning length M_{span}, which is defined as a path starting from one end of the chain to another end *without doubling back along the backbone* (see details the next section) in the flow field [210, 211].

If the total number of repeating units is fixed ($N = N_L + pg$ is fixed), a grafted chain bearing the same monomer (thereby $c = a$) is indeed *more mechanically stable* than a linear counterpart. Suppose $S_1 \approx S_2$, (26) is rewritten as $\sigma_{mid\_graft} = B(N_L{}^2 + N_L p g^{0.5})$ (B is a parameter irrelevant to our discussion). For a linear chain, $p = g = 0$, $\sigma_{mid\_linear} = BN^2$. $\sigma_{mid\_linear} - \sigma_{mid\_graft} = B$

$[(N_L + pg)^2 - N_L{}^2 - N_L pg^{0.5}] = B[(pg)^2 + N_L p(2g - g^{0.5})] > 0$. These deductions imply that the additional drag force resulting from side chains σ_{mid_g} cannot compensate the decrease of σ_{mid} caused by a shorter backbone. Therefore, the drag force at the midpoint of a linear chain is always higher than that in a grafted chain bearing the same N. However, polymers with nonlinear topology were not as effective in drag reduction as linear counterparts of the same total molecular weight, as reported by Gramain and Barreill [212].

Collectively, grafting short side groups shows no influence on chain scission kinetics and activation of mechanophores in ultrasound sonication. Grafting side chains onto a linear backbone appears to decrease the mechanical stability because of the accumulation of additional hydrodynamic drag force on the side chains and/or the repulsive interactions between the side chains. In Argwal's bead-rod model, a grafted chain is more mechanically stable than a linear chain if they have the same number of repeating unit N

6 Mechanochemistry of Star-Shaped Polymers

6.1 Star-Shaped Polymers

In the preceding sections, most of the graft polymers are irregular in topology. It is difficult to separate the effect of chain topology from the effect of chain length on the mechanochemical kinetics. To this end, mechanochemistry of star-shaped polymers has attracted great attention in the last decade. Star-shaped polymers are the simplest class of branched polymers, where several (>2) linear arms connect to a central core (Fig. 26). The core can be an atom, molecule, or even macromolecule, whose radius should be smaller than the dimension of the arm (e.g., the end-to-end distance of the arm R_{arm}) [213]. Depending on the chemical species of the arm, star-shaped polymers are classified into homo-arm star-shaped polymers or miktoarm star-shaped polymers (Fig. 26). Before discussing the mechanochemistry of star-shaped polymers, we first define several key terms. All star-shaped polymers in this section are homo-arm stars having N total repeating units and f_{arm} arms ($N_{arm} = N/f_{arm}$ repeating units per arm). Linear polymers are denoted as **P-L** $\boldsymbol{M}_w$, where P is

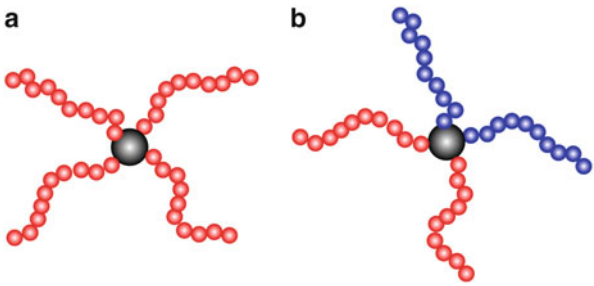

Fig. 26 Schematic drawing of star-shaped molecules with $f_{arm} = 4$ arms: (**a**) homo-arm; (**b**) miktoarm

the abbreviation of the polymer, and M_w is in kDa. Star-shaped polymers are referred to as **P-Sf_{arm} M_{arm}/M_w** ($M_w = M_{arm} f_{arm}$) where M_{arm} is the molar mass of the arm.

Schaefgen and Flory first reported star-shaped polyamides in 1948 [214]. Maurice and co-workers first synthesized well-defined PS through living anionic polymerization in 1962 [215]. The subject of star-shaped polymers has rapidly expanded during the last few decades. The synthesis, characterization, and applications of star-shaped polymers have been extensively reviewed [95, 216–222]. Star-shaped polymers have shown lower crystallization temperatures, lower degrees of crystallinity, and lower melting temperatures [213] than linear polymers of the same molecular weight. They have found a wide range of applications ranging from rheological modifiers [223] to high performance gene delivery [95, 224, 225].

Compared to linear analogues of identical molecular weight and monomer composition, star-shaped polymers have smaller R_G, R_H, and lower intrinsic viscosity [η] [222, 226, 227]:

$$\frac{R_{G,S}^2}{R_{G,L}^2} = \frac{3f_{arm} - 2}{f_{arm}^2} \tag{27}$$

$$\frac{R_{H,S}}{R_{H,L}} \approx f_{arm}^{0.25}\left[2 - f_{arm} + 2^{0.5}(f_{arm} - 1)\right]^{-0.5} \tag{28}$$

$$\frac{[\eta]_S}{[\eta]_L} \approx \left(\frac{3f_{arm} - 2}{f_{arm}^2}\right)^{0.58} \tag{29}$$

where the subscripts S and L denote star-shaped and linear macromolecule, respectively. Equations (27), (28), and (29) are valid in theta solutions. For instance, R_G, R_H, and [η] for a star-shaped molecule bearing eight arms ($f_{arm} = 8$) are 58.6%, 85.2%, and 53.8% of those for a linear chain bearing the same N, respectively. Star-shaped polymers are expected to experience a smaller hydrodynamic drag force and therefore be less susceptible to mechanical degradation. Mechanochemistry of star-shaped polymers has been studied by modeling, experiments, and computer simulations.

6.2 *Mechanical Stability of Star-Shaped Polymers: Bead-Rod Model*

Agarwal and co-workers adopted Odell and Keller's bead-rod model to predict the shear stability of star-shaped polymers [228]. As illustrated in Fig. 27, they adopted a key assumption that all arms are fully stretched before any scission event. For a linear polymer, the tensile force built at the midpoint is $\sigma_{mid} \sim N^2$ (Eq. 13). For a six-arm star molecule bearing the same N, the force at the base of each arm σ_{arm} is

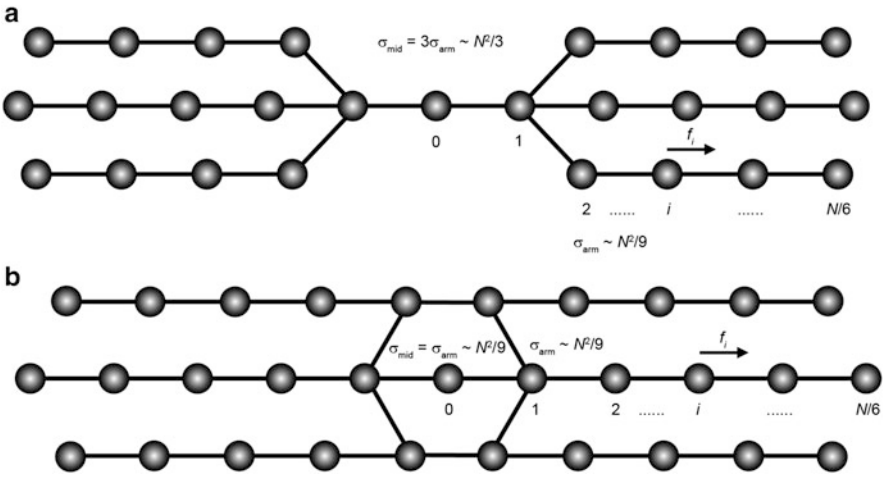

Fig. 27 Schematic drawing of bead-rod model for a star-shaped molecule with $f_{arm} = 6$ arms and N total beads [228]. Each bead experiences a hydrodynamic force f_i. The accumulated tensile force at the 0th bead σ_{mid} depends on the structure of the core: (**a**) a linear core, $\sigma_{mid} \sim 1/3N^2$; (**b**) a fused core, $\sigma_{mid} = \sigma_{arm} \sim 1/9N^2$

$\sigma_{arm} \sim (1/3N)^2 = 1/9N^2$. The force at the midpoint of the core σ_{mid} depends on its structure. If the star has a linear core (Fig. 27a), σ_{arm} in each of the three sets of arms add up to $\sigma_{mid} = 3\sigma_{arm} \sim 1/3N^2$ in the single-bond linkage of the core. If the star has a fused core with three parallel bonds (Fig. 27b), σ_{mid} in each of the three parallel links would scale $\sigma_{mid} = \sigma_{arm} \sim 1/9N^2$. The above deductions can be generalized for star bearing f_{arm} arms and n parallel links in the center of the core. σ_{arm} for each arm is $\sigma_{arm} \sim (2/f_{arm}N)^2 = 4/f^2_{arm}N^2$. Because σ_{arm} in each of $f_{arm}/2$ sets of arms add up and shared by n parallel links, σ_{mid} has the form

$$\sigma_{mid} = \sigma_{arm} f_{arm}/(2n) \sim \frac{2}{nf_{arm}} N^2 \tag{30}$$

If the critical-stress-to-fracture theory is applied, $\dot{\varepsilon}_F$ satisfies the following expression:

$$\dot{\varepsilon}_F \propto nf_{arm}M^{-2} \tag{31}$$

Compared with (14), $\dot{\varepsilon}_F$ of star-shaped polymers follows the same -2 dependence on M but its value is higher than in linear polymers according to (31). The structure of the core in the number of parallel links (n) and the number of arms (f_{arm}) both improve the shear stability of star-shaped polymers.

The bead-rod model implicitly assumes other bonds in the star molecule are as strong as those at the midpoint of the core and favors a core-fracture mechanism. Practically, the linkages which connect the arms to the core may be weaker than the bonds in the core. The fracture may proceed by an arm-loss mechanism.

6.3 *Mechanical Degradation and Activation of Mechanophore in Star-Shaped Polymers*

In 1978, Gramian and Barreill studied the effect of chain topology on the drag reduction of dilute solutions [212]. They found star-shaped PS not to be as effective as linear analogues having the same total molecular weight, but emerged with higher shear stability. They ascribed such enhancement to a lower effective molecular weight (smaller hydrodynamic volume) of star-shaped polymers. Duan and co-workers [229] reported higher shear stability in star poly(ethyleneimine)-PAM in the presence of NaCl.

Here we highlight Striegel's work. He systematically exploited the effects of the number of arms f_{arm} and the molecular weight of each M_{arm} on the scission of star-shaped polymers [230]. In the first set of experiments, he synthesized three samples of similar molecular weights: **PS-L 257**, **PS-S3 85/255**, and **PS-S8 25.5/202** (Fig. 28a) and looked into their shear stability in the acoustic field. M_w of **PS-L 257** decreased to half (c.f., 114 kDa) with an increase of the polydispersity (c.f.,

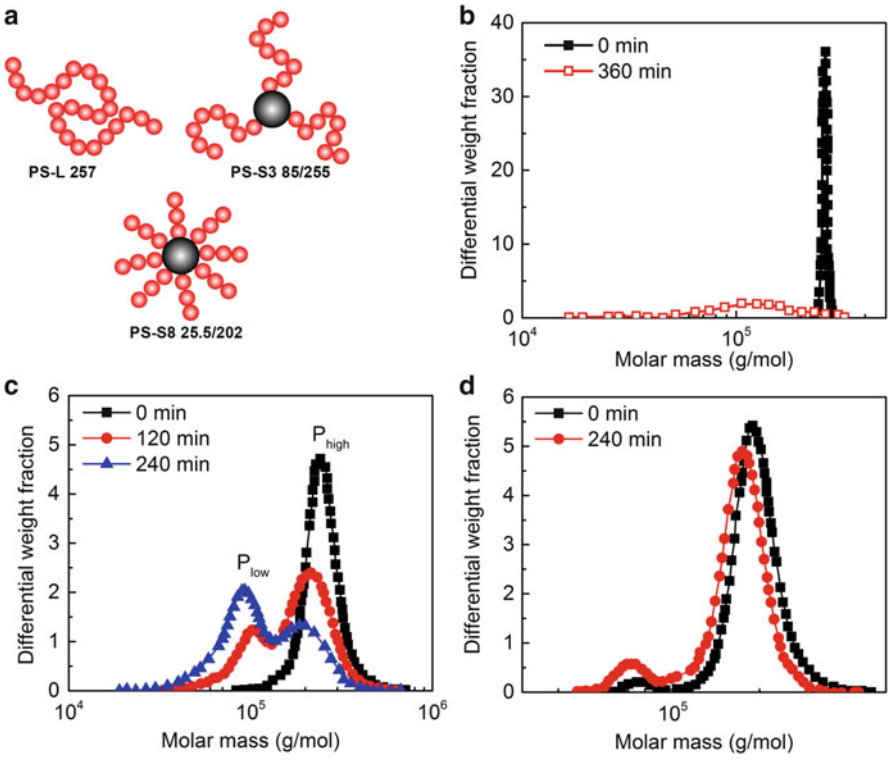

Fig. 28 (**a**) Three polymers used in Striegel's work [230]. Effect of sonication time on the differential molar mass distribution of (**b**) **PS-L 257**, (**c**) **PS-S3 85/255**, and (**d**) **PS-S8 25.5/202**. (Adopted with permission from Striegel [230]. Copyright 2003 Elsevier)

M_w/M_n from 1.001 to 1.262) after 360 min sonication (Fig. 28b). Clearly, the chain is degraded via midpoint scission. For **PS-S3 85/255**, the molecular mass distribution of the molecular weight changed from unimodal to bimodal (Fig. 28c). The peak corresponding to the original star molecules (~250 kDa, thereafter P_{high}) gradually diminished and a peak at lower molecular weight (thereafter P_{low}) grew. The positions of P_{high} and P_{low} shifted and eventually centered at 190 and 90 kDa, respectively. These values support an arm-loss mechanism. Marsalko and co-workers also reported the loss of arm in poly(iso butylene) stars [231]. On the other hand, **PS-S8 25.5/202** is almost inert in the acoustic field (Fig. 28d).

Regarding M_{lim} of linear PS (~65 kDa) under the same experimental conditions, it seems M_{arm} not M is a deterministic factor. However, is $M_{arm} > M_{lim}$ a necessary condition? Striegel then synthesized **PS-S8 45.5/364**, whose $M_{arm} < M_{lim}$. Its degradation behavior is akin to **PS-S3 85/255** and P_{low} centers around 50 kDa after 720 min sonication, indicating arm-loss mechanism.

In the meantime, Striegel also studied the reaction kinetics. For linear analogue **PS-L 257**, a single reaction constant is sufficient to describe the kinetics. On the other hand, **PS-S3 85/255** and **PS-S8 45.5/364** showed a two-step degradation mechanism: (**a**) k_a, arm-loss; (**b**) k_b, simultaneous degradation of the stars with a depleted number of arms and degradation of separated arms (if $M_{arm} > M_{lim}$). For **PS-S3 85/255**, after loss of one arm, the solution is a mixture of linear PS (two arm star molecule) and separated arms with M_w both above M_{lim}. Two degradation behaviors occur simultaneously and $k_a < k_b$. For **PS-S8 45.5/364**, the degradation of separated arms is negligible ($M_{arm} < M_{lim}$) hence $k_a > k_b$.

The degradation of **PS-S8 45.5/364** with $M_{arm} < M_{lim}$ states clearly that $M_{arm} > M_{lim}$ is not a necessary condition. Striegel suggested the criterion $M_{span} > M_{lim}$, where M_{span} is the molar mass of "spanning path." A "spanning path" in a star-shaped molecule is a path starting from the end of one arm going to the end of another arm (red in Fig. 29) *without doubling back along the backbone*. It has N_{span} ($=2N_{arm}+1$, assuming the core only occupies one repeating unit) repeating units, so $M_{span} = 2M_{arm} + M_{core}$ and $M_{span} \approx 2M_{arm}$ for long arm star-shaped polymers. In linear polymers, degradation occurs as $M > M_{lim}$, whereas in star-shaped polymers, $M_{span} > M_{lim}$. For example, **PS-S8 25.5/202** was almost inert in the acoustic field because its $M_{span} \approx 2M_{arm} = 51$ kDa $< M_{lim} = 65$ kDa. The concept of "spanning path" can be extended into other topologies (Fig. 29) [230]. If there is a spanning path in a nonlinear macromolecule with $M_{span} > M_{lim}$, mechanical degradation is possible.

Boydston and co-workers recently revisited the mechanochemical chain scission of star-shaped polymers in acoustic fields using a fluorogenic "turn-on" mechanophore (Fig. 30a) [232]. They synthesized **PMA-L 61.6** and **PMA-S3 28.6/85.9** with $M_{span} = 2M_{arm} = 57.2$ kDa (Fig. 30b). In both samples they linked one of the PMA arms to the core by an anthracene-maleimide Diels–Alder adduct. This mechanophore was previously studied by Bielawski and co-workers [57, 58]. Upon cycloreversion by mechanical force, it produces an anthracene moiety which displays strong UV–Vis and photoluminescence signals.

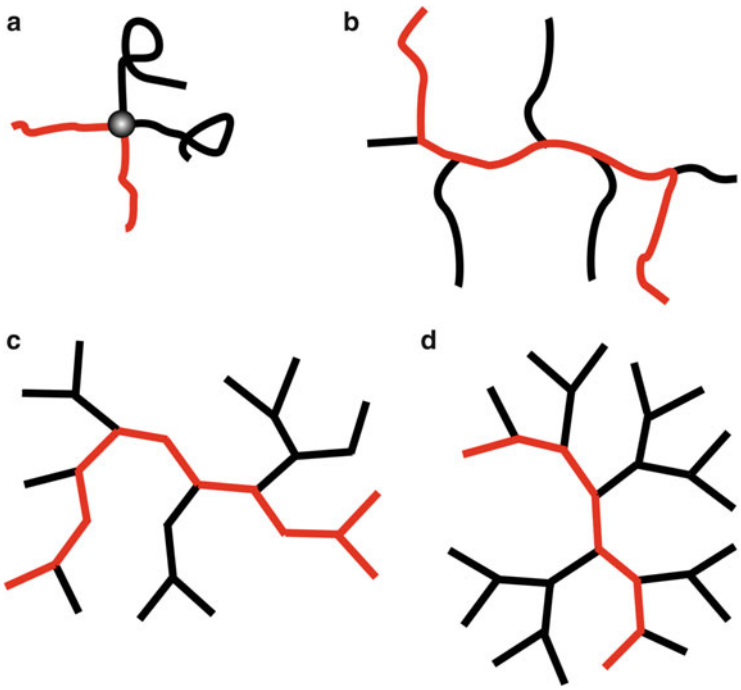

Fig. 29 Schematic drawing of the "spanning path" (highlighted in *red*) in various polymer architectures [230]: (**a**) star-shaped polymer, (**b**) graft polymer, (**c**) hyperbranched polymer, and (**d**) dendrimer. The spanning path is highlighted in *red*

After subjecting the two materials to ultrasonic irradiation, the formation of anthracene was confirmed by photoluminescence spectroscopy. The photoluminescence intensity increases with increasing sonication time (Fig. 30b), which confirms the arm-loss mechanism. Quantifying anthracene (using the photoluminescence intensity at 411 nm) yields two similar reaction constants: $(3.20 \pm 0.14) \times 10^{-2}$ and $(3.26 \pm 0.09) \times 10^{-2}$ min^{-1} for the star and linear polymers, respectively. Boydston also calculated the reaction constant based on refractive index signals (change of M_n). Again, he obtained two similar reaction constants: $(3.13 \pm 0.11) \times 10^{-2}$ and $(3.27 \pm 0.38) \times 10^{-2}$ min^{-1} for star and linear polymers, respectively. His result reveals the equivalence between star-shaped polymers and linear polymers in terms of chain scission rate if M_{span} of star-shaped polymers is equal to M_w of linear polymers.

Unlike previous researchers, Xue and Agarwal were more interested in the effect of core structure on the shear stability of star-shaped polymers. They synthesized six-arm star poly(methyl methacrylate) (PMMA) bearing either a linear core (**A**, $M_w = 2{,}350$ kDa) or a fused core (**B**, $M_w = 2{,}100$ kDa) (Fig. 31) [228, 233]. According to (31), the fused core has a threefold larger $\dot{\varepsilon}_F^B$ ($\sim 3 f_{arm} M^{-2}$)

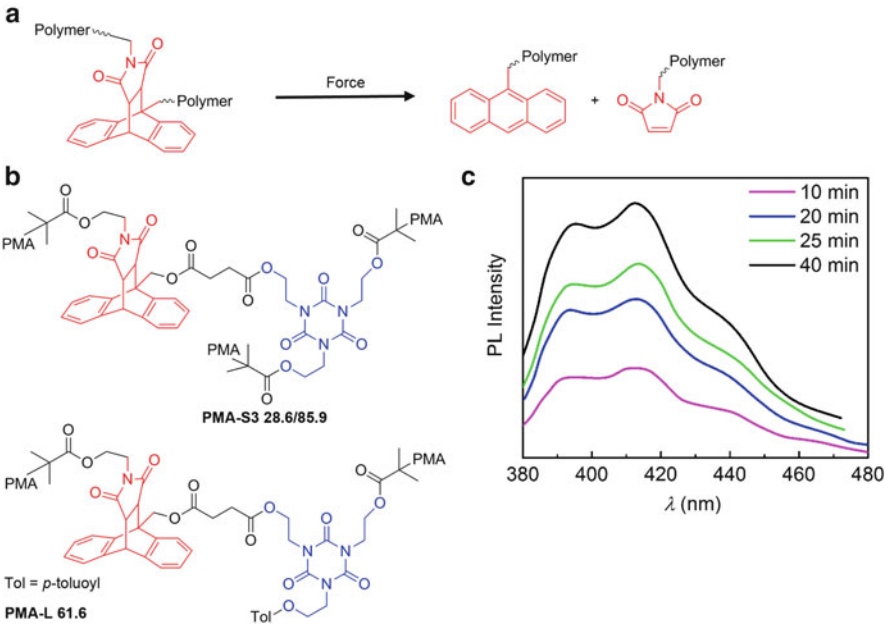

Fig. 30 (**a**) Anthracene-maleimide Diels–Alder adduct that can generally fluoresce an anthracene moiety upon mechanical force. (**b**) Mechanophore-containing star and linear polymers bearing similar M_{span}. (**c**) Photoluminescence spectra in DMF of **PMA-S3 28.6/85.9** upon increasing sonication time indicated in the legend. (Adopted with permission from Church et al. [232]. Copyright 2014 American Chemical Society)

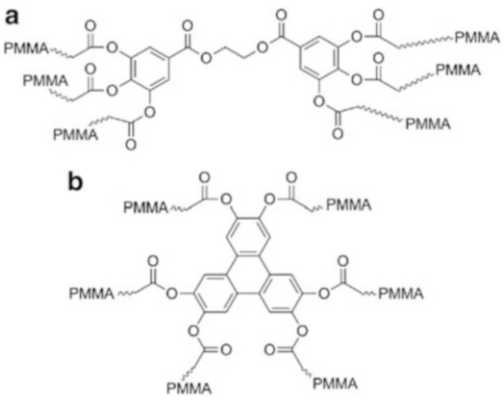

Fig. 31 Star-shaped PMMA polymers bearing (**a**) a linear core and (**b**) a fused core in Xue and Agarwal's work [228]

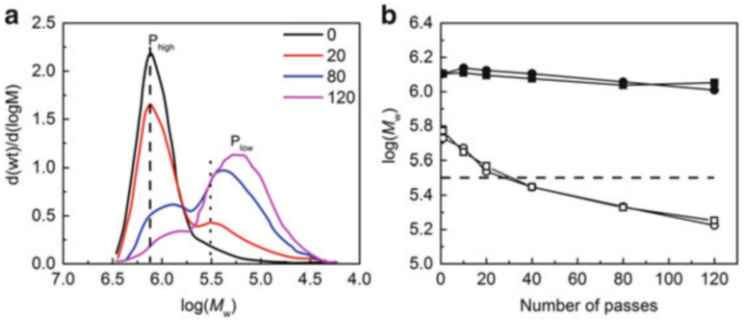

Fig. 32 (**a**) Representative size exclusion chromatography traces of samples for star PMMA with a linear core at different number of passes indicated in the legend. The *dashed line* represents the peak position of the original star molecules and the *dotted line* represents that of the arms. (**b**) Peak molecular weight of the degraded star molecules (*solid symbols*) and arms (*open symbols*). *Square* and *circular symbols* denote fused core and linear core, respectively. (Adopted with permission from Xue et al. [228]. Copyright 2005 American Chemical Society)

than the linear core ($\dot{\varepsilon}_F^{A\sim} f_{arm} M^{-2}$). In this respect, the bead-rod model predicts higher shear stability of **B** than **A**.

Xue carried out the degradation experiment in a cross-slot flow cell and recorded the change of M via size exclusion chromatography. The size exclusion chromatography traces for the linear core **A** are plotted in Fig. 32a at $\dot{\varepsilon} = 46,800\ s^{-1}$ at the central stagnation region. The signal gradually becomes bimodal. The peak corresponding to the original star PMMA (P_{high}) decreases with the appearance of a lower molecular weight peak (P_{low}). After a few passes (<20), the position of P_{low} matches M_{arm} well, suggesting arm-loss of the stars. After around 40 passes, P_{low} shifts to even lower molecular weight. It implies a secondary scission, probably the fracture of cleaved arms. These results strongly support star-shaped polymers degrading by the arm-loss mechanism. The authors summarized the change of the peak molecular weight for both **A** and **B** (Fig. 32b). If **A** were to undergo scission in its core, M_w of P_{high} for **A** should have dropped much faster than that for **B**. However, the traces of P_{high} for **A** and **B** are indistinguishable within experimental error. The author repeated the experiments under different $\dot{\varepsilon}$ (=27,800 and 13,300 s^{-1}) and noted similar results. In short, the degradation of star-shaped polymers is insensitive to the structure of the core in Xue's work.

The key assumption of full extension of all arms before chain scission in Agarwal's model (Fig. 27) is unlikely. It is difficult to reason why all arms should undergo CST at the same time. The arms can arrange in a conformation that prevents the adding up of force at the core (Fig. 33a). Interarm entanglement (Fig. 33b) is also possible and results in force accumulated at the entanglement point, not the linkage in the core. Last, but most important, similar to the concept of molecular individualism [144, 145, 148, 149] (Sect. 3.3.2), each arm may undergo CST at different times and emerge as different conformations (Fig. 33c), i.e., "arm individualism." The assumption that all arms take on fully stretched conformations

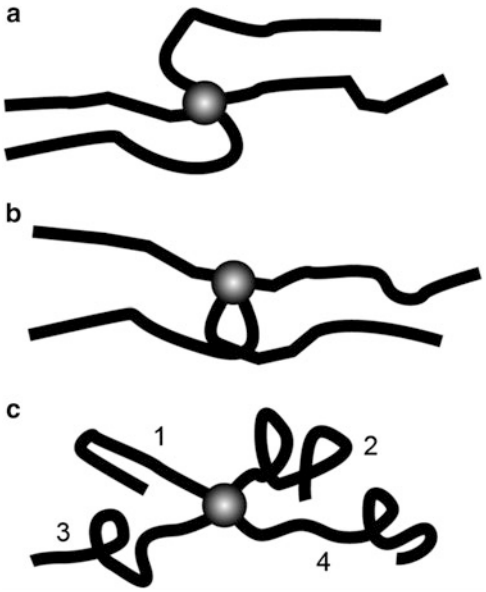

Fig. 33 Schematic drawing of probable conformations of star-shaped polymers in the elongational flow field (*horizontal*). (**a**) Conformation disfavors the building up of force at the core. (**b**) Interarm entanglement leads to stress concentration at the entanglement point. (**c**) "Arm individualism." Each arm may have independent conformations: (*1*) folded, (*2*) coiled, (*3*) kinked, and (*4*) dumbbell

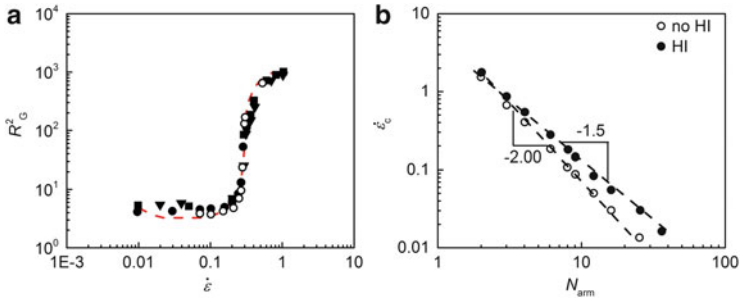

Fig. 34 (**a**) R_G^2 as a function of shear rate for stars with fixed $N_{span} = 13$. *Closed square*: $N = 25$, $f_{arm} = 4$, good solvent; *closed circle*: $N = 37$, $f_{arm} = 6$, good solvent; *closed triangle*: $N = 49$, $f_{arm} = 8$, good solvent; *Open circle square*: $N = 37$, $f_{arm} = 6$, theta solvent. The *red dashed line* is linear chain bearing $N = 13$ beads. (**b**) Dependence of the critical elongational rate with N_{arm} with and without hydrodynamic interactions. (Adopted with permission from Cifre et al. [234]. Copyright 2005 Elsevier)

is oversimplified. In fact, several recent simulation works support the concept of M_{span} and "arm individualism" [235].

May reasoned that the absence of core-fracture in star-shaped polymers is caused by the weaker linkages at the arm–core interface. So he appealingly incorporated SP (Fig. 23) into the core of 4-arm and 8-arm star PMMAs [198]. Although the reaction constant decreases as f_{arm} increases, SP is successfully activated in the acoustic field. His results suggest that it is premature to exclude the core-fraction mechanism.

6.4 CST of Star-Shaped Polymers: Computer Simulations

Computer simulation is a versatile tool to explore the dynamics of polymers with nonlinear topology in great detail [236]. Cifre and Torre studied the effects of N, f_{arm}, hydrodynamic interactions, and the solvent quality on the CST of star-shaped polymers using Brownian dynamics simulation [234, 235]. They observed that CST of star-shaped polymers occurs at a $De = 0.6$, close to that in linear polymers (0.5, see (4)) [235]. If N is fixed (25 beads), the smaller f_{arm}, the sharper CST and the value of $\dot{\varepsilon}_C$. For a given number of arms ($f_{arm} = 6$), the sharpness of CST increases and $\dot{\varepsilon}_C$ shifts to lower values in larger stars (N). The solvent quality has just a minor effect on $\dot{\varepsilon}_C$ in the simulations. The most important results are illustrated in Fig. 34a. The authors varied both N and f_{arm} but kept the spanning path constant ($N_{span} = 2N_{arm} + 1 = 13$ beads). All data points superimpose well about the same $\dot{\varepsilon}_C$ and are very close to the profile of a linear polymer bearing the same number of beads ($N = 13$, red dashed line) [234]. They further exploited the dependence of $\dot{\varepsilon}_C$ on the N_{arm} and the hydrodynamic interactions (Fig. 34b). In both theta solvent and good solvent, $\dot{\varepsilon}_C$ satisfies

$$\dot{\varepsilon}_C = 6.9N_{arm}^{-2.00} \text{ (no hydrodynamic interactions, Rouse Model)} \quad (32)$$

$$\dot{\varepsilon}_C = 4.1N_{arm}^{-1.5} \text{ (hydrodynamic interactions, Zimm Model)} \quad (33)$$

These scaling exponents are consistent with those reported in linear and cyclic polymers (see (5), (6), (21), and (22)) [178, 237], varying only the pre-exponent. Cifre compared the pre-exponent for star-shaped polymers and linear polymers. Take (32) for example (no hydrodynamic interactions). If N_{arm} is replaced with N_{span} ($\approx 2N_{arm}$), the numerical factor in (32) is $6.9 \times 4 = 27.6$, close to the constant $3\pi^2 = 29.6$ predicted theoretically for linear chains [237]. Such consistency is also proved in the case of hydrodynamic interactions (33) and in other simulation work [235].

Cifre also exploited the molecular individualism for the different arms of the same star chain [235]. In Fig. 35, the core-end distance along the flow direction is plotted against time for a star of $N = 49$ beads and $f_{arm} = 6$. The three pairs of arms undergo CST at different times, with the arms in each pair extending in opposite directions. This is a direct observation of the spanning path in a star-shaped molecule by simulation. The author also investigated the distribution of the tensile

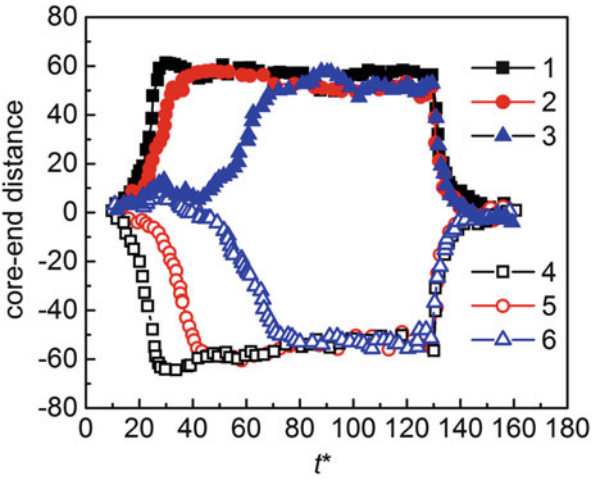

Fig. 35 Time-evolution of the dimensionless core-end distance of the arms of a star chain with $N = 49$ and $f_{arm} = 6$, hydrodynamic interactions, and theta conditions. The *number in the legend* is the label of arms. (Adopted with permission from Cifre et al. [235]. Copyright 2002 Elsevier)

force along the arms [234]. In strong elongational flow, the force is maximum at the linkage connecting the arm to the core. It diminishes along the contour of the arm from the core to the end.

6.5 Design Mechanophores in Star-Shaped Polymers

Collectively, experimental data support the arm-loss mechanism over the core-fracture mechanism and $M_{span} > M_{lim}$ as a necessary condition. These guidelines can aid the design of the mechanophore in star-shaped polymers. As shown in Fig. 36a–c, the core (hereafter "core design"), the interface between the arm and the core (hereafter "interface design"), and the midpoint of the arm (hereafter "arm design") are three possible positions to incorporate mechanophores. The core design is possible [198] but it is not as efficient as other designs. The interface design needs $M_{span} > M_{lim}$ and can work when the arm is short. The arm design is based on a two-step mechanism: arm-loss and then the activation of mechanophores in the separated arms. So M_{span} should satisfy $M_{span} > 2M_{lim}$. This strategy is suitable for long arm star-shaped polymers. For scission type mechanophores, combining interface design and arm design offers the most efficient way to activate mechanophores (Fig. 36d). In this case, $2f_{arm}$ mechanophores can ideally be activated per star molecule. However, such a design is complicated and gives rise to great challenges to synthesis.

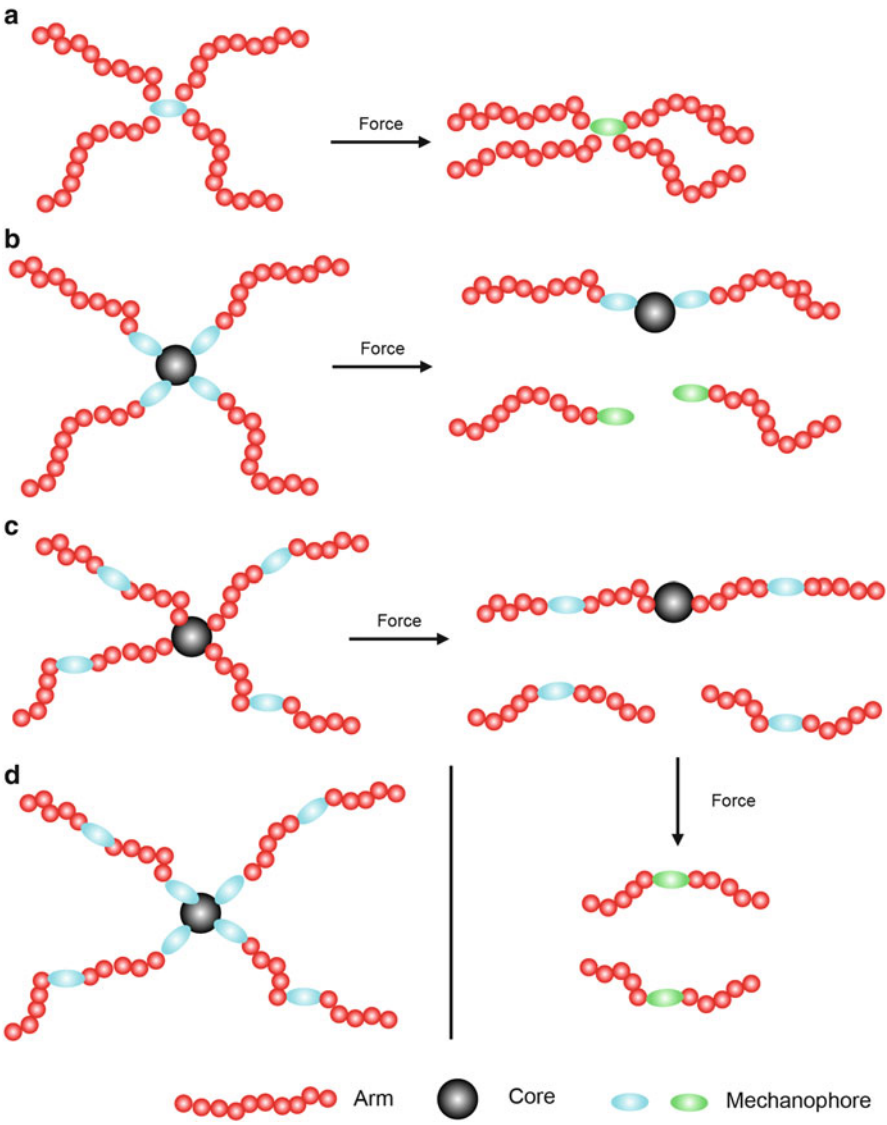

Fig. 36 Design of mechanophores in star-shaped polymers: (**a**) core design, (**b**) interface design, (**c**) arm design, and (**d**) combined interface design and arm design

7 Mechanochemistry of Hyperbranched Polymers and Dendrimers

7.1 Hyperbranched Polymers and Dendrimers

Dendrimers are monodispersed macromolecules with a regular and perfectly branched three-dimensional architecture. A dendrimeric molecule consists of a core, branches, and end groups (Fig. 37a). The branching units are described by generation, which is the number of repeated branching cycles performed during its synthesis. Unlike linear analogues, dendrimers have a well-defined size and, potentially, a huge number of end groups, which can be functionalized. Hyperbranched polymers have similar treelike topologies as dendrimers but they contain some linear units (Fig. 37b). The physical properties of hyperbranched polymers largely depend on the degree of branching (DB). DB, i.e., Frey parameter [238] describes the deviation of hyperbranched polymers from ideal dendrimers. DB is expressed by

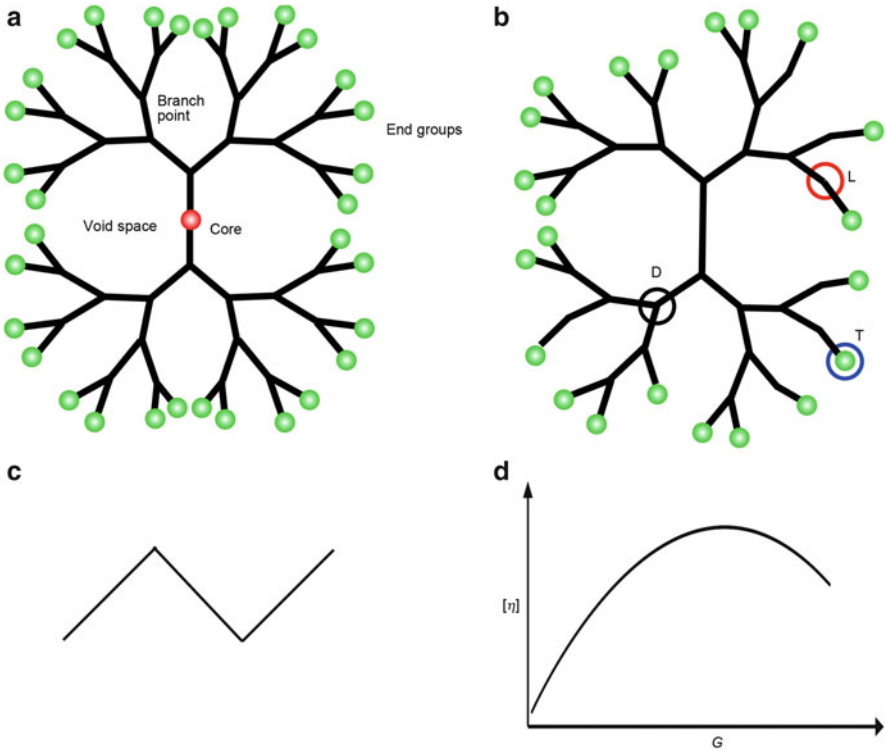

Fig. 37 Schematic drawing of a dendrimer (**a**) and hyperbranched polymers (**b**). D, B, and T denote dendritic, linear, and terminal units, respectively. (**c**) Illustration of an *n*-butane molecule for the explanation of Wiener index. (**d**) Intrinsic viscosity [η] grows non-monotonically as a function of generation *G*

$$\mathrm{DB} = \frac{D + T}{D + T + L} \tag{34}$$

where D is the number of dendritic units, L the number of linear units, and T the number of terminal groups (Fig. 37b). For linear polymers, $D = 0$, $T = 2$, $\mathrm{DB} = 2/L$ and is almost zero for long chain (large L). DB is 1 for dendrimers, and usually around 0.4–0.5 for hyperbranched polymers [239]. DB only accounts for the relative number of branch points. In the study of the rheological properties and CST of dendrimers and hyperbranched polymers, the Wiener index (Wi) is a more suitable descriptor [240]. Wi is defined as the sum of the lengths of the shortest paths between all pairs of vertices in the chemical structure representing the non-hydrogen atoms [241]. For example, an n-butane molecule has three pairs of vertices at distance one, two pairs at distance two, and one pair at distance three, so $Wi = 3 \times 1 + 2 \times 2 + 1 \times 3 = 10$.

Compared with a linear counterpart having the same total molecular weight, dendrimers and hyperbranched polymers are more compact. For instance, the ratio of the hydrodynamic radius R_h to the radius of gyration R_G for dendrimers approaches asymptotically that of a solid sphere (0.77) with the increasing the number of generations G (the ratio is 1.17 for typical linear Gaussian chains, whose end-to-end vectors follow a Gaussian distribution.) [242]. The intrinsic viscosity $[\eta]$ of dendrimers depends weakly on the total molar mass ($[\eta] \sim M_w^{0.05}$) [243], strongly on Wi ($[\eta] \sim Wi^1$) [240], and non-monotonically on the number of generations G (Fig. 37c) [244–247]. The last dependence is ascribed to the change in the fractal dimension of the molecule from polymer type to colloidal type with increasing G [248].

The monodispersity, the large number of surface functionalities, and the unique rheological properties make dendrimers and hyperbranched polymers potential candidates for a variety of applications such as biosensing [249], catalysis [250], gene therapy [251], and lubricant viscosity-index (VI), just to name a few. However, the mechanochemistry of dendrimers and hyperbranched polymers remains little understood.

7.2 *Shear Stability of Hyperbranched Polymers*

Ye and co-workers exploited the shear stability of highly branched, high molecular weight polyethylenes (PEs) as lubricant viscosity index improvers [252, 253]. Viscosity index of a lubricant is a critical parameter which defines its quality and application temperature range. They synthesized PEs with controllable chain topologies ranging from linear to a hyperbranched dendritic structure by chain walking polymerization [254]. The PE samples were blended into a base paraffinic oil (density 0.8659 g mL^{-1} at 15 °C, kinematic viscosity 30.06 cST at 40 °C) to form lubricants. The lubricants were subjected to the Kurt Orbahn (KO) test to measure the shear stability index, which is expressed by

$$\mathrm{SSI} = \frac{\eta_{\mathrm{Fresh}} - \eta_{\mathrm{Shear}}}{\eta_{\mathrm{Fresh}} - \eta_{\mathrm{Base}}} \times 100 \tag{35}$$

where η_{Fresh}, η_{Shear}, and η_{Base} are the kinematic viscosities of the fresh unsheared lubricant, sheared lubricant, and the base oil, respectively.

The lubricants formulated with more hyperbranched topologies displayed extraordinarily high shear stability in the Kurt Orbahn test, and a shear stability index value as low as 1.1. In contrast, lubricants containing linearly structured PE showed a great decrease of kinematic viscosity after 30 Kurt Orbahn test cycles with shear stability index around 46. Because the PEs in their work had similar molecular weights (140–160 kDa), the results convincingly prove that hyperbranched topologies show superior shear stability over their linear cousins. On the other hand, to achieve the same value of viscosity index, a higher polymer concentration is needed for hyperbranched polymers than for linear polymers.

7.3 CST of Hyperbranched Polymers and Dendrimers

Theoretical description of dendritic structures is an active but difficult topic because the length between branched points is close to or even smaller than the Kuhn length, above which the segments can be thought of as if they are freely jointed with each other. Most modeling or simulation work has focused on the quasi-static and rheological properties of hyperbranched polymers and dendrimers in shear flow [240, 244, 255–263]. Limited amounts of data were published for dendrimers and hyperbranched polymers within elongational flow field.

Neelov and Adolf studied CST of dendrimers [264] and hyperbranched polymers [265] under elongational flow by a bead-rod model. In Fig. 38a, the authors simulated the radius of gyration R_G^2 as a function of $\dot{\varepsilon}$ for a fifth-generation dendrimer with $N = 127$ beads. CST of the dendrimer causes the increase of R_G^2 which is significantly smaller as well as less sharp than for a linear chain bearing the same N. This broadened CST is probably because of the smaller value of R_G^2 of the dendrimer even at the completely extended conformation. The dependences of the critical strain for CST $\dot{\varepsilon}_C$ for hyperbranched polymers on N and Wi are illustrated in Fig. 38b and c, respectively [265]. Here, $\dot{\varepsilon}_C$ is defined as the midpoint of CST in the $R_G^2 \sim \dot{\varepsilon}$ plot; $\dot{\varepsilon}_C$ of hyperbranched polymers is virtually constant over the range studied. In the case of dendrimer [264], $\dot{\varepsilon}_C$ is either independent on N or decreases slowly. The power law behaviors observed in the CST of linear, cyclic, and star polymers are no longer valid in hyperbranched polymers and dendrimers. For fixed value of N but varying Wi, the $\dot{\varepsilon}_C$ vs Wi curves follow a power law with an exponent between -3.2 and -3.0. The maximum R_G^2 and the maximum intrinsic elongational viscosity $[\eta_{el}]$ also scale with Wi with similar magnitudes of the exponent. The authors have not yet proposed any physical picture to explain these power laws.

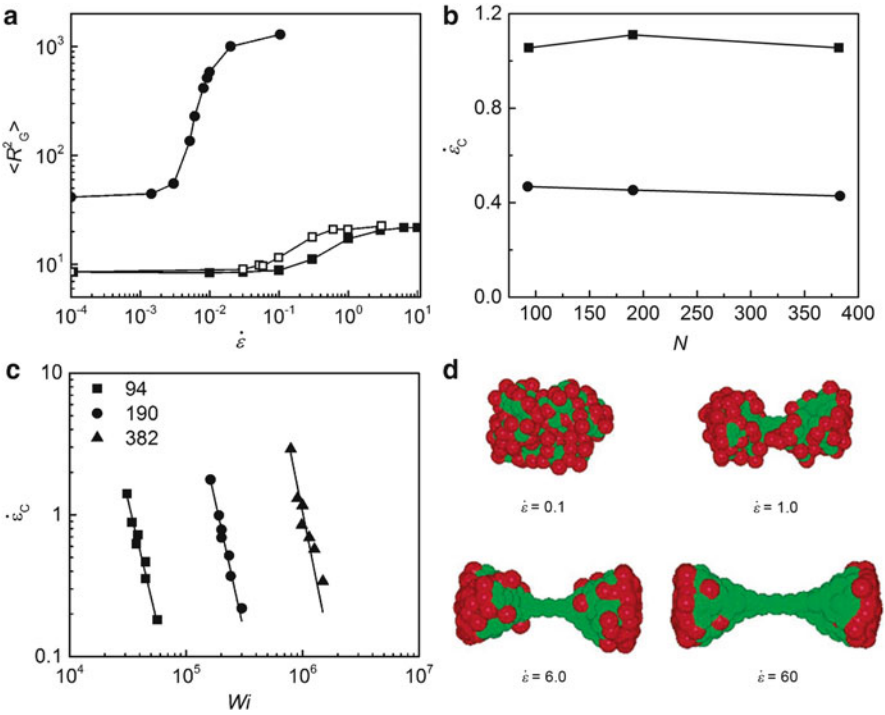

Fig. 38 (**a**) Elongtional flow rate dependence of the radius of gyration $< R_G^2 >$ for a $G = 5$ dendrimers (*squares*) and for a linear chain (*circles*) with the same total number of repeating units $N = 127$. *Filled symbols* represent data with hydrodynamic interactions and *open symbols* denote those without hydrodynamic interactions. (**b**) Critical strain rate for CST $\dot{\varepsilon}_C$ as a function of N for hyperbranched polymers and dendrimer. (**c**) Dependence of $\dot{\varepsilon}_C$ on the Wiener index Wi. The *number in the legend* is N. (**d**) Snapshots of the steady-state shapes of a $G = 6$ dendrimer from simulations in the presence of hydrodynamic interactions under different flow rates. *Red beads* are the end-groups. (**a**) and (**d**) are adopted with permission from Lyulin et al. [263]. Copyright 2005 American Chemical Society. (**b**) and (**c**) are adopted with permission from Neelov and Adolf [264]. Copyright 2004 American Chemical Society

The conformations of a sixth-generation dendrimer at a different elongational rate is illustrated in Fig. 38d [264]. At the midpoint of CST ($\dot{\varepsilon} = 1$), it adopted a dumbbell shape with two "balls" of monomers linked by a short thick stick. As $\dot{\varepsilon}$ increased to six, the balls changed to cone-like shapes, and the linking stick became thinner and longer. At the fully extended conformation ($\dot{\varepsilon} = 60$), it resembled a pair of sharp coaxial cones. According to these snapshots, we notice:

1. The inner part of the dendrimer and hyperbranched polymers is more extended than the outer part. If researchers want to incorporated mechanophores into dendrimers and hyperbranched polymers, we infer the most probable positions are the branch units close to the core.

2. Achieving orientation of all repeating units along the flow axis is unlikely because of the excluded volume effect.
3. Interestingly, the vast majority of the terminal groups lie at the outer edge of the cones.

Collectively, preliminary results reveal that dendrimers and hyperbranched polymers are more shear stable than other linear, cyclic, weakly grafted, and star cousins because of their unique structures. These polymers may fulfill the industry requirements where highly mechanically stable additives are needed. However, more experiments and simulations are required to gain sufficient insights into their CST and mechanochemistry.

8 Mechanochemistry of Polymers Having Temporal Topology Constraints

From Sects. 4 to 8 we have summarized the mechanochemistry of polymers of complex topologies. These topological structures are stable and can only be altered by the scission of covalent bonds. In some other cases, the topology of the molecules (or their assembly) is dynamic and fluctuates in a stress-free state. In this section, we explore the mechanochemistry of two paradigmatic systems.

One class is polymers capable of forming inter- or intra-polymer associations via secondary interactions (electrostatic, hydrogen bonding, host-guest, or hydrophobic interactions). In Fig. 39a, two linear chains form a star-shaped macromolecule by the association of supramolecular motifs. This star-shaped chain obviously behaves differently in the flow field compared with individual linear constituents (Fig. 26).

Another class of dynamic topology is a knotted macromolecule (Fig. 39b) [266–268]. Here we limit our discussion to open knots that can be untied without breaking the covalent bonds (resembling shoelaces and neckties). We do not consider knots formed by closed strings such as Borromean ring and Solomon link (Fig. 39c, d). The knot imposes constraints on the backbone, leading to a potentially different mechanochemical response compared to unknotted cousins.

It should be noted that the two paradigmatic systems are of biological relevance. Proteins and double-strand DNAs have complex topologies with domains held by supramolecular interactions. Knots are widely found in chromosomes [269], viral capsid DNAs [270, 271], and proteins [272, 273], and probably take part in their physiological functions.

8.1 Shear Stability of Macromolecular Aggregates

The study of the shear stability of macromolecular aggregates is promoted by the searching of polymeric drag reduction agents. Linear polymers have an excellent

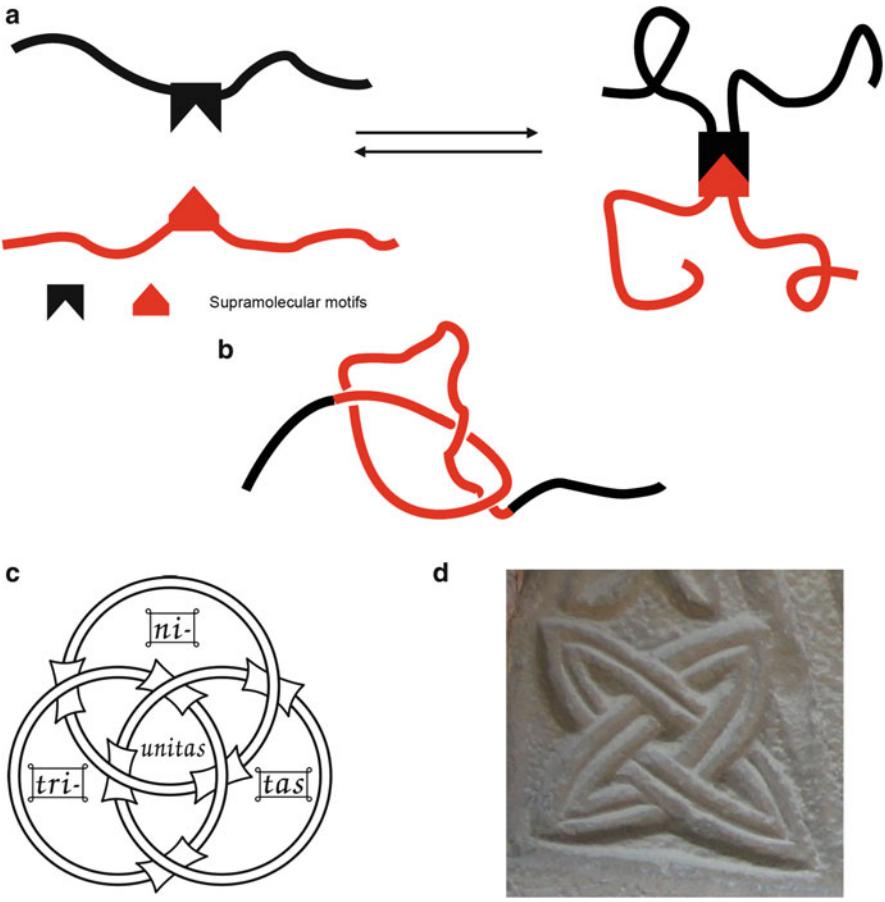

Fig. 39 (**a**) Polymer aggregates having dynamic topologies thought to be the association of supramolecular motifs. (**b**) An open trefoil knot tied in a linear strand. The knotted segments are highlighted in *red*. Knots formed by closed strings: (**c**) Borromean ring and (**d**) Solomon link. The authors of (**c**) and (**d**) have granted anyone the right to use these works for any purpose (http://commons.wikimedia.org/wiki/File:BorromeanRings-Trinity.svg; http://commons.wikimedia.org/wiki/File:San-Tome-Bergamo_(detail).jpg)

DRE, but they are more susceptible to chain scission in the flow field than short polymers. If a macromolecule has a *virtual* high molecular weight and can break and reform, it may have improved shear stability.

Motivated by this simple idea, Ting and Little [274] studied the shear stability of the sodium salt of PAA. They performed the measurements in a turbulent pipe flow apparatus. The decrease of *DRE* of two PAA samples was negligible in eight passes whereas a PEO sample (control) lost about 67% of its ability to reduce drag because of chain degradation. They believed that PAA forms a ladder-like formation in solution (Fig. 40). At pH 7.1, PAA is completely ionized and the neighboring –

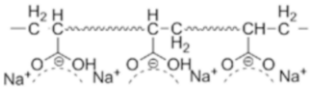

Fig. 40 Proposed ladder-like structure in ionized PAA at pH 7.1 [274]

COO^- groups associate with Na^+, leading to a "chain" parallel to the original –CH–CH_2– backbone. They argued that the associative bonds break and reform in the lower shear region, which should account for the improved shear stability.

Ting and Little's work has encouraged many similar studies since the 1980s [116, 275]. Kowalik and co-workers prepared associative polymers and saw improved shear stability as well as higher *DRE* [276]. Malik and Mashelkar found that polymer aggregates associated either by hydrogen bonding [277] or ionic pair interactions [278] display better resistance to chain degradation than non-associative counterparts.

These authors emphasized the role of supramolecular interactions as sacrificial bonds to prevent the cleavage of the backbone. However, this argument is difficult to reconcile with what we know about mechanochemical degradation of polymers in elongational flow fields. A chain that associates with several other chains is akin to irregularly grafted polymers. According to Agarwal's modified bead-rod model (Sect. 5.5) [209], the "grafting" chains increase the hydrodynamic drag force at the midpoint of the backbone as well as the scission rate. One may argue that such enhanced degradation is unlikely because the "grafting" chains would leave the backbone preferentially by breaking the secondary bonds. Even if this scenario works, the shear stability of the polymer aggregates should not exceed that of the precursor chains.

Agarwal was the first to suggest that the role of supramolecular interactions may go beyond just sacrificial bonds. He extended the bead-rod model to a supramolecular ladder-like polymer [279]. As shown in Fig. 41a, two fully stretched bead-rod chains of equal lengths are arranged parallel to each other along the flow direction and are connected by secondary interactions. The hydrodynamic drag force experienced by the ladder-like chain is the sum of two daughter chains (denoted $2\sigma_{\text{mid\_lad}}$). $2\sigma_{\text{mid\_lad}}$ is obviously larger than σ_{mid} in an isolated chain (Fig. 14) because of the larger surface. Most importantly, the neighboring chain provides additional shielding of hydrodynamic interactions between the beads and the solvent molecules. Therefore, for the same chain, the maximum tension in the backbone is smaller in the aggregates than in isolated conformation under identical flow conditions, i.e., $\sigma_{\text{mid\_lad}} \leq \sigma_{\text{mid}}$. In other words, M_{lim} for a given chain simply increases. Agarwal calculated this effect by comparing the maximum permissible molecular sizes N_{lin} and N_{lad} for the linear and the ladder polymer, assuming that the critical fracture force σ_{F} is the same (critical-stress-to-fracture theory). In Fig. 41b, $N_{\text{lad}}/N_{\text{lin}}$ can increase by as much as 35% by increasing chain length and the normalized bead size a/b. The gain can achieve higher values if more macromolecules orientate along the flow direction and are associated by supramolecular interactions. If the two daughter chains have different lengths, the results are similar.

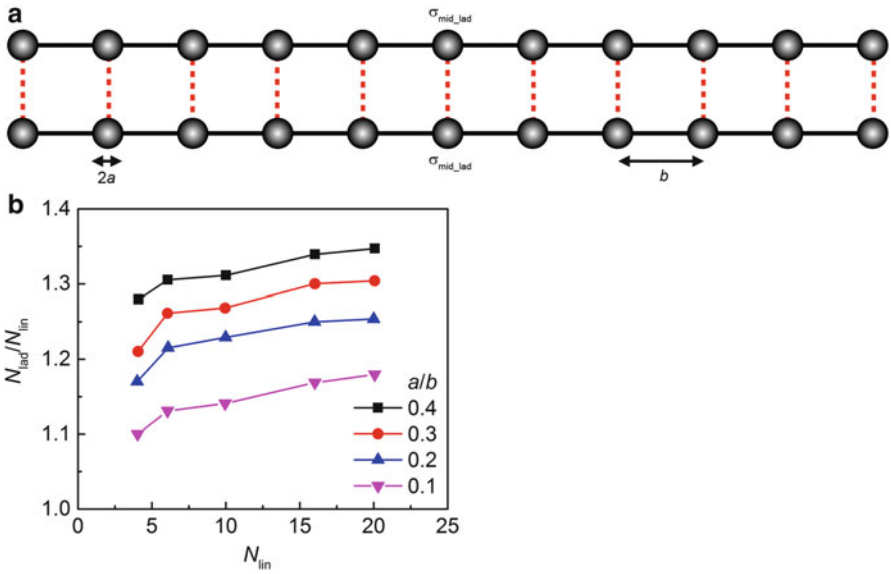

Fig. 41 (**a**) Model of a ladder-like polymer formed by interpolymer associations (highlighted by *red dashed lines*) [279]. The flow direction is horizontal. (**b**) Increase of the maximum length permissible N_{lad}/N_{lin} in the case of a ladder-like polymer as compared to a linear polymer, for the same fracture force. The legend indicates different normalized bead size *a*/*b*. (Adopted with permission from Agarwal et al. [279]. Copyright 1994 American Institute of Physics)

In Agarwal's model, the supramolecular interactions just tie the component chains together and do not bear any load as they are lying perpendicular to the flow direction. The main reasons for the improved shear stability are the redistribution of the hydrodynamic force (because of topology) to the associated chains and the hydrodynamic shielding effect. This may help us to understand the mechanochemistry of biomacromolecules such as double strand DNAs.

8.2 Mechanochemistry of Knotted Polymers

Mathematically, the knotting probability in a self-avoiding chain grows exponentially and asymptotically to 1 as the chain length approaches infinity [280]. The knots can significantly affect the rheological behavior [281] and the mechanochemistry of a polymer.

Saitta and Klein studied the mechanochemistry of isolated hydrocarbon polymer with and without a knot by quantum-chemical calculation [282, 283]. They investigated two model chains ($C_{35}H_{72}$ and $C_{28}H_{58}$) and employed a trefoil knot for each strand. Figure 42 sketches the strain energy distribution in the knotted chains when they are stretched. It is quite different compared to the corresponding distribution in unknotted chains. The bonds at the midpoint of the knot are almost unstrained

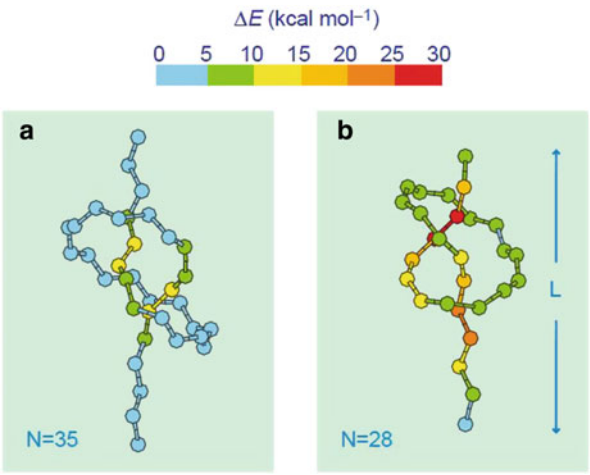

Fig. 42 Strain energy distribution in a knotted hydrocarbon strand with (**a**) $N = 35$ and (**b**) $N = 28$ carbon atoms. (Adopted with permission from Saitta et al. [282]. Copyright 1999 Nature Publishing Group)

whereas those at the entrance and exit of the knot are highly stretched and stress-concentrated. Degradation exclusively occurs at the edge bonds of the knot. The stored strain energy at fracture is 12.7 kcal/mol per C–C bond in the knotted stand but 16.2 kcal/mol per C–C bond in the unknotted stand. Therefore, knots weaken the mechanical properties of polymers, which is consistent with our common sense regarding the fracture of a knotted rope.

The same authors later studied the evolution of the radicals formed after rupture of a single knotted alkane molecule using first-principles molecular dynamics calculation [284]. In knotted chains, recombination of the radicals is totally bypassed in favor of ultrafast (about several hundred femtoseconds) phenomena such as diradicals which generate cyclic alkanes, and disproportionation to form carbon–carbon double bonds. Saitta and Klein suggested that the trefoil knot imposes topological constraints to the velocity distribution of the recoiling radicals at rupture, leading to deviations from the canonical recombination reaction.

So far we have only reviewed the mechanochemistry of isolated knotting polymers. In real systems, the environment should be taken into consideration. Saitta and Klein studied the rupture processes of a bulk-like PE knot [285]. In the first model, a knotted alkane is surrounded by six linear alkanes (unknotted). For the sake of comparison, a linear alkane is also surrounded by six linear alkanes in the second model. Their results show that the bonds at the entrance and the exit of the trefoil knot are more distorted than elsewhere. Quantitatively, the knot weakens the chain to which it is tied by a factor of about 15%. Indeed, the estimated force to break a knotted alkane is 3.5 nN (the value depends on the timescale), 0.5 nN smaller than that of an unknotted alkane of the same length.

To test the simulations experimentally is difficult but possible. Arai and co-workers studied the mechanochemistry of knotted biopolymers [286]. They elegantly prepared a knot in an actin filament using optical tweezers. The manipulation was performed in a viscous solution to suppress the Brownian motion

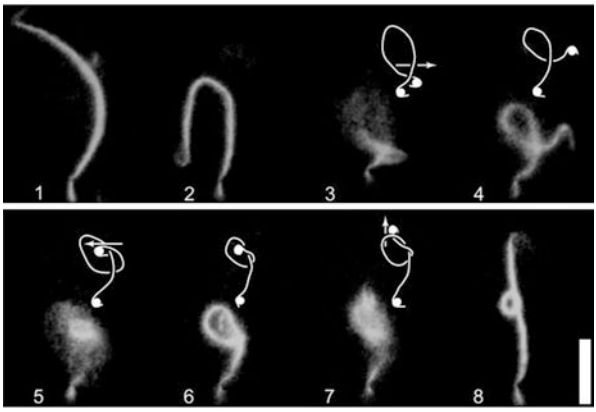

Fig. 43 Tying a knot in an actin filament. *Scale bar*: 10 μm. (Adopted with permission from Arai et al. [286]. Copyright 1999 Nature Publishing Group)

(Fig. 43) and knotting was completed in less than 1 min. They further tightened the knot to establish the relation between the tension and knot diameter. The average knot diameter dropped monotonically as the applied tension increased. The actin filaments broke at the knot when its diameter fell below 400 nm and the tension rose to ~1 pN. This value is two orders of magnitude smaller than the tensile strength of a straight filament ~600 pN [287] and does not change noticeably in different solutions which potentially increase the stability of an actin filament. The authors also prepared a knot in a single DNA molecule, but their apparatus was unable to break either knotted or unknotted DNA.

Our experience of stretching a knotted rope in the macroscopic world is sometimes inconsistent with the observations of stretching a knotted molecule. The knot in highly tightened rope is localized and loses its mobility. However, knots in the highly extended chains behave counter-intuitively. Bao and co-workers prepared knots in single DNA molecules with optical tweezers [288]. All the knots shrink and become highly localized under tension (0.1–2 pN), but they remain surprisingly mobile and undergo thermal diffusion with classical random walk statistics. The diffusion constant varies drastically with increasing complexity of the knot. Recently, Doyle and co-workers demonstrated that it is possible to move the knot at the midpoint to the termini of the chain and untie it by an elongational flow field [289].

In this section, we discuss the mechanochemistry of two systems with temporary topological constraints: molecular aggregates and knotted polymers. Polymer aggregates formed by supramolecular interactions have a superior shear stability as well as drag reduction efficiency over their non-associative cousins. However, the underlying mechanism is unlikely to represent the preferential cleavage of secondary bonds in the flow field. Instead, these supramolecular bonds allow the hydrodynamic drag force to be redistributed and provide enhanced hydrodynamic shielding of the parts of the aggregate. In knotted polymers, the presence of a knot drastically alters the distribution of strain energy along the backbone. Scission

occurs at the entrance and exit bonds of the knot and the corresponding fracture force and the stored strain energy are lower than the values in unknotted chains.

9 Conclusion and Outlook

Polymer mechanochemistry is a multiscale phenomenon, and the ultimate bond scission is the consequence of a series of events. The input of mechanical energy above the threshold level leads to the formation of crazes and cracks on the macroscopic level. To minimize the total free energy, the macromolecules slip, disentangle, and unravel to extended conformations (i.e., CST), generating deformations at the molecular level. The stretching of the bond, the bending of the valence angle, and the rotating of dihedral angle result in a redistribution of the electronic densities of the molecular orbitals and eventually the chemical effect known as mechanochemistry. In earlier days, such mechanochemical effects were to be avoided. However, recent research has demonstrated that mechanochemical changes can be utilized to trigger chemical reactions at certain site of the polymer backbone. This new method opens a way to develop mechanoresponsive materials by the rational design of mechanophores and polymer scaffolds. A better understanding of polymer mechanochemistry is emerging and benefits the design of polymeric materials that are either highly resistant to mechanical failure or respond to mechanical stimuli with desired functions.

Among various factors, the chain architecture critically affects the mechanochemistry of macromolecules. Compared with linear cousins having the same number of monomers, chains with nonlinear topology are more compact. The smaller size causes the chains to either experience less hydrodynamic drag force or have enhanced hydrodynamic shielding effects, or both. In solutions, theoretical works, the simulations, and the experiments all support the fact that the nonlinear chain undergoes coil-to-stretch transition and degrades at higher strain rates ($\dot{\varepsilon}_C$ and $\dot{\varepsilon}_F$), i.e., it is more mechanically stable. However, we are still at the primitive stage of this area and the following issues deserve more attention.

1. Linear polymers. The bead-rod model successfully explained the midpoint scission and the -2 dependence of $\dot{\varepsilon}_F$ on M through frictional loading in quasi-static-state-flow as well as in bulk, where the residence time is sufficient for chains to develop to extended conformations [110]. However, the observed -1 dependence of $\dot{\varepsilon}_F$ on M verified in fast-transient-flow cannot yet be explained by current theories. A theory that can account for both dependences (M^{-1} and M^{-2}) is highly desirable. This theory should explain the interplay between the various conformations observed in the flow field (molecular individualism) and the midpoint scission of the chain. It should also be able to solve the huge discrepancy between the hydrodynamic drag force in fast-transient-flow and the force required to break chemical bonds (~7 nN). Any progress in linear macromolecules can greatly aid the study of other topologies.

2. Cyclic polymers, dendrimers and hyperbranched polymers. The mechanochemistry of these polymers is less understood than that of linear analogues. The experimental observations are either too phenomenological or lack comparison with linear polymers. More experiments should therefore be conducted and compared with simulations in the future.
3. Side groups and graft polymers. Short side groups (up to 19 atoms [197]) show a minor effect on either the degradation of polymer chains or the activation of mechanophores. However, this conclusion was only exploited in ultrasonic degradation. Whether it is valid in other flow fields is largely unknown. For densely grafted chains such as comb polymers, the side chains repulse each other because of the excluded volume effect. The repulsive interaction accumulates along the backbone of the main chain and lowers its dissociative stability. For weakly grafted polymers, the existing results are self-contradictory. Some researchers claimed higher shear stability of graft polymers, which they ascribed to cleavage of the side chains which protects the main chain. However, Agarwal [209] showed that side chains place extra drag force on the main chain and lower its stability. Complex flow fields and the poorly controlled polymer topology may account for these confusing results. To solve this issue, mechanophores can be incorporated either into the main chain or as linkage to connect side chains. The activation of mechanophores in the flow field can aid the elucidation of these contradictory results.
4. Star-shaped polymers. The mechanochemistry of star-shaped macromolecules has been studied more extensively than that of other nonlinear topologies. Although experiments have been consistent with the arm-loss mechanism rather than the core-fracture mechanism of degradation, it is very likely because of the weaker linkages at the core-arm interface. Thanks to the development of mechanophores, the mechanism can be revisited by incorporating weak moieties such as SP or the –S–S– bond into the core. Both simulations and experiments support the idea that the spanning molecular weight M_{span} and not the total molecular weight governs the coil-to-stretch-transition, chain scission, and activation of mechanophore in star-shaped polymers. We reason that the concept of spanning molecular weight is likely the right parameter and can be extended to other nonlinear topologies. However, a limited number of star-shaped polymers have been exploited in the experiments and M_{span} only qualitatively explains the results. The disadvantages of acoustic fields preclude quantitative study of the dependence of $\dot{\varepsilon}_F$ on M_{span}. Last, but equally important, M_{span} may not work well for densely grafted polymers, star-shaped polymers with a large number of arms, dendrimers, and hyperbranched polymers. In these topologies, the excluded volume effect cannot be neglected even in the maximum extended conformations, and contributes considerably to the chain scission. Nevertheless, more experiments need to be conducted in this direction.
5. Dynamic topologies. Polymer aggregates seem most promising for drag reduction applications because both the shear stability, and the performance are improved through supramolecular associations. However, many fundamental questions remain unanswered. How does the strength of the secondary bonds

influence the shear stability of the aggregates? What are the optimum topology and arrangement of the supramolecular motifs? We may probably learn from biomacromolecules. As for knotted polymers, we lack the experimental data to verify the simulations. A facile and high-yield method to prepare knotted polymers (open knots) is highly desirable.

6. Performance. We note that an increase of mechanical stability by altering the chain topology is, in fact, at the cost of a reduced hydrodynamic volume. One side effect is decreased performance in related applications. Star- and comb-shaped PS are not as effective as linear polymers in drag reduction. To achieve the same quality of lubricant viscosity index, higher concentrations of hyperbranched polymers are needed. How to increase the mechanical stability while maintains the performance is a long existing challenge in this subject.
7. Design of mechanophore for nonlinear topologies. As we mentioned in the previous section, the development of polymer mechanochemistry in the last decade is largely promoted by the discovery of mechanophores. The current design of mechanophores in linear polymers is not perfect. We have proposed several adequate positions for mechanophores in nonlinear topologies. These designs are based on the computer simulations of CST and can be tested in the future.
8. Bulk mechanochemistry. Unlike linear polymers, the activation of mechanophore in nonlinear macromolecules in bulk is almost blank. Recently, May found that polymers with branched architectures activate more slowly than linear counterparts in solution, yet more quickly in solid-state tensile experiments [198]. In the bulk, more factors take part in the chain degradation event, including but not limited to chain entanglements, phase separation, crystallization, and supramolecular interactions. Inspections in this direction can aid the design of mechanoresponsive materials in the solid state.

The understanding of topological effect is a fundamental problem in the field of polymer mechanochemistry. We hope this review may provide guidelines for the design of novel polymeric materials with superb mechanical properties and which respond to mechanical stimuli in various productive ways.

Acknowledgement Financial support was provided by National Natural Science Foundation of China (No. 21304076) and China Postdoctoral Science Foundation (No.2013 M541857, No.2014 T70612).

References

1. Ostwald W (1909) Grundriss de Kolloidchemie. Verlag von Theodor Steinkoppff, Dresden
2. Ostwald W (1887) Lehrbuch de Allgemeinen Chemie. 2. Auflage, 2. Band, Engelmann, Leipzig
3. Takacs L (2013) The historical development of mechanochemistry. Chem Soc Rev 42:7649–7659

4. Faraday M (1820) Quart J Sci Lit Art 8:374
5. Lea MC (1866) Researches on the latent image. Brit J Phot 13:84
6. Lea MC (1891) On gold-coloured allotropic silver, part I. Am J Sci 141:179–190
7. Lea MC (1891) On allotropic silver. Part II - relations of allotropic silver with silver as it exists in silver compounds. Am J Sci 141:259–267
8. Lea MC (1892) Disruption of the silver haloid molecule by mechanical force. Am J Sci 143:527–531
9. Lea MC (1893) On endothermic decomposition obtained by pressure. Second part. Transformation of energy by shearing stress. Am J Sci 145:413–420
10. Lea MC (1894) Transformation of mechanical into chemical energy. Third part. Acting of shearing stress continued. Am J Sci 147:377–381
11. Sohma J (1989) Mechanochemistry of polymers. Prog Polym Sci 14:451–596
12. Beyer MK, Clausen-Schaumann H (2005) Mechanochemistry: the mechanical activation of covalent bonds. Chem Rev 105:2921–2948
13. Vasiliu-Oprea C, Dan F (2006) Macromolecular mechanochemistry. Cambridge International Science, Cambridge
14. Balaz P (2008) Mechanochemistry in nanoscience and minerals engineering. Spring-Verlag, Berlin/Heidelberg
15. Caruso MM, Davis DA, Shen Q, Odom SA, Sottos NR, White SR, Moore JS (2009) Mechanically-induced chemical changes in polymeric materials. Chem Rev 109:5755–5798
16. Staudinger H, Bondy HF (1930) Über Isopren und Kautschuk, 19. Mitteil.: Über die Molekülgröße des Kautschuks und der Balata. Ber Dtsch Chem Ges 63:734–736
17. Staudinger H, Heuer W (1934) Über hochpolymere Verbindungen, 93. Mitteil.: Über das Zerreißen der Faden-Moleküle des Poly-styrols. Ber Dtsch Chem Ges 67:1159–1164
18. Staudinger H, Leupold EO (1930) Über Isopren und Kautschuk, 18. Mitteil.: Viscositäts-Untersuchungen an Balata. Ber Dtsch Chem Ges 63:730–733
19. Ayrey G, Moore CG, Watson WF (1956) Mastication. Part III. Chemical verification of the mechanical degradation mechanism of cold mastication. J Polym Sci 19:1–15
20. Basedow AM, Ebert KH (1977) Ultrasonic degradation of polymers in solution. Adv Polym Sci 22:83–148
21. Frenkel Y (1944) Acta Physicochim URSS 19:51
22. Kuhn W, Kuhn H (1944) Wanderungsdoppelbrechung von Fadenmolekelionen im elektrischen Feld. Helv Chim Acta 27:493–499
23. Peterlin A (1966) Hydrodynamics of linear macromolecules. Pure Appl Chem 12:563–586
24. Frank FC (1970) The strength and stiffness of polymers. Proc R Soc Lond A 319:127–136
25. Marucci G (1975) Limiting concepts in extensional flow. Polym Eng Sci 15:229–233
26. De Gennes PG (1974) Coil-stretch transition of dilute flexible polymers under ultrahigh velocity gradients. J Chem Phys 60:5030–5042
27. Keller A, Odell JA (1985) The extensibility of macromolecules in solution-a new focus for macromolecular science. Colloid Polym Sci 263:181–201
28. Odell JA, Keller A (1986) Flow-induced chain fracture of isolated linear macromolecules in solution. J Polym Sci Polym Phys 24:1889–1916
29. Hickenboth CR, Moore JS, White SR, Sottos NR, Baudry J, Wilson SR (2007) Biasing reaction pathways with mechanical force. Nature 446:423–427
30. Lenhardt JM, Ong MT, Choe R, Evenhuis CR, Martinez TJ, Craig SL (2010) Trapping a diradical transition state by mechanochemical polymer extension. Science 329:1057–1060
31. Huang Z, Boulatov R (2011) Chemomechanics: chemical kinetics for multiscale phenomena. Chem Soc Rev 40:2359–2384
32. Davis DA, Hamilton A, Yang J, Cremar LD, Gough DV, Potisek SL, Ong MT, Braun PV, Martínez TJ, White SR, Moore JS, Sottos NR (2009) Force-induced activation of covalent bonds in mechanoresponsive polymeric materials. Nature 459:68–72

33. Berkowski KL, Potisek SL, Hickenboth CR, Moore JS (2005) Ultrasound-induced site-specific cleavage of azo-functionalized poly(ethylene glycol). Macromolecules 38:8975–8978
34. Gossweiler GR, Hewage GB, Soriano G, Wang Q, Welshofer GW, Zhao X, Craig SL (2014) Mechanochemical activation of covalent bonds in polymers with full and repeatable macroscopic shape recovery. ACS Macro Lett 216–219
35. Beiermann BA, Kramer SLB, Moore JS, White SR, Sottos NR (2012) Role of mechanophore orientation in mechanochemical reactions. ACS Macro Lett 1:163–166
36. Beiermann BA, Kramer SLB, May PA, Moore JS, White SR, Sottos NR (2013) The effect of polymer chain alignment and relaxation on force-induced chemical reactions in an elastomer. Adv Funct Mater 24:1529–1537
37. Beiermann BA, Davis DA, Kramer SLB, Moore JS, Sottos NR, White SR (2011) Environmental effects on mechanochemical activation of spiropyran in linear PMMA. J Mater Chem 21:8443–8447
38. Kingsbury CM, May PA, Davis DA, White SR, Moore JS, Sottos NR (2011) Shear activation of mechanophore-crosslinked polymers. J Mater Chem 21:8381–8388
39. Lee CK, Davis DA, White SR, Moore JS, Sottos NR, Braun PV (2010) Force-induced redistribution of a chemical equilibrium. J Am Chem Soc 132:16107–16111
40. Degen CM, May PA, Moore JS, White SR, Sottos NR (2013) Time-dependent mechanochemical response of SP-cross-linked PMMA. Macromolecules 46:8917–8921
41. Lee CK, Beiermann BA, Silberstein MN, Wang J, Moore JS, Sottos NR, Braun PV (2013) Exploiting force sensitive spiropyrans as molecular level probes. Macromolecules 46:3746–3752
42. Chen Y, Zhang H, Fang X, Lin Y, Xu Y, Weng W (2014) Mechanical activation of mechanophore enhanced by strong hydrogen bonding interactions. ACS Macro Lett 3:141–145
43. Jiang S, Zhang L, Xie T, Lin Y, Zhang H, Xu Y, Weng W, Dai L (2013) Mechanoresponsive PS-PnBA-PS triblock copolymers via covalently embedding mechanophore. ACS Macro Lett 705–709
44. Fang X, Zhang H, Chen Y, Lin Y, Xu Y, Weng W (2013) Biomimetic modular polymer with tough and stress sensing properties. Macromolecules 46:6566–6574
45. Hong G, Zhang H, Lin Y, Chen Y, Xu Y, Weng W, Xia H (2013) Mechanoresponsive healable metallosupramolecular polymers. Macromolecules 46:8649–8656
46. Lenhardt JM, Black AL, Beiermann BA, Steinberg BD, Rahman F, Samborski T, Elsakr J, Moore JS, Sottos NR, Craig SL (2011) Characterizing the mechanochemically active domains in gem-dihalocyclopropanated polybutadiene under compression and tension. J Mater Chem 21:8454–8459
47. Lenhardt JM, Black AL, Craig SL (2009) *gem*-Dichlorocyclopropanes as abundant and efficient mechanophores in polybutadiene copolymers under mechanical stress. J Am Chem Soc 131:10818–10819
48. Black Ramirez AL, Ogle JW, Schmitt AL, Lenhardt JM, Cashion MP, Mahanthappa MK, Craig SL (2011) Microstructure of copolymers formed by the reagentless, mechanochemical remodeling of homopolymers via pulsed ultrasound. ACS Macro Lett 1:23–27
49. Diesendruck CE, Steinberg BD, Sugai N, Silberstein MN, Sottos NR, White SR, Braun PV, Moore JS (2012) Proton-coupled mechanochemical transduction: a mechanogenerated acid. J Am Chem Soc 134:12446–12449
50. Lenhardt JM, Ogle JW, Ong MT, Choe R, Martinez TJ, Craig SL (2011) Reactive cross-talk between adjacent tension-trapped transition states. J Am Chem Soc 133:3222–3225
51. Klukovich HM, Kean ZS, Ramirez ALB, Lenhardt JM, Lin J, Hu X, Craig SL (2012) Tension trapping of carbonyl ylides facilitated by a change in polymer backbone. J Am Chem Soc 134:9577–9580
52. Kryger MJ, Ong MT, Odom SA, Sottos NR, White SR, Martinez TJ, Moore JS (2010) Masked cyanoacrylates unveiled by mechanical force. J Am Chem Soc 132:4558–4559

53. Kean ZS, Niu Z, Hewage GB, Rheingold AL, Craig SL (2013) Stress-responsive polymers containing cyclobutane core mechanophores: reactivity and mechanistic insights. J Am Chem Soc 135:13598–13604
54. Kean ZS, Ramirez ALB, Yan YF, Craig SL (2012) Bicyclo 3.2.0 heptane mechanophores for the non-scissile and photochemically reversible generation of reactive bis-enones. J Am Chem Soc 134:12939–12942
55. Klukovich HM, Kean ZS, Iacono ST, Craig SL (2011) Mechanically induced scission and subsequent thermal remending of perfluorocyclobutane polymers. J Am Chem Soc 133:17882–17888
56. Kryger MJ, Munaretto AM, Moore JS (2011) Structure–mechanochemical activity relationships for cyclobutane mechanophores. J Am Chem Soc 133:18992–18998
57. Konda SSM, Brantley JN, Varghese BT, Wiggins KM, Bielawski CW, Makarov DE (2013) Molecular catch bonds and the anti-Hammond effect in polymer mechanochemistry. J Am Chem Soc 135:12722–12729
58. Wiggins KM, Syrett JA, Haddleton DM, Bielawski CW (2011) Mechanically facilitated retro 4 + 2 cycloadditions. J Am Chem Soc 133:7180–7189
59. Brantley JN, Konda SSM, Makarov DE, Bielawski CW (2012) Regiochemical effects on molecular stability: a mechanochemical evaluation of 1,4- and 1,5-disubstituted triazoles. J Am Chem Soc 134:9882–9885
60. Brantley JN, Wiggins KM, Bielawski CW (2011) Unclicking the click: mechanically facilitated 1,3-dipolar cycloreversions. Science 333:1606–1609
61. Chen Y, Spiering AJH, Karthikeyan S, Peters GWM, Meijer EW (2012) Mechanically induced chemiluminescence from polymers incorporating a 1,2-dioxetane unit in the main chain. Nat Chem 4:559–562
62. Tennyson AG, Wiggins KM, Bielawski CW (2010) Mechanical activation of catalysts for C – C bond forming and anionic polymerization reactions from a single macromolecular reagent. J Am Chem Soc 132:16631–16636
63. Paulusse JMJ, Sijbesma RP (2008) Selectivity of mechanochemical chain scission in mixed palladium(II) and platinum(II) coordination polymers. Chem Commun 4416–4418
64. Piermattei A, Karthikeyan S, Sijbesma RP (2009) Activating catalysts with mechanical force. Nat Chem 1:133–137
65. Larsen MB, Boydston AJ (2013) "Flex-activated" mechanophores: using polymer mechanochemistry to direct bond bending activation. J Am Chem Soc 135:8189–8192
66. Larsen MB, Boydston AJ (2014) Successive mechanochemical activation and small molecule release in an elastomeric material. J Am Chem Soc 136:1276–1279
67. Brantley JN, Wiggins KM, Bielawski CW (2013) Polymer mechanochemistry: the design and study of mechanophores. Polym Int 62:2–12
68. Woodward RB, Hoffmann R (1969) The conservation of orbital symmetry. Angew Chem Int Ed 8:781–853
69. Wiggins KM, Brantley JN, Bielawski CW (2012) Polymer mechanochemistry: force enabled transformations. ACS Macro Lett 1:623–626
70. Black AL, Lenhardt JM, Craig SL (2011) From molecular mechanochemistry to stress-responsive materials. J Mater Chem 21:1655–1663
71. Wu D, Lenhardt JM, Black AL, Akhremitchev BB, Craig SL (2010) Molecular stress relief through a force-induced irreversible extension in polymer contour length. J Am Chem Soc 132:15936–15938
72. Ramirez ALB, Kean ZS, Orlicki JA, Champhekar M, Elsakr SM, Krause WE, Craig SL (2013) Mechanochemical strengthening of a synthetic polymer in response to typically destructive shear forces. Nat Chem 5:757–761
73. Brantley JN, Wiggins KM, Bielawski CW (2013) Squeezing new life out of polymers. Angew Chem Int Ed 52:3806–3808
74. Baytekin HT, Baytekin B, Grzybowski BA (2012) Mechanoradicals created in "polymeric sponges" drive reactions in aqueous media. Angew Chem Int Ed 51:3596–3600

75. Chen XX, Dam MA, Ono K, Mal A, Shen HB, Nutt SR, Sheran K, Wudl F (2002) A thermally re-mendable cross-linked polymeric material. Science 295:1698–1702
76. Reutenauer P, Buhler E, Boul PJ, Candau SJ, Lehn JM (2009) Room temperature dynamic polymers based on Diels-Alder chemistry. Chem Eur J 15:1893–1900
77. Jakobs RTM, Ma S, Sijbesma RP (2013) Mechanocatalytic polymerization and cross-linking in a polymeric matrix. ACS Macro Lett 2:613–616
78. Ducrot E, Chen Y, Bulters M, Sijbesma RP, Creton C (2014) Toughening elastomers with sacrificial bonds and watching them break. Science 344:186–189
79. Pike M, Watson WF (1952) Mastication of rubber. I. Mechanism of plasticizing by cold mastication. J Polym Sci 9:229–251
80. Angier DJ, Chambers WT, Watson WF (1957) Mastication of rubber. VI. Viscosity and molecular weight relationships for natural rubber after cold mastication. J Polym Sci 25:129–138
81. Berman NS (1978) Drag reduction by polymers. Annu Rev Fluid Mech 10:47–64
82. Bekard IB, Asimakis P, Bertolini J, Dunstan DE (2011) The effects of shear flow on protein structure and function. Biopolymers 95:733–745
83. Batchelor AW, Stachowiak GW (1996) Arthritis and the interacting mechanisms of synovial joint lubrication. 1. Operating conditions and the environment. J Orthop Rheumatol 9:3–10
84. Turssi CP, Purquerio BDM, Serra MC (2003) Wear of dental resin composites: insights into underlying processes and assessment methods - a review. J Biomed Mater Res B Appl Biomater 65B:280–285
85. Wu T, Zivanovic S, Hayes DG, Weiss J (2008) Efficient reduction of chitosan molecular weight by high-intensity ultrasound: underlying mechanism and effect of process parameters. J Agric Food Chem 56:5112–5119
86. van den Einde RM, Akkermans C, van der Goot AJ, Boom RM (2004) Molecular breakdown of corn starch by thermal and mechanical effects. Carbohydr Polym 56:415–422
87. van den Einde RM, van der Goot AJ, Boom RM (2003) Understanding molecular weight reduction of starch during heating-shearing processes. J Food Sci 68:2396–2404
88. Striegel AM (2007) Influence of anomeric configuration on mechanochemical degradation of polysaccharides: cellulose versus amylose. Biomacromolecules 8:3944–3949
89. Buchholz BA, Zahn JM, Kenward M, Slater GW, Barron AE (2004) Flow-induced chain scission as a physical route to narrowly distributed, high molar mass polymers. Polymer 45:1223–1234
90. Hariadi RF, Yurke B (2010) Elongational-flow-induced scission of DNA nanotubes in laminar flow. Phys Rev E 82:046307
91. Oefner PJ, Hunicke-Smith SP, Chiang L, Dietrich F, Mulligan J, Davis RW (1996) Efficient random subcloning of DNA sheared in a recirculating point-sink flow system. Nucleic Acids Res 24:3879–3886
92. Thorstenson YR, Hunicke-Smith SP, Oefner PJ, Davis RW (1998) An automated hydrodynamic process for controlled, unbiased DNA shearing. Genome Res 8:848–855
93. Lengsfeld CS, Anchordoquy TJ (2002) Shear-induced degradation of plasmid DNA. J Pharm Sci 91:1581–1589
94. Jia Z, Monteiro MJ (2012) Cyclic polymers: methods and strategies. J Polym Sci Polym Chem 50:2085–2097
95. Aloorkar NH, Kulkarni AS, Patil RA, Ingale DJ (2012) Star polymers: an overview. Int J Pharm Sci Nanotech 5:1675–1684
96. Qiu L, Bae Y (2006) Polymer architecture and drug delivery. Pharmaceut Res 23:1–30
97. Odell JA, Keller A, Rabin Y (1988) Flow-induced scission of isolated macromolecules. J Chem Phys 88:4022–4028
98. Müller AJ, Odell JA, Keller A (1988) Elongational flow and rheology of monodisperse polymers in solution. J Nonnewton Fluid 30:99–118

99. Muller AJ, Odell JA, Carrington S (1991) Degradation of polymer solutions in extensional flow. In: Proceedings of the polymer physics: a conference to mark the retirement of A Keller, Bristol UK, pp 3–5
100. Narh KA, Odell JA, Keller A (1992) Temperature-dependence of the conformational relaxation-time of polymer-molecules in elongational flow-invariance of the molecular-weight exponent. J Polym Sci Polym Phys 30:335–340
101. Odell JA, Keller A, Muller AJ (1992) Thermomechanical degradation of macromolecules. Colloid Polym Sci 270:307–324
102. Carrington SP, Odell JA (1996) How do polymers stretch in stagnation point extensional flow-fields? J Nonnewton Fluid 67:269–283
103. Hsieh CC, Park SJ, Larson RG (2005) Brownian dynamics modeling of flow-induced birefringence and chain scission in dilute polymer solutions in a planar cross-slot flow. Macromolecules 38:1456–1468
104. Pope DP, Keller A (1977) Alignment of macromolecules in solution by elongational flow; a study of the effect of pure shear in a four roll mill. Colloid Polym Sci 255:633–643
105. Nguyen TQ, Kausch HH (1986) Degradation of a polymer-solution in transient elongational flow-effect of temperature. Colloid Polym Sci 264:764–772
106. Nguyen TQ, Kausch HH (1988) Chain scission in transient extensional flow kinetics and molecular-weight dependence. J Nonnewton Fluid 30:125–140
107. Nguyen TQ, Kausch HH (1989) Kinetics of polymer degradation in transient elongational flow. Makromol Chem 190:1389–1406
108. Nguyen TQ, Kausch HH (1990) Effects of solvent viscosity on polystyrene degradation in transient elongational flow. Macromolecules 23:5137–5145
109. Nguyen TQ, Kausch HH (1991) Influence of nozzle geometry on polystyrene degradation in convergent flow. Colloid Polym Sci 269:1099–1110
110. Nguyen TQ, Kausch HH (1992) Mechanochemical degradation in transient elongational flow. Adv Polym Sci 100:73–182
111. Nguyen TQ, Kausch HH (1992) Chain extension and degradation in convergent flow. Polymer 33:2611–2621
112. Nguyen TQ (2001) Dynamics of flexible polymer chains in elongational flow. Chimia 55:147–154
113. Nguyen TQ, Liang OZ, Kausch HH (1997) Kinetics of ultrasonic and transient elongational flow degradation: a comparative study. Polymer 38:3783–3793
114. Horn AF (1984) Midpoint scission of macromolecules in dilute-solution in turbulent-flow. Nature 312:140–141
115. Kulicke WM, Kotter M, Grager H (1989) Drag reduction phenomenon with special emphasis on homogeneous polymer-solutions. Adv Polym Sci 89:1–69
116. Morgan SE, McCormick CL (1990) Water-soluble copolymers XXXII: macromolecular drag reduction. A review of predictive theories and the effects of polymer structure. Prog Polym Sci 15:507–549
117. de Gennes PG (1986) Towards a scaling theory of drag reduction. Physica A 140:9–25
118. Tabor M, deGennes PG (1986) A cascade theory of drag reduction. Europhys Lett 2:519–522
119. May PA, Moore JS (2013) Polymer mechanochemistry: techniques to generate molecular force via elongational flows. Chem Soc Rev 42:7497–7506
120. Wiggins KM, Brantley JN, Bielawski CW (2013) Methods for activating and characterizing mechanically responsive polymers. Chem Soc Rev 42:7130–7147
121. Malhotra SL (1983) Ultrasonic modification of polymers. 2. Degradation of polystyrene, substituted polystyrene, and poly(n-vinyl carbazole) in the presence of flexible chain polymers. J Macromol Sci A A18:1055–1085
122. Malhotra SL (1986) Ultrasonic solution degradations of poly(alkyl methacrylates). J Macromol Sci A A23:729–748
123. Morris MJ, Striegel AM (2012) The effect of styrene-methyl methacrylate monomeric arrangement on the ultrasonic degradation of copolymers. Polym Degrad Stab 97:2185–2194

124. Ostlund SG, Striegel AM (2008) Ultrasonic degradation of poly(gamma-benzyl-L-glutamate), an archetypal highly extended polymer. Polym Degrad Stab 93:1510–1514
125. Teraoka I (2002) Polymer solutions: an introduction to physical properties. Wiley, New York
126. Reiner M (1964) The Deborah number. Phys Today 17:62
127. Sim HG, Khomami B, Sureshkumar R (2007) Flow-induced chain scission in dilute polymer solutions: algorithm development and results for scission dynamics in elongational flow. J Rheol 51:1223–1251
128. Ribas-Arino J, Marx D (2012) Covalent mechanochemistry: theoretical concepts and computational tools with applications to molecular nanomechanics. Chem Rev 112:5412–5487
129. Odell JA, Muller AJ, Narh KA, Keller A (1990) Degradation of polymer-solutions in extensional flows. Macromolecules 23:3092–3103
130. Choi HJ, Lim ST, Lai PY, Chan CK (2002) Turbulent drag reduction and degradation of DNA. Phys Rev Lett 89:088302
131. Rabin Y (1987) Polymer fracture in steady and transient elongational flows. J Chem Phys 86:5215–5216
132. Knudsen KD, Hernandez Cifre JG, Lopez Cascales JJ, Garcia de la Torre J (1995) Simulation of fracture of flexible polymer chains in transient elongational flow. Macromolecules 28:4660–4664
133. Knudsen KD, Cifre JGH, dela Torre JG (1996) Conformation and fracture of polystyrene chains in extensional flow studied by numerical simulation. Macromolecules 29:3603–3610
134. Knudsen KD, Cifre JGH, de la Torre JG (1997) Fracture of flexible polymer chains in dilute solution under transient extensional flow. Colloid Polym Sci 275:1001–1009
135. Groote R, Szyja BM, Pidko EA, Hensen EJM, Sijbesma RP (2011) Unfolding and mechanochemical scission of supramolecular polymers containing a metal–ligand coordination bond. Macromolecules 44:9187–9195
136. Islam MT, Vanapalli SA, Solomon MJ (2004) Inertial effects on polymer chain scission in planar elongational cross-slot flow. Macromolecules 37:1023–1030
137. Vijayalakshmi SP, Madras G (2004) Effect of temperature on the ultrasonic degradation of polyacrylamide and poly(ethylene oxide). Polym Degrad Stab 84:341–344
138. Price GJ, Smith PF (1993) Ultrasonic degradation of polymer-solutions. 2. The effect of temperature, ultrasound intensity and dissolved-gases on polystyrene in toluene. Polymer 34:4111–4117
139. Malhotra SL (1982) Ultrasonic degradation of hydroxypropyl cellulose solutions in water, ethanol, and tetrahydrofuran. J Macromol Sci A A17:601–636
140. Price GJ, Smith PF (1993) Ultrasonic degradation of polymer-solutions. 3. The effect of changing solvent and solution concentration. Eur Polym J 29:419–424
141. Desai V, Shenoy MA, Gogate PR (2008) Degradation of polypropylene using ultrasound-induced acoustic cavitation. Chem Eng J 140:483–487
142. Desai V, Shenoy MA, Gogate PR (2008) Ultrasonic degradation of low-density polyethylene. Chem Eng Proc 47:1451–1455
143. Kanwal F, Liggat JJ, Pethrick RA (2000) Ultrasonic degradation of polystyrene solutions. Polym Degrad Stab 68:445–449
144. Smith DE, Chu S (1998) Response of flexible polymers to a sudden elongational flow. Science 281:1335–1340
145. Perkins TT, Smith DE, Chu S (1997) Single polymer dynamics in an elongational flow. Science 276:2016–2021
146. Ballauff M, Wolf BA (1988) Thermodynamically induced shear degradation. Adv Polym Sci 85:1–31
147. Bestul AB (1956) Kinetics of capillary shear degradation in concentrated polymer solutions. J Chem Phys 24:1196–1201
148. Schroeder CM, Babcock HP, Shaqfeh ESG, Chu S (2003) Observation of polymer conformation hysteresis in extensional flow. Science 301:1515–1519
149. deGennes PG (1997) Polymer physics - molecular individualism. Science 276:1999

150. Eyring H (1935) The activated complex and the absolute rate of chemical reactions. Chem Rev 17:65–77
151. Kauzmann W, Eyring H (1940) The viscous flow of large molecules. J Am Chem Soc 62:3113–3125
152. Zhurkov SN (1965) Int J Fracture Mech 1:311
153. Zhurkov SN, Korsukov VE (1974) Atomic mechanism of fracture of solid polymers. J Polym Sci Polym Phys Ed 12:385–398
154. Bell GI (1978) Models for the specific adhesion of cells to cells. Science 200:618–627
155. Ribas-Arino J, Shiga M, Marx D (2010) Mechanochemical transduction of externally applied forces to mechanophores. J Am Chem Soc 132:10609–10614
156. Ribas-Arino J, Shiga M, Marx D (2009) Understanding covalent mechanochemistry. Angew Chem Int Ed 48:4190–4193
157. Dopieralski P, Anjukandi P, Ruckert M, Shiga M, Ribas-Arino J, Marx D (2011) On the role of polymer chains in transducing external mechanical forces to benzocyclobutene mechanophores. J Mater Chem 21:8309–8316
158. Kucharski TJ, Boulatov R (2011) The physical chemistry of mechanoresponsive polymers. J Mater Chem 21:8237–8255
159. Tian Y, Boulatov R (2013) Comparison of the predictive performance of the Bell-Evans, Taylor-expansion and statistical-mechanics models of mechanochemistry. Chem Commun 49:4187–4189
160. Kucharski TJ, Huang Z, Yang Q-Z, Tian Y, Rubin NC, Concepcion CD, Boulatov R (2009) Kinetics of thiol/disulfide exchange correlate weakly with the restoring force in the disulfide moiety. Angew Chem 121:7174–7177
161. Yang QZ, Huang Z, Kucharski TJ, Khvostichenko D, Chen J, Boulatov R (2009) A molecular force probe. Nat Nanotechnol 4:302–306
162. Akbulatov S, Tian Y, Boulatov R (2012) Force–reactivity property of a single monomer is sufficient to predict the micromechanical behavior of its polymer. J Am Chem Soc 134:7620–7623
163. Akbulatov S, Tian Y, Kapustin E, Boulatov R (2013) Model studies of the kinetics of ester hydrolysis under stretching force. Angew Chem Int Ed 52:6992–6995
164. Obukhov SP, Rubinstein M, Duke T (1994) Dynamics of a ring polymer in a gel. Phys Rev Lett 73:1263–1266
165. Bras AR, Goossen S, Krutyeva M, Radulescu A, Farago B, Allgaier J, Pyckhout-Hintzen W, Wischnewski A, Richter D (2014) Compact structure and non-Gaussian dynamics of ring polymer melts. Soft Matter 10:3649–3655
166. Casassa EF (1965) Some statistical properties of flexible ring polymers. J Polym Sci A 3:605–614
167. Clarson SJ, Semlyen JA (1986) Cyclic polysiloxanes. 1. Preparation and characterization of poly(phenylmethyl siloxane). Polymer 27:1633–1636
168. Shin EJ, Jeong W, Brown HA, Koo BJ, Hedrick JL, Waymouth RM (2011) Crystallization of cyclic polymers: synthesis and crystallization behavior of high molecular weight cyclic poly (epsilon-caprolactone)s. Macromolecules 44:2773–2779
169. Bannister DJ, Semlyen JA (1981) Studies of cyclic and linear poly(dimethylsiloxanes). 6. Effect of heat. Polymer 22:377–381
170. Orrah DJ, Semlyen JA, Rossmurphy SB (1988) Studies of cyclic and linear poly(dimethylsiloxanes). 28. Viscosities and densities of ring and chain poly(dimethylsiloxane) blends. Polymer 29:1455–1458
171. Orrah DJ, Semlyen JA, Rossmurphy SB (1988) Studies of cyclic and linear poly(dimethylsiloxanes). 27. Bulk viscosities above the critical molar mass for entanglement. Polymer 29:1452–1454
172. Pasquino R, Vasilakopoulos TC, Jeong YC, Lee H, Rogers S, Sakellariou G, Allgaier J, Takano A, Brás AR, Chang T, Gooßen S, Pyckhout-Hintzen W, Wischnewski A,

Hadjichristidis N, Richter D, Rubinstein M, Vlassopoulos D (2013) Viscosity of ring polymer melts. ACS Macro Lett 2:874–878
173. Kapnistos M, Lang M, Vlassopoulos D, Pyckhout-Hintzen W, Richter D, Cho D, Chang T, Rubinstein M (2008) Unexpected power-law stress relaxation of entangled ring polymers. Nat Mater 7:997–1002
174. Halverson JD, Grest GS, Grosberg AY, Kremer K (2012) Rheology of ring polymer melts: from linear contaminants to ring-linear blends. Phys Rev Lett 108:038301
175. Chen WD, Chen JZ, Liu LJ, Xu XL, An LJ (2013) Effects of chain stiffness on conformational and dynamical properties of individual ring polymers in shear flow. Macromolecules 46:7542–7549
176. Chen WD, Chen JZ, An LJ (2013) Tumbling and tank-treading dynamics of individual ring polymers in shear flow. Soft Matter 9:4312–4318
177. Lang PS, Obermayer B, Frey E (2014) Dynamics of a semiflexible polymer or polymer ring in shear flow. Phys Rev E 89:022606
178. Cifre JGH, Pamies R, Martinez MCL, de la Torre JG (2005) Steady-state behavior of ring polymers in dilute flowing solutions via Brownian dynamics. Polymer 46:267–274
179. Diesendruck CE, Peterson GI, Kulik HJ, Kaitz JA, Mar BD, May PA, White SR, Martínez TJ, Boydston AJ, Moore JS (2014) Mechanically triggered heterolytic unzipping of a low-ceiling-temperature polymer. Nat Chem 6:623–628
180. Sellin RHJ, Hoyt JW, Pollert J, Scrivener O (1982) The effect of drag reducing additives on fluid-flows and their industrial applications. 2. Present applications and future proposals. J Hydraul Res 20:235–292
181. Kenis PR (1971) Turbulent flow friction reduction effectiveness and hydrodynamic degradation of polysaccharides and synthetic polymers. J Appl Polym Sci 15:607–618
182. Fabula AG, Hoyt JW, Crawford HR (1963) Bull Am Phys Soc 8
183. Shenoy AV (1984) A review on drag reduction with special reference to micellar systems. Colloid Polym Sci 262:319–337
184. Dschagarowa E, Bochossian T (1978) Drag reduction in polymer mixtures. Rheol Acta 17:426–432
185. Reddy GV, Singh RP (1985) Drag reduction effectiveness and shear stability of polymer-polymer and polymer-fiber mixtures in recirculatory turbulent-flow of water. Rheol Acta 24:296–311
186. Malhotra JP, Chaturvedi PN, Singh RP (1988) Drag reduction by polymer polymer mixtures. J Appl Polym Sci 36:837–858
187. Malhotra JP, Deshmukh SR, Singh RP (1987) Turbulent drag reduction by polymer-fiber mixtures. J Appl Polym Sci 33:2467–2478
188. Gampert B (ed) (1985) The influence of polymer additives on velocity and temperature fields. Springer, Berlin
189. Brostow W (2008) Drag reduction in flow: review of applications, mechanism and prediction. J Ind Eng Chem 14:409–416
190. Kim O, Little R, Patterson R, Ting R (1974) Polymer structures and turbulent shear stability of drag reducing solutions. Nature 250:408–410
191. Gryte CC, Koroneos C, Agarwal A, Hochberg A (1980) Drag reduction characteristics of graft copolymers prepared by the gamma irradiation of poly (oxyethylene) in the presence of acrylic acid. Polym Eng Sci 20:478–484
192. Deshmukh SR, Singh RP (1987) Drag reduction effectiveness, shear stability and biodegradation resistance of guargum-based graft-copolymers. J Appl Polym Sci 33:1963–1975
193. Ungeheuer S, Bewersdorff HW, Singh RP (1989) Turbulent drag effectiveness and shear stability of xanthan-gum-based graft-copolymers. J Appl Polym Sci 37:2933–2948
194. Hoyt JW (1985) Drag reduction in polysaccharide solutions. Trends Biotechnol 3:17–21
195. Deshmukh SR, Singh RP (1986) Drag reduction characteristics of graft-copolymers of xanthan gum and polyacrylamide. J Appl Polym Sci 32:6163–6176

196. Deshmukh SR, Chaturvedi PN, Singh RP (1985) The turbulent drag reduction by graft copolymers of guargum and polyacrylamide. J Appl Polym Sci 30:4013–4018
197. Malhotra SL (1986) Ultrasonic solution degradations of poly(alkyl methacrylates). J Macromol Sci A 23:729–748
198. May PA (2013) Polymer architecture effects on mechanochemical reactions. University of Illinois at Urbana-Champaign, Urbana
199. Potisek SL, Davis DA, Sottos NR, White SR, Moore JS (2007) Mechanophore-linked addition polymers. J Am Chem Soc 129:13808–13809
200. Sheiko SS, Sun FC, Randall A, Shirvanyants D, Rubinstein M, Lee H, Matyjaszewski K (2006) Adsorption-induced scission of carbon-carbon bonds. Nature 440:191–194
201. Panyukov SV, Sheiko SS, Rubinstein M (2009) Amplification of tension in branched macromolecules. Phys Rev Lett 102:148301
202. Lebedeva NV, Nese A, Sun FC, Matyjaszewski K, Sheiko SS (2012) Anti-Arrhenius cleavage of covalent bonds in bottlebrush macromolecules on substrate. Proc Natl Acad Sci 109:9276–9280
203. Sheiko SS, Panyukov S, Rubinstein M (2011) Bond tension in tethered macromolecules. Macromolecules 44:4520–4529
204. Lebedeva NV, Sun FC, Lee HI, Matyjaszewski K, Sheiko SS (2008) "Fatal adsorption" of brushlike macromolecules: high sensitivity of C-C bond cleavage rates to substrate surface energy. J Am Chem Soc 130:4228
205. Park I, Nese A, Pietrasik J, Matyjaszewski K, Sheiko SS (2011) Focusing bond tension in bottle-brush macromolecules during spreading. J Mater Chem 21:8448–8453
206. Li Y, Nese A, Lebedeva NV, Davis T, Matyjaszewski K, Sheiko SS (2011) Molecular tensile machines: intrinsic acceleration of disulfide reduction by dithiothreitol. J Am Chem Soc 133:17479–17484
207. Park I, Sheiko SS, Nese A, Matyjaszewski K (2009) Molecular tensile testing machines: breaking a specific covalent bond by adsorption-induced tension in brushlike macromolecules. Macromolecules 42:1805–1807
208. Panyukov S, Zhulina EB, Sheiko SS, Randall GC, Brock J, Rubinstein M (2009) Tension amplification in molecular brushes in solutions and on substrates. J Phys Chem B 113:3750–3768
209. Agarwal US, Mashelkar RA (1994) On the stability of grafted polymer-molecules in elongational flows. J Nonnewton Fluid 54:1–10
210. Parker CA, Hedley AH (1974) A structural basis for drag-reducing agents. J Appl Polym Sci 18:3403–3421
211. Merrill EW, Smith KA, Shin H, Mickley HS (1966) Study of turbulent flows of dilute polymer solutions in a couette viscometer. Trans Soc Rheol 10:335–351
212. Gramain P, Borreill J (1978) Influence of molecular weight and molecular structure of polystyrenes on turbulent drag reduction. Rheol Acta 17:303–311
213. Lapienis G (2009) Star-shaped polymers having PEO arms. Prog Polym Sci 34:852–892
214. Schaefgen JR, Flory PJ (1948) Synthesis of multichain polymers and investigation of their viscosities 1. J Am Chem Soc 70:2709–2718
215. Morton M, Helminiak TE, Gadkary SD, Bueche F (1962) Preparation and properties of monodisperse branched polystyrene. J Polym Sci 57:471–482
216. Bywater S (ed) (1979) Preparation and properties of star-branched polymers. Springer, Berlin/Heidelberg
217. Rempp P, Lutz P, Franta E (1994) Applications of anionic-polymerization to macromolecular engineering. J Macromol Sci Pure Appl Chem A31:891–909
218. Quirk RP, Yoo T, Lee BJ (1994) Anionic synthesis of heteroarm, star-branched polymers – scope and limitations. J Macromol Sci Pure Appl Chem A31:911–926
219. Pitsikalis M, Pispas S, Mays JW, Hadjichristidis N (1998) Nonlinear block copolymer architectures. Adv Polym Sci 135:1–137

220. Hadjichristidis N, Pitsikalis M, Pispas S, Iatrou H (2001) Polymers with complex architecture by living anionic polymerization. Chem Rev 101:3747–3792
221. Roovers J (ed) (1999) Solution properties of branched macromolecules. Springer, Berlin/Heidelberg
222. Douglas JF, Roovers J, Freed KF (1990) Characterization of branching architecture through universal ratios of polymer-solution properties. Macromolecules 23:4168–4180
223. Fetters LJ, Kiss AD, Pearson DS, Quack GF, Vitus FJ (1993) Rheological behavior of star-shaped polymers. Macromolecules 26:647–654
224. Nakayama Y, Masuda T, Nagaishi M, Hayashi M, Ohira M, Harada-Shiba M (2005) High performance gene delivery polymeric vector: nano-structured cationic star polymers (star vectors). Curr Drug Deliv 2:53–57
225. Georgiou TK (2014) Star polymers for gene delivery. Polym Int 63:1130–1133
226. Shida K, Ohno K, Kimura M, Kawazoe Y, Nakamura Y (1998) Dimensional and hydrodynamic factors for flexible star polymers in the good solvent limit. Macromolecules 31:2343–2348
227. Zimm BH, Stockmayer WH (1949) The dimensions of chain molecules containing branches and rings. J Chem Phys 17:1301–1314
228. Xue L, Agarwal US, Lemstra PJ (2005) Shear degradation resistance of star polymers during elongational flow. Macromolecules 38:8825–8832
229. Duan M, Fang SW, Zhang LH, Wang FX, Zhang P, Zhang JA (2011) Shear degradation resistance of star poly(ethyleneimine) – polyacrylamides during elongational flow. E Polymers 11:86–99
230. Striegel AM (2003) Influence of chain architecture on the mechanochemical degradation of macromolecules. J Biochem Biophys Methods 56:117–139
231. Marsalkó TM, Majoros I, Kennedy JP (1997) Multi-arm star polyisobutylenes. V. Characterization of multi-arm polyisobutylene stars by viscometry, pour points, electron microscopy, and ultrasonic shear degradation. J Macromol Sci A 34:775–792
232. Church DC, Peterson GI, Boydston AJ (2014) Comparison of mechanochemical chain scission rates for linear versus three-arm star polymers in strong acoustic fields. ACS Macro Lett 3:648–651
233. Xue L, Agarwal US, Zhang M, Staal BBP, Muller AHE, Bailly CME, Lemstra PJ (2005) Synthesis and direct topology visualization of high-molecular-weight star PMMA. Macromolecules 38:2093–2100
234. Cifre JGH, Pamies R, Martinez MCL, de la Torre JG (2005) Steady-state behavior of star polymers in dilute flowing solutions via Brownian dynamics. Polymer 46:6756–6766
235. Cifre JGH, Martinez MCL, de la Torre JG (2002) Conformation and dynamics of star-branched flexible polymer chains in a flowing solution. J Noncryst Solid 307:818–823
236. Ripoll M, Winkler RG, Gompper G (2006) Star polymers in shear flow. Phys Rev Lett 96:188302
237. Cifre JGH, de la Torre JG (1999) Steady-state behavior of dilute polymers in elongational flow. Dependence of the critical elongational rate on chain length, hydrodynamic interaction, and excluded volume. J Rheol 43:339–358
238. Hölter D, Burgath A, Frey H (1997) Degree of branching in hyperbranched polymers. Acta Polym 48:30–35
239. Žagar E, Huskić M, Grdadolnik J, Žigon M, Zupančič-Valant A (2005) Effect of annealing on the rheological and thermal properties of aliphatic hyperbranched polyester based on 2,2-bis (methylol)propionic acid. Macromolecules 38:3933–3942
240. Sheridan PF, Adolf DB, Lyulin AV, Neelov I, Davies GR (2002) Computer simulations of hyperbranched polymers: the influence of the Wiener index on the intrinsic viscosity and radius of gyration. J Chem Phys 117:7802–7812
241. Wiener H (1947) Structural determination of paraffin boiling points. J Am Chem Soc 69:17–20

242. Irzhak VI (2005) Topological structure and relaxation properties of polymers. Usp Khim 74:1025–1056
243. Pavlov GM, Korneeva EV, Mikhailova NA, Roy R, Ortega PC, Perez MA (1999) Molecular characteristics of lactodendrimers based on poly(amidoamine). Vysokomol Soedin Ser A 41:1810–1815
244. Lyulin AV, Davies GR, Adolf DB (2000) Brownian dynamics simulations of dendrimers under shear flow. Macromolecules 33:3294–3304
245. Frechet J (1994) Functional polymers and dendrimers: reactivity, molecular architecture, and interfacial energy. Science 263:1710–1715
246. Lepoittevin B, Matmour R, Francis R, Taton D, Gnanou Y (2005) Synthesis of dendrimer-like polystyrene by atom transfer radical polymerization and investigation of their viscosity behavior. Macromolecules 38:3120–3128
247. Aharoni SM, Crosby CR, Walsh EK (1982) Size and solution properties of globular tert-butyloxycarbonyl-poly(α, iε-L-lysine). Macromolecules 15:1093–1098
248. Ganazzoli F, La Ferla R, Terragni G (2000) Conformational properties and intrinsic viscosity of dendrimers under excluded-volume conditions. Macromolecules 33:6611–6620
249. Caminade A-M, Majoral J-P (2010) Dendrimers and nanotubes: a fruitful association. Chem Soc Rev 39:2034–2047
250. Caminade A-M, Ouali A, Keller M, Majoral J-P (2012) Organocatalysis with dendrimers. Chem Soc Rev 41:4113–4125
251. Boas U, Heegaard PMH (2004) Dendrimers in drug research. Chem Soc Rev 33:43–63
252. Morgan S, Ye Z, Subramanian R, Zhu S (2010) Higher-molecular-weight hyperbranched polyethylenes containing crosslinking structures as lubricant viscosity-index improvers. Polym Eng Sci 50:911–918
253. Wang J, Ye Z, Zhu S (2007) Topology-engineered hyperbranched high-molecular-weight polyethylenes as lubricant viscosity-index improvers of high shear stability. Ind Eng Chem Res 46:1174–1178
254. Dong Z, Ye Z (2012) Hyperbranched polyethylenes by chain walking polymerization: synthesis, properties, functionalization, and applications. Polym Chem 3:286–301
255. Naylor AM, Goddard WA, Kiefer GE, Tomalia DA (1989) Starburst dendrimers. 5. Molecular shape control. J Am Chem Soc 111:2339–2341
256. Lescanec RL, Muthukumar M (1990) Configurational characteristics and scaling behavior of starburst molecules – a computational study. Macromolecules 23:2280–2288
257. Mansfield ML, Klushin LI (1993) Monte-Carlo studies of dendrime macromolecules. Macromolecules 26:4262–4268
258. Lue L, Prausnitz JM (1997) Structure and thermodynamics of homogeneous-dendritic-polymer solutions: computer simulation, integral-equation, and lattice-cluster theory. Macromolecules 30:6650–6657
259. Chen ZY, Cui SM (1996) Monte Carlo simulations of star-burst dendrimers. Macromolecules 29:7943–7952
260. Boris D, Rubinstein M (1996) A self-consistent mean field model of a starburst dendrimer: dense core vs dense shell. Macromolecules 29:7251–7260
261. Sheng YJ, Jiang SY, Tsao HK (2002) Radial size of a starburst dendrimer in solvents of varying quality. Macromolecules 35:7865–7868
262. Murat M, Grest GS (1996) Molecular dynamics study of dendrimer molecules in solvents of varying quality. Macromolecules 29:1278–1285
263. Lyulin AV, Adolf DB, Davies GR (2001) Computer simulations of hyperbranched polymers in shear flows. Macromolecules 34:3783–3789
264. Neelov IM, Adolf DB (2003) Brownian dynamics simulations of dendrimers under elongational flow: bead-rod model with hydrodynamic interactions. Macromolecules 36:6914–6924
265. Neelov IM, Adolf DB (2004) Brownian dynamics simulation of hyperbranched polymers under elongational flow. J Phys Chem B 108:7627–7636

266. Ayme JF, Beves JE, Campbell CJ, Leigh DA (2013) Template synthesis of molecular knots. Chem Soc Rev 42:1700–1712
267. Forgan RS, Sauvage JP, Stoddart JF (2011) Chemical topology: complex molecular knots, links, and entanglements. Chem Rev 111:5434–5464
268. Micheletti C, Marenduzzo D, Orlandini E (2011) Polymers with spatial or topological constraints: theoretical and computational results. Phys Rep 504:1–73
269. Wang JC (1998) Moving one DNA double helix through another by a type II DNA topoisomerase: the story of a simple molecular machine. Q Rev Biophys 31:107–144
270. Arsuaga J, Vazquez M, Trigueros S, Sumners D, Roca J (2002) Knotting probability of DNA molecules confined in restricted volumes: DNA knotting in phage capsids. Proc Natl Acad Sci 99:5373–5377
271. Arsuaga J, Vazquez M, McGuirk P, Trigueros S, Sumners DW, Roca J (2005) DNA knots reveal a chiral organization of DNA in phage capsids. Proc Natl Acad Sci 102:9165–9169
272. Taylor WR (2000) A deeply knotted protein structure and how it might fold. Nature 406:916–919
273. Virnau P, Kardar M, Kantor Y (2005) Capturing knots in polymers. Chaos 15:041103
274. Ting RY, Little RC (1973) Shear stability of drag-reducing polyacrylic acid solutions. Nat Phys Sci 241:42–44
275. Glass JE, Schulz DN, Zukoski CF (1991) Polymers as rheology modifiers - an overview. Acs Symp Ser 462:2–17
276. Kowalik RM, Duvdevani I, Peiffer DG, Lundberg RD, Kitano K, Schulz DN (1987) Enhanced drag reduction via interpolymer associations. J Nonnewton Fluid 24:1–10
277. Malik S, Mashelkar RA (1995) Hydrogen-bonding mediated shear stable clusters as drag reducers. Chem Eng Sci 50:105–116
278. Malik S, Shintre SN, Mashelkar RA (1993) Enhancing the shear stability in drag-reducing polymers through molecular associations. Macromolecules 26:55–59
279. Agarwal US, Mashelkar RA (1994) Hydrodynamic shielding induced stability of zipping macromolecules in elongational flows. J Chem Phys 100:6055–6061
280. Sumners DW, Whittington SG (1988) Knots in self-avoiding walks. J Phys A Math Gen 21:1689–1694
281. Kivotides D, Wilkin SL, Theofanous TG (2009) Entangled chain dynamics of polymer knots in extensional flow. Phys Rev E 80:041808
282. Saitta AM, Soper PD, Wasserman E, Klein ML (1999) Influence of a knot on the strength of a polymer strand. Nature 399:46–48
283. Saitta AM, Klein ML (1999) Polyethylene under tensile load: strain energy storage and breaking of linear and knotted alkanes probed by first-principles molecular dynamics calculations. J Chem Phys 111:9434–9440
284. Saitta AM, Klein ML (1999) Evolution of fragments formed at the rupture of a knotted alkane molecule. J Am Chem Soc 121:11827–11830
285. Saitta AM, Klein ML (2001) First-principles molecular dynamics study of the rupture processes of a bulklike pE knot. J Phys Chem B 105:6495–6499
286. Arai Y, Yasuda R, Akashi K, Harada Y, Miyata H, Kinosita K, Itoh H (1999) Tying a molecular knot with optical tweezers. Nature 399:446–448
287. Tsuda Y, Yasutake H, Ishijima A, Yanagida T (1996) Torsional rigidity of single actin filaments and actin-actin bond breaking force under torsion measured directly by in vitro micromanipulation. Proc Natl Acad Sci 93:12937–12942
288. Bao X, Lee H, Quake S (2003) Behavior of complex knots in single DNA molecules. Phys Rev Lett 91:265506
289. Renner CB, Doyle PS (2014) Untying knotted DNA with elongational flows. ACS Macro Lett 3:963–967

Top Curr Chem (2015) 369: 209–238
DOI: 10.1007/128_2015_641

Published online: 24 June 2015

Mechanochemical Reactions Reporting and Repairing Bond Scission in Polymers

Jess M. Clough, Abidin Balan, and Rint P. Sijbesma

Abstract The past 10 years have seen a resurgence of interest in the field of polymer mechanochemistry. Whilst the destructive effects of mechanical force on polymer chains have been known for decades, it was only recently that researchers tapped into these forces to realize more useful chemical transformations. The current review discusses the strategic incorporation of weak covalent bonds in polymers to create materials with stress-sensing and damage-repairing properties. Firstly, the development of mechanochromism and mechanoluminescence as stress reporters is considered. The second half focuses on the net formation of covalent bonds as a response to mechanical force, via mechanocatalysis and mechanically unmasked chemical reactivity, and concludes with perspectives for the field.

Keywords Catalysis • Chemiluminescence • Chromism • Cycloreversion • Dioxetane • Flex activation • Mechanochemistry • Polymers • Self-healing

Contents

J.M. Clough, A. Balan, and R.P. Sijbesma (✉)
Laboratory of Supramolecular Polymer Chemistry, Department of Chemical Engineering and Chemistry, Institute for Complex Molecular Systems, Eindhoven University of Technology, PO Box 513, 5600 MB Eindhoven, The Netherlands
e-mail: r.p.sijbesma@tue.nl

Over the past century, polymers have become ubiquitous in modern life and in many of their applications they are expected to be able to withstand mechanical stress. Ultimately, polymeric mechanical behaviour is an expression of multiple processes operative at the molecular level: upon application of force to a bulk sample, mechanical energy may first be expended in driving conformational changes and disentanglements of polymer chains, after which bond deformation and covalent bond scission occur. Generally, these processes lead to irreversible damage and deterioration in the material properties, as first reported in the 1930s when Staudinger observed an MW reduction in rubber subjected to mastication. With the advent of polymer mechanochemistry nearly a decade ago, however, chemists and material scientists began to make use of the large macroscopic forces endured by polymers for constructive ends. Polymers present an attractive platform for the study of mechanical effects on chemical bonds: the typical macroscopic forces applied to polymers (in the Newton range) are many order of magnitude larger than the force required to break covalent bonds (of the order of a few nN), ensuring plentiful activation; in contrast to other forms of chemical activation with heat or light, mechanoactivation is strongly directional, with the potential to pull or push specific nuclei via choice of polymer attachment point [1]. A flurry of publications has established polymer mechanochemistry as a tool of wide utility, detailing the exploration of many new concepts such as the incorporation of specific functionalities ("mechanophores") [2] in the main chain that break selectively on application of force; the use of supramolecular polymers as reversible "force mediators" [3] and the activation of unique mechanochemical reaction pathways, giving rise to reactions that are not promoted by thermal or photochemical activation [4]. Theoretical and experimental studies have also demonstrated that applying force to a polymer chain does not universally lead to bond scission.

The acceleration in rate of the mechanochemical transformation depends strongly on the orientation of the scissile bond relative to the applied force [5–7]. With a view to materials applications, mechanochemical reactions offer exciting opportunities for early stage detection of damage in polymers with high sensitivity and the self-healing of materials following damage via mechanochemical processes that lead to the net formation of chemical bonds.

Recent efforts to report and to repair mechanical damage with mechanochemical reactions form the subject of the current chapter. We start with a brief discussion of the use of the spiropyran unit as a mechanophore for reporting strain. Spiropyran mechanochemistry inspired the development of another stress probe, the highly sensitive mechanoluminescent dioxetane, whose application as scission reporter in several types of polymeric materials is discussed. The chapter continues with a description of recent efforts to develop productive mechanochemistry, where initial scission leads to the formation of new bonds. Bond formation is either induced by the scission of covalent bonds, e.g. by the opening of rings, or bonds are formed under the action of a latent catalyst when it is activated by mechanochemical dissociation of a Lewis acid–base pair. These examples of productive mechanochemistry offer exciting possibilities to develop new modes of self-healing in

polymeric materials. We conclude the chapter with a brief overview of productive mechanochemical reactions that release small molecules.

1 Spiropyran Mechanochromism

Pericyclic transformations form a major part of the mechanochemistry canon, with examples ranging from electrocyclic ring-openings of benzocyclobutenes [4] and *gem*-dihalocyclopropanes (gDHCs) [8] to cycloreversions of Diels–Alder adducts [9], cyclobutanes [10] and dioxetanes [11]. Two of the most practicable, real-time reporters of mechanical stress in polymeric materials to have emerged from the mechanochemistry field fall into this broad class of mechanically-induced transformations. The first and most mature is the mechanochromic spiropyran, beautifully demonstrated by Davis et al. in their seminal Nature paper of 2009 [12], building on preliminary successes with this mechanophore within the Moore group [2]. First reported in the early twentieth century, spiropyran forms the intensely coloured fluorophore merocyanine upon heating, irradiation with UV light or mechanochemical grinding via a 6π electrocyclic ring-opening. The transformation can be reversed upon irradiation with visible light to reform the C–O spiro bond and regenerate the spiropyran. In their Nature report, Davis and colleagues bi-functionalised spiropyran with α-bromo or methacryolyl esters for living radical and free radical polymerisations, respectively, to covalently incorporate spiropyran as a mechanophore within acrylate polymers (Fig. 1a). Tensile testing of elastomeric poly(methyl acrylate) PMA and diametric compression of glassy poly(methyl methacrylate) PMMA samples showed that the electrocyclic ring-opening of spiropyran could be activated with mechanical force in the solid state, giving polymers that turned visibly red at plastic strains. As greater strain was applied to the sample, a concomitant increase in the intensity of the colour and the fluorescence was observed, permitting quantification of mechanically-induced polymeric damage. This publication also detailed simple mechanical models used to rationalise the choice of polymer attachment points, on the 5′ and 8 positions, as being the most efficient for transduction of the mechanical force to the spiro C–O bond (rather than the spiro C–C bond). Others have since explored the effect of directing mechanotransduction via choice of polymer attachment point in more detail with electronic structure calculations for a selection of different mechanophores, including the spiropyran [6].

The spiropyran unit has since been established as an effective molecular force probe. Following their initial discovery, the Moore group published detailed studies investigating the role of polymer architecture, mobility [16] and chain orientation [17, 18] in the mechanical response of PMA and PMMA, rubbery and glassy polymers, respectively, upon the application of tensile and torsional stress. A study by Beiermann et al. examined the fluorescence anisotropy of the ring-opened merocyanines as a means to characterise their degree of orientation relative to the direction of the applied tensile force. In PMA, they found strong preferential activation of the spiropyrans in the direction of the tensile force [17]. On tensile

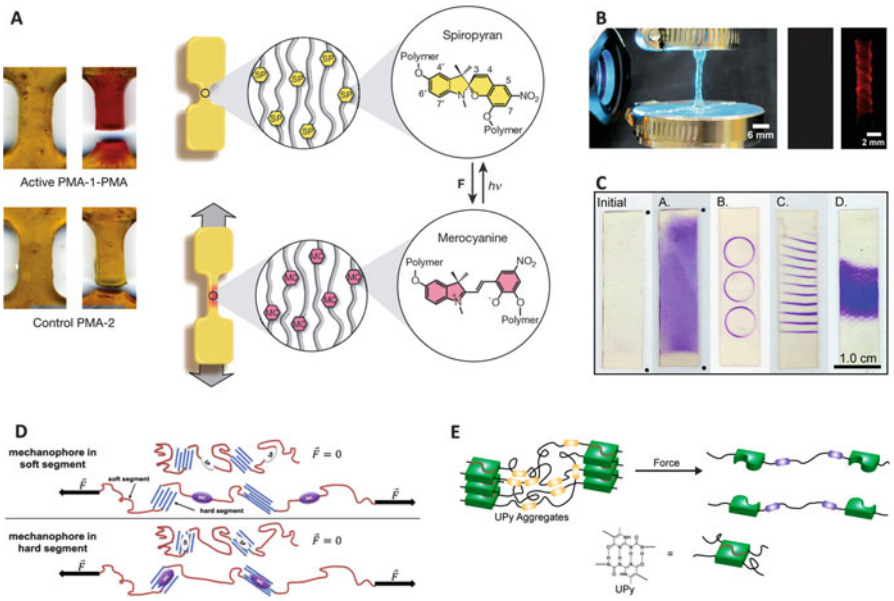

Fig. 1 The spiropyran stress reporter: (**a**) the spiropyran undergoes electrocyclic ring-opening to form strongly coloured merocyanine in bulk PMA samples subjected to tensile force; (**b**) mechanoactivation can also be achieved in torsion and characterised with fluorescence; (**c**) activation at reversible strains was found possible in PDMS, for example, by pressing patterns in a PDMS sheet; (**d**) incorporation of spiropyran in thermoplastic elastomers and in (**e**) gels cross-linked with hydrogen-bonded UPy dimers. Reprinted with permission from [12] (Copyright © Nature Publishing Group 2009), [13] (Copyright © The Royal Society of Chemistry 2011), [9] (Copyright © American Chemical Society 2014), [14] (Copyright © American Chemical Society 2013) and [15] (Copyright © American Chemical Society 2013)

testing of PMMA, brittle failure was found to precede mechanoactivation at room temperature; [16] by contrast, activation could be obtained when heating close to its *T*g (90–105°C) or plasticising the matrix with 15–20 wt% methanol, suggesting some mobility of the polymer chains is necessary for mechanoactivation [16]. Similar conclusions were drawn from shear-based studies. On shear testing PMMA samples, Kingsbury et al. imaged the merocyanine fluorescence in situ to characterise the onset shear stress, or the shear stress needed to activate a detectable proportion of the spiropyran moieties [13]. The onset stress increased with shear rate, as greater shear rates do not allow the polymer chains time to rearrange and accommodate the applied stress. Increasing the length of the primary crosslinker with respect to the spiropyran led to a decrease in activation stress, which was attributed to the spiropyran bearing a greater proportion of the strain with shorter non-functional crosslinkers. Torsion combined with in situ fluorescence imaging was also used to probe the time-dependent activation of spiropyran upon creep loading, employing a similar methodology to characterise the onset stress [19]. Smaller creep stresses required a longer time to reach the detectable threshold of fluorescence intensity, but correspondingly smaller strains to initiate the activation. It was also revealed that the detectable threshold is exceeded when the creep

strain rate reaches a maximum, which is associated with the onset of strain-hardening, and a peak in polymer chain mobility.

The Moore group and others have ventured more recently into other modes of activation outside the realm of traditional mechanical testing, such as solvent swelling [20] and laser-generated acoustic shockwaves [21]. Inspired by the reversible activation of chromophores in cephalopod skins to generate coloured markings, Wang et al. in a collaboration between the groups of Craig and Zhao made use of the electrically-induced deformations in poly(dimethyl siloxane) to activate covalently incorporated spiropyran in a diverse array of patterns [22]. In addition, the range of polymeric materials amenable to spiropyran stress-sensing has expanded significantly in the past 5 years. Aside from polyacrylates, this range now encompasses widely-used engineering polymers, such as polyurethanes [14], thermoplastic elastomers (TPEs) [23] (Fig. 1d), poly(dimethylsiloxane) (PDMS) [9] (Fig. 1c) and rubber-toughened PMMA [24]. Polyurethane proved to be a better platform than PMA and PMMA to characterise the kinetics and thermodynamics of the mechanically induced transformation from spiropyran to merocyanine – PMA is too soft, with activation only at high strains, and PMMA too brittle, giving minimal plastic deformation. In particular, merocyanine was found not to revert to the spiropyran in polyurethane when held at constant strain. Furthermore, if a sample was stretched, activating the spiropyrans, then irradiated with light whilst being held at constant strain to close the merocyanines, it was found that the spiropyrans opened once more after 1–2 h, demonstrating force-induced change in the energy landscape of the spiropyran-merocyanine transformation. Lastly, spiropyran has also been employed in combination with supramolecular cross-links, such as hydrogen-bonding dimers [15] and transition metal or lanthanide complexes [25], to create stress-reporting, self-healing gels.

2 Mechanoluminescence

These developments by Moore and others prompted the Sijbesma group to look to the cycloreversion of the high-stability thermochemiluminescer, bis(adamantyl)-1,2-dioxetane, as a potential stress reporter. The strained, central four-membered dioxetane ring is known to decompose at elevated temperatures into two ketones, one of which can take an excited state and relax with the emission of a photon, producing the signature bright blue chemiluminescence. Amongst the 1,2-dioxetane family, the bis(adamantyl) derivative is striking for its stability, with an energy barrier to decomposition of 35 kcal/mol and a half-life at room temperature of around 40 years [26], largely because of the steric lock posed by the two adamantyl groups. In 2012, it was shown that the chemiluminescent cycloreversion of this dioxetane could be activated mechanically, giving mechanoluminescence (Fig. 2) [11]. This transformation converts mechanical energy directly into electronic excitation energy without the need for an additional excitation source, in contrast to the fluorescent spiropyran. The stress response is also transient in time, rather than cumulative. Provided that the background signal

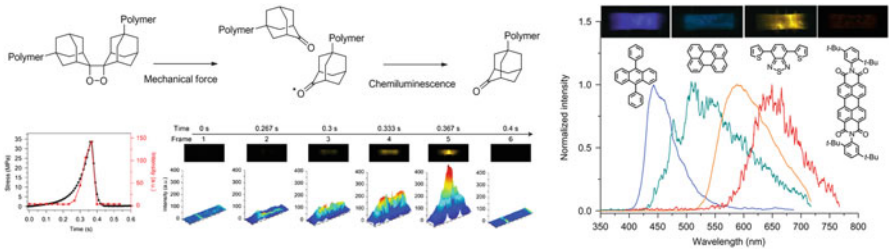

Fig. 2 Mechanoluminescence from bulk cross-linked PMA samples subjected to tensile testing was recorded with a high-speed camera and found to increase in intensity in concert with the stress in the sample. The emission colour can be tuned by doping with fluorescent acceptors. Reprinted with permission from [11] (Copyright © Nature Publishing Group)

is sufficiently low, mechanoluminescence offers significant enhancements in sensitivity over mechanochromism in the imaging of covalent bond scission within polymeric materials, potentially comparable to those obtained with the introduction of chemiluminesence to biochemical assays. In the current section, the use of the latent excitation energy of the bis(adamantyl)dioxetane mechanophore for stress-reporting in polymers is discussed.

As for the spiropyran, sonication served as an initial test-bed for the mechanoluminescence concept, to ascertain whether the chemiluminescent decomposition of bis(adamantyl)-1,2-dioxetane could be triggered mechanically. Although mechanochemical transformations in bulk polymers have the most technological relevance, solution-based sonochemistry generally requires less material and can be coupled more easily with traditional analytical techniques. In addition, the strain rates accessible with sonochemistry are greater than with other solution-based flow techniques such as opposed jets or cross slots, allowing mechanical activation to be obtained in polymers of lower molecular weight and at greater scission rates. The potential of polymer sonochemistry as a platform for studying polymer degradation was recognised as early as the 1930s and in the past decade it has become a popular method of screening mechanochemical reactivity. Whilst the exact mechanism of mechanical activation in sonochemistry remains under debate, it is generally accepted that chain scission is induced by the solvodynamic shear forces associated with bubble cavitation in the solution. Pressure oscillations induced by ultrasound waves in solution lead to the formation of micro-sized cavitation bubbles which upon their collapse generate a local shear field [27]. Polymers situated in the vicinity of this shear field experience a velocity gradient, with the part of the chain closest to the centre of cavitation being pulled in at a greater velocity. The high resultant elongational stresses first cause the polymer to uncoil, after which the covalent bonds along the polymer backbone begin to deform, leading ultimately to chain scission [28]. The “coil-to-stretch” transition is thought to be an important step preceding covalent bond scission.

The mechanism by which polymers interact with cavitation-induced shear fields informs the design and interpretation of mechanochemical experiments making use of sonochemistry. First, it is observed that scission occurs preferentially around the mid-point of the polymer chain, as the solvodynamic forces are greatest at this point

[29]. The reactivity of a new mechanophore, such as bis(adamantyl)-1,2-dioxetane, is therefore examined by incorporating it at the centre of a polymer chain, where the probability of chain scission and mechanoactivation are highest. This behaviour contrasts with that on thermal activation, in which scission occurs in a random fashion. Furthermore, a typical control to demonstrate that the reactivity of a mechanophore is mechanical in origin and not thermal is to end-functionalise a polymer chain with the mechanophore; under genuine mechanoactivation, no significant transformation should be observed. Second, mechanoactivation exhibits a characteristic dependence upon the molecular weight of the polymer in which the mechanophore is incorporated, which is not displayed by thermal activation. The higher the molecular weight of the polymer, the longer the relaxation time of the polymer chain and hence the lower the strain rates required to induce a coil-to-stretch transition, giving greater rates of mechanical activation. In addition, it is typically found that bond scission and mechanoactivation do not occur to a significant extent below a lower molecular weight limit, known as the limiting molecular weight, M_{lim}, typically derived by plotting rate constants of scission against molecular weight and extrapolating to a rate constant of zero. In this limit, the polymer chains become too short to accumulate the force required to break chemical bonds as the strain rates required for chain scission are higher than those that can be provided by sonication [30]. M_{lim} varies with conditions and polymer type: for example, covalent pTHF has an M_{lim} of 50–60 kDa, whereas for PMMA it is in the region of 90–100 kDa; incorporation of a weak bond into a polymer chain lowers M_{lim} significantly [31]. Finally, the conditions of sonication strongly influence the efficiency of formation and collapse of cavitation bubbles, and hence the shear forces achieved. Mechanoactivation is enhanced at lower temperatures, at lower concentrations of polymer, in solvents with lower vapour pressure, in better-solvating solvents and when the dissolved gas has a lower heat capacity [27].

In the first sonochemistry-based investigations on the dioxetane mechanophore, the mechanically reactive moiety was centrally incorporated in poly(methyl acrylate) (PMA) by synthesising a dioxetane-functionalised bis-initiator for single electron transfer living radical polymerisation and growing a PMA chain from both ends (a similar strategy to that employed by Davis et al. with the spiropyran). Upon sonicating dilute solutions of this polymer, light emission could be observed from the sonication flask and chain scission was monitored via GPC; adamantanone formation was additionally demonstrated by functionalisation with a chromophore-bearing hydrazine [11]. Controls established the mechanical origin of the luminescence. Neither sonication of bis(adamantyl)-1,2-dioxetane not covalently bound to a polymer in the presence of polymer nor sonication of polymer end-functionalised with dioxetane showed any light emission or hydrazine functionalisation, and the thermal decomposition behaviour of the bis(adamantyl)dioxetane was found to be unchanged by the tethering of polymer chains.

Whilst sonication is a convenient tool to screen for mechanical reactivity, a probe for mechanical stress such as the bis(adamantyl)dioxetane is most likely to provide the most technologically relevant insights in the solid state, where most polymeric materials find their application. To this end, poly(methyl acrylate)

networks were fitted out with the bis(adamantyl)-1,2-dioxetane mechanophore as a cross-linker via a UV-initiated free radical polymerisation; bulk samples were tested in a rheometer with an extensional fixture [11]. Application of tensile strain resulted in the emission of mechanoluminescence, which could be recorded with a high-speed camera. As can be seen in Fig. 2, the mechanoluminescence emission correlated directly with the stress exhibited by the material. Furthermore, the spectrum of the light emission could be tuned by doping the polymeric matrix with different fluorescent acceptors. This work served as a foundation for subsequent ventures with mechanoluminescence in the solid state.

Since 2012, the Sijbesma group in collaboration with others has employed mechanoluminescence as a means to investigate a variety of polymeric materials, ranging from entirely novel designer systems to common engineering polymers. A particularly satisfying example in the former category was the use of dioxetane mechanoluminescence to demonstrate a new toughening approach for elastomers [32] (Fig. 3a). The group of Prof. Creton at ESPCI developed elastomers comprising multiple interpenetrating networks generated via sequential free radical

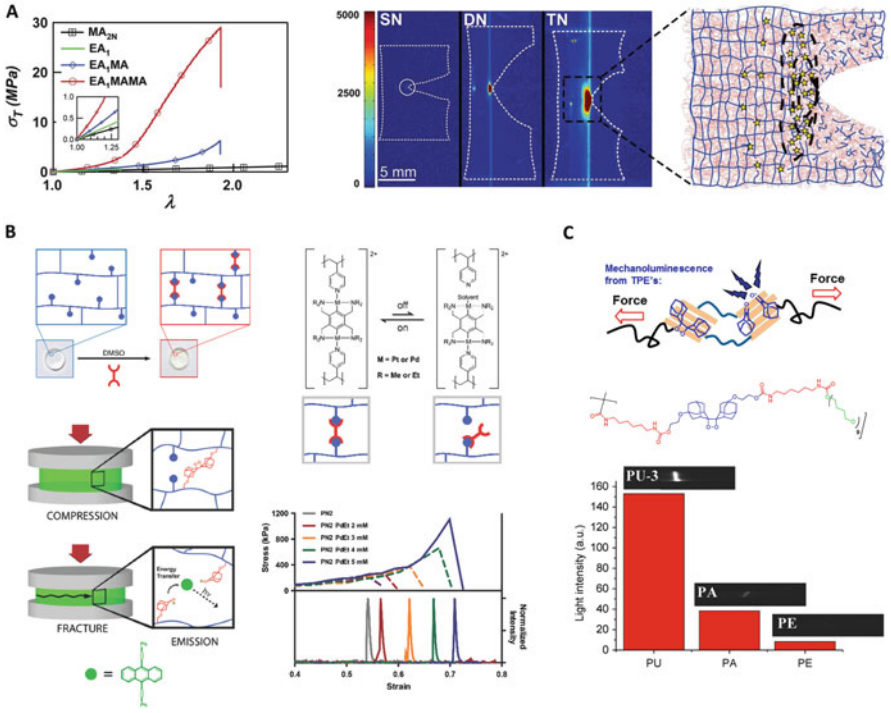

Fig. 3 Development of mechanoluminescence as a stress probe within polymeric materials: (**a**) in multiple network elastomers; (**b**) in swollen gels supramolecularly cross-linked with transient metal-ligand bonds and (**c**) in thermoplastic elastomers. Reprinted with permission from [32] (Copyright © AAAS 2014), [33] (Copyright © Wiley VCH 2014) and [34] (Copyright © American Chemical Society 2014)

polymerisations, similar to the multiple network hydrogels already well known in the literature. In this strategy, a first cross-linked network is polymerised and then swollen with the monomer of the second network (plus cross-linker and initiator), isotropically stretching the chains of the first network. Upon polymerisation, a double network is obtained and the swelling/polymerisation procedure can be repeated once more to give a triple network. Under stress at a crack tip, the prestretched chains in the first and second networks serve as sacrificial stress-bearers, breaking and dissipating energy prior to material failure. The yield stress of the material was shown to be dependent on the monomer used to make the first sacrificial network. The rationale for the reinforcement strategy was affirmed quite beautifully by dioxetane mechanoluminescence. In single edge notch tests, mechanoluminescence was highly localised at the crack tip for the single network, becoming more intense for the double network and for the triple network, a large yielding zone being observed over an extended region ahead of the crack tip. The mechanoluminescence traces were rich in information about the yielding zone, revealing its extent and shape, which could be controlled by the extensibility of the second network chains. In future work, it is hoped that this information could be compared with predictions from more advanced damage models.

The dioxetane mechanophore also assisted in understanding another novel toughening approach, developed in the context of metallosupramolecular gels [33] (Fig. 3b). This reinforcement strategy, conceived by Prof. Craig and colleagues, made use of their group's extensive study of networks based on poly (vinyl pyridine) cross-linked with bifunctional van Koten-type pincer complexes. The pincer complexes coordinate reversibly to the free pyridines, resulting in weak, transient supramolecular interactions which control the bulk dynamical properties of the gel. Key to this strategy is the ability to tune the lifetime of the supramolecular interaction, either by varying the central metal ion within the complex or by making small structural changes to the complex. In such a system, the supramolecular cross-links have little effect on the modulus and structure of the material, but still allow greater strain to be borne at failure by serving as mediators of molecular-scale "force management", homogenising the distribution of stress and inhibiting crack formation. Such a mechanism would be consistent with the substantial increase in fracture energies upon incorporation of the supramolecular cross-linkers. In this model system study, the dioxetane mechanophore was incorporated as a covalent cross-linker within these gels in order to demonstrate that covalent bond scission could be inhibited by the addition of reversible cross-linkers to the network. Upon increasing the concentration of mechanically invisible cross-linker, an increase in strain at break was observed and the onset of mechanoluminescence was correspondingly delayed. This approach to material design, improving fracture toughness independently of the elastic modulus, is of particular interest to the development of materials where a high modulus is a disadvantage, for example, in biomaterials.

In addition to these collaborations, the deformation mechanisms of more commonplace polymeric materials have been visualised with mechanoluminescence. Bis(adamantyl)dioxetane was incorporated into the main chains of segmented copolymers comprising poly(tetramethylene oxide) (PTMO) soft segments with

different hydrogen-bonding hard segments, one of the most prevalent types of thermoplastic elastomers (TPEs) [34]. The fatigue and failure of these commercially important materials is strongly influenced by the microphase separation of these segments into soft and hard blocks. Over the years this has stimulated the use of mechanochromism to investigate their mechanical behaviour: diacetylenes, OPVs, azobenzenes and more recently spiropyran [23] have all been used to interrogate the organisation and role of the hard blocks within TPEs under tensile stress. Mechanoluminescence was used to examine chain slippage out of the hard blocks and the strength of the hydrogen-bonding interaction within the hard blocks in the mechanical behaviour of TPEs (Fig. 3c).

Among the most salient findings was the observation of stronger mechanoluminescence emission in block copolymers with hard segments better able to engage in hydrogen-bonding, such as polyurethane, as compared with hard segments displaying much weaker hydrogen-bonding, such as polyester. With stronger hydrogen-bonding interactions, the rate of disentanglement of the polymer chains decreases relative to the rate of strain, preventing the chains from accommodating the applied stress, thereby leading to a greater degree of chain scission. At higher strain rates, little difference in the intensity of the mechanoluminescence between TPEs with different hard blocks was observed, suggesting that the hydrogen-bonding slows down entanglement but ultimately is not a prerequisite for bond scission. Regarding the role of chain slippage, it was found that increasing the molecular weight led to an increase in emission intensity, interpreted as an indicator of decreased chain slippage at higher molecular weights when there are more hard segments to anchor the polymer chain. Even in chains with more than 50 hard segments, slippage could still be reduced (and the mechanoluminescence emission increased) by increasing the molecular weight still further. More recent work with the bis(adamantyl)dioxetane mechanophore has examined swelling-induced mechanoluminescence and the mechanical behaviour of PDMS, which will be reported on in due course.

Complementary to efforts to establish the general utility of this mechanophore, the excited state products of the mechanical scission process have been characterised, specifically, the ratio of singlet and triplet excited ketone products and the total chemiexcitation yield [35]. From a practical viewpoint, such information is useful as singlet and triplet excited ketones require different acceptors to maximise light emission efficiency. In addition, the thermochemiluminescent decomposition of alkyl dioxetanes nearly always gives an excess of triplet products, in spite of triplet formation being formally spin-forbidden [36]. A fascinating collection of studies dating back to the 1960s and 1970s, from Turro, Wilson, Adam and others, reveals the drive of these pioneers to ascertain the excited state products of an ever-expanding family of dioxetanes with the aim of elaborating on the mechanism of decomposition [37]. Even today, the exact details of the decomposition mechanism remain enigmatic, although high-level calculations indicate substantial step-wise character with O–O bond scission leading. The products of scission are therefore an interesting target for study, especially given that polymer mechanochemistry has been shown to open up new reaction pathways inaccessible to thermal or photochemical activation.

For this, linear PMA polymers incorporating a central dioxetane unit were sonicated, principally for reasons of precision (the failure of solid state samples under tensile testing, and hence the total mechanoluminescence emission, depends more strongly on the defects within the sample). A sensitised relay scheme was devised with a europium complex, $Eu(TTA)_3Phen$, as a phosphorescent acceptor to monitor the formation of singlet and triplet excited states; the quantum yields were then extracted via fitting to a model including all the relevant photophysical processes. Within the relatively wide error margins, the singlet-triplet ratios and quantum yields were found to be similar upon mechanical activation as compared with thermal activation. This was attributed to the region of intersystem crossing being located in a region of high degeneracy between the ground and excited state surfaces, as indicated by the results of high-level CASSCF calculations on the thermal decomposition of 1,2-dioxetane [38, 39]. The relative rates of formation of the excited states and by extension the singlet-triplet ratio and quantum yields would therefore be similarly affected by the application of force. Calculations at a comparable level of theory would need to be conducted for the mechanical pathway to substantiate this argument.

3 Mechanically-Induced Bond Creation

Alongside stress reporters, such as the spiropyran and the dioxetane, another burgeoning area of research in mechanochemistry involves the development of mechanophores for constructive bond-forming. These mechanophores are particularly desirable against the backdrop of intensive research into self-healing polymers. One approach to address this aim is mechanically induced catalysis, where a single scission event can lead to the creation of many bonds (see below). Others have pioneered the use of pericyclic transformations to this end, which is the focus of the remainder of the review. Here, the mechanophore has latent chemical reactivity (as distinct from latent chemiexcitation energy in the dioxetane mechanophore), which upon unmasking with mechanical force can undergo further reaction, for example, with a bifunctional cross-linker. Under thermal activation, the pericyclic transformations needed to generate the reactive species often require high temperatures, limiting the potential to exploit the reactivity of the products. The mild conditions in mechanochemistry thus become advantageous. Furthermore, the high degree of localisation of mechanical forces intimates the possibility of inducing reinforcing bond-forming reactivity where it is most needed, i.e. in the areas where bond scission is most prevalent.

One of the early, ground-breaking papers within the polymer mechanochemistry field was also one of the first to raise the possibility of constructive bond formation upon mechanical activation. On the back of preliminary successes from the Moore group, Hickenboth et al.'s Nature paper of 2007 describes the force-induced electrocyclic ring-opening of benzocyclobutene centrally incorporated within a PEG polymer to the *ortho*-quinodimethide product [4] (Fig. 4). The significance

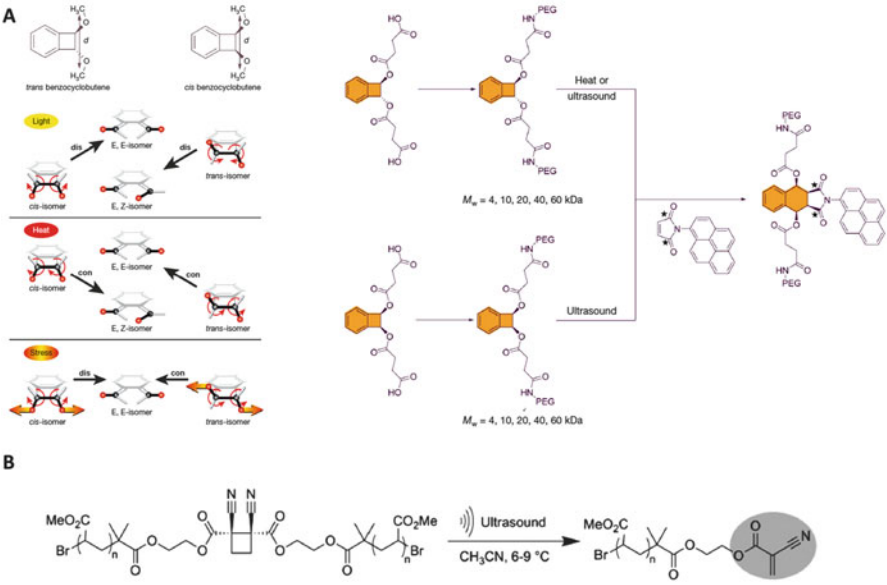

Fig. 4 Examples of mechanically induced formation of reactive species from the Moore group: (**a**) both *cis*- and *trans*-benzocyclobutene undergo electrocyclic ring-opening to the same *ortho*quinomethide product, in contrast to the behaviour under thermal and photochemical activation. This product can then go on to react with dienophiles such as the fluorophore-bearing maleimide; (**b**) generation of highly reactive cyanoacrylates upon sonication. Reprinted with permission from [4] (Copyright © Nature Publishing Group 2009) and [40] (Copyright © American Chemical Society 2010)

of this work lies in its demonstration of mechanical force as a means to drive transformations inaccessible to other forms of activation in a selective fashion: it was found that both *cis*- and *trans*-benzocyclobutene give the E,E-isomer of the *ortho*-quinodimethide, indicating that the *cis*-benzocyclobutene undergoes the thermally disallowed disrotatory ring-opening. This electrocyclic ring-opening was interrogated in a more quantitative fashion as part of a more recent atomic force microscopy (AFM)-based investigation into a selection of mechanophores, conducted by the Craig group [41]. On the timescale of these experiments (~0.1 ms), the symmetry-forbidden reactivity of *cis*-benzocyclobutene was found to occur at a force threshold of 1,370 pN, slightly lower than the required force to induce the symmetry-allowed reactivity of the *trans*-benzocyclobutene isomer (1,500 pN), agreeing well with previous results from modelling the force-modified potential energy surfaces by Ribas-Arino et al. [30]. These experiments show quantitatively that the symmetry-forbidden pathway proceeds at a greater rate than its symmetry-allowed analogue.

Aside from the fascinating fundamental implications, the mechanical production of a highly reactive group, trapped in this work by a maleic anhydride dienophile, was intriguing for material science applications. In a similar vein, the Moore group also worked on dicyanocyclobutanes, which were shown to undergo mechanically

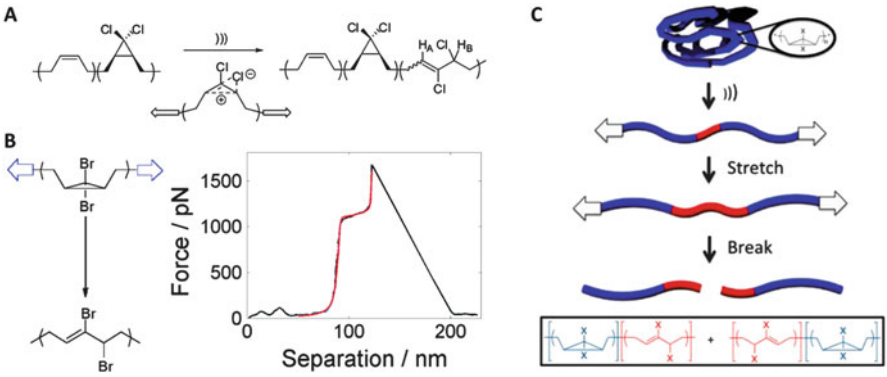

Fig. 5 Characterising gDCC and gDBC mechanochemical reactivity: (**a**) force-induced electrocyclic ring-opening of gDCC within poly(gDCC) to 2,3-dichloroalkene; (**b**) elongation upon ring-opening measured by SMFS provides molecular level toughening; (**c**) sonochemical formation of block copolymers from poly(gDHC)s. Reprinted with permission from [8] (Copyright © American Chemical Society 2009), [44] (Copyright © American Chemical Society 2012) and [45] (Copyright © American Chemical Society 2010)

activated cycloreversion to produce highly reactive cyanoacrylates [40, 42]. Upon sonication in solution, these were successfully trapped with chromophore-functionalised amines via Michael addition, although to date this system has yet to be realised in the solid state.

Those working in the group of Craig were also inspired to pursue force-induced covalent bond formation with mechanophore-bearing systems of their own design, which recently came to fruition with their report of the first material to self-strengthen under mechanical force [43]. Their contributions to this area follow from their pioneering development of the *gem*-dihalocyclopropane (gDHC)-based mechanophores (Fig. 5). In addition to being easy to synthesise, the dichloro and dibromo members of this family undergo thermally or mechanically induced electrocyclic ring-opening to generate 2,3-dihaloalkenes. The advantages of the gDHC-based system for mechanochemical bond formation are threefold. First, gDHCs can be readily incorporated en masse in the polymer main chain, increasing the chances of a mechanophore being situated at a point of increased stress; second, upon opening, the mechanophore lengthens, thereby relieving stress and allowing polymer chains to survive otherwise catastrophic stresses; finally, the 2,3-dihaloalkenes are reactive to nucleophilic substitution, opening the way to mechanically induced bond-forming reactions.

In 2009, sonication was first used to examine the potential of gDHCs as mechanophores [8]. Reacting polybutadiene with dichlorocarbene, as first described in the 1960s, yielded polymers with multiple gDCCs along the backbone that underwent conversion to the 2,3-dichloroalkene upon sonication (over 80% after 4 h sonication). The selectivity of the transformation was clear from these early sonication-based studies, with 35% of the gDCCs in a chain undergoing ring-opening prior to scission of the polymer chain (Fig. 6a). Sonication experiments also permitted elucidation of the mechanically induced ring-opening mechanism. In

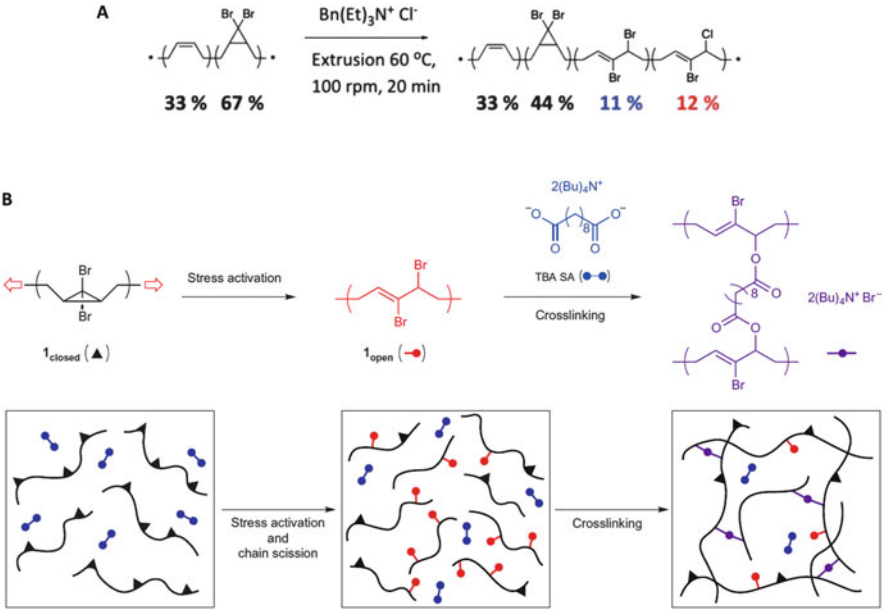

Fig. 6 Activation of gDBCs and subsequent bond creation in the solid state: (**a**) under extrusion of poly(gDBC) in the presence of chloride, 250 chloride substitutions occur on the mechanically generated 2,3-dibromoalkene for every 9 chain scissions; (**b**) extrusion of poly(gDBC) in the presence of a dicarboxylate leads to force-induced cross-linking. Reprinted with permission from [43] (Copyright © Nature Publishing Group 2013) and [46] (Copyright © The Royal Society of Chemistry 2011)

contrast to thermal activation, in which *cis*-gDCC reacts around 20 times faster than the *trans* isomer, the two isomers react with comparable rates in sonication. Whilst it might be expected that the *cis* is accelerated more, it is thought the shear stresses generated upon sonication give rise to regions of high, localised stress along the backbone of the polymer, in which the gDCC mechanophores react regardless of their stereochemistry. Solution-based sonication of gDCC polymers found application in the synthesis of block copolymers [44]. This study made use of the fact that ultrasound induces not only multiple gDHC ring-opening but covalent scission of the polymer chain, with an average of one such scission event per chain. As the gDHC ring-opening is strongly localised around the mid-point of the polymer chain, each chain scission event generates two polymers with AB character. The blockiness of the two phases was confirmed by selective degradation of the ring-opened alkenes via ozonolysis, leaving behind only those sections of polymer chain in which the gDCCs had not undergone mechanical activation. Furthermore, the polymers resulting from sonication, with blocks of gDCC and 2,3-dichloroalkene, were found to self-assemble into ordered lamellar phases in the solid state, as characterised by small angle X-ray scattering.

SMFS experiments furnished further information about the structural changes upon mechanochemical ring-opening. From a conformational transition at 1.2 nN of force, it was possible to deduce that the polymer chain lengthens by 1.28 Å per gDBC opened under mechanical force, corresponding to an extension of 28% in the contour length of the polymer [45]. Typically, at these high restoring forces, extending the polymer by even a few percent leads to catastrophic rupture; a mechanically induced extension of 28% in this force range therefore provides a substantial increase in toughness (as measured by the net energy absorbed prior to rupture, or the area under force-extension curve up to the point of scission). Compared to gDBC, gDCC exhibits more surprising behaviour under SMFS in that the *cis*-gDCC undergoes the preferred disrotatory ring-opening at a force threshold of 1.3 nN, but the *trans*-isomer is thought to open via the disallowed conrotatory process, forming the Z-isomer of the alkene product, at a force of 2.3 nN [41]. The force-induced extension was found to be consistent with the conrotatory mechanism. Additionally, SMFS experiments with gDCC revealed sensitivity to the stereochemistry of an α-alkene substituent, three bonds away from the mechanophore: the E-alkene substituted gDCC opened at a force 0.4 nN lower than the gDCC with the Z-alkene substituent, in spite of their similar thermal reactivities [47]. In a polymer containing both E- and Z-alkene substituted gDCCs along its backbone, two extension plateaus are observed in the force-extension curve, in contrast to just one with the gDBC.

Spurred on by these successes, the group took this concept further into the solid state, trialling two different modes of activation: compression and extrusion (tension activates only a very small proportion of the mechanophores in the solid state). Upon compressing bulk polymer samples of gDHC-functionalised polybutadiene with a steel press, 0.1% of the gDCCs and 0.4% of the gDBCs was found to undergo ring-opening to the 2,3-dihaloalkene, as determined by 1-H NMR [48]. It appeared that stresses were concentrated over very short segments of the polymer chain corresponding to only a few monomers, longer than would be expected for thermally activated ring-opening but somewhat less than the entanglement density of the polymer. Extrusion, by contrast, gave higher conversions, ranging from 6% to 30% after 1 h of extrusion, depending on polymer composition and the shear stress applied [46]. Crucially, the 2,3-dibromoalkene formed from the mechanically-induced ring-opening of gDBC underwent subsequent nucleophilic substitution by chloride ions during extrusion in the presence of benzyltriethylammonium chloride at 60°C and 100 rpm. Molecular weight analysis indicated an average of over 500 ring-openings and 250 substitution reactions for every 9 scission events per polymer chain, corresponding to 25 new intermolecular covalent bond formations per covalent bond scission.

These promising indications paved the way for the above-mentioned Nature Chemistry paper [43]. Here, the mechanophore chosen was gDBC, embedded as previously shown in polybutadiene, and extruded at 40°C for 30 min and 50 rpm (corresponding to bulk stresses of 0.15–0.25 MPa), leading to a 7% conversion of the gDBCs into their open form and a reduction in the MW from 780 to 560 kDa. Extruding in the presence of a dicarboxylate, the ditetrabutylammonium salt of

sebacic acid, led to an insoluble polymer that appeared to become stronger after approximately 13 min of extrusion: the Young's modulus increased from 8 to 150 MPa, suggesting that the mechanically-induced cross-linking was outcompeting destructive chain scission (Fig. 6b) In addition to dynamic viscosity and nanoindentation measurements, IR confirmed the formation of the desired ester. Sonication of polymer solutions and monitoring the molecular weight change with GPC corroborated the solid state observations, with the solutions forming insoluble cross-linked precipitates after 30 min. Capitalising on this finding, they then moved to a one-component system, in which cross-linking carboxylates were incorporated in the polybutadiene backbone, along with the gDBCs. Upon sonicating this polymer, a still greater remodelling response was observed: on leaving sonicated solutions to stand in the absence of shear, the solutions formed a gel with elastic moduli two orders of magnitude greater than the starting material.

Alongside the gDCC and gDBC mechanophores, the Craig group has also explored the *gem*-difluoro derivative, gDFC, which displays complementary behaviour to the gDCC and gDBC mechanophores. in that it undergoes a net contraction under the action of mechanical force, rather than a lengthening (Fig. 7). Unlike gDCC and gDBC, gDFC does not undergo electrocyclic ring-opening to the difluorohalide, but instead isomerises via a 1,3-diradical transition state. Mechanically induced ring-opening was found to promote the formation of the *cis*-isomer, which has a shorter end-to-end distance than the *trans*, leading to the overall contraction. In this sense, gDFC is less useful as a mechanophore for covalent bond formation, but its mechanochemical reactivity is nonetheless remarkable. When synthesised, a *cis*:*trans* ratio of 1:1.2 is obtained, which increases to 1:2.6 when heated overnight at 210°C, consistent with the 1 kcal/mol difference in stability, which has been measured previously at 275°C. By contrast, when a gDFC PB polymer is sonicated for less than 1 h, the *cis*:*trans* ratio becomes 3.5:1, indicating that mechanical force favours the kinetically and thermodynamically less stable *cis* isomer, as reported in a seminal paper of the field in 2010 [49]. This phenomenon is thought to result from a mechanically induced inversion of the potential energy surface, as revealed in molecular dynamics simulations. On the force-modified potential energy surface, the s-trans/s-trans diradical transition state is an energy minimum, when on the force-free surface it is a saddle point. Upon releasing the force, the mechanically-produced diradical preferentially forms the *cis* isomer of gDFC by disrotatory ring-closing, which was observed to occur within 500 fs in the force-free simulation; no ring closure under mechanical force was observed on the timescale of these simulations (1 ps). Indeed, the 1,3-diradical proved to be sufficiently stabilised by mechanical force to undergo a radical addition to a fluorescent coumarin tag.

The mechanism of gDFC ring-opening was further clarified in a more recent study of this mechanophore by SMFS. As with the gDCC and gDBC mechanophores, it proved possible to follow the chain extension as the gDFCs opened, with the *cis*-gDFC undergoing a disrotatory ring-opening at a force of 1.29 nN and the *trans*-gDFC a conrotatory ring-opening at 1.82 nN, both via the same s-trans/s-trans transition state [41]. In this context, it is interesting to compare

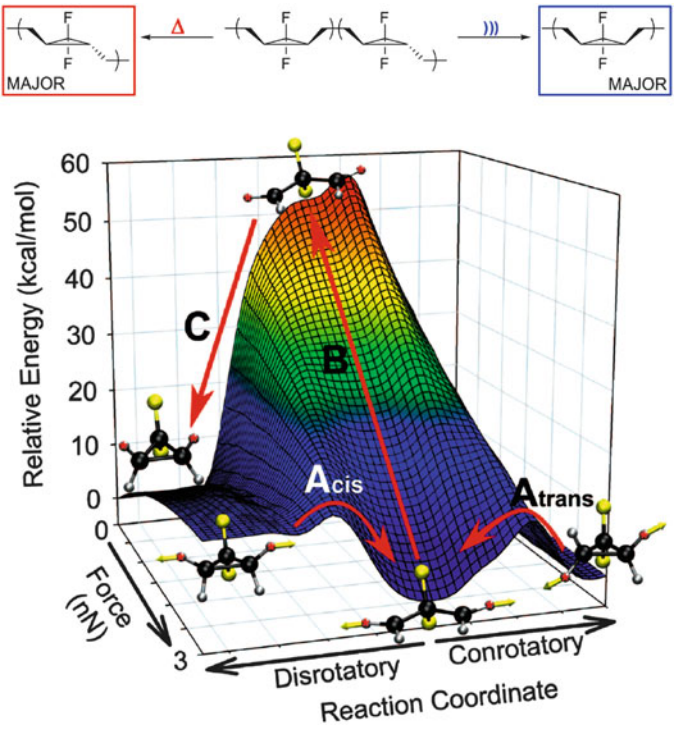

Fig. 7 Mechanochemical reactivity of gDFC. At high forces, *cis*- and *trans*-gDFC open to form a 1,3-diradical intermediate (A_{cis} and A_{trans} respectively). Upon releasing the force (*B*), the intermediate becomes a high energy transition state which forms the *cis* isomer via the thermally allowed disrotatory ring-closing. Conrotatory ring closure to give the *trans* isomer (*C*) is disfavoured by a small energy barrier

the derived force-induced barriers to ring-opening of the gDFC and the gDCC. Whilst the *trans*-gDCC, similar to the *trans*-gDFC, was also found to undergo the disallowed conrotatory ring-opening, the force barrier was much greater relative to that of the allowed disrotatory ring-opening of its *cis*-counterpart than for the gDFC. This can be thought intuitively as a consequence of the greater propenyl cation character in the transition state of gDCC ring-opening, leading to a more pronounced preference for the favoured disrotatory process.

Furthermore, the mechanical reactivity of gDFC was found to depend upon the microstructure of the polymer in which the mechanophore finds itself [50]. The first indications of this more complex behaviour were that the extent of gDFC isomerisation to the *cis* isomer appeared to be inversely dependent upon the gDFC content of the polymer; the mechanical reactivity of gDCCs and gDBCs are by contrast independent of gDHC content. To account for this, it was proposed that activation of gDFCs directly adjacent to one another leads to the formation of a tetraradical that can undergo a radical elimination reaction, thereby cleaving the polymer backbone. The gDFCs remaining in the two cleaved segments are much less susceptible to activation and hence a lower overall degree of activation is

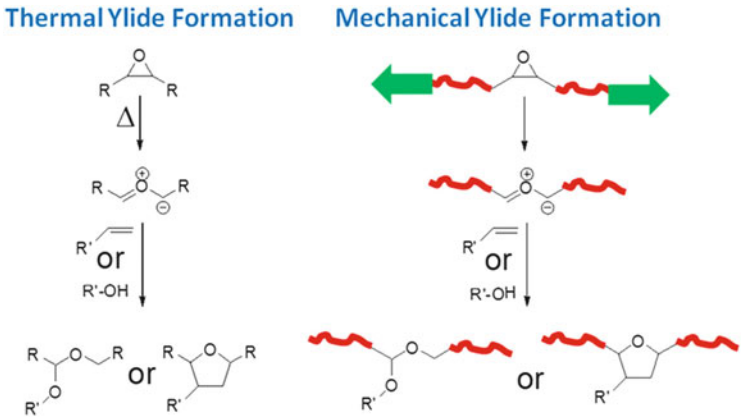

Fig. 8 Sonochemical generation of reactive ylides from epoxides. Reprinted with permission from [51] (Copyright © American Chemical Society 2012)

observed within one scission cycle. This hypothesis was confirmed by synthesising a polymer in which a gDFC was present on every third repeat unit so that none of the gDFCs were adjacent to each other; as expected, this polymer showed a much higher activation than the random polymer with the same gDFC content.

More recently, the efforts of the Craig group to develop mechanophores with latent bond-forming reactivity have extended to encompass a wide range of chemical functionalities, including epoxides, perfluorocyclobutanes and bicycloheptanes. Similar to the gDHCs, epoxides undergo thermally induced electrocyclic ring-opening to give a reactive intermediate and can be readily incorporated in large numbers within a polymer backbone. In this case, a carbonyl ylide is formed which can react further, for example, with protic solvents or dipolarophiles in a dipolar cycloaddition reaction. The force-free barrier to ring-opening is somewhat higher than for the gDHCs (65 vs 35–40 kcal/mol), although this is amenable to tuning with substituents on the epoxide. Epoxidised polynorbornene underwent the predicted ring-opening upon sonication, giving carbonyl ylides which were trapped by alcohols and a dipolarophile, dimethyl acetylenedicarboxylate, and a net isomerisation of *cis* to *trans* epoxide was observed [51]. Interestingly, epoxidised polybutadiene showed no mechanical reactivity, underlining the importance of not just the mechanophore itself but the polymer backbone in determining mechanochemical reactivity (Fig. 8) [52].

Perfluorocyclobutane groups were also of interest in the context of polymers capable of regeneration, although in this case the polymer reforms only upon heating to elevated temperature, as opposed to in situ under mechanical force, as shown for the gDBCs. On sonicating perfluorocyclobutane-containing polymers, trifluorovinylethers were found to form from the cycloreversion of the cyclobutanes, in a decomposition process significantly different under thermal activation [53]. The perfluorocyclobutane groups can be regenerated by heating the polymer solution to above 150°C (Fig. 9).

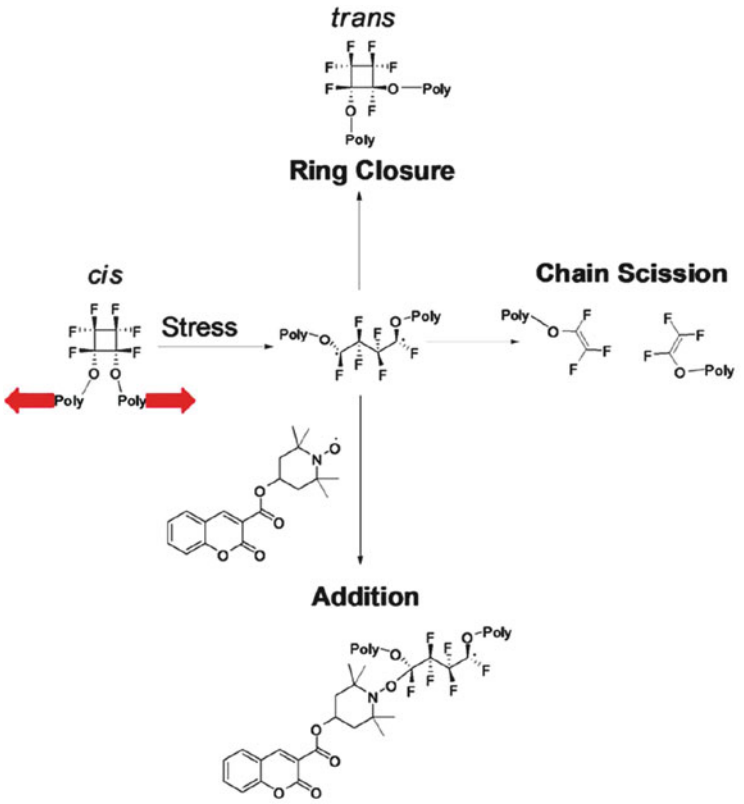

Fig. 9 Sonochemically induced scission and thermal remending of perfluorocyclobutane-containing polymers. Reprinted with permission from [53] (Copyright © American Chemical Society 2011)

Finally, two detailed studies on bicyclo[3.2.0]-heptanes emerged from the Craig group in 2013 and 2014 [10, 54] (Fig. 10). These mechanophores undergo cycloreversion of the cyclobutane ring and, similar to the gDHCs, are non-scissile, initially elongating on activation rather than breaking. Whilst a relatively new addition to the field, the BCH mechanophore holds promise in the area of mechanically induced bond creation and can potentially improve upon the gDHC-based systems. The elongation upon scission is much greater than with the gDHC (7 Å), giving greater stress relief and, in contrast to the gDCC and gDBC mechanophores, the BCH can be reformed upon photoactivation. The α,-β-unsaturated esters formed have been shown to react subsequently via conjugate addition with thiols to form cross-linked polymer networks upon sonication. Through examining the products formed from a series of stereoisomers and substituted derivatives, it was inferred that the cycloreversion proceeds via a 1,4-diradical intermediate, rather than a concerted mechanism as under thermal activation. In combination with their accessible synthesis and ability to be

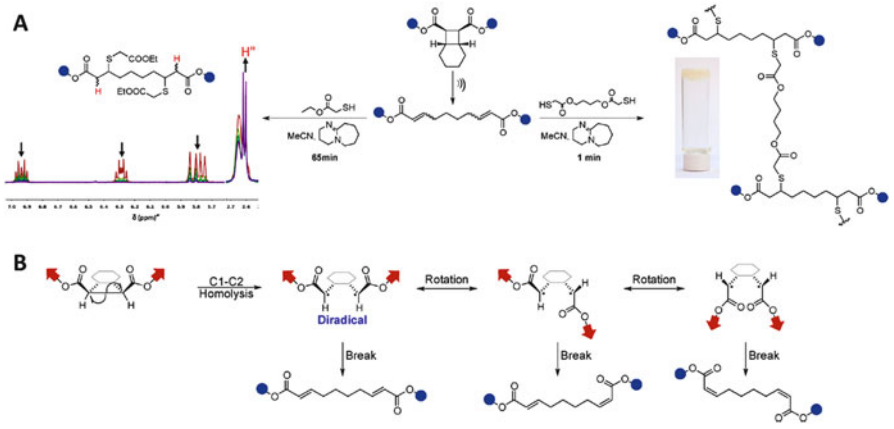

Fig. 10 Towards new mechanophores for bond creation: the bicyclo[3.2.0]-heptanes. The alpha, beta-unsaturated ester formed from mechanically induced [2+2] cycloreversion can undergo subsequently react with nucleophiles (**a**), such as thiols to form functionalised copolymers (*left*) and cross-linked gels (*right*). Analysis of the stereoisomerism of the products (**b**) supported a stepwise mechanism for the ring-opening via a 1,4-diradical intermediate

plentifully incorporated in polymer backbones, these show great potential as mechanophores for constructive force-induced bond-forming.

4 Mechanical Release of Small Molecules in Polymer Matrices

The proliferation of mechanophores capable of producing useful reactive intermediates within the polymer main chain has prompted others to investigate different modes of chemically productive mechanical reactivity. One such mode is the mechanically-induced release of small molecules, a recent addition to the mechanochemistry field. Mechanophores are incorporated into elastomeric networks and an applied force leads to conformational changes and subsequent scission of bonds that are not part of the polymer backbone, whilst maintaining the overall mechanical integrity of the polymer matrix [55]. The range of accessible reactivities remains limited, but researchers in this fledgling area are starting to make use of the small molecule products for further reactions, including polymerisation. This type of activation displays the potential for applications in mechanochemical catalysis, mapping deformations and damage in polymer networks and self-healing or self-reinforcing elastomers [56].

The first example of this type of activation was the mechanochemical generation of an acid, developed by Diesendruck et al. Inspired by Craig's gDHC system, they incorporated *gem*-dichlorotetrahydro cyclopropanated indene into polymethyl acrylate matrix (PMA) and showed that compression resulted in ring-opening of

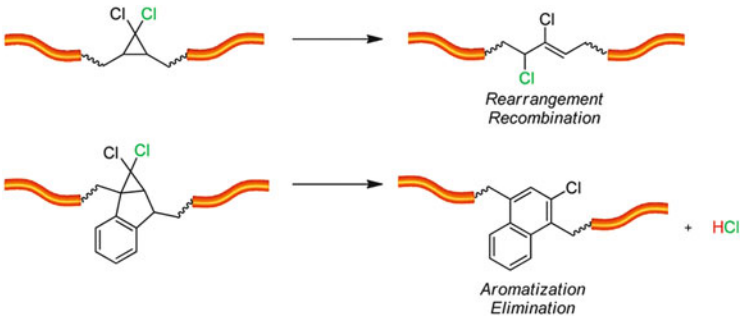

Fig. 11 Potential indole-based mechanocatalyst for acid generation. Reprinted with permission from [57] (Copyright © American Chemical Society 2012)

cyclopropane to give the elimination product 2-chloronaphthalene, with the release of HCl [57] (Fig. 11) Calorimetric analysis of the sample before and after compression demonstrated that up to 20% mechanophore conversion was achieved at a load of 352 MPa. Control polymer in which the mechanophore was not covalently incorporated into the PMA matrix showed 6% conversion under the same conditions. Although a significantly high thermal background reaction observed with control polymer might limit its practical applications, this work represented an important step towards the realisation of autonomous self-healing materials, as the mechanogenerated acid could be used to catalyse cross-linking reactions in situ, thereby allowing the material to respond actively and constructively to mechanical force

Reports have also emerged from the Boydston group describing the flex, or bond-bending, activation of an oxanorbornadiene, a Diels–Alder adduct of furan and dimethyl acetylenedicarboxylate [58]. They incorporated the mechanophore into poly(methyl acrylate) (PMA) matrix and showed that the furan derivative could be released under stress applied to the bulk polymer (Fig. 12). The main-chain alkene moieties are thus converted into alkynes, not only preserving the overall macromolecular structure but making bonds in the main chain shorter and stronger following the application of mechanical force. After compression, the polymer was soaked in dichloromethane and the small molecules released mechanically diffused out of the matrix; they could then be identified by and monitored with GC–MS and NMR. However, the forces required to activate the mechanophore caused failure in the PMA matrix, limiting the number of loading cycles. In a second publication, the authors partly addressed this issue by incorporating the same mechanophore in a segmented PU matrix, which required lower stress loadings for successive mechanophore activation [59]. Nevertheless, only a maximum of 7% mechanophore activation could be reached after 15 compression cycles, which was attributed to random scission of the chemical crosslinks and the destruction of physical crosslinks within the hard domains of the segmented PU matrix.

Finally, in a significant departure from the more traditional pericyclic-based mechanophores, colleagues in the Moore group were able to induce mechanically the heterolytic depolymerisation of cyclic and linear poly(*ortho*-phthalaldehyde)

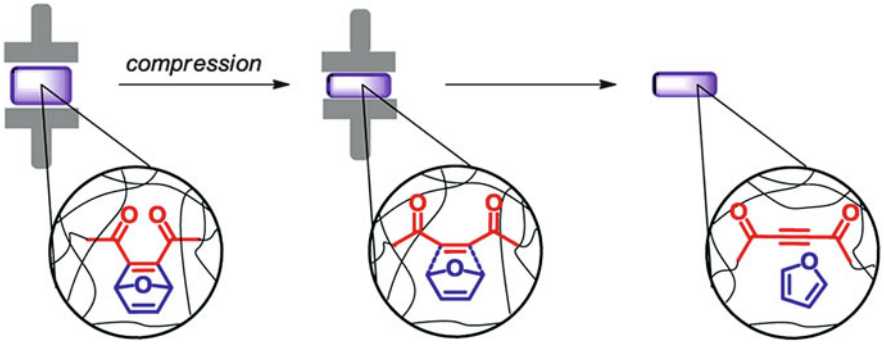

Fig. 12 Solid state mechanoactivation of oxanorbornadiene, producing an alkyne in the polymer backbone and releasing a small molecule furan. Reprinted with permission from [58] (Copyright © American Chemical Society 2013)

(PPA) to its constituent monomers upon sonication in dilute solution, constituting small molecule release en masse [60]. The heterolytic nature of the scission was confirmed by sonicating linear PPA in the presence of nucleophilic and electrophilic trapping agents, which reduced the rate of polymer degradation, and was further supported by molecular dynamics simulations. Crucially, the reactive *ortho*-phthalaldehyde (OPA) monomers could then be repolymerised with a chemical initiator, regenerating PPA. The system represents an exciting reimagining of the mechanically induced remodelling concept, inspired in part by the recycling of monomeric building blocks such as amino acids, carbohydrates and nucleic acids in nature. Nevertheless, whilst ground-breaking as a proof-of-principle, the present design seems unlikely to find general application, primarily because PPA exhibits limited thermal and chemical stability. The sensitivity of the polymerisation to the electronics of the monomer also constrains the possibilities for further modification and functionalisation, although others in collaboration with the Moore group are starting to explore this avenue of enquiry.

5 Mechanochemical Catalysis

Mechanocatalysts are catalysts of which the activity or specificity is modified under the influence of mechanical force. Two distinct modes of activation can be envisioned: steric modification or unblocking of active sites. In steric activation, the activity of the catalyst is modified by a change in the steric environment of the active site, e.g. by changing the relative position of catalytically active groups forming the active site or by changing the configuration of the binding site.

A second class of mechanocatalysts is activated by separating two interacting sites (Lewis acid–Lewis base), at least one of which has catalytic activity. In the current chapter we discuss the nature of biological and the design of synthetic

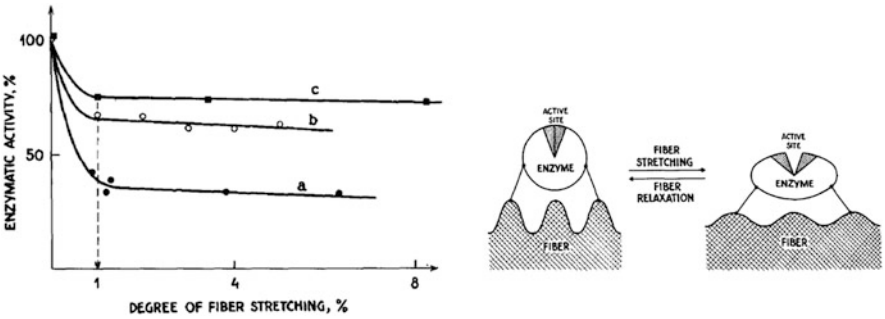

Fig. 13 Dependence of relative activity of enzymes covalently bound to different elastic supports on the degree of stretching of the supports. (*a*) chymotrypsin on protein coated nylon fibre; (*b*) trypsin on human hair; (*c*) chymotrypsin on viscose (cellulose) fibre. Schematic representation of the deformation of enzyme bound to a mechanically stretched elastic fibre. Reprinted with permission from [62] (Copyright © Elsevier 1976)

mechanocatalysts, present recent work on mechanical catalyst activation, and propose potential fields of application for this fascinating class of responsive systems.

Proteins fold in many different conformations which change the activity of enzymes associated with them. The free energy difference between different folded states is usually much lower than the energy of a covalent bond and this makes it possible to 'force' a protein into a different conformation and alter its enzymatic activity, even at low stress [61]. Klibanov et al. have investigated the effect of mechanical stretching on enzyme activity by covalently attaching chymotrypsin and trypsin to nylon, human hair and viscose fibres [62]. They showed that stretching of these polymer supports induced a deformation on protein molecules and thus a threefold decrease in enzyme activity. Upon relaxation, the initial level of activity was reached, instantaneously revealing that enzyme activity can be altered reversibly by a stretch-relax process (Fig. 13).

In contrast to enzymes, synthetic catalysts have hardly been explored for the possibility of modifying their catalytic activity by changing the steric environment of the active site. Only very recently, research was published that investigated the effect of a photochemical switch coupled to a chelating bisphosphine on the activity profile of the catalyst. The photochemical switch, a biindane, changes the bite angle of the chelating ligand, and influences the enantioselectivity of reactions catalysed by Pd complexes of the photoresponsive ligand. It was found that the effect of switching was largest for Heck arylation reactions (Fig. 14) [63].

However, the most common approach to mechanocatalysis in synthetic systems has been to activate the catalysts by modifying electronic properties. Catalysts that are in a latent state because of pairing of acidic and basic sites are well known for their capability to be activated thermally, and are employed in a number of different reactions. Some of the most striking examples of this kind of catalysts are *N*-heterocyclic carbenes (NHCs) [64]. These Lewis bases have been used as catalysts in various organic transformations, including condensation, 1,2- and 1,4-addition,

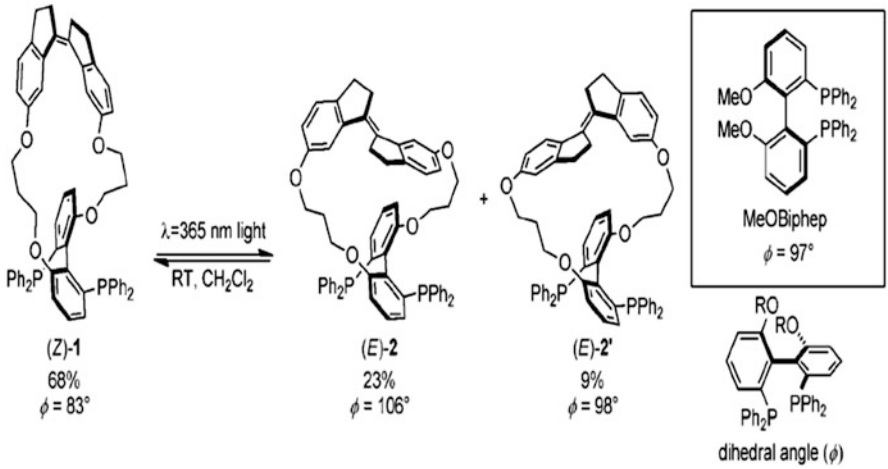

Fig. 14 Photomechanoactivation of a palladium catalyst for Heck arylation. Reprinted with permission from [63] (Copyright © Wiley VCH 2014)

transesterification and ring-opening reactions [65, 66]. Because of their nucleophilicity they show high reactivity towards various substrates but they can also be masked in thermally labile precursors [67]. NHC−metal complexes have been applied as thermally latent catalysts in the preparation of a number of polymers, such as poly(urethane), poly(methyl methacrylate), poly(caprolactone) and poly (amide) [68–72].

By their nature, latent transition metal (TM) catalysts [73, 74] with strongly bound ligands can be adapted to form mechanocatalysts by providing the ligands with 'handles' to transfer mechanical force. These handles can be (linear) polymer chains, which provide drag in a viscous system that is sheared or undergoes elongational strain, or the ligands can be connected to a polymer network in an elastic system.

Much of the work done in recent years on polymer mechanochemistry has made use of the high elongational strain rates observed around collapsing cavitation bubbles in sonicated solutions, as outlined in the section on mechanoluminescence [27]. In addition to the distinctive features of sonochemically-induced mechanical reactivity described above, further attention needs to be paid to the sonication conditions in the case of mechanochemical catalysis, because catalyst lifetime and turnover number are reduced by sonochemical byproducts. Implosion of cavitation bubbles is essentially an adiabatic process which leads to formation of local hotspots within the bubble in which temperature and pressure increases drastically. The content of cavitation bubbles pyrolyses under these extreme conditions and results in formation of reactive species, such as radicals and persistent secondary byproducts; acidic byproducts may also form from the degradation of the substrates [75]. Chemical impurities deactivate the reactive catalyst partially if not completely. Recent studies in our group have shown that heat capacity of gas

dissolved in solution influences the formation of sonochemical impurities. For instance, use of methane (CH_4) instead of argon (Ar) decreases the production of radicals significantly [76]. Higher heat capacity and possible energy dissipation produced by increased degrees of freedom in CH_4, compared to those of monoatomic Ar, decrease the temperature in hotspots and suppress reactive impurity formation. On the other hand, solubility of the saturation gas may also have a negative influence on ultrasound induced mechanical chain scission. A gas with higher solubility decreases the intensity of cavitation effects and so leads to lower scission rates. The selection of saturation gas is crucial for both scission rate and sonochemical impurity formation [75]. Therefore, the mechanochemical catalysis should be performed under a gas which increases the lifetime of the active catalyst, at the same time still leading to strong cavitation.

Groote et al. investigated mechanochemical scission of metal–ligand bonds in supramolecular polymer complexes by ultrasound using viscosity measurements and molecular dynamics simulations (MD) combined with constrained geometry optimisation calculations (COGEF) [77]. Calculations indicated that the force required to break the metal−ligand bond is between 400 and 500 pN on the 10 ps timescale of the simulation; a reduction of 15–25% in this value is thought to be appropriate to account for the longer (microsecond) timescale of sonication-induced scission. This value is much lower than the force typically required to break covalent bonds (several nN), confirming that coordination bonds, weaker than covalent bonds on polymer backbone, break more easily, resulting in lower M_{lim} for supramolecular polymers compared to their covalent counterparts.

Recently in the Sijbesma group, high-molecular-weight linear coordination polymers of diphenylphosphine telechelic polytetrahydrofuran with palladium (II) dichloride were developed [3]. Molecular weights of these polymers could be altered reversibly by ultrasound and it has been shown that polytetrahydrofuran chains remain intact during sonication [78]. This implies that only the reversible palladium–phosphorus bonds are broken and coordinatively unsaturated palladium complexes were produced by the application of mechanical forces on these coordination polymers [79]. Furthermore, polymers which include both Pd^{II} and Pt^{II} were sonicated and it was shown that force selectively breaks the weaker Pd–phosphine bonds which were randomly distributed along the polymer backbone [80].

Following the work on metal–phosphine coordination polymers, the group started investigating mechanical dissociation of silver(I)-coordination complexes with *N*-heterocyclic carbene (NHC) functionalised polymers [81]. It has been shown that polymers with an $Ag(NHC)_2$ coordination complex in the pTHF main chain have significantly lower M_{lim} values. pTHF has an M_{lim} around 40 kg mol^{-1} whereas the M_{lim} for $Ag(NHC\text{-}pTHF)_2PF_6$ is lower than 13 kg mol^{-1} [75]. Thus external force selectively breaks Ag–NHC bonds and yields free NHC, which was used to catalyse the transesterification of benzyl alcohol and vinyl acetate under sonication [82, 83] (Fig. 15). The complex form of the carbene displayed no activity, proving the latency of the catalyst. Control experiments confirmed that the catalyst was activated mechanically.

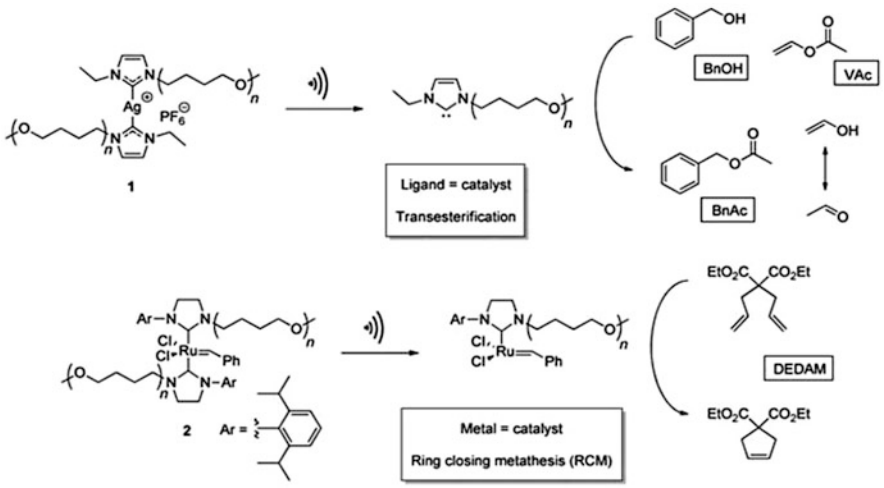

Fig. 15 Mechanically activated catalysts and the corresponding catalytic reactions studied within the Sijbesma group

After successful application of the concept of mechanocatalysis, its generality was tested with bis-NHC ruthenium–alkylidene complex [84]. Mechanistic studies revealed that ligand dissociation is a crucial step in catalyst activation for Ru mediated olefin metathesis reactions to form coordinatively unsaturated reactive Ru species [85]. Among several effective Ru catalysts, bis-NHC ruthenium–alkylidene complexes were shown to be latent at ambient temperature because dissociation of the strong Ru–NHC bond requires elevated temperatures [86]. Piermattei showed that Ru catalysts with pTHF chains attached bis NHC ligands resulted in a latent metathesis catalyst that can be activated by mechanical force [82]. Sonicating a solution of diethyl diallylmalonate (DEDAM) in the presence of mechanically responsive Ru catalysts (36 kg mol^{-1}) resulted in approximately 20% conversion after 1 h (Fig. 15). Control experiments were conducted to prove that catalyst activation is mechanical rather than thermal in nature. A lower MW analogue of the catalyst (18 kg mol^{-1}) showed lower activity because of the slower chain scission rate that decreased the amount of active catalyst formed in the timespan of sonication. Replacing polymer actuators by butyl chains attached to NHC resulted in mechanically silent latent catalysts, showing less than 0.2% conversion in the presence of DEDAM after 1 h of sonication.

In a later study, bis-NHC ruthenium–alkylidene complex was activated under compressive strain [87] (Fig. 16). In order to initiate Ru-mediated polymerisation of norbornene in solid state, polymer catalyst (34 kg mol^{-1}) and a norbornene monomer were incorporated in a high molecular weight poly(tetrahydrofuran) (pTHF) matrix (Mn = 170 kDa, PDI = 1.3) which provided the physical cross-linking through the crystalline domains and allowed macroscopic forces to be transferred to the metal–ligand bonds. Consecutive compressions showed that up to 25% of norbornene monomer was polymerised after five loading cycles.

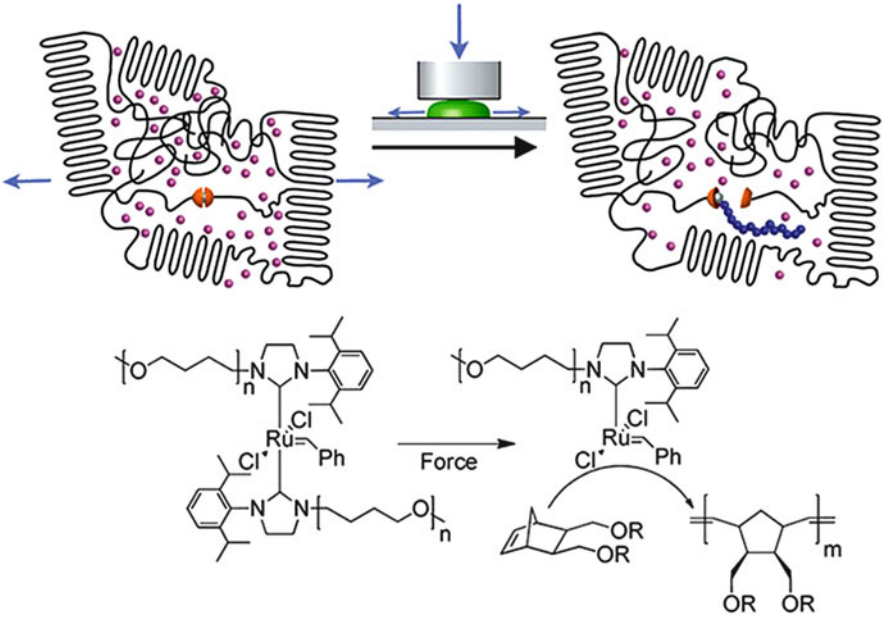

Fig. 16 Mechanoactivation of latent ruthenium catalyst in the solid state, initiating in situ polymerisation of norbornene monomer in response to stress. Reprinted with permission from [87] (Copyright © American Chemical Society 2013)

6 Conclusion

The recent revival of polymer mechanochemistry has resulted in a variety of highly innovative concepts for reporting and repairing bond scission in polymers. In the current chapter we have tried to summarise the most important work in this area. Most of the published papers in this field provide 'proofs of concept', and need further elaboration before mechanochemical processes can begin to play a substantial role in improving polymeric material. By providing a treasure trove of highly stimulating ideas, these papers witness the potential of the field to provide the tools for developing smart, responsive materials that may eventually incorporate the capability to actively restore mechanical properties by mechanically triggered molecular scale repair.

References

1. Beyer MK, Clausen-Schaumann H (2005) Chem Rev 105:2921
2. Potisek SL, Davis DA, Sottos NR, White SR, Moore JS (2007) J Am Chem Soc 129:13808
3. Paulusse JMJ, Sijbesma RP (2004) Angew Chem Int Ed 43:4460
4. Hickenboth CR, Moore JS, White SR, Sottos NR, Baudry J, Wilson SR (2007) Nature 446:423

5. Hermes M, Boulatov R (2011) J Am Chem Soc 133:20044
6. Konda SSM, Brantley JN, Varghese BT, Wiggins KM, Bielawski CW, Makarov DE (2013) J Am Chem Soc 135:12722
7. Huang Z, Boulatov R (2011) Chem Soc Rev 40:2359
8. Lenhardt JM, Black AL, Craig SL (2009) J Am Chem Soc 131:10818
9. Gossweiler GR, Hewage GB, Soriano G, Wang Q, Welshofer GW, Zhao X, Craig SL (2014) ACS Macro Lett 3:216
10. Kean ZS, Black Ramirez AL, Yan Y, Craig SL (2012) J Am Chem Soc 134:12939
11. Chen Y, Spiering AJH, Karthikeyan S, Peters GWM, Meijer EW, Sijbesma RP (2012) Nat Chem 4:559
12. Davis DA, Hamilton A, Yang J, Cremar LD, Van Gough D, Potisek SL, Ong MT, Braun PV, Martínez TJ, White SR, Moore JS, Sottos NR (2009) Nature 459:68
13. Kingsbury CM, May PA, Davis DA, White SR, Moore JS, Sottos NR (2011) J Mater Chem 21:8381
14. Lee CK, Davis DA, White SR, Moore JS, Sottos NR, Braun PV (2010) J Am Chem Soc 132:16107
15. Fang X, Zhang H, Chen Y, Lin Y, Xu Y, Weng W (2013) Macromolecules 46:6566
16. Beiermann BA, Davis DA, Kramer SLB, Moore JS, Sottos NR, White SR (2011) J Mater Chem 21:8443
17. Beiermann BA, Kramer SLB, Moore JS, White SR, Sottos NR (2012) ACS Macro Lett 1:163
18. Beiermann BA, Kramer SLB, May PA, Moore JS, White SR, Sottos NR (2014) Adv Funct Mater 24:1529
19. Degen CM, May PA, Moore JS, White SR, Sottos NR (2013) Macromolecules 46:8917
20. Lee CK, Diesendruck CE, Lu E, Pickett AN, May PA, Moore JS, Braun PV (2014) Macromolecules 47:2690
21. Grady ME, Beiermann BA, Moore JS, Sottos NR (2014) ACS Appl Mater Interfaces 6:5350
22. Wang Q, Gossweiler GR, Craig SL, Zhao X (2014) Nat Commun 5:4899
23. Lee CK, Beiermann BA, Silberstein MN, Wang J, Moore JS, Sottos NR, Braun PV (2013) Macromolecules 46:3746
24. Celestine A-DN, Beiermann BA, May PA, Moore JS, Sottos NR, White SR (2014) Polymer 55:4164
25. Hong G, Zhang H, Lin Y, Chen Y, Xu Y, Weng W, Xia H (2013) Macromolecules 46:8649
26. Wieringa JH, Strating J, Wynberg H, Adam W (1972) Tetrahedron Lett 13:169
27. Caruso MM, Davis DA, Shen Q, Odom SA, Sottos NR, White SR, Moore JS (2009) Chem Rev 109:5755
28. Kuijpers MWA, Iedema PD, Kemmere MF, Keurentjes JTF (2004) Polymer 45:6461
29. Odell JA, Muller AJ, Narh KA, Keller A (1990) Macromolecules 23:3092
30. Ribas-Arino J, Shiga M, Marx D (2009) Chem Eur J 15:13331
31. Encina MV, Lissi E, Sarasúa M, Gargallo L, Radic D (1980) J Polym Sci Polym Lett Ed 18:757
32. Ducrot E, Chen Y, Bulters M, Sijbesma RP, Creton C (2014) Science 344:186
33. Kean ZS, Hawk JL, Lin S, Zhao X, Sijbesma RP, Craig SL (2014) Adv Mater 26:6013
34. Chen Y, Sijbesma RP (2014) Macromolecules 47:3797
35. Clough JM, Sijbesma RP (2014) ChemPhysChem 15:3565
36. Scaiano J (1989) In: Scaiano J (ed) CRC handbook of organic photochemistry, vol 2. CRC, Boca Raton, pp 271–327
37. Turro NJ, Devaquet A (1975) J Am Chem Soc 97:3859
38. De Vico L, Liu Y-J, Krogh JW, Lindh R (2007) J Phys Chem A 111:8013
39. Farahani P, Roca-Sanjuán D, Zapata F, Lindh R (2013) J Chem Theory Comput 9:5404
40. Kryger MJ, Ong MT, Odom SA, Sottos NR, White SR, Martinez TJ, Moore JS (2010) J Am Chem Soc 132:4558
41. Wang J, Kouznetsova TB, Niu Z, Ong MT, Klukovich HM, Rheingold AL, Martinez TJ, Craig SL (2015) Nat Chem. doi:10.1038/nchem.2185, advance online publication
42. Kryger MJ, Munaretto AM, Moore JS (2011) J Am Chem Soc 133:18992

43. Ramirez ALB, Kean ZS, Orlicki JA, Champhekar M, Elsakr SM, Krause WE, Craig SL (2013) Nat Chem 5:757
44. Black Ramirez AL, Ogle JW, Schmitt AL, Lenhardt JM, Cashion MP, Mahanthappa MK, Craig SL (2012) ACS Macro Lett 1:23
45. Wu D, Lenhardt JM, Black AL, Akhremitchev BB, Craig SL (2010) J Am Chem Soc 132:15936
46. Black AL, Orlicki JA, Craig SL (2011) J Mater Chem 21:8460
47. Wang J, Kouznetsova TB, Kean ZS, Fan L, Mar BD, Martínez TJ, Craig SL (2014) J Am Chem Soc 136:15162
48. Lenhardt JM, Black AL, Beiermann BA, Steinberg BD, Rahman F, Samborski T, Elsakr J, Moore JS, Sottos NR, Craig SL (2011) J Mater Chem 21:8454
49. Lenhardt JM, Ong MT, Choe R, Evenhuis CR, Martinez TJ, Craig SL (2010) Science 329:1057
50. Lenhardt JM, Ogle JW, Ong MT, Choe R, Martinez TJ, Craig SL (2011) J Am Chem Soc 133:3222
51. Klukovich HM, Kean ZS, Ramirez ALB, Lenhardt JM, Lin J, Hu X, Craig SL (2012) J Am Chem Soc 134:9577
52. Klukovich HM, Kouznetsova TB, Kean ZS, Lenhardt JM, Craig SL (2012) Nat Chem 5:110
53. Klukovich HM, Kean ZS, Iacono ST, Craig SL (2011) J Am Chem Soc 133:17882
54. Kean ZS, Niu Z, Hewage GB, Rheingold AL, Craig SL (2013) J Am Chem Soc 135:13598
55. Sottos NR (2014) Nat Chem 6:381
56. Wiggins KM, Brantley JN, Bielawski CW (2013) Chem Soc Rev 42:7130
57. Diesendruck CE, Steinberg BD, Sugai N, Silberstein MN, Sottos NR, White SR, Braun PV, Moore JS (2012) J Am Chem Soc 134:12446
58. Larsen MB, Boydston AJ (2013) J Am Chem Soc 135:8189
59. Larsen MB, Boydston AJ (2014) J Am Chem Soc 136:1276
60. Diesendruck CE, Peterson GI, Kulik HJ, Kaitz JA, Mar BD, May PA, White SR, Martínez TJ, Boydston AJ, Moore JS (2014) Nat Chem 6:623
61. Zocchi G (2009) Annu Rev Biophys 38:75
62. Klibanov AM, Samokhin GP, Martinek K, Berezin IV (1976) Biochim Biophys Acta BBA Enzymol 438:1
63. Kean ZS, Akbulatov S, Tian Y, Widenhoefer RA, Boulatov R, Craig SL (2014) Angew Chem Int Ed 53:14508
64. Fèvre M, Pinaud J, Gnanou Y, Vignolle J, Taton D (2013) Chem Soc Rev 42:2142
65. Marion N, Díez-González S, Nolan SP (2007) Angew Chem Int Ed 46:2988
66. Hopkinson MN, Richter C, Schedler M, Glorius F (2014) Nature 510:485
67. Moore JL, Rovis T (2010) Top Curr Chem 291:77
68. Bantu B, Pawar GM, Decker U, Wurst K, Schmidt AM, Buchmeiser MR (2009) Chem Eur J 15:3103
69. Naumann S, Schmidt FG, Schowner R, Frey W, Buchmeiser MR (2013) Polym Chem 4:2731
70. Naumann S, Schmidt FG, Frey W, Buchmeiser MR (2013) Polym Chem 4:4172
71. Naumann S, Schmidt FG, Speiser M, Böhl M, Epple S, Bonten C, Buchmeiser MR (2013) Macromolecules 46:8426
72. Naumann S, Speiser M, Schowner R, Giebel E, Buchmeiser MR (2014) Macromolecules 47:4548
73. Kantchev EAB, O'Brien CJ, Organ MG (2007) Angew Chem Int Ed 46:2768
74. Monsaert S, Lozano Vila A, Drozdzak R, Van Der Voort P, Verpoort F (2009) Chem Soc Rev 38:3360
75. Rooze J, Groote R, Jakobs RTM, Sijbesma RP, van Iersel MM, Rebrov EV, Schouten JC, Keurentjes JTF (2011) J Phys Chem B 115:11038
76. Groote R, Jakobs RTM, Sijbesma RP (2012) ACS Macro Lett 1:1012
77. Groote R, Szyja BM, Pidko EA, Hensen EJM, Sijbesma RP (2011) Macromolecules 44:9187
78. Paulusse JMJ, Huijbers JPJ, Sijbesma RP (2005) Macromolecules 38:6290
79. Paulusse JMJ, Sijbesma RP (2006) J Polym Sci Part Polym Chem 44:5445

80. Paulusse JMJ, Sijbesma RP (2008) Chem Commun 37:4416
81. Karthikeyan S, Potisek SL, Piermattei A, Sijbesma RP (2008) J Am Chem Soc 130:14968
82. Piermattei A, Karthikeyan S, Sijbesma RP (2009) Nat Chem 1:133
83. Groote R, van Haandel L, Sijbesma RP (2012) J Polym Sci Part Polym Chem 50:4929
84. Jakobs RTM, Sijbesma RP (2012) Organometallics 31:2476
85. Dias EL, Nguyen ST, Grubbs RH (1997) J Am Chem Soc 119:3887
86. Van der Schaaf PA, Kolly R, Kirner H-J, Rime F, Mühlebach A, Hafner A (2000) J Organomet Chem 606:65
87. Jakobs RTM, Ma S, Sijbesma RP (2013) ACS Macro Lett 2:613

Top Curr Chem (2015) 369: 239–284
DOI: 10.1007/128_2014_623

Published online: 10 April 2015

Interplay Between Mechanochemistry and Sonochemistry

Pedro Cintas, Giancarlo Cravotto, Alessandro Barge, and Katia Martina

Abstract Ultrasonic irradiation-based mechanochemical strategies have recently been the subject of intensive investigation because of the advantages they offer. These include simplicity, energy savings and wide applicability. Traditional areas of sonoprocessing such as cleaning, efficient mixing and solid activation have been extended to both macromolecular and micro/nanostructures, some of which are biologically significant, ultrasound-responsive actuators and crystal design, among others. Unlike conventional mechanochemical protocols, which require little solvent usage if any at all, mechanical (and chemical) effects promoted by ultrasound are observed in a liquid medium. Tensile forces, which share similarities with solid mechanochemistry, are generated by virtue of nonlinear effects, notably cavitation, when high-amplitude waves propagate in a fluid. This work aims to provide insight into some recent developments in the multifaceted field of sono-mechanochemistry using various examples that illustrate the role of ultrasonic activation, which is capable of boosting hitherto sterile transformations and inventing new crafts in applied chemistry. After a preliminary discussion of acoustics, which is intended to provide a mechanistic background, we mainly focus on experimental developments, while we often mention emerging science and occasionally delve into theoretical models and force simulations.

Keywords Cavitation · Mechanical effects · Mechanotransduction · Self-assembly · Streaming · Ultrasound-responsive systems

P. Cintas (✉)
Departamento de Química Orgánica e Inorgánica, Universidad de Extremadura, Avenida de Elvas s/n, 06006 Badajoz, Spain
e-mail: pecintas@unex.es

G. Cravotto (✉), A. Barge, and K. Martina
Dipartimento di Scienza e Tecnologia del Farmaco and NIS, Centre for Nanostructured Interfaces and Surfaces, University of Turin, Via P. Giuria 9, 10125 Turin, Italy
e-mail: giancarlo.cravotto@unito.it

Contents

1 Introduction: Sound and Energy

Sound is essentially mechanical energy. This simple assumption, well known by physicists and acousticians in particular, is however overlooked (if not ignored) by other scientists [1, 2]. A sound wave propagating in air or any other fluid is a compressional wave, which can be characterised by a series of properties such as frequency, pitch and intensity. The latter is the average power transmission per unit area perpendicular to the direction of the wave. The unit is the bel (B), although a unit which is ten times smaller, the decibel (dB) is commonly employed. Conversational speech has an intensity of ca. 60 dB at a distance of about 1 m from the mouth, while traffic in a noisy street can supply ca. 75–80 dB. The propagation of sound may be regarded as a form of transmission of energy through matter. Thus work is done (and hence energy is expanded) when a fluid is disturbed at a point. The reappearance of the disturbance (compression) at another point corresponds to energy transfer via wave propagation (sound has a longitudinal nature). Following on from the preceding statements, average energy transfer rate per unit time per unit area of the wave front is also the intensity. In practice it is expressed as the average flow of power per unit area, whose unit is the watt per square centimetre (W/cm^2). The lowest amount of sound energy humans can hear is about 10^{-20} J (or in other words, a minimum audible intensity of ca. 10^{-16} W/cm^2). The upper limit of sound intensity that can be generated is set by atmospheric pressure and such a wave would have an intensity of approximately 190 dB. Mathematical analysis shows that the intensity of a plane sound wave is given by

$$I = p^2{}_{\mathrm{emax}} / \, 2\rho_{\mathrm{o}} V,$$

in which $p_{\max}$ is the maximum excess pressure in the wave, ρ_{o} is the average (equilibrium) density of the medium and V is the sound velocity. It should be noted that this *expression is independent of frequency*. For dry air at 20°C and standard atmospheric pressure, the equilibrium density (ρ_{o}) is only 0.001205 g/cm^3

and $V = 344$ m/s. When such values are substituted into the above equation and then converted to W/cm^2, an intensity (I) of about 10^{-9} W/cm^2 results, or 70 dB above the minimum audible intensity. It should also be noted from the above equation that the intensity for given excess pressure depends on the medium and in particular on the ρ_oV product. The latter is the *specific acoustic resistance* of the medium for a plane wave. For water under standard conditions, $\rho_o V$ is ca. 3,800 times that for air. It takes an excess pressure ca. 60 times that for air to generate a comparable intensity.

Nonlinear effects, however, limit the maximum pressure that can be obtained. Sound waves of large amplitudes ultimately break into a shock with morphologies that deviate from a sinusoidal curve (see below).

The term sonochemistry indicates the use of sound waves to generate chemical and physical effects which can be harnessed in multiple applications (Fig. 1). Although such effects can be obtained at a wide range of frequencies, the word "sonochemical" is invariably linked to ultrasound, i.e. sound we cannot hear (typically above 20 kHz). Natural phenomena are good sources of both ultrasonic (e.g. animal communication or navigation) and infrasonic waves (such as earthquakes and tidal motion). Ultrasonics is currently of interest to lay people because of medical imaging, metal cleaning, industrial and dental drills and non-destructive material characterisation.

Although cavitational effects were first identified in the late 1890s and were subsequently modelled by Lord Raleigh, ultrasound was no more than a scientific curiosity until around 1910 [1, 3]. Technical interest grew during World War I after the successful development of piezoelectric transducers in early forms of sonar to detect submarines. The field of ultrasonics can be divided into two large domains: low-energy waves and high-energy waves. In the former, the amplitude (i.e. the height of the wave from its highest point to its lowest point) is low enough so that

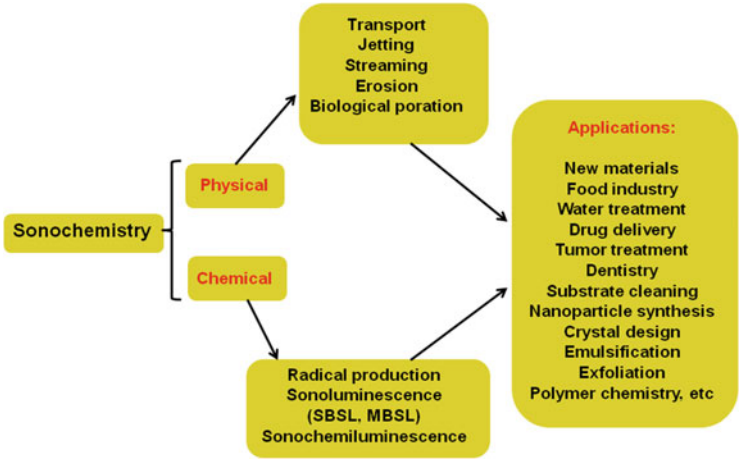

Fig. 1 Roadmap for sonochemical research

the wave is not appreciably distorted in passing through the medium, which remains largely unchanged except for a slight rise in temperature (caused by variation in intensity, directly proportional to wave amplitude). For high-energy waves, however, physical and chemical effects occur as the medium undergoes changes caused by the generation of significant mechanical stress and/or intense local heating. The interaction between high-energy sinusoidal waves and a medium causes distortion and leads to important nonlinear effects which fall into the admittedly difficult field of physical acoustics. Such effects include shock wave formation, acoustic streaming, cavitation and acoustic levitation. Both mechanical and chemical effects of interest and benefit to the molecular (or supramolecular) world arise from cavitation (Sect. 2). This quasi-adiabatic phenomenon entails the rapid nucleation, growth and implosion of microbubbles in a liquid which releases an enormous amount of kinetic energy to drive a chemical reaction to completion. This is different to a direct interaction between ultrasound and matter [4]. A more detailed description follows; pressure in a liquid falls (below zero) sharply as an ultrasonic wave of sufficient intensity (i.e. acoustic pressure) exceeds the normal average pressure in a liquid. The liquid then ruptures and generates small cavities which become unstable and collapse quickly. In the end, the gas entrapped within the cavity is highly compressed (hydrodynamic models point to several hundreds of atmospheres and temperatures as high as 5,000 K). Such high pressures are relieved by the accompanying radiation of shock waves. As already mentioned, shock waves are a nonlinear effect which arise from explosions (e.g. cavitational collapse) or which are emitted from an object moving faster than sound.

Bubble collapse generates a disturbance which starts out with a sinusoidal curve, given by a linear equation, but soon develops into a sawtooth or triangular curve when excess pressure is plotted vs distance in the direction of wave propagation (Sect. 2). This wave shows discontinuities in pressure, density and flow velocity, which all become large changes over very small liquid intervals (about 10^{-4} cm). As a result, the discontinuities travel through the medium faster than the ambient acoustic velocity. Mechanical effects thus caused by shock waves, liquid jets and shear forces in the bulk medium and bubble vicinity result in enhanced mass and energy transfer, particle size reduction, liquid emulsification and surface activation. Purely chemical effects, such as molecular sonolysis, which leads to discrete radicals or excited species, polymer rupture and changes in solvation and ligand-metal coordination, mainly occur inside the bubbles (so long as reagents possess sufficient volatility) or at the bubble interface. Given the complex nature of acoustic cavitation, both mechanical and chemical effects are juxtaposed and may work cooperatively (Fig. 2). Accordingly, a clear-cut dissection of mechanical effects is problematic, although they may be prevalent at suitable frequencies and intensities, as we see later.

This chapter aims to describe the mechanical bias of cavitational effects and how they are related to conventional mechanochemistry and force-induced physical fields in general. This subject has been well documented over the last decade [5–9], and particular attention has been paid to scenarios such as mechanically responsive polymers [10–12], micro- and nano-structured materials [13–15] and

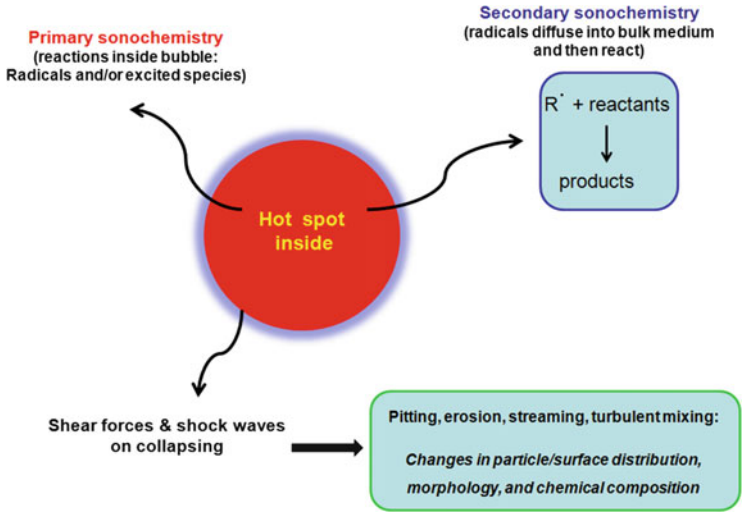

Fig. 2 Primary and secondary effects of acoustic cavitation

sonocrystallisation [16], which are all expected to have a major impact on the fabrication of novel and smart materials as well as the pharmaceutical industry. Although we briefly mention these past achievements, our goal is to focus on the aspects of sono-mechanochemistry that have been overlooked in recent thematic issues. We emphasise soft matter, both synthetic and biological, as well as the less-well-known, yet hugely promising, applications of acoustic fields, such as CO_2 capture and acoustically-driven micro- and nano-motors. Mechanistic frameworks should be investigated in these cases, although, unfortunately, space limitations prevent in-depth analysis. Our readers are referred to recent and comprehensive works such as those by Boulatov and associates [17] and Ribas-Arino/Marx [18]. They largely deal with attempts to understand chemical reactivity under mechanical loads in general and some models may certainly be extrapolated to ultrasound-induced forces. Much more futuristic areas, where a coupling of sound wave mechanical energy and nonlinear effects certainly provide both a technological and societal impact, can be found in the creation of acoustic metamaterials and phononic crystals [19–22]. These issues, however, lie beyond the bounds of this chapter.

2 Cavitation and Secondary Mechanical Effects

As mentioned in the introductory remarks, ultrasound waves transport both kinetic energy (particles of the medium oscillate and displace from their equilibrium position in the direction of propagation) and potential energy (fluid compression), as fluids can support negative pressure for short times. When a sufficiently large

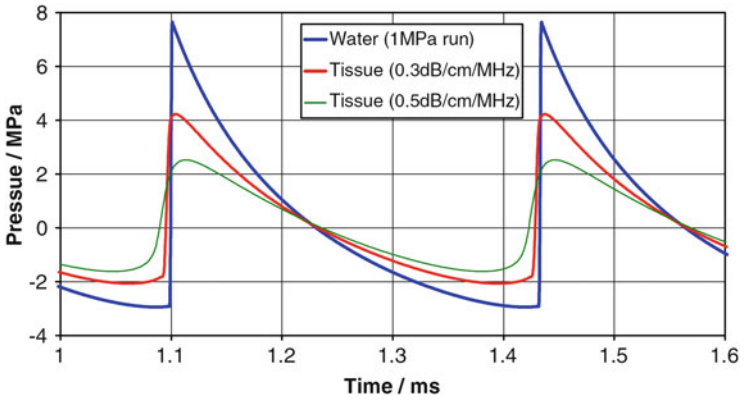

Fig. 3 Model predictions of shock waves from a transducer (3.0 MHz) focused at 70 mm, propagating in water and homogeneous tissues at different sound attenuation values. The average amplitude at the face of the transducer is 1.0 MPa. Reproduced with permission from [23]. Copyright 2006 Elsevier Ltd

negative pressure is applied to the liquid (here it is the pressure on rarefaction) so that the distance between the molecules exceeds the critical molecular distance to hold the liquid intact, the latter inevitably breaks down and microbubbles form. The characteristic linearity of sinusoidal acoustic waves is no longer valid at high amplitudes and nonlinear phenomena cause sudden changes in pressure and fluid properties, such as the generation of shock waves. The rate of pressure change is determined by sound attenuation in the medium, which also depends on frequency. In water, the shock rise time (i.e. the time interval for the wave to vary from 10% to 90% of its peak value) may be much shorter than the wave period, whilst for other materials, such as biological tissues, the pressure variations are less pronounced. Figure 3 shows numerical predictions of waveform distortion produced by nonlinear propagation, at different sound attenuations, in water and homogeneous tissues. The waveforms are generated in the focal region at a range of 52 mm from a rectangular 3.0 MHz [23]. The waveforms lack symmetry and tend to have a shorter compression phase followed by a longer rarefaction phase. The overall effect is a reduction in rarefaction pressure, with respect to linear propagation, leading to the generation of harmonics which may extend to many times the original frequency.

Enhanced sound attenuation can also lead to other secondary effects that include local heating and streaming. Both radiation pressure and streaming are prominent phenomena associated with the propagation of ultrasonic waves [23, 24]. These subjects require a significant mathematical background, which may be tedious and/or mislead the readership of this chapter. It is sufficient first to introduce the concept of excess pressure and then recall previous statements. For a harmonic wave in a fluid, its displacement (ξ) can be replaced by the excess pressure (p_e) generated by the wave, which is defined by the difference between the actual pressure (p) at any point and time and the normal pressure (p_o) in the initially

undisturbed fluid. Thus, $p_e = p - p_o$ and that excess pressure gives spatio-temporal variations such as ξ in the harmonic equation

$$\xi = A \sin 2\pi(ft - x/\lambda),$$

where A is the amplitude, f the frequency, t the elapsed time, x the distance from the origin and λ the wavelength. For plane harmonic waves the excess pressure vanishes over time, although this premise only holds for low intensity sound. At higher intensity, excess pressure that does not become zero on average is also present, thereby making a net contribution to the static pressure prevailing in the fluid, which is known as the *radiation pressure*. In a simplified form, radiation pressure can be roughly expressed as the ratio of the intensity of the sound (I) to its velocity (c), i.e.

$$P_{rad} \cong I/c.$$

Radiation pressure is a steady constant pressure for continuous wave signals. For acoustic pulses, however, this pressure varies periodically at the pulsing frequency. Radiation pressure thus provides a mechanism for producing force at frequencies other than the normal ultrasonic frequencies and potentially in the audible zone. For small particles and non-absorbing interfaces, radiation pressure has a direction and amplitude which depend on the elastic properties of the material in question. This extra force may also result in particle movement.

Likewise, acoustic streaming stems from high-amplitude waves travelling through a medium. In linear behaviour, particles are expected to vibrate about their equilibrium position; in other words, with no net flow. In stark contrast to this and as a result of ultrasonic waves' attenuation with distance, there is a pressure gradient in the fluid which gives rise to a net flow. The magnitude and pattern of the flow depends on the wave properties as well as the type of fluid and reaction vessel. The flow usually moves axially away from the transducer with recirculation vortices that bring fluid back to the transducer face. Visualisation of streaming in liquids can easily be accomplished using thymol blue indicator [23–25]. The maximum axial streaming velocity (v_{max}) for a focused beam of intensity I and radius r, can be approximately estimated as

$$v_{max} \cong \alpha I r^2 G / c_o \mu,$$

where α is the amplitude attenuation coefficient, μ is the shear viscosity of the fluid and G a constant which depends on beam characteristics and vessel geometry. It is convenient to recall that sound attenuation involves the loss of wave amplitude produced by different mechanisms such as absorption or scattering. Attenuation is measured in dB per unit length and also depends on the frequency of the incident beam. Accordingly, the attenuation coefficient (α) is usually given in dB/(kHz or MHz) · cm.

Globally considered, fluid streaming developed around a solid particle or surface greatly increases both mass and heat transfer. The sonoprocessing of fluidised beds is an important application with environmental connotations (Sect. 6), as the entrainment of fine particles in the sound wave improves fluidisation in dense beds and alternatively induces particle agglomeration in diluted beds [26].

The above-mentioned mechanical effects can be significantly enhanced if cavitation takes place in the ultrasonic field. A threshold intensity, which in turn depends upon frequency, must be reached for cavitation to occur, although the process is largely influenced by external parameters, such as solvent properties, temperature or dissolved gases. Cavitation in liquids decreases as one moves to higher frequencies (e.g. the MHz region). This can easily be explained as the rarefaction (as well as compression) phase shortens. With shorter cycles, the finite time required for molecules to be pulled apart, thus generating a cavity, becomes too short. Accordingly, higher amplitudes (power) are required to make liquids cavitate at high frequencies. The fact that most sonochemical applications are run between 20 and 100 kHz is not a coincidence [4, 27].

Sonochemists recognise two types of cavitation – *stable* and *transient*. The former means that bubbles oscillate around their equilibrium position, possibly over prolonged compression/rarefaction cycles. Stable cavitation simply emerges because the acoustic pressure serves as a force that drives the bubble and varies its radius. Experimental observations show that a pulsating bubble under stable cavitation grows progressively. This effect is associated with another phenomenon – *rectified diffusion*. During the compression phase, the gas inside the bubble is at a pressure higher than the equilibrium value and diffuses from the bubble. Conversely, the pressure within the cavity decreases during rarefaction, so that some gas diffuses into the bubble. Because of the larger area present during expansion than under compression, there is a net increase in gas content in the bubble over a cycle. Obviously, a bubble cannot grow indefinitely. During expansion, bubbles reach a critical size and then collapse violently because of the inertial forces of the spherically converging liquid [23, 24]. This transient (or inertial) cavitation triggers well-established mechanical (shocks) and potential chemical effects (highly excited species formation or light emission = *sonoluminescence*). The disturbance caused by the presence of pulsating bubbles also generates a small fluid flow, i.e. microstreaming. Because this flow varies with distance from the bubble, high shear stress near the bubble also occurs and this mechanical action alone is sufficient to cause cell and soft tissue deformations or damage.

This discussion of cavitation certainly overlooks specific details, but it highlights how the nonlinear propagation of ultrasound causes inhomogeneities and physical effects which may have consequences for molecules present in the medium. It is also worth mentioning that suitable cavitation nuclei may also be created at the expense of existing bubbles in a liquid or formed in crevices in suspended particles

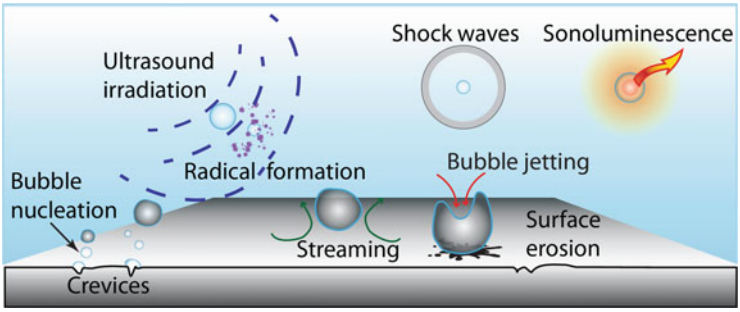

Fig. 4 Schematic representation of nonlinear effects produced by bubble collapse. Reproduced with permission from [28]. Copyright 2012 David Fernández Rivas, Enschede, The Netherlands

where very small amounts of gas can be trapped. An illustrative picture of this cascade process which involves several mechanisms that account for the mechanical action of ultrasonic waves is supplied in Fig. 4 [28].

It is hoped that enhanced mechanical action takes place in association with high intensities and frequencies. However, harmonic generation and sound attenuation provide secondary mechanisms capable of inducing effects within a wide range of frequencies. An assessment of mechanical effects as a function of nominal frequency is not immediately obvious. Mason and associates have monitored, using SEM (scanning electron microscopy) and XPS (X-ray photoelectron spectroscopy), the abrasive action of sound waves on a glass-filled polystyrene blend by measuring weight loss at different frequencies (20, 40, 582, 863 and 1,142 kHz) [29]. At low frequencies (20-kHz probe or 40-kHz bath), the high weight loss correlated well with significant surface changes which were caused purely by mechanical effects, such as micro-jetting. Less pronounced changes occurred at higher frequencies, although surface oxidation was ascribed to enhanced radical specie production. These conclusions, attained in aqueous solutions, agree with previous observations on dextran degradation. Here, mechanical action was important at 35 kHz, whereas extensive degradation took place at 500 kHz and higher frequencies caused by radical reactions [30]. A recent study by Tran and coworkers furnished similar conclusions on the inverse dependence of mechanical and chemical effects on ultrasonic frequencies. Because power intensity (usually measured by calorimetry) decreases as frequency increases, these authors insisted on the use of constant power intensity. By measuring the degradation rates and viscosity ratios of poly (ethylene oxide) (in water and benzene) and polystyrene (in benzene only) under ultrasonic irradiation (from 20 kHz to 1 MHz), this group found a decrease in mechanical effects above 100 kHz [31].

3 Assembly and Scission in Molecular and Supramolecular Arrangements

That ultrasonic waves promote both molecular association and the extensive disruption of structural arrangements may, at first sight, appear somewhat counterintuitive. Once again, such effects depend on the characteristics of the ultrasonic field. Numerical methods and simulations have been introduced to predict the active zones while bearing in mind that, by definition, a cavitating field is a heterogeneous system (liquid and bubbles) [32–34]. In general, reproducible results are attained as long as external factors and reactor shape are optimised, although some practitioners often ignore the critical issue of power control.

Because acoustic radiation lacks quantum character, mechanical oscillations can be harnessed at various frequency ranges, especially via large molecular structures which respond by triggering chemical and biochemical events. Surface acoustic waves (SAWs), for instance, which operate in the MHz zone, have been used for the actuation of fluids, polymer patterning and the directional manipulation of particles on surfaces [35–37]. Atomistic explanations remain largely obscure in view of the frequency mismatch between SAWs and the vibrational states of the adsorbed species. The acoustic enhancement of surface diffusion has recently been suggested [38], which might also account for well-known cases of surface catalysis [39, 40] and molecular desorption [41, 42]. The experimental observation of ultrasonically-induced birefringence is also relevant [43, 44]. On the other hand, low-frequency mechanical vibrations have been shown to be useful in lattice crystallisation as they favour higher ordering and packing [45, 46]. The process depends on vibrational amplitude and frequency and is also related to the appearance of convective flow. Flow configuration and velocity can be altered by changing the acoustic parameters. The particle aggregation mechanism is herein described in terms of stochastic resonance, which contrasts with the usual approach of maintaining equilibrium conditions during crystallisation [47]. Similar analogies can be encountered, within the broad context of mechanochemistry, in granules climbing along a vibrating tube, where the force between the tube and the particles varies periodically, thus causing a directional effect [48].

3.1 Organogel and Hydrogel Formation

If there is a paradigmatic case of ultrasound-assisted formation and the structural manipulation of soft matter, it would most likely be gelation. The process is hardly new and can historically be ascribed to early observations of pattern formation in liquids and solids induced by mechanical vibrations, although the field has experienced a further renaissance over the last two decades, thus launching molecular level investigations [49]. Low-molecular weight (LMW) molecules (usually with molar masses below 3,000 and not involving polymeric chains) are capable of

immobilizing significant amounts of organic solvents or water, thereby serving as organogels or hydrogels, respectively. These substances self-assemble in a given solvent, via non-covalent interactions such as hydrogen bonding (which is probably the most prevalent intermolecular interaction), van der Waals interactions and π–π stacking, which all cooperatively drive the one-dimensional growth of LMW molecules, leading to fibres and strands. These further assemble into three-dimensional networks which encapsulate the solvent and impede flow. This kind of supramolecular soft material, which responds to sonication and stress, may find numerous applications in biomedical research and the preparation of self-healing substances or mechanical switches [50, 51].

It is fair to recognise that the 2005 paper by Naota and Koori triggered subsequent developments in this discipline. The paper reported rapid gelation upon the sonication of solutions containing a dinuclear Pd-salicylidene complex, which is stabilised by intramolecular π-stacking interactions [52]. When solutions of complex *anti*-**1** (Fig. 5) were irradiated with ultrasound (40 kHz, 0.45 W/cm^2) at room temperature, gelation took place within a few seconds. The resulting gels were thermoreversible and clear solutions were obtained via heating to temperatures above T_{gel}. Derivatives with longer hydrocarbon spacers ($n = 6$–8) failed to gelate, although precipitation was sometimes observed. The process also exhibited marked stereoselectivity as the *syn* isomer of **1** did not give gels under the same conditions. These complexes also show planar chirality and this feature was instrumental in elucidating the putative role of ultrasound. When enantiopure *anti*-**1** was subjected to prolonged sonication, it remained unaffected in solution. By stark contrast, scalemic mixtures of *anti*-**1** (42% *ee*) gave gelation, although the resulting gel showed no optical activity. In other words, gelation proceeds with racemisation. This points to a process involving the heterochiral association of (*R*)- and (*S*)-configured monomers which alters the cofacial bent structure of the parent isomer. Without sonication, the conformation is stable enough and avoids aggregation, but irradiation leads to interpenetrative and consecutive planar monomers stacking (Fig. 5).

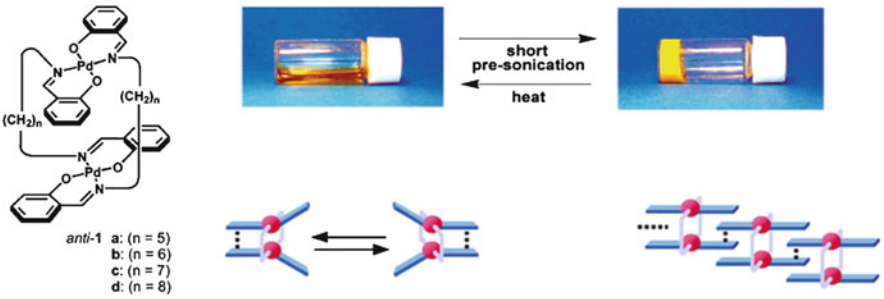

Fig. 5 Reversible sol–gel transformation of Pd-salicylidene complexes. Sonication favours gelation and induces a conformational change, from bent to interlocked structures. Reproduced with permission from [52]. Copyright 2005 American Chemical Society

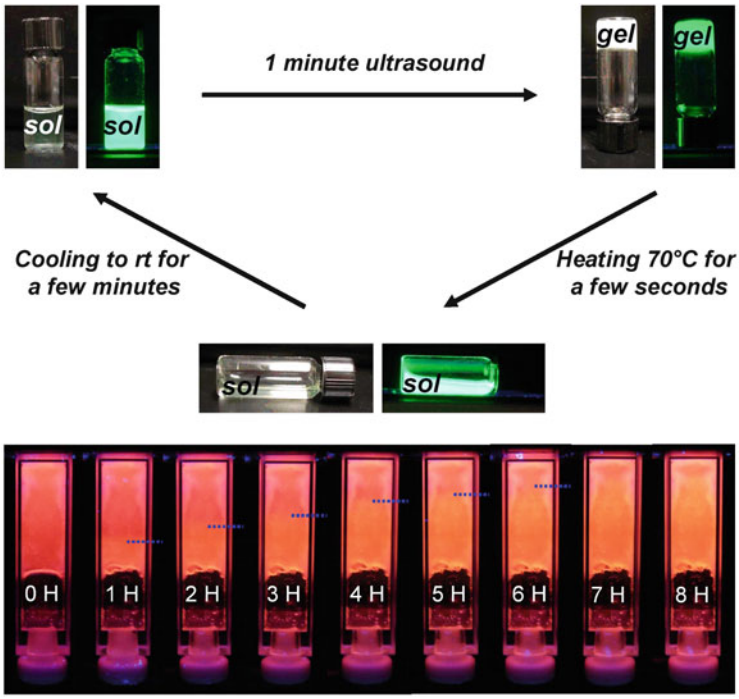

Fig. 6 *Top*: Hexane solutions containing a dipeptide plus QD_{524} undergo gelation after 1-min of irradiation, followed by heating and slow cooling. The procedure can be repeated as the dipeptide precipitates at the bottom of the vial. *Bottom*: Use of ultrasound-generated gels containing QD_{598} for vapour sensing (2-mercaptoethanol). Reproduced with permission from [53]. Copyright 2008 Wiley-VCH Verlag GmbH & Co. KGaA

The advantages and versatility of this type of gelation, which allows the synthesis of complex structures to be carried out, is illustrated by the incorporation of quantum dots (QDs) into hydrogels [53]. Thus, hexane suspensions of a dipeptide derivative and CdSe/ZnS covered with trioctylphosphine oxide, as a surface ligand, undergo gelation in minutes under sonication. The resulting gels are luminescent under UV irradiation and can revert into the sol state upon heating and slow cooling (Fig. 6). The procedure can be used for vapour sensing in the gel state, as shown for 2-mercaptoethanol (Fig. 6, bottom). The gel was prepared using QD_{598} and excess dipeptide in decane after 2 min of sonication. The QD-doped gel was then exposed to 2-mercaptoethanol vapours, as a function of time, under UV irradiation. The increase in photoluminescence can easily be detected over time as the gel becomes progressively more fluorescent as the QD reagent diffuses inside the organogel from the bottom to the top of the vial.

That sonication and shearing stress stimulates gelation, rather than structural disruption, is in principle challenging from a mechanistic point of view. Analysis is complicated because most experimental protocols do not always indicate intensity measurements. Nor do they report other parameters that affect the acoustic field.

However, unlike gels controlled by chemical stimuli, mechanical force and moderate sonication do not generally modify (or destroy) the structure of a molecule in the gel network. The role of sonication appears to be twofold [50]. First, ultrasound can transform intramolecular interactions into favourable intermolecular interactions that lead to aggregation. Second, sonication may induce conformational changes on the resulting organogel, i.e. after formation of the supramolecular network assembled by non-covalent interactions. This aspect is noticeable in the case of two-component organogels as irradiation often results in strengthening infinite hydrogen bonding and other intermolecular interactions that assist gel formation. The latter is well exemplified by melamine–uric acid hydrogels. Neither of the parent molecules is appreciably soluble in water, but gels formed at or above 0.8 wt% concentrations after sonication and shaking for short times (ca. 5 min) [54]. Likewise, sonication triggers morphological changes such as the formation of fibres from a polypeptide organogelator that exists as vesicles in solution. This morphological switch is reversible and repeatable and the fibre–vesicle transition occurs on incubating the gel at 60°C [55]. Similar morphological variations have been reported for a multifunctional adamantane-based gelator, for which a 5-min irradiation affords partial gelation (in the form of vesicles), while prolonged sonication gives rise to a 3D network. Again, the process is reversible over a wide concentration range via sonication and heating-cooling cycles. Gelation can also be fine-tuned by further host–guest interactions in the presence of β-cyclodextrin under sonication, with structures evolving from nanoribbons to ordered nanothreads [56].

A fibrillar structure appears to be the dominant and terminal motif in supramolecular gels generated by shear forces or sonication in liquids. This holds additional significance in biomimetic studies. For instance, silica nanofibers (~30 nm average diameter and ~100 μm length) have recently been obtained via the sonication of an emulsion containing tetraethyl orthosilicate as the silica precursor [57]. The protocol is relatively inexpensive, conducted in a conventional ultrasonic bath and overcomes difficulties associated with other methods such as electrospinning or heating. SEM images show that nanofibres grow on the tips of silica rods, with both co-existing in the same solution (Fig. 7). Only silica rods would be obtained in the absence of sonication, thus showing that irradiation does effectively promote fibrillation. The authors largely attributed this improved preparation to fluid motion created by ultrasound (i.e. microstreaming). Apparently, silica rods act as a micromotor and the torque produced by sound waves results in rod rotational motion, thereby spinning off nanofibres at the rod tips.

The influence of ultrasonic force on aggregation morphologies can be obtained from crystallisation experiments, especially en route to fluorescent materials with enhanced emission [58, 59]. The striking conclusion reached is that luminescent properties are tuneable and can be controlled by molecular packing, which is greatly affected by the ultrasonic treatment and sensitive to its power. At low-energy ultrasonic power, a polar molecule, namely 4-[bis(4-aminophenyl) amino]-*N*,*N*-diphenylbenzamide (ITPADA), containing imide and amino groups, with spherical structure undergoes self-assembly via intermolecular hydrogen

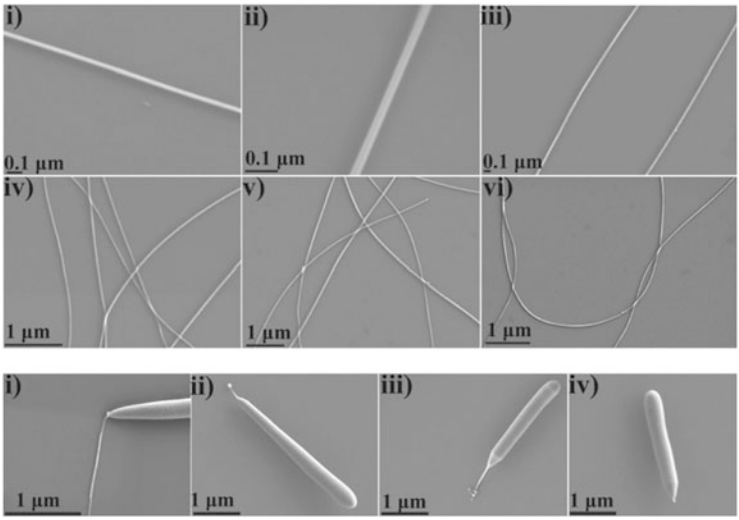

Fig. 7 Scanning electron microscopy (SEM) images of silica nanofibres (*i–iii* zoom in and *iv–vi* zoom out images) and a visualisation of nanofibre growth on rod tips. Reproduced with permission from [57]. Copyright 2014 The Royal Society of Chemistry

bonding which is stronger along the *x* and *y* axes than along the *z* axis. When the ultrasonic power increases, the layer-by-layer structure would be peeled off (see next section). As a result, the initially generated four-side prismatic structure becomes thinner and thinner, as power increases, and converts into a rhombic nanosheet array (Fig. 8). Theoretical conclusions corroborate this finding as ITPADA molecules in single crystals lack coplanarity, caused by intermolecular interactions, and their band gaps were accordingly higher (>4 eV) than those of free molecules (~3.7 eV), thus accounting for blue-shifted fluorescence wavelengths [59].

3.2 Exfoliation of Layered Materials

With the advent and fast development of graphene as the flagship material for futuristic technology, including interfaces with biology [60], the search for economic and large-scale syntheses of few-layer (ideally monolayer) graphene and other carbonaceous structures has become a front-line objective. Exfoliation is clearly a compulsory step and this goal can be achieved by numerous physical and chemical methods which can be extended to layered structures other than graphite, such as BN, MoS_2, MoO_3 and clays [61]. Ultrasonic exfoliation is routinely performed in numerous solvents and then applied to a variety of chemical modifications [62], although the characterisation of the ultrasonic field (power in particular) is not explicitly mentioned in most cases. As expected, bubble collapse

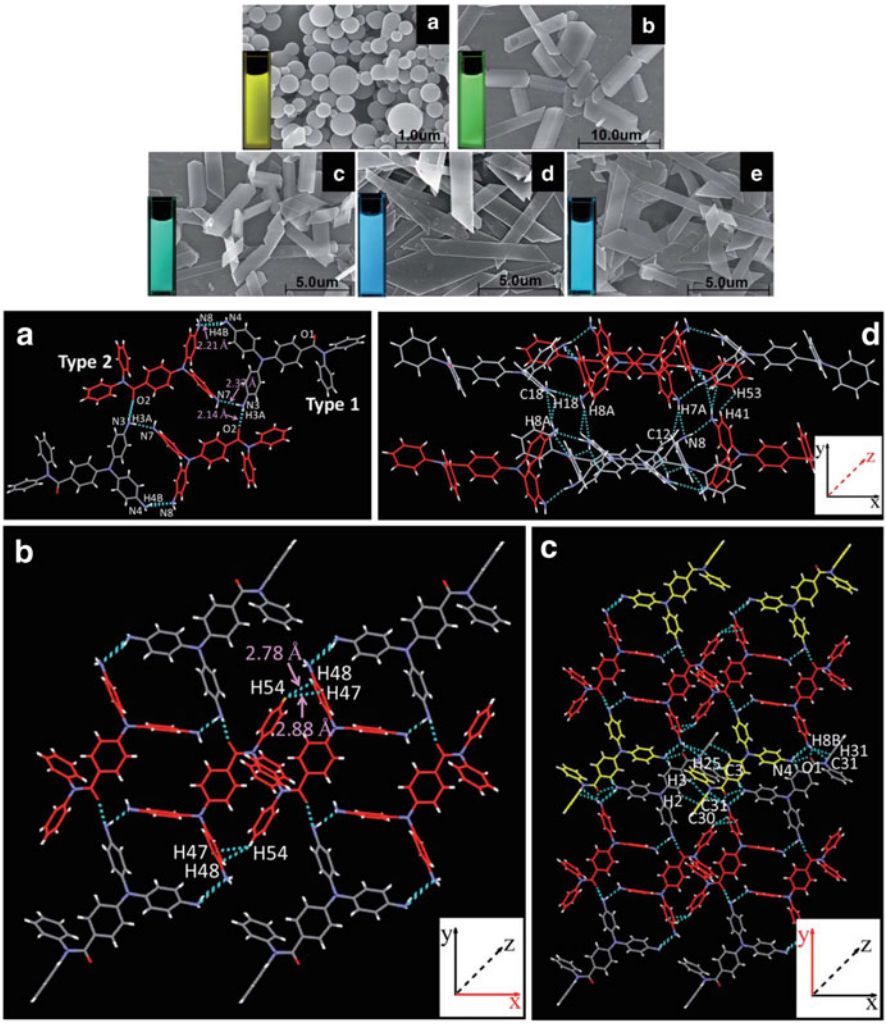

Fig. 8 *Top*: Influence of US power (40 kHz) on the morphology and fluorescence color of ITPADA suspensions in THF-H_2O mixtures (90% water content): (**a**) non-ultrasonic; (**b**) 80 W; (**c**) 120 W; (**d**) 160 W; (**e**) 200 W. *Bottom*: Crystal packing of ITPADA single crystals: (**a**) basic unit of single crystals; (**b**) interactions along the *x*-axis; (**c**) interactions along the *y*-axis; (**d**) interactions along the *z*-axis. Reproduced with permission from [59]. Copyright 2014 The Royal Society of Chemistry

generates mechanical force which is able to disrupt the weak intermolecular interactions present in layered materials (e.g. stacked graphene monolayers in the case of graphite).The liquid-phase exfoliation of graphene has recently been accomplished by means of a high-shear mixer, as long as the local shear rate exceeds 10^4 s^{-1} [63]. In this context, parallelisms with ultrasound-induced shear forces should be scrutinised in terms of acoustic power [64], as exfoliation and

dispersion depend on inertial cavitation and not on the stable stages [65]. Short ultrasound times at lower power generally produce high-quality graphene layers with defects that are mainly located at layer edges. Prolonged irradiation is, however, detrimental and causes bulk defects, as shown by Raman spectroscopy in a recent study conducted in *N*-methyl-2-pyrrolidone (NMP), a typical solvent for graphene exfoliation. Such defects are essentially topological, while vacancies, atomic substitutions and sp^3-like defects should be ruled out [66].

Together with sonication, microwave (MW) irradiation enables the exfoliation of graphene precursors, leading to graphene itself [67] and other forms of porous carbon [68]. Some effort has also been expended on the combined use of MW and ultrasound, either combined or separately, for the purification and surface functionalisation of layered materials such as carbon nanotubes. In a study aimed at evaluating both mechanochemical and frequency effects in the oxidation of multi-walled carbon nanotubes (MWCNTs), some conclusions were inferred from TEM (transmission electron microscopy) and Raman spectroscopy data [69]: (1) MW irradiation causes rupture, because of fast heating and metal content, and the surface becomes highly oxidised (with OH and COOH groups); (2) the combined use of MW and US leads to surface oxidation along with structural defects, although this protocol efficiently removes the amorphous external layer; (3) sonication (20 kHz) accelerates surface oxidation and damage, although partial exfoliation was observed (graphene sheets are noticeable); (4) at high frequency (300 kHz), ultrasound promotes oxidation, but the tubular arrangement of CNTs is preserved (Fig. 9).

Emerging hyphenated techniques, such as the use of MW and ultrasound beams, offer substantial rewards. The sequential approach mentioned above provides inherent advantages as sonication enables rapid exfoliation, while the chemical derivatisation of graphene sheets is largely improved under MW irradiation. This strategy can be exemplified in the synthesis of graphite halides (Fig. 10) [70]. The first step (halogenation reaction), involving the intercalation of the halogen between the graphite layers, is accelerated by microwaves so that the modified material can then easily be exfoliated into monolayer graphene in organic solvents under mild sonication. Alternatively, stable suspensions of few-layer graphene have been obtained via the sonication of graphite flakes in benzylamine which were then subjected to cyclopropanation under MW irradiation [71].

If all-carbon graphene has so far attracted enormous attention in mass media, the fact that polymerised organic crystals can also be exfoliated to create two-dimensional sheets should likewise open a new age of innovation in materials design. The subject is in its infancy, but two recent papers in Nature Chemistry pave the way for these exciting 2D-polymers [72, 73]. Both studies exploit the photopolymerisation of single crystals, in particular anthracene-based monomers, where photochemical dimerisation is facilitated by aromatic unit stacking. The resulting 2D-photopolymerised crystals can be exfoliated into sheets by dispersion in NMP at 50°C. Analyses by SEM and AFM (atomic force microscopy) reveal that multilayer materials were isolated in most cases, although a few monolayer sheets were also detected (Fig. 11). As expected, the role of sonication in exfoliation

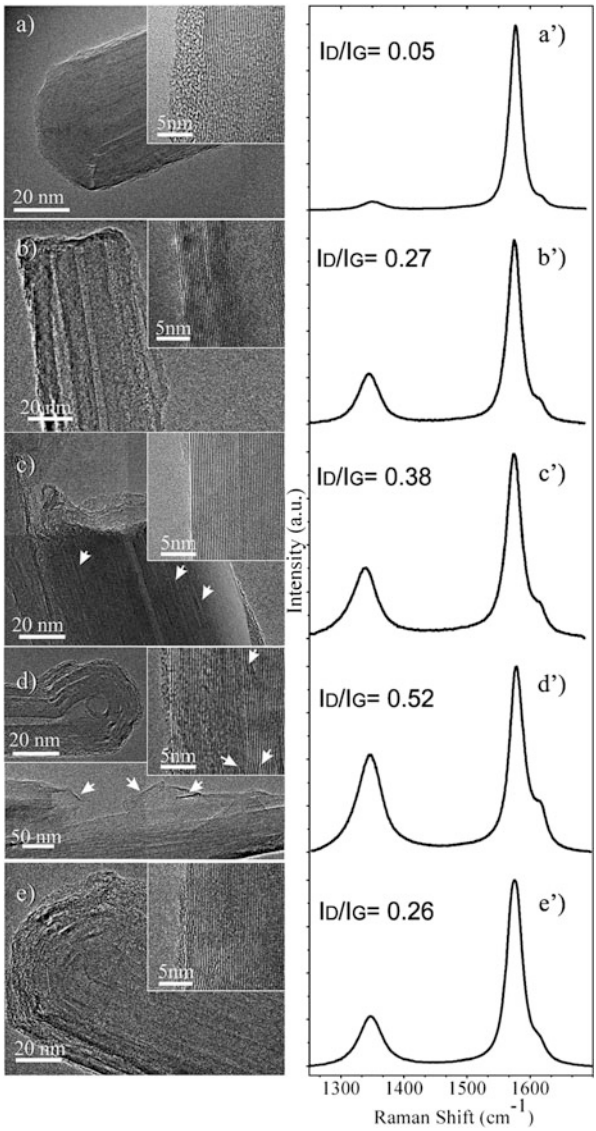

Fig. 9 TEM images and D/G Raman bands for (**a**) pristine MWCNT, (**b**) after MW irradiation (2.45 GHz), (**c**) after sequential MW-US (20 kHz) irradiation, (**d**) sonication at 20 kHz, and (**e**) sonication at 300 kHz. Reproduced with permission from [69]. Copyright 2011 The Royal Society of Chemistry

proved decisive, although the protocols are far from optimised. Short irradiation of NMP dispersions led to multilayer sheets, whereas full exfoliation to monolayers was only achieved by lengthy operations (1–2 weeks) that involved slow rotation in round-bottomed flasks or the use of a fluorinated acid as the intercalating agent. It should be noted that the exfoliation of covalent organic frameworks (COFs) and molecular organic frameworks (MOFs) is not new. However, the resulting sheets were not robust enough. In the present cases, the exploitation of covalent bonding in

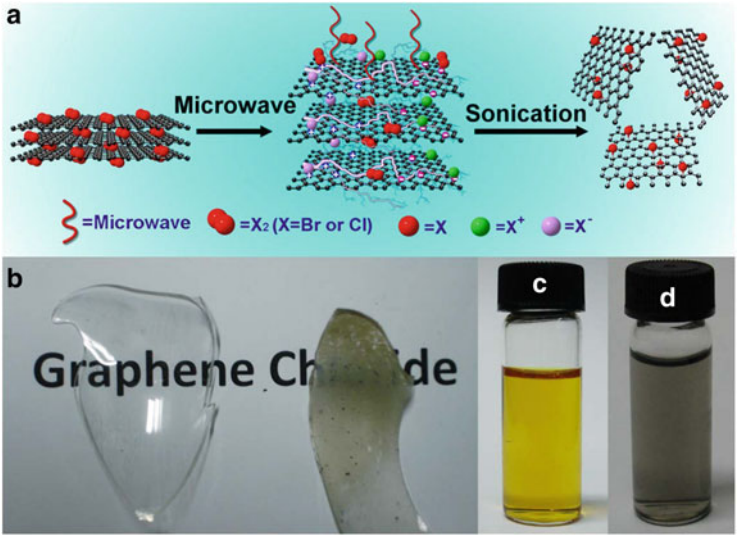

Fig. 10 (**a**) Scheme showing sequential MW-assisted graphite halogenation followed by ultrasound-promoted exfoliation. Photographs of graphite chloride (**b**), a graphite chloride dispersion in DMF (**c**), and graphite bromide dispersion in DMF (**d**). Reproduced with permission from [70]. Copyright 2012 Macmillan Publishers Ltd

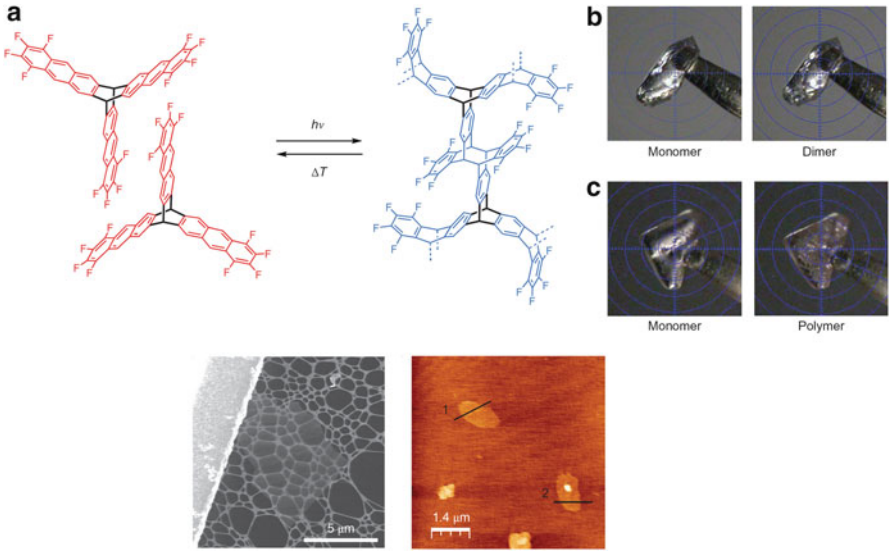

Fig. 11 (**a**) Chemical structure of a tetrafluoro-triptycene-based monomer (fantrip) and the corresponding 2D-polymer, poly(fantrip). (**b**) A single crystal of the monomer before and after irradiation (223 K, 460 nm, 80 min). (**c**) A single crystal of the monomer before and after irradiation (223 K, 460 nm, 150 min) followed by a second irradiation (223 K, 400 nm, 70 min). The *bottom panel* shows SEM and AFM images of exfoliated sheets. Reproduced with permission from [72]. Copyright 2014 Macmillan Publishers Ltd

2D-structures means that the sheets were able to support their own weight when aggregates were suspended across μm-scale holes. These properties make these structures suitable for use in optoelectronics or artificial membranes.

3.3 Modification of Polymeric Structures

The generation and properties of mechanically responsive polymers has most certainly become a hot topic in macromolecular science. Mechanical energy can be harnessed in multiple chemical transformations, such as mechanochromism, analyte detection and self-healing. The basic strategy relies upon the concept of the mechanophore; small structural units embedded into long chain polymers which undergo site-selective scission [6–8, 12]. Although numerous solid-state and solution methods can be used to activate polymers [11], sonication has the unique ability of providing shear forces and strain in solution by virtue of the mechanical events associated with cavitational collapse. A seminal study in the early 1980s reported the fast degradation of weak peroxide linkages along a polymer backbone under sonication (relative to control polymers) [74]. This was followed by more precise explorations by Moore and coworkers showing how azo or benzocyclobutene mechanophores, approximately installed in the centre of a polymer chain and subjected to ultrasonic irradiation, underwent site-specific cleavage [75, 76]. The latter was particularly appealing to modern literature, not only because it showed the accelerating effect of ultrasound-induced force, but also because it showed reaction pathways that challenge the current Woodward–Hoffmann rules-based interpretation. Thus, both *cis*- and *trans*-functionalised benzocyclobutenes undergo ring opening, leading to the *E*,*E*-configured diene, a result that was further corroborated by derivatisation with an appropriate chromophore (Fig. 12). This finding is unexpected from a thermal activation point of view (only the *trans* isomer should afford the *E*,*E*-diene while the *cis* isomer is expected to give the *E*,*Z*-diene). Alternatively, a photochemical mechanism would give the reverse result (*cis* and *trans* isomers leading to *E*,*E* and *E*,*Z*-dienes, respectively).

This "nonclassical" electrocyclic ring-opening reaction, along with other striking results which are markedly different from what is expected from thermochemical pathways, clearly require an extension of theoretical models to mechanical forces and distortion-induced instabilities [18, 77, 78]. This is not discussed here, although a few, merely qualitative, conclusions should be mentioned: (1) mechanical scission caused by strain after bubble collapse is most likely responsible for polymer cleavage; (2) radical production has a negligible effect; (3) thermally forbidden mechanisms may become *mechanically allowed* pathways within a certain range of forces.

If one assumes that, at least intuitively, sonication offers efficient mixing in liquids where forces are generated by turbulent regimes and elongational flows, this framework may be invoked in tracking mechanophore evolution [10]. There are actually some similarities between ultrasonic and transient elongational flow

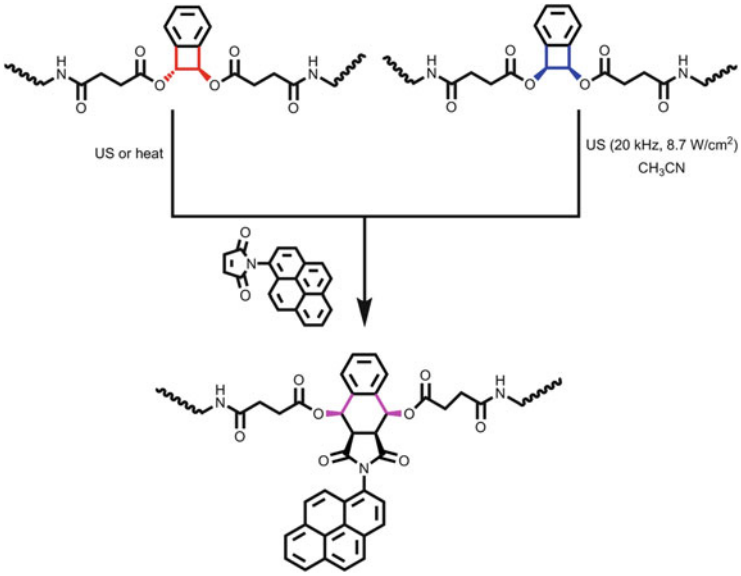

Fig. 12 Ultrasound-induced ring-opening transformations of benzocyclobutene mechanophores installed in polymer chains

degradation of polymers, such as the propensity for midchain cleavage and molecular weight dependence. There should be some resemblance between the adiabatic compression triggered by bubble generation as ultrasound propagates and transient elongational flow, which is obtained by forcing a liquid across a constriction. As a result, a high velocity gradient is created. However, some divergences exist between the hydrodynamic types and these have been discussed in detail by Nguyen et al. as they evaluate the kinetics of ultrasonic degradation for dilute solutions of polystyrene in decalin [79]. First, the cavity is filled with a gas that undergoes constant compression and expansion cycles and, second, acoustic pressure varies along the bulk medium as a function of time. Accordingly, the strain rate changes at various time intervals during bubble collapse. As viewed in Fig. 13, the temporal evolution of strain rates depends on the radius of the collapsing bubble. The latter is created above an intensity threshold and becomes unstable enough after reaching a critical diameter.

Unlike transient elongational flow, the flow induced by sonication at the collapse stage is time dependent. This means that the important factor in kinetics modelling is not spatial distribution but temporal variation in the fluid strain rate [79]. In an ultrasonic experiment, both the limiting molecular weight (M_{lim}, i.e. the molecular weight below which no chain scission takes place regardless of the degradation time) and the degradation rate are dictated by an effective strain rate ($\dot{e}_{\mathrm{eff}}$), which prevails during bubble collapse. By extrapolating the kinetics results obtained in transient elongational flow to ultrasonic degradation, and bearing in mind the M_{lim} values determined in sonication experiments, Nguyen and coworkers concluded

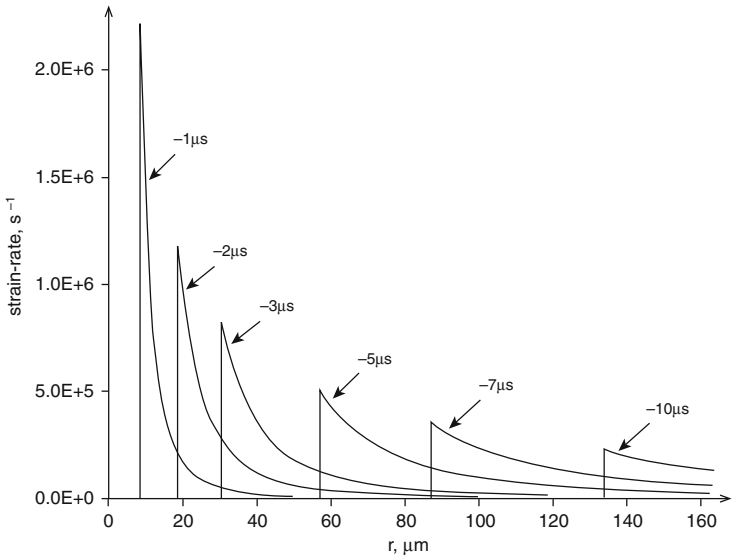

Fig. 13 Strain rate distribution during bubble collapse vs various implosion times. The distance from the cavity centre (r) is given in μm and full collapse occurs at $t = 0$. Reproduced with permission from [79]. Copyright 1997 Elsevier Science Ltd

that $\dot{e}_{\text{eff}}$ should be $\geq 3 \times 10^6\ \text{s}^{-1}$ (Fig. 14). The curve suggests that a polymer chain near the cavitating bubble undergoes a range of strain rates and therefore multiple fragmentations may occur if the daughter chains are larger than M_{lim}. Similar behaviour can be inferred from transient elongational flow experiments, as midchain scission is the dominant process at low strain rates. At higher strain rates, however, shorter molecular chains appear in solution and the resulting molecular weight distribution of the degraded polymer is close to the distributions obtained by cavitational flow [79].

As stated previously, the advancements in controlled polymer scission via *sono-mechanochemistry* are remarkable with new exploration occurring at great pace. Whatever the actual mechanism may be, recent synthetic schemes focus on new functional groups and applications. Thus, a dioxetane mechanophore inserted into a polymer chain represents another weak linkage which can be selectively cleaved under sonication [80]. Blue luminescence, whose intensity and colour was modified by the presence of energy-transfer acceptors, was observed from the resulting excited ketone species (Fig. 15). This protocol also constitutes a valuable step towards detecting failures or structural defects in polymeric materials. Moore and associates have also introduced a biomimetic-like material with reversible responses in the form of a metastable poly(*ortho*-phthalaldehyde) which undergoes ultrasound-induced mechanical depolymerisation to its components via a heterolytic mechanism. Repolymerisation can subsequently be achieved by a chemical initiator [81]. It is worth pointing out that repeatable force-induced cycles which incorporate flex-activated mechanophores (serving as crosslinkers) into elastomeric

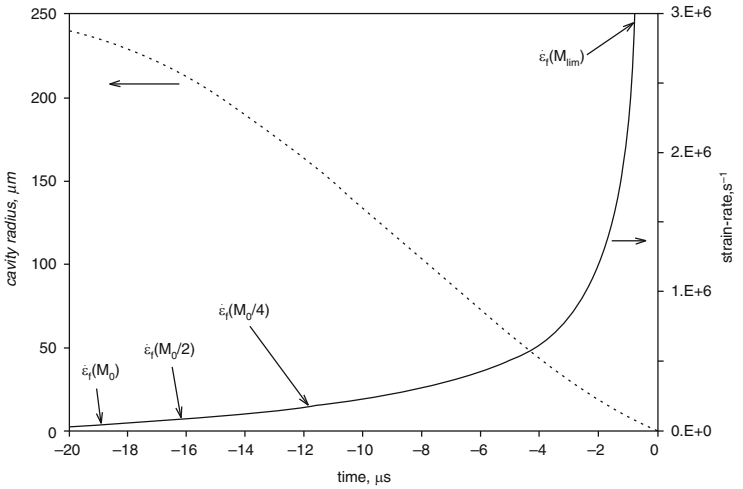

Fig. 14 Temporal evolution of the bubble radius (*left axis*, in μm) and strain rate maximum (*right axis*, in s^{-1}) during bubble implosion. Reproduced with permission from [79]. Copyright 1997 Elsevier Science Ltd

networks have recently been demonstrated. Activation takes place by applying compressive stress, thus releasing a small molecule which diffuses out of the polymer matrix [82, 83].

A new productive chemical change was also observed when mechanical stress caused by ultrasonic irradiation was applied to triple bonds centred on a poly (methyl acrylate) backbone [84]. Further reaction with azides gives rise to an isoquinoline derivative, which points to *transoidal* bending activation which deviates from the expected product (1,2,3-triazole) observed for Huisgen-type cycloadditions of azides with *cisoidal* triple bond arrangements in strained alkynes. Once again, this result is outstanding and illustrates how mechanochemistry can do things which are otherwise difficult or impossible under conventional conditions. Nevertheless, site-selective polymer scission under mechanical stress should be neither a universal trend nor a chemical panacea. A retro-click reaction which has caused enormous excitement in the chemical community, given the wide applicability of the bio-orthogonal alkyne-azide ligation, might not be genuine; an editorial expression of concern has been published and the subject is under confidential investigation [85]. Nevertheless, as rightly pointed out by experts in the field, these circumstances have consequences for specific transformations and do not weaken the principle message conveyed by polymer mechanochemistry which has been based on numerous and testable examples [86]. Thus, a recent application to surface functionalisation should be mentioned in the present context. Silica nanoparticles (SiO_2-NPs) grafted with a polymer chain containing a maleimide-anthracene cycloadduct were also subjected to ultrasonication and afforded mechanophore scission via a retro-[4+2] cycloaddition. The mechanophore-anchored polymer-grafted SiO_2-NPs were prepared by standard protocols (immobilisation of

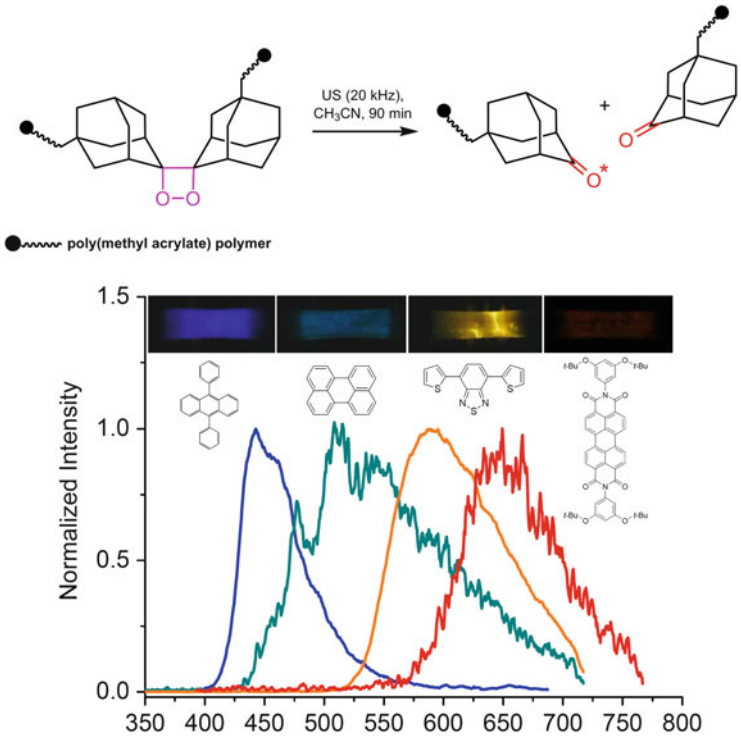

Fig. 15 *Top*: Sono-scission of a polymer chain which includes a 1,2-dioxetane mechanophore to form an adamantanone-excited species with blue light emission. *Bottom*: Luminescence spectra obtained during the mechanical stretching of polymers containing organic acceptors show different colours and intensities. Reproduced with permission from [80]. Copyright 2012 Macmillan Publishers Ltd

triethoxysilane-terminated monomer initiator to silica particles followed by surface-based living radical polymerisation). As expected, sonication was able to generate elongational flow after bubble collapse, thereby transducing mechanical force into the polymer chains. The weakest point should be the polymer-SiO_2-NP heterointerface, which underwent preferential cleavage. Polymer chains of various molecular weights linked to SiO_2-NPs were also tested. Results evidenced a linear response to polymer chain sizes plus a threshold molecular weight dependence similar to that of homopolymers. Moreover, mechanophore scission altered the morphology of the grafted SiO_2-NPs, which exhibited irregular patterns, unlike hexagonal arrangements before sonication [87].

Mechanochemical transduction aided by sonication can also be achieved at a supramolecular level. Given the dynamic character (self-assembly and disassembly) of non-covalent interactions, reversible transformations to create new responsive polymers may potentially be accomplished. As shown in Fig. 16, a cross-linked network containing a europium(III) salt undergoes metal–ligand dissociation upon

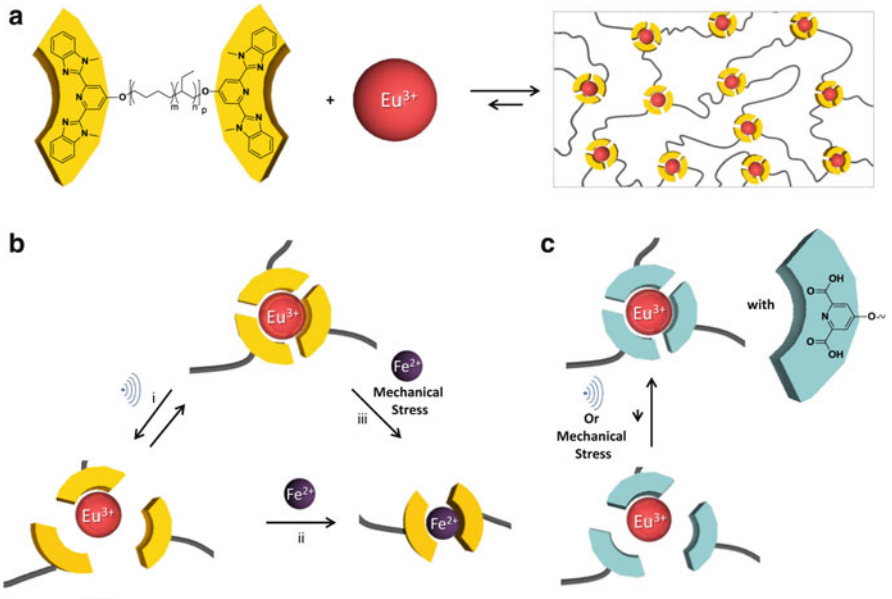

Fig. 16 Mechanochemical evolution of metallosupramolecular polymers generated by (**a**) combination of an Eu(III) salt and a telechelic poly(ethylene-*co*-butylene) with 2,6-bis(1-′-methylbenzimidazolyl)pyridine ligands at the termini; counterions are omitted for clarity. (**b**) Reversible dissociation upon ultrasonication (*i*); irreversible metal exchange with Fe(II) ions as a result of (*ii*) ultrasonication or (*iii*) other mechanical forces. (**c**) Dipicolinic acid ligands bind strongly to Eu(III) and the supramolecular network cannot easily be disassembled under mechanical stress. Reproduced with permission from [88]. Copyright 2014 American Chemical Society

exposure to pulsed ultrasound in solution. This disassembly is only possible with a high molecular weight supramolecular entity, thus again showing the same size dependence as reported for covalent polymer mechanophores. The strength of the metal–ligand interaction is also critical, as polymers containing more strongly coordinating ligands do not dissociate under irradiation [88]. Interestingly, the authors searched for mechanically healable responses and, to this end, polymer films were cut into pieces, gently pressed and exposed to ultrasound, while either directly immersed in a CH_3CN solution or in a sealed bag. In both cases, piece welding was observed and the original mechanical properties of the material were fully restored by this ultrasonic mending protocol.

Aida and coworkers have investigated the influence of low-frequency, audible range sound on macromolecular alignment. The group synthesised a zinc porphyrin which undergoes self-assembly via coordination and hydrogen bonding interactions. The resulting supramolecular nanofibre preferentially aligns itself parallel to the propagation of audible sound (Fig. 17), a fact that can be visualised by linear dichroism (LD) spectroscopy [89]. Observations point to an alignment of the nanofibres flowing around the sidewall of the cuvette and them becoming oriented parallel to the direction of liquid vibration. Because a large hydrodynamic gradient

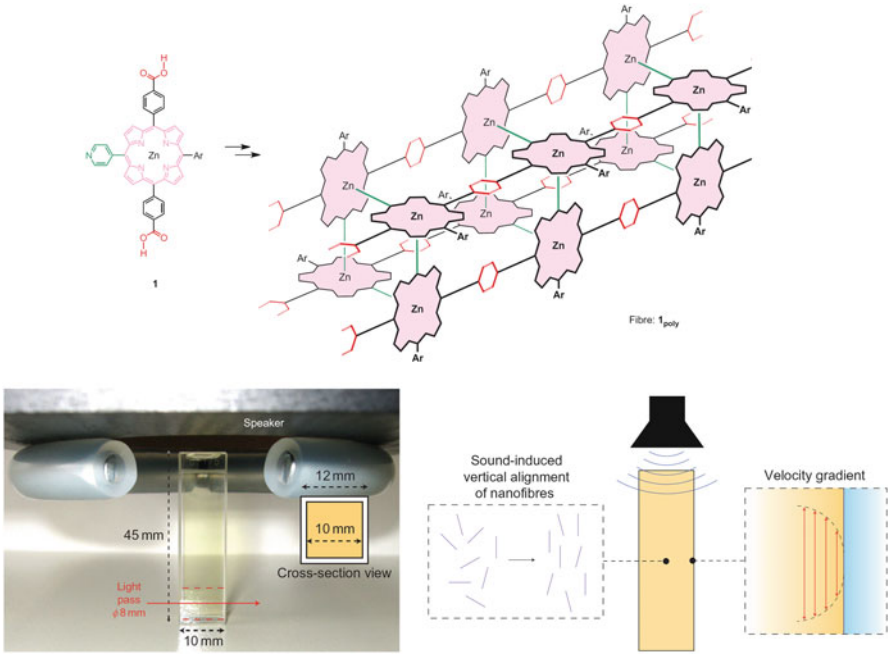

Fig. 17 *Top*: Self-assembled zinc porphyrin leading to supramolecular nanofibres. *Bottom*: Designed nanofibres can be acoustically aligned in solution with audible sound emitted from a loudspeaker located 20 mm above the cuvette. Linearly polarised light was used to record LD spectroscopy. Reproduced with permission from [89]. Copyright 2010 Macmillan Publishers Ltd

(i.e. velocity gradient) should occur at the boundary layer of the liquid flowing near the wall surface, a large LD intensity could also be recorded at the sidewall. The phenomenon appears to be quite general for linear nanofibres, while dendritic zinc porphyrins exhibit a similar effect at higher concentrations. On the other hand, no acoustic LD responses were detected for rod-shaped structures. The protocol may find potential applications in vibration sensing technologies.

In line with the preceding example, hydrodynamic orientation has also been detected in molecules that are first subjected to light and then exposed to audible sound capable of eliciting macromolecular changes. Thus, a linear molecule containing a central azobenzene moiety and three long alkyl chains at each end self-aggregates into supramolecular nanofibres when the azo group is *trans*-configured. Photochemical irradiation (UV light) causes its isomerisation into the *cis*-azobenzene derivative, which leads to amorphous aggregates (Fig. 18) [90]. It should be noted that the assembly process was highly dependent on the length of the alkyl chains and only a 12-carbon chain gave rise to aggregation from the *trans*-isomer. In the *cis*-isomer, 6-, 12- and 16-carbon chains aggregated in an amorphous fashion. LD spectroscopy showed no preferential orientation in solution. However, when samples were irradiated with audible sound, the nanofibres were found to

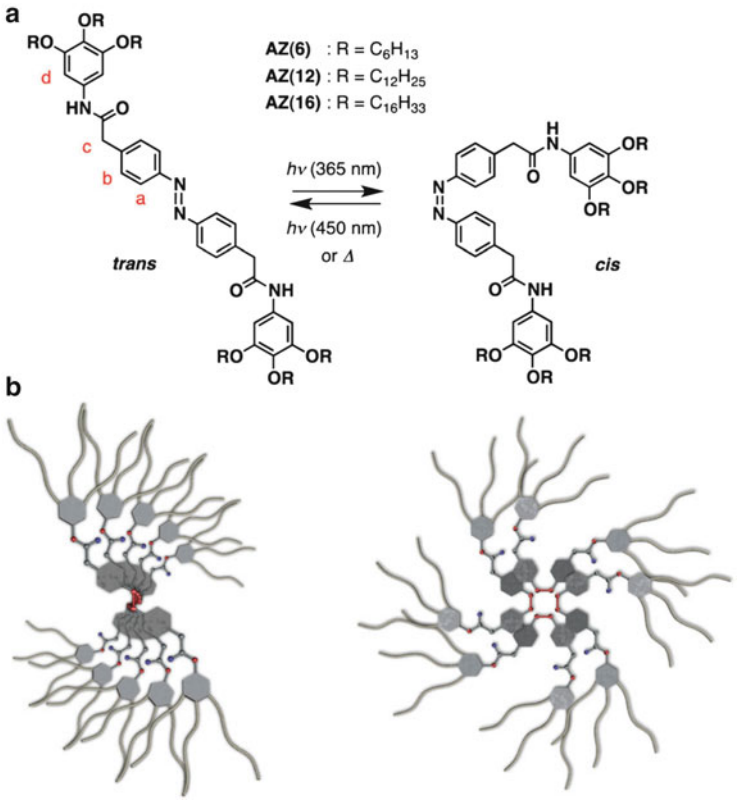

Fig. 18 (**a**) Chemical structures of *trans*- and *cis*-azobenzene derivatives which undergo reversible photoisomerisation. (**b**) Putative self-assemblies; only nanofibres generated from the *trans*-isomer aligned in a sound-induced fluid flow. Reproduced with permission from [90]. Copyright 2014 The Royal Society of Chemistry

align with each other, whereas no change was detected in the amorphous *cis*-aggregates.

4 Mechanical Action on Biostructures

The effects of sound waves on biological tissues and structures have long been known. In general, prolonged sonication is detrimental, leading to extensive cellular damage and chemical biomolecule modification via cavitation processes. Ultrasonic biophysics deals with the study of mechanisms which account for the interaction of ultrasound and biological materials [91]. This damage can, however, be harnessed for specific therapeutic applications [92, 93]. Furthermore, the changes experienced by sound waves in biological media can also be viewed as

the basis for diagnostic ultrasound and biomedical imaging [94, 95]. In particular, drug delivery may be greatly enhanced under sonication. Shock waves induce mechanical forces which transiently open polymeric micelles and polymersomes, thus releasing their contents. This mechanism is well accepted (see below), although the effects of ultrasound on cell apoptosis or genotoxicity must still be elucidated [96]. Likewise, copolymer micelles, which are a suitable, FDA-approved vehicle for drug delivery, can be functionalised to respond to multiple stimuli. For instance, the incorporation into the micelle of a mechanophore which can be selectively cleaved under ultrasound plus the inclusion of a disulfide bond which is sensitive to the reducing action of glutathione illustrates this aspect [97].

It is generally considered that ultrasound waves change the permeability properties of liposome membranes caused by transient cavitation, where the collapse of air bubbles near the lipid membrane creates pores which alter the orientation and hydrophobicity of the lipid structure [98]. Drug delivery via acoustically sensitive liposomes is also largely influenced by the content and structure of the lipid systems. Drug transport can be facilitated by means of lipid molecules, within the liposome membrane, which are capable of creating local instabilities. While such instabilities do not disturb membrane integrity before sonication, they respond once the acoustic stimulus is applied and then heal when the irradiation is turned off [99]. Thus, at appropriate phosphatidylethanolamine (PE) phospholipid levels, the membrane displays a typically lamellar structure with zero intrinsic curvature ($H = 0$) which undergoes topological changes after exposure to ultrasound and converts into a non-lamellar structure, with negative intrinsic curvature ($H < 0$), forming pores through which the drug can readily be released (Fig. 19).

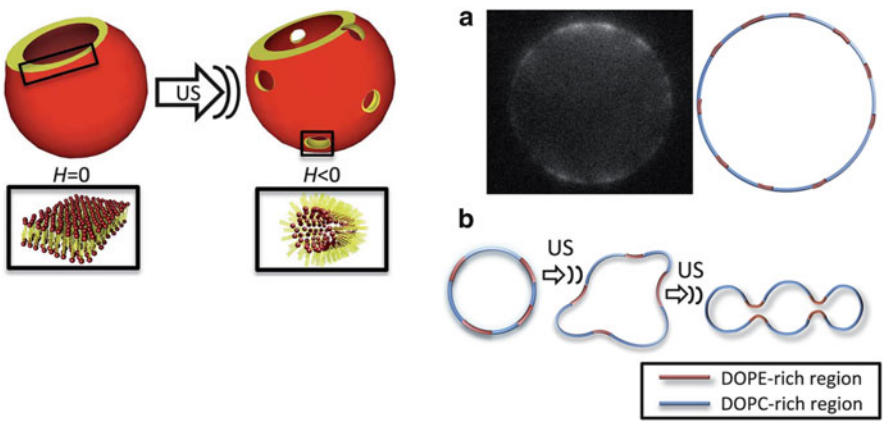

Fig. 19 *Left*: Schematic representation of the proposed mechanism for topological changes in dioleoyl phosphoethanolamine (DOPE) based liposomal membranes upon ultrasound irradiation. *Right*: (**a**) Giant DOPE-based unilamellar vesicle, before sonication, which shows an inhomogeneous membrane; DOPE-rich domains of negative curvature are marked in *red*, embedded in zones rich in dioleoyl phosphocholine (DOPC) of zero mean curvature. (**b**) Illustration of shape changes upon ultrasound stimuli. Reproduced with permission from [99]. Copyright 2014 The Royal Society of Chemistry

A recent simulation using molecular dynamics has evaluated the creation of pores in lipid bilayer membranes by inducing shock waves in a system containing an array of nanobubbles next to those membranes [100]. This model shows that the extent of damage depends on the orientation of the bubbles relative to the shock wave direction as well as the distance between the bubbles. The argument may, in principle, be extrapolated to the context of cavitation-induced microbubbles. However, the authors used a simplified bubble system which did not contain any water vapour molecules, but did include specific bubble alignment to the membrane. Simulations thus point to temporary lipid bilayer disruption under such conditions. This disruption would then be recovered after the damage, which contrasts with the permanent alteration that cavitation creates in solid surfaces.

An indirect and clever method for inducing drug release is the inclusion, inside the liposomes, of magnetic nanoparticles which can be activated by a pulsating magnetic field that triggers the generation of ultrasonic vibrations (~30 kHz). Proof of concept lies in the release of molecules, such as $MgSO_4$ and 5(6)-carboxyfluorescein, being accomplished from magneto liposomes loaded with Fe_3O_4 or FePt nanoparticles, both in homogeneous and inhomogeneous magnetic fields [101].

More productive chemical results, which still harness the destructive action of ultrasound on certain bonds, can be attained when sonication is applied to biological fluids (e.g. protein solutions) en route to bionanomaterials [15]. A conspicuous example can be found in sonochemically-prepared protein microspheres, in which the interplay of mechanical effects (emulsification) and chemical effects (formation of transient species) is noticeable. A protein emulsion is readily created at the interface between two immiscible liquid phases, while radicals generated by water sonolysis promote disulfide bond cross-linking between cysteine residues. Surface modifications, via conjugation with monoclonal antibodies or RGD-containing peptides, can also be carried out [102, 103]. The sonochemical preparation of chitosan microspheres also exploits the intermolecular cross-linking of imine bonds from the sugar precursor [104].

Cell disruption under the action of sound waves appears to be of particular benefit in the case of biofilm elimination. A bacterial biofilm is a microbial community attached to a substrate or interface and which is also embedded in a matrix of polymeric substances generated by such bacteria. Biofilms are a major problem in prostheses as opportunistic pathogens (e.g. *Escherichia coli*, *Staphylococcus aureus* or *Staphylococcus epidermidis*) develop rapidly after surgery. Ultrasound has been frequently used as an effective tool for biofilm removal. Surprisingly, the literature also describes an antagonistic effect, i.e. bacterial viability may be enhanced under sonication. The subject has recently been reviewed and it was found that both effects depend on factors such as frequency, intensity, materials used for ultrasound diffusion, the presence or absence of cavitation and the type of bacteria [105]. The combined use of therapeutic ultrasound with antibiotics usually decreases bacterial viability in vitro and in vivo [106]. On the other hand, sonication at high frequency is unable to kill bacteria, although some damage to the surrounding tissue occurs [107].

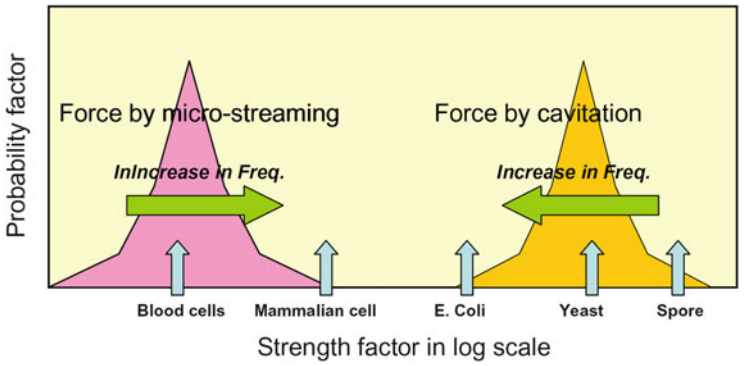

Fig. 20 Schematic diagram showing the relationship between cavitational forces and cell surface strength. Rigid structures are broken by bubble collapse, with little or no microstreaming effect. The *x*-axis (*strength factor*: no numerical values are given) provides an indication on the shear forces required to disrupt mammalian or microbial cells. Reproduced with permission from [109]. Copyright 2008 Elsevier Science Ltd

Cavitational effects on cells and bacteria can be assessed by culturing a specific strain into a container that is then exposed to cavitation generated by ultrasound, shock waves or a laser. The so-called Harvey chamber was a pioneering model with which to evaluate the biophysical effect of ultrasound. Here, the pressure values from the impact of a liquid jet, produced during bubble collapse and the accompanying shock wave, are compared against the maximum stress the cell surface can withstand before rupture [108]. Damage to microbial cells and degradation of their polymer chains also reflect the shear stress triggered around oscillating or collapsing microbubbles. Thus, the rate of intercellular protein release from yeast cells has been used to quantify the mechanical effects of ultrasound. Yeast cells are relatively rigid and fragmentation only occurs in the vicinity of cavitation bubbles, while microstreaming is largely inefficient in fragmenting [109]. Figure 20 shows a merely qualitative relationship between forces in the ultrasonic field and the strength of different classes of biological cells. The frequency effect of cavitation is indicated by the amount of protein released at 20 and 130 kHz. The frequency effect under microstreaming is based on the boundary layer, of thickness δ, separating the inner and outer streaming vortices:

$$\delta = (2\eta/\omega\rho)^{1/2},$$

where η is the shear viscosity, ω the angular frequency and ρ the density of the liquid. The boundary layer has a thickness of about 4 μm at 20 kHz and 0.56 μm at 1 MHz in water. The smaller size of the layer at high frequencies results in high velocity gradients and shearing stress of ca. 550 Pa. Bubbles vibrating at 20 kHz as a source of microstreaming are capable of breaking erythrocytes which leak haemoglobin when shear stress exceeds 450 Pa [109] (Fig. 20).

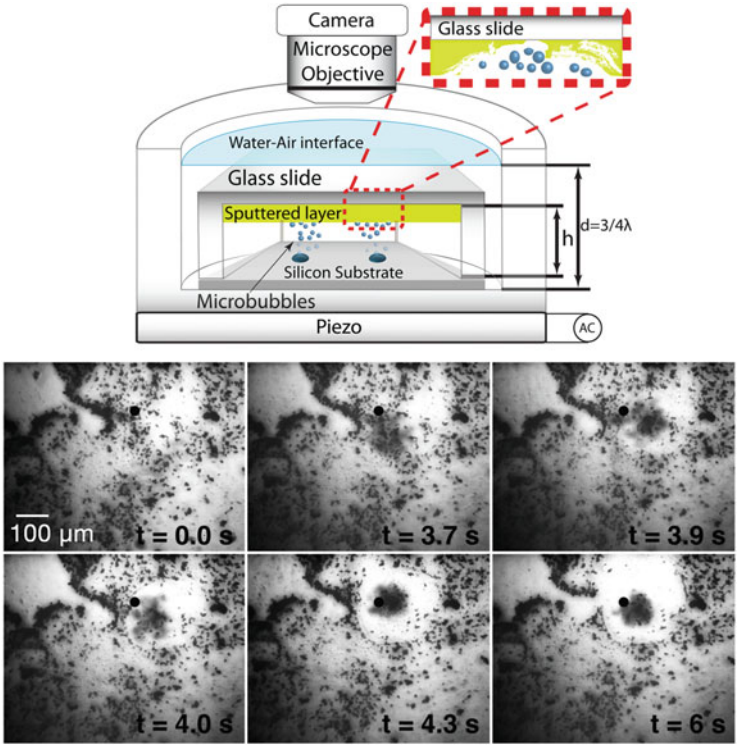

Fig. 21 *Top*: Schematic setup of an ultrasonically vibrating micropitted silicon surface. The cavitation chamber is filled with pure liquids or a cell cultivation liquid for biological assays. *Bottom*: Temporal recording of a biofilm removed by microbubbles. The grey area with black dots is the zone covered by biofilm. The pit is indicated with a large black dot. Microbubbles can be identified as the blurred dark region surrounding the pit. Reproduced with permission from [110]. Copyright 2012 AIP Publishing

Similar conclusions on the negligible effect microstreaming has on biofilm disruption have been reached by Fernandez Rivas et al. using a small-scale ultrasonic device with the ability of locally remove layers of metals, polymers or biomaterials from a glass slide (Fig. 21) [110, 111]. The innovative idea here is the use of a silicon surface containing micropits where individual gas bubbles can be entrapped. Ultrasonic vibration not only gives rise to acoustic streaming from the oscillating surface but also results in gas bubble pinch-off from the micropits at a high enough pressure. The glass cavitation chamber (25 mm outer diameter and 6 mm depth) is glued to a piezo element working at a frequency of 200 ± 5 kHz at the bottom. The biofilm was quickly removed when the bubble cloud was attracted by the biofilm-covered substrate (Fig. 21). However, no removal was observed by streaming alone or by bubble clusters not attracted to the glass surface. This behaviour was also observed for a hydrogel mimicking biofilm characteristics.

The increasing growth of neuropathologies, especially in Western countries, which are associated with prions and other aggregates of misfolded proteins, has become a serious concern in biomedical research. Amyloid fibril formation, for instance, appears to be the critical step in Alzheimer's disease. Ultrasound has been used to evaluate both the formation and disruption of amyloids, although contradictory results may be found as sonication parameters are often overlooked, as in biofilms.

Sonication-induced fibrils, generated in thermostated baths at short irradiation times (ca. 1 min), cause the formation of subsequent fibrils (self-seeding). The process is pH-dependent and AFM images indicate that fibrils with diameters of more than 7 nm are obtained at pH 7.0, which are thicker than those formed at pH 2.5 [112]. Fibril breakage occurs at longer irradiation times, although ultrasound also produces a uniform fibril length distribution. A recycling model has been proposed as the fibrils in the sonicated samples markedly increase their length when left undisturbed [113]. The homogeneous size achieved under sonication bears some resemblance to the pluses associated with sonocrystallisation, thereby favouring the nucleation step. The growth phase proceeds in a template-like manner by incorporating monomers into the ends of seed fibrils. Without sonication, the energy landscape is broad and additional breakdown or re-agglomeration mechanisms would result in a wide range of fibril lengths. The elongational field triggered by sonication modulates the free energy profile and leads to monodispersed fibrils with uniform size, as shown in Fig. 22 (average molecular weight of ~1,660,000 daltons or 140 mer) [114].

Molecular dynamics simulations have recently been performed to ascertain the disruption of amyloid fibrils, which sheds light onto the cavitational event [115]. No significant changes in the peptide structure are observed at positive pressures. At

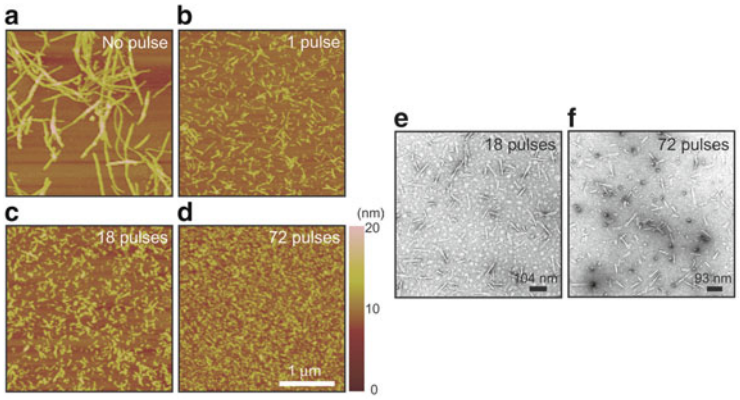

Fig. 22 Effects of pulsed ultrasound on the fragmentation of β_2-microglobulin. (**a–b**) show AFM images of the fibrils before sonication and after 1, 18 and 72 pulses, respectively. (**e, f**) show the corresponding electron microscopy images. Pulses were applied for 1 min with variable quiescent periods. Sonication was run at 37°C in a bath (ca. 17–20 kHz). Reproduced with permission from [114]. Copyright 2009 American Association for the Advancement of Science

negative pressures, however, a bubble is created, mainly around the hydrophobic residues of the transmembrane region. Most β-sheet structures are maintained even in the bubble, although the latter collapses after reaching a positive pressure and water molecules impact against the hydrophilic residues in the non-transmembrane region and disrupt the amyloid. Shorter amyloids require longer irradiation times for disruption to occur, because the number of hydrophobic residues is insufficient to serve as bubble nuclei, which is consistent with the above-mentioned experimental results. These simulations, however, assume that bubbles are generated from water vapour and do not take into account the formation of microbubbles from existing gases in solution. Likewise, fragmentation induced by shearing forces was also not considered. Further molecular modelling reveals that force-assisted fragmentation and fracture times in amyloids depend on polymorphic substructures [116]. Fibrillation also appears to be strongly dependent on chemical composition as shown in another study into chitin derivatives under ultrasonication and gas bubbling in water [117].

5 Ultrasonically-Driven Motion

If any aspect of ultrasonic irradiation is tightly linked to molecular biology, it must surely be mechanotransduction, by which mechanical input is harnessed for autonomous motion or converted into (bio)chemical signals. Although the morphologies of living organisms are encoded in their genomes, cells are otherwise active gels and the evolutionary processes that lead ultimately to shape are rooted in mechanical forces. The emerging field of *mechanobiology* aims to understand how mechanical information translates into complex processes such as cell growth, differentiation or motility [118, 119]. Mechanical energy makes sense in this context as numerous cellular processes involve the activation of stress-sensitive molecules or fluid flow generation. On the other hand, overlooked pathologies caused by low-power sound and low-frequency noise (up to 500 Hz) are most likely associated with changes in mechanotransduction cellular signalling [120].

In close mimicry of biological systems, mechanical motion and other chemical responses can be performed by external stimuli. A plethora of micro/nanomotors have been designed in recent years, with varied degree of functionalisation, which work under physical force, including ultrasonic acoustic waves [121, 122]. Surface acoustic waves (SAWs) that can be generated in miniaturised devices are ideal for lab-on-a-chip applications. A seminal demonstration by Hu and associates showed how an acoustic needle that vibrates under the action of a piezoelectric transducer was able to trap and rotate small particles around its tip in water. The rotation of trapped particles can be controlled by the acoustic pressure near the tip or by controlling the frequency and power (via voltage) of the transducer [123]. An extension of this concept is the use of SAWs on a piezoelectric substrate (made of lithium niobate) with a pair of interdigital transducers to induce rotation of a

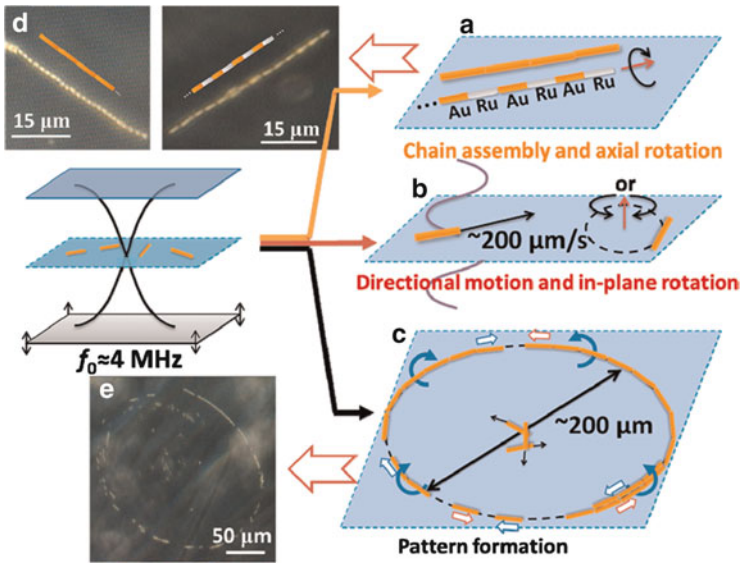

Fig. 23 Schematic illustration of the different types of motion: (**a**) axial directional motion with chain assembly, (**b**) in-plane rotation, and (**c**) axial spinning and pattern formation, of metal microrods in a 3.7-MHz acoustic field. AuRu rods (gold-silvery colour in dark image) showed similar behaviour to of Au rods, except that they moved from the Ru ends (silvery end in the image) forward and aligned heat-to-tail into chains. Images (**d**) and (**e**) show chain structures and ring patterns formed by Au and AuRu rods. Reproduced with permission from [125]. Copyright 2012 American Chemical Society

small disk (5 mm diameter) immersed in a water drop. Large radial accelerations (172 m/s^2) were obtained and hold potential for microcentrifugation [124].

The autonomous motion of metallic microrods, in the form of levitation, rotation, propulsion, alignment and particle assembly has been induced in water or saline solutions using SAWs at 3.7 MHz [125]. Moreover, results obtained with metallic and polymer (polystyrene) materials are substantially different and depend strongly on shape and symmetry (Fig. 23). Metal rods induce strong vortices upon alignment and display preferential axial motion, while spherical metal particles induce vortices as well, but scarcely show directional motion. Polymer particles show neither directional motion nor induce vortex formation, irrespective of shape. The fact that polymer rods display no directional motion, but weak axial rotation, when aligned suggests that such trends are influenced by different acoustic field effects. Thus, axial propulsion arises chiefly from the scattering of acoustic waves travelling in the z-direction and its rate can be altered either by modifying the amplitude and frequency of the continuous irradiation or by means of pulsed sonication. It would appear that the swimming trajectory of an object is governed by the balance between the orienting force induced by the physical field and the effects that randomise particle orientations, such as rotary Brownian motion and/or a tumbling mechanism resembling that of flagella in bacteria [126].

Wang et al. have recently displayed the modulating effect of an ultrasonic field on the bubble propulsion of a chemically-fuelled microengine [127]. The latter, fabricated by electrodeposition, consists of a poly(3,4-ethylenedioxythiophene) (PEDOT)/Ni/Pt tubular arrangement (15 μm long, 5 μm diameter at its wide side). The catalytic decomposition of hydrogen peroxide fuel on the inner Pt surface releases oxygen microbubbles, which leads to microengine propulsion. The application of ultrasound disrupts bubble evolution, thus hindering and stopping movement. In the absence of sonication, the microengine moves at high speed (231 μm/s) with a characteristic bubble tail. When irradiation is applied (at 10 V of the US transducer), the microengine almost stops completely within 0.1 s and only maintains a negligible velocity of 0.6 μm/s. When the ultrasonic field is turned off, the original speed is regained once again within 0.1 s. Reproducible on/off cycles are observed and different velocities can be obtained by simply tuning ultrasonic power.

Acoustic propulsion in biological fluids and cells opens the door to biomedical applications, from drug delivery to the selective transport or capture of biological targets (e.g. bacteria) [128], and has perhaps taken its inspiration from the film "Fantastic Voyage". The fuel-free propulsion of a nanomotor by means of acoustic energy can be additionally oriented in the presence of a magnetic field, thus targeting specific cells and tissues. As a proof of the concept, a ferromagnetic nickel stripe has been electrochemically grown between diamagnetic Au and Ru segments, which then responds to a weak external magnetic field (40–45 mT) used to orient nanowires moving along their long axes, propelled by SAWs (~3.7 MHz) [129]. These features enable μm-level precision toward living human cervical cancer cells (HeLa cells) cultured in an aqueous phosphate buffer (Fig. 24). Moreover, viability tests showed no significant cell degradation in the presence of metallic nanowires after 20 min of acoustic irradiation (at 10 V peak values). This experiment demonstrates clever random motion suppression in microengines which were fine-tuned by a second controlling field. Ultrasound-excited motion (at ~4 MHz resonant frequency) of Au nanorods inside HeLa cells, which remain viable after ultrasonic exposure, has also been reported and shows the aforementioned directionality patterns of axial propulsion and spinning [130].

In a different strategy to achieve ultrasound-guided motion, Wang and coworkers prepared microbullets with an inner Au layer which permits conjugation to a monolayer of thiolated cysteamine. The entire functionalisation also enables electrostatic attachment to perfluorocarbon (PFC) (either perfluoropentane or perfluorohexane) droplets to be carried out. Under ultrasonic irradiation, the PFC droplets are vaporised, leading to the net motion of microbullets towards lamb kidney tissue. Propulsion can be modulated by adjusting external parameters such as acoustic pressure, pulse duration or surfactant concentration [131].

Although not directly related to acoustic nanomotors, one might wish to pay attention to the selective binding control of single molecules in biological media. As an illustrative example, low-power ultrasound radiation, mediated by magnetic particles, can selectively dissociate non-covalent bonds according to their inherent strengths [132]. Consider, for instance, as shown in Fig. 25, two types of

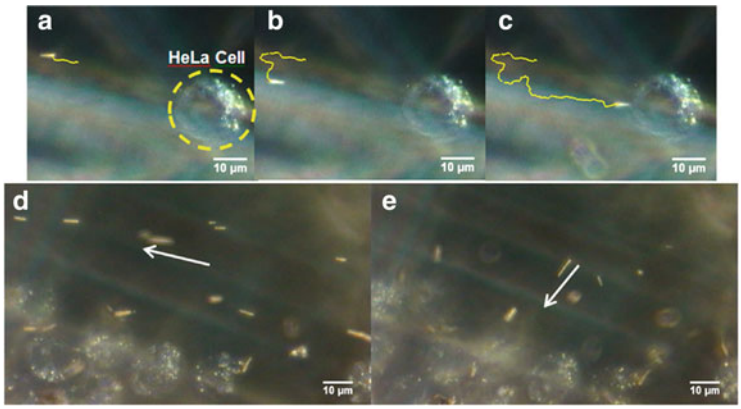

Fig. 24 Acoustically-propelled nanomotor targeted at a HeLa cell (**a–c**). (**d**) Nanowires are moving parallel to a group of cells, with their direction indicated by the arrow. (**e**) When the external field is turned, nanowires are magnetically steered toward the cells through an approximately 90° turn. Reproduced with permission from [129]. Copyright 2013 American Chemical Society

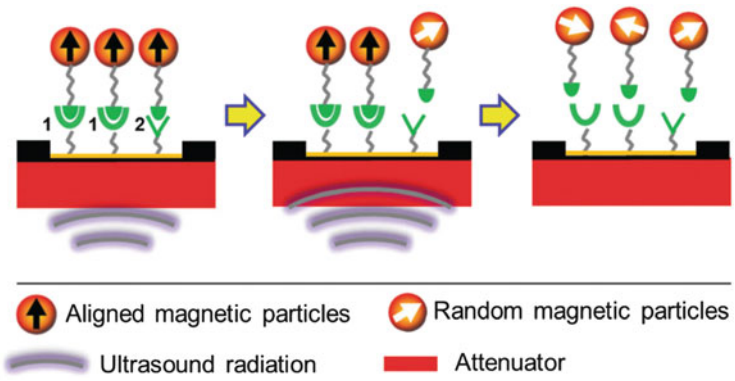

Fig. 25 Schematic illustration of the acoustic radiation force (ARF)-based FIRMS (force-induced remnant magnetisation spectroscopy) approach for the selective cleavage of non-covalent bonds. Reproduced with permission from [132]. Copyright 2014 The Royal Society of Chemistry

non-covalent bonds to biological receptors, one occurring between a magnetically labelled ligand and receptor 1, the other involving interaction between the ligand and receptor 2, which is assumed to have a weaker binding constant than the former. Low-power sonication is only able to dissociate the weaker bond selectively. The dissociated magnetic particles cause a decrease in the magnetic signal because of the randomisation of their magnetic dipoles. Subsequent application of a slightly higher-power ultrasound dissociates the stronger bond between the ligand and receptor 1. Different antibodies and DNA duplexes have been mechanically resolved using this approach.

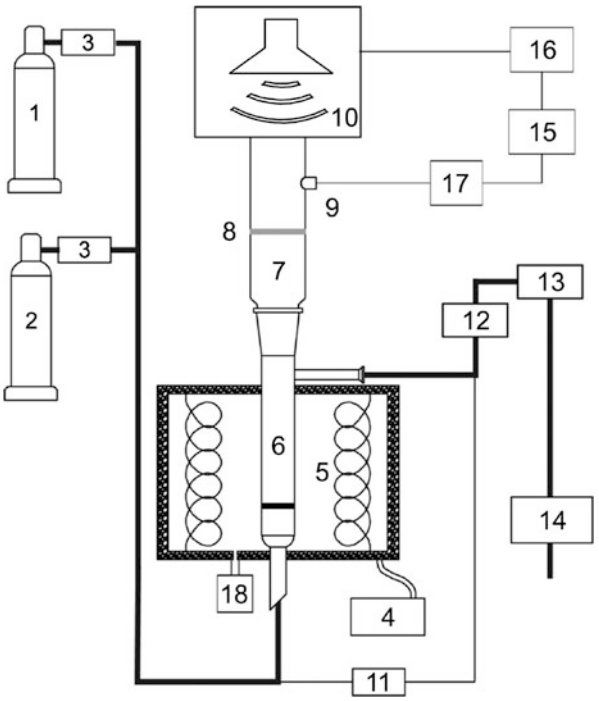

Fig. 26 Diagram showing Ca-looping sonoprocessing. 1: Compressed gas used for carbonation (15 vol.% CO_2/ 85 vol.% N_2); 2: compressed gas used for calcinations (dry air); 3: mass flow controllers; 4: temperature controller; 5: furnace; 6: quartz reactor; 7: sound waveguide; 8: elastic membrane; 9: microphone; 10: loudspeaker; 11: differential pressure transducer; 12: particulate filter; 13: mass flow meter; 14: gas analyzer; 15: signal amplifier; 16: signal generator; 17: oscilloscope; 18: air cooling system. Reproduced with permission from [133]. Copyright 2013 American Chemical Society

6 Cleaning, Erosion and Streaming: New Developments

Cleaning, erosion, emulsification and streaming are paradigmatic effects of the mechanical action of high-amplitude waves and cavitating bubbles. This penultimate section does not intend to re-emphasise these aspects, as they are well established and lie at the core of sonochemistry. Rather, we provide glimpses of a few recent applications which harness these mechanical mechanisms.

Fluid recirculation enhancing acoustic streaming [26] can be used in the sonoprocessing of solid particles and, most notably, make use of low-cost commercially available devices which operate at low frequencies. The so-called Ca-looping process is a viable technology with which to perform post-combustion CO_2 capture with high efficiency. In short, it involves the separation of CO_2 via the carbonation of CaO in a fluidised bed at high temperature, followed by limestone calcination to regenerate the sorbent. Capture is increased under low frequency acoustic vibration (ca. 100 Hz) and intensities of around 140 dB [133, 134]. The operational setup is shown in Fig. 26. Fine particles (with diameters smaller than 100 μm) are entrained in the oscillating gas flow induced by the low-frequency field, which leads to the strong agitation of the bed and enhances gas-solid contact. Moreover, acoustic streaming (i.e. intense convection of gas flow) is generated on the surface of larger particles (otherwise immovable by the acoustic wave) and promotes both heat and mass transfer at the gas–solid interface. These mechanisms, used combined or

separately, increase carbonation/decarbonation rates, but depend heavily on average particle size and sound parameters.

It should be noted that audible sound (generated by cheap loudspeakers) can be used for related separation techniques, even on large scales (pilot plant). A reduction in particle emissions from coal combustion fumes has been achieved using an array of stepped-plate piezoelectric transducers, which produce a homogeneous distribution of high-intensity waves (145–165 dB), located along the wall of the chamber at that high-temperature environment [135].

Cleaning and erosion can be visualised on the small scale using miniaturised devices and provide fine details of the mechanical action. Material removal experiments have been conducted using the setup shown in Fig. 21 (top) for the elimination of biofilms [110]. The cavitation cell does not enable an optical visualisation of the cavitating bubbles because of the opaque character of materials deposited on the glass slide. However, some observations, which are also dependent on the pit arrangement and intensity (Fig. 27),were made. For deposited gold, a small opening in the Au layer (right on top) is seen (where the pits are located) when low power irradiation is applied (0.182 W). At constant power, the size of the removed layer increases slowly. The maximum area removed for one pit is ca. 0.03 mm^2. This increases proportionally upon increasing the power for two, three or four pit geometries (linear, triangular or rectangular shapes, respectively, are seen). While this kind of surface removal is observed for both Au and Pt, deposited Cr and Ti (expected to have harder passivating coatings) do not undergo removal under the above conditions and the bubbles are able to detach small pieces only occasionally. When the ultrasound is switched off, the pits are filled with water and, if a bubble is still inside a pit, further bubble nucleation can no longer be attained. When ultrasound is turned on, no cavitation is observed from the micropits. As mentioned in Sect. 4, streaming does not account for surface removal

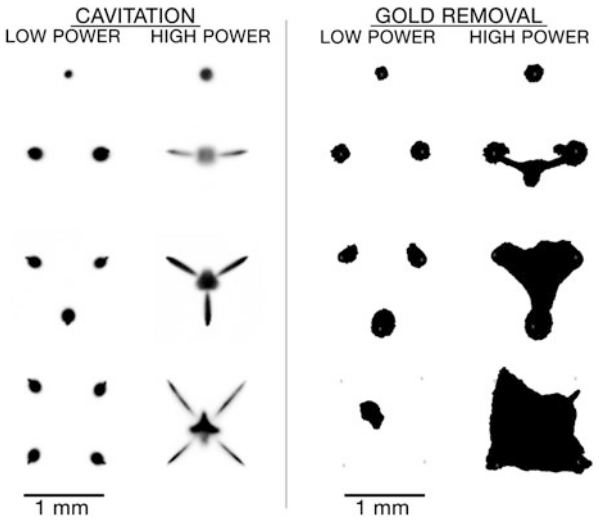

Fig. 27 From *top to bottom* (and *left to right*): bubble generation from 1 to 4 pit arrangements at low and high power. *Left*: Bright field illumination (*inverted colour*) showing bubble patterns at slow speed imaging. *Right*: Shapes of cleaned areas in gold (*black*) caused by bubble cavitation. Reproduced with permission from [110]. Copyright 2012 AIP Publishing

and the cleaning effect is locally restricted to the pits and how close the nucleated bubbles are from the surface to be removed.

The influence of radical production by the cavitation bubbles was also investigated by exposing all the metal surfaces to hydrogen peroxide. No Au reaction was observed in the first 5 min, although some small regions showed tiny amounts of detachment (ca. 1 mm^2) after that time. Some chemical activity was detected in Pt in the form of bubbling and gas formation, most likely H_2/O_2 generation, which led to the removal of the entire layer in a few seconds. On the other hand, Cr and Ti did not undergo reaction after 10 min of irradiation. The latter allows one to conjecture that any contribution from radical species (such as H· or HO·) to the removal rates is minimal under the conditions employed to produce cavitating bubbles, which nucleate from the pits [110].

Surface damage can be caused by bubble cavitation and shock waves on non-coinage metals. Silicon is an oft-studied case where surface erosion has been studied in various crystallographic orientations – namely (100), (110) and (111) surfaces at 191 kHz [136]. The most significant damage caused by cavitation was observed on the (100) face, with an eroded area which was ca. 2.5 times larger than in other crystallographic orientations after 180 min of irradiation. Erosion pits increased at a constant rate for (110) and (111), although this effect stopped in (100) after 120 min.

More complex transformations have been observed for crystalline silicon under acoustic cavitation in water sparged with Ar at temperatures of between 10 and 20°C [137]. Spectroscopic investigation reveals that Ar, which is bubbled continuously through the liquid phase, is ultrasonically excited via mechanoluminescence, i.e. light emission produced by mechanical action on the Si surface. This phenomenon also triggers physico-chemical transformations at the solid–liquid interface (Fig. 28), thus causing stress and defects as well as an increase in

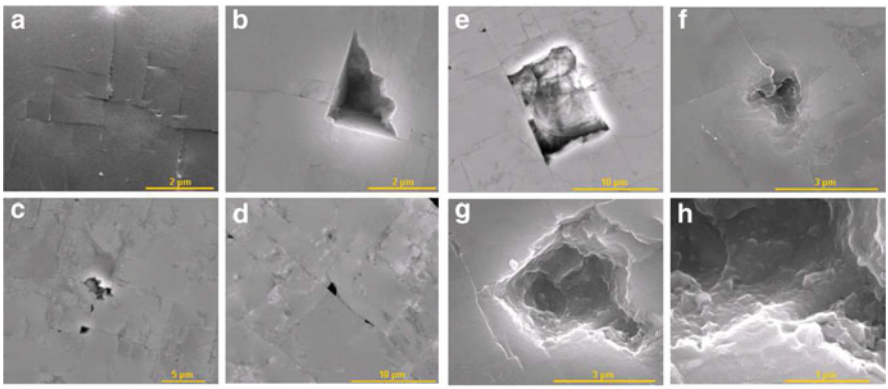

Fig. 28 SEM images of crystalline silicon showing the propagation of cracks and defects after sonication for (**a**) 5 h, (**b**, **c**) 7 h, (**d**) 9 h, (**e**) 12 h, and (**f**–**h**) 15 h. Acoustic intensity is 32 W/cm^2, Ar bubbling at 20°C in water (250 mL). Reproduced with permission from [137]. Copyright 2012 American Chemical Society

roughness and wettability. Interestingly, progressive amorphisation of the crystalline was also observed. The latter can be attributed to a loss of lattice stability during the high-energy environment created by the collapsing bubbles in compression/decompression cycles. This shock wave-caused mechanical effect should also be considered as the local pressures generated by such waves are similar to those employed in high-pressure transformations of crystalline silicon.

7 Concluding Remarks: Open Questions

It should now be unnecessary to underline the mechanical connection between sonochemistry and other subfields of mechanochemistry. The former clearly possesses a series of inherent characteristics by virtue of various forces generated in a liquid under the action of pressure waves. Both chemical and physical activation, especially when cavitation is present, are able to drive numerous transformations and often provide a useful mechanistic rationale.

As a leading sonochemist [9], who was paraphrasing Churchill, once said: *sonochemists and mechanochemists are one people separated by a common phenomenon*. This phenomenon is obviously the conversion of mechanical energy into chemistry, which includes a vast territory of applications worthy of exploration. The present survey simply summarises a few fundamentals plus some scenarios of current and active interest. The interplay between sonochemistry and its mechanical relationships invariably leaves open questions and new avenues to investigate. To mention a few:

1. Further developments in theoretical modelling, particularly via high-level quantum-mechanical calculations, are required and can boost our understanding of the forces involved. Cavitational modelling is, in any case, a challenge because of its nonlinear effects.
2. How can selectivity be controlled in macromolecular or supramolecular arrangements?
3. What kind of physical effects are involved in the acoustically-promoted formation of metastable crystals, co-crystals and nanostructures?
4. How do cavitation and other physical effects influence or alter phenomena such as mechanoluminescence or chemiluminescence?
5. How does reactor design affect efficiency and reproducibility?
6. Should energy efficiency also be analyzed in terms of batch vs continuous processes?
7. How different are acoustic fields from other forms of flowing energy? (e.g. hydrodynamic cavitation).
8. What kind of safety concerns should be addressed? (in particular mechanical input in single cells and biofluids).

9. How can we assess sonomechanical mechanisms? Are there suitable molecular probes?
10. Can we probe cell mechanics with ultrasonics via non-invasive and innocuous techniques?

Ultrasonication tells us that liquid flows may offer rich science, merging physics and chemistry. We are often fascinated by liquid patterns observed in common and cheap cleaning baths or bubble clouds around an ultrasonic horn. Many years ago, Leonardo da Vinci, the prototypical Renaissance genius, was a man who loved fluids [138]. His drawings reflect passion and curiosity and show swirling, curving, revolving and wavy patterns with precision. He recognised that flow was an essential ingredient of life. Had Leonardo known more about the action of sound in liquids, he would certainly have conveyed science and beauty to mesmerise future generations forever.

Acknowledgments Financial support from the following agencies is gratefully acknowledged: University of Turin (fondi ricerca locale 2013) and the Junta de Extremadura-FEDER (Ayuda a Grupos Consolidados, Grant No. GR10049). The authors are also deeply indebted to Dr. David Fernández-Rivas (University of Twente, The Netherlands, and BubClean) for his stimulating feedback and permission to reproduce Fig. 4.

References

1. Gooberman GL (1990) Sound. In: Gwinn RP, Norton PB, Goetz PW (eds) The new encyclopaedia britannica vol. 27, Encyclopaedia Britannica Inc, Chicago, pp 629–631 (ultrasonics); entire chapter on sound, pp 604–632
2. Rossing TD (2007) Introduction to acoustics. In: Rossing TD (ed) Springer handbook of acoustics. Springer, New York, pp 1–6
3. Cravotto G, Cintas P (2011) Introduction to sonochemistry: a historical and conceptual overview. In: Chen D, Sharma SK, Mudhoo A (eds) Handbook on applications of ultrasound and sonochemistry. CRC/Taylor & Francis, Boca Raton, pp 23–40, Ch 2
4. Mason TJ, Lorimer JP (2002) Applied sonochemistry. The uses of power ultrasound in chemistry and processing. Wiley-VCH, Weinheim
5. Cravotto G, Cintas P (2006) Power ultrasound in organic synthesis: moving cavitational chemistry from academia to innovative and large-scale applications. Chem Soc Rev 35:180–196
6. Caruso MM, Davis DA, Shen Q, Odom SA, Sottos NR, White SR, Moore JS (2009) Mechanically-induced chemical changes in polymeric materials. Chem Rev 109:5755–5798
7. Cravotto G, Cintas P (2012) Harnessing mechanochemical effects with ultrasound-induced reactions. Chem Sci 3:295–307
8. Cravotto G, Calcio Gaudino E, Cintas P (2013) On the mechanochemical activation by ultrasound. Chem Soc Rev 42:7521–7534
9. Suslick KS (2014) Mechanochemistry and sonochemistry: concluding remarks. Faraday Discuss 170. doi:10.1039/c4fd00148f
10. May PA, Moore JS (2013) Polymer mechanochemistry: techniques to generate molecular force via elongational flows. Chem Soc Rev 42:7497–7506

11. Wiggins KM, Brantley JN, Bielawski CW (2013) Methods for activating and characterizing mechanically responsive polymers. Chem Soc Rev 42:7130–7147
12. Brantley JN, Wiggins KM, Bielawski CW (2013) Polymer mechanochemistry: the design and study of mechanophores. Polym Int 62:2–12
13. Bang JH, Suslick KS (2010) Applications of ultrasound to the synthesis of nanostructured materials. Adv Mater 22:1039–1059
14. Ariga K, Mori T, Hill JP (2012) Mechanical control of nanomaterials and nanosystems. Adv Mater 24:158–176
15. Xu H, Zeiger BW, Suslick KS (2013) Sonochemical synthesis of nanomaterials. Chem Soc Rev 42:2555–2567
16. Sander JRG, Zeiger BW, Suslick KS (2014) Sonocrystallization and sonofragmentation. Ultrason Sonochem 21:1908–1915
17. Huang Z, Boulatov R (2011) Chemomechanics: chemical kinetics for multiscale phenomena. Chem Soc Rev 40:2359–2384
18. Ribas-Arino J, Marx D (2012) Covalent mechanochemistry: theoretical concepts and computational tools with applications to molecular nanomechanics. Chem Rev 112:5412–5487
19. Kildishev AV, Boltasseva A, Shalaev VM (2013) Planar photonics with metasurfaces. Science 339:1232009. doi:10.1126/science.1232009
20. Brunet T, Leng J, Mondain-Monval O (2013) Soft acoustic metamaterials. Science 342:323–324
21. Maldovan M (2013) Sound and heat revolutions in phononics. Nature 503:209–217
22. Gustafsson MV, Aref T, Kockum AF, Ekström MK, Johansson G, Delsing P (2014) Propagating phonons coupled to an artificial atom. Science 346:207–211
23. Humphrey VF (2007) Ultrasound and matter-physical interactions. Prog Biophys Mol Biol 93:195–211
24. Lepoint T, Lepoint-Mullie F (1998) Theoretical bases. In: Luche JL (ed) Synthetic organic sonochemistry. Plenum, New York, pp 1–49, Ch 1
25. Nyborg WL (1998) Acoustic streaming. In: Hamilton MF, Blackstock DT (eds) Nonlinear acoustics. Academic, San Diego, pp 207–228
26. Valverde JM (2013) Acoustic streaming in gas-fluidized beds of small particle. Soft Matter 9:8792–8814
27. Mason TJ, Peters D (2002) Practical sonochemistry. Power ultrasound uses and applications, 2nd edn. Woodhead Publishing, Oxford, pp 1–46
28. Fernández Rivas D (2012) Taming acoustic cavitation, PhD Thesis. University of Twente, The Netherlands, Ch 2, p 10. doi:10.3990/1.9789036534192
29. Mason TJ, Cobley AJ, Graves JE, Morgan D (2011) New evidence for the inverse dependence of mechanical and chemical effects on the frequency of ultrasound. Ultrason Sonochem 18:226–230
30. Portenlänger G, Heusinger H (1997) The influence of frequency on the mechanical and radical effects for the ultrasonic degradation of dextranes. Ultrason Sonochem 4:127–130
31. Tran KVB, Kimura T, Kondo T, Koda S (2014) Quantification of frequency dependence of mechanical effects induced by ultrasound. Ultrason Sonochem 21:716–721
32. Tudela I, Sáez V, Esclapez MD, Díez-García MI, Bonete P, González-García J (2014) Simulation of the spatial distribution of the acoustic pressure in sonochemical reactors with numerical methods: a review. Ultrason Sonochem 21:909–919
33. Son Y, Lim M, Ashokkumar M, Khim J (2011) Geometric optimization of sonoreactors for the enhancement of sonochemical activity. J Phys Chem C 115:4096–4103
34. Merouani S, Ferkous H, Hamdaoui O, Rezgui Y, Guemini M (2015) A method for predicting the number of active bubbles in sonochemical reactors. Ultrason Sonochem 22:51–58
35. Alvarez M, Friend JR, Yeo LY (2008) Surface vibration induced spatial ordering of periodic polymeric patterns on a substrate. Langmuir 24:10629–10632

36. Friend JR, Yeo LY, Arifin DR, Mechler A (2008) Evaporative self-assembly assisted synthesis of polymeric nanoparticles by surface acoustic wave atomization. Nanotechnology 19:145301
37. Shilton R, Tan MK, Yeo LY, Friend JR (2008) Particle concentration and mixing in microdrops driven by focused surface acoustic waves. J Appl Phys 104:014910
38. Wu C, Zaitsev VY, Zhigilei LV (2013) Acoustic enhancement of surface diffusion. J Phys Chem C 117:9252–9258
39. Kelling S, Mitrelias T, Matsumoto Y, Ostanin VP, King DA (1997) Acoustic wave enhancement of the catalytic oxidation of carbon monoxide over Pt{110}. J Chem Phys 107:5609–5612
40. Inoue Y (2007) Effects of acoustic waves-induced dynamic lattice distortion on catalytic and adsorptive properties of metal, alloy and metal oxide surfaces. Surf Sci Rep 62:305–336
41. Zinovev AV, Veryovkin LV, Moore JF, Pellin MJ (2007) Laser-driven acoustic desorption of organic molecules from back-irradiated solid foils. Anal Chem 79:8232–8241
42. Dow AM, Wittrig AR, Kenttämaa HI (2012) Laser-induced acoustic desorption (LIAD) mass spectrometry. Eur J Mass Spectrom 18:77–92
43. Lipeles R, Kivelson D (1980) Experimental studies of acoustically induced birefringence. J Chem Phys 72:6199–6208
44. Nomura H, Matsuoka T, Koda S (2004) Ultrasonically induced birefringence in polymer solution. Pure Appl Chem 76:97–104
45. Khunsin W, Amann A, Kocher-Oberlehner G, Romanov SG, Pullteap S, Seat HC, O'Reilly EP, Zentel R, Torres CMS (2012) Noise-assisted crystallization of opal films. Adv Funct Mater 22:1812–1821
46. Avetissov I, Sadovskiy A, Belov S, Khomyakov A, Rekunov K, Kostikov V, Sukhanova E (2013) Thermodynamic features of axial vibrational control technique for crystal growth from the melt. CrystEngComm 15:2213–2219
47. Ende DJA, Anderson SR, Salan JS (2014) Development and scale-up of cocrystals using resonant acoustic mixing. Org Process Res Dev 18:331–341
48. Liu C, Wu P, Wang L (2013) Particle climbing along a vibrating tube: a vibrating tube that acts as a pump for lifting granular materials from a silo. Soft Matter 9:4762–4766
49. Cravotto G, Cintas P (2009) Molecular self-assembly and patterning induced by sound waves. The case of gelation. Chem Soc Rev 38:2684–2697
50. Yu X, Chen L, Zhang M, Yi T (2014) Low-molecular-mass gels responding to ultrasound and mechanical stress: towards self-healing materials. Chem Soc Rev 43:5346–5371
51. Ye E, Chee PL, Prasad A, Fang X, Owh C, Yeo VJJ, Loh XJ (2014) Supramolecular soft biomaterials for biomedical applications. Mater Today 17:194–202
52. Naota T, Koori H (2005) Molecules that assemble by sound: an application to the instant gelation of stable organic fluids. J Am Chem Soc 127:9324–9325
53. Bardelang D, Zaman MB, Moudrakovski IL, Pawsey S, Margeson JC, Wang D, Wu X, Ripmeester JA, Ratcliffe CI, Yu K (2008) Interfacing supramolecular gels and quantum dots with ultrasound: smart photoluminescent dipeptide gels. Adv Mater 20:4517–4520
54. Anderson KM, Day GM, Paterson MJ, Byrne P, Clarke N, Steed JW (2008) Structure calculations of an elastic hydrogel from sonication of rigid small molecule components. Angew Chem Int Ed 47:1058–1062
55. Ke D, Zhan C, Li ADQ, Yao J (2011) Morphological transformation between nanofibers and vesicles in a controllable bipyridine-tripeptide self-assembly. Angew Chem Int Ed 50:3715–3719
56. Zhang M, Jiang M, Meng L, Liu K, Mao Y, Yi T (2013) Fabrication of multiplicate nanostructures via manipulation of the self-assembly between an adamantine based gelator and cyclodextrin. Soft Matter 9:9449–9454
57. Datskos P, Chen J, Sharma J (2014) Synthesis of very small diameter silica nanofibers using sound waves. Chem Commun 50:7277–7279

58. Koenig M, Torres T, Barone V, Brancato G, Guldi DM, Bottari G (2014) Ultrasound-induced transformation of fluorescent organic nanoparticles from a molecular rotor into rhomboidal nanocrystals with enhanced emission. Chem Commun 50:12955–12958
59. Sun H, Zhang Y, Yan W, Chen W, Lan Q, Liu S, Jiang L, Chi Z, Chen X, Xu J (2014) A novel ultrasound-sensitive mechanofluorochromic AIE-compound with remarkable blue-shifting and enhanced emission. J Mater Chem C 2:5812–5817
60. Kostarelos K, Novoselov KS (2014) Exploring the interface of graphene and biology. Science 344:261–263
61. Nicolosi V, Chhowalla M, Kanatzidis MG, Strano MS, Coleman JN (2013) Liquid exfoliation of layered materials. Science 340:1226419. doi:10.1126/science.1226419
62. Cravotto G, Cintas P (2010) Sonication-assisted fabrication and post-synthetic modification of graphene-like materials. Chem Eur J 16:5246–5259
63. Paton KR, Varrla E, Backes C, Smith RJ, Khan U, O'Neill A, Boland C, Lotya M, Istrate OM, King P, Higgins T, Barwich S, May P, Puczharski P, Ahmed I, Moebius M, Pettersson H, Long E, Coelho J, O'Brien SE, McGuire EK, Sanchez BM, Duesberg GS, McEvoy N, Pennycook TJ, Downing C, Crossley A, Nicolosi V, Coleman JN (2014) Scalable production of large quantities of defect-free few-layer graphene by shear exfoliation in liquids. Nat Mater 13:624–630
64. Buzaglo M, Shtein M, Kober S, Lovrincic R, Vilan A, Regev O (2013) Critical parameters in exfoliating graphite into graphene. Phys Chem Chem Phys 15:4428–4435
65. Sesis A, Hodnett M, Memoli G, Wain AJ, Jurewicz I, Dalton AB, Casey JD (2013) Influence of acoustic cavitation on the controlled ultrasonic dispersions of carbon nanotubes. J Phys Chem B 117:15141–15150
66. Bracamonte MV, Lacconi GI, Urreta SE, Foa Torres LEF (2014) On the nature of defects in liquid-phase exfoliated graphene. J Phys Chem C 118:15455–15459
67. Janowska I, Chizari K, Ersen O, Zafeiratos S, Soubane D, Da Costa V, Speisser V, Boeglin C, Houllé M, Bégin D, Plee D, Ledoux MJ, Pham-Huu C (2010) Microwave synthesis of large few-layer graphene sheets in aqueous solution of ammonia. Nano Res 3:126–137
68. Zhu Y, Murali S, Stoller MD, Ganesh KJ, Cai W, Ferreira PJ, Pirkle A, Wallace RM, Cychosz KA, Thommes M, Su D, Stach EA, Ruoff RS (2011) Carbon-based supercapacitors produced by activation of graphene. Science 332:1537–1541
69. Cravotto G, Garella D, Calcio Gaudino E, Turci F, Bertarione S, Agostini G, Cesano F, Scarano D (2011) Rapid purification/oxidation of multi-walled carbon nanotubes under 300 kHz-ultrasound and microwave irradiation. New J Chem 35:915–919
70. Zheng J, Liu HT, Wu B, Di CA, Guo YL, Wu T, Yu G, Liu YQ, Zhu DB (2012) Production of graphite chloride and bromide using microwave sparks. Sci Rep 2:662. doi:10.1038/srep00662
71. Economopoulos SP, Rotas G, Miyata Y, Shinohara H, Tagmatarchis N (2010) Exfoliation and chemical modification using microwave irradiation affording highly functionalized graphene. ACS Nano 4:7499–7507
72. Kissel P, Murray DJ, Wulftange WJ, Catalano VJ, King BT (2014) A nanoporous two-dimensional polymer by single-crystal-to-single-crystal photopolymerization. Nat Chem 6:774–778
73. Kory MJ, Wörle M, Weber T, Payamyar P, van de Poll SW, Dshemuchadse J, Trapp N, Schlüter AD (2014) Gram-scale synthesis of two-dimensional polymer crystals and their structure analysis by X-ray diffraction. Nat Chem 6:779–784
74. Encina MV, Lissi E, Sarasúa M, Garagallo L, Radic D (1980) Ultrasonic degradation of polyvinylpyrrolidone: effect of peroxide linkages. J Polym Sci Polym Lett Ed 18:757–760
75. Berkowski KL, Potisek SL, Hickenboth CR, Moore JS (2005) Ultrasound-induced site-specific cleavage of azo-functionalized poly(ethylene glycol). Macromolecules 38:8975–8978
76. Hickenboth CR, Moore JS, White SR, Sottos NR, Baudry J, Wilson SR (2007) Biasing reaction pathways with mechanical force. Nature 446:423–427

77. Luty T, Ordon P, Eckhardt CJ (2002) A model for mechanochemical transformations: applications to molecular hardness, instabilities, and shock initiation of reaction. J Chem Phys 117:1775–1785
78. Tian Y, Boulatov R (2013) Comparison of the predictive performance of the Bell-Evans, Taylor-expansion and statistical-mechanics models of mechanochemistry. Chem Commun 49:4187–4189
79. Nguyen TQ, Liang QZ, Kausch HH (1997) Kinetics of ultrasonic and transient elongational flow degradation: a comparative study. Polymer 38:3783–3793
80. Chen Y, Spiering AJH, Karthikeyan S, Peters GWM, Meijer EW, Sijbesma RP (2012) Mechanically induced chemiluminescence from polymers incorporating a 1,2-dioxetane unit in the main chain. Nat Chem 4:559–562
81. Diesendruck CE, Peterson GI, Kulik HJ, Kaitz JA, Mar BD, May PA, White SR, Martinez TJ, Boydston AJ, Moore JS (2014) Mechanically triggered heterolytic unzipping of a low-ceiling-temperature polymer. Nat Chem 6:623–628
82. Larsen MB, Boydston AJ (2014) Successive mechanochemical activation and small molecule release in an elastomeric material. J Am Chem Soc 136:1276–1279
83. Gossweiler GR, Hewage GB, Soriano G, Wang Q, Welshofer GW, Zhao X, Craig SL (2014) Mechanochemical activation of covalent bonds in polymers with full and repeatable macroscopic shape recovery. ACS Macro Lett 3:216–219
84. Diesendruck CE, Zhu L, Moore JS (2014) Alkyne mechanochemistry: putative activation by transoidal bending. Chem Commun 50:13235–13238
85. McNutt M (2014) Editorial expression of concern. Science 344:1460
86. Halford B (2014) Texas student falsified data. Chem Eng News December 15 issue, p 9
87. Li J, Shiraki T, Hu B, Wright RAE, Zhao B, Moore JS (2014) Mechanophore activation at heterointerfaces. J Am Chem Soc 136:15925–15928
88. Balkenende DWR, Coulibaly S, Balog S, Simon YC, Fiore GL, Weder C (2014) Mechanochemistry with metallosupramolecular polymers. J Am Chem Soc 136:10493–10498
89. Tsuda A, Nagamine Y, Watanabe R, Nagatani Y, Ishii N, Aida T (2010) Spectroscopic visualization of sound-induced liquid vibrations using a supramolecular nanofibre. Nat Chem 2:977–983
90. Hotta Y, Suiko S, Motoyanagi J, Onishi H, Ihozaki T, Arakawa R, Tsuda A (2014) A physical operation of hydrodynamic orientation of an azobenzene supramolecular assembly with light and sound. Chem Commun 50:5615–5618
91. O'Brien WD Jr (2007) Ultrasound-biophysics mechanisms. Prog Biophys Mol Biol 93:212–255
92. Kennedy JE (2005) High-intensity focused ultrasound in the treatment of solid tumours. Nat Rev Cancer 5:321–327
93. Yu T, Zhang Y, He H, Zhou S, Liu Y, Huang P (2011) Anticancer potency of cytotoxic drugs after exposure to high-intensity focused ultrasound in the presence of microbubbles and hematoporphyrin. Mol Pharmaceutics 8:1408–1415
94. Wang LV, Hu S (2012) Photoacoustic tomography: in vivo imaging from organogelles to organs. Science 335:1458–1462
95. Guo C, Jin Y, Dai Z (2014) Multifunctional ultrasound contrast agents for imaging guided photothermal therapy. Bioconjugate Chem 25:840–854
96. Alvarez-Lorenzo C, Concheiro A (2014) Smart drug delivery systems: from fundamentals to the clinic. Chem Commun 50:7743–7765
97. Tong R, Lu X, Xia H (2014) A facile mechanophore functionalization of an amphiphilic block copolymer towards remote ultrasound and redox dual stimulus responsiveness. Chem Commun 50:3575–3578
98. Frenkel V (2008) Ultrasound mediated delivery of drugs and genes to solid tumors. Adv Drug Deliv Rev 60:1193–1208
99. Kang M, Huang G, Leal C (2014) Role of lipid polymorphism in acoustically sensitive liposomes. Soft Matter 10:8846–8854

100. Santo KP, Berkowitz ML (2014) Shock wave induced collapse of arrays of nanobubbles located next to a lipid membrane: coarse-grained computer simulations. J Phys Chem B. doi:10.1021/jp505720d
101. Podaru G, Ogden S, Baxter A, Shrestha T, Ren S, Thapa P, Dani RK, Wang H, Basel MT, Prakash P, Bossmann SH, Chikan V (2014) Pulsed magnetic field induced fast drug release from magneto liposomes via ultrasound generation. J Phys Chem B 118:11715–11722
102. Toublan FJJ, Boppart S, Suslick KS (2006) Tumor targeting by surface-modified protein microspheres. J Am Chem Soc 128:3472–3473
103. Baram-Pinto D, Shukla S, Richman M, Gedanken A, Rahimipour S, Sarid R (2012) Surface-modified protein nanospheres as potential antiviral agents. Chem Commun 48:8359–8361
104. Skirtenko N, Tzanov T, Gedanken A, Rahimipour S (2010) One-step preparation of multifunctional chitosan microspheres by a simple sonochemical method. Chem Eur J 16:562–567
105. Erriu M, Blus C, Szmukler-Moncler S, Buogo S, Levi R, Barbato G, Madonnaripa D, Denotti G, Piras V, Orrù G (2014) Microbial biofilm modulation by ultrasound: current concepts and controversies. Ultrason Sonochem 21:15–22
106. Ensing GT, Roeder BL, Nelson JL, van Horn JR, van der Mei HC, Busscher HJ, Pitt WG (2005) Effect of pulsed ultrasound in combination with gentamicin on bacterial viability in biofilms on bone cements in vivo. J Appl Microbiol 99:443–448
107. Bigelow TA, Northagen T, Hill TM, Sailer FC (2009) The destruction of *Escherichia coli* biofilms using high-intensity focused ultrasound. Ultrasound Med Biol 35:1026–1031
108. Miller DL (1976) Instrument for microscopical observation of the biophysical effects of ultrasound. J Acoust Soc Am 60:1203–1212
109. Iida Y, Tuziuti T, Yasui K, Kozuka T, Towata A (2008) Protein release from yeast cells as an evaluation method of physical effects in ultrasonic field. Ultrason Sonochem 15:995–1000
110. Fernandez Rivas D, Verhaagen B, Seddon JRT, Zijlstra AG, Jiang LM, van der Sluis LWM, Versluis M, Lohse D, Gardeniers HJGE (2012) Localized removal of layers of metal, polymer, or biomaterial by cavitating microbubbles. Biomicrofluidics 6:034114
111. Fernández Rivas D (2012) Taming acoustic cavitation, PhD thesis, University of Twente, The Netherlands, Ch 7, pp 119–141
112. Ohhashi Y, Kihara M, Naiki H, Goto Y (2005) Ultrasonication-induced amyloid fibril formation of β_2-microglobulin. J Biol Chem 280:32843–32848
113. Carulla N, Caddy GL, Hall DR, Zurdo J, Gairí M, Feliz M, Giralt E, Robinson CV, Dobson CM (2005) Molecular recycling within amyloid fibrils. Nature 436:554–558
114. Chatani E, Lee YH, Yagi H, Yoshimura Y, Naiki H, Goto Y (2009) Ultrasonication-dependent production and breakdown lead to minimum-sized amyloid fibrils. Proc Natl Acad Sci USA 106:11119–11124
115. Okumura H, Itoh SG (2014) Amyloid fibril disruption by ultrasonic cavitation: nonequilibrium molecular dynamics simulations. J Am Chem Soc 136:10549–10552
116. Lee M, Baek I, Chang HJ, Yoon G, Na S (2014) The bond survival time variation of polymorphic amyloid fibrils in the mechanical insight. Chem Phys Lett 600:68–72
117. Tanaka K, Yamamoto K, Kadokawa JI (2014) Facile nanofibrillation of chitin derivatives by gas bubbling and ultrasonic treatments in water. Carbohydr Res 398:25–30
118. Editorial (2014) Mechanobiology in harness. Nat Mater 13:531
119. Iskratsch T, Wolfenson H, Sheetz MP (2014) Appreciating force and shape–the rise of mechanotransduction in cell biology. Nat Rev Mol Cell Biol. doi:10.1038/nrm3903
120. Alves-Pereira M, Castelo Branco NAA (2007) Vibroacoustic disease: biological effects of infrasound and low-frequency noise explained by mechanotransduction cellular signalling. Prog Biophys Mol Biol 93:256–279
121. Guix M, Mayorga-Martinez CC, Merkoçi A (2014) Nano/micromotors in (bio)chemical science applications. Chem Rev 114:6285–6322
122. Gao W, Wang J (2014) The environmental impact of micro/nanomachines: a review. ACS Nano 8:3170–3180

123. Hu J, Tay C, Cai Y, Du J (2005) Controlled rotation of sound-trapped small particles by an acoustic needle. Appl Phys Lett 87:094104
124. Shilton RJ, Glass NR, Chan P, Yeo LY, Friend JR (2011) Rotational microfluidic motor for on-chip microcentrifugation. Appl Phys Lett 98:254103
125. Wang W, Castro LA, Hoyos M, Mallouk TE (2012) Autonomous motion of metallic microrods propelled by ultrasound. ACS Nano 6:6122–6132
126. Takatori SC, Brady JF (2014) Swim stress, motion, and deformation of active matter: effect of an external field. Soft Matter 10:9433–9445
127. Xu T, Soto F, Gao W, Garcia-Gradilla V, Li J, Zhang X, Wang J (2014) Ultrasound-modulated bubble propulsion of chemically powered microengines. J Am Chem Soc 136:8552–8555
128. Garcia-Gradilla V, Orozco J, Sattayasamitsathit S, Soto F, Kuralay F, Pourazary A, Katzenberg A, Gao W, Shen Y, Wang J (2013) Functionalized ultrasound-propelled magnetically guided nanomotors: toward practical biomedical applications. ACS Nano 7:9232–9240
129. Ahmed S, Wang W, Mair LO, Fraleigh RD, Li S, Castro LA, Hoyos M, Huang TJ, Mallouk TE (2013) Steering acoustically propelled nanowire motors toward cells in a biologically compatible environment using magnetic fields. Langmuir 29:16113–16118
130. Wang W, Li S, Mair L, Ahmed S, Huang TJ, Mallouk TE (2014) Acoustic propulsion of nanorod motors inside living cells. Angew Chem Int Ed 53:3201–3204
131. Kagan D, Benchimol MJ, Claussen JC, Chuluun-Erdene E, Esener S, Wang J (2012) Acoustic droplet vaporization and propulsion of perfluorocarbon-loaded microbullets for targeted tissue penetration and deformation. Angew Chem Int Ed 51:7519–7522
132. De Silva L, Yao L, Xu S (2014) Mechanically resolving noncovalent bonds using acoustic radiation force. Chem Commun 50:10786–10789
133. Valverde JM, Ebri JMP, Quintanilla MAS (2013) Acoustic streaming enhances the multicyclic CO_2 capture of natural limestone at Ca-looping conditions. Env Sci Technol 47:9538–9544
134. Valverde JM, Raganati F, Quintanilla MAS, Ebri JMP, Ammendola P, Chirone R (2013) Enhancement of CO_2 capture at Ca-looping conditions by high-intensity acoustic fields. Appl Energy 111:538–549
135. Gallego-Juarez JA, Riera-Franco de Sarabia E, Rodriguez-Corral G, Hoffmann TL, Galvez-Moraleda JC, Rodriguez-Maroto JJ, Gomez-Moreno FJ, Bahillo-Ruiz A, Martin-Espigares M, Acha M (1999) Application of acoustic agglomeration to reduce fine particle emissions from coal combustion plants. Env Sci Technol 33:3843–3849
136. Fernandez Rivas D, Betjes J, Verhaagen B, Bouwhuis W, Bor TC, Lohse D, Gardeniers HJGE (2013) Erosion evolution in mono-crystalline silicon surfaces caused by acoustic cavitation bubbles. J Appl Phys 113:064902
137. Virot M, Pflieger R, Skorb EV, Ravaux J, Zemb T, Möhwald H (2012) Crystalline silicon under acoustic cavitation: from mechanoluminescence to amorphization. J Phys Chem C 116:15493–15499
138. Ball P (2009) Flow–nature's patterns. A tapestry in three parts. Oxford University Press, pp 1–20, Ch 1

Top Curr Chem (2015) 369: 285–316
DOI: 10.1007/128_2015_644

Published online: 30 June 2015

Huxley's Model for Muscle Contraction Revisited: The Importance of Microscopic Reversibility

R.Dean Astumian

Abstract Andrew Huxley's model for muscle contraction is the first mechanistic description of how an energy-providing chemical reaction, ATP hydrolysis, can be coupled by a molecule (myosin) to do work in the environment in a cyclic process. The model was originally used to fit experimentally obtained force vs velocity curves, and has served as a paradigm for understanding mechanochemical coupling ever since. Despite the remarkable success in fitting kinetic data, Huxley's model is thermodynamically inconsistent in several regards, most notably in its failure to include thermal noise in the description of the mechanical transitions by which motion occurs. This inconsistency has led subsequent workers to incorrect conclusions regarding the importance of mechanical transitions for determining the direction of motion, the efficiency of energy conversion, the ratio of forward to backward steps, and the applied force necessary to stop the motion of chemically driven molecular motors. In this chapter an extension of Huxley's model is described where the principle of microscopic reversibility provides a framework for developing a thermodynamically consistent description of a molecular machine. The results show clearly that mechanical strain and the so-called "power stroke" are irrelevant for determining the directionality and thermodynamic properties of any chemically driven molecular motor. Instead these properties are controlled entirely by the chemical specificity that describes how the relative rates of the ATP hydrolysis reaction depend, by allosteric interactions, on the mechanical state of the molecule. This mechanism has been termed an "information ratchet" in the literature. In contrast to the results for chemical driving, a power stroke can be a key component for the operation of an optically driven motor, the transitions of which do not obey microscopic reversibility.

R.D. Astumian (✉)
Department of Physics, University of Maine, Orono, ME 04469, USA
e-mail: astumian@maine.edu

Keywords Actin · ATP hydrolysis · Mechanochemical energy transduction · Molecular motor · Myosin

Contents

1 Introduction

In 1938, A.V. Hill proposed [1] a remarkably simple hyperbolic equation,

$$(F + a)(V + b) = c,$$

which captures the experimentally observable relationship between the shortening velocity of muscle, V, and a load force, F. This phenomenological expression for the force-velocity curve can be recast in terms of a single fit parameter as

$$\tilde{V} = \frac{K(1 - \tilde{F})}{K + \tilde{F}}, \tag{1}$$

where $\tilde{V} = V/V_0$ is the sliding velocity normalized by the velocity at zero load and $\tilde{F} = F/F_{\text{stall}}$ is the load force normalized by the stall force F_{stall} – the force necessary to bring the sliding velocity to zero – and $K = a/F_{\text{stall}} = b/V_0$ is a fit parameter.

In 1957, Andrew Huxley described [2] an explicit mechanistic model for muscle contraction based on consideration of the structure of muscle [3, 4]. These early structural studies, along with subsequent work, have been featured in a Nature retrospective web focus (http://www.nature.com/nature/focus/slidingfilaments/) on the sliding filament model of muscle contraction. Huxley's model introduced position-dependent rate constants for reversible binding of actin to myosin followed by an energetically downhill process that completes hydrolysis of ATP and triggers release of actin by myosin. This model is perhaps the first mechanistic description of how energy released by a chemical reaction can be coupled to do mechanical work in a cyclic (repeatable) process. Significantly, the force-velocity relation derived from Huxley's picture, with a few additional assumptions, can be cast in the form of A.V. Hill's earlier phenomenological expression at (1) [5].

Subsequent workers, notably Terrell Hill and colleagues [6], extended the model to include back reactions for the chemical processes so that thermodynamic parameters such as efficiency can be calculated. In their analysis the motion of the myosin while attached to actin is modeled as a deterministic elastic relaxation often termed a "power stroke." Unfortunately, this treatment of the mechanical motion as a deterministic process is not thermodynamically consistent and leads to incorrect predictions about the importance of the mechanical properties of the myosin.

Here, Huxley's model [2] and its extension by Hill, Eisenberg, Podolsky, and Chen [6] is revisited in light of the principle of microscopic reversibility [7]. The conclusion is that, when the rate constants for the chemical reactions of ATP hydrolysis and for the mechanical transitions of the motor are constrained by microscopic reversibility, the "power stroke" is seen to be irrelevant for determining the direction of motion, the optimal efficiency, the stopping force of the motor, or the ratio of forward to backward steps. These thermodynamic quantities are controlled entirely by molecular recognition that allows the rates of the different steps in ATP hydrolysis to depend strongly on the mechanical state of the myosin head [8]. Consistent incorporation of microscopic reversibility gives rise to a model known as a Brownian information ratchet [9] and leads to a simple relation for the force/velocity curve which, although not strictly hyperbolic, is practically indistinguishable from plots of A.V. Hill's (1) in the region between zero force and stall force.

2 Huxley's Model

The basic idea of Huxley's model is that the myosin filament has a subgroup (termed a head) attached to the main filament by a spring-like element. This subgroup fluctuates back and forth because of thermal noise and can form temporary interactions and attach to sites on the adjacent actin filament with a rate, denoted by $f(x)$, which depends on its position x. The temporary interactions can be broken by a free-energy releasing process (ATP hydrolysis) that detaches the myosin from actin with a rate $g(x)$ that also depends on position. These two

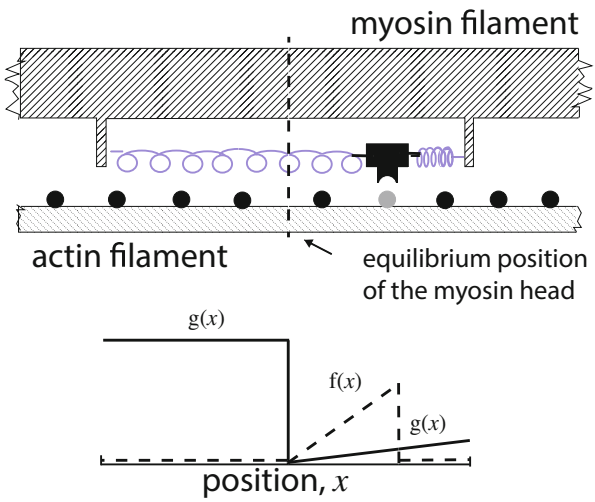

Fig. 1 Huxley's model for how a cyclic binding of myosin to actin (with rate $f(x)$) and release of actin (with rate $g(x)$) can cause net translation of the actin, and ultimately leads to contraction of the actin-myosin fiber bundle

mechanical states of myosin are often described as attached (A) and detached (D), respectively.

In any interval $x \pm \mathrm{d}x$ a certain fraction, $n(x,t)$, of the myosin heads is attached, and a fraction $1 - n(x,t)$ is detached. When the head is attached to actin, the spring pulls the actin with a force given by the deviation of the spring from its equilibrium position. Given the spring constant and equilibrium position (or equivalently the free energy profile $U(x)$), it is straightforward to relate the distribution $n(x,t)$ to the instantaneous force exerted on actin.

2.1 Steady-State Analysis

At steady state the sliding velocity is constant and the fraction of actin/myosin pairs attached at any x does not change with time. The time-independent spatial distribution $n(x)$ is then given by the differential equation

$$-V\frac{\mathrm{d}n(x)}{\mathrm{d}x} = f(x) - [f(x) + g(x)]n(x), \tag{2}$$

where V is the experimentally observed velocity of sliding. Using simple piecewise linear functions $g(x)$ and $f(x)$ (see Fig. 1), Huxley calculated the fraction $n(x)$, and hence the average force on actin as a function of velocity. The fit to experimental results such as force vs velocity curves and rate of energy dissipation – the same data that had led A.V. Hill to the phenomenological (1) – is very good. With a few plausible assumptions regarding the dependence of the rates on the velocity [5], Huxley's model can be cast into the identical mathematical form as Hill's phenomenological equation describing a hyperbolic relation between velocity and force.

2.1.1 Microscopic Reversibility and Chemical Transitions

Despite excellent success in fitting kinetic data, however, Huxley's model is not thermodynamically complete because there is no explicit dependence of the velocity or average force on the free-energy released by ATP hydrolysis ($\Delta\mu = \mu_{\mathrm{ATP}} - \mu_{\mathrm{ADP}} - \mu_{\mathrm{P_i}}$). Huxley recognized that the process described by $g(x)$ is not the microscopic reverse of the process described by $f(x)$ and that each cycle of attaching by $f(x)$ and detaching by $g(x)$ implicitly involves hydrolysis of one ATP molecule, but (2) cannot be used to investigate such important questions as "what happens when the ATP hydrolysis reaction is near equilibrium?," or "does externally driving the muscle to slide with a negative velocity lead to the synthesis of ATP?" To probe these thermodynamic questions, the rates of the microscopic reverses for both attachment and detachment, $f'(x)$ and $g'(x)$, respectively, must be included in the description. The rates in general depend on position, but obey an important thermodynamic constraint,

$$\frac{f(x)g(x)}{f'(x)g'(x)} = \mathrm{e}^{\Delta\mu}\,, \tag{3}$$

which must hold at any particular value of x. To make the notation as compact as possible, all energies are written in units of the thermal energy $k_{\mathrm{B}}T$, and we choose length units in which the period along the myosin is unity.

2.1.2 Chemical Specificity

Hypothetical energy profiles for ATP hydrolysis are shown for two different positions, 0 and α, in Fig. 2. At any position, ATP hydrolysis obeys the simple Michaelis–Menten mechanism shown at the bottom of Fig. 2. The chemical specificities (i.e., the relative rates of the "f" and "g" processes) depend on the transition state energy difference $\Delta\mathcal{E}^{\ddagger}(x) = \mathcal{E}^{\ddagger}_{\mathrm{g}}(x) - \mathcal{E}^{\ddagger}_{\mathrm{f}}(x)$. We can write relationships between the rate constants in terms of these transitions state energy differences:

$$\frac{f(0)\,g'(\alpha)}{g'(0)\,f(\alpha)} = \frac{f'(\alpha)\,g(0)}{g(\alpha)\,f'(0)} = \mathrm{e}^{-\Delta\mathcal{E}^{\ddagger}(0)+\Delta\mathcal{E}^{\ddagger}(\alpha)}. \tag{4}$$

The transition state energies are not thermodynamically constrained and are thus subject to evolution or to chemical design. Some of the individual rate constants, $f(x)$, $f'(x)$, $g(x)$ and $g'(x)$, depend on the concentrations [ATP], [ADP], and [$\mathrm{P_i}$], but the ratios in (4) do not.

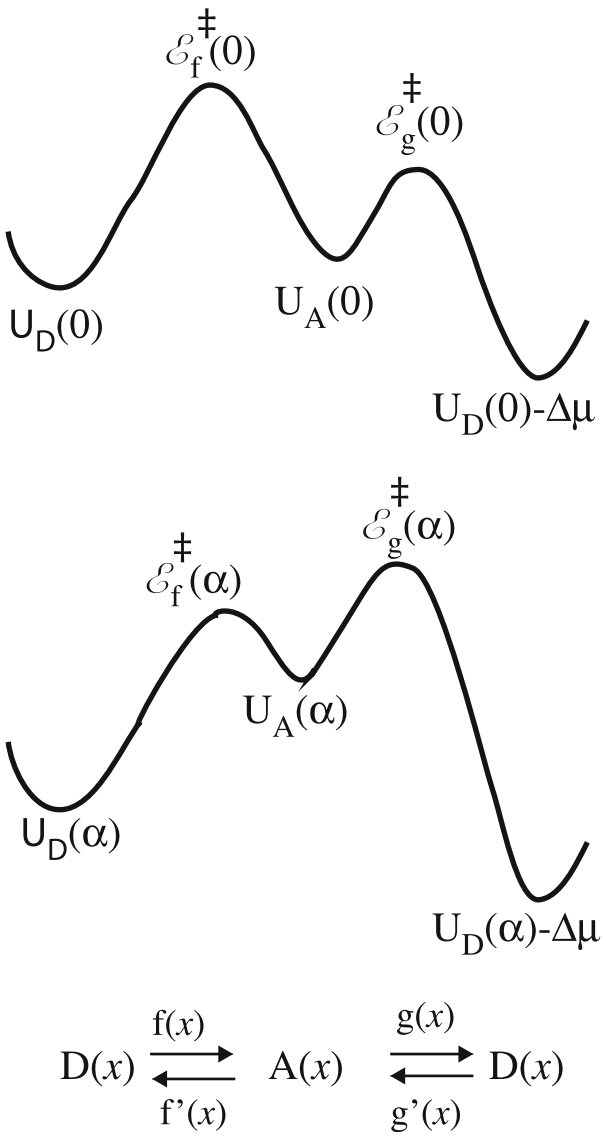

Fig. 2 Free energy profiles for the chemical process at two different positions 0 and α. The selection between the "f" and "g" processes depends on the transition state energy differences. In Fig. 3 $\mathcal{E}_f^{\ddagger}(0) - \mathcal{E}_g^{\ddagger}(0) > 0$ and $\mathcal{E}_f^{\ddagger}(\alpha) - \mathcal{E}_g^{\ddagger}(\alpha) < 0$, so at position 0 the myosin is specific for the g process and at position α the myosin is specific for the f process. The energy of the bound state at position α, $U_A(\alpha)$, is greater than the energy of the bound state at position 0, $U_A(\alpha)$. The energy-releasing mechanical transition from position α to 0 (see Fig. 4) is termed the power stroke

2.1.3 Focusing on Trajectories

A model that is consistent with the constraint on the transition rates expressed in (3) is essential for understanding the thermodynamics of energy coupling – stoichiometry, thermodynamic efficiency, stopping force, ratio of forward to backward steps, etc. Further, to address what is perhaps the most basic question about muscle – "why does ATP hydrolysis drive myosin to move actin one way and not the other?" the velocity must be an output of the theory rather than an input as it is in Huxley's model. We can better understand this question in terms of a mechanistic description

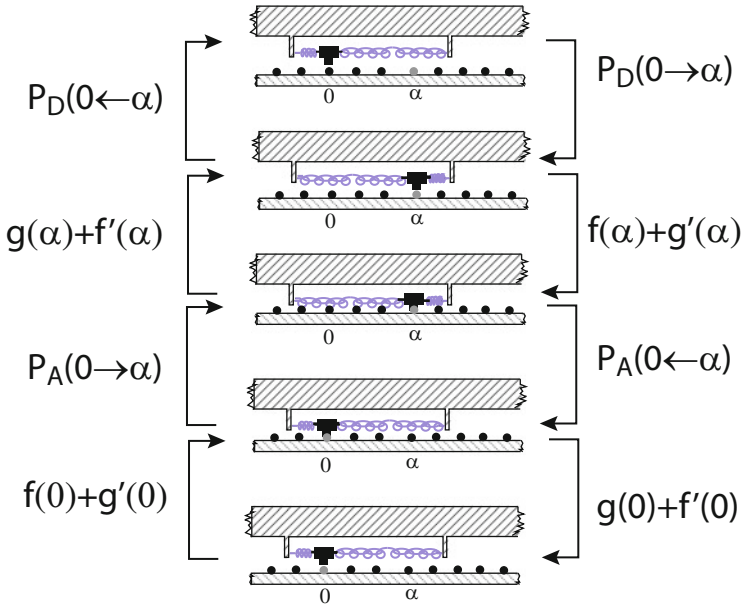

Fig. 3 Possible sequence of steps by which myosin transports an actin site, shown in *light gray*, between points α and 0. The sequence from *top* to *bottom* transports actin to the *left* relative to the myosin, a direction we call a forward step, whereas the sequence from *bottom* to *top* transports actin to the *right* relative to the myosin, a direction we call a backward step

of possible trajectories between the two points labeled 0 and α shown in Fig. 3. Starting at the top of Fig. 3, movement to position α while detached, then binding at position α with subsequent movement to position 0 while attached, followed by dissociation at position 0 results in movement of actin a distance α to the left. This path is illustrated going from top to bottom in Fig. 3 by the arrows at the right. Starting at the bottom, however, binding at position 0 with subsequent movement to position α while attached, followed by dissociation and return to position 0 results in movement of actin a distance α to the right, as indicated by the arrows at the left in Fig. 3. What parameters govern whether a forward step (the sequence from top to bottom in Fig. 3) or a backward step (the sequence from bottom to top in Fig. 3) is more likely?.

2.2 Terrell Hill's Extension of Huxley's Model

A natural answer proposed by Terrell Hill and colleagues [6] is that the direction of motion is governed by the asymmetry of the spring. Hill et al. [6] explicitly described the motion of the actin filament in terms of an asymmetric free-energy landscape for the actin site as shown in Fig. 4, where in the attached state the myosin exerts a position-dependent force on the actin, and in the detached state

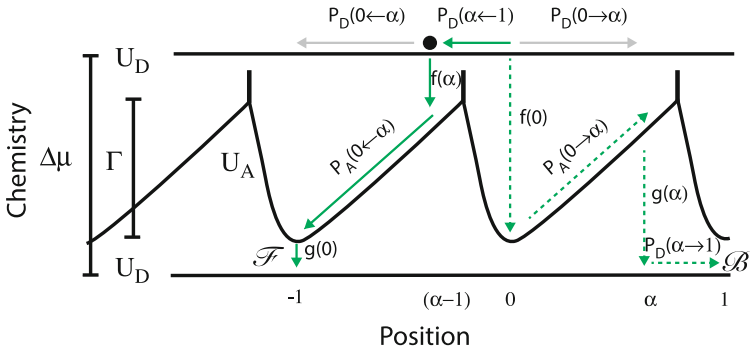

Fig. 4 Schematic illustration of the free-energy functions for the attached (A) and detached (D) states similar to that given by Hill, Eisenberg, Chen, and Podolsky [6]. The energy change $\Delta\mu$ is the total energy provided by ATP hydrolysis, and Γ is the energy released during the "power stroke" in which the myosin pulls the actin filament to the *left*. Hill et al. gave only a single period of the functions $U_A(x)$ and $U_D(x)$, and showed only the *solid green* transitions representing a step (denoted $\mathscr{F}$) in which the myosin moves the actin to the *left* (forward) while hydrolyzing ATP. The unnormalized probabilities for all transitions are shown on the diagram. By periodicity $P_S(i \leftarrow \alpha + i) \equiv P_S(0 \leftarrow \alpha)$; $P_S(\alpha + i \leftarrow 1 + i) \equiv P_S(\alpha \leftarrow 1)$; $P_S(i \rightarrow \alpha + i) \equiv P_S(0 \rightarrow \alpha)$; and $P_S(\alpha + i \rightarrow 1 + i) \equiv P_S(\alpha \rightarrow 1)$ for S = A, D

the myosin head does not exert a force on actin. There may be a load force which is typically modeled as being homogeneous and giving rise to a net tilt of both $U_A(x)$ and $U_D(x)$.

The asymmetry in the harmonic potential guides the eye to recognize that diffusion from the dissociation site i, for $i = \ldots, -1, 0, 1 \ldots$, over the short distance $(1 - \alpha)$ to the binding site at $(\alpha - i) - 1$ is more likely than diffusion over the greater distance α to the binding site at $i + \alpha$. In the limit $\alpha \approx 1$, no diffusion is required and, seemingly, the myosin would then work almost deterministically. The only stochastic aspect of the motion would reside in the chemistry described by the "f" and "g" processes, and each hydrolysis would result in motion of actin one step to the left. Hill et al. [6] presented only a single period of the schematic potential energy landscape and included only the transitions represented as solid green lines in which the myosin moves the actin to the left (forward) while hydrolyzing ATP according to the path denoted $\mathscr{F}$. They described this path as having a near "optimal efficiency," arguing that "it is clear there is no way the efficiency could be greater than $\Gamma/\Delta\mu$." These seemingly commonsense assertions are wrong.

For a complete analysis we must recognize the possibility of another sequence [10], shown by the dashed arrows in Fig. 4, in which myosin moves the actin a period to the right, *while also hydrolyzing* ATP. This backward path, denoted $\mathscr{B}$, is often ignored because it contains the macroscopically implausible (and deterministically impossible) uphill motion on the potential U_A from the energy minimum at the position zero to a strained configuration at the position α.

2.3 Microscopic Reversibility and Mechanical Transitions

For chemically driven motors the asymmetric well with depth Γ is a *trompe l'oeil* that fools the reader into concluding that the directionality of motion and other thermodynamic aspects of muscle behavior are governed by the spring and its anharmonicity. As is shown using the principle of microscopic reversibility, this is not the case. In fact, the intrinsic (zero load) direction of motion, and every thermodynamic property of muscle behavior, is governed solely by the activation barrier differences $\Delta\mathcal{E}^{\ddagger}(\alpha)$ and $\Delta\mathcal{E}^{\ddagger}(0)$ that determine the chemical specificities, and not by the energy difference $U_{\mathrm{A}}(\alpha) - U_{\mathrm{A}}(0)$ that drives the power stroke.

We can most easily see the importance of the $\Delta\mathcal{E}^{\ddagger}(x_{\mathrm{i}})$ by first considering the relationship between forward and reverse mechanical motions. Using the Onsager–Machlup thermodynamic action theory [11], Bier et al. [12] provided explicit relations based on the principle of microscopic reversibility for the relative probability of a down-slide vs an up-slide on an energy surface, which for Fig. 4 can be expressed as

$$\begin{aligned}
\frac{P_{\mathrm{A}}(0 \rightarrow \alpha)}{P_{\mathrm{A}}(0 \leftarrow \alpha)} &= \mathrm{e}^{U_{\mathrm{A}}(0) - U_{\mathrm{A}}(\alpha) + \alpha F}, \\
\frac{P_{\mathrm{A}}(\alpha \rightarrow 1)}{P_{\mathrm{A}}(\alpha \leftarrow 1)} &= \mathrm{e}^{-U_{\mathrm{A}}(0) + U_{\mathrm{A}}(\alpha) + (1-\alpha)F}, \\
\frac{P_{\mathrm{D}}(0 \rightarrow \alpha)}{P_{\mathrm{D}}(0 \leftarrow \alpha)} &= \mathrm{e}^{\alpha F}, \\
\frac{P_{\mathrm{D}}(\alpha \rightarrow 1)}{P_{\mathrm{D}}(\alpha \leftarrow 1)} &= \mathrm{e}^{(1-\alpha)F},
\end{aligned} \tag{5}$$

where αF is the force $\times$ distance work done in moving the actin a distance α in the presence of an external homogeneous force, F, and we choose as a sign convention that positive F tends to move the actin filament to the right.

We can obtain an additional constraint on the rate constants for the chemical transitions with these relations by using a "thermodynamic" box, as shown in Fig. 5. The product of the probabilities for the clockwise transitions must equal the product of the probabilities for the counterclockwise transitions,

$$P_{\mathrm{A}}(0 \leftarrow \alpha) P_{\mathrm{D}}(0 \rightarrow \alpha) f(\alpha) f'(0) = P_{\mathrm{D}}(0 \leftarrow \alpha) P_{\mathrm{A}}(0 \rightarrow \alpha) f'(\alpha) f(0), \tag{6}$$

with an analogous relation holding for the transitions of a thermodynamic box (not shown) formed using the "g" rates:

$$\frac{g'(\alpha) g(0)}{g'(0) g(\alpha)} = \frac{f(\alpha) f'(0)}{f(0) f'(\alpha)} = \mathrm{e}^{[U_{\mathrm{A}}(0) - U_{\mathrm{A}}(\alpha)]}. \tag{7}$$

The ratio of the probabilities for path $\mathscr{F}$ and path $\mathscr{B}$ is then seen to be

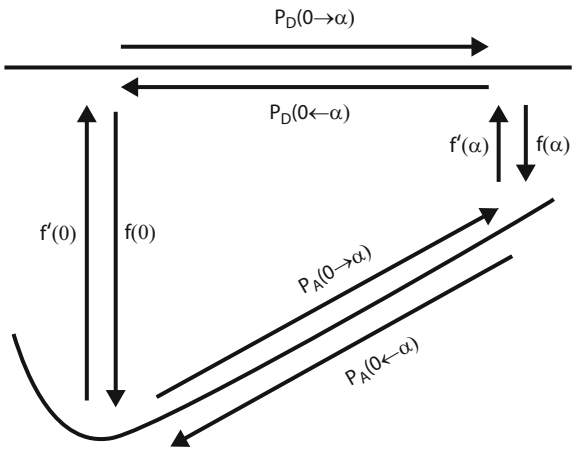

Fig. 5 Illustration of a thermodynamic box used to derive a relationship between the rate constants $f(0), f'(0), f(\alpha)$ and $f'(\alpha)$. A similar box (not shown) that involves the "g" rates can be drawn. Irrespective of the magnitude of $\Delta\mu$, or of whether there is a load force, the product of the probabilities in the clockwise direction must be equal to the product of the probabilities in the counter-clockwise direction (see (6)), resulting in (7)

$$\frac{P_{\mathscr{B}}}{P_{\mathscr{F}}} = \frac{P_{\mathrm{A}}(0 \rightarrow \alpha) P_{\mathrm{D}}(\alpha \rightarrow 1)\, f(0)\, g(\alpha)}{P_{\mathrm{A}}(0 \leftarrow \alpha)\, P_{\mathrm{D}}(\alpha \leftarrow 1) f(\alpha)\, g(0)} = \mathrm{e}^{\left[\Delta\mathcal{E}^{\ddagger}(\alpha) - \Delta\mathcal{E}^{\ddagger}(0)\right]}\, \mathrm{e}^{\mathrm{F}}, \tag{8}$$

where the second equation is obtained by using (7) and (4). In the absence of an applied force, the selection between the path in which ATP is hydrolyzed and actin moves a period to the left ($\mathscr{F}$) and the path in which ATP is hydrolyzed and actin moves a period to the right ($\mathscr{B}$) is determined solely by $\Delta\mathcal{E}^{\ddagger}(\alpha) - \Delta\mathcal{E}^{\ddagger}(0)$ (the chemical specificities) and is independent of the shape, $U_{\mathrm{A}}(x)$, or amplitude, Γ, of the mechanical potential energy landscape! In other words, myosin operates as a Brownian information motor [9] or ratchet [13], the directionality of which is determined by allosteric interactions that allow the relative activation barriers for the "f" and "g" chemical processes to vary as a function of position. When $\left[\Delta\mathcal{E}^{\ddagger}(\alpha) - \Delta\mathcal{E}^{\ddagger}(0)\right] < 0$ the path $\mathscr{F}$ is favored and when $\left[\Delta\mathcal{E}^{\ddagger}(\alpha) - \Delta\mathcal{E}^{\ddagger}(0)\right] > 0$ the path $\mathscr{B}$ is favored, irrespective of the shape or details of the mechanical potential profile $U_{\mathrm{A}}(x)$.

2.4 General Coupled Transport Relations

2.4.1 Microscopic Reversibility and Path Probabilities

In addition to paths $\mathscr{F}$ and $\mathscr{B}$ (and their microscopic reverses $\mathscr{F}_R$ and $\mathscr{B}_R$, respectively) there are also paths in which the motor moves without hydrolyzing ATP (slip), or in which ATP is hydrolyzed without moving (futile cycling). To add further complexity, to evaluate explicitly all terms, we would have to integrate over

all possible values for α. We can cut through this complexity by focusing on possible outcomes in the environment for every complete cycle that starts and ends at periodically related positions, e.g., $0 \pm i$ with myosin in the detached state [14]. These paths can be summarized:

$\mathscr{F}/\mathscr{F}_{\mathrm{R}}$ Actin to left with ATP hydrolysis/actin to right with ATP synthesis
$\mathscr{B}/\mathscr{B}_{\mathrm{R}}$ Actin to right with ATP hydrolysis/actin to left with ATP synthesis
$\mathcal{S}/\mathcal{S}_{\mathrm{R}}$ Actin to left without chemistry/actin to right without chemistry
$\mathcal{C}/\mathcal{C}_{\mathrm{R}}$ Hydrolysis of ATP without motion/synthesis of ATP without motion

The ratio for the probability of any process and its microscopic reverse is a thermodynamic identity [14]:

$$\frac{P_{\mathscr{F}}}{P_{\mathscr{F}_{\mathrm{R}}}} = \mathrm{e}^{-F+\Delta\mu}; \quad \frac{P_{\mathscr{B}}}{P_{\mathscr{B}_{\mathrm{R}}}} = \mathrm{e}^{F+\Delta\mu}; \quad \frac{P_{\mathcal{S}}}{P_{\mathcal{S}_{\mathrm{R}}}} = \mathrm{e}^{-F}; \quad \frac{P_{\mathcal{C}}}{P_{\mathcal{C}_{\mathrm{R}}}} = \mathrm{e}^{\Delta\mu}. \tag{9}$$

The net probabilities to take a forward step, and for an ATP to be hydrolyzed, in terms of these probabilities are

$$\begin{aligned} P_{\text{forward}} - P_{\text{backward}} &= \underbrace{(P_{\mathscr{F}} + P_{\mathscr{B}_{\mathrm{R}}} + P_{\mathcal{S}})}_{\text{forward steps}} - \underbrace{(P_{\mathscr{F}_{\mathrm{R}}} + P_{\mathscr{B}} + P_{\mathcal{S}_{\mathrm{R}}})}_{\text{backward steps}}, \\ P_{\text{hydrolysis}} - P_{\text{synthesis}} &= \underbrace{(P_{\mathscr{F}} + P_{\mathscr{B}} + P_{\mathcal{C}})}_{\text{ATP hydrolysis}} - \underbrace{(P_{\mathscr{F}_{\mathrm{R}}} + P_{\mathscr{B}_{\mathrm{R}}} + P_{\mathcal{C}_{\mathrm{R}}})}_{\text{ATP synthesis}}. \end{aligned} \tag{10}$$

To calculate the overall ratio between the forward and backward paths we need to integrate $\mathrm{P}_{\mathscr{F}}$ and $\mathrm{P}_{\mathscr{B}}$ over α for a complete period (i.e., from 0 to 1) and take the ratio of their integrals. For each value of α we can use the relation (8) so we have

$$\frac{\int_0^1 P_{\mathscr{B}} \mathrm{d}\alpha}{\int_0^1 P_{\mathscr{F}} \mathrm{d}\alpha} = \frac{\mathrm{e}^F \int_0^1 \mathrm{e}^{\Delta\Delta\mathcal{E}^{\ddagger}} P_{\mathscr{F}} \mathrm{d}\alpha}{\int_0^1 P_{\mathscr{F}} \mathrm{d}\alpha} = \left\langle \mathrm{e}^{\Delta\Delta\mathcal{E}^{\ddagger}} \right\rangle e^F \equiv q\mathrm{e}^F, \tag{11}$$

where $\Delta\Delta\mathcal{E}^{\ddagger} = \Delta\mathcal{E}^{\ddagger}(\alpha) - \Delta\mathcal{E}^{\ddagger}(0)$ and the parameter "q" is the no load ratio of the overall likelihood for an ATP driven backward step to the likelihood for an ATP driven forward step.

2.4.2 General Equations for Velocity and Rate of ATP Hydrolysis

The average velocity and rate of ATP hydrolysis can be obtained by dividing the net probabilities (10) by a common time constant and then using the thermodynamic identities in (9) and the definition in (11) to simplify the resulting expression to obtain

$$V = \tau^{-1}\left\{[(1-e^{F-\Delta\mu}) - qe^{F}(1-e^{-F-\Delta\mu})] + \frac{P_S}{P_F}(1-e^{F})\right\},$$
$$v_{ATP} = \tau^{-1}\left\{[(1-e^{F-\Delta\mu}) + qe^{F}(1-e^{-F-\Delta\mu})] + \frac{P_C}{P_F}(1-e^{-\Delta\mu})\right\}. \quad (12)$$

The equations (12) are exact. The terms in brackets ($[\cdots]$) describe the coupled transport and the terms $\frac{P_S}{P_\mathcal{F}}(1-e^{F})$ and $\frac{P_C}{P_\mathcal{F}}(1-e^{-\Delta\mu})$ describe the slip (stepping without ATP hydrolysis/synthesis) and futile cycling (ATP hydrolysis/synthesis without stepping), respectively. It should be noted that when $F, \Delta\mu << 1$ the exponentials in the general (10) can be expanded and truncated to first order in F and $\Delta\mu$. Onsager reciprocity [15] is apparent in that the coefficient of $\Delta\mu$ in the expanded equation for V and the coefficient of F in the expanded equation for v_{ATP} are equal.

We arrive at an important conclusion by examining the ratio of net forward to backward steps ("the step ratio") $= P_{backward}/P_{forward}$,

$$\text{step ratio} = \left(\frac{1 + qe^{-\Delta\mu} + \frac{P_S}{P_F}}{q + e^{-\Delta\mu} + \frac{P_S}{P_F}}\right)e^{-F}. \quad (13)$$

It should be noted that the velocity can be written most simply as

$$V = \tau^{-1}(1 - \text{step ratio}) \quad (14)$$

It is immediately apparent from (13) that when $\Delta\mu = 0$ the factor in parentheses $(\cdots)$ is unity as expected for a system in chemical equilibrium. On close examination we also see that when $q = 1$ this factor is unity irrespective of the value of $\Delta\mu$ [16]. Directed motion of a molecular machine requires both that the system be away from equilibrium ($\Delta\mu \neq 0$) and also that the symmetry of the system be broken, $q \neq 1$. For a chemically driven motor, this symmetry breaking has nothing to do with the amplitude, Γ, or with the underlying mechanical potential, U_A, and is governed solely by the spatial dependence of the transition state energies that determine "q." The dependence of the term $\frac{P_S}{P_\mathcal{F}}$ on [ATP] can be obtained for specific models and has been used to fit [16] the ATP concentration dependence of the velocity and stopping force observed by Clancy et al. [17] for a mutated form of kinesin which displays incomplete coupling (i.e., significant slip and futile cycling).

2.5 *Simple Approximations for ATP Hydrolysis-Driven Processes: The Fully Coupled Limit*

In the situation of our interest, muscle contraction, the free energy released by ATP hydrolysis, $\Delta\mu$, is typically between 50 and 70 kJ/mol ($\Delta\mu = 17 - 20$ in our units)

and $q << 1$ so the term $qe^{-\Delta\mu}$ can be neglected in comparison with the other terms. Further, ATP hydrolysis is almost fully coupled to actin transport so slip and futile cycling (the third term in the first and second equations at (12), respectively) can be neglected. This is the fully coupled limit in which every ATP hydrolysis or synthesis is associated with one step forward or backward [16]. We find simple approximations

$$\begin{aligned} V &\approx \tau^{-1}[1-(q+e^{-\Delta\mu})e^{F}], \\ v_{\mathrm{ATP}} &\approx \tau^{-1}[1+(q-e^{-\Delta\mu})e^{F}]. \end{aligned} \tag{15}$$

Setting

$$A = \left(q + e^{-\Delta\mu}\right);\ A^{*} = \left(q - e^{-\Delta\mu}\right) \tag{16}$$

the velocity and rate of ATP hydrolysis at zero load and the stall force can easily be calculated from (15) to be

$$V_0 \approx \tau_0^{-1}[1-A]\,;\ \ v^0_{\mathrm{ATP}} \approx \tau_0^{-1}\left[1+A^{*}\right]\,;\ \ F_{\mathrm{stall}} \approx \ln\left((A)^{-1}\right). \tag{17}$$

2.5.1 Almost Hyperbolic Relation from an Information Ratchet Model

Taking a Boltzmann expression for the force dependence of the time constant $\tau^{-1} = e^{-a\tilde{F}}\tau_0^{-1}$ we find the normalized velocity

$$\tilde{V} = A^{a\tilde{F}}\left(\frac{1-A^{(1-\tilde{F})}}{1-A}\right) \tag{18}$$

and the normalized rate of ATP hydrolysis

$$\tilde{v}_{\mathrm{ATP}} = A^{a\tilde{F}}\left(\frac{1+A^{*(1-\tilde{F})}}{1+A^{*}}\right), \tag{19}$$

where $\tilde{v}_{\mathrm{ATP}} = v_{\mathrm{ATP}}/v^0_{\mathrm{ATP}}$. Plots of the hyperbolic expression (1) and of the exponential expression (18) are shown in Fig. 6. The plots are very close to one another between zero load and stall force with $a = 1$ and $A = 0.015$. Nevertheless, the underlying physical pictures behind these two equations are very different.

The hyperbolic expression can be derived from a picture in which the mechanical motion involves a deterministic power stroke. Although this power stroke model can be generalized to include thermodynamically consistent rate constants (see (3)), the description of the mechanical transitions as deterministic processes is not consistent with microscopic reversibility and is incorrect.

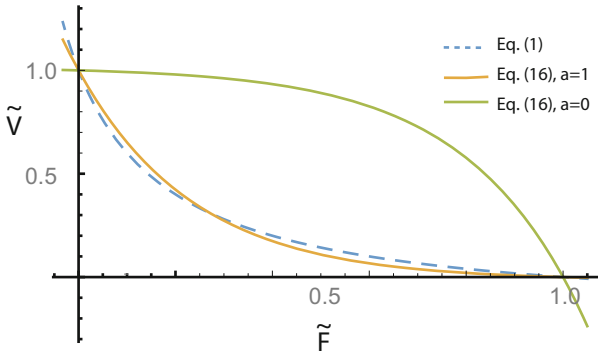

Fig. 6 Plots of (1) (*blue dashed line*) with $K = 0.2$ (consistent with the fit in Hill's original paper), and (16) with $A = 0.015$ and $\alpha = 1$ (*orange solid line*) and with $A = 0.015$ and $\alpha = 0$ (*green solid line*). Although the *orange* and *dashed blue curves* virtually overlap in the region between no load and stall force, the symmetry is different. Equation (1) is invariant under the transformation $\tilde{F} \leftrightarrow \tilde{V}$ whereas (16) is not. Predictions of the two equations can be easily distinguished in the super-stall and assisting force regimes

In contrast, the information ratchet model [9], on which (18) and (19) are based, is consistent with microscopic reversibility for both the chemical and the mechanical processes. The shape of the curve described by (18) is governed by both the force dependence of τ^{-1} and by the term q that parameterizes the relative likelihood of a forward ATP driven step vs a backward ATP-driven step. The force velocity curve is close to hyperbolic with $a = 1$, but with $a = 0$, the velocity is nearly constant up to a force of slightly more than half the stopping force and then dramatically decreases to zero at the stopping force, and with $a = 0.25$ (not shown) the velocity is a nearly linearly decreasing function of the applied force up to F_{stall}. The thermodynamic properties such as the step ratio, stoichiometry, efficiency, and stall force are independent of τ^{-1}.

Plots of $\tilde{V}$ and $\tilde{v}_{\text{ATP}}$ vs applied force $\tilde{F}$ are shown in Fig. 7 for $a = 0.5$. As predicted by Astumian and Bier [10], the rate of ATP hydrolysis falls with applied force, but then increases again beyond the stopping force when the motor moves backward. This prediction was supported experimentally by Nishiyama et al. [18] and by Carter and Cross [19], whose results are consistent with ATP stimulated backward stepping at forces greater than the stall force. Their observations are not consistent with so-called tight coupling models [20] in which every ATP hydrolysis leads to a forward step, but are consistent with fully coupled models [16] in which every hydrolysis or synthesis of ATP is associated with a forward or backward step and *vice versa*.

We can obtain a better understanding of the relative importance of the kinetic splitting factor q and the thermodynamic driving force $\Delta\mu$ by considering two limits to the behavior of a molecular motor.

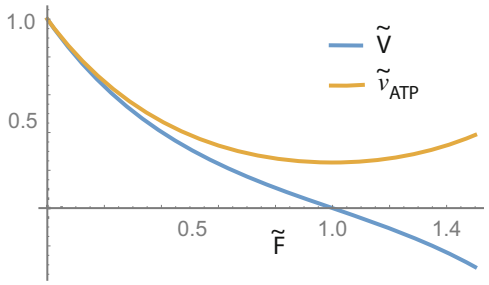

Fig. 7 Plot of $\tilde{V}$ and $\tilde{v}_{ATP}$ from (16), with $K = 0.015$ and with $a = 1/2$. As predicted by Astumian and Bier based on a kinetic model for a Brownian motor, the ATP hydrolysis rate increases beyond the stall force, F_{stall}. A concomitant prediction – that ATP can stimulate rather than inhibit backstopping – was supported experimentally by Nishiyama et al. [18] and by Carter and Cross [19]

2.6 *Thermodynamic vs Kinetic Control*

2.6.1 Thermodynamic Control

When $q << e^{-\Delta\mu}$, $A \approx -A^* \approx e^{-\Delta\mu}$, and the motor is thermodynamically controlled. This limit is also known as the tight coupling limit in which each hydrolysis of an ATP is associated with one forward step and each backward step is associated with synthesis of one ATP. The step ratio and the thermodynamic efficiency are

$$(\text{step ratio})_{th} = e^{F-\Delta\mu}; \quad \eta_{th} = \frac{F}{\Delta\mu}\tanh\left[\frac{\Delta\mu - F}{2}\right]. \tag{20}$$

This thermodynamic limit represents the optimal behavior for a molecular motor where all the evolvable (or designable) features are such that the behavior of the motor is limited only by energy conservation. With $\Delta\mu = 20$ the efficiency is maximized at about 80% when $F = 18$, and there is no fundamental limit lower than unity [21]. The FoF1-ATPase is an example of a thermodynamically controlled motor. The difference in activation barriers for the kinetic processes are $>2 \times (40)$ kJ/mol as can be seen from the energy landscape for rotation [22]. This value is indeed significantly larger than the $\Delta\mu$ for ATP hydrolysis. When an ATP-driven thermodynamically controlled motor is forced backward, ATP is synthesized.

2.6.2 Kinetic Control

When $e^{-\Delta\mu} << q$ then $A \approx A^* \approx q$ and the motor is under kinetic control. The step ratio and efficiency are well approximated as

$$(\text{step ratio})_{\text{kin}} = q\mathrm{e}^{F}; \quad \eta_{\text{kin}} = \frac{F}{\Delta\mu}\tanh\left[\frac{\langle \Delta\Delta\mathcal{E}^{\ddagger}\rangle - F}{2}\right]. \tag{21}$$

This kinetic limit is clearly appropriate for muscle. The value $q = 0.015$ corresponds to $\Delta\Delta\mathcal{E}^{\ddagger} = \Delta\mathcal{E}^{\ddagger}(0) - \Delta\mathcal{E}^{\ddagger}(\alpha) \approx 10\,\text{kJ/mol}$. Myosin V is another example of a kinetically controlled motor. The difference in activation barriers for the $\mathscr{F}$ and $\mathscr{B}$ kinetic processes are ≈40 kJ/mol, as can be seen from the energy landscapes for the functional ($\mathscr{F}$) and non-functional ($\mathscr{B}$) paths [23]. Both of these values are indeed significantly smaller than the $\Delta\mu$ for ATP hydrolysis. Forcing an ATP-driven kinetically controlled motor backwards causes enhanced ATP hydrolysis, not synthesis, a behavior predicted by Astumian and Bier [10].

3 Ratchet Models of Molecular Machines

3.1 Understanding Ratchets in Terms of Chemical Specificities

The major conclusion of our reinvestigation of Huxley's model for muscle contraction is that the power stroke, long thought to be an essential element of the operation of many molecular machines, is in fact a red herring and is irrelevant for determining the direction and thermodynamic behavior of any chemically driven molecular motor. To understand better how the chemical specificity and not the mechanical potential governs the directionality of a molecular machine, let us consider a so-called power stroke model (Fig. 8) which has been used to describe the bacterial flagellar motor [24], where the position variable x is now replaced with an angle variable θ.

Xing et al. [24] included only the downward pointing green arrows in the shaded reaction windows of the potentials $U_1(\theta)$ (deprotonated) and $U_2(\theta)$ (protonated), giving rise to a simple story. Two protons bind from the periplasm in the reaction window at the bottom of potential $U_1(\theta)$. The motor finds itself in a strained configuration on the protonated state potential $U_2(\theta)$, thus deterministically initiating power stroke 1 as the system relaxes to the bottom of the well on $U_2(\theta)$. Then, at the bottom of the well, the two protons dissociate to the cytoplasm, thereby inducing a transition to a strained state on $U_1(\theta)$ which deterministically initiates power stroke 2 as the system relaxes to the bottom of the well. In each complete cycle, two protons are transported from the periplasm to the cytoplasm and the motor makes one step to the right.

Neglect of the backward transitions (short arrows) is justifiable based on the large proton electrochemical potential, $\Delta\mu$, which drives the process. Neglect of the red arrows is justifiable based on structural considerations showing that at one angle the proton binding site is open to the periplasm but not to the cytoplasm, and at

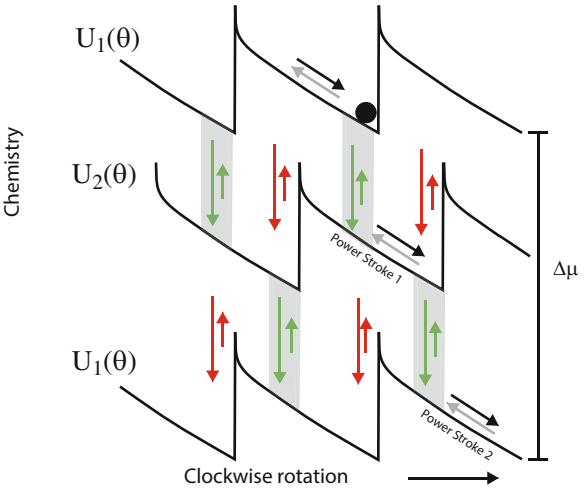

Fig. 8 A power stroke model for a bacterial flagellar motor that has been described in terms of two asymmetric sawtooth potentials whose spatial periods are out of phase with one another. In the original depiction [24], only the *long green arrows* pointing downward in the *shaded reaction windows* were drawn for the chemical (proton binding and release) transitions, but this approximation represents a logically impossible limit

another angle the proton binding site is open to the cytoplasm but not to the periplasm. Either of these approximations is perfectly sensible – very large $\Delta\mu$ implies kinetic control where $e^{-\Delta\mu} << q$. A very large difference between high (closed) and low (open) energy barriers implies thermodynamic control where $q << e^{-\Delta\mu}$. However, making both approximations is not correct and is equivalent to assuming that q is both much greater than and simultaneously much less than $e^{-\Delta\mu}$, a logical impossibility. When the analysis is carried out correctly, using rate constants consistent with microscopic reversibility, we find, contrary to the visual impression conveyed by Fig. 8, the direction of motion, the step ratio, and the stall force are governed solely by the chemical specificities and by $\Delta\mu$ and are independent of the forces produced by the slopes of the potentials $\partial U_1(\theta)/\partial\theta$ and $\partial U_2(\theta)/\partial\theta$.

To reify this very important point further, let us consider the two ratchet models shown in Fig. 9. At first glance it would seem that the ratchet in Fig. 9a is designed for transport to the right and that in Fig. 9b is designed for transport to the left. Despite appearances, however, both ratchets operate as Brownian information motors [9]. When the rate constants are assigned consistent with microscopic reversibility, the intrinsic directionality of each ratchet is controlled by the parameter

$$q = \frac{g_1 f_2'}{f_1' g_2}. \tag{22}$$

When $q < 1$ the motion is to the right for both ratchets, and when $q > 1$ the motion is to the left. Further, the step ratio and stall force for both ratchets are identical, and in the fully coupled limit the efficiencies are identical as well. The essential feature determining the directionality and stall force is the allosteric interaction by which

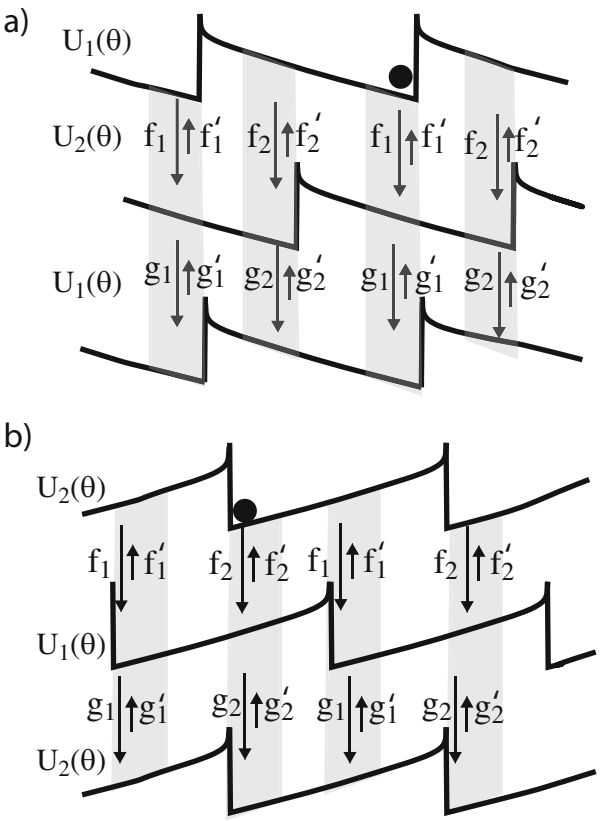

Fig. 9 Two shift ratchets with different mechanical potentials $U_1(x)$ and $U_2(x)$. Appearance suggests that the ratchet in (**a**) is designed to move to the *right* and that in (**b**) is designed to move to the *left* when $\Delta\mu > 0$. However, when rate constants consistent with microscopic reversibility are used in the description of the chemical transitions, this is seen not to be the case, and that the direction is controlled by the chemical specificity $q = \frac{g_1 f_2'}{f_1' g_2}$

the chemical rates are position dependent and not the slopes of the mechanical potentials.

3.2 *Plausible Logic and Incorrect Conclusions: A Cautionary Tale*

It is, however, easy to fool ourselves by making natural, but subtly incorrect, assignments of the rate constants. A simple assignment for Fig. 9,

$$\begin{aligned} f_1 = f_2 = g_1 = g_2 = \sigma e^{\Delta\mu/4}, \\ f_1' = f_2' = g_1' = g_2' = \sigma e^{-\Delta\mu/4}, \end{aligned} \tag{23}$$

is patently consistent with the constraint of microscopic reversibility expressed in (3). In a linear approximation the forward rate constants can be written as $\sigma + \varepsilon$ and the reverse rate constants as $\sigma - \varepsilon$, where $\varepsilon = \sigma\Delta\mu/4$. According to Presse

et al. [25] "ε represents some driving force, the degree to which detailed balance is broken to drive the system in one direction. In biology, ε may depend on the amount of ATP concentration driving a motor, for example."

When we use the assignment of rate constants in (23) to analyze the ratchets in Fig. 9, we find, just as naive and superficial expectation leads us to believe, that the ratchet in Fig. 9a drives motion to the right and the ratchet in Fig. 9b drives motion to the left. Doesn't this prove the importance of the power stroke? The answer is no. The assignment of the rate constants in (23), although consistent with one requirement of microscopic reversibility, (3), is not consistent with the second requirement, (7). In explicit terms of the rate constants shown in Fig. 9, these two requirements are

$$\frac{f_1 g_1}{f_1^{'} g_1^{'}} = \frac{f_2 g_2}{f_2^{'} g_2^{'}} = \mathrm{e}^{\Delta\mu} \tag{24}$$

and

$$\frac{f_1 f_2^{'}}{f_1^{'} f_2} = \frac{g_2 g_1^{'}}{g_2^{'} g_1} = \mathrm{e}^{\Delta U(\theta_1) - \Delta U(\theta_2)}, \tag{25}$$

where $\Delta U(\theta) = U_1(\theta) - U_2(\theta)$. Maintaining consistency with both requirements of microscopic reversibility assures that, for any values θ_1 and θ_2, the product of clockwise and counterclockwise transitions for the thermodynamic boxes corresponding to that shown in Fig. 5 are equal:

$$\begin{aligned} P_1(\theta_1 \rightarrow \theta_2) f_2 P_2(\theta_1 \leftarrow \theta_2) f_1^{'} &= f_1 P_2(\theta_1 \rightarrow \theta_2) f_2^{'} P_1(\theta_2 \leftarrow \theta_1), \\ P_1(\theta_1 \rightarrow \theta_2) g_2^{'} P_2(\theta_1 \leftarrow \theta_2) g_1 &= g_1^{'} P_2(\theta_1 \rightarrow \theta_2) g_2 P_1(\theta_2 \leftarrow \theta_1). \end{aligned} \tag{26}$$

This relationship must hold irrespective of whether the system is or is not at equilibrium. When we take rate constants that are consistent with all requirements of microscopic reversibility[1] we once again arrive at the correct conclusion that the step ratio (i.e., the directionality) and stall force are independent of the slopes of the mechanical potentials and are governed solely by the parameter q.

Equation (26) describes the discreet version of a curl free vector field [26–28]. We can thus define a scalar field by specifying the potential energies (i.e., $U_1(\theta)$ or $U_2(\theta)$) and transition state energies $\mathcal{E}_{\mathrm{f}}(\theta)$ and $\mathcal{E}_{\mathrm{g}}(\theta)$, and linearly interpolating between these specified energies . In the resulting two-dimensional potential

[1] Using windowing functions where some of the rate constants are zero except in certain windows is mathematically incorrect. The ratios of the rate constants specified by microscopic reversibility must hold everywhere, even if the magnitudes of some of the rate constants become very small in some regions. Note that the relationships (26) hold when the ratios of rate constants are proportional to the exponentials of the energy differences $f(\theta)/f^{'}(\theta) \propto \mathrm{e}^{\Delta U(\theta)}$ and $g^{'}(\theta)/g(\theta) \propto \mathrm{e}^{\Delta U(\theta)}$ with θ independent proportionality constants.

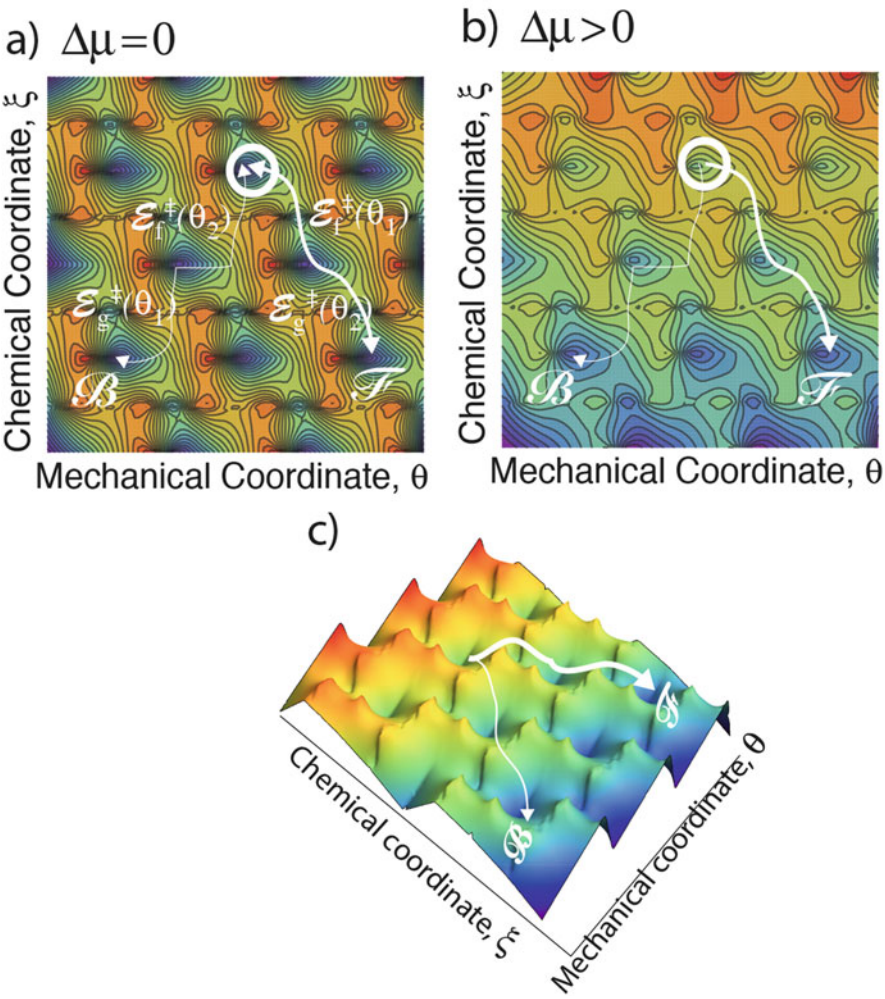

Fig. 10 Plots of the 2-D potential calculated by taking piece-wise linear functions for the shift ratchet shown in Fig. 9b with amplitude of 13 along the mechanical coordinate, and transition state (*saddle point*) energies of $\mathcal{E}_{\mathrm{f}}^{\ddagger}(\theta_1) = \mathcal{E}_{\mathrm{g}}^{\ddagger}(\theta_2) = 8.5$ and $\mathcal{E}_{\mathrm{f}}^{\ddagger}(\theta_2) = \mathcal{E}_{\mathrm{g}}^{\ddagger}(\theta_1) = 0$. Two periods in each direction are shown. In (**a**) we set $\Delta\mu = 0$. In (**b**) the system is away from chemical equilibrium with $\Delta\mu = 20$. Already in (**a**) we see that the difference in saddle point energies (i.e., $q = \mathrm{e}^{-10}$) strongly selects the path $P_{\mathscr{T}}/P_{\mathscr{T}_{\mathrm{R}}}$ over the path $P_{\mathscr{B}}/P_{\mathscr{B}_{\mathrm{R}}}$, but the ratios between forward and microscopic reverse pairs are unity so there is no net directional motion. Then in (**b**), where $\Delta\mu = 20$ the path $P_{\mathscr{T}}$ is strongly favored over its microscopic reverse, $P_{\mathscr{T}_{\mathrm{R}}}$, resulting in net motion to the right on the mechanical coordinate driven by chemical energy. Even so, there is nothing that could sensibly be called "torque generation". (**c**) Three-dimensional representation of the contour plot shown in (**b**). The selection between $\mathscr{T}$ and $\mathscr{B}$ is because of the lower energy barriers for $\mathscr{T}$

energy surface, one coordinate (often denoted ξ) represents chemistry and the other coordinate (θ here) represents the mechanical process as shown in Fig. 10a. Energy landscapes have recently been explored using computational models explicitly based on structural studies for the F0F $_1$-ATPase [22].

3.3 Visualizing the Mechanism of Chemically Driven Motors on a 2-D Potential Energy Surface

Contour plots of the shift ratchet in Fig. 9b are shown in Fig. 10a for $\Delta\mu = 0$ and in Fig. 10b for $\Delta\mu > 0$, where the effect of chemical free energy gradient is modeled as a homogeneous force acting along the chemical coordinate ξ. The applied load is zero in both cases. Figure 10a is the equilibrium case but already we see nascent directionality – starting from the white circle, the path $\mathscr{F}$ with motion to the right and hydrolysis of an ATP is much more likely than the path $\mathscr{B}$ with motion to the left and hydrolysis of an ATP. Of course it is also true that the path $\mathscr{F}_{\mathrm{R}}$ with motion to the left and synthesis of an ATP is much more likely than the path $\mathscr{B}_{\mathrm{R}}$ with motion to the right and synthesis of an ATP, so there is no net left/right directionality because $P_{\mathscr{F}} = P_{\mathscr{F}_{\mathrm{R}}}$ and $\mathrm{P}_{\mathscr{B}} = \mathrm{P}_{\mathscr{B}_{\mathrm{R}}}$ – see (9). What then can having excess ATP do to cause directed motion? In Fig. 10b we see a contour plot with the effect of $\Delta\mu > 0$ incorporated as a homogeneous force acting along the chemical coordinate ξ. Now $P_{\mathscr{F}} > P_{\mathscr{F}_{\mathrm{R}}}$ and the nascent directionality already apparent in the equilibrium plot $P_{\mathscr{F}} > \mathrm{P}_{\mathscr{B}}$ is manifest.

From this picture we recognize that even such ubiquitously used phrases as "torque generation" or "force generation" are imprecise at best and very misleading at worst when applied to chemically driven molecular machines. In a recent paper, Mukherjee and Warshel [29] asserted "In particular, it is important to explain that the experimentally observed torque and related observations cannot be reproduced without proper coupling to the chemical energy that leads to the torque." Of course there is no such thing as "experimentally observed torque." What is observed is rotational motion. In the macroscopic or even mesoscopic world the inference that the observed motion is produced by a torque $(-\partial U/\partial\theta)$ is certain. For *molecular* machines, however, thermal noise causes random translational and rotational motion even without forces or torques apparent from the energy landscape on which the motion occurs. The idea behind a Brownian motor [30] is to use input energy to prevent backward motion, rather than to cause forward motion, and then allow thermal noise to do the job of moving the motor along the least energy path hewn out by structural features that surround the path with high barriers. Let us explore this idea in the context of the energy landscape shown in Fig. 10.

In the absence of an external load, the average torque over a period,

$$\oint \frac{\partial U(\theta,\xi)}{\partial \theta} d\theta|_{\xi=\text{constant}} = 0, \tag{27}$$

is zero for any fixed value of the chemical coordinate for any rotary molecular motor, irrespective of the value of $\Delta\mu$. The value of the integral over the forward path $\mathscr{F}$

$$\int_{\mathcal{F}} \left\{ \underbrace{\left[\frac{-\partial U(\theta,\xi)}{\partial \theta} d\theta\right]}_{\text{Torque}} + \underbrace{\left[\frac{-\partial U(\theta,\xi)}{\partial \xi} d\xi\right]}_{\text{Chemistry}} \right\} = \Delta\mu \tag{28}$$

gives the work done by/on the environment, $\Delta\mu$, in moving along this path. The separation of terms into "torque" and "chemistry" follows from the fact that the forces or torques are derived from a potential (scalar) field, which in turn follows from the constraints of microscopic reversibility. It is tempting to see in this separation a validation of the "power stroke" model for molecular motors in which torque is generated by the release of chemical energy, but this idea is horribly wrong. For the model shown in Fig. 10b, the term describing torque in the least energy path is negative – i.e., work is done on the rotor by the environment rather than vice versa – and the term describing chemistry is greater than $\Delta\mu$ by this same amount. We can most easily see this in the context of Fig. 9b from which the potential energy landscape in Fig. 10 is derived. With $q < 1$ and $\Delta\mu > 0$, the most probable mechanism is that in which the motor moves from $U_2(\theta_2)$ to $U_2(\theta_1)$ by thermal noise, reacts by process f_1 to arrive at $U_1(\theta_1)$, moves to $U_1(\theta_2)$ by thermal noise, then reacts by process g_2 to arrive again at the starting point $U_2(\theta_2)$, having transported two protons from the cytoplasm to the periplasm while completing one clockwise rotation of 360°.

The value of the integral in (28) is path independent and depends only on the start and end points. The values of each of the terms identified as torque and chemistry, however, depend on path. Further, had we chosen the ratchet in Fig. 9a rather than that in Fig. 9b on which to base the 2-D potential landscape, the term describing torque in the integral over the least energy forward path $\mathscr{F}$ would be positive and that for the chemistry would be less than $\Delta\mu$. It is therefore perhaps tempting to categorize mechanisms for which $\int_{\mathscr{F}} \frac{-\partial U(\theta,\xi)}{\partial \theta} \mathrm{d}\theta > 0$ as power stroke motors, and those for which $\int_{\mathscr{F}} \frac{-\partial U(\theta,\xi)}{\partial \theta} \mathrm{d}\theta \leq 0$ as Brownian motors, but this separation seems artificial and misleading – the essential mechanism by which directed motion occurs in either ratchet is the selection between $P_{\mathscr{F}}$ and $P_{\mathscr{B}}$. This selection, governed solely by the specificity parameter q, is already evident at equilibrium, although directed motion is manifest only when $\Delta\mu \neq 0$. The answer to the quintessential question regarding molecular machines: "How does ATP hydrolysis drive directed motion," is seen to be the doubtless unsatisfying, but

nonetheless accurate, description – mass action. Irrespective of whether $\int_{\mathscr{F}} \frac{-\partial U(\theta,\xi)}{\partial \theta} d\theta$ is positive or negative, the mechanism works as a Brownian information ratchet.

3.4 *FoF$_1$ ATP Synthase: A Beautiful Illustration of a Brownian Information Ratchet*

Recent computational work on the FoF$_1$ ATP synthase offers a beautiful, experimentally connected, illustration of the basic Brownian information motor principle. Figure 11a shows the energy landscape for the different chemical and rotational states of the F$_1$ ATPase calculated by Mukherjee and Warshel [22]. The diagram is drawn without incorporating the effect of $\Delta\mu$ and can be thought of as the equilibrium case. The critical feature determining the coupling is the zigzag diagonal energy valley running from the lower left to upper right corner, already present at equilibrium. Of course, at equilibrium the probability of a transition from the bottom left to top right corner is exactly as likely as a transition from the top right to lower left corner. When $\Delta\mu > 0$ there is effectively a net tilt from left to right driving the system to the right $\cdots \rightarrow D_1E_2T_3 \rightarrow E_1T_2D_3 \rightarrow T_1D_2E_3 \rightarrow \cdots$, and, because of the zigzag diagonal energy valley, upward (clockwise rotation) as well.

Key points on an energy landscape are energy minima (the states A/C and B with energies $U_{A/C}$ and U_B) and saddle points (transition states with energies $\mathcal{E}^{\ddagger}_H$ and $\mathcal{E}^{\ddagger}_L$). If the state energies are exchanged $U_{A/C} \leftrightarrow U_B$, nothing significant changes with regard to the overall appearance of the energy landscape – there is still a zigzag energy valley running from the lower left to the upper right corner. In stark contrast, if the transition state energies are interchanged $\mathcal{E}^{\ddagger}_H \leftrightarrow \mathcal{E}^{\ddagger}_L$, the appearance of the landscape is dramatically changed – the zigzag energy valley runs from the upper left corner to the lower right corner. On such an energy landscape, an imposed $\Delta\mu$ drives motion downward (counterclockwise rotation). As pointed out by Mukherjee and Warshel "once the free energy surface is determined, the motor functionality and the corresponding vectorial process becomes clear because the individual rate constants follows the Boltzmann-based transition state theory" [22]. As is clear from the present chapter, the specific features of the energy landscape that govern the coupling are the saddle points – the transition states – as predicted by a Brownian motor model and not the energy differences between the states as predicted by the mechanical paradigm in which the power stroke plays a crucial role.

The presentation of Mukherjee and Warshel [22] of the energy landscape for the F$_1$ ATPase echoes earlier descriptions of generic molecular machines based on discrete kinetic lattice models such as shown in Fig. 11b [31]. The selection between the light gray zigzag path from the lower left to upper right corners and the dark gray zigzag path between the upper left to lower right corners is

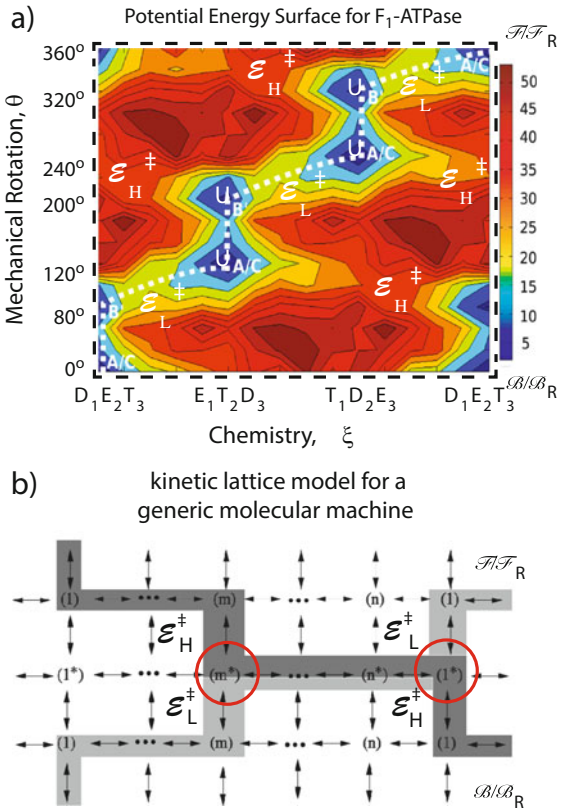

Fig. 11 (**a**) Two-dimensional potential energy profile calculated for the different rotational and chemical states for the F_1 part of the FoF_1 ATP synthase, where the energies are given in kcal/mol. The calculation is carried out without adding the effect of a non-zero $\Delta\mu$ and can thus be considered an equilibrium result. The underlying potential energy surface is taken from [22]. (**b**) Kinetic lattice for a generic chemically driven molecular machine redrawn from [31]. The selection between the paths $\mathscr{T}/\mathscr{T}_R$ and $\mathscr{B}/\mathscr{B}_R$ is determined at the kinetic switching points highlighted by the *red circles*. For $\mathcal{E}_H^\ddagger >> \mathcal{E}_L^\ddagger$ (i.e., $q << 1$) the *dark gray path* $\mathscr{B}/\mathscr{B}_R$ is negligible. If the rate constants for all transitions are consistent with the constraints of microscopic reversibility, a potential energy landscape can be drawn for the mechanism and is qualitatively similar to that shown in (**a**), with a pronounced energy valley running from the *lower left* to *upper right corner*

independent of the equilibrium constants, and depends only on the ratio of the rate constants out of the states circled in red. As noted, "The equilibrium energies of the states and of the barriers between the states constrain the motion on the multidimensional lattice to one or a few paths in which completion of a chemical cycle is coupled to moving forward by a spatial period. The function of a Brownian machine is specified entirely by the equilibrium energies of the states (stabilities) and of the barriers between them (labilities). Structure is important only insofar as it determines the energies. Addition of the chemical substrate such that the free energy

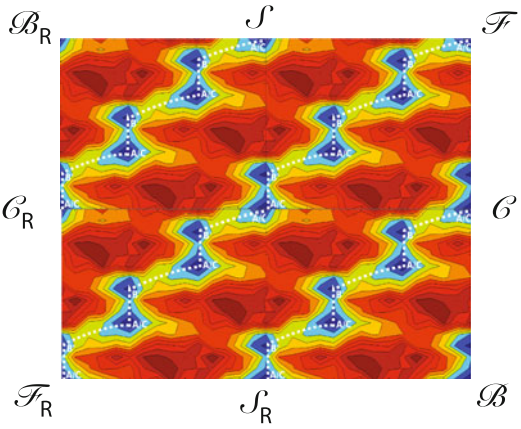

Fig. 12 Two periods in each direction for the F_1 ATPase, with the trajectories corresponding to hydrolysis of three ATPs and clockwise rotation/microscopic reverse ($\mathcal{F}/\mathcal{F}_R$), hydrolysis of three ATPs and counterclockwise rotation/microscopic reverse ($\mathcal{B}/\mathcal{B}_R$), hydrolysis of three ATPs without rotation/microscopic reverse ($\mathcal{C}/\mathcal{C}_R$), and clockwise rotation without ATP hydrolysis or synthesis/microscopic reverse ($\mathcal{S}/\mathcal{S}_R$)

released is greater than the increase in the potential energy produced by motion against an applied load causes the system to undergo directed motion by mass action" [32]. In an important recent advance, Share, Parimal, and Flood have demonstrated chemical control of a bi-labile system [33].

We can best understand the general principles of energy coupling in terms of an energy landscape by zooming out to view the landscape from a distance where several periods in each direction can be seen, rather than by zooming in to examine the details of individual motions where attention is focused on less than a single period. This is consistent with Terrell Hill's emphasis on viewing energy coupling in terms of complete cycles rather than steps within the cycles [34]. This approach is illustrated in Fig. 12, where two periods in each direction are plotted for the F_1 ATPase calculated by Mukherjee and Warshel [22]. Each of the four possible pairs of forward and microscopic reverse trajectories – $\mathcal{F}/\mathcal{F}_R$, $\mathcal{B}/\mathcal{B}_R$, $\mathcal{C}/\mathcal{C}_R$, and $\mathcal{S}/\mathcal{S}_R$ – are shown on the perimeter of the plot. At this level of detail we see immediately that the essential feature for coupling chemical reaction and mechanical rotation is the deep zigzag energy valley surrounded by high energy barriers. The details of the energies within the valley are more or less irrelevant – the relative probability of moving left and up vs right and down is a thermodynamic identity $P_{\mathcal{F}_R}/P_{\mathcal{F}} = e^{-\Delta\mu}$ irrespective of whether the energy of state A/C is greater than, less than, or equal to the energy of state B. The key feature that assures coupling such that a large $\Delta\mu$ drive clockwise rotation is the high energy barrier $\mathcal{E}_H^{\ddagger} >> \mathcal{E}_L^{\ddagger}$. The relative likelihood of completing a backward, counterclockwise rotation while hydrolyzing ATP vs completing a forward, clockwise rotation is $q = e^{2\times\left(\mathcal{E}_L^{\ddagger} - \mathcal{E}_H^{\ddagger}\right)}$. Because $q \ll e^{-\Delta\mu}$ the F_1 ATPase is under thermodynamic control and forcing the molecule to rotate

counter-clockwise results in the synthesis of ATP, rather than enhanced hydrolysis of ATP as appears to be the case for kinesin and myosin which are under kinetic control.

4 Unreasonable Effectiveness of Equilibrium Theory

It has become almost obligatory when writing about molecular machines to stress that they operate far from equilibrium. Unfortunately, this is a very confusing observation, not because the statement is wrong, but because the statement is correct in a misleading way. The chemical energy $\Delta\mu$ that drives the motion of molecular motors is quite large in comparison to thermal energy, and hence, in general, the probability distribution for an ensemble of molecular motors amongst the possible states of the motor is very different from that predicted based on a simple Boltzmann model for an equilibrium distribution function. An individual molecular machine, however, is, in the only sense meaningful for an individual molecule, very, very close to equilibrium – there is no inertia. This regime of motion is known as the low Reynold's number limit [35], and gives rise to what has been termed an unreasonable effectiveness of equilibrium theory [36, 37]. For example, see (20) and (21) where the step ratios for both thermodynamic and kinetic control are seen to be simple exponential functions.

The unreasonable effectiveness of equilibrium theory is very important for understanding why Onsager's theory is so important in the analysis of bio-molecular machines. It is often stated that the Onsager reciprocal relations [15], and the Onsager–Machlup thermodynamic action theory [11] by which the constraints of microscopic reversibility were derived (see (5)), are valid only near equilibrium in the linear response regime. Although this is technically true, it is important to consider Onsager and Machlup's own words describing the limitations of their approach: "The essential physical assumption about the irreversible processes is that they are linear; i.e., that the fluxes depend linearly on the forces that cause them."

For individual trajectories on an energy surface such as shown in Figs. 4 or 11, this is simply the statement that the motion occurs in the low Reynold's number regime where inertia is negligible, and hence where the velocity is proportional to the local gradient of the potential. Thus, by using the Onsager–Machlup approach [11] it is straightforward to derive many relationships between forward and microscopic reverse trajectories [12] which provide important constraints for any model of a molecular machine.

We have seen that the so-called power stroke has no role in determining the thermodynamics of chemo-mechanical coupling by molecular motors. This irrelevance of the power stroke does not hold for optically driven motors as can be demonstrated experimentally [38–40]. Let us investigate this difference between chemically and optically driven motors in detail for a hypothetical molecular walker.

5 Three-State Mechanism for Energy Transduction: Optical vs Chemical Driving

Biological [41] and synthetic [42] molecular walkers can often be described in terms of a three-state mechanism shown that involves a mechanical transition L ⇌ R along with two energy-driven processes, E ⇌ L and E ⇌ R, in which one of the heads dissociates/binds to the molecular track as shown in Fig. 12. This mechanism can also be written as a triangle reaction:

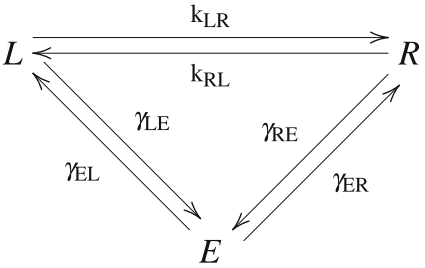

(29)

where $K_{\mathrm{LR}} = \frac{k_{\mathrm{LR}}}{k_{\mathrm{RL}}} = \mathrm{e}^{\Delta U_{\mathrm{LR}} - F}$. Each completion of a clockwise cycle results in one step to the right, and each completion of a counter-clockwise cycle results in one step to the left. The step ratio is the product of clockwise rate constants divided by the product of counter-clockwise rate constants:

$$\text{step ratio} = \frac{\gamma_{\mathrm{RE}}\gamma_{\mathrm{EL}}}{\gamma_{\mathrm{LE}}\gamma_{\mathrm{ER}}}\mathrm{e}^{\Delta U_{\mathrm{LR}} - F}. \tag{30}$$

As a reminder, we are working in energy units where $k_{\mathrm{B}}T = 1$ and in length units such that the step length is also unity.

The triangle reaction was introduced by Onsager [15] to illustrate the importance of microscopic reversibility for chemical processes, and has been used by many subsequent authors as a paradigm for understanding free-energy transduction from a chemical reaction. This cyclic scheme may rightly be regarded as the simplest mechanism encapsulating the essential features of coupled transport. Let us consider two distinct cases for an autonomous molecular machine depending on how energy is put into the transitions E ⇌ L and E ⇌ R (Fig. 13).

5.1 Optical Driving

The fundamental constraint on optical transitions between two states "i" and "j" of a molecule is that given by Einstein [43] for absorption, spontaneous emission, and stimulated emission:

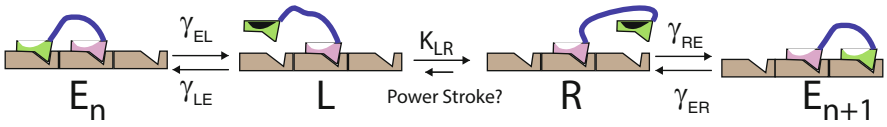

Fig. 13 A simple model for a molecular walker in which attachment and detachment of a head is mediated by a reaction with rates γ_{iE} and γ_{Ei}, respectively, where i = L if the rear head attaches/detaches, and i = R if the front head attaches/detaches. The conformational change L ⇌ R (power stroke?) shifts the position of the free head relative to the attached head

$$\frac{\omega_{\mathrm{i\,j}}}{\omega_{\mathrm{ji}}} = \frac{\rho\left(\nu_{\mathrm{ij}}\right)}{\left[\frac{8\pi h\nu_{\mathrm{ij}}^3}{c^3} + \rho\left(\nu_{\mathrm{ij}}\right)\right]}, \tag{31}$$

where for simplicity we take the degeneracies of states "i" and "j" to be the same. If the transitions between states E and L and between E and R are driven by light, the ratios of the transition constants $\gamma_{\mathrm{EL}}/\gamma_{\mathrm{LE}}$ and $\gamma_{\mathrm{ER}}/\gamma_{\mathrm{RE}}$ are given by the Einstein relations for absorption and spontaneous and stimulated emission and we have

$$\left(\text{step ratio}\right)_{\mathrm{opt}} = \left\{\frac{\rho(\nu_{\mathrm{ER}})\left[\frac{8\pi h\nu_{\mathrm{EL}}^3}{c^3} + \rho(\nu_{\mathrm{EL}})\right]}{\rho(\nu_{\mathrm{EL}})\left[\frac{8\pi h\nu_{\mathrm{ER}}^3}{c^3} + \rho(\nu_{\mathrm{ER}})\right]}\right\} \mathrm{e}^{\Delta U_{\mathrm{LR}} - F}, \tag{32}$$

where $\rho(\nu_{\mathrm{ij}})$ is the radiation density at frequency $\nu_{\mathrm{ij}} = \Delta U_{\mathrm{ij}}/\hbar$ and $\hbar$ is Planck's constant. When the photon density is that of a blackbody radiator,

$$\rho_{\mathrm{bb}}\left(\nu_{\mathrm{ij}}\right) = 8\pi\hbar\nu_{\mathrm{ij}}^3 c^{-3}\left(\mathrm{e}^{\Delta U_{\mathrm{ij}}} - 1\right)^{-1},$$

the factor in braces reduces to $\{\cdots\} = \mathrm{e}^{-\Delta U_{\mathrm{LR}}}$ and then the $\left(\text{step ratio}\right)_{\mathrm{opt}} = \mathrm{e}^{-F}$. However, in very bright light, where $\rho\left(\nu_{\mathrm{ij}}\right) >> 8\pi\hbar\nu_{\mathrm{ij}}^3/c^3$, the factor in braces reduces to $\{\cdots\} = 1$ and $\text{step ratio}_{\mathrm{opt}} = \mathrm{e}^{\Delta U_{\mathrm{LR}} - F}$. Clearly, directed motion requires both a non-equilibrium light source and a power stroke, $\Delta U_{\mathrm{LR}} \neq 0$.

5.2 *Chemical Driving*

In contrast to the Einstein constraints for optical driving, transition coefficients for chemical driving obey microscopic reversibility, where for any transition i ⇌ j the ratio of forward to backward transition constants is given by

$$\frac{k_{ij}}{k_{ji}} = A_{ij} e^{\Delta U_{ij}}, \tag{33}$$

where A_{ij} is a proportionality constant which may depend on the concentration of ligands that bind in the reaction $i \rightleftharpoons j$. For chemical driving, the transitions of the triangle reaction (29) are $\gamma_{EL} = g_L + f_L^{'}$; $\gamma_{ER} = g_R + f_R^{'}$; $\gamma_{LE} = g_L^{'} + f_L$; and $\gamma_{RE} = g_R^{'} + f_R$. Inserting these relationships into (30) we find [16]

$$(\text{step ratio})_{\text{chem}} = \frac{(1 + qe^{-\Delta\mu}) + \left(s_R + s_L^{-1} e^{-\Delta\mu}\right)}{(q + e^{-\Delta\mu}) + (s_R + s_L^{-1} e^{-\Delta\mu})} e^{-F}, \tag{34}$$

where $s_i = g_i^{'}/f_i$ are the specificities in terms of which $q = s_L/s_R$. If either $\Delta\mu = 0$ or $q = 1$ the $(\text{step ratio})_{\text{chem}} = e^{-F}$. Clearly, the step ratio and stall force depend only on the specificities and not on ΔU_{LR}, and directed motion requires both a non-equilibrium chemical driving and a kinetic bias, $q \neq 1$, but does not require a power stroke.

6 Conclusions: "Power Stroke" Model is Just Plain Wrong as a Description of Chemically Driven Molecular Machines

It is important to state the conclusion of this paper clearly – the power stroke model, on which so much attention has been focused over the last five decades, is wrong as a description of a chemically driven molecular motor. This is not to say that there aren't energy releasing conformational changes in the cyclic mechanisms by which molecular motors work, but only that they are irrelevant to the understanding of the basic mechanism by which a chemical reaction (often ATP hydrolysis or proton transport across a membrane) drives directed motion. One of the key results of the present study is the understanding that, for chemically driven molecular motors, the ability of a molecular machine to discriminate between substrate and product depending on the state of the machine [44] is far more important for determining the intrinsic directionality and thermodynamics of chemo-mechanical coupling than are the details of the internal mechanical conformational motions of the machine. The organizing principle by which we can best understand chemically driven molecular machines is the principle of microscopic reversibility. In Fig. 9, if the rate constants used in the analysis are not consistent with microscopic reversibility, we arrive at the false conclusion that the slopes of the potentials (the forces or torques) govern the direction of motion. If, however, the analysis is carried out with rate constants that are consistent with microscopic reversibility, we arrive at the correct conclusion that the direction of motion is governed solely by the single kinetic parameter "q" and is independent of the slopes of the potentials.

We further recognize that the often used phrases “force generation” and “torque generation” to describe the action of molecular machines are imprecise and potentially very misleading. In a viscous medium, the translation of a macroscopic, or even mesoscopic, object requires a force, and rotation requires a torque. In contrast, thermal noise can drive both rotational and translational diffusion of molecules. The diffusion is random and does not of itself produce net directed motion. However, the presence of diffusion opens to a molecular machine the possibility of using input energy to control energy barriers to prevent “backward” motion, and then letting thermal noise do the job of producing the forward motion. This mechanism does not violate the second law of thermodynamics because free-energy, or more precisely information, is used to control the positioning of the barriers behind but not in front of the desired motion of a molecular machine [30]. Directed translation is driven without “generating force,” and directed rotation is driven without “generating torque.” In both cases, the motion can occur against a load, thereby storing energy. It is possible and useful to ask “what constant force or torque would be necessary to cause the observed velocity or angular velocity?” [21]. The answer to this question can be used to determine the minimum energy needed to cause the observed motion, and forms the basis for definition of a generalized efficiency (minimum energy or power needed divided by actual energy or power used) which characterizes the molecular machine even when the only output work is done on the viscous environment [21].

The Brownian information ratchet mechanism by which all chemically driven molecular machines work can be much better described in terms of a chemical paradigm involving specificity gating, as discussed for ion pumps [45], than in terms of a mechanical paradigm anticipated by Bustamante, Cheng, and Mejia [46]. Chemically driven Brownian information ratchets based on this principle have recently been synthesized [47, 48]. In contrast to the conclusions for chemical driving, a power stroke is very important for the directionality and efficiency of light-driven molecular machines and for molecular machines driven by external modulation of thermodynamic parameters. These results are very important not only for understanding biomolecular motors and pumps [14] but also in the design of synthetic molecular machines [49, 50].

References

1. Hill AV (1938) The heat of shortening and the dynamic constants of muscle. Proc R Soc Lond B 126:136–195
2. Huxley AF (1957) Muscle structure and theories of contraction. Prog Biophys Biophys Chem 7:255–318
3. Huxley AF, Niedergerke R (1954) Structural changes in muscle during contraction; interference microscopy of living muscle fibres. Nature 173:971–973
4. Huxley H, Hanson J (1954) Changes in the cross-striations of muscle during contraction and stretch and their structural interpretation. Nature 173:973–976

5. Seow CY (2013) Hill's equation of muscle performance and its hidden insight on molecular mechanisms. J Gen Physiol 142:561573
6. Hill TL, Eisenberg E, Chen YD, Podolsky RJ (1975) Some self-consistent two-state sliding filament models of muscle contraction. Biophys J 15:335–372
7. Astumian RD (2012) Microscopic reversibility as the organizing principle of molecular machines. Nat Nanotechnol 7:684–688. doi:10.1038/nnano.2012.188
8. Lehn JM (1990) Perspectives in supramolecular chemistry—from molecular recognition towards molecular information processing and self-organization. Angew Chem Int Ed Engl 29:1304–1319
9. Astumian RD, Derenyi I (1998) Fluctuation driven transport and models of molecular motors and pumps. Eur Biophys J 27:474–489
10. Astumian RD, Bier M (1996) Mechanochemical coupling of the motion of molecular motors to ATP hydrolysis. Biophys J 70:637–653
11. Onsager L, Machlup S (1953) Fluctuations and irreversible processes. Phys Rev 91:1505–1512. doi:10.1103/PhysRev.91.1505
12. Bier M, Derenyi I, Kostur M, Astumian RD (1999) Intrawell relaxation of overdamped Brownian particles. Phys Rev E Stat Phys Plasmas Fluids Relat Interdiscip Topics 59:6422–6432
13. Ait-Haddou R, Herzog W (2003) Brownian ratchet models of molecular motors. Cell Biochem Biophys 38:191–213. doi:10.1385/CBB:38:2:191
14. Astumian RD (2010) Thermodynamics and kinetics of molecular motors. Biophys J 98:2401–2409
15. Onsager L (1931) Reciprocal relations in irreversible processes. I. Phys Rev 37:405–426. doi:10.1103/PhysRev.37.405
16. Astumian RD (2015) Irrelevance of the power stroke for the directionality, stopping force, and optimal efficiency of chemically driven molecular machines. Biophys J 108:291–303. doi:10.1016/j.bpj.2014.11.3459
17. Clancy BEB, Behnke-Parks WMW, Andreasson JOLJ et al (2011) A universal pathway for kinesin stepping. Nat Struct Mol Biol 18:1020–1027. doi:10.1038/nsmb.2104
18. Nishiyama M, Higuchi H, Yanagida T (2002) Chemomechanical coupling of the forward and backward steps of single kinesin molecules. Nat Cell Biol 4:790–797. doi:10.1038/ncb857
19. Carter NJ, Cross RA (2005) Mechanics of the kinesin step. Nature 435:308–312. doi:10.1038/nature03528
20. Fisher ME, Kolomeisky AB (1999) Molecular motors and the forces they exert. Phys A 274:241–266
21. Derenyi I, Bier M, Astumian R (1999) Generalized efficiency and its application to microscopic engines. Phys Rev Lett 83:903–906. doi:10.1103/PhysRevLett.83.903
22. Mukherjee S, Warshel A (2012) Realistic simulations of the coupling between the protomotive force and the mechanical rotation of the F0-ATPase. Proc Natl Acad Sci 109:14876–14881. doi:10.1073/pnas.1212841109
23. Mukherjee S, Warshel A (2013) Electrostatic origin of the unidirectionality of walking myosin V motors. Proc Natl Acad Sci 110:17326–17331. doi:10.1073/pnas.1317641110
24. Xing J, Bai F, Berry R, Oster G (2006) Torque-speed relationship of the bacterial flagellar motor. Proc Natl Acad Sci U S A 103:1260–1265. doi:10.1073/pnas.0507959103
25. Press S, Ghosh K, Lee J, Dill KA (2013) Principles of maximum entropy and maximum caliber in statistical physics. Rev Mod Phys 85:1115–1141. doi:10.1103/RevModPhys.85.1115
26. Astumian R, Bier M (1994) Fluctuation driven ratchets: molecular motors. Phys Rev Lett 72:1766–1769
27. Magnasco M (1994) Molecular combustion motors. Phys Rev Lett 72:2656–2659. doi:10.1103/PhysRevLett.72.2656
28. Keller D, Bustamante C (2000) The mechanochemistry of molecular motors. Biophys J 78:541–556. doi:10.1016/S0006-3495(00)76615-X

29. Mukherjee S, Warshel A (2015) Dissecting the role of the γ-subunit in the rotary-chemical coupling and torque generation of F1-ATPase. Proc Natl Acad Sci 112:2746–2751. doi:10.1073/pnas.1500979112
30. Astumian RD (2001) Making molecules into motors. Sci Am 285:56–64
31. Astumian RD (2002) Protein conformational fluctuations and free-energy transduction. Appl Phys Mater Sci Process 75:193–206. doi:10.1007/s003390201406
32. Astumian RD (2007) Design principles for Brownian molecular machines: how to swim in molasses and walk in a hurricane. Phys Chem Chem Phys 9:5067–5083. doi:10.1039/b708995c
33. Share AI, Parimal K, Flood AH (2010) Bilability is defined when one electron is used to switch between concerted and stepwise pathways in Cu(I)-based bistable [2/3]pseudorotaxanes. J Am Chem Soc 132:1665–1675. doi:10.1021/ja908877d
34. Hill TL (1983) Some general principles in free energy transduction. Proc Natl Acad Sci U S A 80:2922–2925
35. Purcell EM (1977) Life at low Reynolds number. Am J Phys 45:3–11
36. Astumian RD (2006) The unreasonable effectiveness of equilibrium theory for interpreting nonequilibrium experiments. Am J Phys. doi:10.1119/1.2205883
37. Garcia HG, Kondev J, Orme N et al (2011) Thermodynamics of biological processes. Methods Enzymol 492:27–59. doi:10.1016/B978-0-12-381268-1.00014-8
38. Conyard J, Addison K, Heisler IA et al (2012) Ultrafast dynamics in the power stroke of a molecular rotary motor. Nat Chem 4:547–551. doi:10.1038/nchem.1343
39. Bruns CJ, Stoddart JF (2014) Rotaxane-based molecular muscles. Acc Chem Res 47:2186–2199. doi:10.1021/ar500138u
40. Ragazzon G, Baroncini M, Silvi S et al (2014) Light-powered autonomous and directional molecular motion of a dissipative self-assembling system. Nat Nanotechnol. doi:10.1038/nnano.2014.260
41. Kull FJ, Endow SA (2013) Force generation by kinesin and myosin cytoskeletal motor proteins. J Cell Sci 126:9–19. doi:10.1242/jcs.103911
42. Leigh DA, Lewandowska U, Lewandowski B, Wilson MR (2014) Synthetic molecular walkers. In: Molecular machines and motors. Springer, Cham, pp 111–138
43. Einstein A, Ehrenfest P (1923) Zur Quantentheorie des Strahlungsgleichgewichts. Z Phys 19:301–306
44. Lehn JM (2013) Perspectives in chemistry-steps towards complex matter. Angew Chem Int Ed. doi:10.1002/anie.201208397
45. Jencks WP (1997) From chemistry to biochemistry to catalysis to movement. Annu Rev Biochem 66:1–18. doi:10.1146/annurev.biochem.66.1.1
46. Bustamante C, Cheng W, Mejia YX (2011) Revisiting the central dogma one molecule at a time. Cell 144:480–497. doi:10.1016/j.cell.2011.01.033
47. Alvarez-Prez M, Goldup SM, Leigh DA, Slawin AMZ (2008) A chemically-driven molecular information ratchet. J Am Chem Soc 130:1836–1838. doi:10.1021/ja7102394
48. Carlone A, Goldup SM, Lebrasseur N et al (2012) A three-compartment chemically-driven molecular information ratchet. J Am Chem Soc 134:8321–8323. doi:10.1021/ja302711z
49. Kay ER, Leigh DA, Zerbetto F (2007) Synthetic molecular motors and mechanical machines. Angew Chem Int Ed 46:72–191. doi:10.1002/anie.200504313
50. Coskun A, Banaszak M, Astumian RD et al (2012) Great expectations: can artificial molecular machines deliver on their promise? Chem Soc Rev 41:19–30. doi:10.1039/c1cs15262a

Top Curr Chem (2015) 369: 317–344
DOI: 10.1007/128_2015_643

Published online: 25 June 2015

Mechanical Properties and Failure of Biopolymers: Atomistic Reactions to Macroscale Response

GangSeob Jung, Zhao Qin, and Markus J. Buehler

Abstract The behavior of chemical bonding under various mechanical loadings is an intriguing mechanochemical property of biological materials, and the property plays a critical role in determining their deformation and failure mechanisms. Because of their astonishing mechanical properties and roles in constituting the basis of a variety of physiologically relevant materials, biological protein materials have been intensively studied. Understanding the relation between chemical bond networks (structures) and their mechanical properties offers great possibilities to enable new materials design in nanotechnology and new medical treatments for human diseases. Here we focus on how the chemical bonds in biological systems affect mechanical properties and how they change during mechanical deformation and failure. Three representative cases of biomaterials related to the human diseases are discussed in case studies, including: amyloids, intermediate filaments, and collagen, each describing mechanochemical features and how they relate to the pathological conditions at multiple scales.

Keywords Amyloidosis · Biological materials · Bone · Lamin

Contents

G. Jung, Z. Qin, and M.J. Buehler (✉)
Laboratory for Atomistic and Molecular Mechanics, Department of Civil and Environmental Engineering, Massachusetts Institute of Technology, 77 Massachusetts Ave, Cambridge, MA 02139, USA
e-mail: mbuehler@MIT.EDU

1 Introduction

Biological materials are intriguing because of their mechanical properties and diverse physiological roles. Most biomaterials have hierarchical structures and they derive their mechanical properties from multiple mechanisms at different scales, ranging from nano- to macro-levels. Typically, each level of structure features its own failure mechanism and, thus, failure of biomaterial is typically complicated and dissipates large amounts of energy at different scales. Previous studies have attempted to reveal various toughening mechanisms of biological materials, and much progress has been made over the past decade or so. A prominent mechanism is when a collection of weak sacrificial bonds dissipates a large amount of energy in silk, which leads to a very high fracture toughness [1], and concentrated stress at cracks or flaws is redistributed because of the inelasticity of materials in nacre [2]. Many biological materials exhibit a combination of these and other mechanisms that exist concurrently, enabled by the existence of hierarchical structures. However, the fundamental deformation and fracture mechanisms of many biological protein materials remain unknown for several reasons. First, in many cases, the information about the structural assembly at each hierarchy is not well known. Second, the deformation behavior and the fracture properties at a lower hierarchy level affect the mechanical property of a higher hierarchy level nonlinearly and in complicated ways. Finally, the responses of all hierarchy levels to the macroscale mechanical loads can change under different loading conditions, and hence be altered during the use of a material or as an organism evolves [3]. Because materials failure basically arises from the chemical bond breaking, studying the behaviors of chemical bonds is critical to understanding their deformation and failure mechanisms. This connection between the chemical scale and meso- and macro-level properties remains a fertile area of materials science and engineering.

The robustness of biomaterials is important for performing their biological functions which work in various physiological conditions. Over 6,000 diseases

are directly or indirectly caused by genetic mutations [4]. Because the components of biomaterials are complex and numerous, it is challenging to specify the roles of all components and to distinguish the important parts from others. Thus, it is useful to focus on their mutations and effects causing serious diseases to understand their properties. Even a single base in a genetic sequence changed by random mutation can cause serious disease in the human body because of the reordering of the protein's finely tuned chemical bond network, weakening the structural stability and altering the mechanical properties of the associated biopolymer.

Moreover, some diseases are linked to reactions with foreign peptide deposits in tissues (such as Alzheimer's disease, Parkinson's disease, etc.) [5]. Other diseases, such as Hutchinson–Gilford progeria syndrome (HGPS, a genetically-caused rapid ageing disease), are triggered by a genetic defect occurring in the building block of the nuclear membrane structure of lamins [6–8]. Genetic disorders in collagenous tissues, such as *Osteogenesis imperfecta*, have been linked to the variation of material structure caused by mutations in genes that encode the tropocollagen molecules [9–11].

In a given system, the deformation and fracture processes where the thermodynamic state variables (e.g., the energy and stress) change because of mechanical loadings is a very intriguing topic in mechanochemistry [12]. In particular, failure mechanisms and their criteria have been examined extensively for engineering applications. Not only for engineering materials such as metal and silicon, but also for biomaterials, a detailed knowledge of their mechanical properties is crucial for understanding their functions and malfunctions in the human body. For instance, the mechanical robustness of amyloid fibrils makes it difficult to decompose them in the human body [13]. Hutchison–Gilford progeria changes the deformation and failure mechanisms of cells from allowing large deformation to localizing stress [14, 15].

The deformation and fracture accompanying the remodeling of chemical bonds in biological systems, the mechanochemical properties, provide a set of interesting research questions with significant practical impacts. However, studying mechanochemical processes from a purely experimental point of view can be quite difficult because of the limitation of experiments caused by associated time- and length-scales [12]. To be specific, because the newly created surfaces during fracture can feature a high reactivity because of unsatisfied valences on atoms or missing counterparts, structural relaxation occurs on relatively short time scales via rearranging of chemical bonds. The brevity of these time scales makes the phenomena elusive to experimental approaches. However, advances in molecular dynamics simulations, including powerful techniques such as steered molecular dynamics (SMD), metadynamics, and replica exchange molecular dynamics (REMD), make it possible to analyze the stable structures of biomaterials and the behavior of chemical bonds under extreme loading on an extremely short time scale (i.e., femtoseconds to nanoseconds).

Several earlier computational and experimental studies have revealed how chemical bonds behave in biological systems during deformation and failure. Although their structures and mechanical properties are significantly different,

Biomaterials	Mechanochemical Features	Related chemical bonds			
		covalent	ionic	hydrogen	salt-bridge
Amyloid	self-strengthening			✓	
	length dependency			✓	
	periodicity			✓	✓
Intermediate Filaments (IF)	alpha-beta transition			✓	
	crosslink (IF network)	✓	✓		✓
Mineralzied Collagen (MC)	mineral stiffening	✓	✓	✓	
	thickness dependency		✓		
IF & MC	rate dependency	✓		✓	

Fig. 1 Summary of major chemical bonds and mechanochemical features in biological materials discussed in this review. The mechanical properties result from interplay between chemical bonds and deformation of biomaterials. The effect of each chemical bond becomes distinct or obscure because of the states of deformation and loading

they share some common important features in terms of their mechanochemical behavior. In biological materials, three different types of interaction are crucial for their mechanical properties and structures: covalent bonds, ionic bonds, and hydrogen bonds. These bonds behave differently under external loads, affecting the stability and mechanical properties of biological systems. Because of their complex chemical bond networks, the different types of interactions interplay to maximize the resistance to failure of materials or weaken mechanical properties in the cases related to diseases. The key mechanochemical features of three representative materials, amyloids, intermediate filaments, and collagen molecules, which closely relate to human diseases and the different types of bonds related to their features are summarized in Fig. 1.

In the following we focus on describing the behavior of these chemical bonds of amyloids, intermediate filaments, and collagen under mechanical loads on the atomic length scale. Understanding the complicated behavior and interplay of these chemical bonds in biological materials can help us to analyze and predict the mechanochemical processes in other bio/nano-materials, leading to the development of new medical treatments, detecting tools for diseases, and new strategies to design biomedical materials with novel functions [16–19].

2 Mechanochemical Mechanisms of Amyloidosis

2.1 Introduction

In general, the failure of proteins to remain in their native functional conformational state leads to various human diseases. These misfolded proteins can no longer play

their ordinary roles in organisms [20]. Amyloidosis is a disease caused by the deposition of misfolded proteins called amyloids. These misfolded proteins are polypeptide molecules with highly ordered and stable β-sheets.

Alzheimer's disease is a representative amyloidosis, which is a neurodegenerative disorder where the deposition and self-assembly of amyloid may block cell-to-cell signaling at synapses. Once amyloid plaques are formed, they typically grow uncontrollably. This formation leads to neurotoxicity hindering the normal biological function of native tissues. Based on the knowledge of mechanical stabilities and rigidities of amyloid plaques, new treatments of amyloidosis, such as weakening the mechanical strength of the amyloid deposits, could be developed. This exemplifies a materials-driven approach to develop a treatment that invokes controlled failure as a driving mechanism.

Most protein polypeptides possibly form amyloids through a structural transition from their native soluble conformation into insoluble fibrillar depositions [18], but their formation, including their forming rate and their structural stability, mainly depends on their sequence [21]. In addition to the effect of sequence, there are several factors affecting the formation of amyloids. Because the aggregation of amyloid occurs in aqueous solution, the hydrophobicity of side chains determines the aggregation propensity of a sequence; a series of hydrophobic residues facilitates the aggregation. Previous studies have shown that replacement of hydrophobic residues of peptides (e.g., 17–19 residues of Aβ (1-43)) by hydrophilic residues can reduce aggregation and enhance solubility [22–24]. Another critical factor of aggregation is a net charge of the polypeptide. Because a high net charge can make the protein unstable in a compact folded state because of the intra-molecular repulsions, decreasing the positive net charge of the protein by mutations leads to an accelerated formation of β-sheet containing aggregates [25, 26].

Although amyloids are associated with the neurodegenerative disorders in organs, because of their exceptional sturdiness, strength, and stability under diverse conditions, their highly ordered hierarchical structures can be utilized as a powerful tool for creating future devices or interesting nanostructured molecular materials. For example, several studies have shown the possibility of using amyloid fibrils as a template for fabrication of conductive nanowires [16–19]. These great potentials for technological applications increase the interest in amyloid protein material from various fields of science.

2.2 Formation and Structure

Many mechanisms of aggregation of amyloids have been studied and provide us with the insight into ways to control amyloid formation. Among the variety of protein amyloids, β-amyloids (i.e., Aβ (1-40), Aβ (1-42), Aβ (1-43)) have been considered critical to understanding Alzheimer's disease [27]. The plaques in brain tissue with Alzheimer's disease are predominantly comprised of two Aβ amyloids, Aβ (1-40) and Aβ (1-42).

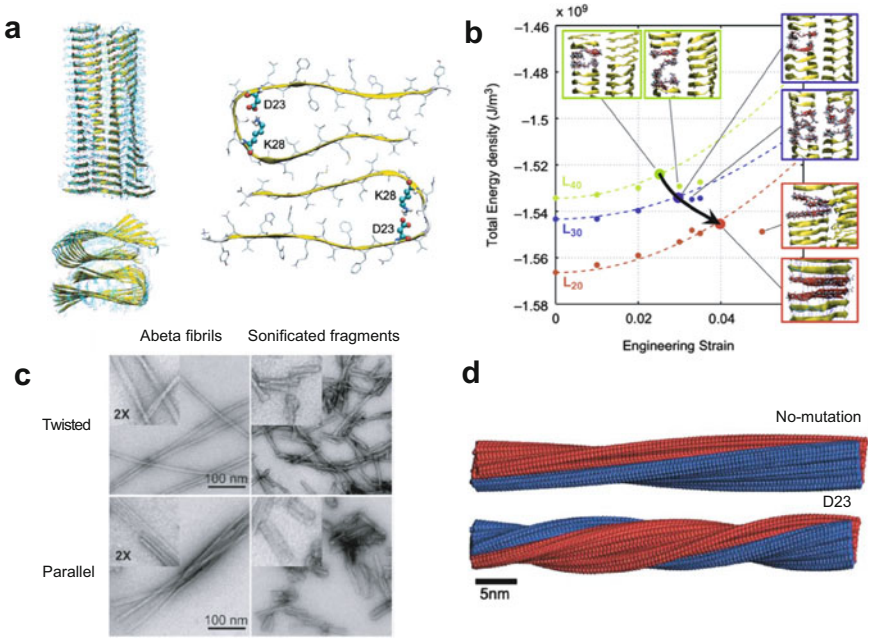

Fig. 2 Structures of normal and mutated amyloid fibrils and mechanical responses under tensile loadings. (**a**) Visualization of molecular structure of twofold symmetric amyloid Aβ (1-40) fibril showing the characteristic twisting structure and one layers of amyloid fibril with highlighted salt bridge (charged side chains) site at residue D23 (aspartate) and K28 (lysine). (**b**) Size dependency of critical strain under tensile loading: the energy density as function of the applied strain with different lengths, $L_{20} = 91.87$, $L_{30} = 144.33$ and $L_{40} = 189.75$ Å. (Adapted with permission from [95]. Copyright (2010), with permission from Elsevier). (**c**) TEM images of amyloid Aβ (1-40) fibril with two different morphologies: twisted and parallel after synthesized (*left*), TEM images of sonicated amyloid fibrils fragments (*right*) [32]. (**d**) Periodicity of mutated and normal Aβ (1-40) fibrils (figures in **a** and **d**). (Reprinted with permission from [43]. Copyright (2010) American Chemical Society)

The structural information about the amyloid fibrils can be obtained by imaging technique such as TEM (Transmission Electron Microscopy), AFM (Atomic Force Microscopy), and X-ray diffraction [28, 29]. The analysis of amyloid structure is challenging because of their extremely large size and the difficulty of forming crystallized structures for NMR (Nuclear Magnetic Resonance) spectroscopy.

However, the progress in methods to grow microcrystals of small peptide fragments and in preparation of amyloid fibrils for ssNMR (Solid State Nuclear Magnetic Resonance) spectroscopy has contributed to identifying the structure of amyloid fibrils [30]. Human Aβ (1-40) is composed of 40 amino acids: Asp-Ala-Glu-Phe-Arg-His-Asp-Ser-Gly-Tyr-Glu-Val-His-His-Gln-Lys-Leu-Val-Phe-Phe-Ala-Glu-Asp-Val-Gly-Ser-Asn-Lys-Gly-Ala-Ile-Ile-Gly-Leu-Met-Val-Gly-Gly-Val-Val (DAEFR HDSGY EVHHQ KLVFF AEDVG SNKGA IIGLM VGGVV), and Aβ (1-40) peptide can form fibrils from the peptide solutions purified with

1.0 mM at pH 7.4 by incubation for 5–24 days [31]. In the models obtained from the ssNMR data and by the energy minimization of the molecular structure with CHARMM force field, residues 1–8 are fully disordered, and the peptide conformation is composed of two β-strands, separated by a 180° turned bend formed by residues 25–29. The cross-β unit is a double-layered structure, with parallel β-sheets formed by residues 12–24 and 30–40. The assembly of these double-layered β-sheets using hydrogen bonds constitutes a long fibril with an axis coinciding with the direction of the intermolecular backbone (Fig. 2a) [30].

The self-assembled amyloid fibrils exhibit distinct morphologies, often characterized as twisted or parallel assemblies of finer filaments in TEM images (Fig. 2c). The morphology of Aβ (1-40) depends subtly on synthetic conditions, showing significantly different toxicities in neuronal cell cultures [32]. This shows that the structures of amyloid fibrils are not determined solely by the amino acid sequence. However, the sequence of the peptides is important as it controls the formation of the basic structural motifs. Because Aβ (1-42) has a different sequence, the structure shows different features from Aβ (1-40). Aβ (1-42) also can be synthesized and form fibrils in vitro with slightly different conditions from that of Aβ (1-40) and the structural information can be analyzed by the ssNMR as well. Unlike Aβ (1-40), it has been revealed that residues 1–17 are disordered and residues 18–26 and 31–42 form two intermolecular β-sheets in Aβ (1-42) [33].

2.3 Mechanochemical Properties

The molecular mechanism determining the chemical response induced by mechanical loading is crucial to identifying the mechanochemical properties of materials. Although it is challenging to address directly the behavior of the chemical bonds experimentally, the behavior of chemical bonds is reflected in mechanical properties in deformation. Thus, it is crucial to make an effort to measure the mechanical properties of materials and compare them with the computational results. From the computational methods, we could find reliable mechanisms that explain the behavior of chemical bonds on the atomic scale.

The AFM indentation method has been used to measure the elastic properties of molecular materials with high spatial resolution [34, 35]. The reported Young's modulus of amyloid fibrils by AFM indentation ranges from a few tens of MPa [36, 37] to a few tens of GPa [38, 39] depending on the sample size of fibrils, experimental approach, and loading conditions.

Because the mechanical properties of amyloid fibrils are derived from AFM nanoindentation measurements on the basis of assumptions about the geometry of the fibrils, they cannot provide highly accurate information about deformation. Because of the vague information on structures, to determine how different loading conditions affect the amyloid fibrils' structures and mechanical properties, we must resort to simulation. Thanks to the development of the molecular dynamics approach, one can obtain the Young's modulus of a biological system

computationally and literally see how the system deforms and fails under various loading conditions.

Molecular dynamics simulations have been used to study the structure and mechanical properties of the amyloid fibrils, revealing the deformation mechanism of the compressive and tensile loading of amyloid fibrils [19, 40]. The results have shown good agreement with experimental findings, showing that the computational method is reliable for studying amyloid fibrils under various loading conditions such as compression and tension.

Under both compression and tension, the Young's modulus of amyloid fibrils increases as the compressive or tensile strain is increased. Because the major chemical bonds supporting the structural stability of amyloid fibrils are the hydrogen bonds in the β-sheets, the mechanical response to the external load comes from the adjustment of the hydrogen bond network. The crucial deformation mechanism is associated with the torsional twisting of amyloid fibrils along the fibril axis which occurs with change in the density of the hydrogen bonds between β-sheets.

Under compressive loading, the number of hydrogen bonds increases because of the contraction of the distance among the β-strands, resulting in self-strengthening. This outstanding self-strengthening mechanical response to the compression could explain why the amyloid is so stable and can withstand high stresses without failure. On the other hand, as the amyloid fibril stretches under the tensile loading, the average distance between interlayers increases. The increased distance leads to a continuous decrease of hydrogen bond density until the fibril fails. However, the energy of amyloid fibrils still increases (Fig. 2b) in spite of the continuous decrease in the number of hydrogen bonds during the deformation. The increase in energy is coupled with a torsional motion of the amyloid fibrils, showing a higher Young's modulus than under compression. Although the fibrils have little chance to increase the number of hydrogen bonds under the tension, they can enhance their stiffness produced by the behavior of the covalent bonds rather than hydrogen bonds. Both compression and tension are associated with a torsional twisting deformation, in which a variation of the interlayer twist angle is proportional to both the applied stress and the measured strain. As described above, the different chemical and structural rearrangements of the amyloid fibrils play a primary role in strengthening their stiffness in responding to both compressive and tensile loading.

In addition to the Young's modulus, measured by atomic force microscopy and spectroscopy, the strength of amyloid fibrils is found to range from a few hundred megapascals (MPa) to one gigapascal (GPa) [38]. Recent molecular dynamics simulations studied the failure mechanism of amyloid fibrils under tensile stress [41], demonstrating a length dependency of the failure strain and stress (Fig. 2b). As described above, the number of hydrogen bonds continuously decreases as the tensile strain increases. Intriguingly, during the failure, the density of hydrogen bonds increases because of rearrangements and stabilization of the structures of broken parts of fibrils, making it difficult to break the whole system. As the amyloid fibril breaks into two parts, it is required to break a number of hydrogen bonds between the β-sheets. However, only one set of hydrogen bonds breaks and others

recover from damage after the amyloid fibril fails. This partial self-healing mechanism prevents the whole system from breaking into several parts.

Longer amyloid fibrils are more likely to be brittle and weak than shorter ones (Fig. 2b). Because the hydrogen bond interaction is a relatively short-range force (~4 Å), the critical strain and critical stress of the shorter amyloid fibrils can have higher values than the longer amyloids based on the fibrils' elastic response under tensile loading. Previous studies have shown that the number of hydrogen bonds that break simultaneously can be determined theoretically, providing a critical strand length of hydrogen bond clusters [42]. Beyond the critical length, the deformation of the system is more likely to be localized and the failure force of the system decreases to a certain value. On the other hand, under the critical length, the failure of the system is governed by the displacement rather than the critical strength. The reported theoretical critical length and reference failure strength of amyloid fibrils are about 1,000 nm and 175 pN, respectively [42]. These critical length and strength predictions mainly originate from the behavior of hydrogen bond clusters at the nanoscale, and are critical to understanding their ability to develop a significant mechanical strength in human brain tissue.

2.4 Mutation Effects

The stability and mechanical properties of amyloid fibrils result from the highly regular stacking of β-sheets and the dense network of hydrogen bonds. Because the sequence of the peptide plays a key role in aggregation, it is worth studying the effects of mutations to clarify the role of chemical bonds in structural stability and formation by comparing the properties and structures between normal and abnormal amyloid fibrils. The salt bridge between aspartate (D) 23 and lysine (K) 28 (Fig. 2a) is the key to understanding geometric properties of amyloid fibrils, as disrupting these salt bridges by replacing the amino acid with glycine (G) affects the stability and mechanical properties of amyloid fibrils [43].

The mutations damaging the salt bridge by replacing one of the residues (D23 or K28) or both (D23K28) by G can change three important features of amyloid fibrils: the length periodicity (Fig. 2d), failure strain, and Young's modulus. The periodicity is defined as the length of the amyloid fibrils needed to cover a complete twist turn. The D23 increases the twisting angle between β-sheets from 1.32° to 3.11°, decreasing the periodicity length to less than half. Removing one of the salt bridges is the primary reason for the change in the twisting angle, because the twisting angle of D23K28 remains less changed at 1.72°.

The modification of chemical bond networks is crucial to determining the pathways of the mechanochemical behavior. This changes the critical strain and the Young's modulus of the amyloid fibril. Interestingly, the mutations weaken the ability of fibrils to rearrange their internal structure through the twisting movement described in Sect. 2.3. For example, the angle change at 0.4% strain decreases from 23% to 7% in K28 and from 23% to 2% in D23, the D23K28 unwinding under the

compression. The Young's modulus of the mutated fibrils shows significant variation from about 4 GPa (D23 and K28) to 19 GPa (D23K28). It is evident that because of changes in their structure and chemical characteristics, the mutated components of the amyloid fibrils can have significant influence on the aggregation and mechanical properties of the amyloid fibrils.

3 Intermediate Filaments: Structure, Mechanics, and Disease

3.1 Introduction

The intermediate filament protein (IF protein) is a major component of animal cells along with microfilaments and microtubules. Compared to microtubules and microfilaments, a single intermediate filament tends to be rather flexible, extensible, and tough [44].

IF proteins assemble into a filament with a diameter of 8–12 nm which is the intermediate size between those of microtubules (25 nm) and microfilaments (7–9 nm). Whereas microtubules and microfilaments are more likely to be related to many basic cellular functions [44, 45], intermediate filaments play a key role in mechanical properties of tissues and cells, such as the stiffness and maximum strain, and the mechanical integrity of various tissues such as muscle, liver, and skin [44, 46].

More than 65 functional genes are related to the intermediate filaments and at least 30 diseases are related to the mutations in these genes [47]. The intermediate filaments gene family can be classified into five distinct types (I–V) based on their primary structure, gene, and their regulated tissue expression pattern [48, 49].

Intermediate filament protein types I and II are acidic keratin and basic keratin, found in epithelial cells. Vimentin, desmin, glial fibrillary acidic protein, synemin, and peripherin comprise the type III intermediate filaments. The type IV intermediate filaments include nestin and syncoilin, which are located in nervous systems and mostly found in neurons. The nuclear intermediate filaments, lamin A, its splice variant lamin C, and lamin B1 and B2 (type V), form a filamentous support inside the inner nuclear membrane [50].

Each intermediate filament type is closely related to a genetic disease associated with certain mutations. For example, HGPS is a rare genetic disease caused by a structural defect in the lamina nuclear membrane changing the mechanical properties at the cellular level [6]. This genetic disease causes the segmental premature aging in children, who suffer from failing to reach full stature and experience hair loss, thin wrinkled skin, and joint stiffness. Patients usually die of cardiovascular disease or stroke in their early teens [51]. Various skin diseases have also been associated with keratin mutations, which cause cytoplasmic aggregates and weaken the mechanical properties of epithelial cells [52, 53].

As with other biological materials, the change of nanostructure and the mechanical properties of the intermediate filaments are crucial to understanding diseases related to the intermediate filament mutations. Because the mechanical properties reflect the chemical bond network at the crack surfaces or in the entire system, the modification of structures by mutations severely affects how the chemical bonds at the crack surface interact and respond to mechanical loads [15, 49, 54]. Understanding how the different types of bonds in intermediate filaments react together under various mechanical loadings can give us opportunities to control and utilize the properties for medical applications.

3.2 Formation and Structure

Although various primary proteins form a variety of intermediate filaments, all intermediate filaments have a similar structural design. The basic building block, a monomer of IF protein, is a long central α-helix, called 'rod' domain, interrupted by 'linkers' and flanked by an N-terminal 'head' and a C-terminal 'tail' domain as shown in Fig. 3a [49, 55, 56]. Two monomers twist around each other to form a coiled-coil dimer, which is stabilized by a hydrophobic left-handed stripe that winds around the axis of each α-helix [57]. This rod-like domain controls the mechanical property of the single intermediate filament. Despite these similarities, there are distinct differences at the tail domain between nuclear IF proteins (e.g., lamin) and cytoplasmic IF proteins (e.g., vimentin) [58].

Although physical features of intermediate filaments look similar, different types of intermediates form different types of crosslinks affecting the elastic properties of the filament networks. The strong covalent bonds among the individual filaments are formed in keratin [59, 60], or divalent cations such as Ca^{2+} and Mg^{2+} glue vimentin intermediate filaments through coulombic interactions [61].

Vimentin filaments are the most widely distributed type among all IFs and are the focal point in this section. Their basic unit is a long monomer made up of 466 amino acid residues consisting of four main segments: 1A, 1B, 2A, and 2B divided by three linkers: L1, L12, and L2 as shown in Fig. 3a. Segment 2A (residues 264–282) is the shortest of all the segments. Segment 2B with 115 amino acids (residues 291–405) features an α-helical coiled-coil geometry for the major segment. One of the discontinuities found in heptad repeats of an α-helical coiled-coil protein is the 'stutter' region as pointed out in Fig. 3a [62, 63]. It can be seen that the stutter is located at the end of the eighth heptad, in the vicinity of residue 351 [64]. An analysis of the amino acid sequence revealed that the vicinity of the stutter region is hydrophilic, showing a parallel arrangement of two coils in the α-helix rather than a coiled-coil configuration. Although parts of the vimentin dimer structure have been revealed separately in independent experiments, a complete atomistic-level model of the basic constituents of this kind of protein material remains elusive.

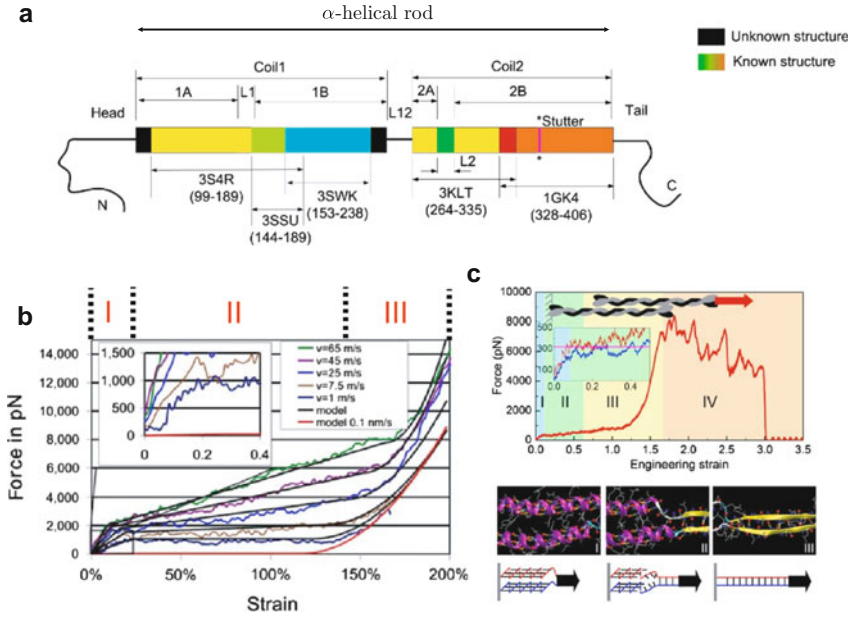

Fig. 3 Schematic view of the human vimentin protein and force-strain curves of coiled-coil intermediate filament under tensile loadings. (**a**) Schematic representation of vimentin structure. (**b**) Force-strain behaviors of a coiled-coil α-helical structures revealing the loading rate dependency of the molecular-level stiffness under tensile loading. (Reprinted from [66], with kind permission from Springer Science and Business Media). (**c**) α-β secondary structural transition of coiled-coil α-helix under tensile loading. (Reprinted from [67])

The known structures largely comprise the rod-like domain of the vimentin dimer, as illustrated in Fig. 3a. However, some segments have unknown structures. Experimental work using diffraction techniques has identified certain structural characteristics, and work based on Electron Paramagnetic Resonance measurements have revealed that the local stiffness of the L1 and L2 domains (both helical structures) is close to that of the rod-like domain [65]. There appear to be persistent experimental challenges in identifying the remaining parts of vimentin IF structures. However, the intrinsic limitations in experimental methods call for the development of complementary computational methods that can provide a more controlled condition to assess the relation between the nanostructure and the nanomechanics of this class of materials.

3.3 Mechanochemical Properties

To understand the mechanical properties of intermediate filament networks, knowledge of the mechanical behavior of single intermediate filaments is required. The

mechanical properties of coiled-coil α-helix dimers, basic building block of vimentin intermediate filaments, under tensile loading were studied in molecular dynamics simulations [66, 67]. The stretching process can be divided into three regimes (Fig. 3b). Because the coiled-coil structure has multiple hydrogen bonds, the number of hydrogen bonds could be a critical measure to distinguish different regimes of the deformation. In the first regime at small strains (<50%), most hydrogen bonds are stretched, and their mechanical response shows elastic behavior as described in Fig. 3b. Unfolding of the α-helices leads to the second plateau regime (around up to 90%). The third strain-hardening regime (leading up to 180%) is associated with the stretching covalent bonds once all hidden length in the protein is exhausted. This highly nonlinear mechanical feature of coiled-coil α-helices results from the structural transitions of the chemical bond network which is changing because of the mechanical loading.

The different stages of mechanical response of the intermediate filaments show another important feature of the biological materials. In the second regime, the hydrogen bonds rupture and the α-helices unfold; the unfolded structure is stretched in the third regime. The transition between these two regimes and the stress–strain behavior depends on the loading rate. In other words, the mechanochemical properties of intermediate filaments show rate dependency (Fig. 3b). At low loading speed, the α-helices unfold smoothly by rupturing hydrogen bonds without covalent bond stretching. At high loading speed, the covalent bonds extend in their folded structure because there is less rupturing of hydrogen bonds. Thus, different levels of pulling speeds control the ratio between hydrogen bond rupturing and covalent bond stretching.

The ratio in which two different types of bonds respond to the mechanical loading is governed by the molecules' intermediate structures. It is a notable observation that mechanochemical properties can be controlled through the modification of structures, and the structures can, in turn, also be controlled by loading speeds. The intermediate filament protects its structure from rapid and small deformation (such as an impact) by utilizing the strong covalent bonds. The intermediate filament can also maintain its structure in spite of large and smooth deformation by recovering broken hydrogen bonds and folding upon release of the mechanical load.

In addition to the behavior of the hydrogen bonds, an α-β structural transition is observed in both experiment and computational simulation in the final regime (Fig. 3c) [67–69]. Because of rearrangement of the β-sheet structure during deformation, the stress–strain behavior shows a plateau region (Fig. 3c **IV**) before rupture, corresponding to the sticky sliding of β-strands with respect to each other. In the plateau region, a large amount of energy is dissipated by forming and breaking multiple hydrogen bonds as the protein fiber fails.

Different types of crosslinks play a key role in the higher structure of intermediate filament networks. As shown in previous studies, the intermediate filament network is involved not only in the mechanical role but also in the cellular role. It is intriguing that the intermediate filament network can withstand extreme deformation >100% without rupture, even with the existence of defects [14,

70]. This extreme capacity for deformation mainly results from the highly nonlinear properties of the coiled-coil structures by sacrificing individual protein filaments [65]. Also, the flaw-tolerant characteristic results from the stiffening behavior during the secondary structural transitions for a single filament. In addition to the properties of a single filament, the crosslinks between intermediate filaments are also critical to the mechanical behavior of the intermediate filament network [42].

3.4 Mutation Effects

The important role of lamins in genetic diseases has been identified by recent studies [49, 71, 72]. For example, HGPS is a rare genetic disease causing premature aging early in life and leading to cardiovascular disease and death before age 16 years. The A- and B-type lamins comprise the intermediate filament that is the main component of the nucleoskeleton at the inner face of the nuclear membrane of the cell [73]. The *LMNA* gene encodes several A-type lamin proteins, mainly Lamin A and C. The *LMNB1* and *LMBN2* gene encode B-type lamins (lamins B1 and B2). Among the various lamin proteins, lamin A has received significant attention for its mechanical role in biology. Because the loss of lamin A affects nuclear mechanics more than other lamins in HGPS, a single point mutation in the *LMNA* gene activates a cryptic splice site, causing 50 amino acids encoded by exon 11 to be deleted, and the resulting mutant protein is called D50 lamin A (D50 LA) [7].

The properties of the hierarchical structure where individual intermediate filaments strongly form crosslinks with each other and flexibility of lamin filaments lead to the extremely large capacity of the larger-scale protein network to deform without failure. Replica exchange MD simulations and experiments reveals that D50 LA tail domain is more compact and displays less heterogeneity than the mature lamin A tail domain [74]. The compact and stable lamin may lead to more stiffness and reduced toughness. The increased stiffness could reduce the viability of cells by impairing their ability to recover from damage [75].

4 Collagenous Diseases

4.1 Introduction

Collagenous protein is the most abundant biological material in the human body. The three main types (I, II, and III) of collagen form 80–90% of the collagen in people. Type I collagen is a crucial structural protein material which maintains the integrity of many tissues such as bones, teeth, tendons, and ligaments. Many tissue disorders are associated with structural alterations of tropocollagen molecules that can be caused by over 300 mutations.

One of the most intriguing tissues composed of collagen protein is bone. Bone is extremely tough yet light, and can adapt to mechanical stimulus by changing its structure and repairing itself. Bone is, similar to other biomaterials, a hierarchical composite material composed of the soft tropocollagen and strong hydroxyapatite minerals (HAP). The hierarchical structures allow bone to have extreme toughness, dissipating high deformation energy without crack propagation. Distinct toughening mechanisms govern the mechanical properties at each level of hierarchy.

Osteogenesis imperfecta (OI) is a genetic disease characterized by high bone fragility, also referred to as "brittle bone syndrome." Patients with OI exhibit associated symptoms such as short stature and loose joints. The origin of the disease is the changes of the structure of tropocollagen molecules caused by the substitution of a single glycine amino acid. The OI mutations lead to serious reductions in the ultimate strength and the critical strain of OIM (Osteogenesis imperfecta murine) collagen [76].

A basic building block of the bone is the mineralized collagen fibril. With various percentages of mineralization, different types of bones have specialized properties for their own purposes. As with other biomaterials, the atomistic mechanical properties of its basic constitutive units are strongly correlated with their chemical bond network induced by their structural stability, and their reactivity during deformation and fracture.

4.2 Formation and Structure

Several hierarchical structure levels play a role in the superior mechanical properties of bone. The most fundamental building block is a polypeptide composed of a series of amino acids. Three strands of polypeptide assemble into the triple helical tropocollagen molecules. The molecular structure of mineralized-collagen fibrils is shown in Fig. 4a. The molecular segments repeat within a single unit cell called the 'D period' (length $D = 67$ nm). The D period consists of an overlap region ($0.46D = 30.8$ nm) and a gap region ($0.54D = 36.2$ nm) [77]. Because of their staggered geometry, which creates the gap regions, the tropocollagen molecules form collagen fibrils mineralized by the hydroxyapatite crystals mainly in those gaps [77].

The mechanism of nucleation of the minerals in bone has been intensively studied. Although it is not clearly understood, previous studies show that amorphous calcium phosphate (ACP) is a precursor phase in bone formation. After ACP is deposited as a first-formed mineral phase, it transforms into matured mineral phase, HAP [5, 78].

Recent studies revealed the process of mineralization of type I collagen by using horse tendon in solutions contacting $CaCl_2$, K_2HPO_4, and polyaspartic acid (pAsp). The time-resolved study shows that mineralized calcium phosphate particles are found close to the gap regions after 24 h. After ACP diffuses into fibrils, it develops to the oriented apatite (plate-shaped crystals with 2–5 nm thick, 15–55 nm long and 5–25 nm wide) (Fig. 4b) [79].

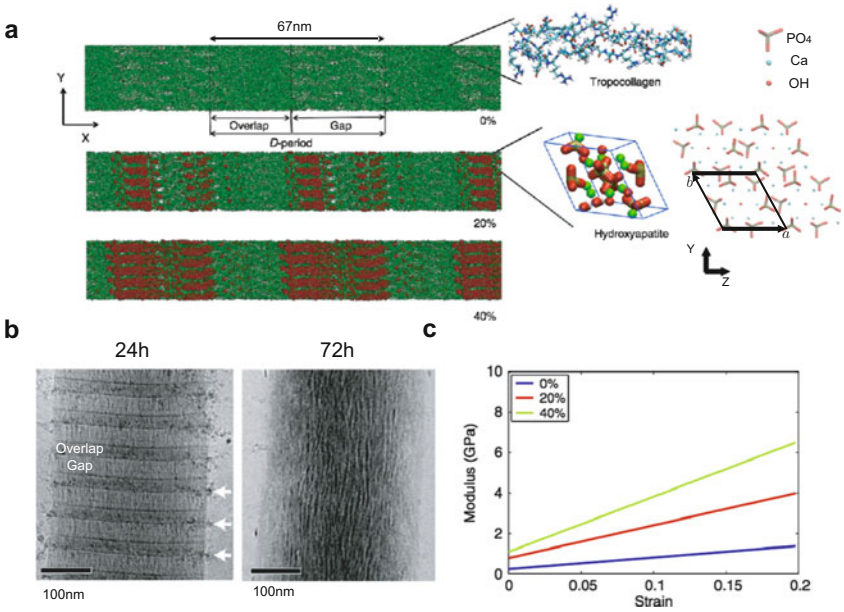

Fig. 4 (**a**) Collagen fibril model with 0%, 20%, and 40% mineralization. (**b**) Cryogenic TEM image of different stages of mineralization in vitro of type I collagen of horse tendon in the presence of 10 μg ml^{-1} polyaspartic acid (pAsp) which is an inhibitor of hydroxyapatite crystallization [96]; mineralization calcium phosphate particles were found outside the fibrils after 24 h (*white arrows*), plate-shape crystal (2–5 nm thick, 15–55 nm long and 5–25 nm wide) after 72 h. (Reprinted by permission from Macmillan Publishers Ltd: [79], Copyright (2010)). (**c**) Modulus-strain curves showing HAP volume dependency in simulation. (**a** and **c** are reprinted from [43])

The structure of HAP ($Ca_{10}(PO_4)_6(OH)_2$) is shown in Fig. 4a. The basic unit comprises pairs of positively charged calcium ions (C-sites) and clusters of six negatively charged phosphates (P-sites). Because the collagen protein is not stiff, the distribution of HAP in mineralized-collagen fibril plays a key role in the stiffness of bone. On the other hand, the mineral is less tough than the collagen molecule. Bone is naturally designed to utilize the unique properties of both minerals and proteins.

4.3 Mechanochemical Properties

Because tropocollagen is one of the basic components of bone tissue, it is critical to understand the mechanical properties of a single tropocollagen molecule. The Young's modulus of the tropocollagen has been estimated both in experiments and molecular dynamics simulations. The Young's modulus of tropocollagen has a wide range of values [80] and this wide variation comes from the tropocollagen

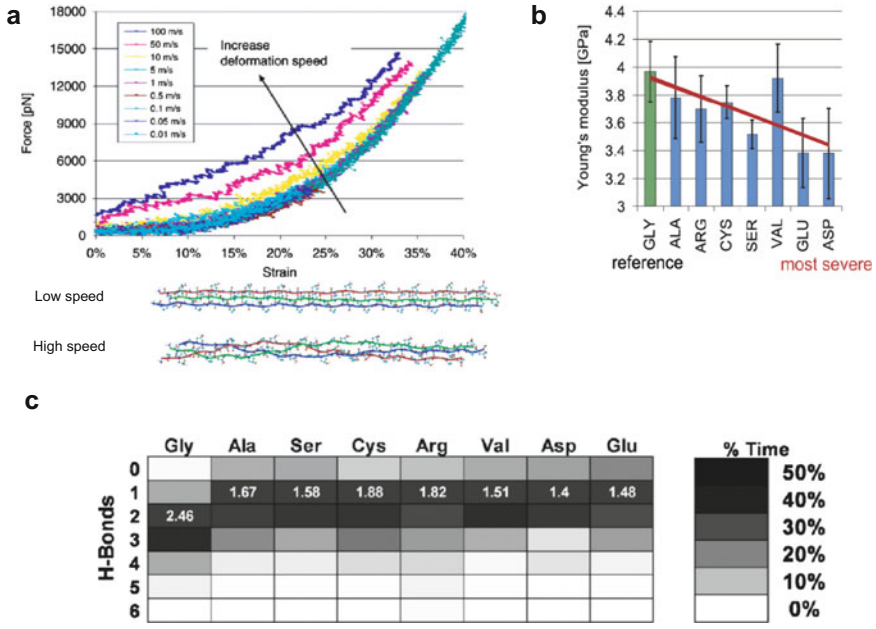

Fig. 5 (**a**) Force-strain curves of tropocollagen under tensile loading showing rate dependency. (Reprinted from [80], Copyright (2009), with permission from Elsevier). (**b**) Young's modulus of a single tropocollagen molecule, as a function of the amino acid replacing and as a function of OI severity. (Reprinted from [86], Copyright (2009), with permission from Elsevier). (**c**) Effects of mutation types on interchain hydrogen bonds. (Reproduced from [97], with permission of The Royal Society of Chemistry)

nanostructure. A full atomistic simulation performed by Gautieri et al. reveals that tropocollagen has three different deformation stages.

Initially, the tropocollagen molecules unwind with rotation in the first stage and then the hydrogen bonds break, and release energy in the second stage. The behavior of tropocollagen molecules in the second stage, where multiple hydrogen bonds break, is the major mechanism mediating the deformation of collagen fibrils. This process may allow the bone to dissipate large amounts of energy through large deformation. In the final stage, the backbones of molecules are stretched and the mechanical response is stronger than in previous stages because the deformation is mainly related to the covalent bonds. It is also revealing that the Young's modulus depends on the loading rate (Fig. 5a), as with other biological materials described in previous chapters, and the dependency results from the not fully unfolded structure of tropocollagen molecules. Figure 5a shows how the structure changes with different loading speeds. Although the tropocollagen molecules can fully unwind under low-speed loading, partially unfolded structures are observed at high-speed loading. The effects of differently deformed structures at different loading speeds demonstrate the nonlinear elasticity or hyperelasticity of the collagen materials.

Because the mineral has higher modulus than the collagen molecules, it is commonly believed that the presence of HAP is important to the stiffness of bone [81, 82]. The mechanical and failure properties of bone depend on the relative amount of the mineral deposited in the collagen fibrils [83, 84]. From tests on various bone samples of mammals, it is known that the Young's modulus of the mineralized-collagen fibrils increases linearly with the mineral contents [81].

A full-atomistic mineralized-collagen fibril atomic model for MD simulations was recently developed by Nair et al. (Fig. 4a) [85]. They performed tensile tests with different volume fractions of mineralization. Their study reveals that mineral content increases the stiffness of the mineralized-collagen fibrils (Fig. 4c). These simulations show that the mineral crystals can withstand four times more stress than the collagen, and the collagen can deform more than the mineral. Because the HAP is largely deposited in the gap regions, as the HAP percentage increases, the gap regions become stiffer because of the strong ionic forces in the HAP. On the other hand, the collagen can deform more than the mineral because of its softness under the external loadings. It is evident that the volume fraction of HAP is critical for the stiffness of mineralized-collagen fibrils. In addition, the different stiffness between the gap region and the overlap region can lead to the different structural deformation states, affecting the kind of unfolding that accompanies the hydrogen bond breaking and strong electrostatic force between the HAP and proteins. The variation may allow the mineralized-collagen fibrils to have a wide range of stiffness and critical strain points. Similar to the intermediate filaments, this variation can play a critical role in toughening bone at the macroscale.

4.4 Mutation Effects

Because the structure of the tropocollagen depends on its amino acid components and sequence, the mutations replacing an amino acid affect the tropocollagen structures. This structural difference leads to changes in the intermolecular interactions in the system, affecting the collagen fibril packing and the space of the gap regions, thus changing the mechanical properties of bone.

Molecular dynamics studies of the effects of OI at the molecular level have shown a reduction in the Young's modulus of up to 15% [86] (Fig. 5b). The structural changes caused by OI mutations induce localized stress concentration at the collagen fibril level, leading to lower stiffness and more brittleness than observed in normal collagen fibrils. It was suggested that the decrease of the Young's modulus is strongly correlated with the density of the hydrogen bonds. Figure 5c shows the effects of the mutated acids on the hydrogen bond density of stabilized structures. As the density of hydrogen bonds decreases, the collagen molecules become softer, and this effect is more pronounced as the severity of mutation increases (Fig. 5b). Also, as a result of elongated equilibrium distance between the collagen molecules by the mutation, the adhesion energy between the molecules decreases. This weakened intermolecular interaction results in the

reduction of the intermolecular crosslinks in the collagen fibrils. Molecular level studies clearly show that even a single substitution induced by mutations has a significant effect on the higher level of structures, critical for understanding the mechanical properties and the catastrophic failure mechanism of bone.

Because of the different structures of the collagen proteins, the deposition of the mineral in the gap regions can change. The X-ray diffraction data show that the mineral plates in OI mineralized-collagen fibrils are more structurally disordered and thinner than those of normal fibrils. The qualities of mineral crystals, such as shape, thickness, and alignment, are related to a drastic change in the ability of tropocollagen to bind to the minerals [87]. However, how these kinds of qualities affect the mechanical properties of bone is still little understood. Modeling the different mineral qualities in the mineralized-collagen fibrils remains challenging because the mechanism of crystallization from the amorphous structures is not clear yet. It would be interesting for future studies to clarify the crystallization process and how the mechanical properties change.

Although the main mechanism of crystallization is not yet known, we can see how the quality of mineral is important in the fibrils. In a previous study, how the interaction between minerals and collagens changes as a function of HAP thickness is reported [88]. Although the interaction between collagens and minerals is crucial for understanding the mechanical properties of mineralized-collagen fibrils, the strength and stiffness of each component should be considered individually to obtain an accurate description of mechanical behavior. However, the changes in those mechanical properties produced by the mineral qualities have not yet been studied in atomic simulations. Here, we aim to shed light on the importance of the qualities of minerals to the study of mineralized-collagen fibrils of OI bone by performing simple tensile tests with different thicknesses of HAP minerals. Based on experiments on mice and rats, the earliest measurable thickness of HAP is under 2 nm and it increases to more than 3 nm in 3 months [89]. Because the average thickness of mineral crystals of OI mice is around $1.7 \sim 1.8$ nm [87], we performed tensile tests of HAP with different thicknesses ($T = 1.7$, 3.4, 5.1 nm).

Tensile tests are performed under different environments, in a vacuum and in water. Although our model is extremely simplified, the results show meaningful effects of mineral thickness usually ignored up to now. We observed that the mechanical properties such as Young's modulus, strength, and critical strain are sensitive to thicknesses less than 5 nm. As the thickness increases, the sensitivity decreases and the mechanical properties become closer to those of bulk materials. In the vacuum, the critical strength of 1.7 nm HAP does not show a peak point (~2.0 GPa under 8% tensile strain) because the structure is not so well ordered as with the bulk crystals because of the lack of other layers in the thickness direction. Because the ionic interaction based on Coulombic interaction reaches a longer distance than other interactions, it is important to have enough layers to be stabilized in a specific structure. However, because of the thinness of the minerals, the interactions with environments such as proteins and water can disturb the structure, making the minerals lose their bulk properties.

On the other hand, in the water, we observe a clearer critical strength point of 1.7 nm HAP than that of 1.7 nm HAP in the vacuum. This means the mechanical properties are affected by the interactions between HAP and the environments. Thin HAP (under 2 nm) shows more ductility and fluidity because of the relatively disordered structure. Although the structure is more amorphous and the structural deformation occurs across the entire system during the tensile deformation with the thin HAP, the deformation and failure of HAP become more localized as the thickness of HAP increases. Because of the thinness of the minerals, the interactions with environments such as proteins and water can disturb or stabilize the HAP structure, making the minerals lose or gain their bulk properties.

We note that the drastic difference in the strength of 3.4 and 1.7 nm samples of HAP is observed in both vacuum and water (50% and 30% difference in vacuum and water, respectively). When the forces HAP can withstand in the fibrils with the real size are considered, the effect of thickness is more significant. In the case of 15 nm width, the forces drop from to 200 to 50 nN in vacuum, and from 250 to 80 nN in water. Because the mutation of collagen molecules changes the structure of collagen and, thus, the thickness of HAP, the brittleness of OI bone may derive from the failure of HAP crystal. Although we do not consider the changes of shapes, grains, or alignments of HAP produced by the collagen proteins, mineral crystal qualities and their roles are intriguing subjects for future study.

The single point mutant of collagen and volume of mineral phase have a significant effect on the mechanical properties and toughness of bone. Although previous experiments suggest mutations change the mineral quality, the role of mineral quality is still unclear. We performed tensile tests of HAP with different thicknesses to address the importance of HAP quality in mineralized-collagen fibrils. Even though the simulation is limited to only the thickness effect of HAP, it has been shown that not only volumetric factor but also the quality of the minerals has effects on the strength, stiffness, critical strain, and failure mechanism of mineralized-collagen fibrils. To determine in more detail the roles of the quality of mineral, understanding the formation mechanism of HAP in vivo and more precise information about HAP are essential for future work.

4.5 Simulation Details

In our simulations we used the empirical force fields for the interaction among ions of HAP reported earlier [90, 91]. Two-body ionic short-range interaction potential of the Buckingham type and Coulombic interaction term were adopted. A Morse potential was adopted for both O-H and P-O bond interactions. The harmonic three-body potential was used to describe the tetrahedral configuration of oxygen ions around phosphorus. The force fields describe the structures and the mechanical properties of HAP reasonably well, and show excellent agreement with the experimental data. For the interactions between water molecules and ions of HAP, we adopted the same approach as in the previous study [92].

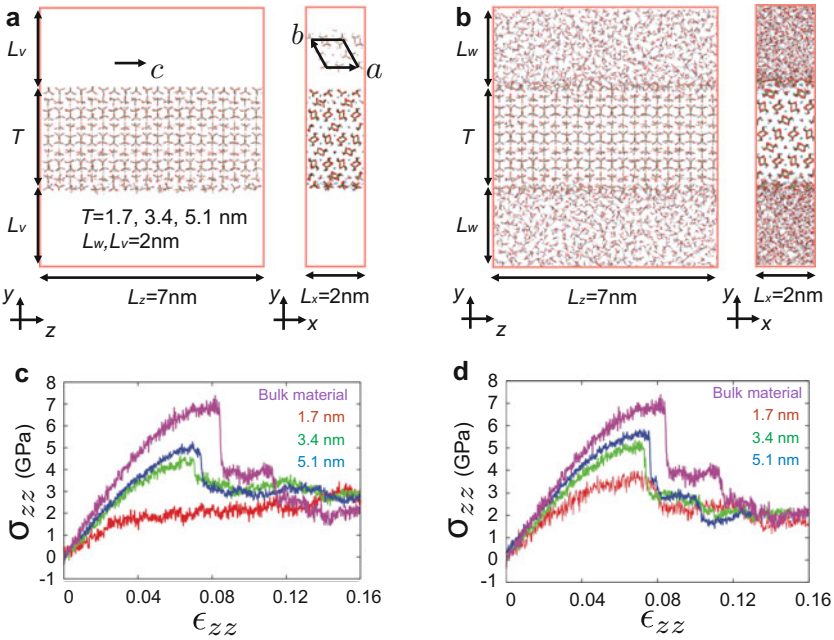

Fig. 6 The relaxed structure of HAP mineral crystals: (**a**) in a vacuum; (**b**) in water. (**c**, **d**) Stress–strain curves of HAP as a function of different thicknesses

We generated the HAP crystal structures using Visual Molecular Dynamics (VMD) [93]. Because we aim to test the effects of thickness (in the y direction), we build a slap system by inserting a vacuum layer (4 nm, Fig. 6a) and a water layer (4 nm, Fig. 6b) around the HAP slap. After energy minimization, the temperature of the system is initially set to 5 K with a Berendsen thermostat for 10,000 steps. Then we apply a Berendsen barostat to relax the simulation box for 30,000 steps. Then we gradually increase the temperature to room temperature (300 K). We relaxed the system with the additional 70,000 steps. After relaxation, we fixed the edge part of the longest side (the z direction) and deformed the system in the z direction as quickly as 1.0 m/s. We performed the same tensile test for the bulk material with the same geometry of 1.7 nm to show that the weakening strength mainly comes from the finite thickness. All relaxations and running simulations were performed with a 0.5 fs time step. Our MD simulations were performed using LAMMPS [94] and VMD was used for visualization.

5 Remarks

Biological materials are important not only because of their physiological roles but also because they hold significant potential for future applications in various areas of technology, such as nanodevices. In this review, we have shown that the mechanochemical properties of biomaterials are closely related to their structure and loading conditions. Because of the mechanical stimuli, the behavior of different types of chemical bonds can either enhance or weaken the mechanical properties of biopolymers by affecting the failure and deformation mechanism at each deformation stage. The breaking and reforming of hydrogen bonds play the most crucial role in defining the stability and capacity of protein materials to withstand extreme mechanical loadings. First, the hydrogen bonds allow the system to have large deformation by continuously changing the structures under the slow loading (e.g., unwinding the collagen and the coiled-coil alpha helix in the intermediate filaments). Second, the weak hydrogen bonds can be relatively more easily recovered than most engineering materials after the loading is removed, enabling the system to recover from the damage (e.g., failure of amyloid fibrils under the tensile loading). Finally, the hydrogen bond network controls the point where the covalent bonds in the system start to withstand the external loadings (such as rate dependency of the collagen fibrils and intermediate filaments).

We also discussed the mutation effects on mechanical properties of the materials. Basically, the mutation can change the stabilized structure of biomaterials, affecting the chemical bond networks. The altered structures can change the mechanochemical properties of materials under the various external loadings, weakening or enhancing the strength and toughness of materials. In addition, mutations can change the density of crosslinks between the basic units, critical to determining the properties at a higher hierarchical level of the biological systems.

Because the rupture and fracture occur over an extremely short time span, computational methods such as molecular dynamics and newly developed MD techniques become essential tools to analyze the structure of materials and the relations between mechanochemical processes and loading conditions. Through the simple MD simulations of HAP crystals, we have shown that the thickness of HAP can affect the behavior of ionic bonds under the tensile loadings, showing the importance of the chemical environments of HAP crystals and the crystal quality. The details of the effects of the HAP crystal quality and the nucleation mechanism would make an interesting follow-up study in the future.

The hierarchical structures of biological materials are critical to understanding the mechanical properties in the different level of structures. As discussed above, the single mutation of the most fundamental building block of biomaterials affects the chemical bond network, density, and structure. The fact that different types of bonds respond differently to mechanical loadings and interact with each other makes the biomaterials extremely intriguing. The knowledge of mechanochemical properties and processes under various loading conditions provide valuable opportunities and insight for new materials design and applications in the future.

Acknowledgements We acknowledge support from DOD-PECASE, NSF, and ARO, and additional funding from NIH-U01.

References

1. Smith BL, Schäffer TE, Viani M, Thompson JB, Frederick NA, Kindt J et al (1999) Molecular mechanistic origin of the toughness of natural adhesives, fibres and composites. Nature 399 (6738):761–763
2. Wang RZ, Suo Z, Evans AG, Yao N, Aksay IA (2011) Deformation mechanisms in nacre. J Mater Res 16(09):2485–2493
3. Buehler M, Keten S (2010) Colloquium: failure of molecules, bones, and the Earth itself. Rev Mod Phys 82:1459–1487
4. Amberger JS, Bocchini CA, Schiettecatte F, Scott AF, Hamosh A (2014) OMIM.org: Online Mendelian Inheritance in Man (OMIM®), an online catalog of human genes and genetic disorders. Nucleic Acids Res 43:D789–D798
5. Mahamid J, Aichmayer B, Shimoni E, Ziblat R, Li C, Siegel S et al (2010) Mapping amorphous calcium phosphate transformation into crystalline mineral from the cell to the bone in zebrafish fin rays. Proc Natl Acad Sci 107(14):6316–6321
6. Eriksson M, Brown WT, Gordon LB, Glynn MW, Singer J, Scott L et al (2003) Recurrent de novo point mutations in lamin A cause Hutchinson–Gilford progeria syndrome. Nature 423 (6937):293–298
7. De Sandre-Giovannoli A, Bernard R, Cau P, Navarro C, Amiel J, Boccaccio I et al (2003) Lamin A truncation in Hutchinson-Gilford progeria. Science 300(5628):2055
8. Csoka AB, Cao H, Sammak PJ, Constantinescu D, Schatten GP, Hegele RA (2004) Novel lamin A/C gene (LMNA) mutations in atypical progeroid syndromes. J Med Genet 41 (4):304–308
9. Primorac D, Rowe DW, Mottes M, Barisić I, Anticević D, Mirandola S et al (2001) Osteogenesis imperfecta at the beginning of bone and joint decade. Croat Med J 42(4):393–415
10. Prockop JD (1995) Collagens: molecular biology, diseases, and potentials for therapy. Annu Rev Biochem 64(1):403–434
11. Byers PH, Wallis GA, Willing MC (1991) Osteogenesis imperfecta: translation of mutation to phenotype. J Med Genet 28(7):433–442
12. Baláž P, Achimovičová M, Baláž M, Billik P, Cherkezova-Zheleva Z, Criado JM et al (2013) Hallmarks of mechanochemistry: from nanoparticles to technology. Chem Soc Rev 42 (18):7571–7637
13. Huang YY, Knowles TPJ, Terentjev EM (2009) Strength of nanotubes, filaments, and nanowires from sonication-induced scission. Adv Mater 21(38–39):3945–3948
14. Dahl KN, Scaffidi P, Islam MF, Yodh AG, Wilson KL, Misteli T (2006) Distinct structural and mechanical properties of the nuclear lamina in Hutchinson–Gilford progeria syndrome. Proc Natl Acad Sci 103(27):10271–10276
15. Buehler MJ, Yung YC (2009) Deformation and failure of protein materials in physiologically extreme conditions and disease. Nat Mater 8(3):175–188
16. Reches M, Gazit E (2005) Self-assembly of peptide nanotubes and amyloid-like structures by charged-termini-capped diphenylalanine peptide analogues. Isr J Chem 45(3):363–371
17. Yemini M, Reches M, Rishpon J, Gazit E (2005) Novel electrochemical biosensing platform using self-assembled peptide nanotubes. Nano Lett 5(1):183–186
18. Cherny I, Gazit E (2008) Amyloids: not only pathological agents but also ordered nanomaterials. Angew Chem Int Ed 47(22):4062–4069

19. Paparcone R, Keten S, Buehler MJ (2010) Atomistic simulation of nanomechanical properties of Alzheimer's Aβ(1-40) amyloid fibrils under compressive and tensile loading. J Biomech 43 (6):1196–1201
20. Chiti F, Dobson CM (2006) Protein misfolding, functional amyloid, and human disease. Annu Rev Biochem 75(1):333–366
21. Goldschmidt L, Teng PK, Riek R, Eisenberg D (2010) Identifying the amylome, proteins capable of forming amyloid-like fibrils. Proc Natl Acad Sci 107(8):3487–3492
22. Otzen DE, Kristensen O, Oliveberg M (2000) Designed protein tetramer zipped together with a hydrophobic Alzheimer homology: a structural clue to amyloid assembly. Proc Natl Acad Sci 97(18):9907–9912
23. Wurth C, Guimard NK, Hecht MH (2002) Mutations that reduce aggregation of the Alzheimer's Aβ42 peptide: an unbiased search for the sequence determinants of Aβ amyloidogenesis. J Mol Biol 319(5):1279–1290
24. Chiti F, Taddei N, Baroni F, Capanni C, Stefani M, Ramponi G et al (2002) Kinetic partitioning of protein folding and aggregation. Nat Struct Biol 9(2):137–143
25. Chiti F, Calamai M, Taddei N, Stefani M, Ramponi G, Dobson CM (2002) Studies of the aggregation of mutant proteins in vitro provide insights into the genetics of amyloid diseases. Proc Natl Acad Sci 99(Suppl 4):16419–16426
26. Schmittschmitt JP, Scholtz JM (2003) The role of protein stability, solubility, and net charge in amyloid fibril formation. Protein Sci 12(10):2374–2378
27. Jarrett JT, Berger EP, Lansbury PT (1993) The carboxy terminus of the beta amyloid protein is critical for the seeding of amyloid formation: implications for the pathogenesis of Alzheimer's disease. Biochemistry 32(18):4693–4697
28. Jansen R, Dzwolak W, Winter R (2005) Amyloidogenic self-assembly of insulin aggregates probed by high resolution atomic force microscopy. Biophys J 88(2):1344–1353
29. Morris KL, Serpell LC (2012) X-Ray fibre diffraction studies of amyloid fibrils, vol 849, Amyloid proteins. Humana Press, Totowa, pp 121–135
30. Petkova AT, Ishii Y, Balbach JJ, Antzutkin ON, Leapman RD, Delaglio F et al (2002) A structural model for Alzheimer's β-amyloid fibrils based on experimental constraints from solid state NMR. Proc Natl Acad Sci 99(26):16742–16747
31. Antzutkin ON, Balbach JJ, Leapman RD, Rizzo NW, Reed J, Tycko R (2000) Multiple quantum solid-state NMR indicates a parallel, not antiparallel, organization of β-sheets in Alzheimer's β-amyloid fibrils. Proc Natl Acad Sci 97(24):13045–13050
32. Petkova AT, Leapman RD, Guo Z, Yau W-M, Mattson MP, Tycko R (2005) Self-propagating, molecular-level polymorphism in Alzheimer's ß-amyloid fibrils. Science 307(5707):262–265
33. Lührs T, Ritter C, Adrian M, Riek-Loher D, Bohrmann B, Döbeli H et al (2005) 3D structure of Alzheimer's amyloid-β(1-42) fibrils. Proc Natl Acad Sci 102(48):17342–17347
34. Shulha H, Zhai X, Tsukruk VV (2003) Molecular stiffness of individual hyperbranched macromolecules at solid surfaces. Macromolecules 36(8):2825–2831
35. Dimitriadis EK, Horkay F, Maresca J, Kachar B, Chadwick RS (2002) Determination of elastic moduli of thin layers of soft material using the atomic force microscope. Biophys J 82 (5):2798–2810
36. Guo S, Akhremitchev BB (2006) Packing density and structural heterogeneity of insulin amyloid fibrils measured by AFM nanoindentation. Biomacromolecules 7(5):1630–1636
37. del Mercato LL, Maruccio G, Pompa PP, Bochicchio B, Tamburro AM, Cingolani R et al (2008) Amyloid-like fibrils in elastin-related polypeptides: structural characterization and elastic properties. Biomacromolecules 9(3):796–803
38. Smith JF, Knowles TPJ, Dobson CM, MacPhee CE, Welland ME (2006) Characterization of the nanoscale properties of individual amyloid fibrils. Proc Natl Acad Sci 103 (43):15806–15811
39. Kol N, Adler-Abramovich L, Barlam D, Shneck RZ, Gazit E, Rousso I (2005) Self-assembled peptide nanotubes are uniquely rigid bioinspired supramolecular structures. Nano Lett 5 (7):1343–1346

40. Xu Z, Paparcone R, Buehler MJ (2010) Alzheimer's Aβ(1-40) amyloid fibrils feature size-dependent mechanical properties. Biophys J 98(10):2053–2062
41. Paparcone R, Buehler MJ (2011) Failure of Aβ(1-40) amyloid fibrils under tensile loading. Biomaterials 32(13):3367–3374
42. Keten S, Xu Z, Ihle B, Buehler MJ (2010) Nanoconfinement controls stiffness, strength and mechanical toughness of β-sheet crystals in silk. Nat Mater 9(4):359–367
43. Paparcone R, Pires MA, Buehler MJ (2010) Mutations alter the geometry and mechanical properties of Alzheimer's Aβ(1-40) amyloid fibrils. Biochemistry 49(41):8967–8977
44. Kreplak L, Fudge D (2007) Biomechanical properties of intermediate filaments: from tissues to single filaments and back. Bioessays 29(1):26–35
45. Wang J, Zohar R, McCulloch CA (2006) Multiple roles of α-smooth muscle actin in mechanotransduction. Exp Cell Res 312(3):205–214
46. Lazarides E (1980) Intermediate filaments as mechanical integrators of cellular space. Nature 283(5744):249–255
47. Hesse M, Magin TM, Weber K (2001) Genes for intermediate filament proteins and the draft sequence of the human genome novel keratin genes and a surprisingly high number of pseudogenes related to keratin genes 8 and 18. J Cell Sci 114(14):2569–2575
48. Strelkov SV, Herrmann H, Aebi U (2003) Molecular architecture of intermediate filaments. Bioessays 25(3):243–251
49. Omary MB, Coulombe PA, McLean WHI (2004) Intermediate filament proteins and their associated diseases. N Engl J Med 351(20):2087–2100
50. Qin Z, Buehler MJ (2012) Computational and theoretical modeling of intermediate filament networks: structure, mechanics and disease. Acta Mech Sinica 28(4):941–950
51. Uitto J (2002) Searching for clues to premature aging. Trends Mol Med 8(4):155–157
52. Vassar R, Coulombe PA, Degenstein L, Albers K, Fuchs E (1991) Mutant keratin expression in transgenic mice causes marked abnormalities resembling a human genetic skin disease. Cell 64 (2):365–380
53. Albers K, Fuchs E (1987) The expression of mutant epidermal keratin cDNAs transfected in simple epithelial and squamous cell carcinoma lines. J Cell Biol 105(2):791–806
54. Ma L, Yamada S, Wirtz D, Coulombe PA (2001) A 'hot-spot' mutation alters the mechanical properties of keratin filament networks. Nat Cell Biol 3(5):503–506
55. Fuchs E, Cleveland DW (1998) A structural scaffolding of intermediate filaments in health and disease. Science 279(5350):514–519
56. Herrmann H, Bär H, Kreplak L, Strelkov SV, Aebi U (2007) Intermediate filaments: from cell architecture to nanomechanics. Nat Rev Mol Cell Biol 8(7):562–573
57. Smith TA, Strelkov SV, Burkhard P, Aebi U, Parry DAD (2002) Sequence comparisons of intermediate filament chains: evidence of a unique functional/structural role for coiled-coil segment 1A and linker L1. J Struct Biol 137(1–2):128–145
58. Herrmann H, Aebi U (2004) Intermediate filaments: molecular structure, assembly mechanism, and integration into functionally distinct intracellular scaffolds. Annu Rev Biochem 73 (1):749–789
59. Wiita AP, Ainavarapu SRK, Huang HH, Fernandez JM (2006) Force-dependent chemical kinetics of disulfide bond reduction observed with single-molecule techniques. Proc Natl Acad Sci 103(19):7222–7227
60. Parbhu AN, Bryson WG, Lal R (1999) Disulfide bonds in the outer layer of keratin fibers confer higher mechanical rigidity: correlative nano-indentation and elasticity measurement with an AFM. Biochemistry 38(36):11755–11761
61. Lin Y-C, Broedersz CP, Rowat AC, Wedig T, Herrmann H, MacKintosh FC et al (2010) Divalent cations crosslink vimentin intermediate filament tail domains to regulate network mechanics. J Mol Biol 399(4):637–644
62. Ackbarow T, Sen D, Thaulow C, Buehler MJ (2009) Alpha-helical protein networks are self-protective and flaw-tolerant. PLoS One 4(6):e6015

63. Strelkov SV, Herrmann H, Geisler N, Lustig A, Ivaninskii S, Zimbelmann R et al (2001) Divide-and-conquer crystallographic approach towards an atomic structure of intermediate filaments. J Mol Biol 306(4):773–781
64. Strelkov SV, Herrmann H, Geisler N, Wedig T, Zimbelmann R, Aebi U et al (2002) Conserved segments 1A and 2B of the intermediate filament dimer: their atomic structures and role in filament assembly. EMBO J 21(6):1255–1266
65. Aziz A, Hess JF, Budamagunta MS, Voss JC, Kuzin AP, Huang YJ et al (2012) The structure of vimentin linker 1 and rod 1B domains characterized by site-directed spin-labeling electron paramagnetic resonance (SDSL-EPR) and X-ray crystallography. J Biol Chem 287 (34):28349–28361
66. Ackbarow T, Buehler MJ (2007) Superelasticity, energy dissipation and strain hardening of vimentin coiled-coil intermediate filaments: atomistic and continuum studies. J Mater Sci 42 (21):8771–8787
67. Qin Z, Kreplak L, Buehler MJ (2009) Hierarchical structure controls nanomechanical properties of vimentin intermediate filaments. PLoS One 4(10):e7294
68. Fudge DS, Gardner KH, Forsyth VT, Riekel C, Gosline JM (2003) The mechanical properties of hydrated intermediate filaments: insights from hagfish slime threads. Biophys J 85 (3):2015–2027
69. Kreplak L, Doucet J, Dumas P, Briki F (2004) New aspects of the α-helix to β-sheet transition in stretched hard α-keratin fibers. Biophys J 87(1):640–647
70. Panorchan P, Schafer BW, Wirtz D, Tseng Y (2004) Nuclear envelope breakdown requires overcoming the mechanical integrity of the nuclear lamina. J Biol Chem 279 (42):43462–43467
71. Wilson KL, Zastrow MS, Lee KK (2001) Lamins and disease. Cell 104(5):647–650
72. Rowat AC, Lammerding J, Herrmann H, Aebi U (2008) Towards an integrated understanding of the structure and mechanics of the cell nucleus. Bioessays 30(3):226–236
73. Wilson KL, Berk JM (2010) The nuclear envelope at a glance. J Cell Sci 123(12):1973–1978
74. Qin Z, Kalinowski A, Dahl KN, Buehler MJ (2011) Structure and stability of the lamin A tail domain and HGPS mutant. J Struct Biol 175(3):425–433
75. Verstraeten VLRM, Ji JY, Cummings KS, Lee RT, Lammerding J (2008) Increased mechanosensitivity and nuclear stiffness in Hutchinson–Gilford progeria cells: effects of farnesyltransferase inhibitors. Aging Cell 7(3):383–393
76. Misof K, Landis WJ, Klaushofer K, Fratzl P (1997) Collagen from the osteogenesis imperfecta mouse model (oim) shows reduced resistance against tensile stress. J Clin Invest 100(1):40–45
77. Orgel JPRO, Irving TC, Miller A, Wess TJ (2006) Microfibrillar structure of type I collagen in situ. Proc Natl Acad Sci 103(24):9001–9005
78. Olszta MJ, Cheng X, Jee SS, Kumar R, Kim Y-Y, Kaufman MJ et al (2007) Bone structure and formation: a new perspective. Mater Sci Eng R Rep 58(3–5):77–116
79. Nudelman F, Pieterse K, George A, Bomans PHH, Friedrich H, Brylka LJ et al (2010) The role of collagen in bone apatite formation in the presence of hydroxyapatite nucleation inhibitors. Nat Mater 9:1004–1009
80. Gautieri A, Buehler MJ, Redaelli A (2009) Deformation rate controls elasticity and unfolding pathway of single tropocollagen molecules. J Mech Behav Biomed Mater 2(2):130–137
81. Currey JD (1990) Physical characteristics affecting the tensile failure properties of compact bone. J Biomech 23(8):837–844
82. Jäger I, Fratzl P (2000) Mineralized collagen fibrils: a mechanical model with a staggered arrangement of mineral particles. Biophys J 79(4):1737–1746
83. Currey J (2001) Sacrificial bonds heal bone. Nature 414:699
84. Gao H, Ji B, Jäger IL, Arzt E, Fratzl P (2003) Materials become insensitive to flaws at nanoscale: lessons from nature. Proc Natl Acad Sci 100(10):5597–5600
85. Nair AK, Gautieri A, Chang S-W, Buehler MJ (2013) Molecular mechanics of mineralized collagen fibrils in bone. Nat Commun 4:1724

86. Gautieri A, Uzel S, Vesentini S, Redaelli A, Buehler MJ (2009) Molecular and mesoscale mechanisms of osteogenesis imperfecta disease in collagen fibrils. Biophys J 97(3):857–865
87. Fratzl P, Paris O, Klaushofer K, Landis WJ (1996) Bone mineralization in an osteogenesis imperfecta mouse model studied by small-angle X-ray scattering. J Clin Invest 97(2):396–402
88. Qin Z, Gautieri A, Nair AK, Inbar H, Buehler MJ (2012) Thickness of hydroxyapatite nanocrystal controls mechanical properties of the collagen-hydroxyapatite interface. Langmuir 28(4):1982–1992
89. Fratzl P, Fratzl-Zelman N, Klaushofer K, Vogl G, Koller K (1991) Nucleation and growth of mineral crystals in bone studied by small-angle X-ray scattering. Calcif Tissue Int 48 (6):407–413
90. Mostafa NY, Brown PW (2007) Computer simulation of stoichiometric hydroxyapatite: structure and substitutions. J Phys Chem Solid 68(3):431–437
91. de Leeuw NH, Bowe JR, Rabone JAL (2007) A computational investigation of stoichiometric and calcium-deficient oxy- and hydroxy-apatites. Faraday Discuss 134:195–214
92. Raiteri P, Gale JD (2010) Water is the key to nonclassical nucleation of amorphous calcium carbonate. J Am Chem Soc 132(49):17623–17634
93. Humphrey W, Dalke A, Schulten K (1996) VMD: visual molecular dynamics. J Mol Graph 14 (1):33–38
94. Plimpton S (1995) Fast parallel algorithms for short-range molecular dynamics. J Comput Phys 117(1):1–19
95. Paparcone R, Buehler MJ (2010) Failure of Alzheimer's Aβ(1-40) amyloid nanofibrils under compressive loading. JOM 62(4):64–68
96. Deshpande AS, Beniash E (2008) Bioinspired synthesis of mineralized collagen fibrils. Cryst Growth Des 8(8):3084–3090
97. Gautieri A, Vesentini S, Redaelli A, Buehler MJ (2012) Osteogenesis imperfecta mutations lead to local tropocollagen unfolding and disruption of H-bond network. RSC Adv 2:3890–3896

Top Curr Chem (2015) 369: 345–376
DOI: 10.1007/128_2015_640

Published online: 9 June 2015

Mechanochemistry in Polymers with Supramolecular Mechanophores

Alexander P. Haehnel, Yoshimitsu Sagara, Yoan C. Simon, and Christoph Weder

Abstract Mechanochemistry is a burgeoning field of materials science. Inspired by nature, many scientists have looked at different ways to introduce weak bonds into polymeric materials to impart them with function and in particular mechano-responsiveness. In the following sections, the incorporation of some of the weakest bonds, i.e. non-covalent bonds, into polymeric solids is being surveyed. This review covers sequentially π–π interactions, H-bonding and metal-ligand coordination bonds and tries to highlight some of the advantages and limitations of such systems, while providing some key perspective of what may come next in this tantalizing field.

Keywords Mechanochemistry • π–π interactions • H-bonding • Metal-ligand • Non-covalent • Solid polymers

Contents

A.P. Haehnel, Y. Sagara, Y.C. Simon (✉), and C. Weder (✉)
Adolphe Merkle Institute, University of Fribourg, Chemin des Verdiers 4, 1700 Fribourg, Switzerland
e-mail: yoan.simon@unifr.ch; christoph.weder@unifr.ch

1 Introduction

Touch is one of the most primal senses in living organisms and can be broadly defined as the ability to transduce a mechanical cue into an electrical signal, which in turn can be transcribed by the cerebrum [1]. Whether dealing with stretching motions, hair movement, or pressure, the detection of mechanical stimuli is based on mechanotransducing cells which are capable of generating events that eventually lead to the creation of an action potential traveling along the afferent neuron. The paradigm for cellular transduction is based on the opening of transmembrane proteins, which allow the formation of an ionic imbalance which triggers the electrical signaling. It is important to recognize the general non-covalent nature of the mechanotransduction pathways in living cells. In an attempt to emulate such pathways and bestow mechanoresponsiveness upon synthetic materials systems, researchers have begun to utilize weak bonds to impart polymers with new, mechanically triggered functionalities such as catalysis, healability, and color or pH changes [2–4]. Although many of the recently developed materials rely on mechanically responsive motifs – also referred to as mechanophores – which dissociate upon cleavage of weak covalent bonds, a subset of mechanically responsive materials has emerged based on the dissociation of assemblies formed through weak, dynamic, non-covalent interactions. The development of such materials systems is rooted in the realization that a myriad of natural processes happen through weak interactions [5, 6], such as the opening of transmembrane proteins, pre-catalytic enzyme-substrate complexes, or actin polymerization. Although some of the early work in the area of polymer mechanochemistry had largely focused on fundamental experiments often involving sonochemical processes in dilute solution [7–10], there has been a growing interest in solid materials capable of selectively transducing macroscopic mechanical forces into molecular events that trigger desirable macroscopic materials responses [2, 3, 8, 11]. Indeed, this emerging design approach has recently permitted the development of a range of adaptive solid-state polymers in which pre-programmed functions can be triggered by external stimuli, including mechanical triggers [12]. Although the general aspects of mechanochemistry with polymers have been the subject of several recent reviews and articles [13–15], this report summarizes the development of polymer mechanochemistry involving non-covalent mechanophores with pertinent examples from the recent literature. The materials are organized according to the types of non-covalent interactions exploited (π–π, metal–ligand, and hydrogen bonding). This account encompasses an extensive number of examples of molecular level experiments – mostly based on sonochemistry in solutions – and also emphasizes mechanochemical effects in solid-state materials. Because there are many examples of thixotropic gels or otherwise mechanically responsive physical gels, this chapter does not cover extensively this burgeoning field of supramolecular chemistry. However, a selection of key systems that have influenced the direction of the field is presented in relevant contexts.

2 π–π Interactions

Whether transduction is based on the scission or disassembly of covalent or non-covalent bonds, one of the perhaps most useful and most widely investigated mechanically triggered responses is a color change. The latter is an effective reporting handle that rapidly indicates the occurrence of a pre-defined mechanical transduction event. Consequently, mechanochromic materials have garnered a great deal of attention in the past decade, as they provide a one-of-a-kind solution to harness mechanical force and investigate stress transfers down to the molecular level [16]. In organic materials, colors and color changes are often introduced by utilizing (poly)aromatic molecules with unique optical properties. In such systems, π–π interactions have been shown to play a critical role in the mechanochemical transduction process, because the absorption and/or photoluminescence properties of aggregated organic or organometallic molecules are often significantly different from those of individual molecules [17, 18]. Some chromophores undergo complete quenching of photoluminescence in their aggregated states, others exhibit aggregation-induced emission, and a third group displays different photoluminescence and/or absorption colors in assembled or isolated (or monomeric) states. Different molecular origins lead to such responses as excimer formation [19, 20], charge-transfer complexes [21, 22], or exciton coupling [23], together with changes in molecular mobility [24]. Thus, it is possible to influence the photophysical properties of polymer-based materials by altering the aggregation state of embedded π-conjugated chromophores through the application of mechanical forces [25–28].

One of the first attempts to use strategically the mechanically induced disassembly of aggregated chromophores in a polymer matrix involved a family of fluorescent dyes which form (static) excimers in their aggregated states [29]. Such complexes between two identical photoluminescent (PL) molecules, one in an electronically excited and one in its ground state, were discovered by Förster and Kasper 60 years ago [30, 31]. The excimer has a lower potential energy than the separated components (i.e., a molecule in its first electronically excited state and a molecule in its ground state) and therefore excimers emit at higher wavelengths (lower energy) than the monomer species from which they are constituted (in line with the common terminology, the term ‘monomer’ is used here to describe optically active structures that involve single-molecule excited states, as opposed to excimers). In solution, excimer formation is frequently a dynamic, diffusion-controlled process [32, 33]. By contrast, diffusion of dye molecules in solid polymers is slow in comparison to the lifetime of the excited states, so that in this environment excimers predominantly arise from preformed ground-state aggregates, which may also display different absorption characteristics compared to the monomeric species [34].

Early work on the mechanically induced deformation of supramolecular assemblies of chromophores in polymer matrices was inspired by the surprising discovery that solid-state tensile deformation of blends of minute amounts of the highly

fluorescent, conjugated polymer poly(2,5-(2-ethylhexyloxy)-*p*-phenylene ethynylene) (EHO-OPPE) and ultra-high-molecular-weight poly(ethylene) not only led to uniaxial orientation of the conjugated guest molecules along the elongational axis, but also promoted the break-up of *small* aggregates comprising *a few* of these molecules into well-individualized structures (Fig. 1) [35]. This process was monitored by single-molecule spectroscopy (Fig. 2) and did not cause any noticeable color changes. Although the study did not involve well-defined supramolecular assemblies, the results paved the way for subsequent work on mechanochromic polymers comprising assemblies of aggregachromic, excimer-forming cyano-substituted oligo(*p*-phenylene vinylene)s (cyano-OPVs) (Figs. 2, 3, and 4) [36–49].

Building on the above-summarized findings, Löwe and Weder reported the first example of mechanoresponsive luminescent polymers comprising self-assembled cyano-OPVs in 2002 [37]. This chromophore family was chosen because of several attractive features, including high thermal stability, ease of color tuning through peripheral group functionalization (Fig. 3a), and a strong tendency towards excimer formation. The significant red-shift of the emission maxima (up to 140 nm) upon aggregation makes them especially interesting, because the photoluminescence color changes can be easily detected by the naked eye (Fig. 3b, c). Furthermore, cyano-OPVs are readily accessible and their solubility and aggregation behavior in

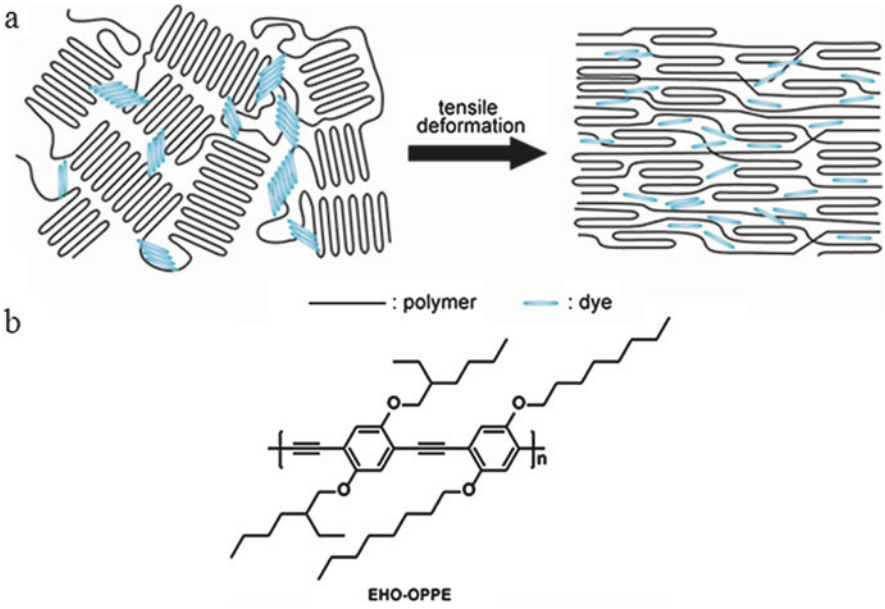

Fig. 1 (**a**) Schematic representation of the mechanically induced transformation of a disordered semicrystalline polymer comprising small aggregates of self-assembled chromophores (small-molecule or polymeric) into an oriented structure in which the guest molecules are well dispersed. (**b**) Structure of EHO-OPPE, a poly(*p*-phenylene ethynylene) derivative

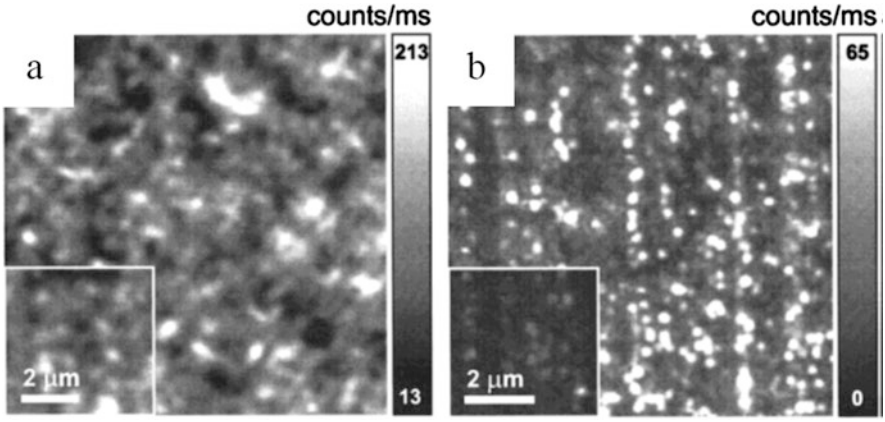

Fig. 2 Scanning confocal microscopy images of blend films of ultra-high-molecular-weight polyethylene and 10^{-4} wt% EHO-OPPE (see Fig. 1). (**a**) As prepared film. (**b**) Uniaxially deformed sample drawn to a draw ratio of 80. Both images were acquired by detecting the polarization direction oriented parallel to the (eventual) deformation direction. *Inset* shows images acquired by detecting the orthogonal polarization direction. Adapted with permission from [35]. Copyright 2000 American Chemical Society

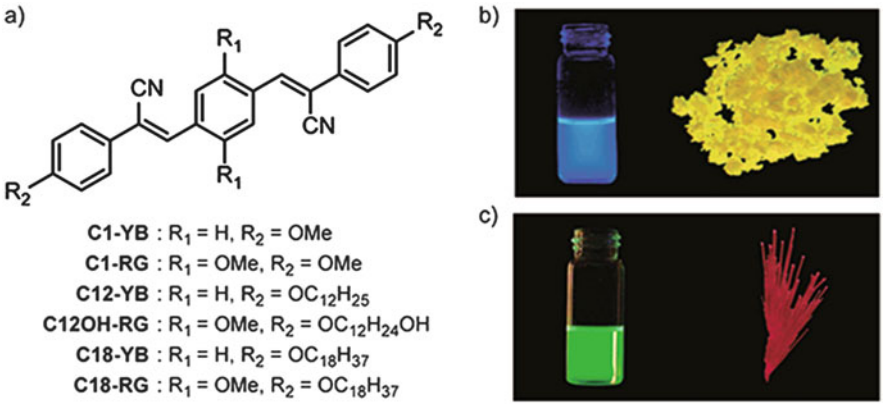

Fig. 3 (**a**) Examples of molecular structures of cyano-OPVs. (**b**, **c**) Images of **C1-YB** (**b**) and **C1-RG** (**c**) recorded under excitation with ultraviolet light in chloroform (*left*) and in the crystalline state (*right*). (**b**, **c**) reprinted with permission from [36]. Copyright 2003 American Chemical Society

different host polymers can easily be modified via the choice of the peripheral groups. The electronic properties of cyano-OPVs can be tuned over a wide range and depend on both the electron-donating or electron-accepting character of the substituents attached to the conjugated core [53, 54], as well as the nature of the supramolecular assemblies [42, 55]. For example, in **C1-RG** (red-to-green), the introduction of two alkoxy groups into the central aromatic ring reduces the

HOMO–LUMO gap compared to the **C1-YB** (yellow-to-blue) analog, resulting in a shift of the emission color in solution as well as in the crystalline state (Fig. 3). The crystal structure of **C1-RG** features a parallel arrangement of neighboring molecules, which are organized so that the electron-poor cyano-vinylene moiety of one molecule overlaps with the electron-rich central ring of its neighbor. These assemblies display excimer emission. Surprisingly, increasing the length of the peripheral alkyloxy groups in the YB series to dodecyloxy (**C12-YB**) or octadecyloxy (**C18-YB**) leads to crystal structures in which the molecules do not adopt a "staggered" array and where blue monomer emission is dominant [34]. This observation shows that π–π and aliphatic (or other) interactions in cyano-OPVs must be carefully balanced in order to achieve self-assembled structures that support excimer formation.

A guest-diffusion technique was employed to introduce **C1-YB** and **C1-RG** into linear low-density poly(ethylene) (LLDPE). Through optimization of the dyeing conditions, i.e., dye concentration, temperature, and swelling time, cyano-OPV-doped polymer films that exhibit a mechanically induced photoluminescence color change were produced. Figure 4 shows the emission spectra of a **C1-RG**-doped LLDPE film at different draw ratios. In the undrawn state, samples with sufficiently high dye content display a broad emission band with a maximum at 650 nm, characteristic of excimer emission. Emission bands with well-resolved vibronic structures at 470–570 nm are also observed, which correspond to emission from molecularly dispersed chromophores. Figure 4 shows clearly that, with increasing strain, the intensity of the excimer band decreases relative to the monomer emission bands. This relative intensity change suggests that nanoscale aggregates of **C1-RG**, which are present in the as-prepared polymer film, are converted into monomeric

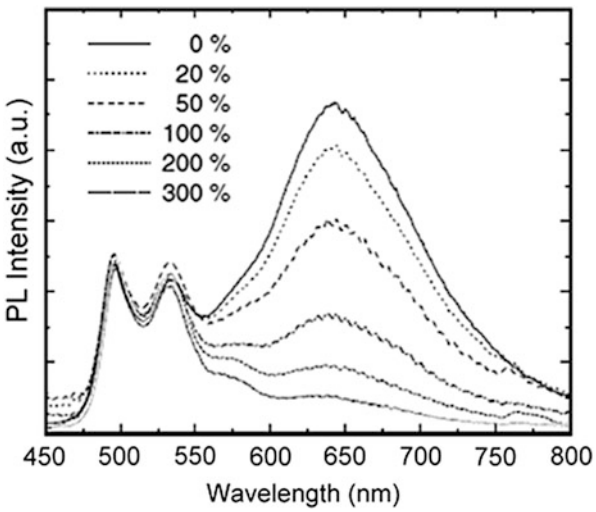

Fig. 4 Photoluminescence spectra of an LLDPE/**C1-RG** blend as function of draw ratio. Adapted with permission from [37]. Copyright 2002 Wiley-VCH

species in response to tensile deformation, as depicted in Fig. 1a. Thus, even though the functionality-imparting motifs are not covalently attached to the polymer matrix, stresses can effectively be transferred and cause the disassembly of aggregates which are presumably small and held together by weak, non-covalent forces. In the context of currently applied terminology, the cyano-OPV *stacks* should probably be referred to as the mechanophores, although it can be argued that it would be appropriate to utilize the term for the cyano-OPV motif itself. It is noted that this comment applies to many of the mechanically responsive moieties discussed in this text.

Crenshaw et al. subsequently demonstrated that mechanically responsive blends can also be produced by melt-processing LLDPE/cyano-OPV blends and presented a detailed investigation of the phase behavior of these materials.[36] To avoid large-scale phase separation, blend films were prepared by melt-mixing and compression-molding at 180°C to form thin films (choosing the dye concentration so that at this temperature thermodynamic miscibility is achieved; in case of **C1-RG**, only 0.18 wt% was used) and subsequently quenching the blends into a kinetically-trapped state. Because of the sub-ambient glass transition temperature of LLDPE, the blends are thermodynamically unstable and the dyes slowly aggregate under ambient conditions. The process was shown to span several months by monitoring the increase of the excimer emission band (Fig. 5a). The aggregation process was significantly accelerated when the blend films were immersed in hexane (Fig. 5b), which swells the LLDPE and increases the translational mobility of the guest molecules, but is a poor solvent for **C1-RG**. Mechanically responsive behavior was demonstrated for polymer blends in which the cyano-OPVs had been allowed to aggregate by either of the above-mentioned processes. The photoluminescence color of blend films comprising either **C1-RG** or **C1-YB** exhibited a

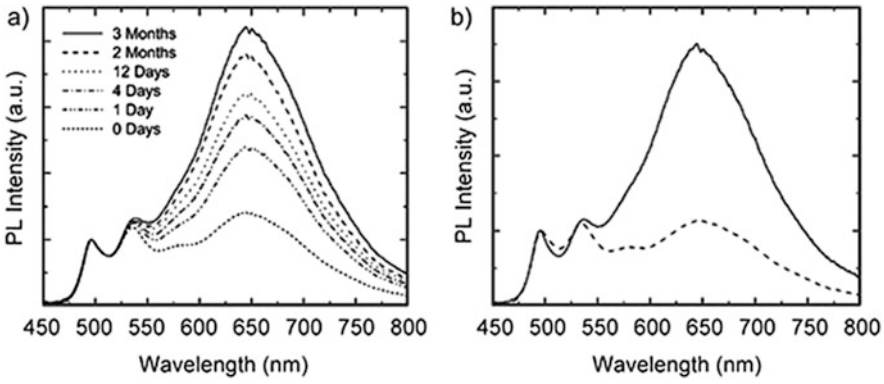

Fig. 5 (**a**) Photoluminescence spectra of a blend film of LLDPE and 0.18 wt% **C1-RG** as function of storage time under ambient conditions. (**b**) Photoluminescence spectra of a blend film of LLDPE and 0.18 wt% **C1-RG** freshly prepared (*dashed line*) and after swelling the film for 15 min in hexane and subsequent drying (*solid line*). All spectra were normalized to the intensity of the monomer peak. Adapted with permission from [36]. Copyright 2003 American Chemical Society

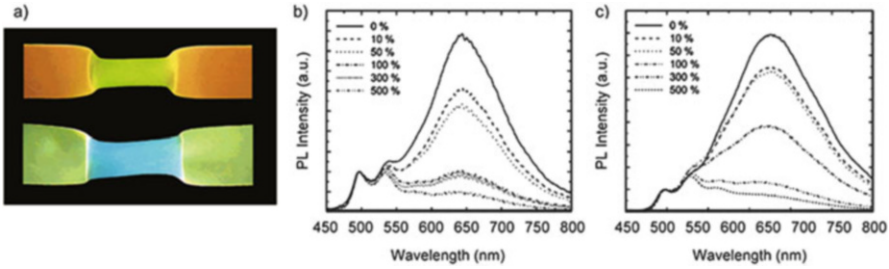

Fig. 6 (**a**) Pictures of blend films of LLDPE and 0.18 wt% **C1-RG** (*top*) and 0.20 wt% **C1-YB** (*bottom*) stretched at room temperature. The pictures were taken under excitation with ultraviolet light. (**b**, **c**) Photoluminescence spectra of blend films of LLDPE and 0.20 wt% **C1-RG** (**b**) or **C1-YB** (**c**) as a function of draw ratio. All spectra were normalized to the intensity of the monomer peak. Adapted with permission from [36]. Copyright 2003 American Chemical Society

significant change upon tensile deformation (Fig. 6a), concomitant with a substantial reduction of the relative intensity of the excimer bands (Fig. 6b, c). When LLDPE/**C1-RG** blends were slowly cooled from the melt, the formation of large dye aggregates with dimensions exceeding several micrometers was observed, which could not be mechanically dispersed, leading to materials in which no mechanochromic response was observed.

Based on the above-mentioned discovery that the size of excimer-forming aggregates matters, Crenshaw et al. subsequently investigated how substituents attached to the outer benzene rings of cyano-OPVs influence the aggregation behavior of these dyes in poly(ethylene) blends [38]. **C18-RG**, featuring octadecyloxy instead of methoxy groups in the lateral positions (Fig. 3a), was shown to nucleate much more efficiently than **C1-RG**. The comparably inefficient nucleation of **C1-RG** appears to limit the number of dye aggregates formed, which results in the slow growth of larger aggregates. Smaller dye aggregates of **C18-RG** in LLDPE film are more easily dispersed during tensile deformation, leading to a more substantial photoluminescence color change compared to their **C1-RG** analogs. However, it appears that in the case of **C18-RG** a semicrystalline matrix is also required or is at least beneficial to nucleate dye crystal growth. Other effects on the mechanoresponsive luminescence properties, i.e., the ability of the polymer host to transfer stress and break up the chromophore aggregates upon deformation, have also been investigated, such as matrix crystallinity or polarity. In poly(ethylene) with higher crystallinity, dye aggregates are more easily disassembled than in poly (ethylene) with lower crystallinity. The ability of the polymer host to break up dye aggregates upon deformation, and thus the extent of color change observed upon deformation, is related to the plastic deformation process of PE crystallites – specifically those arranged in a lamellar morphology – and increases with increasing polymer crystallinity, decreasing dye aggregate size, and decreasing rates of deformation. The color-strain traces (where color was expressed by the ratio of monomer to excimer emission intensity, I_M/I_E) of PE/**C18-RG** blends all mirror the stress–strain profiles. In these cases, I_M/I_E increases steeply upon yielding, grows

moderately during neck propagation, and displays a slightly steeper increase during strain hardening. Beyond poly(ethylene)s, the Weder group has used poly(ethylene terephthalate) [39] and a semicrystalline fluoropolymer [40] as host matrices to create mechanochromic materials based on cyano-OPVs.

Reversible, mechanically induced dissociation of cyano-OPVs has been achieved in thermoplastic elastomers in which the chromophores were covalently incorporated into the polymer backbones [41]. Although chromophore aggregation and disassembly in these materials are intermolecular processes, the design is reminiscent of more recently developed mechanoresponsive polymers with built-in "mechanophores", i.e., weak links designed to break upon application of a load to the polymer chain. Several elastomers were prepared and the hard segment to soft segment ratio and the dye content were systematically varied. Upon deformation, all compression-molded, quenched polymer films containing **C12OH-RG** showed a combination of monomer and excimer emission. In the best compositions, the prepared polyurethane exhibited a pronounced change of the photoluminescence color from an orange-red, excimer-dominated emission to green fluorescence characteristic of molecularly dispersed chromophores (Fig. 7a, b). In situ opto-mechanical studies, in which samples were exposed to a cyclic triangular strain pattern, demonstrated that the fluorescence color change nicely mirrored the reversible stress–strain response of the polymer (Fig. 7c).

Although the property of interest in all of the above-mentioned cyano-OPV-containing materials was a mechanically induced change of the photoluminescence color (i.e., a mechanically induced transformation from an excimer-rich to a monomer-dominated emission), certain cyano-OPVs also display a changed of their absorption color upon (dis)assembly. Thus, Kunzelman et al. reported mechanochromic blend films based on **C18-RG** and either poly(ethylene

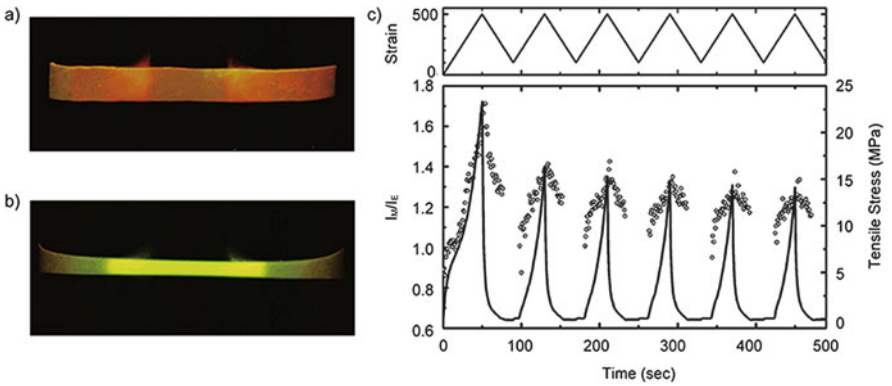

Fig. 7 (**a**) Picture of a mechanochromic elastomer made by integrating **C12OH-RG** into a thermoplastic polyurethane backbone in the unstretched state. (**b**) Picture of the same material in the stretched state. Both pictures were taken under illumination with ultraviolet light. (**c**) Ratio of monomer to excimer emission I_M/I_E (*circles*) and tensile stress (*solid line*) under a triangular strain cycle between 0% and 500% at a frequency of 0.0125 Hz. Adapted with permission from [41]. Copyright 2006 American Chemical Society

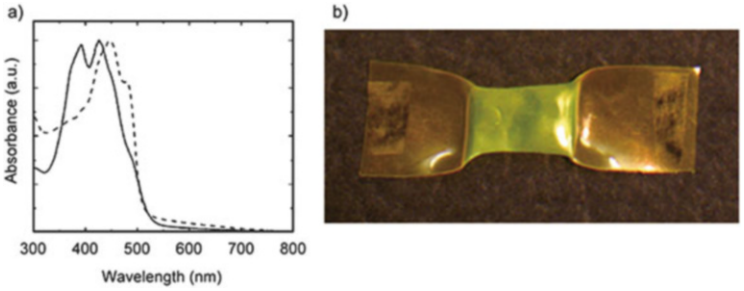

Fig. 8 (**a**) Normalized absorption spectra of a 0.5 wt% LLDPE/**C18-RG** blend film before (*solid line*) and after (*dashed line*) stretching at room temperature to a draw ratio of ca. 300%. (**b**) Picture of the same material in which the center portion has been uniaxially deformed. The image was taken under ambient illumination. Adapted with permission from [42]. Copyright 2006 Wiley-VCH

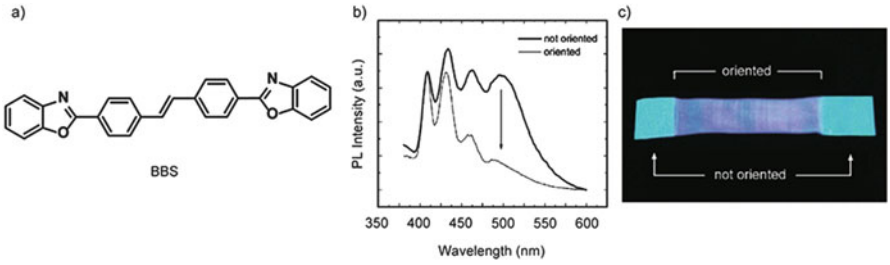

Fig. 9 (**a**) Molecular structure of bis(benzoxazolyl)stilbene (BBS). (**b**) Fluorescence spectra of a PP/BBS blend film containing 0.5 wt% of BBS before and after tensile deformation (**c**) Picture of the same material in which the center portion was uniaxially deformed. The image was taken under excitation with ultraviolet light. (**b**, **c**) adapted with permission from [50]. Copyright 2005 Wiley-VCH

terephthalate glycol) (PETG) [43] or LLDPE [42]. Figure 8 shows how the absorption spectrum (Fig. 8a) and visual appearance (Fig. 8b) of an LLDPE/**C18-RG** blend film change in response to solid-state tensile deformation. The spectral shift indicates that small dye aggregates are molecularly dispersed upon elongation. Similar changes in absorption have also been reported for PETG-based polymer films in which a cyano-OPV dye was covalently introduced into the polymer chain [43].

Beyond cyano-OPVs, several other dyes that form excimers in their aggregated state have also been used for mechanosensing purposes. Pucci and coworkers have reported that poly(propylene) (PP) films containing bis(benzoxazolyl)stilbene (BBS) (Fig. 9a) change photoluminescence color upon tensile deformation [50]. In the as-prepared state, the emission spectrum (Fig. 9b) shows a broad excimer emission band around 500 nm, along with sharper monomer emission bands at 410, 430, and 455 nm. Mechanical deformation lowers the intensity of the excimer band, resulting in a photoluminescence color change (Fig. 9c).

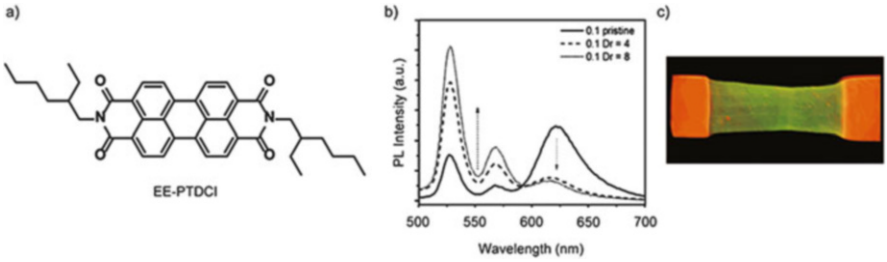

Fig. 10 (**a**) Molecular structure of *N*,*N*′-bis-(2′-ethylhexyl)perylene-3,4,9,10-tetracarboxyldiimide (EE-PTCDI). (**b**) Fluorescence spectra of a LLDPE/EE-PTCDI blend film containing 0.1 wt% EE-PTCDI before and after uniaxial deformation to different draw ratios (Dr). (**c**) Picture of the same material in which the center portion has been uniaxially deformed to a draw-ratio of 4. The image was taken under excitation with ultraviolet light. (**b**, **c**) adapted with permission from [52]. Copyright 2008 American Chemical Society

Mechanosensing behavior of blend films of poly(1,4-butylene succinate) and BBS have also been studied by the same group [51].

Pucci and coworkers have also reported LLDPE-based films containing perylene bisimide derivatives [52], which have been intensively examined because of their attractive optoelectronic character and propensity to assemble into supramolecular architectures. Blend films comprising *N*,*N*′-bis-(2′-ethylhexyl)perylene-3,4,9,10-tetracarboxyldiimide (EE-PTCDI) in LLDPE were obtained by melt-mixing procedures and blend films with 0.1 wt% of the dye exhibited mechanoresponsive behavior as shown in Fig. 10. The intensity of the emission band around 620 nm, which is ascribed to emission from EE-PTCDI aggregates, decreased drastically after drawing, indicating that the perylene compound became molecularly dispersed. The transition dipole moment of EE-PTCDI was also shown to align along the direction of drawing.

Most of the materials systems described above are based on blends of conventional dyes to which small amounts of self-assembling polymers were added. Another promising approach to mechanoluminescent polymeric materials is the covalent attachment of mechanoresponsive luminescent molecular assemblies on the surface of polymers. Sagara et al. have recently reported poly(lactic acid) (PLA) beads that feature mechanoresponsive luminescent micelles on their surface (Fig. 11) [56]. The latter consist of 1,6-disubstituted pyrene derivative **Py1** (Fig. 12), and were attached to the surface of the PLA beads through covalent bonds. Compound **Py1** self-assembles in aqueous conditions to form micelles, on account of its amphiphilic nature. Upon application of a sufficiently large mechanical forces to the micelles (in aqueous conditions), their photoluminescence color changes from yellow to green. The yellow emission is ascribed to excimer formation of the luminescent core of **Py1**. Using the amino groups introduced in the peripheral positions of the dendrons, the resulting micelles could be covalently attached to a variety of surfaces that had also been decorated with amine groups using the amine-reactive crosslinker **L2** (Fig. 12). Thus, the authors succeeded in

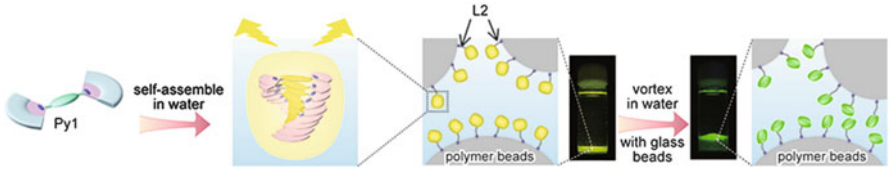

Fig. 11 Schematic illustration of polylactic acid (PLA) beads with mechanoresponsive luminescent micelles on the surface and change of their photoluminescent color upon application of a mechanical force. The pictures were taken under excitation with ultraviolet light. Adapted with permission from [56]. Copyright 2014 American Chemical Society

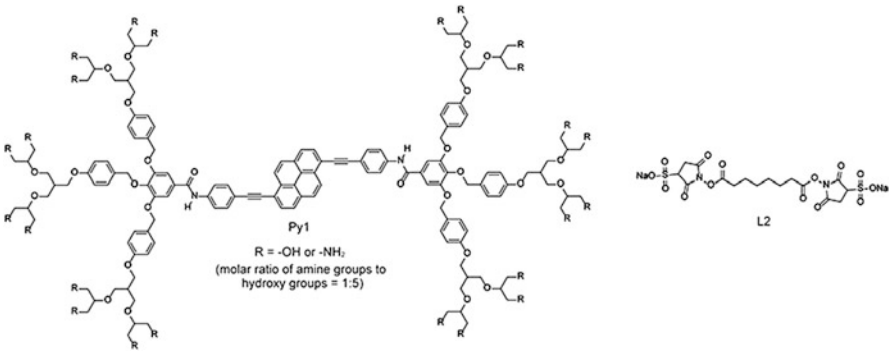

Fig. 12 Molecular structure of pyrene-based amphiphile **Py1** and water-soluble cross-linker **L2**

attaching the micelles to PLA beads ($\Phi = 70-150$ μm) with amino groups on their surfaces, which was confirmed by confocal fluorescence microscopy. Mechanical stimulation was applied by vortexing the glass vial containing water and the micelle-decorated PLA beads. A photoluminescent color change could easily be observed by the naked eye when the PLA beads with the mechanoresponsive micelles were vortexed in the presence of glass beads, which are heavier than PLA beads. By contrast, no obvious change in emission spectra was observed when micelle-bearing PLA beads were vortexed in the absence of said glass beads. The mechanoresponsive luminescent PLA beads seem to have a threshold below which no photoluminescence color change occurs. This threshold behavior stems from the uniform size of the micelles consisting of **Py1**. In contrast to polymer blends comprising mechanosensing dyes, no elongation or contraction of the polymer beads themselves is required to induce a change in photoluminescence color.

Mechanically responsive π–π interactions have also been utilized in supramolecular polymers, where π–π stacking between electronically complementary (i.e., electron-rich and electron-poor) π-conjugated groups has been utilized to achieve supramolecular polymerization [57–60]. For example, pairs of naphthalene diimide groups that were introduced into the backbone and termini of polymer **P1** (Fig. 13) bind to pyrene moieties that were introduced to both ends of polymer **P2**.

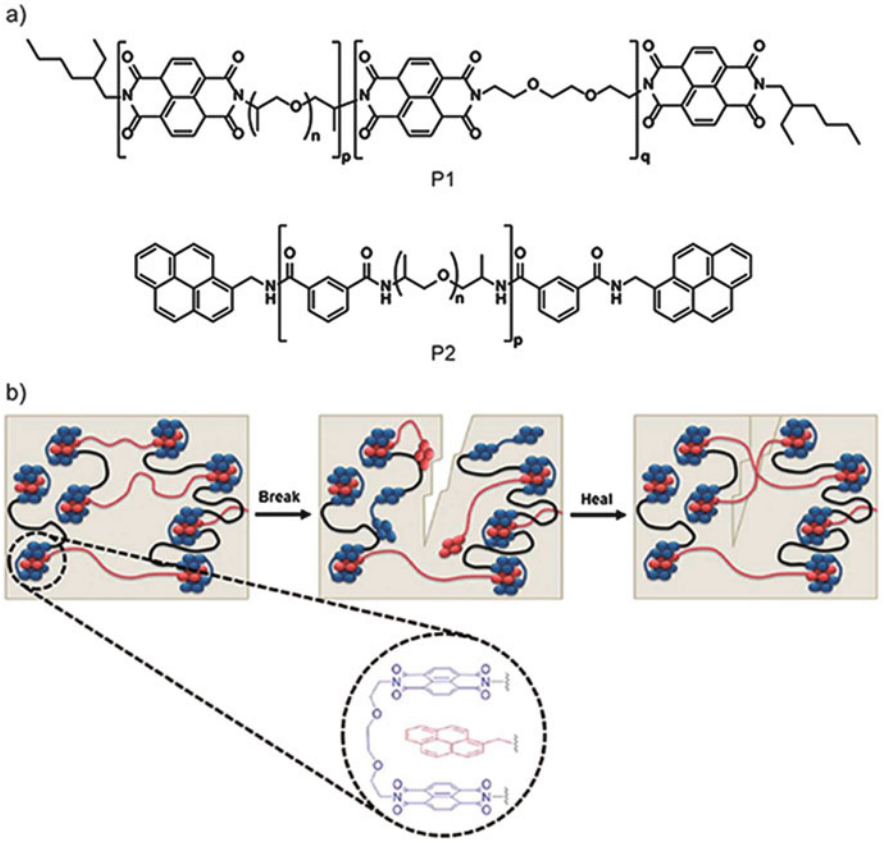

Fig. 13 (**a**) Molecular structures of **P1** and **P2**, building blocks used to assemble a healable mechanochromic supramolecular polymer. (**b**) Schematic illustration of the healable supramolecular polymers using donor–acceptor interactions between **P1** and **P2**. (**b**) reprinted with permission from [60]. Copyright 2014 The Royal Society of Chemistry

Combination of **P1** and **P2** leads to the formation of a supramolecular network structure, in which cross-links are based on intermolecular interactions between electron donor and acceptor groups [58]. The formation of donor-acceptor stacked structures is not only evidenced through the material's mechanical properties, but can also be inferred from the appearance of a characteristic reddish color, which arises from the naphthalene diimide/pyrene charge transfer interactions. The materials system at hand was designed to be healable after being damaged. Indeed, after breaking samples of the **P1/P2** mixture, the defect could be healed and the tensile modulus could be completely restored by heating for 5 min to 50°C. The observed healing efficiency was maintained over several cycles of breaking and heating. Therefore, the π–π stacking moieties composed of donor and acceptor groups are regarded as reversible units in polymeric materials. Although the authors did not exploit this color change for mechanochemical purposes, one can easily foresee that

such systems would be prone to color change upon mechanochemical activation and that adequately connected charge-transfer complexes in general should yield similar mechanochromic behavior.

3 Hydrogen Bonds

This section focuses on supramolecular polymers based on complementary hydrogen-bonding motifs that exhibit association-dissociation in response to mechanical stimuli. Hydrogen bonds are one of the most commonly utilized types of intermolecular interaction in the fabrication of supramolecular polymers because of their directional character and ideal strength [61–64]. Furthermore, the associative character of a given supramolecular motif can be fine-tuned by controlling the number of hydrogen-bonding sites. The inherent reversible nature of hydrogen bonds bestows supramolecular polymers made from such motifs with adaptive characters such as thermo-, photo-, chemo-, and mechanoresponsive properties [61–66]. In the last 15 years, a large number of hydrogen-bonding supramolecular polymers have been investigated [67, 68]. Interestingly, however, only a few reports have described mechanically active hydrogen bonds in supramolecular polymers with unambiguous experimental evidence that shows dissociation and formation of hydrogen bonds in response to mechanical stimulation [69–72].

Some of the most compelling examples of mechanoactive hydrogen bonds in polymers have been inspired by the natural protein titin [69]. Titin is a giant protein of muscle sarcomeres and has 200–300 repeating modules which are unfolded sequentially when a mechanical force is applied (Fig. 14a), leading to a saw-tooth pattern in the force-extension curve. Each peak is ascribed to individual unfolding events of the repeating modules and reflects the constant force required to unfold each of them. Using a biomimetic design, a modular polymer with multiple loops (Fig. 14b) was developed by the Guan group. Module polymer **P3-1** featuring the

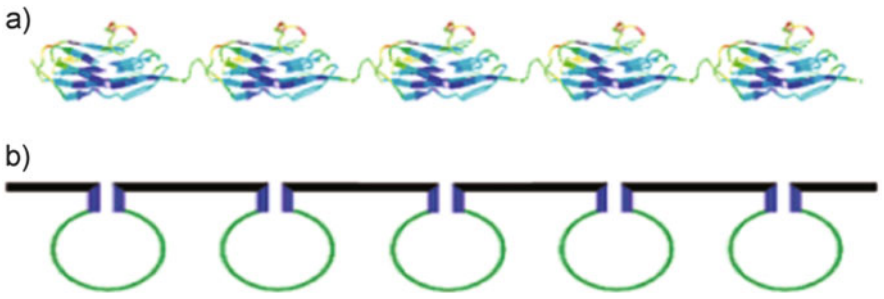

Fig. 14 Concept of biomimetic modular polymer design. (**a**) A small section of titin, which has 200–300 repeating immunoglobulin domains. (**b**) Design of modular polymer containing multiple loops held by secondary forces. Reprinted with permission from [69]. Copyright 2004 American Chemical Society

quadruple-hydrogen-bonding motif 2-ureido-4[1*H*]-pyrimidinone (**UPy**) was prepared using pre-polymer **3-1** and free **UPy** monomer **3-2** (Fig. 15). Control polymer **P3-2** was also synthesized using pre-polymer **3-1** and protected **UPy** monomer **3-3**. Single-molecule force-extension studies using atomic force microscopy were carried out for both modular polymer **P3-1** and control polymer **P3-2**. A distinct saw-tooth pattern appeared in the force-extension curve for modular polymer **P3-1** (Fig. 16a), whereas the force-extension curves for control polymer **P3-2** did not show the saw-tooth character. Instead, only one peak was observed, which is

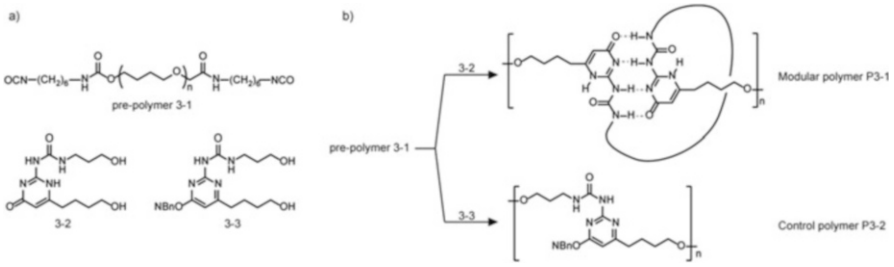

Fig. 15 (**a**) Molecular structures of pre-polymer **3-1**, free UPy monomer **3-2**, and protected UPy monomer **3-3**. (**b**) Scheme illustrating the synthesis of **P3-1** and **P3-2**

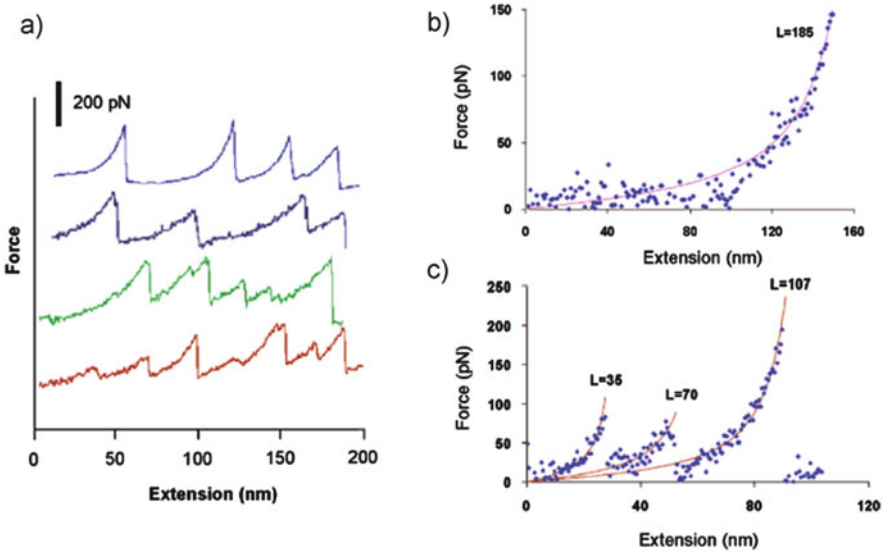

Fig. 16 AFM single chain force-extension data. Both the modular polymer **P3-1** and the control polymer **P3-2** were subjected to single-chain force-extension studies in toluene. (**a**) An overlay of several force-extension curves for modular polymer **P3-1**. (**b**) One representative single chain force-extension curve for the control polymer **P3-2**. (**c**) A typical single-chain force-extension curve for the modular polymer **P3-1**. In (**b**) and (**c**), all *scattered dots* represent experimental data and the *solid lines* are fitting results. Reprinted with permission from [69]. Copyright 2004 American Chemical Society

typical for the entropic extension of a random coil chain. These observations indicate that sequential unfolding of **UPy** dimers in the modular polymer **P3-1** occurs along the polymer chain during single-molecule force-extension studies. When the modular polymer chain is gently pulled, the force increases until the **UPy** dimers can no longer withstand the load. As a result, the quadruple hydrogen bonding between two **UPy** moieties yields and the loop opens, extending the chain length of the modular polymer. Therefore, the peak force shown in Fig. 16 represents the force required to disassemble the **UPy** dimers, and the gaps between two peaks are characteristic of the unfolding of the extra slack provided by the loop following dimer dissociation. Because the **UPy** dimers can be connected in different ways during the synthesis, the force needed to deform the dimer varied between ca. 200 pN for the preferred head-to-head arrangement vs ca.100 pN for the less favorable head-to-tail or tail-to-tail connectivity. Additionally, the force-extension curve showed different length between force peaks because of the chain length distribution of the pre-polymer **3-1**.

To overcome several limitations of the modular polymer **P3-1** (e.g., interchain interactions), a newly designed monomer **3-4** which forms quadruple hydrogen bonds was subsequently prepared by Guan and coworkers using peptidomimetic β-sheet motif (Fig. 17a) [70]. Two loops were used to promote proper intrachain dimerization, thereby limiting dimerization with a nonadjacent unit within the same polymer or with units in different polymer chains. Alkyl chains were used as the loop-forming unit in lieu of polydisperse poly(tetramethyleneoxide), which led to constant gaps between force peaks in the force-extension curve. The double-closed loop (DCL) polymer **P3-3** (Fig. 17b) was obtained by reacting equimolar amounts of 4,4′-methylenebis-(phenyl-isocyanate) (MDI) and the DCL monomer. Single-molecule force-extension studies using atomic force microscopy were also carried out for the DCL polymer (Fig. 18). Compared to the modular polymer **P3-1**, the saw-tooth pattern showed greater uniformity. The force required to break each module was, however, smaller (~50 pN), which was explained by the smaller dimerization constant of the peptidomimetic β-sheet units (~10^4) compared to that of UPy dimers (~10^7). Despite the increased uniformity, a distribution of the contour length (ΔL) between consecutive peaks in the force-extension curves was observed ($\Delta L \approx 5$–21 nm). This phenomenon was thought to arise from π–π stacking

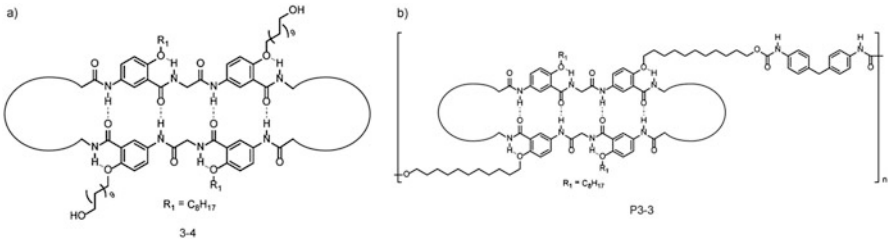

Fig. 17 Molecular structures of (**a**) double-closed loop monomer **3–4** and (**b**) the resulting polymer **P3-3**

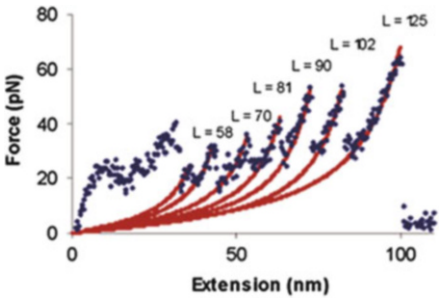

Fig. 18 AFM single-molecule force-extension curves for the DCL modular polymer shown in Fig. 17b. Reprinted with permission from [70]. Copyright 2004 American Chemical Society

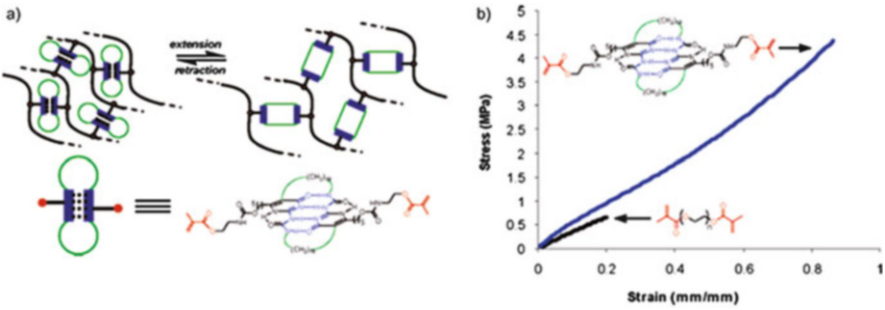

Fig. 19 (**a**) Schematic representation of the design of a biomimetic modular cross-linker. (**b**) Stress–strain curves for 6% cross-linked poly(*n*-butyl acrylate) rubber for the sample (*blue*) and control specimen (strain rate: 100 mm/min at room temperature). Reprinted with permission from [71]. Copyright 2007 American Chemical Society

between dimerizing units. The association energy between two dimerizing modules is comparable to that of the four hydrogen bonds in each dimerizing module. Therefore, during the polymer extension, the four hydrogen bonds in each module as well as π–π stacking between modules dissociate simultaneously.

Taking into account the knowledge obtained from both modular systems, Guan and coworkers prepared UPy-based cross-linker **3–5** having two alkyl chain loops (Fig. 19a) in the module unit [71]. The authors expected that the mechanical properties of the resulting cross-linked polymers would be significantly enhanced because of the reversible nature of the UPy-based module and strength of quadruple hydrogen bonds in each module. Cross-linked poly(*n*-butyl acrylate) was chosen as the backbone because of its elastomeric character. Poly(ethylene glycol) dimethacrylate was chosen as the control cross-linker. Several films were prepared by copolymerization of *n*-butyl acrylate and cross-linker **3–5** or poly(ethylene glycol) dimethacrylate. Figure 19b shows the stress–strain curves for samples cross-linked with 6 mol% of either the cross-linker **3–5** or the poly(ethylene glycol) dimethacrylate control. Upon cross-linking with **3–5**, both modulus and tensile strength substantially increased without sacrificing the maximum extensibility. By contrast, the covalently cross-linked control suffered from a much smaller strain

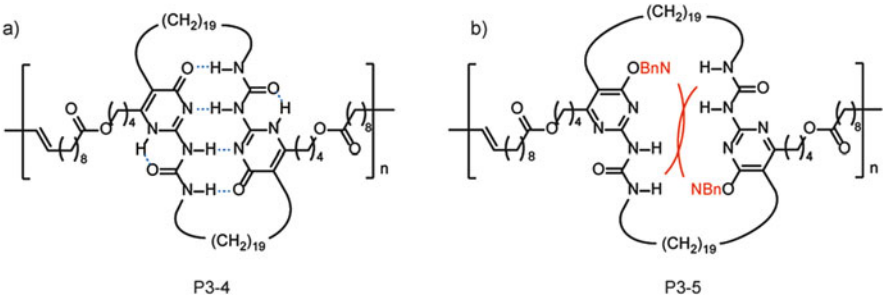

Fig. 20 Molecular structure of (**a**) linear double-closed loop module polymer **P3-4** and (**b**) control polymer **P3-5**

at break. The striking difference between the two materials was attributed to the increased energy dissipation ability of cross-linker **3–5**.

The same group also developed linear polymer **P3-4** using UPy-based double closed-loop modules (Fig. 20) [72]. To avoid undesired hydrogen-bonding and prevent complicated folding structures, the polymer did not possess any hydrogen-bonding sites other than the UPy moieties in each module. Linear module polymer **P3-4** and control polymer **P3-5** were obtained by acyclic diene metathesis using corresponding monomers. In control polymer **P3-5**, an *o*-nitrobenzyl (NBn) protection group was introduced to suppress hydrogen-bond formation in each module. As shown in Fig. 20a, the stress–strain curves of **P3-4** and **P3-5** are completely different from each other. Control polymer **P3-5** fractures at 7% strain. By contrast, modular polymer **P3-4** exhibited large deformation with a maximal strain of >100%. At low strains, **P3-4** is quite stiff and showed a relative high Young's modulus. After 5% elongation, **P3-4** exhibited a large deformation with modest increase in stress, which means that a large amount of energy is absorbed as a result of the sequential unfolding of UPy-based modules upon stretching.

The shape-memory properties of the linear polymer **P3-4** and its mechanical behavior have also been investigated in a later study. After ten loading-unloading cycles, the polymer was set at 135% of its original length. By leaving this sample at room temperature for 18 h, **P3-4** recovered up to 110% of its original length (Fig. 21). The complete recovery of original mechanical properties of **P3-4** was achieved by heating the sample at ~ 80°C for ~30 s after loading-unloading cycles. Moreover, when the sample was heated and elongated to 250% strain and then cooled to 5°C, the temporary shape was fixed. A gradual temperature increase led to sample retraction and further heating resulted in complete shape recovery of **P3-4** film. The observed stress–strain responses and the shape-memory characters of **P3-4** are derived from the dynamic nature of UPy dimerization, as further corroborated by the absence of similar properties for control polymer **P3-5**. The mechanism to explain the observed phenomena is illustrated by the authors (Fig. 21). UPy homodimers are unfolded upon mechanical or thermal stimulation. When the stimulus is removed, UPy interchain cross-dimers form in the polymer films. Subsequent heating induces recombination of UPy moieties and leads to the recovery of the original shape and mechanical properties.

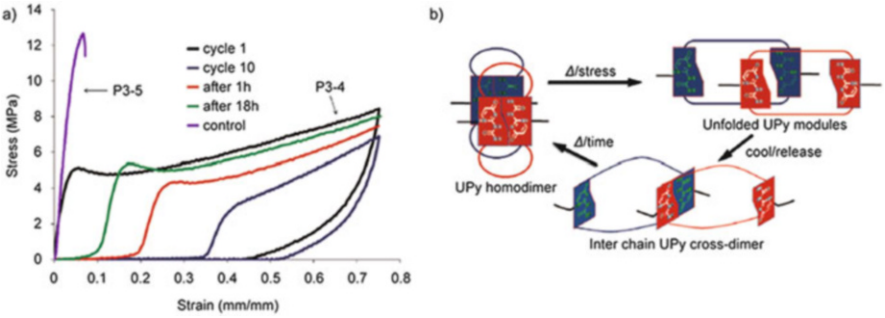

Fig. 21 (**a**) Stress–strain curves for polymer **P3-4** and control **P3-5** shown in Fig. 20. (**b**) Proposed molecular mechanism for shape-memory behavior. Adapted with permission from [72]. Copyright 2009 American Chemical Society

4 Metal–Ligand Interactions

Metal–ligand interactions represent another class of non-covalent supramolecular motifs, which have been shown to be very useful in the context of designing stimuli-responsive supramolecular polymers. The motif type represents great versatility, as the strength of the interaction between a polymer-bound ligand and metal ions, the responsiveness to various stimuli, and the response can be varied over a broad range via the variation of both metal ion and ligand. A major advantage of metallo-supramolecular polymers is the possibility of combining the processability of polymers, at the same time retaining some of the unique properties of the metal centers. In 2003, a seminal contribution of Rowan and coworkers introduced "multistimuli, multiresponsive metallo-supramolecular polymers" [73]. The material introduced by the Rowan group consisted of a poly(ethylene glycol) (PEG) backbone which was functionalized at both ends with a bis(2,6-bis(1′-methylbenzimidazolyl)-4-hydroxypyridine) ligand (Mebip; Fig. 22). Such building blocks can be used to construct longer polymer chains by adding various metal ions in the form of weakly coordinating salts, such as nitrates, perchlorates, or bistriflimides. Chain extension is achieved by stoichiometric complexation of the metal by the polymer-bound ligands. Of course, the nature of the metal ion plays a pivotal role in the overall molecular architecture of the materials. In the most common case, i.e., where ditopic polymeric ligands are used, the metal center determines whether linear connections (as in the case of bivalent ions) or branching/network points are formed (as in the case of trivalent ions), because they are coordinated by two or three telechelic ligands. Many properties of the resulting material can be adjusted by carefully choosing the metal ion. For instance, luminescent europium ions may be used as an internal probe indicating the status of the metal–ligand bond, because they exhibit luminescence through an "antenna effect," i.e., the energy initially absorbed by the ligand is channeled to the metal through a metal-to-ligand charge transfer [74, 75].

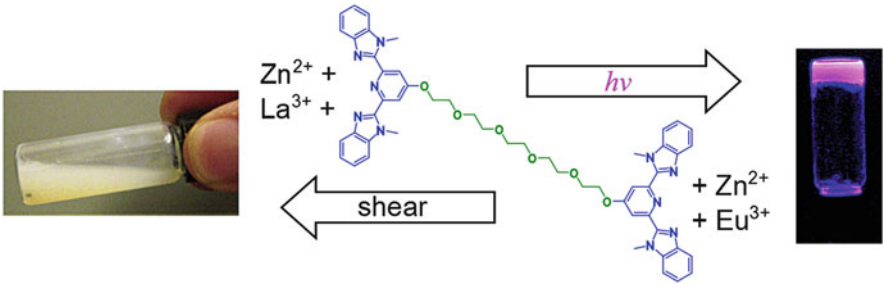

Fig. 22 Illustration of chemical structure, mechanical response, and optical characteristics of multi-stimuli responsive metallo-supramolecular polymers. Adapted with permission from [73]. Copyright 2003 American Chemical Society

Although metallo-supramolecular polymers had been previously studied [76], the work of Beck et al. opened new avenues by demonstrating that metal–ligand bonds could be mechanically activated [73], although the materials studied were gels, and thus not, strictly speaking, solid materials because of the presence of solvent (here acetonitrile). The mechanical activation of weak coordination bonds was demonstrated in metallo-supramolecular gels containing the telechelic building block shown in Fig. 22 and Zn^{2+}:La^{3+} (ratio 97:3) through the characteristic thixotropic (shear-thinning) behavior of the gels. Upon manual agitation, stable gels were rapidly liquefied as a result of the disengagement of the ligands from the metal ions. When the system was allowed to rest, stable gels were reformed. The behavior was shown to depend upon the amount of solvent present. Furthermore, thermal stimuli-responsiveness was demonstrated, and lanthanide ions were shown to separate from the ligands more easily than transition metal ions. Additionally, responsiveness to chemical stimuli, such as a competing ligand (i.e., formate anion, which binds preferentially to the Eu^{3+} ions in comparison to the Mebip ligands), was also demonstrated. On account of the supramolecular nature of the binding motifs, all stimuli, i.e., mechanical, thermal, and, chemical, could be used to dissociate reversibly the metallopolymers studied.

A broad range of stimuli-responsive metallopolymers based on Mebip-terminated macromonomer–metal ion interactions has in the meantime been investigated, not only with respect to the mechanical activation of the weak links, but also in terms of kinetic formation of the metal–ligand complex [77], influence of the metal centers (dynamic vs inert, two- vs three functional, and variation of optical properties), and the polymers (e.g., polar vs nonpolar, rubbery vs glassy vs semi-crystalline). It is noted that in solid materials the morphology has a great influence on the mechanical properties and the underlying stress-transfer processes of these materials [78]. Although mechanically induced disassembly of the metal–ligand motifs has in some cases been inferred, this process has rarely been experimentally supported. For example, the groups of Weder and Rowan demonstrated that optical healing can be achieved in metallo-supramolecular polymers assembled from a rubbery telechelic poly(ethylene-*co*-butylene) (**15**) that was chain-terminated with

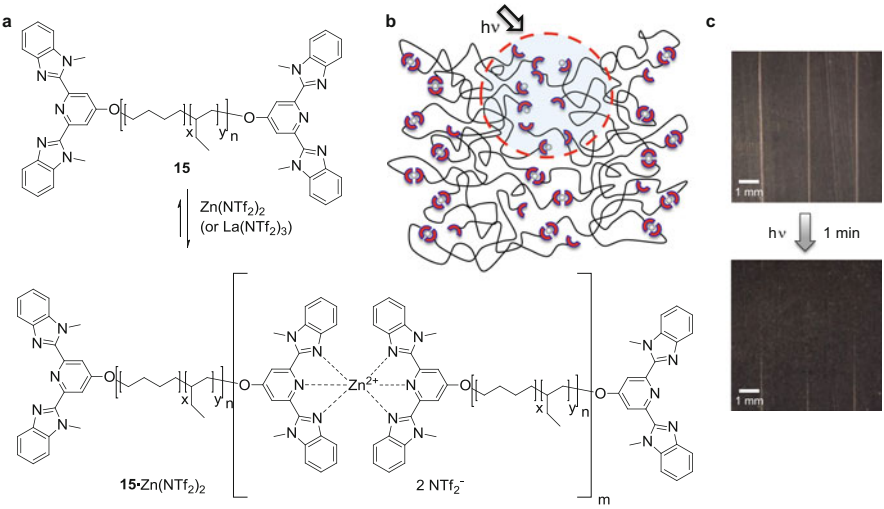

Fig. 23 (**a**) Chemical structure of macromonomer **15** and the metallo-supramolecular polymers **15**·[$M(NTf_2)_v$] where M=Zn^{2+} ($v=2$) or M=La^{3+} ($v=3$). (**b**) Schematic representation of the lamellar structure of **15**·[$M(NTf_2)_v$]. (**c**) Image illustrating the optical healing of a film of **15**·[$Zn(NTf_2)_2$] (ratio of **15**:$Zn(NTf_2)_2 = 1{:}0.7$) with UV light ($\lambda = 320$–390 nm, 950 mW/cm^2, 2×30 s). Figures are adapted from [79]

2,6-bis(1′-methylbenzimidazolyl)-pyridine (Mebip) ligands and $Zn(NTf_2)_2$ or $La(NTf_2)_3$ to afford **15**·$Zn(NTf_2)_2$ and **15**·$La(NTf_2)_3$ (Fig. 23) [79]. The metal–ligand binding is dynamic (more so in the case of La^{3+} than Zn^{2+}) and the polymers can be depolymerized upon exposure to certain external stimuli such as light, heat, and presumably mechanical forces. Small-angle X-ray diffraction experiments and electron microscopy revealed that these metallo-supramolecular materials microphase separate into lamellar structures, in which the metal–ligand complexes form a "hard" phase, which serves to crosslink physically the "soft" phase formed by the poly(ethylene-*co*-butylene) cores. The Mebip ligands and Mebip/metal complexes absorb ultraviolet (UV) light and exhibit a low fluorescence quantum yield. Thus, when the materials are irradiated with UV light, the absorbed energy is converted to heat. This results in the temporary disengagement of the metal complexes, or, in other words, depolymerization of the metallopolymer and formation of a low-viscosity melt. Upon removal of the light source, the metal–ligand complexes reform and the material's original properties are restored. This transformation allows for optical healing of (mechanically induced) damaged areas of the material. When deliberately damaged films of **15**·$Zn(NTf_2)_2$ or **15**·$La(NTf_2)_3$ were exposed to UV light with an intensity of ~950 mW/cm^2, the defects were repaired in less than 1 min. Mechanical analysis showed that the original mechanical properties of the materials could be fully restored and it was shown that the materials can be repeatedly damaged and healed. It was shown that, under comparable conditions, films of **15**·[$La(NTf_2)_3$] healed more readily than films made from **15**·[$Zn(NTf_2)_2$], consistent with the lower stability of La^{3+}/Mebip complexes vis-à-vis the Zn^{2+}/

Mebip-based counterparts and a higher level of light-induced depolymerization of the former. The concept of photothermally induced healing of supramolecular materials is applicable to any supramolecular polymer with a sufficiently dynamic binding motif and the concept has now been utilized in a variety of materials systems [80–82].

The repeated healability of the metallo-supramolecular polymers discussed above implies that, on the molecular level, mechanical damage exclusively causes (reversible) disassembly of the metal–ligand motifs, as shown schematically in Fig. 23, and not cleavage of covalent bonds. However, until recently, this mechanism had not been confirmed. With the objective of probing the mechanistic aspects of mechanotransduction in such materials, the Weder group recently embarked on the investigation of mechanically-induced responses of metallo-supramolecular networks. Their study showed that metallo-supramolecular polymers based on macromonomer **5** (a telechelic poly(ethylene-*co*-butylene) with Mebip ligands at the termini) and the europium salt $Eu(ClO_4)_3$ (Fig. 24a) are mechanoresponsive [83, 84]. The Eu^{3+}:Mebip complexes serve both as mechanically responsive binding motifs and built-in optical probes that can monitor the extent of (dis)assembly

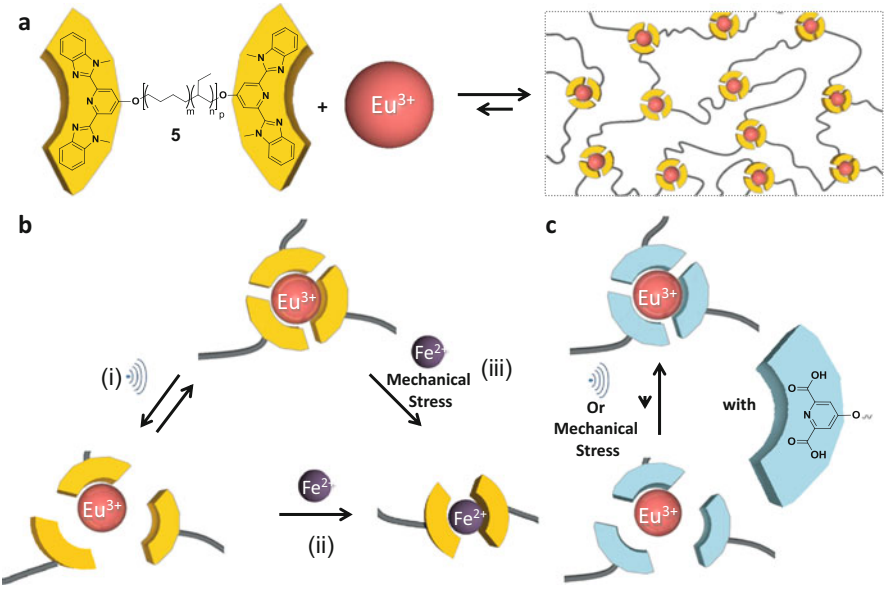

Fig. 24 Structure of a mechanoresponsive metallo-supramolecular polymer network and schematic representation of (dis)assembly mechanisms. (**a**) Formation of $(\mathbf{5})_{1.5}\cdot[\mathbf{Eu(ClO_4)_3}]$ networks by assembly of **5** and $Eu(ClO_4)_3\cdot 6H_2O$ (ClO_4^- counterions are omitted for clarity). (**b**) (i) Reversible dissociation of the Eu^{3+}-ligand complexes upon ultrasonication and irreversible exchange with Fe^{2+} ions in films of $(\mathbf{5})_{1.5}\cdot[\mathbf{Eu(ClO_4)_3}]$ soaked in a $Fe(ClO_4)_2$ solution as a result of (ii) ultrasonication or (iii) other mechanical forces. (**c**) Deprotonated dipicolinic acid ligands bind strongly to Eu^{3+} and these complexes can hardly be mechanically dissociated (triethylammonium ions are omitted for clarity). Reprinted with permission from [83]. Copyright 2014 American Chemical Society

because of their characteristic photoluminescent properties. Dose-dependent and reversible metal–ligand dissociation occurs upon exposure to ultrasound in solution (Fig. 24a, b). The absence of ultrasound-induced dissociation of a low-molecular weight model complex and in-depth studies of temperature effects confirm that the dissociation is indeed the result of mechanical activation (for an extensive review of sonochemical activation please refer to [10, 13]). The influence of the strength of the metal–ligand interactions on the mechanically induced dissociation was also explored. Metallo-supramolecular polymers in which the Mebip ligands were substituted with more strongly coordinating dipicolinate ligands (Fig. 24c) do not dissociate upon exposure to ultrasound. Finally, it was shown that mechanochemical transduction in metallo-supramolecular polymers is also possible in the solid state. This permitted the mending of damaged objects through ultrasound (Fig. 25c) as well as mechanochromic behavior based on metal-exchange reactions in metallo-supramolecular polymers infused with an auxiliary metal salt (Fig. 25b). This was achieved by immersing the metallo-supramolecular polymer in an $Fe(ClO_4)_2$ solution and subjecting the material thus treated to ultrasound or a macroscopic force. Gratifyingly, no color change occurred by immersion in the salt solution, and only upon mechanochemical activation was an irreversible color change, characteristic of the $Fe(Mebip)_2$ complexes, observed (Fig. 25b).

In all of the studies summarized above, the Mebip ligands were covalently attached to a telechelic core and served either to chain-extend or cross-link these building blocks, in connection with various metal ions, into linear or cross-linked metallo-supramolecular polymers. Rowan et al. took a different approach when they blended complexes based on monofunctional dodecyl-Mebip and metal ions into methacrylate-based polymer matrices [85]. Interestingly, when complexes with platinum ions were used, a mechanically responsive material was obtained, which

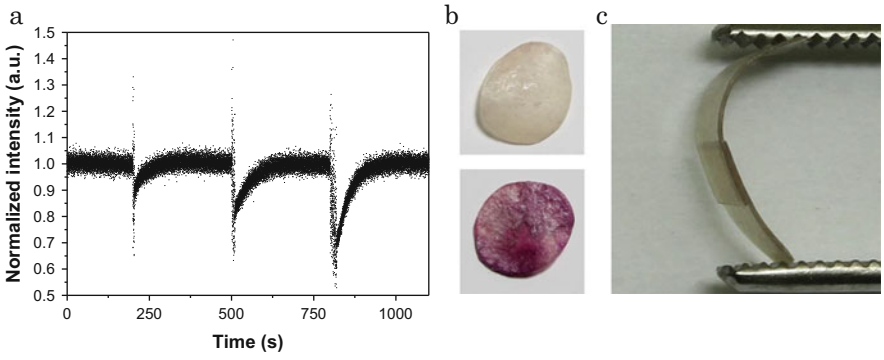

Fig. 25 (**a**) Emission of $(\mathbf{5})_{\mathbf{1.5}}\cdot[\mathbf{Eu(ClO_4)_3}]$ in $CHCl_3$ monitored at 620 nm over time. The solution was subjected to three ultrasonication pulses of 10 s each. (**b**) Images of $(\mathbf{5})_{\mathbf{1.5}}\cdot[\mathbf{Eu(ClO_4)_3}]$ films swollen in an acetonitrile solution of $Fe(ClO_4)_2$ for 5 days before (*top*) and after (*bottom*) ultrasonication. (**c**) Image of two films of $(\mathbf{5})_{\mathbf{1.5}}\cdot[\mathbf{Eu(ClO_4)_3}]$ mended together by ultrasonication. Adapted with permission from [83]. Copyright 2014 American Chemical Society

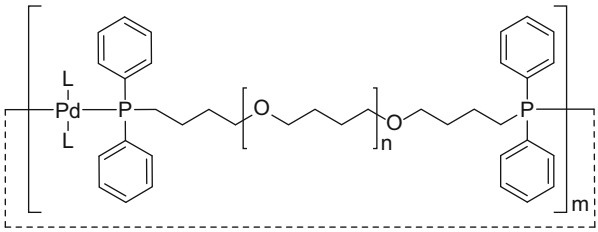

L = e.g. Cl
n = degree of polymerization of the macromonomer
m = degree of polymerization of the supramolcular aggregate
The dashed line indicates possible cyclic structures.

Fig. 26 General structure of the mechanically responsive Pd–phosphine-containing metallo-supramolecular polymers studied by Sijbesma and co-workers [86]

displayed a mechanically induced color change both in absorption and photoluminescence. The mechanically induced optical changes were related to a variation of the Pt–Pt interactions (i.e., the distances in small Pt-ligand crystallites that formed in the glassy matrix), which were stable after applying mechanical forces in the glassy state but could be deliberately reverted by heating to above the T_g of the polymer matrix.

The discovery that mechanochemistry can be at play in metal-containing polymers goes back to 2004, when Sijbesma and coworkers demonstrated mechanochemical activation in polymers comprising phosphine ligands that were coordinating late transition metals such as palladium or iridium. Specifically, poly(tetrahydrofuran) (pTHF) with telechelic phosphine moieties was used to complex $PdCl_2$, which resulted in the formation of linear supramolecular polymers and smaller cyclic structures (Fig. 26) [86]. The Pd–phosphine bonds could be selectively broken upon ultrasonication solutions of the metallopolymer and no by-products could be identified by NMR spectroscopy. Also, because no irreversible polymer degradation upon multiple cycles of breaking and reformation was observed, one can conclude that the Pd phosphine connection could be reversibly and selectively cleaved. The reformation of the metallo-supramolecular polymer was shown to be much slower than in the previously described Mebip systems (dozens of hours vs minutes). Ultrasonication was shown to disrupt longer chains preferentially, which is indicative that mechanical activation as a thermal process should affect short and long chains alike. A most interesting feature of the mechanically responsive Pd-containing material is the catalytic potential of the metal centers, which can be reversibly activated. This feature was used, for example, to induce the activation of an olefin metathesis catalyst mechanically [4, 87–89].

In a subsequent study, Paulusse et al. quantified the extent of the sonochemically induced dissociation of slightly modified phosphine ligands (cyclohexyl instead of phenyl substituents at the phosphorus) from the Pd centers by adding 1-(dicyclohexylphosphino)dodecane as a competing ligand [90]. The metallopolymer was kinetically stable when it was mixed in solution with the alkyldiphenylphosphine, because exchanges within the Pd coordination sphere are very slow. However, upon ultrasonication, a significant and irreversible

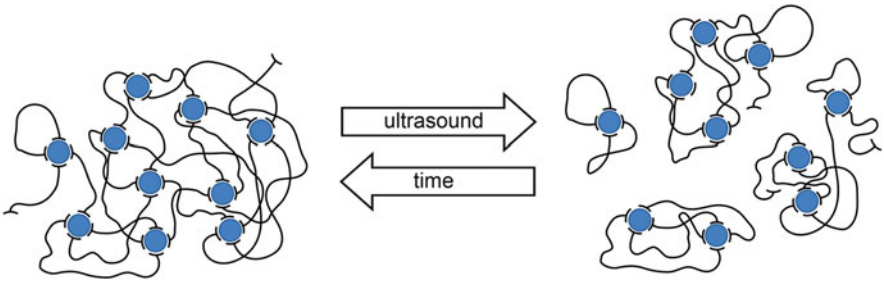

Fig. 27 Proposed mechanism for the liquefaction of phosphine-Rh or phosphine-Ir supramolecular gels upon ultrasonication [91]

reduction of the molecular weight of the metallopolymer was observable, on account of mechanically induced dissociation of the metallopolymer and subsequent irreversible binding of 1-(dicyclohexylphosphino)dodecane to the free Pd. The study revealed that the dissociation rate of the current system upon ultrasonication was too slow for a practical application in catalysis.

Similar metallopolymers based on diphenylphosphine-terminated macromonomers in combination with Rh^+ or Ir^+ ions resulted in the formation of gel-like networks when the building blocks were combined in a solvent such as dichloromethane or chloroform [91]. These gels could be liquefied upon ultrasonication (Fig. 27) as a result of ligand exchanges that preserved the coordination stoichiometry of the metal centers while reducing the number of cross-links. After sonication, the equilibrium network reformed almost immediately in the case of Rh^+ (gel phase after 1 h at +20°C), whereas the process was much slower in the case of the Ir^+-based gel (sol phase still present after 3 days at −20°C).

Through the study of "mixed" metallopolymers based on Pd^{2+} and Pt^{2+} salts and phosphine-terminated telechelic macromonomers, Sijbesma and coworkers were able to address the question of how selective ultrasonication induced chain scission of metallopolymers can be [92]. Moore and coworkers had previously reported that selectivity in chain scission requires that the bond energy of the "weak links" – also referred to as mechanophores – is approximately 100–125 kJ mol^{-1} lower than that of the other (residual) bonds [93]. The hybrid system containing both Pd^{2+} and Pt^{2+} metal ions focused on very small bond energy differences; according to density functional theory calculations the complex formed between $PtCl_2$ and pentyl-dicyclohexylphosphine features a metal-P bond that is ca. 30 kJ mol^{-1} stronger than the corresponding Pd complex. Although such a small difference in coordination strength should preclude complete selectivity, ultrasonication experiments of solutions of the metallopolymer demonstrated that chain scission at the Pd centers was favored over chain scission at Pt centers. Similarly, the degradation kinetics were studied by ultrasonication of solutions that contained palladium(II) dichloride bis (1-dodecyl)diphenylphosphine, where the phosphine serves as a competing ligand [92]. An important factor limiting the selectivity is the position of the metal center in the original metallopolymer. Degradation experiments with other polymers have established a minimum molecular weight of ca. 30,000 g mol^{-1} at the time of the

experiments for vinylic polymers such as poly(styrene) or poly(methyl methacrylate) [94]. The macromonomers used in this study have a number-average molecular weight of 12,000 g mol^{-1} and therefore the relative position of the complexes to the middle of the chain (where the mechanical force reaches its maximum) might significantly influence the selectivity because of a differing effective force felt by each segment.

Another metallo-supramolecular system, on the basis of 2,6-bis(1,2,3-triazol-4-yl)pyridine (BTP) as well as Zn^{2+} and Eu^{3+}, respectively, was introduced by Weng and coworkers [95]. The approach is quite different from the majority of mechanically responsive metallo-supramolecular polymers heretofore described: the ligands were designed to be part of the polymer backbone instead of being located at the end of the polymer chains. Telechelic pTHF was thus copolymerized with the dihydroxy-functionalized BTP ligand and hexamethylene diisocyanate to produce a polyurethane that was further cross-linked through the addition of metal ions (Fig. 28a). The metal-rich domains phase-separate from the pTHF soft

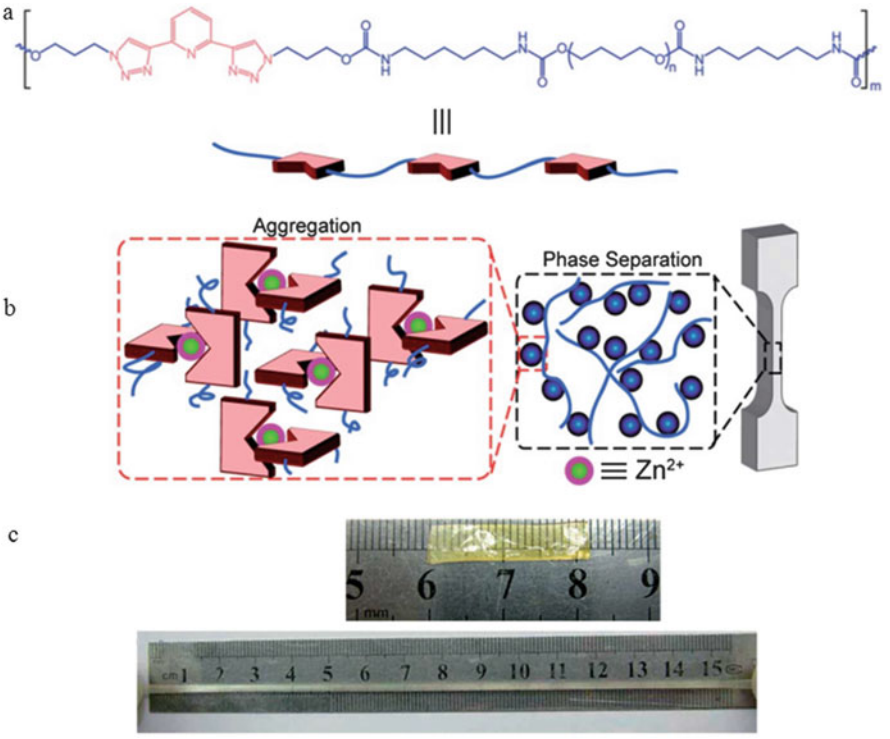

Fig. 28 (**a**) Chemical structure of a poly(THF)-BTP polyurethane. (**b**) Schematic representation of structure and morphology of the metallo-supramolecular polymer network formed by combination of poly(THF)-BTP and Zn^{2+}. (**c**) Pictures of a film of the metallo-supramolecular polymer network made from poly(THF)-BTP and Eu^{3+} before and after stretching. Adapted with permission from [95]. Copyright 2013 The Royal Society of Chemistry

segments, forming a hard phase. This phase-segregated morphology results in additional physical crosslinks (Fig. 28b). The material featured – depending on the ratios of BTP ligands to Zn^{2+} and to Eu^{3+} ions – high tensile strengths (up to 18 MPa), large strains at break (in excess of 1,000%, Fig. 28c), and high toughness (up to 70 MPa), whereas these maximum values were observed for the material containing solely Eu^{3+} metal centers. The metal–ligand hard phase was found to be thermally stable but mechanically labile. Mechanical stress caused the disruption of the hard phase domains and the dissociation of metal–ligand complexes, leading to a mechanical behavior reminiscent of the titin-mimics designed by the Guan group (see above). It is noted that in this case the mechanical properties are not the result of the unfolding of modular domains, but the metal–ligand-based cross-links appear to act as sacrificial bonds. The authors also demonstrated that UV-light induced "reshuffling" of the supramolecular network under mechanical constraint allowed for stress reduction upon irradiation with UV light on account of an increased dissociation rate of the metal–ligand complexes under these conditions.

Most recently, Liang et al. reported an example system for mechanically triggered drug release from metallo-supramolecular diblock copolymer micelles (Fig. 29) [96]. The latter were based on bis(TPy)-Cu^{2+} (TPy=2,2′:6′,2″-terpyridine) complexes employed to link poly(propylene glycol) (PPG) and poly(ethylene glycol) (PEG) into an amphiphilic block copolymer. The material was shown to be able to self-assemble in aqueous solution into spherical micelles with hydrophobic PPG cores. The micelles can be opened/disrupted via ultrasound, which reversibly breaks the Cu^{2+}-ligand complexes and thereby allows the release of hydrophobic cargo molecules encapsulated in the micelles. After halting the sonication, the metal–ligand bonds were shown to reform, resulting in the re-assembly

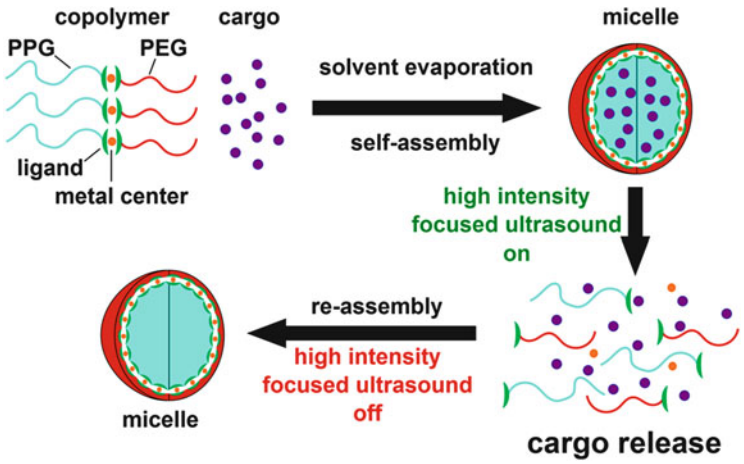

Fig. 29 Schematic illustration of the self-assembly of amphiphilic metallo-supramolecular block copolymers under encapsulation of cargo into micelles and disassembly of the micelles under release of the drug upon ultrasound sonication via dissociation of the metal–ligand complex. Upon cessation of the ultrasonication, the micelles re-assemble again [96]

of (slightly smaller) micelles. In reference experiments with micelle systems based on otherwise the same chemistry but stronger ruthenium–TPy complexes or covalent bonds (block copolymer PEO-PPG-PEO), no drug release under similar ultrasonication conditions was observed.

In addition to the work previously described, the studies of Bielawski and coworkers in which hemi-telechelic pyridine-end-terminated poly(methyl acrylate) was utilized to initiate ionic polymerization upon mechanically activated scission of the boron-nitrogen coordination bond should be mentioned [97]. Although the design of these systems is in principle very interesting, an "expression of concern" was published and editorial review is currently underway to investigate "the reliability of the data reported in the article." Nevertheless, at this stage, no definitive conclusion has been drawn.

5 Summary and Outlook

Chemical bond activation through mechanical force, a hallmark of many biological materials, has long been known to occur in artificial materials, but such processes have traditionally been regarded as a challenge and not an opportunity. Although mechanical force is well known to be capable of altering the electronic states of chemical bonds and thereby cause changes in chemical reactivity, optical properties, electrical conductivity, magnetic response, and other properties, it has been a veritable challenge to harness this knowledge to design functional mechanoresponsive materials rationally. The last decade, though, has witnessed tremendous progress in this domain. Researchers have been able to create mechanoresponsive systems in different material families, including small organic molecules, polymers, and inorganic materials. These materials have exploited a broad range of mechanophores. Although the development of the field of mechanically responsive polymers appears to have been catalyzed by early research involving supramolecular motifs, efforts have shifted in the last 5 years towards polymers comprising mechanophores that involve breaking of covalent bonds. Nevertheless, as summarized in this overview, a number of supramolecular polymers have emerged in which exposure to mechanical force fields causes the selective dissociation of supramolecular motifs. Studies have evolved from proof-of-concept experiments to the design of a range of functional materials in which the mechanically triggered disassembly permits execution of a pre-programmed function. It appears that the general concept of mechanochemistry in supramolecular materials is versatile and can be exploited using a broad range of non-covalent interactions, that is, mechanophores relying on hydrogen bonding, π–π stacking, metal–ligand binding, and other non-covalent bonds. As the strength of such interactions can be tailored over a broad range, and the molecular-level changes imparted by the (dis)assembly appear to be virtually limitless, this framework opens up avenues for the development of a plethora of new materials capable of transducing (weak) mechanical

forces into a useful outcome, including, as discussed here, healing, color changes, catalytic functions, and many others.

Acknowledgments This work was supported by the National Center of Competence in Research (NCCR) Bio-Inspired Materials, a research instrument of the Swiss National Science Foundation. The authors acknowledge further support from the U.S. Army Research Office (W911NF-12-1-0339), the Swiss National Science Foundation (Grant No. 135405 and 152968), the European Research Council (ERC-2011-AdG 291490-MERESPO), and the Adolphe Merkle Foundation. Y.S. acknowledges JSPS Postdoctoral Fellowships for Research Abroad.

References

1. Lumpkin EA, Caterina MJ (2007) Nature 445:858. doi:10.1038/Nature05662
2. Chen Y, Spiering AJH, Karthikeyan S, Peters GWM, Meijer EW, Sijbesma RP (2012) Nat Chem 4:559. doi:10.1038/nchem.1358
3. Davis DA, Hamilton A, Yang JL, Cremar LD, Van Gough D, Potisek SL, Ong MT, Braun PV, Martinez TJ, White SR, Moore JS, Sottos NR (2009) Nature 459:68. doi:10.1038/Nature07970
4. Groote R, Jakobs RTM, Sijbesma RP (2013) Polym Chem 4:4846. doi:10.1039/C3py00071k
5. Heinrichs A (2009) Nat Rev Mol Cell Biol 10:163. doi:10.1038/Nrm2642
6. Gillespie PG, Walker RG (2001) Nature 413:194. doi:10.1038/35093011
7. Brantley JN, Konda SSM, Makarov DE, Bielawski CW (2012) J Am Chem Soc 134:9882. doi:10.1021/Ja303147a
8. Lenhardt JM, Black AL, Craig SL (2009) J Am Chem Soc 131:10818. doi:10.1021/ja9036548
9. Beyer MK, Clausen-Schaumann H (2005) Chem Rev 105:2921. doi:10.1021/Cr030697h
10. Cravotto G, Cintas P (2012) Chem Sci 3:295. doi:10.1039/C1sc00740h
11. Lee CK, Davis DA, White SR, Moore JS, Sottos NR, Braun PV (2010) J Am Chem Soc 132:16107. doi:10.1021/Ja106332g
12. Stuart MAC, Huck WTS, Genzer J, Muller M, Ober C, Stamm M, Sukhorukov GB, Szleifer I, Tsukruk VV, Urban M, Winnik F, Zauscher S, Luzinov I, Minko S (2010) Nat Mater 9:101. doi:10.1038/Nmat2614
13. Caruso MM, Davis DA, Shen Q, Odom SA, Sottos NR, White SR, Moore JS (2009) Chem Rev 109:5755
14. Black AL, Lenhardt JM, Craig SL (2011) J Mater Chem 21:1655. doi:10.1039/C0jm02636k
15. Black AL, Orlicki JA, Craig SL (2011) J Mater Chem 21:8460. doi:10.1039/C0jm03875j
16. Weder C (2015) In: Kobayashi S, Müllen K (eds) Encyclopedia of polymeric nanomaterials. Springer, Weinheim, Germany
17. Turro NJ (1978) Modern molecular photochemistry. Benjamine/Cummings Publishing Co. Menlo Park, California, USA
18. Valeur B (2002) Molecular fluorescence: principles and applications. Wiley-VCH. Weinheim, Germany
19. Birks JB (1975) Rep Prog Phys 38:903
20. Winnik FM (1993) Chem Rev 93:587
21. Goetz KP, Vermeulen D, Payne ME, Kloc C, McNeil LE, Jurchescu OD (2014) J Mater Chem C 2:3065. doi:10.1039/C3TC32062F
22. Weber CD, Robinson SG, Stay DP, Vonnegut CL, Lonergan MC (2012) ACS Macro Lett 1:499. doi:10.1021/mz300046x
23. Kasha M, Rawls HR, El-Bayoumi MA (1965) Pure Appl Chem 11:371
24. Hong Y, Lamab JWY, Tang BZ (2011) Chem Soc Rev 40:5361
25. Sagara Y, Kato T (2009) Nat Chem 1:605. doi:10.1038/nchem.411
26. Pucci A, Ruggeri G (2011) J Mater Chem 21:8282. doi:10.1039/c0jm03653f

27. Pucci A, Bizzarri R, Ruggeri G (2011) Soft Matter 7:3689. doi:10.1039/C0SM01038C
28. Ciardelli F, Ruggeri G, Pucci A (2013) Chem Soc Rev 42:857. doi:10.1039/c2cs35414d
29. Makowski B, Kunzelman J, Weder C (2011) In: Urban M (ed) Handbook of stimuli-responsive materials. Wiley-VCH, New York, p 117
30. Förster T, Kasper KZ (1954) Physik Chem NF 1:275
31. Förster T, Kasper KZ (1955) Elektrochem Angew Physik Chem 59:976
32. Döller E, Förster TZ (1962) Phys Chem 34:132
33. Birks JB, Dyson DJ, Munro IH (1963) Prog R Soc 275 (Ser. A):575
34. Spies C, Gehrke RJ (2002) Phys Chem 106:5348
35. Trabesinger W, Renn A, Hecht B, Wild UP, Montali A, Smith P, Weder C (2000) J Phys Chem B 104:5221
36. Crenshaw BR, Weder C (2003) Chem Mater 15:4717. doi:10.1021/Cm034447t
37. Löwe C, Weder C (2002) Adv Mater 14:1625. doi:10.1002/1521-4095(20021118)14:22<1625::AID-ADMA1625>3.0.CO;2-Q
38. Crenshaw BR, Burnworth M, Khariwala D, Hiltner A, Mather PT, Simha R, Weder C (2007) Macromolecules 40:2400. doi:10.1021/ma062936j
39. Kinami M, Crenshaw BR, Weder C (2006) Chem Mater 18:946. doi:10.1021/cm052186c
40. Lott J, Weder C (2010) Macromol Chem Phys 211:28. doi:10.1002/macp.200900476
41. Crenshaw BR, Weder C (2006) Macromolecules 39:9581. doi:10.1021/ma061685b
42. Kunzelman J, Crenshaw BR, Kinami M, Weder C (2006) Macromol Rapid Comm 27:1981. doi:10.1002/marc.200600642
43. Kunzelman J, Gupta M, Crenshaw BR, Schiraldi DA, Weder C (2009) Macro Mater Eng 294:244. doi:10.1002/mame.200800299
44. Crenshaw BR, Weder C (2005) Adv Mater 17:1471. doi:10.1002/adma.200401688
45. Crenshaw BR, Kunzelman J, Sing CE, Ander C, Weder C (2007) Macromol Chem Phys 208:572. doi:10.1002/macp.200600622
46. Kunzelman J, Chung T, Mather PT, Weder C (2008) J Mater Chem 18:1082. doi:10.1039/b718445j
47. Sing CE, Kunzelman J, Weder C (2009) J Mater Chem 19:104. doi:10.1039/b813644k
48. Kunzelman J, Crenshaw BR, Weder C (2007) J Mater Chem 17:2989. doi:10.1039/b705880b
49. Tang L, Whalen J, Schutte G, Weder C (2009) ACS Appl Mater Interfaces 1:688. doi:10.1021/am800199u
50. Pucci A, Bertoldo M, Bronco S (2005) Macromol Rapid Comm 26:1043. doi:10.1002/marc.200500227
51. Pucci A, Di Cuia F, Signori F, Ruggeri G (2007) J Mater Chem 17:783. doi:10.1039/b612033d
52. Donati F, Pucci A, Cappelli C, Mennucci B, Ruggeri G (2008) J Phys Chem B 112:3668
53. Löwe C, Weder C (2002) Synthesis 9:1185
54. Makowski BT, Lott J, Valle B, Singer KD, Weder C (2012) J Mater Chem 22:5190. doi:10.1039/c2jm15846a
55. Kunzelman J, Kinami M, Crenshaw BR, Protasiewicz JD, Weder C (2008) Adv Mater 20:119. doi:10.1002/adma.200701.772
56. Sagara Y, Komatsu T, Ueno T, Hanaoka K, Kato T, Nagano T (2014) J Am Chem Soc 136:4273. doi:10.1021/ja412670g
57. Burattini S, Colquhoun HM, Greenland BW, Hayes W (2009) Faraday Discuss 143:251
58. Burattini S, Colquhoun HM, Fox JD, Friedmann D, Greenland BW, Harris PJ, Hayes W, Mackay ME, Rowan SJ (2009) Chem Commun (Camb) 6717. doi:10.1039/b910648k
59. Burattini S, Greenland BW, Merino DH, Weng W, Seppala J, Colquhoun HM, Hayes W, Mackay ME, Hamley IW, Rowan SJ (2010) J Am Chem Soc 132:12051
60. Hart LR, Hunter JH, Nguyen NA, Harries JL, Greenland BW, Mackay ME, Colquhoun HM, Hayes W (2014) Polym Chem 5:3680. doi:10.1039/c4py00292j
61. Brunsveld L, Folmer BJB, Meijer EW, Sijbesma RP (2001) Chem Rev 101:4071. doi:10.1021/cr990125q
62. Hoeben FJM, Jonkheijm P, Meijer EW, Schenning A (2005) Chem Rev 105:1491. doi:10.1021/cr030070z
63. Aida T, Meijer EW, Stupp SI (2012) Science 335:813. doi:10.1126/science.1205962

64. Kato T, Mizoshita N, Kishimoto K (2005) Angew Chem Int Ed Engl 45:38. doi:10.1002/anie.200501384
65. Wojtecki RJ, Meador MA, Rowan SJ (2011) Nat Mater 10:14. doi:10.1038/nmat2891
66. Guimard NK, Oehlenschlaeger KK, Zhou J, Hilf S, Schmidt FG, Barner-Kowollik C (2012) Macromol Chem Phys 213:131. doi:10.1002/macp.201100442
67. Sijbesma RP, Beijer FH, Brunsveld L, Folmer BJB, Hirschberg JHKK, Lange RFM, Lowe JKL, Meijer EW (1997) Science 278:1601
68. Sivakova S, Bohnsack DA, Mackay ME, Suwanmala P, Rowan SJ (2005) J Am Chem Soc 127:18202
69. Guan Z, Roland JT, Bai JZ, Ma SX, McIntire TM, Nguyen M (2004) J Am Chem Soc 126:2058
70. Roland JT, Guan Z (2004) J Am Chem Soc 126:14328
71. Kushner AM, Gabuchian V, Johnson EG, Guan Z (2007) J Am Chem Soc 129:14110
72. Kushner AM, Vossler JD, Williams GA, Guan Z (2009) J Am Chem Soc 131:8766
73. Beck JB, Rowan SJ (2003) J Am Chem Soc 125:13922. doi:10.1021/ja038521k
74. Lis S (2002) J Alloy Comp 341:45. doi: 10.1016/S0925-8388(02)00055-5
75. Sabbatini N, Guardigli M, Lehn J-M (1993) Coord Chem Rev 123:201. doi:10.1016/0010-8545(93)85056-A
76. Schubert US, Eschbaumer C (2002) Angew Chem Int Ed 41:2892. doi:10.1002/1521-3773(20020816)41:16<2892::AID-ANIE2892>3.0.CO;2-6
77. Rowan SJ, Beck JB (2005) Faraday Discuss 128:43. doi:10.1039/B403135K
78. Kumpfer JR, Wie JJ, Swanson JP, Beyer FL, Mackay ME, Rowan SJ (2011) Macromolecules 45:473. doi:10.1021/ma201659d
79. Burnworth M, Tang L, Kumpfer JR, Duncan AJ, Beyer FL, Fiore GL, Rowan SJ, Weder C (2011) Nature 472:334. doi:10.1038/nature09963
80. Coulibaly S, Roulin A, Balog S, Biyani M, Foster EJ, Rowan SJ, Fiore GL, Weder C (2014) Macromolecules 47:152
81. Biyani MV, Foster EJ, Weder C (2013) ACS Macro Letters 2:236–240
82. Fiore G, Rowan SJ, Weder C (2013) Chem Soc Rev 42:7278
83. Balkenende DWR, Coulibaly S, Balog S, Simon YC, Fiore GL, Weder C (2014) J Am Chem Soc 136:10493. doi:10.1021/Ja5051633
84. Simon YC, Fiore GL, Weder C (2014) Chimia 68:666. doi:10.2533/chimia.2014.666
85. Kumpfer JR, Taylor SD, Connick WB, Rowan SJ (2012) J Mater Chem 22:14196. doi:10.1039/C2JM32160B
86. Paulusse JMJ, Sijbesma RP (2004) Angew Chem Int Ed 43:4460. doi:10.1002/anie.200460040
87. Groote R, Szyja BM, Leibfarth FA, Hawker CJ, Doltsinis NL, Sijbesma RP (2014) Macromolecules 47:1187. doi:10.1021/ma4022339
88. Jakobs RTM, Ma S, Sijbesma RP (2013) ACS Macro Lett 2:613. doi:10.1021/mz400201c
89. Jakobs RTM, Sijbesma RP (2012) Organometallics 31:2476. doi:10.1021/Om300161z
90. Paulusse JMJ, Huijbers JPJ, Sijbesma RP (2006) Chem Eur J 12:4928. doi:10.1002/chem.200600120
91. Paulusse JMJ, van Beek DJM, Sijbesma RP (2007) J Am Chem Soc 129:2392. doi:10.1021/ja067523c
92. Paulusse JMJ, Sijbesma RP (2008) Chem Comm 4416. doi:10.1039/B806978F
93. Berkowski KL, Potisek SL, Hickenboth CR, Moore JS (2005) Macromolecules 38:8975. doi:10.1021/ma051394n
94. Nguyen TQ, Liang OZ, Kausch HH (1997) Polymer 38:3783. doi:10.1016/S0032-3861(96)00950-0
95. Yuan J, Zhang H, Hong G, Chen Y, Chen G, Xu Y, Weng W (2013) J Mater Chem B 1:4809. doi:10.1039/C3TB20647E
96. Liang B, Tong R, Wang Z, Guo S, Xia H (2014) Langmuir 30:9524. doi:10.1021/la500841x
97. Wiggins KM, Hudnall TW, Tennyson AG, Bielawski CW (2011) J Mater Chem 21:8355. doi:10.1039/C0JM03619F

Top Curr Chem (2015) 369: 377–424
DOI: 10.1007/128_2015_626

Published online: 20 March 2015

Responsive Polymers as Sensors, Muscles, and Self-Healing Materials

Qiang Matthew Zhang and Michael J. Serpe

Abstract Responsive polymer-based materials can adapt to their surrounding environment by expanding and shrinking. This swelling and shrinking (mechanotransduction) can result in a number of functions. For example, the response can be used to lift masses, move objects, and can be used for sensing certain species in a system. Furthermore, responsive polymers can also yield materials capable of self-healing any damage affecting their mechanical properties. In this chapter we detail many examples of how mechanical responses can be triggered by external electric and/or magnetic fields, hygroscopicity, pH, temperature, and many other stimuli. We highlight how the specific responses can be used for artificial muscles, self-healing materials, and sensors, with particular focus on detailing the polymer response yielding desired effects.

Keywords Artificial muscles · Mechanochemistry · Responsive polymers · Self-healing materials · Sensors

Contents

Q.M. Zhang and M.J. Serpe (✉)
Department of Chemistry, University of Alberta, Edmonton, Alberta, Canada, T6G 2G2
e-mail: michael.serpe@ualberta.ca

1 Introduction

Sea cucumbers rapidly change their stiffness by several orders of magnitude in the face of danger, Venus flytraps close their leaves and trap insects in response to stimulation of their trigger hairs, and octopus, squid, and cuttlefish quickly change their color for camouflage or to warn potential predators [1]. These are just a few of the many examples of nature's ability to respond to external stimuli. Polymer scientists and engineers have been working very hard to develop novel materials that can mimic this incredible behavior. To accomplish this, stimuli-responsive polymers are often the materials of choice. Stimuli-responsive polymers (also called smart/intelligent polymers) are capable of significantly changing their properties such as shape, mechanical properties, solubility, permeability, optical properties, and electrical properties upon the application of a stimulus; common stimuli include temperature, pH, light, magnetic field, electrical field, sonication, solvents, ions, enzymes, and specific organic compounds [2–8].

Several classes of stimuli-responsive polymers have been reported. Polysaccharides, proteins, and nucleic acids represent one group of stimuli-responsive biopolymers which can be found widely in living systems [9–11]. Indeed, these materials belong to the oldest class of substances in Nature with stimuli-responsive properties. However, for many years, synthetic polymers with stimuli-responsive properties have attracted a similar level of attention within the scientific community [12]. Table 1 lists some examples of stimuli-responsive polymers, and the stimuli that can be used elicit a response [13].

Of all stimuli-responsive polymers, temperature-responsive polymers are the best known and most studied. Among those, polymers that exhibit a lower critical solution temperature (LCST) have found the widest applicability [14]. The LCST is a fascinating phenomenon found for various polymer solutions. Polymer solutions often exhibit both an LCST and an upper critical solution temperature (UCST). For the LCST, at temperatures below the LCST the polymer is completely miscible in the solvent, whereas at temperatures above the LCST a phase separation occurs. In fact, the most investigated temperature-responsive polymer featuring a LCST in water is poly(*N*-isopropylacrylamide) (pNIPAm). The LCST of pNIPAm is ~32°C,

Table 1 Abbreviated names of polymers with their associated responsivities

	Polymer	Types of stimulus
BIS	Bisacrylamide	
PAA	Poly(acrylic acid)	pH
PAAEM	Poly(acetoacetoxyethyl methacrylate)	
PAm	Poly(acrylamides)	
PBA	Poly(butyl acrylate)	
PDEA	Poly[2-(diethylamino) ethyl methacrylate]	pH
PDMS	Poly(dimethylsiloxane)	[a]E-field, [b]T-field
PDPA	Poly[2-(diisopropylamino) ethyl methacrylate]	pH
PEO	Poly(ethylene oxide)	T-field
PGMA	Poly(glycerol monomethacrylate)	
PHEMA	Poly(hexyl ethyl methacrylate)	
PHFBMA	Poly(hexafluoro butylmethacrylamide)	T-field
PLG	Poly (glutamic acid)	pH
PLLA	Poly(L-lactides)	
PMMA	Poly(methyl) methacrylate	
PMPC	Poly[2-(methacryloyloxy) ethyl phosphorylcholine]	E-field, T-field
PNaA	Poly(sodium acrylate)	pH
PNaVBA	Poly(sodium-4-vinylbenzoate)	pH
PNCL	Poly(*N*-vinylcaprolactone)	T-field, pH
PNIPAM	Poly(*N*-isopropylacrylamide)	T-field
PPO	Poly(propylene oxide)	T-field
PSMA	Poly(stearyl methacrylate)	
PVIm	Poly(*N*-vinylimidazole)	pH

Reproduced with permission from [13]
[a]Electrical field
[b]Thermal field

which is close to human body temperature [15]. Consequently, by altering the temperature of pNIPAm in water, its solubility can be tuned, e.g., pNIPAm transitions from hydrophilic (soluble) to hydrophobic (insoluble) as the LCST is exceeded. Other N-substituted polyacrylamides [16, 17] and other classes of polymers such as poly(oligoethyleneoxide-(meth)acrylate)s [18] or poly(2-oxazoline)s [19] have also been shown to exhibit thermoresponsivity and exhibit an LCST.

Another class of responsive polymers that have been found to be useful is light responsive polymers. The response of the polymer, and its reversibility, depends greatly on the functional groups making up the polymer. For example, some photochromic molecules undergo a reversible isomerization upon irradiation [20]. This process is usually accompanied with a polarity change as well as a color change in the chromophoric units. Such phenomena can be observed in chemical compounds such as azobenzene [21], spiropyran [22], and triphenylmeth-

ane leuco [23]. Irreversible light responsivity is achieved when polymers contain photocleavable units, which subsequently yield the polymer response [24]. For example, the ester bond of *o*-nitrobenzyl ester (ONB) [25, 26] irreversibly breaks upon exposure to UV light. Photocleavage reactions are generally initiated by UV-light; however, under certain conditions, near infrared (NIR)-light can also be used for cleavage of ONB-groups [25].

Mechanochemistry, even though a relatively new topic, has matured considerably over recent years. It has implications for material wear, abrasion, friction, and lubrication; this ultimately affects the performance of materials and their properties. Most important for this submission are volume/conformational changes of responsive polymers, which can yield a specific function [27]. While this kind of mechanochemistry is not a result of molecular scale bond breaking and reformation, it is nevertheless mechanochemistry. This is because the system's volume/conformational changes are in response to the environment, which changes the *chemistry* of the system and yields a response. For example, as pointed out in examples below, polymers composed of a weak acid can be ionized in a pH-dependent fashion; the "chemical reaction" of base with the polymer causes its ionization and a "mechanochemical" swelling response. Up to now, most reviews on responsive polymers focus on its applications such as drug delivery and biomaterials [28]. In this review, we showcase specific responsive polymers and their use as muscles, self-healing materials, and sensors.

2 Artificial Muscles

The ability to mimic the muscles in humans, both for the improvement of the quality of human life and in some cases simply for our amusement, has been a topic of great interest for some time. The performance of the emerging polymer actuators exceeds that of natural muscle in many respects, making them particularly attractive for real world applications. For example, muscle-like behavior is desirable in medical devices, prostheses, robotics, toys, biomimetic devices, and micro/nanoelectromechanical systems [29, 30]. Several "smart materials" have been proposed as artificial muscles, such as shape memory alloys, magnetostrictive alloys, piezoelectrics, and responsive polymers [31]. Polymer-based artificial muscle technologies are being developed, which produce high strains and stresses in response to electrostatic forces, electrostriction, ion insertion, and molecular conformational changes [32]. Materials used include elastomers, conducting polymers, ionically conducting polymers, and gels.

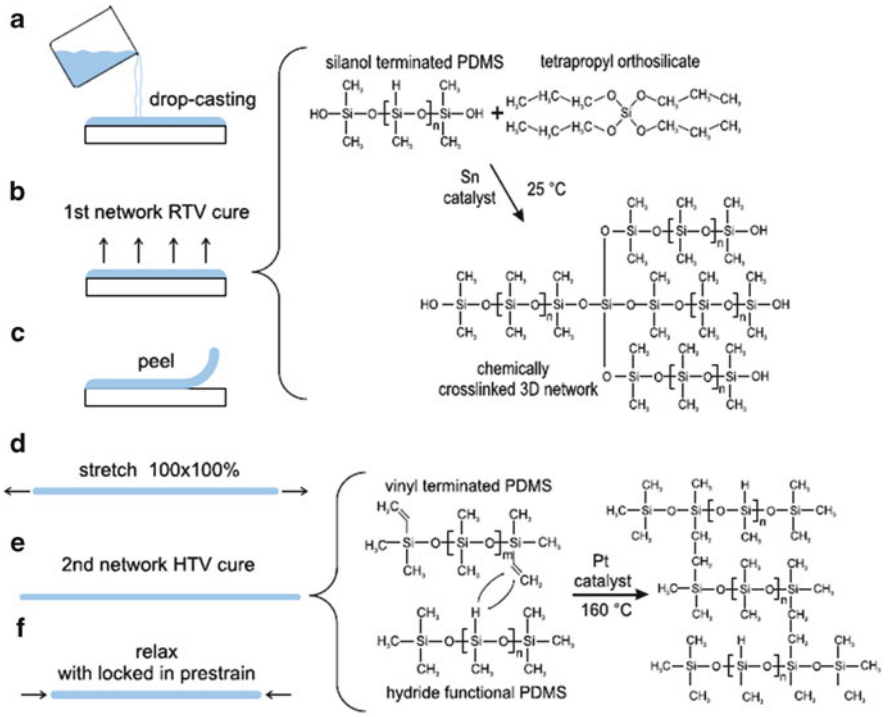

Fig. 1 Process for preparing S-IPN films: (**a**) solution is drop cast onto treated glass; (**b**) solvent is allowed to evaporate and the RTV silicone cures at room temperature; (**c**) film is peeled off of the glass substrate; (**d**) film is stretched biaxially by 100 × 100%; (**e**) HTV silicone is cured at 180°C for 30 min; (**f**) film is relaxed and some prestrain is preserved. Reproduced with permission from [34]

2.1 Dielectric Elastomers

Dielectric elastomers (DEs) behave as compliant capacitors, expanding in area and shrinking in thickness when a voltage is applied [33]. They consist of a thin elastomeric film coated on two sides with compliant electrodes. When an electric field is applied across the electrodes, a stress is generated on the film because of electrostatic attraction between opposite charges on these electrodes as well as repulsion from similar charges on each electrode. This stress causes the film to contract in thickness and expand in area. Most elastomers used are essentially incompressible, so any decrease in thickness results in a concomitant increase in the planar area. An all-silicone pre strain-locked interpenetrating polymer network (all-S-IPN) elastomer has been developed as a muscle-like actuator [34]. The elastomer was fabricated using a combination of two silicones: a soft room temperature vulcanizing (RTV) silicone as the host elastomer matrix, and a more rigid high temperature vulcanizing (HTV) silicone to preserve the prestrain in the host network (Fig. 1). In the S-IPN fabrication procedure, the RTV and HTV silicones

were codissolved in a common solvent, cast into thin films, and the RTV silicone allowed to cure before applying prestrain and finally curing the HTV silicone to lock in the prestrain. A performance improvement of the prestrain-locked silicones over standard silicone films was achieved, with a linear strain of 25% and an area strain of 45% when tested in a diaphragm configuration. The process can also be used to improve electrode adhesion and stability as well as improve the interlayer adhesion in multilayer actuators. The improved interlayer adhesion showed a long-life (>30,000 cycles at >20% strain) and repeated high-performance actuation (>500 cycles at ~40% strain) of prestrained free-standing multilayer actuators.

A number of approaches have been explored for increasing the dielectric constant of DEs. This is most commonly achieved by adding a high dielectric constant filler material to an elastomer host, such as aluminum oxide, titanium oxide, and barium titanium oxide [35–37]. For example, Standard Thai Rubber 5 L (STR 5 L)/aluminum oxide (Al_2O_3) composite (60 wt% Al_2O_3) was modified by cross-linking with 1 wt% dicumyl peroxide (DCP)/Irganox 1076 and cured at 170°C [35]. The deflection responses of the dielectric elastomer actuators were investigated under electrical field strengths of 0 and 650 V/mm at room temperature (27°C). The devices deflect toward the anode side at the electrical field strength of 200 V/mm; the degree of bending increases monotonically with increasing electrical field strength up to 650 V/mm [38]. Upon removal of the applied electric field, the device returns to its original position and shape (Fig. 2). The X-ray diffraction pattern of the film suggests that the Al_2O_3 generates dipole moments in the elastomer matrix, while scanning electron microscope images of the composites show that Al_2O_3 particles were uniformly distributed in the natural rubber matrix.

A polymer-based device capable of lifting many times its own mass was fabricated by drying a solution of the polycation poly(diallyldimethyl ammonium chloride) (pDADMAC) on a flexible surface coated with charged poly(*N*-isopropylacrylamide)-based microgels (Fig. 3) [39–41]. Upon drying of the pDADMAC solution on the microgel-modified surface, it bends. The authors proposed that the microgels serve as "glue" that allows the contraction of the pDADMAC layer to be translated to the underlying substrate. That is, there are multiple, electrostatic interactions between pDADMAC and the charged microgels. Therefore, the contraction of the pDADMAC layer upon drying can be translated to the substrate through its interaction with the microgels, and the microgels transfer the contraction to the Au-coated surface, thereby pulling the sides of the substrate up. Flexible surfaces then curl up into scroll-like structures, which can be opened up at high humidity. These arms are able to lift relatively large masses, and resist forces many times their own mass.

2.2 *Ionic Polymers*

An alternative means of producing actuation in a polymer is to employ ions that are mobile within the polymer phase. An applied field drives the motion of these ions and entrained solvent, leading to swelling or contraction when the ions enter or

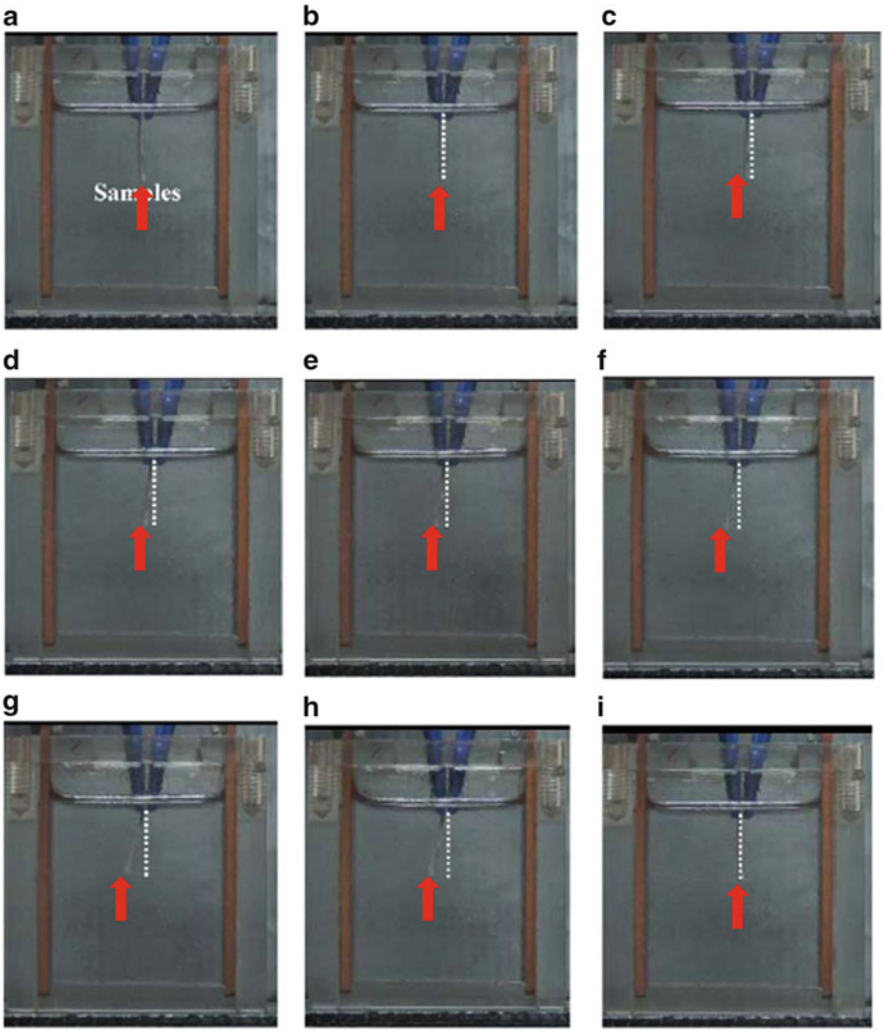

Fig. 2 Photographs of deflection responses under electrical field strength of 100–650 V/mm of the dielectric elastomer compounds of formula 8: (**a**) measured at 0 V/mm; (**b**) measured at 100 V/mm; (**c**) measured at 200 V/mm; (**d**) measured at 300 V/mm; (**e**) measured at 400 V/mm; (**f**) measured at 500 V/mm; (**g**) measured at 600 V/mm; (**h**) measured at 650 V/mm; (**i**) after switching off the electrical field for 60 s. The tip of the *red arrow* is pointing at the device. Reproduced with permission from [38]

leave regions of the polymer. If the polymer phase is electrically conductive, then the ions serve to balance charge generated on these conductors as the potential is changed, creating very strong local fields (but overall low voltage). The voltages employed in these materials are low (1–7 V), but the energies are nonetheless high

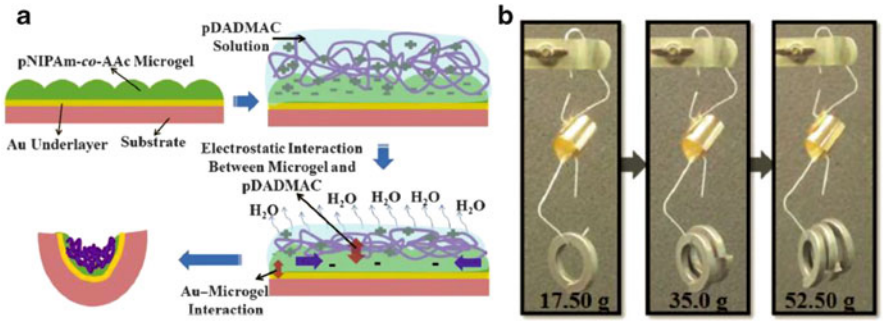

Fig. 3 The preparation process (**a**) and strength test (**b**) of the device. Reproduced with permission from [39]

because of the close spacing between ions and electronic charges and the large amount of charge that can be transferred.

A high-performance electro-active artificial muscle was prepared using pendent sulfonated chitosan (PSC) and functionalized graphene oxide (GO), which exhibited strong electro-chemomechanical interactions with ionic liquid (IL) in an open air environment (Fig. 4) [42]. The GO-PSC-IL nano-biopolymer membrane shows an increased tensile strength with ionic exchange capacity up to 83.1% which increased ionic conductivity over 18 times. The high ionic conductivity results in twice the bending actuation compared to the pure chitosan actuator under the same electrical input signals. The GO-PSC-IL actuators could show robust and high-performance actuation at low applied voltages (5 V) which are required in realistic applications.

Ionic polymer–metal composites (IPMCs) have received enormous research interest as unique electroactive polymers (EAPs) over the past decade because of their soft and flexible structure, relatively large electromechanical bending, and low driving voltage [43, 44]. With the ability to operate in an aqueous environment and closely mimic the motion of biological muscles, IPMC materials are particularly attractive for artificial muscle applications [43]. In one example, a nanostructured electrode surface was fabricated using platinum nanothorn assemblies and a Nafion membrane [37]. The nanostructured actuator shows a new way to achieve highly enhanced electromechanical performance over existing flat/featureless electrodes. The authors demonstrated that the formation and growth of the nanothorn assemblies at the electrode interface lead to a dramatic improvement (three- to fivefold increase) in actuation range, as shown in Fig. 5. These advances are attributed to the high capacitance of the nanothorn assemblies, which increases significantly the charge transport speed during the actuation process.

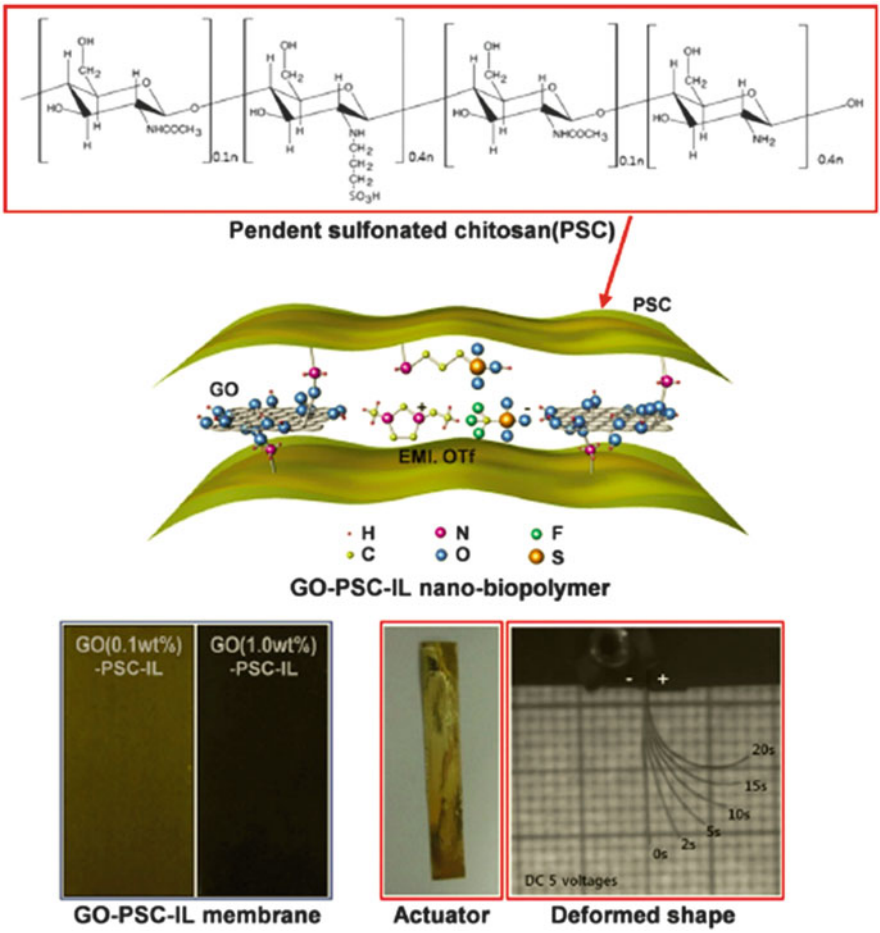

Fig. 4 Schematic illustration for pendent sulfonated chitosan and graphene oxide-pendent sulfonated chitosan-ionic liquid (GO-PSC-IL) nano-biopolymer actuator. Reproduced with permission from [42]

2.3 Conducting Polymers

Conducting polymers are typically semiconducting when undoped and conducting when doped with donor or acceptor ions [45]. The conformational changes of conducting polymer-based artificial muscles are a result of electrochemical ion insertion and removal, possibly along with other associated solvating species.

One example utilizing conducting polymers showed that interpenetrating polymer networks (IPN) could be prepared using a hot pressing method to combine a polytetrahydrofuran network for mechanical resistance and a poly(ethylene oxide) (PEO) as a solid polymer electrolyte [46]. After interpenetration of two poly

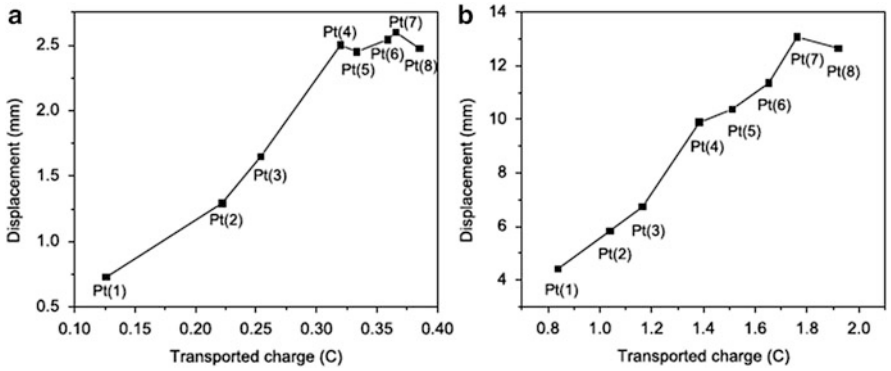

Fig. 5 Transported charge/displacement correlation. Peak-to-peak displacement vs transported charge (**a**) at 0.1 Hz, 61 V and (**b**) at 0.1 Hz, ±3 V AC square-wave input. Reproduced with permission from [43]

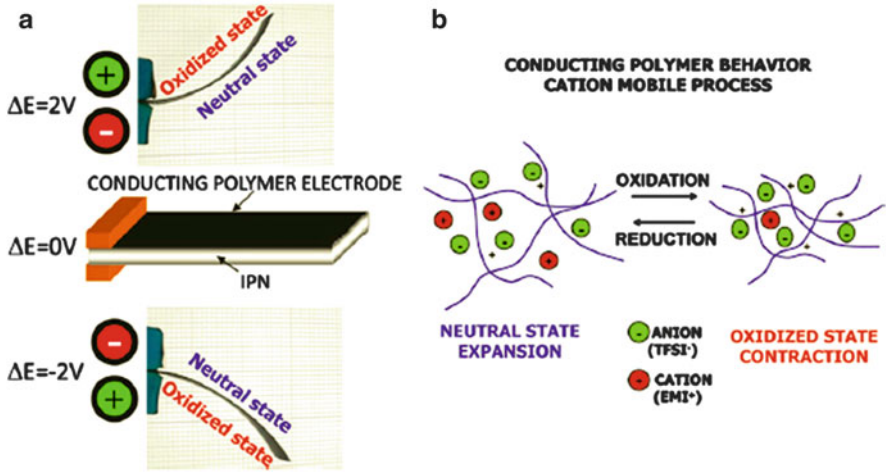

Fig. 6 (**a**) Beam shaped IPN macroactuator ($\triangle E = \pm 2$ V). (**b**) Oxidation-reduction process of conducting polymer. Reproduced with permission from [46]

(3,4-ethylenedioxythiophene) (PEDOT) electrodes in both faces of the IPN film and swelling in an ionic liquid, a 20 μm thick conducting IPN actuator was obtained, which moved with large displacement at a 125 Hz fundamental frequency (Fig. 6).

A humidity-sensitive conducting polymer actuator made up of PEDOT doped with poly(4-styrenesulfonate) (PEDOT/PSS) was fabricated [47]. Water vapor sorption and electro-active actuating behavior of free-standing PEDOT/PSS films were investigated by sorption isotherm and electromechanical analyses. The non-porous PEDOT/PSS film, with a specific surface area of 0.13 $m^2\ g^{-1}$, sorbed water vapor of 1,080 $cm^3(STP)\ g^{-1}$, corresponding to 87 wt%, at relative water

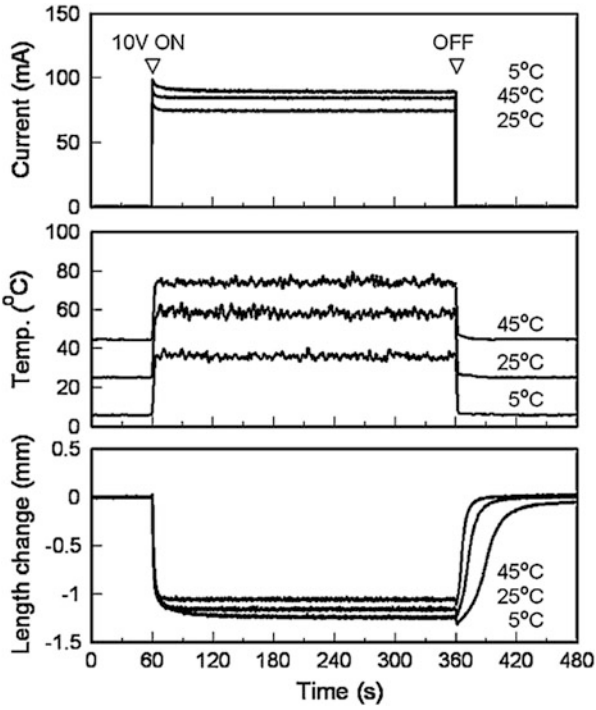

Fig. 7 Time profiles of electric current, surface temperature, and length change of PEDOT/PSS films (50 mm long, 2 mm wide, and 10 μm thick) under 10 V measured at 50% RH and various temperatures. Reproduced with permission from [47]

vapor pressure of 0.95. As temperature increased from 25°C to 40°C, the actuator exhibited a lower sorption degree, which is an indicator of an exothermic process. Isosteric heat of sorption decreased with increasing water vapor sorption and the value reached 43.9 kJ mol^{-1}, consistent with the heat of water condensation (44 kJ mol^{-1}). Upon application of 10 V, the film underwent 2.46% contraction at 5°C, which was caused by desorption of water vapor, and the contraction slightly decreased to 2.10% at 45°C (Fig. 7). The speed of contraction was an order of magnitude faster than that of expansion and less dependent on the temperature. This behavior is attributed to water vapor in the film desorbing at high temperature. In contrast, the higher the temperature the faster the film expansion because the diffusion coefficient at higher temperature is increased.

A series of strong and flexible polymer films were developed by combining both a rigid matrix (polypyrrole (PPy)) and a dynamic network (polyol-borate (PEE)) [16]. Upon water sorption and desorption, the borate ester of PPy can be hydrolyzed and reformed, which changes the mechanical properties of the composite at different humidity (Fig. 8). Intermolecular hydrogen bonding between the PEE network and PPy also modulates intermolecular packing of the polymer composite, altering its mechanical properties in response to water. The polymer composite exhibits fast, reversible, and dramatic mechanical deformation and recovery in response to environmental moisture, visually reminiscent of "fast twitch" muscle activity.

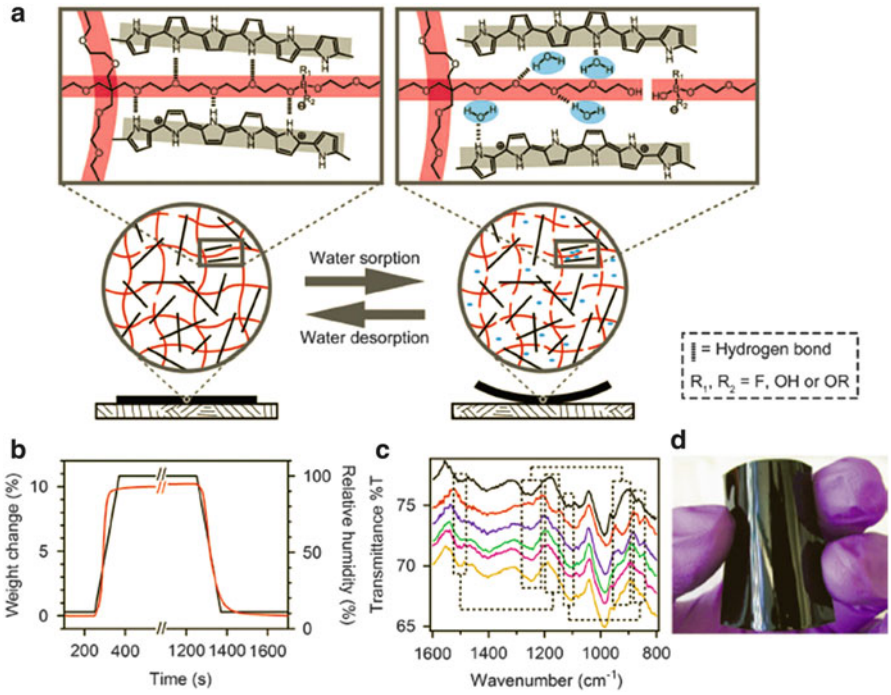

Fig. 8 Characterization of PEEPPy composite films. (**a**) A PEEPPy composite film (*black*) is composed of PPy polymer chains (*gray lines*) and a PEE-borate network (*red lines*). The structure changes (involving H bonds and borate ester bonds) in response to water (*blue dots*) sorption and desorption. (**b**) PEE-PPy weight change (*red*) synchronizes with air humidity change (*black*). (**c**) ATR-IR spectra showing H/D exchange between the PEE-PPy film and water vapor. *Top* to *bottom*: before D_2O exposure and 0, 1, 2, 3, and 4 min after D_2O exposure. *Dashed lines* indicate the three pairs of shifting peaks. (**d**) A PEE-PPy film maintains its flexibility and mirror-like surface after 6 months of open storage. Reproduced with permission from [48]

2.4 Liquid Crystal Elastomers

Liquid-crystalline polymers (LCPs) contain mesogens which are attached to the polymer backbones with uniform alignment. Once the molecular alignment of the mesogens is disordered by external stimuli such as heat [49] and/or electricity [50], LCPs show contraction along the mesogen's alignment direction. For example, UV light can cause photoisomerization of azobenzene moieties; the conformation change of azobenzene moieties causes the mesogens to become disordered. By incorporating azobenzene chromophores into LCPs using monofunctional (monomer) and difunctional (crosslinker) azobenzene monomers (Fig. 9), deformation can be induced upon irradiation with UV light [51].

Photoinduced motion of the 10 μm thick LCP films was examined as shown in Fig. 10. To irradiate the LCP films under the same experimental condition, part of the LCP film was covered with a glass substrate and irradiated from above. By irradiation with UV light at 240 mW cm^{-2}, LCP films with a high azobenzene

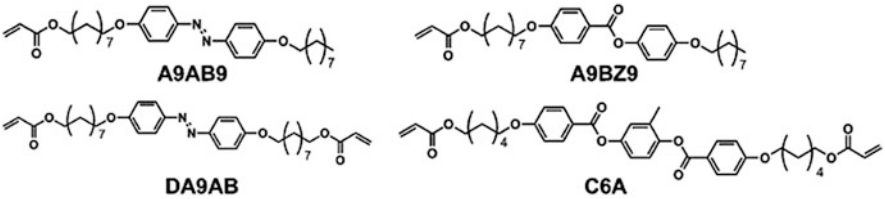

Fig. 9 Chemical structures of monofunctional (monomer) and difunctional (crosslinker) azobenzene monomers. Reproduced with permission from [51]

content (a46) bent beyond 90° toward the UV light source (Fig. 10B-a), while LCP films with a low azobenzene content (a42 and a20) are not capable of bending to such an extent (Fig. 10B-b). The high azobenzene content films reverted completely back to the initial flat conformation (Fig. 10B-c). The bending behavior is affected by the thickness of the film and UV light intensity. When 20 μm thick LCP films or UV light with low intensity (25 mW cm^{-2}) were used, the films did not exhibit such a "reverting motion." A plausible mechanism for the unbending behavior is the relaxation of the gradient of the deformation along the depth direction as described in Fig. 10c. Because the incident light penetrates deep areas from the surface of the film, photoinduced contraction occurs at the opposite side of the film and at the irradiated surface. Consequently, the bent films revert to the initial shape.

A plastic belt was prepared by connecting both ends of the LCP laminated film and then the belt was placed on a pulley system as illustrated in Fig. 11a [52]. By irradiating the belt with UV light from top right and visible light from top left simultaneously, a rotation of the belt was induced that drove the two pulleys in a counterclockwise direction at room temperature, as shown in Fig. 11b. A plausible mechanism of the rotation is as follows: Upon exposure to UV light, a local contraction force is generated at the irradiated part of the belt near the right pulley along the alignment direction of the azobenzene mesogens. This contraction force is parallel to the long axis of the belt and acts on the right pulley, leading it to rotate in the counterclockwise direction. At the same time, as the other side is irradiated by visible light, there is a local expansion force at the irradiated part of the belt near the left pulley. That causes a counterclockwise rotation of the left pulley. These contraction and expansion forces generated simultaneously at the different parts along the long axis of the belt give rise to rotation of the pulleys and belt in the same direction. The rotation then brings new parts of the belt to be exposed to UV and to visible light, which enables the motor system to rotate continuously.

3 Self-Healing Polymers

Self-healing polymers are defined as polymeric materials capable of reforming bonds, and healing, in response to damage [53]. This research is driven by the vision that, in the future, damaged materials may not have to be replaced so often,

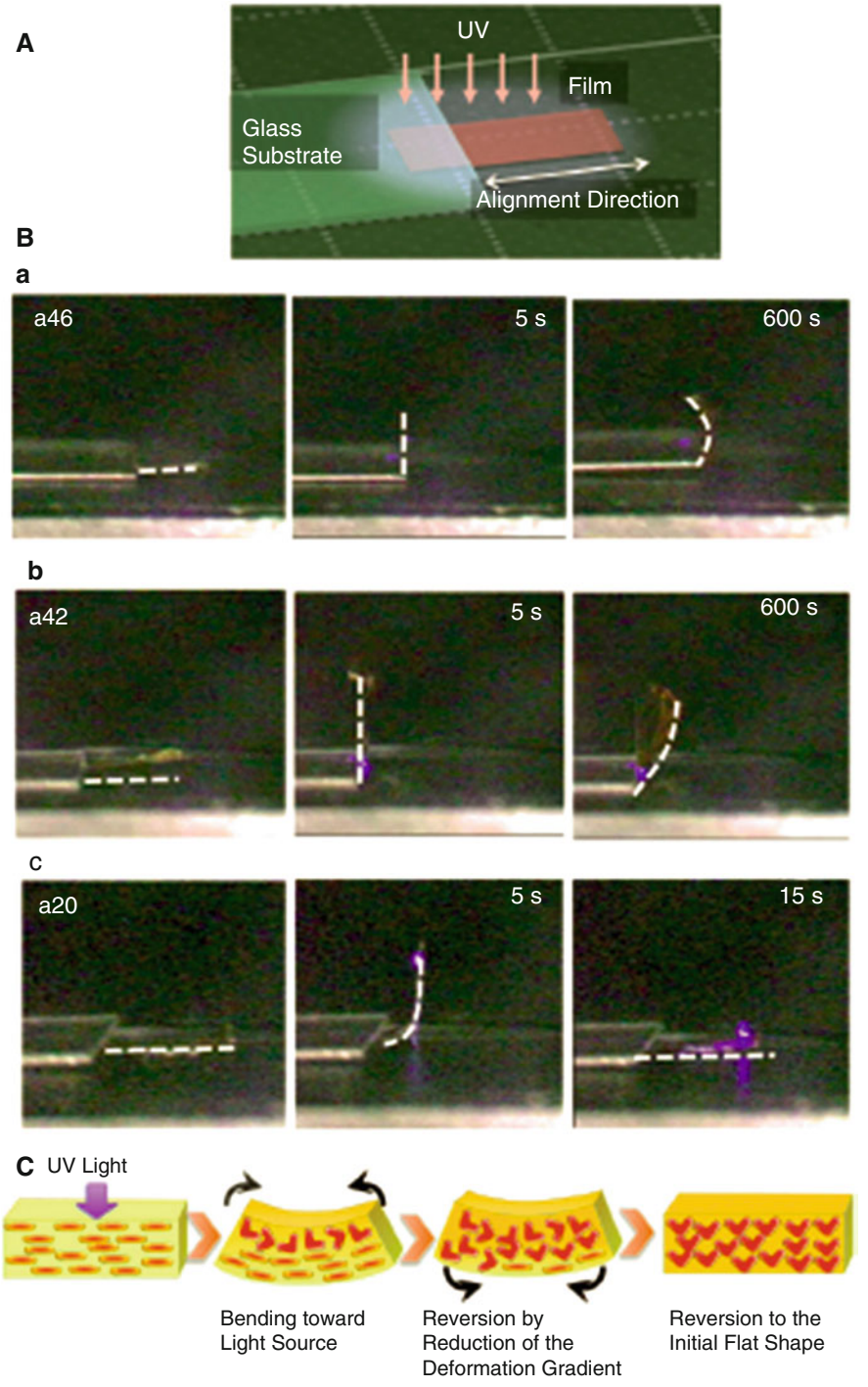

Fig. 10 Schematic illustration of the experimental setup (**A**), photographs of LCP films exhibiting photoinduced deformation (**B**), and schematic illustrations of the photoinduced deformation

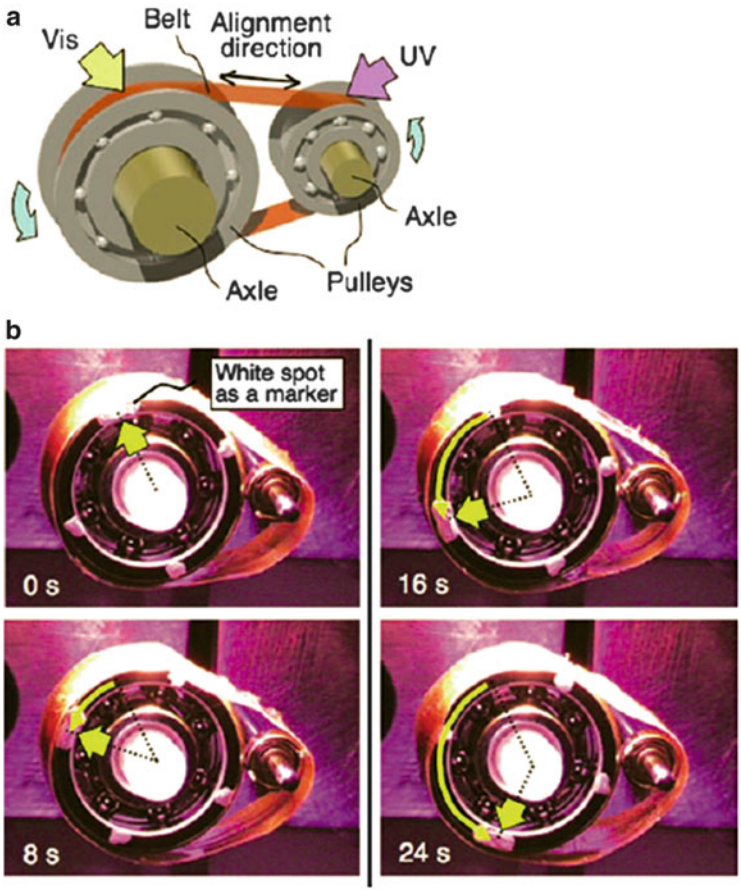

Fig. 11 (**a**) Schematic illustration of a light-driven plastic motor system used in this study, showing the relationship between light irradiation positions and a rotation direction. (**b**) Series of photographs showing time profiles of the rotation of the light-driven plastic motor with the LCP laminated film induced by simultaneous irradiation with UV (366 nm, 240 mW cm^{-2}) and visible light (>500 nm, 120 mW cm^{-2}) at room temperature. Diameter of pulleys: 10 mm (*left*), 3 mm (*right*). Size of the belt: 36 × 5.5 mm. Thickness of the layers of the belt: PE, 50 μm; LCE, 18 μm. Reproduced with permission from [52]

Fig. 10 (continued) mechanism (flat shape: film before UV irradiation; *yellow*: film; *red*: mesogens) (**C**). The series of photographs in (**B**) show the motion of LCP films by irradiation with UV light (366 nm, 240 mW cm^{-2}) at room temperature: the first frame, before irradiation; the second frame, after irradiation for 5 s; the third frame, after continuous irradiation with UV light. The films showed different photoinduced deformation: (*a*) bending alone; (*b*) partly unbending after bending by 90°; (*c*) completely unbending. Size of the film: 2 × 3 mm × 10 μm. The *white dashed line* in the photographs describes the edges of the film. Reproduced with permission from [51]

which would result in cost and efficiency savings in many applications. Work in this area is diverse, ranging from airplane and automotive part manufacturing to computer circuit board generation and the development of high quality lubricants [53]. Reversible systems have been based on either covalent bonds or non-covalent interactions such as hydrogen bonding or π–π stacking [53]. The rational design of self-healing materials is based on the interaction of chemical functionalities with various forms of input energy/stimulus [54–56].

3.1 *Thermoresponsive Cycloaddition-Based Polymeric Smart Materials*

Diels–Alder (DA) cycloadditions are one convenient route for the formation of carbon–carbon bonds via a facile reaction under undemanding conditions [57]. As a thermoreversible reaction, DA cycloaddition does not require the addition of chemicals/catalyst to promote reaction [58]. This property makes it an ideal reaction for the synthesis of self-healing polymers.

Functionalization of polymer chains with the chemical groups (furan and maleimide) is a convenient approach to prepare DA-adduct based crosslinked networks. Furan- (PA-F) and maleimide- (PA-MI) modified polyamides have been prepared for the construction of crosslinked polyamides (Fig. 12)

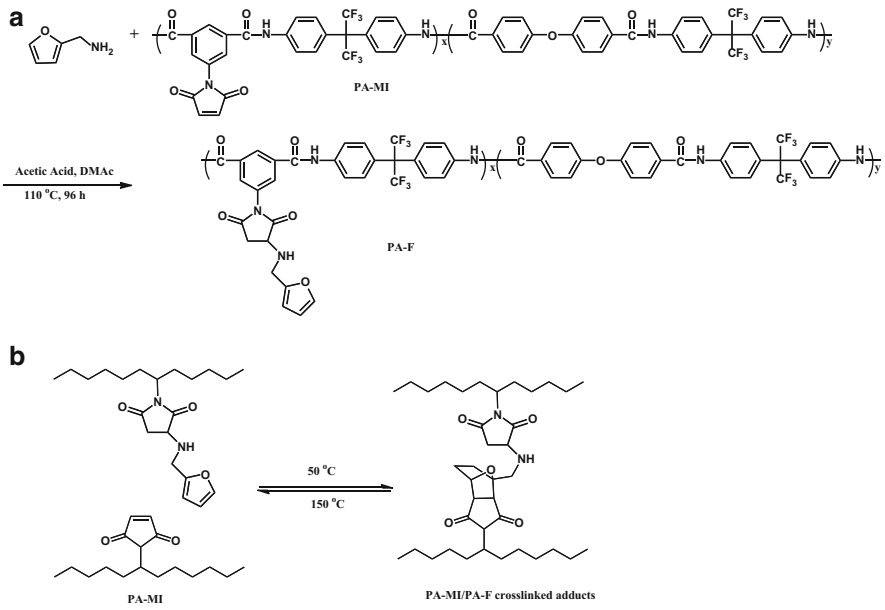

Fig. 12 (**a**) Preparation of furan-containing polyamides PA-F. (**b**) Thermally reversible crosslinking reactions between PA-MI and PA-F. Reproduced with permission from [59]

[59]. PA-MI/PA-F cross-linked polymers showed thermally reversible crosslinking behavior via DA and retro-DA reactions. Cross-linked PA-MI/PA-F films exhibited enhanced toughness and mechanical properties over PA-MI and PA-F precursors. Moreover, PA-MI/PA-F films also showed excellent thermal self-repairing behavior.

However, the number of suitable DA pairings which can be cycled in a reasonable temperature range (i.e., below the materials' degradation temperature) are scarce. To date, only a few DA systems are used in self-healing materials with cyclability at mild temperatures within reasonable times. To address this limitation, a reversible system based on hetero Diels–Alder (HDA) reactions, utilizing acid activated dithioesters as dienophiles and cyclopentadiene (Cp), has been developed (Fig. 13) [60]. A novel self-healing material was prepared using a cyanodithioester (CDTE) compound/Cp HDA pair. By employing CDTE/Cp multifunctional building blocks, healing can be achieved in a very short time (5 min) at relatively low temperatures (120°C).

In another example, mechanical force can induce chain cleavage of perfluorocyclobutane (PFCB), shown in Fig. 14, generating trifluorovinyl esters (TFVE), which are also reformed by cycloreversion [61]. The chain cleavage proceeds via a stepwise mechanism with 1,4-diradical intermediates. This thermal remending is similar to that of other DA chain scission mechanisms, but is shown here to proceed through a reactive intermediate which can participate in intermolecular radical addition reactions.

3.2 Dynamic Covalent Bonds

Another class of reactions utilized in self-healing involves covalent bonding capable of chain exchange reactions, as shown in Fig. 15 [62]. Dynamic acylhydrazone bonds were first utilized in a crosslinked self-healing network by condensation reactions of acylhydrazines of polyethylene oxide (PEO) and aldehyde groups of tris[(4-formylphenoxy)methyl]ethane [63]. Taking advantage of the equilibrium acylhydrazone bond formation, as shown in Fig. 15a, these networks exhibit self-healing properties under ambient conditions.

Trithiocarbonates (TTC) also offer an interesting alternative platform by dynamic covalent reshuffling reactions of TTC via a free radical mechanism shown in Fig. 15b. It was first introduced into poly(methyl methacrylate) (PMMA) and polystyrene (PS) gels as a covalent crosslinker, which exhibited dynamic properties [64]. Following this, it was found that the C–S bonds of TTC can be photostimulated, and high segmental mobility of the polymer matrix obtained by RAFT copolymerization of *n*-butyl acrylate (BA) and a TTC crosslinker can facilitate repetitive network repairs using UV radiation at 330 nm [64].

Disulfide bonds can also undergo metathesis exchange reactions in which two neighboring S–S bonds can be disrupted and reformed through free radical or ionic

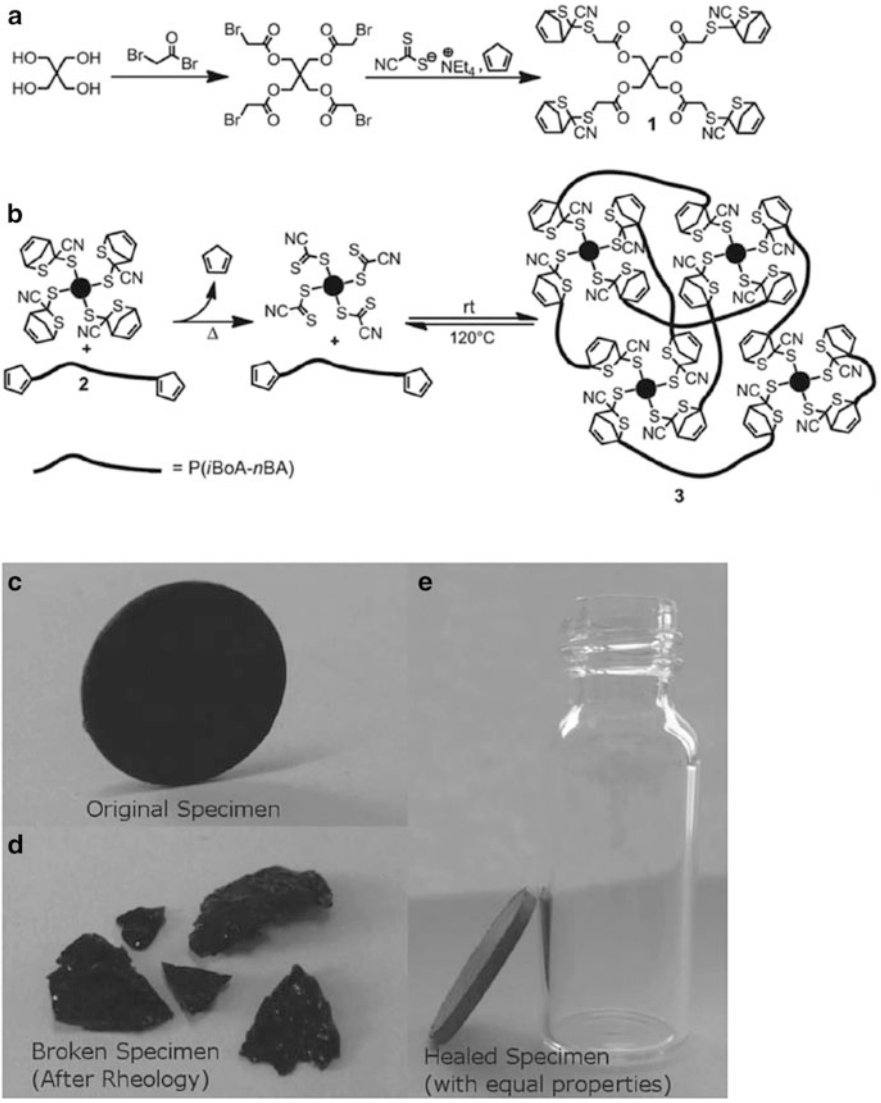

Fig. 13 (**a**) Reaction scheme for the preparation of the CDTE based tetra-linker **1**. (**b**) Network formation of **3** via DA/rDA chemistry during the deprotection reaction and the cycling process. (**c**) Pressed pellet of **3**. (**d**) Broken specimen after rheology experiments. (**e**) Healed specimen with identical mechanical properties as the original one. Reproduced with permission from [60]

intermediates (Fig. 15c) [65]. The reversibility of S–S bonds can be achieved by reduction reactions to form two thiol (S–H) groups which can be reversed by oxidation. Once S–S bonds are incorporated into low glass transition temperature (T_g) gel networks, room-temperature bond interchange is possible. Poly(*n*-butyl acrylate) grafted star polymers were prepared by chain extension atom transfer

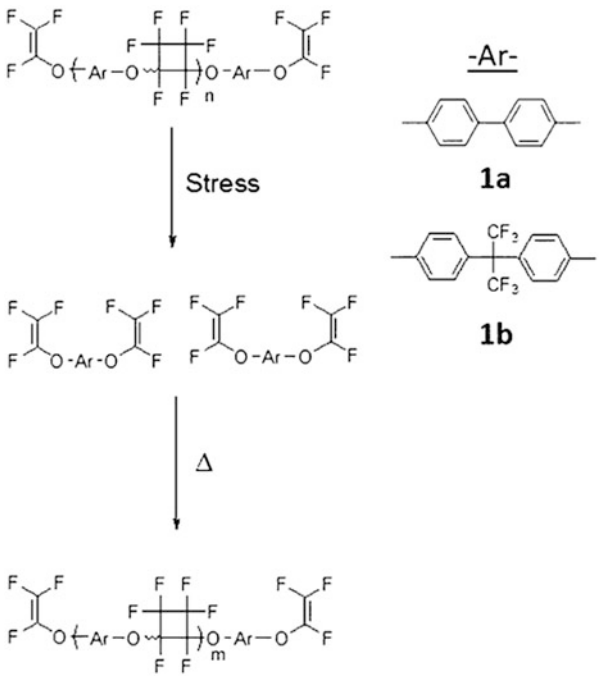

Fig. 14 Mechanical chain scission in PFCB polymers generates trifluorovinyl ether end groups that can be repolymerized thermally. Reproduced with permission from [61]

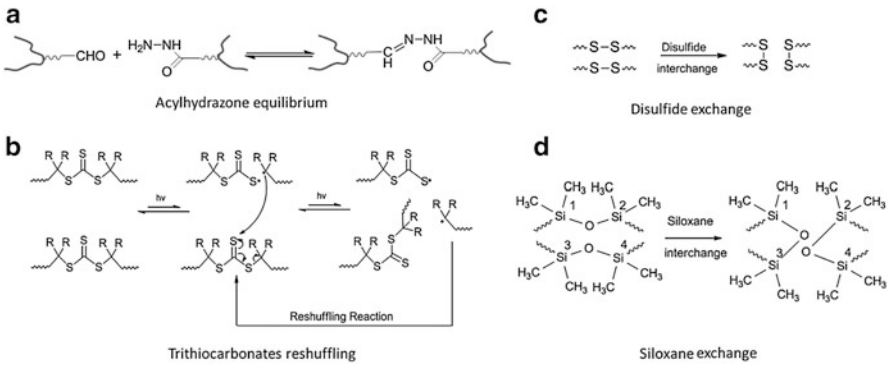

Fig. 15 Self-healing via covalent bond reformation using chain exchange reactions: (**a**) acylhydrazone equilibrium; (**b**) reshuffling reaction of trithiocarbonates (TTC); (**c**) disulfide chain exchange; (**d**) siloxane chain exchange. Reproduced with permission from [62]

radical polymerization (ATRP) from cross-linked cores. The cross-linked core is comprised of poly(ethylene glycol diacrylate), which was further utilized as macroinitiator for the consecutive chain extension of bis(2-methacryloyloxyethyl disulfide) [66]. This approach introduces disulfide (S–S) reversible crosslinks into

the branch peripheries of crosslinked star copolymers. It can be self-repaired by oxidation/reduction equilibrium between S–H and S–S at ambient temperature. When thiuram disulfide was incorporated into low T_g polyurethane networks, repair could be accomplished using visible light under ambient conditions via radical exchange reactions [67].

Silicone-based materials have been known for their ability to restructure under certain conditions [68]. Recently, tetramethylammonium silanolate-initiated ring-opening copolymerization of octamethylcyclotetrasiloxane (D4) and bis (heptamethylcyclotetrasiloxanyl) ethane (bis-D4) showed that these crosslinked polymers with ethylene bridges and active silanolate end groups are able to be restructured [69]. Figure 15d depicts siloxane interchange reactions, which maintain their activity under ambient conditions, thus providing "ready-to-respond" active groups.

3.3 Hydrogen Bonding

Taking advantage of high segmental mobility, low T_g self-healing materials were also reported utilizing hydrogen bonding-like attributes as a function of temperature or pH [70]. Self-healing supramolecular plastics were prepared by oligocondensation of a mixture of fatty mono-, di-, and triacids with diethylenetriamine (DETA) (Fig. 16) [71]. The molecular weight and the degree of branching of the backbones can be controlled and adjusted by selection of the ratio of di- and triacids to 2-aminoethylimidazolidone (UDETA), which plays the role of a self-complementary hydrogen bonding moiety. Additional complementary hydrogen bonding units are introduced by grafting urea onto all secondary amines of DETA. At room temperature they behave as viscoelastic melts. The highest molecular weight materials, where the mechanical relaxation time is particularly long, behave

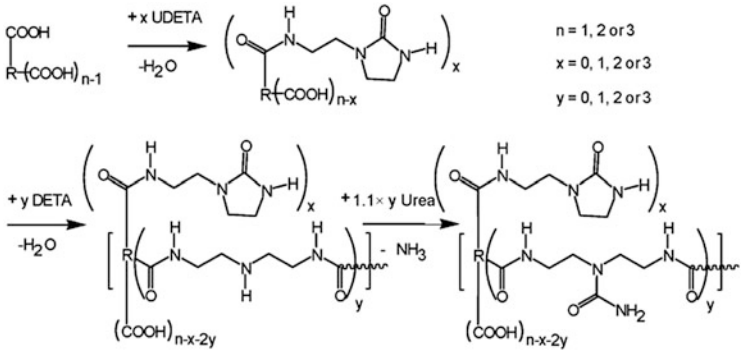

Fig. 16 Synthesis of supramolecular plastics in three steps. Fatty acids: *n* avg 2.03. (1) aminoethyl imidazolidone (UDETA), (2) diethylenetriamine (DETA), (3) urea. Branching is shown in *parentheses*; *brackets* indicate polymers. Reproduced with permission from [71]

as supramolecular self-healing rubbers: they can be reversibly extended several times their initial size with little creep under stress, and when cut and put together, they self-repair.

Self-healing poly(butyl acrylate) (PBA) copolymers containing comonomers with 2-ureido-4[1*H*]-pyrimidinone quadruple hydrogen bonding groups (UPy) were prepared (Fig. 17) [72]. The adhesion strengths of PBA–UPy polymers depend on the UPy content, contact time, temperature and humidity level. The increase of adhesion strengths is attributed to the strong UPy–UPy hydrogen bonding interactions. Fractured PBA–UPy films can fully recover their self-adhesion strength to 40, 81, and 100% in 10 s, 3 h, and 50 h, respectively, under almost zero external loads.

Dimethylnorbornene ester (DNE) has been used as a cohealing agent, which copolymerizes with dicyclopentadiene (DCPD). DCPD can form a hydrogen bond with an epoxy matrix (Fig. 18) [73]. Dimethylphthalate (DMP) is structurally

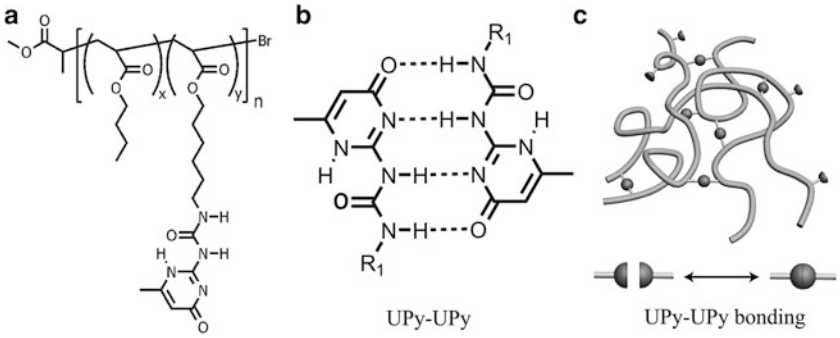

Fig. 17 Schematic of (**a**) the chemical structure of P(nBA- *r* -UPy), (**b**) hydrogen bonds between two UPy groups, and (**c**) polymer chains functionalized with UPy groups. Reproduced with permission from [72]

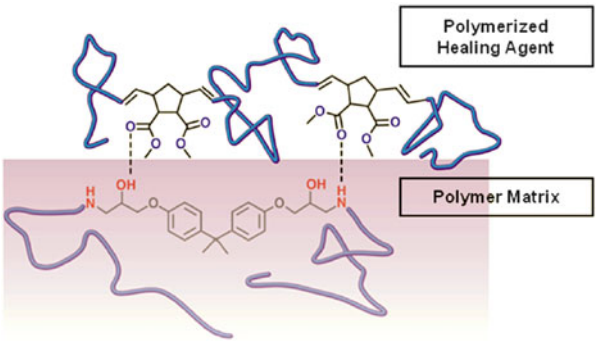

Fig. 18 Schematic of noncovalent adhesion promotion in a self-healing system. The polymer formed in the crack plane contains hydrogen-bond-donating groups that interact with hydrogen-bond-accepting groups present in the epoxy matrix. Reproduced with permission from [73]

similar to DNE because it contains ester groups capable of hydrogen bonding with an epoxy matrix. An optimized blend of the monomers was encapsulated using a urea-formaldehyde microencapsulation procedure, and the resulting capsules were used for in situ self-healing experiments. Improved healing efficiency was observed for samples containing the DCPD/DNE capsules.

3.4 Metal–Ligand Coordination

Because of their optical and photophysical properties, metal complexes offer many advantages compared to other systems [74]. Reversibility and tunability by incorporating different metal ion and ligand substituents make coordination chemistry particularly attractive.

A series of metallosupramolecular polymers have been reported, comprising an amorphous poly(ethylene-*co*-butylene) core with 2,6-bis(19-methylbenzimidazolyl) pyridine ligands at the termini that coordinated metal ions through ligand binding (Fig. 19). These polymers can be mended by exposure to light [75]. Upon exposure to ultraviolet light, the metal–ligand motifs are electronically

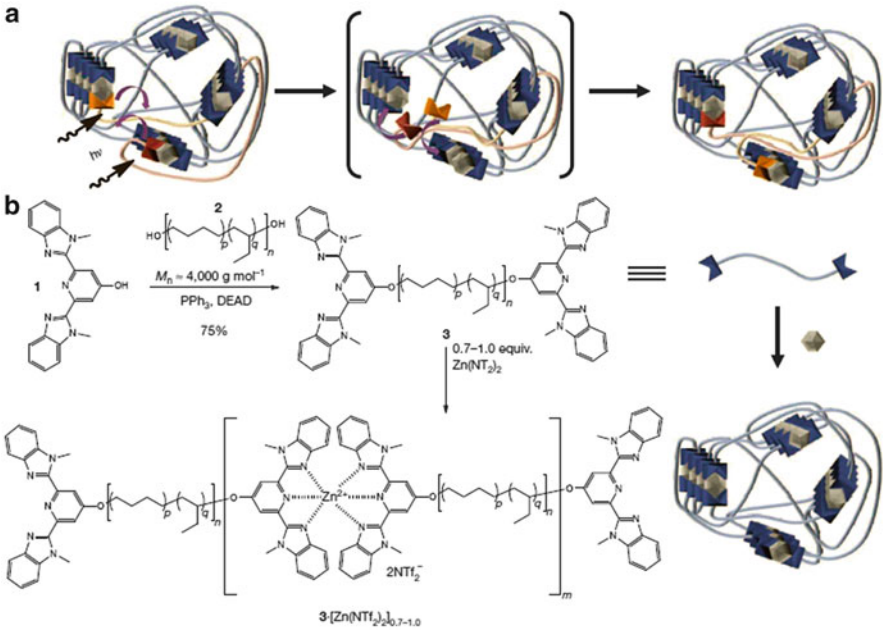

Fig. 19 Mechanism and synthesis of photohealable metallosupramolecular polymers. (**a**) Proposed optical healing of a metallosupramolecular, phase separated network. (**b**) Synthesis of macromonomer 3 and polymerization by addition of $Zn(NTf_2)_2$. DEAD, diethyl azodicarboxylate. Reproduced with permission from [75]

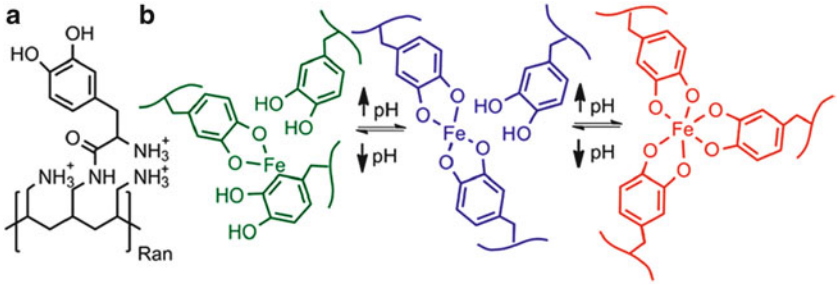

Fig. 20 (**a**) DOPA was randomly grafted onto polyallylamine. There are several pH responsive parts of the polymer. The amine side chain itself is involved in an acid/base equilibrium with a pK_a around 9.3–9.7, which has been determined by potentiometric titrations. (**b**) Furthermore, the catechol can be oxidized to the quinone form or it can be cross-linked by Fe^{III} in the pH-dependent manner. Reproduced with permission from [77]

excited and the absorbed energy is converted into heat. It caused temporary disengagement of the metal–ligand motifs and a concomitant reversible decrease in the polymers' molecular mass as well as viscosity, thereby allowing healing of mechanical damage.

There is increasing evidence that metal–ligand coordination plays an important role in the dynamics of biological rearrangements. Molecular engines that generate mechanical energy can be powered by chemical processes, resulting in swelling and shrinking of macromolecular segments caused by metal–ligand interactions. Recent studies took advantage of coordination between Fe^{3+} and catechol ligands, which resulted in pH-induced crosslinked self-healing polymer with near-covalent elastic moduli [76]. By attaching dopamine (DOPA) to an amine-functionalized polymer, a multiresponsive system is formed upon reaction with iron (Fig. 20) [77]. The degree of polymer crosslinking is pH controlled through the pH-dependent DOPA/iron coordination chemistry. That is, when the solution is made more basic, the hydrogels can self-heal. Close to the pK_a value, or more precisely the pI (isoelectric point) value, of the polymer, the gel collapses because of reduced repulsion between polymer chains. Thereby a bistable gel-system is obtained. The polymer system closely resembles mussel adhesive proteins and thus also serves as a model system for mussel adhesive chemistry.

3.5 π–π Stacking Interactions

π–π stacking interactions were utilized in the development of thermally triggered reversible self-healing supramolecular polymer networks. This was achieved using end-capped π-electron-deficient groups which interacted with other π-electron-rich aromatic molecules [78]. Upon heating, the π–π stacking interactions were interrupted, enabling π-electron-rich aromatic molecules to disengage from

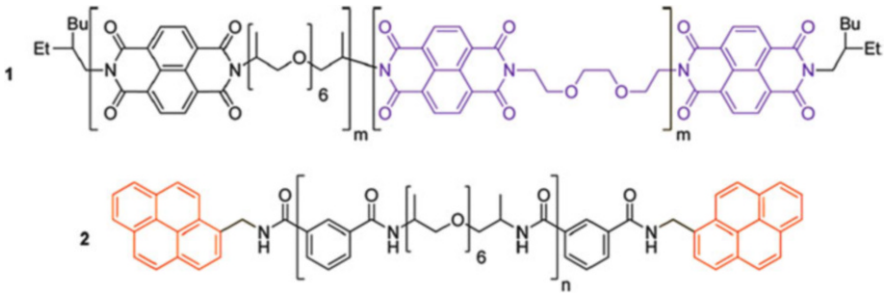

Fig. 21 Molecular structure of healing polymer blend 1 · 2 (1:3 w/w ratio). Reproduced with permission from [80]

π-electron-deficient groups and flow because of the presence of a flexible "soft" spacer [79]. Thus, repair of damage and restoration of mechanical strength was achieved by reformation of π–π stacking.

A supramolecular healable polymer blend was formed via π–π interactions, which is comprised of a π-electron-rich pyrenyl end-capped oligomer and a chain-folding oligomer containing pairs of π-electron poor naphthalene-diimide (NDI) units as well as cellulose nanocrystals (CNCs) for reinforcement (Fig. 21) [80]. All the nanocomposites could be rehealed upon exposure to elevated temperatures. It was found that the healing rate was reduced with increasing CNC content. The best combination of healing efficiency and mechanical properties was obtained with the 7.5 wt% CNC nanocomposite. It exhibited a tensile modulus enhanced by as much as a factor of 20 over the matrix material alone and could be fully rehealed at 85°C within 30 min. Thus it is demonstrated that supramolecular nanocomposites can afford greatly enhanced mechanical properties over the unreinforced polymer, while still keeping efficient thermal healing.

4 Mechanotransducing Sensors

"Sensor" is derived from the Latin word "sensus", which directly translated means "sense," or to "sense something." When one thinks of "sensing," we can turn to the basic five human senses: sight, hearing, taste, smell, and touch. These senses allow the human body to receive signals or sense stimuli from the environment and react or respond to them [81]. If a sense gives the ability to receive and respond to a signal, we can transfer this to the technical level and define a sensor as: "A device that receives and responds to signals and stimuli from the environment". There has been a consistent increase in research output related to the development and application of optical chemical sensors in the late twentieth century. The development of novel molecular sensors capable of detecting environmental changes (temperature, pH, concentration of enzyme or ionic species, etc.) has been pursued

in medical, biological, and environmental applications [9, 82]. In this section, we highlight pH sensors, chemical sensors, and biosensors.

4.1 Mechanotransducing pH Sensors

pH is a key parameter to measure for a broad range of applications, e.g., in life sciences, food and beverage processing, soil examination, and marine and pharmaceutical research to name a few. The development of an optical pH sensor, which can be used in real world applications, is not trivial. pH-sensitive hydrogels can be weakly acidic or weakly basic, depending on the nature of the ionizable moieties on the polymer backbone. Therefore, charges can be generated on the polymer backbone in a pH-dependent fashion. The charges formed on the polymer backbone at certain pHs yields the polymer response caused by electrostatic interactions and osmotic pressure effects [83].

In one example, a poly(acrylic acid-*co*-isooctyl acrylate) hydrogel was coupled with a magnetoelastic sensor, the resonance frequency of which corresponds with applied mass load [84]. The gels were found to respond rapidly to changes in solution pH, reversible swelling and shrinking, leading to mass changes; the mass changes can be detected as a shift in the resonance frequency of the sensor (Fig. 22). The response of the pH sensor is accurately fitted using the equation $\mathrm{fr} = 49.891 - 1.04\ \mathrm{pH} + 0.048\ \mathrm{pH2}$. The average change in sensor resonance

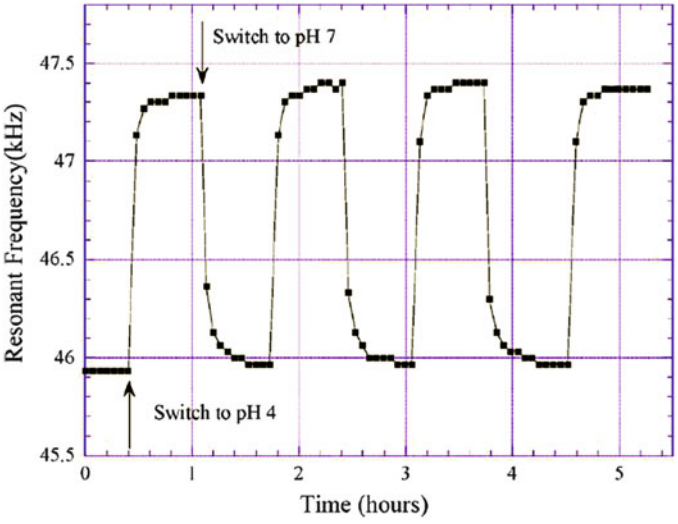

Fig. 22 Resonance frequency of the pH sensor, as it is repeatedly cycled between pH 4.03 and 7.02 solutions. The pH-sensitive polymer layer is approximately 1.36 μm thick. Reproduced with permission from [84]

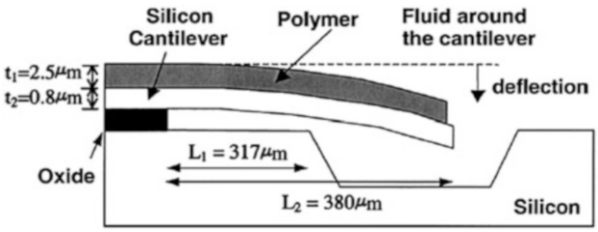

Fig. 23 Schematic of the cantilever/polymer structure with associated dimensions. Reproduced with permission from [85]

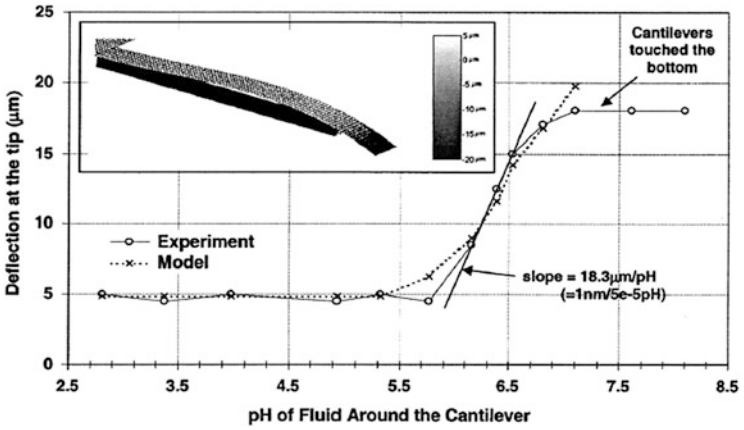

Fig. 24 Equilibrium cantilever deflection as a function of solution pH. The *solid line* is experimental results and a sensitivity of 5×10^{-5} pH for a 10 nm bending deflection resolution can be obtained. The *dotted line* is obtained with the cantilever and polymer modeled as a composite beam with no slip at the boundary. Small deflections with respect to the length are assumed. Polymer elastic modulus of 85 MPa is used to fit the model to experiments. The *inset* shows a three-dimensional plot of the deflection of the cantilever/polymer at pH 7.0, obtained from the model. Reproduced with permission from [85]

frequency is 506 Hz/pH, approximately 1%/pH of the resonance frequency value, from pH 4.4 to 8.5.

A pH sensor with ultrahigh sensitivity could be fabricated using microcantilever-based technology (Fig. 23) [85]. Silicon-on-insulator wafers were used to fabricate cantilevers on which a polymer consisting of poly(methacrylic acid-*co*-ethylene glycol) was patterned using UV-initiated free-radical polymerization. When the pH around the cantilever was increased above the pK_a of poly(methacrylic acid), negative charges were formed in the polymer network, which resulted in its expansion and caused the microcantilever to bend. Excellent mechanical amplification of polymer swelling as a function of pH change within the dynamic range was obtained, with a maximum deflection sensitivity of 1 nm/5×10^{-5} $\triangle$pH [85].

At low pH, the cantilever is bent downwards as the hydrogel is swollen because of the liquid around it, when compared to the dry state. As the pH is increased above

5.7, the polymer swells rapidly and eventually the cantilever touches the bottom of the well. Between pHs of about 5.9 and 6.5 (dynamic range of the sensor), the slope of the deflection at the tip vs pH curve, and hence the sensitivity, is maximum at about 18.3 μm/pH (Fig. 24). If a laser-based deflection measurement system is used, such as the one used in conventional atomic force microscope, where deflections of 1 nm can easily be detected, the above number translates to a sensitivity of 5×10^{-5} pH for a 1-nm bending detection resolution. These sensitivities are among the highest reported for any micro-scale pH detectors.

The color changes of some sensors can be detected by the naked eye, making them especially useful and inexpensive. One unique class of materials is obtained from the self-assembly of colloidal particles to form crystalline arrays (CCA) [86]. These arrays exhibit bright, visible colors similar to the opal gemstone, which can be "locked" into place by polymerization of a hydrogel into the interstices of the array to form a soft photonic material which possess the volume-phase transition phenomenon of polymer gels [87]. Specifically, when light impinges on the periodic structure, it is reflected/refracted/diffracted from each interface formed by the particles. This light, under suitable conditions, interferes constructively/destructively and reflects/transmits certain wavelengths of light according to the well-known Bragg condition, modified for the photonic crystals, given by [88–91]

$$m\lambda = 2\, n\, d \quad \sin \quad \theta, \tag{1}$$

where m is the diffraction order, λ the wavelength of the reflected light, n the mean refractive index of the periodic structure, d the lattice period of the crystalline direction of propagation of light, and θ the angle between the incident light and diffraction crystal planes.

The pH-dependent volume-phase transitions of a hydrogel network surrounding a CCA could be monitored using Bragg diffraction/color [92]. The pH-dependent charges on the polymer network induce the polymer to change volume, and hence size. The hydrogel size changes yield a change in the lattice spacing of the CCA, and a concomitant color change. The Young's modulus of the hydrogel could be determined from the CCA hydrogel Bragg diffraction to determine the elastic restoring forces [93]. They describe a detailed hydrogel volume-phase model, which accurately models swelling with no adjustable parameters. Finally, the results demonstrate that carboxylated CCA photonic crystals are excellent pH and ionic strength sensors.

Poly(hydroxyethyl methacrylate)-based photonic materials were also prepared and used as a pH sensor [94]. To accomplish this, the surface of monodisperse silica particles was coated with a thin layer of polystyrene. Surface charge groups were attached by a grafting polymerization of styrene sulfonate. The resulting highly charged monodisperse silica particles were self-assembled into a CCA in deionized water. Polymerization of hydroxyethyl methacrylate (HEMA) occurred around the CCA to form a HEMA-CCA. Hydrofluoric acid was utilized to etch out the silica particles to produce a three-dimensional periodic array of voids in the HEMA-CCA. The authors also fabricated a CCA by utilizing a second polymerization to incorporate carboxyl groups into the HEMA CCA. They were also able to model

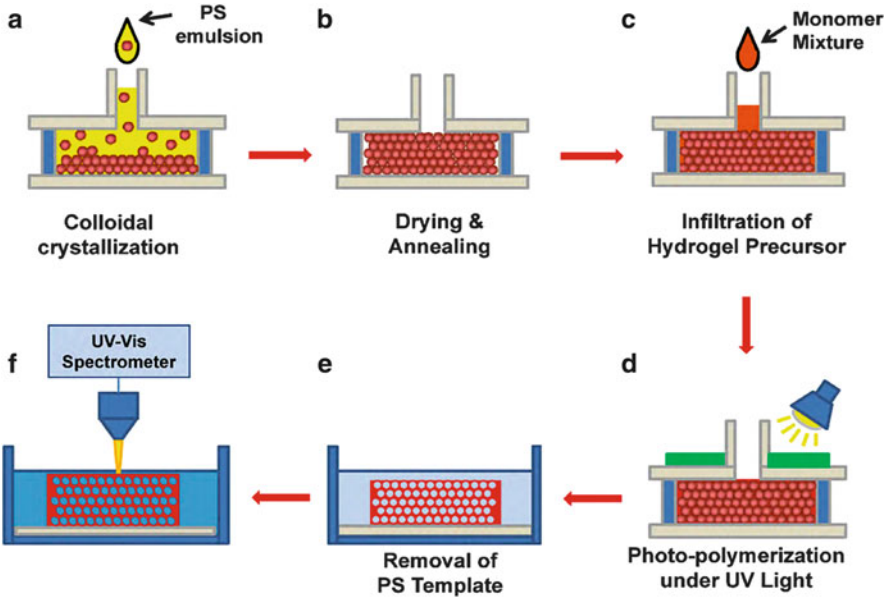

Fig. 25 Schematic illustration of experimental procedures. Reproduced with permission from [96]

the pH dependence of diffraction of the HEMA-CCA by using Flory theory. An unusual feature of the pH response is a hysteresis in response to titration to higher or lower pH. The kinetics of equilibration is very slow because of the ultralow diffusion constant of protons in the carboxylated CCA as predicted earlier by the Tanaka group [95].

In spite of its simplicity, the long response time of the hydrogel photonic crystal materials has limited their utility as sensors. This is because of the slow diffusion of analytes in the hydrogel to influence the optical properties. New fabrication procedures of these hydrogel photonic crystal sensors were used to improve the response time. The Lee Group [96] demonstrated a mechanically robust and fast responsive photonic crystal pH sensor, which was fabricated by templated photopolymerization of hydrogel monomers within the interstitial space of a self-assembled colloidal photonic crystal, as shown in Fig. 25.

By optimization of photopolymerization conditions, these pH sensors show a response time of less than 10 s upon a pH change. The fast response behavior is a result of the void spaces in the structure. Most of the ionic species are expected to diffuse rapidly through the voids, and then into the hydrogel, resulting in an aqueous diffusion limited response time. Experiments revealed that the device's response was reproducible over many cycles, and the response was consistent for $>$6 months. Mangeney's group made a novel photonic crystal pH sensor for fast pH response by incorporating a planar defect inside the photonic crystals, as shown in Fig. 26a [97]. Figure 26b shows the typical SEM images of the used colloidal-

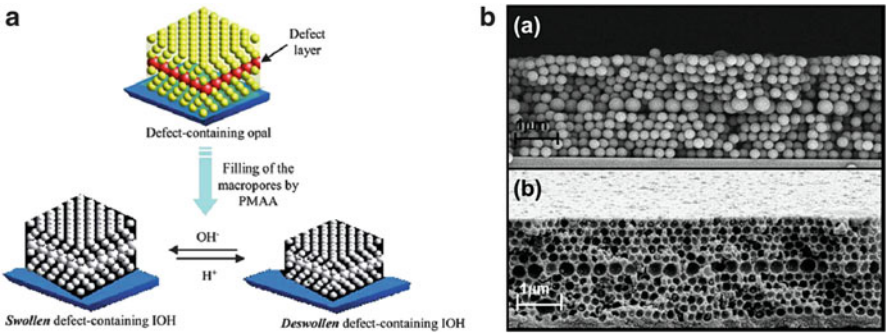

Fig. 26 (**a**) Schematic illustration of the defect-containing direct opal and inverse opal hydrogel (IOH) films. (**b**) SEM images of (**a**) the colloidal-crystal template with embedded planar defect layer of larger particles and (**b**) the resulting inverse opal hydrogel film with a defect layer of larger macropores. The resulting materials consists of a three-dimensional, highly-ordered, and interconnected macroporous array of poly(methacrylic acid) which is sensitive to pH. Reproduced with permission from [97]

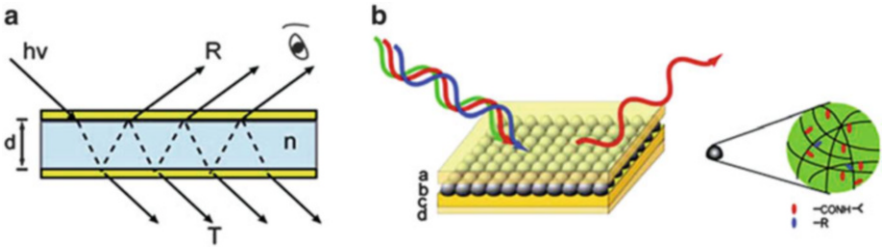

Fig. 27 (**a**) Schematic of a traditional Fabry-Perot etalon (d, distance between two mirrors; n, refractive index of the dielectric). (**b**) Schematic structure and proposed mechanism for our poly (*N*-isopropylacrylamide) microgel based etalons fabricated by sandwiching (b) a microgel layer between (a, c) two reflective Cr/Au surfaces, all on (d) a cover glass. Reproduced with permission from [102]

crystal template with an embedded planar defect layer and the resultant photonic polymer hydrogel films.

The Serpe group recently reported on structures that are colored, and their color is capable of changing in response to stimuli [98–101]. These materials were constructed by "painting" temperature and pH responsive poly(*N*-isopropylacrylamide)-*co*-acrylic acid (pNIPAm-*co*-AAc) microgels onto an Au coated glass substrate [99]. Following further treatment, another Au layer is deposited onto the microgel layer. As can be seen in Fig. 27 [102], this yields a mirror–dielectric–mirror structure akin to a classic Fabry–Perot etalon. When the device was immersed in water, the pNIPAm-*co*-AAc microgels swell and separate the Au layers from one another. Light impinging on the structure scan enter the microgel-based cavity and resonate between the two Au layers, which results in

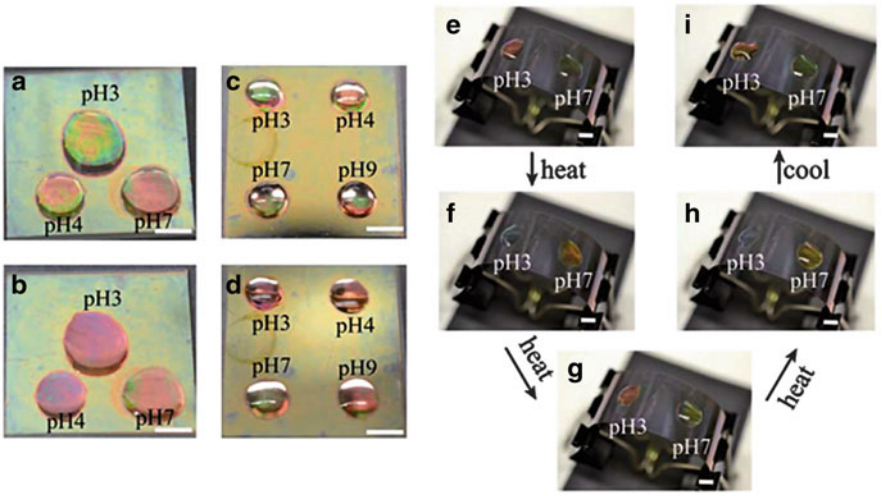

Fig. 28 Photographs of an etalon with solutions of various pH spotted on a single surface (**a**, **c**, **e**, **i**) 25°C and (**b**, **d**, **f**, **g**, **h**) 37°C. (**f**) 3 min after heating; (**g**) 5 min after heating; (**h**) 6 min after heating. In each panel, the *scale bar* is 5 mm. Reproduced with permission from [102]

specific wavelengths of light being reflected/transmitted according to the following equation:

$$m\lambda = 2\, n\, d\, \cos\ \theta, \tag{2}$$

where λ is the wavelength maximum of the peak(s), m is the peak order, n is the refractive index of the dielectric, d is the spacing between the mirrors, and θ is the angle of incidence [98, 103].

Once AAc groups are deprotonated in high pH solution, the microgel layer swells because of Coulombic repulsion in the microgels [102]. Figure 28 shows the visual color change which can be observed as a function of pH, as well as the fact that different regions on a single device can be modulated independently, which could have implications for display device technology [102].

Förster resonance energy transfer (FRET) is a promising method for sensing at a molecular level where FRET is generally referred to as an energy transfer between fluorescent donor and acceptor [104]. Because the efficiency of FRET is very sensitive to the distance between FRET donor and acceptor, FRET has been traditionally used for monitoring single molecular events such as the conformational transition of macromolecules by labeling fluorophores at specific sites [105]. A polymeric pH sensor with a FRET donor and a FRET acceptor attached to both ends of a pH-sensitive polymeric linker has been reported [106]. The pH sensor exhibits a blue color corresponding to the emission of the FRET donor at pHs higher than 7.6, but the pH sensor emits green light when the pH is lower than 6.8. This is a direct result of FRET, induced by the conformational change of polymeric linker bringing the FRET pair together (Fig. 29).

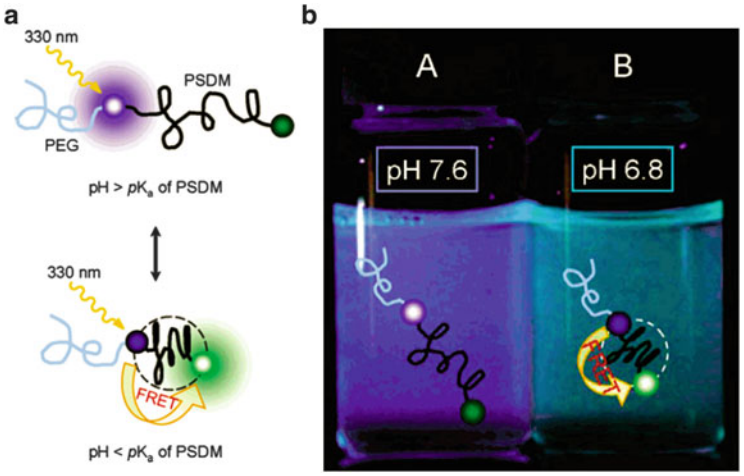

Fig. 29 (**a**) Diagrammatic representation of the induced FRET triggered by pH. (**b**) Fluorescence images of solutions at (*A*) pH 7.6 and (*B*) pH 6.8 when the solutions are irradiated at 330 nm. Both solutions have a concentration of 2.0×10^{-2} g/L. Reproduced with permission from [106]

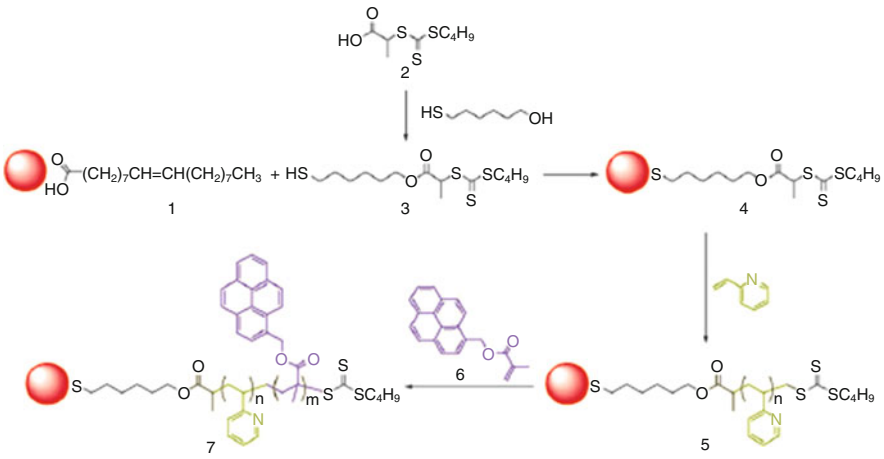

Fig. 30 Synthesis of (PyMMP-*b*-P2VP)-CdSe/ZnS core-shell quantum dots. Reproduced with permission from [107]

Relatedly, cadmium selenide/zinc sulfide (CdSe/ZnS) core-shell quantum dots (QDs) were coated with pH responsive and fluorescent poly((1-pyrene)methyl-2-methyl-2-propenoate))-*b*-poly(2-vinylpyridine) (PyMMP-*b*-P2VP) block copolymers [107]. The synthesis and chemical structure of (PyMMP-*b*-P2VP)-CdSe/ZnS QDs is shown in Fig. 30. FRET between these two distinguishable chromophores of red emitting CdSe/ZnS cores and blue emitting polypyrene-based shells is governed by the interspacing between them, which can be controlled through the

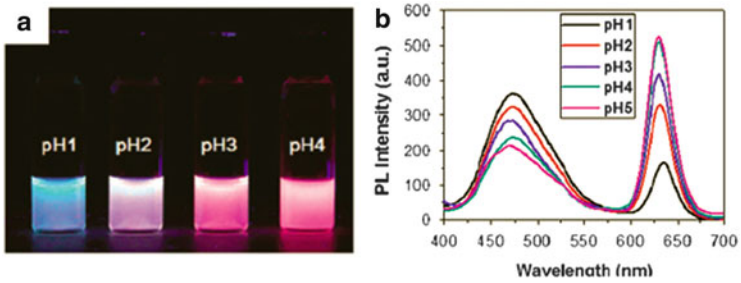

Fig. 31 (**a**) Photographic image of (PyMMP-*b*-P2VP)-QDs solutions under irradiation at 365 nm using a UV lamp. (**b**) PL spectra of (PyMMP-*b*-P2VP)-QDs. Reproduced with permission from [107]

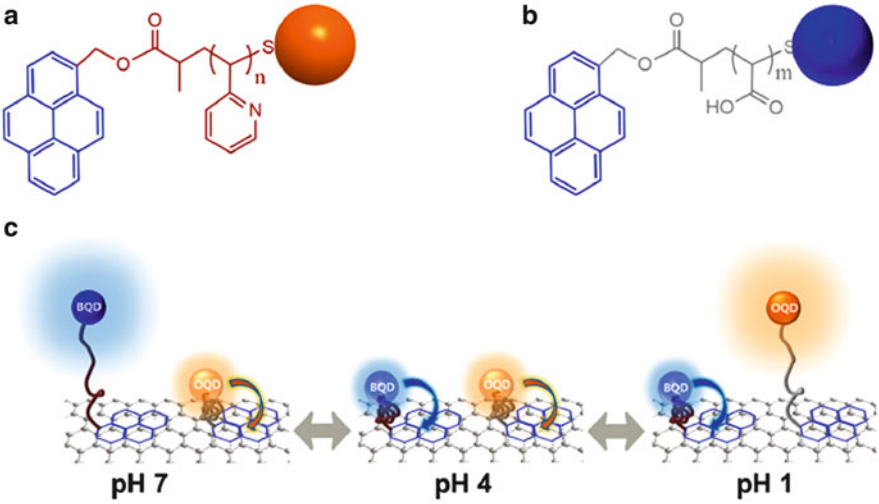

Fig. 32 Structure of (**a**) P2VP-OQD and (**b**) PAA-BQD. (**c**) Schematic illustration of the conformation and behavior of MQD-GO at a given pH value. Reproduced with permission from [108]

pH-dependent conformation of the P2VP chains [107]. Furthermore, the emission intensity ratio between the QDs and pyrene blocks can easily be balanced and controlled by simply tuning the number of repeating pyrene units in the (PyMMP-*b*-P2VP) chain. Therefore, polymer-coated QDs can exhibit not only ratiometric pH-dependent fluorescence spectra but also a clear color change from blue to purple to red as the solution pH is increased. These colors match well with the corresponding photoluminescence (PL) spectra shown in Fig. 31.

A versatile platform for an efficient graphene oxide (GO)-based optical sensor which exhibits distinctive ratiometric color responses has been developed [108]. A key strategy for generating a colorimetric, wide pH range sensor is to use two different blue- and orange-colored QDs anchored to a single GO sheet, as shown in Fig. 32. The pH-dependent emissions of the blue and orange QDs were controlled

by using linkers of two different pH-responsive polymers which changed their conformation in response to a different, but complementary, range of pH values [108]. The conformational changes caused the QDs to approach the GO surface, which influenced their emission properties. In addition, the GO-based sensor exhibits excellent dispersion stability in aqueous media and reversibility, all of which satisfy the critical requirements for a pH sensor.

4.2 Mechanotransducing Chemical Sensors

The emission of gaseous pollutants such as sulfur oxide, nitrogen oxide, and toxic gases as a result of a variety of industrial processes has become a serious environmental concern, especially in specific parts of the world. As a result, sensors are needed to monitor the concentration of various contaminants, which can prevent or limit uncontrolled releases of toxic compounds.

In one example, polyaniline (PAN) films were prepared by Langmuir–Blodgett (LB) and self-assembly (SA) techniques [109]. NO_2 is an oxidizing gas, which on contact with the π-electron network of polyaniline results in the transfer of an electron from the polymer to the gas. When this occurs, the polymer becomes positively charged. The charge carriers thus created give rise to the increased conductivity of the films, and a concomitant decrease in resistance. The response time to NO_2 and the relative change of resistance of films increase with increase of the number of film layers, as show in Fig. 33. Thin films allow more contact with NO_2 than thick films, which increases the response time.

Quartz crystal microbalance (QCM)-based SO_2 gas sensors were fabricated using amino-functionalized poly(styrene-*co*-chloromethyl styrene) derivatives [110]. SO_2 can be absorbed by the polymer's amine groups, which causes the mass to change such that it can be detected by the QCM. The sensor reaches equilibrium within 50 min in 50 ppm SO_2. The sensors exhibit complete

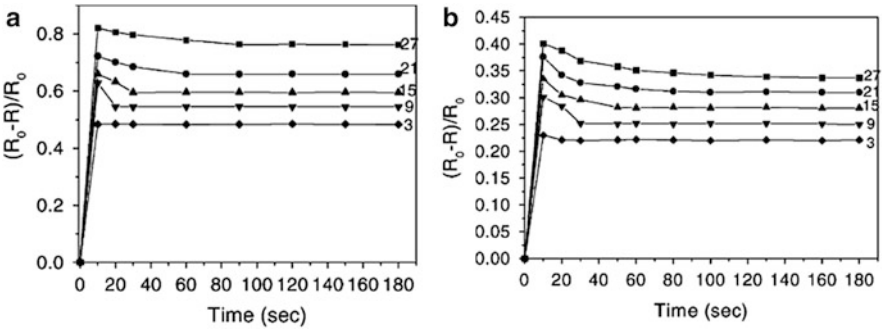

Fig. 33 Plots of the relative change of resistance of polyaniline-based films prepared by LB technique with various number of layers vs response time at 20 ppm NO_2. (**a**) PAN; (**b**) PAA-AA. Reproduced with permission from [109]

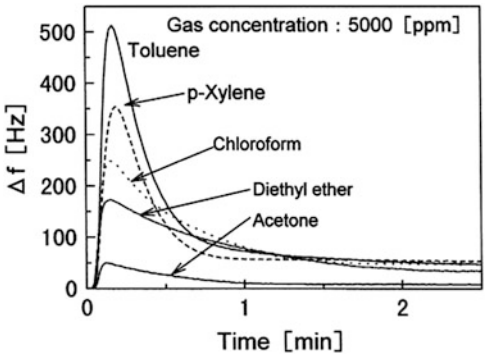

Fig. 34 Typical transient responses of the copolymerized propylene–butyl-film-coated sensor for various gases with concentrations of 5,000 ppm. Δf: quartz resonator frequency. Reproduced with permission from [111]

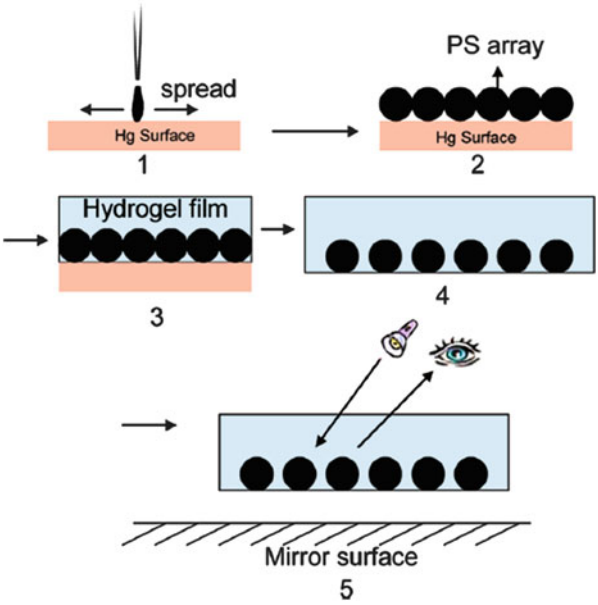

Fig. 35 Fabrication of a two-dimensional (2D) photonic crystal for sensing applications. (1, 2) PS particles self-assembled into a 2D close-packed array, (3) A hydrogel film is polymerized around the 2D array, (4) The swollen hydrogel with the embedded 2D array is peeled from the glass substrate. (5) Diffraction from the 2D array/hydrogel sandwich is monitored visually. Reproduced with permission from [112]

reversibility at 70°C. A similar system for the detection of aromatic gases (e.g., toluene and *p*-xylene) was also reported [111]. The copolymerized propylene–butyl film was chosen as the sensing membrane coated on the QCM [111]. The system exhibits high sensitivity and excellent selectivity for aromatic solvent gases such as toluene and xylene (Fig. 34).

In order to detect heavy metals, a single layer of polystyrene particles was immobilized in hydrogel thin films, which contained molecular recognition agents. In this case, 4-acryloylamidobenzo-18-crown-6 (4AB18C6) was the active component in the hydrogel network, which responds specifically to Pb^{2+} (Fig. 35) [112]. When exposed to Pb^{2+} solution, 4AB18C6 selectively complexed Pb^{2+}, which increased the charge density in the polymer network. This resulted in

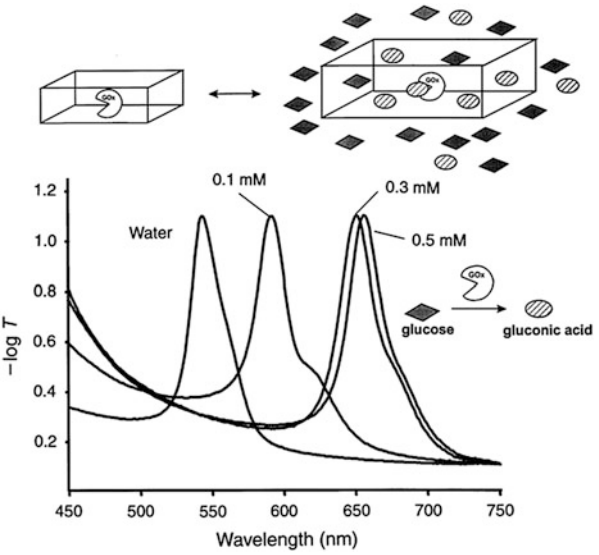

Fig. 36 Visible extinction spectra showing how diffraction depends on glucose concentration for a 125-mm-thick CCA glucose sensor. Reproduced with permission from [114]

hydrogel swelling and correspondingly increased the distance between PS particles and resulted in a color change of the thin film.

In another example, the Asher group showed that a periodic array of polystyrene spheres could be locked in a polyacrylamide hydrogel [113]. The enzyme glucose oxidase was incorporated into this system, which worked as a glucose sensor (Fig. 36) [114]. These materials were shown to exhibit Bragg diffraction in the visible wavelengths. Glucose solutions can then cause the hydrogel to swell, resulting in a red shift of the diffracted light. The hydrogel swelling is a result of the formation of a reduced glucose oxidase upon glucose turnover. The oxidized glucose oxidase is uncharged at neutral pH; however, the reduced glucose oxidase is anionic at pH 7. The reduced glucose oxidase is reoxidized by O_2, as detailed in the below reactions.

$$\begin{aligned} GO_x(\text{ox}) + \text{glucose} &\rightarrow GO_x - (\text{red}) + \text{gluconic acid} + H + H + + GO_x(\text{red}) + O_2 \\ &\rightarrow H_2O_2 + GO_x(\text{ox}). \end{aligned}$$

No response occurs for similar concentrations of sucrose or mannose because of the enzyme selectivity.

Bisphenol A (BPA) is a common compound used in the synthesis of many plastics and epoxy resins. However, recent studies have determined BPA is an emerging contaminant, which can disrupt the endocrine system and potentially cause cancer [115]. By molecular imprinting, Gao's group created numerous nanocavities in polymethyl methacrylate (PMMA) spheres, which can specifically target BPA (Fig. 37). The monodisperse PMMA spheres can be made into a CCA-based optical sensor. When the sensor is exposed to BPA solution, binding

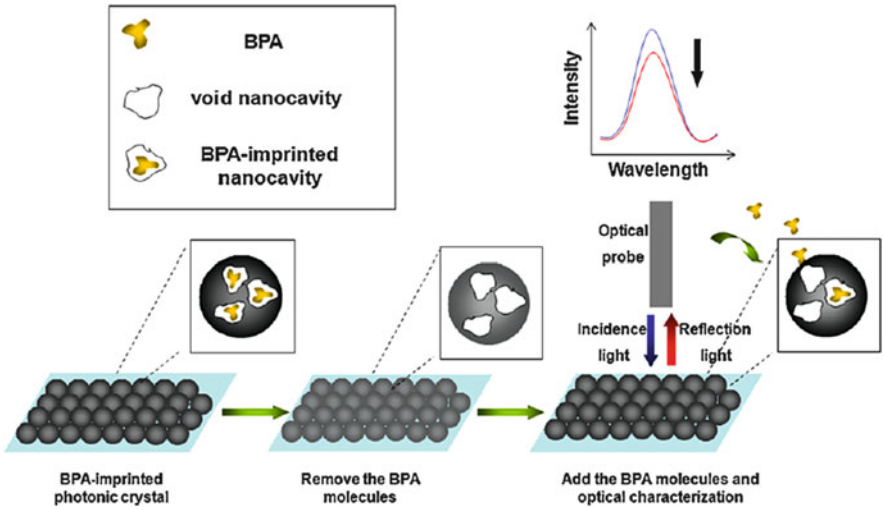

Fig. 37 Experimental procedures for the reflectometric detection of BPA using an imprinted nanocavity opal photonic crystal sensor. Reproduced with permission from [117]

occurs because of the hydrogen bonding and spatial effects, and the recognition process can swell the microspheres, resulting in smaller average refractive index and decreasing the diffraction peak intensity [117].

Li's group also developed imprinted photonic polymers for detecting the pesticide atrazine (Fig. 38) [116]. This pesticide has recently shown up as a contaminant in drinking water and consumption of this pesticide above the maximum contaminant level (MCLs) has been associated with adverse human health effects. To accomplish this, the authors deposited silica colloids onto a glass substrate to form a 3D ordered array as a template. Pre-gel solution containing template molecule (atrazine) was filled into the void space of the 3D ordered array. After polymerization, silica and the atrazine molecular templates were removed from the hydrogel film. The system now had highly ordered porous arrays with specific nanocavities capable of recognizing atrazine through noncovalent interactions. When exposed to different concentrations of atrazine, hydrogen bonding occurred between atrazine and gels, and hence the gel swelled, resulting in a visual color change.

4.3 Mechanotransducing Biosensors

One of the most common and well-known sensors for the detection of biomolecules is the blood glucose biosensor. Initially described by Clark and Lyons in 1962, the sensor relies on monitoring the oxygen concentration in solution (using an oxygen selective electrode); the amount of oxygen can be related to glucose concentration from the reaction of glucose oxidase and oxygen [118]. With glucose sensing

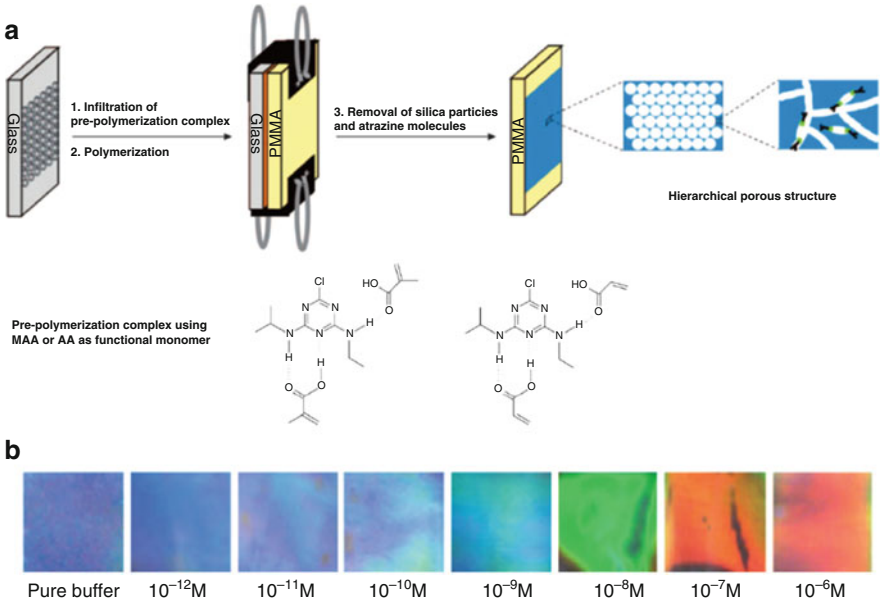

Fig. 38 (**a**) Schematic illustration of the procedure used for the preparation of the molecularly imprinted photonic polymer (MIPP). (**b**) Color change induced by exposure to atrazine at different concentrations. Reproduced with permission from [116]

solved, attention has shifted to the development of sensors that can detect specific DNA sequences, metal ions, small molecules, proteins, and cells. Biosensors were recently prepared by attaching DNA to synthetic polymer backbones [119]. Two strands of acrydite-modified DNA, S1 (50-acrydite-AAAACTCATCTGTGAAAG AACCTGGGGGAGTATTGCGGAGGAAGGT-30) and S2 (50-acrydite-AAACCCA GGTTCTTCTAGAGGGAGAC-30), were copolymerized with linear polyacrylamide polymers to form polymer strands P-S1 and P-S2 in a transparent liquid form, respectively (Fig. 39) [120]. S1 was designed to contain an ATP aptamer fragment. A crosslinker L1 (50-GGGAGACAAGGATAAATCCTT CAATGAAGTGGGTCTCCCTCTACTCACAGATGAGT-30), containing a cocaine aptamer fragment, was designed to hybridize with S1 and S2. The polymers transform into a gel as the hybridization proceeds during the mixture of P-S1, P-S2 with L1. In the presence of cocaine and ATP, the specific aptamer–target recognition causes the DNA hydrogels to undergo a macroscopic gel–sol transition.

In a related example, polyacrylamide hydrogel-based sensors functionalized with a thymine rich DNA which can simultaneously detect and remove mercury from water were fabricated [121]. Specifically, in the absence of Hg^{2+}, the DNA is in a random coil conformation, and the addition of SYBR Green I gives a weak fluorescence (Fig. 40a, yellow line). In the presence of Hg^{2+}, the DNA forms a hairpin structure yielding a ~ninefold emission increase. Using the naked eye, the

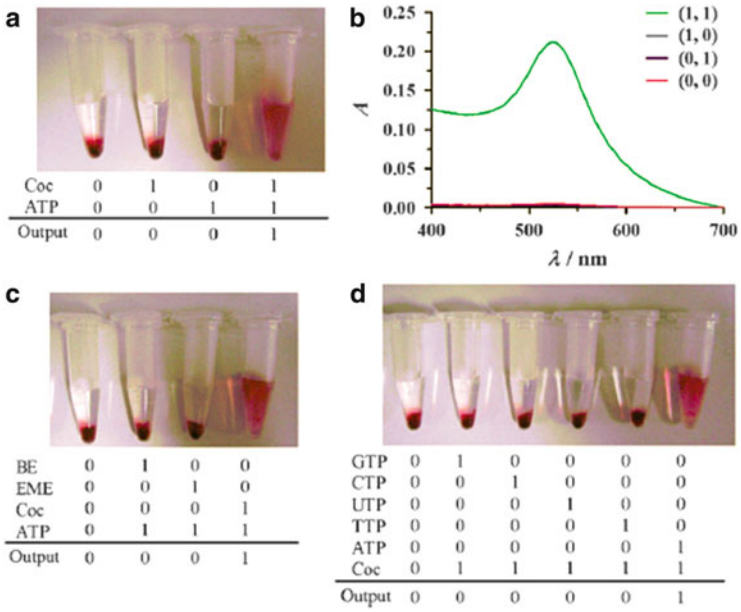

Fig. 39 (**a**) Photograph of aptamer-crosslinked hydrogels visualized with trapped BSA-GNPs before and after addition of cocaine and ATP. (**b**) UV–vis spectrum of the results of the AND logic gate. (**c**) Photograph of selectivity of the system to cocaine. (**d**) Photograph of selectivity of the system to ATP. The input stimulus concentration was 1 mM. Reproduced with permission from [120]

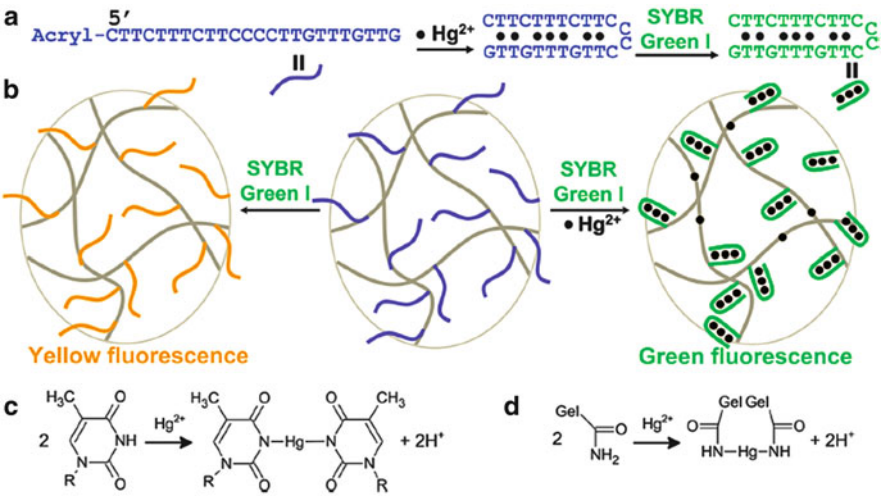

Fig. 40 (**a**) DNA sequence of acrydite-Hg-DNA and fluorescence signal generation for Hg^{2+} detection. The 5′-end is modified with an acrydite group for hydrogel attachment. (**b**) Covalent DNA immobilization within a polyacrylamide hydrogel and interaction with Hg^{2+} and SYBR Green I produces a visual fluorescence signal. (**c**, **d**) Chemical reaction schemes of Hg^{2+} binding with thymine base pairs (**c**) and polyacrylamide in hydrogel (**d**), where "Gel" in the molecular formula denotes the hydrogel matrix. Reproduced with permission from [121]

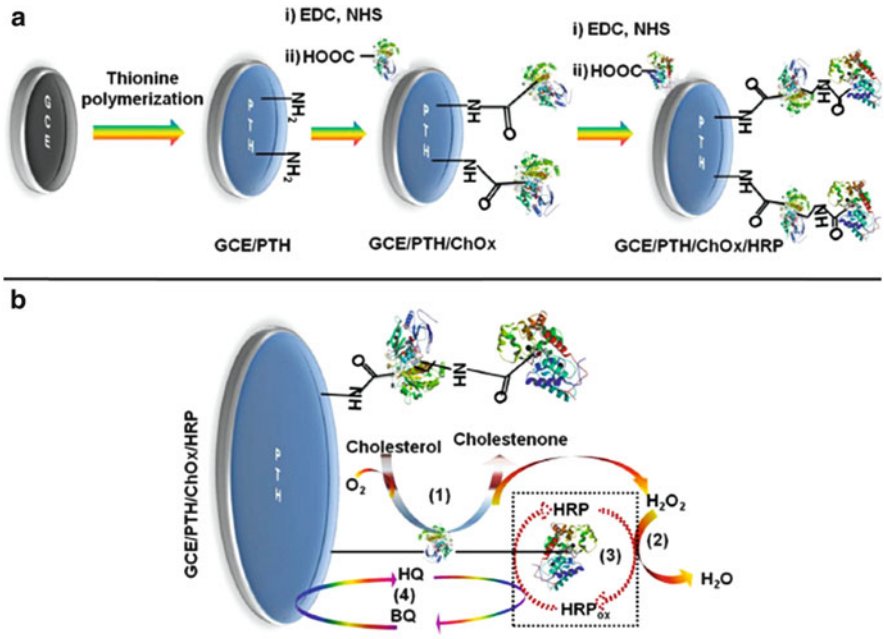

Fig. 41 Schematic representation of the fabrication of GCE/PTH/ChOx/HRP biosensor (**a**) and the reaction processes at the GCE/PTH/ChOx/HRP biosensor (**b**). The crystal structures of cholesterol oxidase (ChO*x*) and horseradish peroxidase (HRP) enzyme was obtained from Protein Data Bank (ID: 2IOK.pdb and IHCH.pdb, respectively). Reproduced with permission from [122]

detection limit in water solution is 10 nM Hg^{2+}. This sensor can be regenerated using a simple acid treatment, which removes Hg^{2+} from water within 1 h.

A simple and inexpensive cholesterol biosensor was fabricated by immobilizing cholesterol oxidase (ChOx) and horseradish peroxidase (HRP) onto a poly (thionine) modified glassy carbon electrode (GCE/PTH) (Fig. 41) [122]. Hydroquinone (HQ) was used as a mediator to promote the electron transfer between the enzyme and the electrode. It results in excellent electrocatalytic activity of immobilized HRP for H_2O_2 reduction, which was produced from cholesterol by the enzymatic reaction with ChOx. The linear range for cholesterol spanned from 25 to 125 μM, with a detection limit and a sensitivity of 6.3 μM and 0.18 μA/cm^2/μM, respectively. The highly reproducible and sensitive GCE/PTH/ChOx/HRP sensor exhibited an interference-free signal for cholesterol detection with excellent recoveries for real sample analysis.

There has recently been a growing interest in the use of block copolymer photonic gels for biosensing applications[123]. Block copolymers offer the flexibility of fabricating 1D, 2D, and 3D photonic materials through self-assembly. Some photonic gels are extremely sensitive to changes in charge, the dielectric environment, and biomolecules such as proteins and DNA. Exposure of the photonic gels to species that can alter the electrostatic and dielectric environment of the

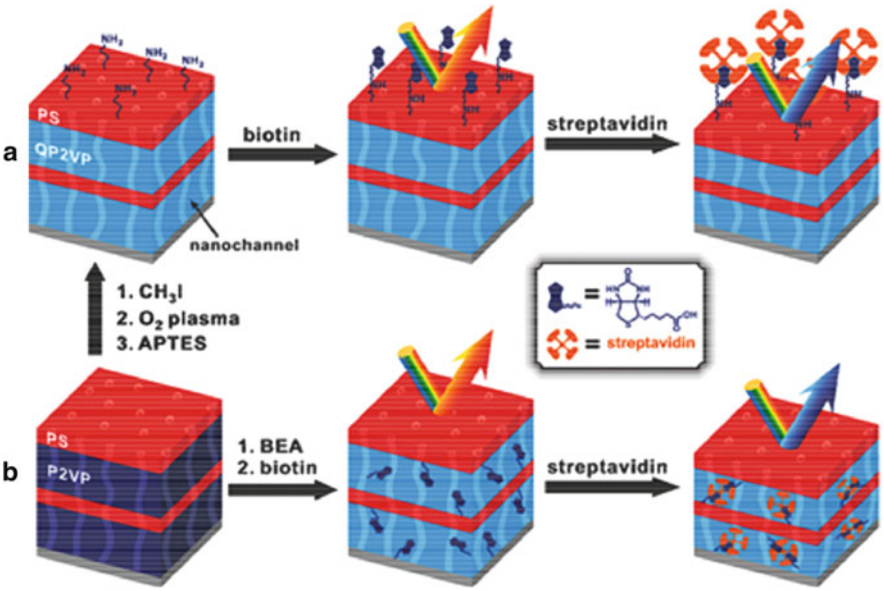

Fig. 42 Preparation of biotinylated photonic gels. Reproduced with permission from [123]

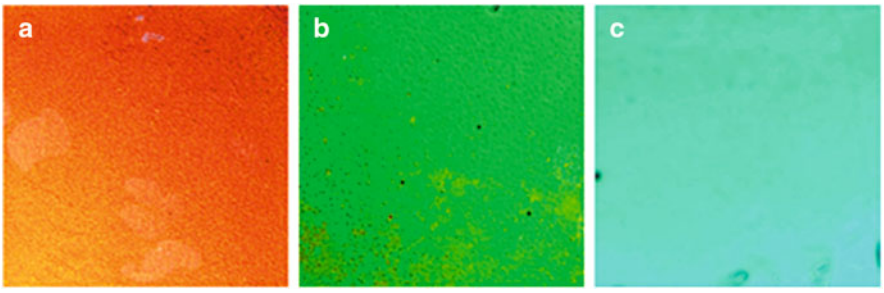

Fig. 43 Color changes of the inside-biotinylated photonic gels in response to streptavidin; (**a**) [S] = 0 M; (**b**) [S] = 0.5 mM; (**c**) [S] = 10 mM. Reproduced with permission from [123]

photonic gels can change the photonic gel's optical properties dramatically [123]. Kang and coworkers have reported a photonic gel sensor using polystyrene-*b*-quaternized poly(2-vinyl pyridine) (PS-*b*-QP2VP) modified with biotin molecules for detecting streptavidin (Fig. 42) [123]. This was achieved by on-gel (Fig. 42a) and in-gel (Fig. 42B) modification with biotin via the conventional carbodiimide coupling reaction. An apparent visual color change with streptavidin binding was observed for the in-gel photonic materials (Fig. 43). The color change was induced by binding of a streptavidin to multiple biotin molecules, which acted as a crosslinker, and resulted in the deswelling of the gels.

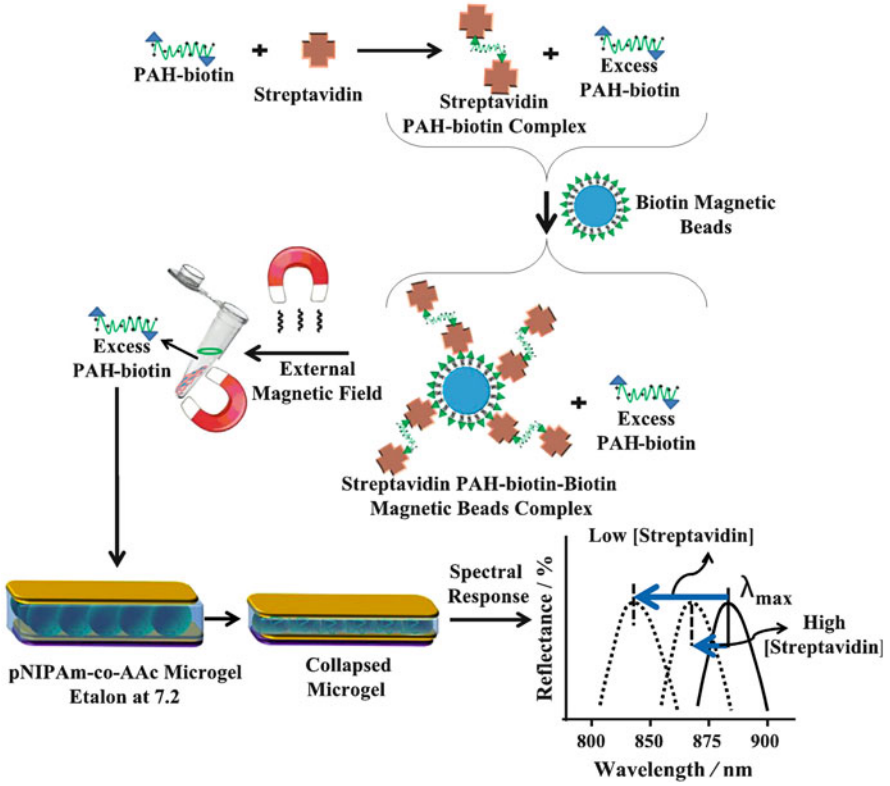

Fig. 44 Streptavidin (the analyte) is added to an excess amount of biotin-modified poly (allylamine hydrochloride) (PAH). The streptavidin–biotin–PAH complex is then removed from solution using biotin modified magnetic particles, leaving behind free, unbound PAH. The unbound PAH is subsequently added to a pNIPAm-*co*-AAc microgel-based etalon immersed in aqueous solution at pH 7.2 which renders both the microgel layer and the PAH charged. As a result, the etalon's spectral peaks shift in proportion to the amount of PAH–biotin that was added. This, in turn can be related back to the original amount of streptavidin added to the PAH–biotin. Reproduced with permission from [124]

The Serpe group recently developed etalon-based biosensors [124]. They first showed that biotinylated polycationic polymer can penetrate through the Au overlayer of an etalon and cause the layer of negatively charged microgels to collapse. The extent of peak shift depends on the amount of biotinylated polycation added to the etalon; high polycation concentration yields a large shift, and vice versa. This phenomenon can be exploited to sense the concentration of streptavidin in solution at μM concentrations, as detailed in Fig. 44. Etalons are very interesting because, unlike most biosensors, a large signal is obtained for low analyte concentration, as can be seen in Fig. 45 [124].

The Serpe group went on to show that a similar concept can be used to detect μM concentrations of target DNA in solutions [125, 126]. This detection originates

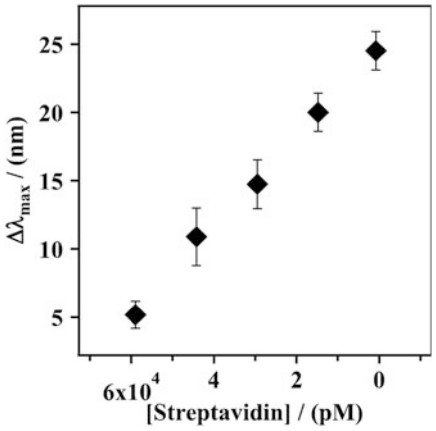

Fig. 45 Cumulative shift of the etalon's reflectance peak upon addition of the indicated amounts of streptavidin to PAH–biotin100:1. The pNIPAm-*co*-AAc microgel-based etalon was soaked in pH 7.2 throughout the experiment, while the temperature was maintained at 25°C. Each data point represents the average of at least three independent measurements, and the *error bars* are the standard deviation for those values. Reproduced with permission from [124]

from the penetration of polyanionic DNA into the etalon's positively charged microgel layer. DNA interacts electrostatically with the positively charged microgels and crosslinks them. The crosslinking results in shrinking of the confined microgel between Au layers resulting in the peaks shifts, as predicted in (2). The extent of shift can be related to the concentration of target DNA present in the sample solution.

5 Summary and Conclusions

Various responsive polymer-based systems were reviewed here, and their utility as artificial muscles, self-healing materials, and sensors detailed. These polymers, expanding in area and shrinking in thickness during exposure to stimuli, have been investigated as artificial muscles. Stimuli include electrostatic forces, pH, light, magnetic fields, and others. Self-healing polymeric materials were also detailed, where damage to materials can "automatically" result in a healing response. We have shown examples using reversible covalent interactions or non-covalent interactions such as hydrogen/ion bonding or π–π stacking. We have also detailed many examples of sensors that use mechanotransduction mechanisms to yield responses from materials which can be quantified and related to the concentration of various species in solutions.

This review has detailed how mechanochemistry can be used to yield desired functions, and has illustrated the tremendous opportunities for both fundamental and technological advances. Furthermore, many of the examples detailed in this

chapter are not only useful for the specific applications detailed here, but are responsible for pushing the field of polymer science forward. While much progress has been made, many challenges still exist which prevent the use of these materials in everyday applications. For example, regarding sensing, polymers with enhanced sensitivities to specific species need to be developed and investigated. Furthermore, response times need to be enhanced, and the strength of the muscles improved. Additionally, many of the systems described here are prohibitively expensive for real world applications, so less expensive functional components therefore need to be identified. Finally, biocompatibility is a major issue; many of these materials are difficult to use in biological settings. Regardless of the challenges, continuous development of new responsive polymers and related technologies makes us optimistic about the future positive impacts these materials can have on human life.

Acknowledgements MJS acknowledges funding from the University of Alberta (the Department of Chemistry and the Faculty of Science), the Natural Sciences and Engineering Research Council of Canada (NSERC), the Canada Foundation for Innovation (CFI), the Alberta Advanced Education & Technology Small Equipment Grants Program (AET/SEGP), Grand Challenges Canada, and IC-IMPACTS.

References

1. Derby CD (2007) Escape by inking and secreting: marine molluscs avoid predators through a rich array of chemicals and mechanisms. Biol Bull 213:274
2. Rapoport N (2007) Physical stimuli-responsive polymeric micelles for anti-cancer drug delivery. Prog Polym Sci 32:962
3. Schmaljohann D (2006) Thermo-and pH-responsive polymers in drug delivery. Adv Drug Deliv Rev 58:1655
4. Ionov L (2010) Actively-moving materials based on stimuli-responsive polymers. J Mater Chem 20:3382
5. Liu F, Urban MW (2010) Recent advances and challenges in designing stimuli-responsive polymers. Prog Polym Sci 35:3
6. Stuart MAC, Huck WT, Genzer J, Müller M, Ober C, Stamm M, Sukhorukov GB, Szleifer I, Tsukruk VV, Urban M (2010) Emerging applications of stimuli-responsive polymer materials. Nat Mater 9:101
7. Roy D, Cambre JN, Sumerlin BS (2010) Future perspectives and recent advances in stimuli-responsive materials. Prog Polym Sci 35:278
8. Meng H, Li G (2013) A review of stimuli-responsive shape memory polymer composites. Polymer 54:2199
9. Zhang J, Zhang M, Tang K, Verpoort F, Sun T (2014) Polymer-based stimuli-responsive recyclable catalytic systems for organic synthesis. Small 10:32
10. Huo M, Yuan J, Tao L, Wei Y (2014) Redox-responsive polymers for drug delivery: from molecular design to applications. Polym Chem 5:1519
11. Gil ES, Hudson SM (2004) Stimuli-reponsive polymers and their bioconjugates. Prog Polym Sci 29:1173
12. Zhai L (2013) Stimuli-responsive polymer films. Chem Soc Rev 42:7148

13. Ahn S-k, Kasi RM, Kim S-C, Sharma N, Zhou Y (2008) Stimuli-responsive polymer gels. Soft Matter 4:1151
14. Dimitrov I, Trzebicka B, Müller AHE, Dworak A, Tsvetanov CB (2007) Thermosensitive water-soluble copolymers with doubly responsive reversibly interacting entities. Prog Polym Sci 32:1275
15. Schild H (1992) Poly (N-isopropylacrylamide): experiment, theory and application. Prog Polym Sci 17:163
16. Maeda Y, Nakamura T, Ikeda I (2001) Changes in the hydration states of poly (N-alkylacrylamide) s during their phase transitions in water observed by FTIR spectroscopy. Macromolecules 34:1391
17. Idziak I, Avoce D, Lessard D, Gravel D, Zhu X (1999) Thermosensitivity of aqueous solutions of poly (N,N-diethylacrylamide). Macromolecules 32:1260
18. Lutz JF (2008) Polymerization of oligo (ethylene glycol)(meth) acrylates: toward new generations of smart biocompatible materials. J Polym Sci A Polym Chem 46:3459
19. Hoogenboom R (2009) Poly (2-oxazoline)s: a polymer class with numerous potential applications. Angew Chem Int Ed 48:7978
20. Dai S, Ravi P, Tam KC (2009) Thermo-and photo-responsive polymeric systems. Soft Matter 5:2513
21. Zhang QM, Li X, Islam MR, Wei M, Serpe MJ (2014) Light switchable optical materials from azobenzene crosslinked poly (N-isopropylacrylamide)-based microgels. J Mater Chem C 2:6961
22. Liu D, Chen W, Sun K, Deng K, Zhang W, Wang Z, Jiang X (2011) Resettable, multi-readout logic gates based on controllably reversible aggregation of gold nanoparticles. Angew Chem Int Ed 50:4103
23. Zhang QM, Xu W, Serpe MJ (2014) Optical devices constructed from multiresponsive microgels. Angew Chem Int Ed 53:4827
24. Schumers JM, Fustin CA, Gohy JF (2010) Light-responsive block copolymers macromol. Rapid Commun 31:1588
25. Kumar S, Dory YL, Lepage M, Zhao Y (2011) Surface-grafted stimuli-responsive block copolymer brushes for the thermo-, photo-and pH-sensitive release of dye. Macromolecules 44:7385
26. Yan B, Boyer J-C, Branda NR, Zhao Y (2011) Near-infrared light-triggered dissociation of block copolymer micelles using upconverting nanoparticles. J Am Chem Soc 133:19714
27. May PA, Moore JS (2013) Polymer mechanochemistry: techniques to generate molecular force via elongational flows. Chem Soc Rev 42:7497
28. Mura S, Nicolas J, Couvreur P (2013) Stimuli-responsive nanocarriers for drug delivery. Nat Mater 12:991
29. Madden JD, Vandesteeg NA, Anquetil PA, Madden PG, Takshi A, Pytel RZ, Lafontaine SR, Wieringa PA, Hunter IW (2004) Artificial muscle technology: physical principles and naval prospects. IEEE J Oceanic Eng 29:706
30. Madden JD, Schmid B, Hechinger M, Lafontaine SR, Madden PG, Hover FS, Kimball R, Hunter IW (2004) Application of polypyrrole actuators: feasibility of variable camber foils. IEEE J Oceanic Eng 29:738
31. Colgate JE, Lynch KM (2004) Mechanics and control of swimming: a review. IEEE J Oceanic Eng 29:660
32. Mirfakhrai T, Madden JD, Baughman RH (2007) Polymer artificial muscles. Mater Today 10:30
33. Brochu P, Pei Q (2010) Advances in dielectric elastomers for actuators and artificial muscles. Macromol Rapid Commun 31:10
34. Brochu P, Stoyanov H, Niu X, Pei Q (2013) All-silicone prestrain-locked interpenetrating polymer network elastomers: free-standing silicone artificial muscles with improved performance and robustness. Smart Mater Struct 22:055022

35. Zhang Z, Liu L, Fan J, Yu K, Liu Y, Shi L, Leng J (2008) In: The 15th international symposium on: smart structures and materials & nondestructive evaluation and health monitoring. International Society for Optics and Photonics p 692610
36. Lotz P, Matysek M, Lechner P, Hamann M, Schlaak HF (2008) In: The 15th international symposium on: smart structures and materials & nondestructive evaluation and health monitoring. International Society for Optics and Photonics p 692723
37. Pei Q, Rosenthal MA, Pelrine R, Stanford S, Kornbluth RD (2003) Smart structures and materials. International Society for Optics and Photonics p 281
38. Tangboriboon N, Datsanae S, Onthong A, Kunanuruksapong R, Sirivat A (2013) Electromechanical responses of dielectric elastomer composite actuators based on natural rubber and alumina. J Elastom Plast 45:143
39. Islam MR, Li X, Smyth K, Serpe MJ (2013) Polymer-based muscle expansion and contraction. Angew Chem Int Ed 52:10330
40. Islam MR, Serpe MJ (2014) Poly (N-isopropylacrylamide) microgel-based thin film actuators for humidity sensing. RSC Adv 4:31937
41. Li X, Serpe MJ (2014) Understanding and controlling the self-folding behavior of polymer-based muscles. Adv Funct Mater 24:4119
42. Jeon JH, Cheedarala RK, Kee CD, Oh IK (2013) Dry-type artificial muscles based on pendent sulfonated chitosan and functionalized graphene oxide for greatly enhanced ionic interactions and mechanical stiffness. Adv Funct Mater 23:6007
43. Jo C, Pugal D, Oh I-K, Kim KJ, Asaka K (2013) Recent advances in ionic polymer–metal composite actuators and their modeling and applications. Prog Polym Sci 38:1037
44. Palmre V, Pugal D, Kim KJ, Leang KK, Asaka K, Aabloo A (2014) Nanothorn electrodes for ionic polymer-metal composite artificial muscles. Sci Rep 4:6176
45. Kumar D, Sharma R (1998) Advances in conductive polymers. Eur Polym J 34:1053
46. Khaldi A, Plesse C, Soyer C, Cattan E, Vidal F, Legrand C, Teyssié D (2011) Conducting interpenetrating polymer network sized to fabricate microactuators. Appl Phys Lett 98:164101
47. Okuzaki H, Hosaka K, Suzuki H, Ito T (2010) Effect of temperature on humido-sensitive conducting polymer actuators. Sensor Actuat A Phys 157:96
48. Ma M, Guo L, Anderson DG, Langer R (2013) Bio-inspired polymer composite actuator and generator driven by water gradients. Science 339:186
49. Thomsen DL, Keller P, Naciri J, Pink R, Jeon H, Shenoy D, Ratna BR (2001) Liquid crystal elastomers with mechanical properties of a muscle. Macromolecules 34:5868
50. Lehmann W, Skupin H, Tolksdorf C, Gebhard E, Zentel R, Krüger P, Lösche M, Kremer F (2001) Giant lateral electrostriction in ferroelectric liquid-crystalline elastomers. Nature 410:447
51. Kondo M, Sugimoto M, Yamada M, Naka Y, J-i M, Kinoshita M, Shishido A, Yu Y, Ikeda T (2010) Effect of concentration of photoactive chromophores on photomechanical properties of crosslinked azobenzene liquid-crystalline polymers. J Mater Chem 20:117
52. Yamada M, Kondo M, Mamiya Ji YY, Kinoshita M, Barrett CJ, Ikeda T (2008) Photomobile polymer materials: towards light-driven plastic motors. Angew Chem Int Ed 47:4986
53. Syrett JA, Becer CR, Haddleton DM (2010) Self-healing and self-mendable polymers. Polym Chem 1:978
54. Russell T (2002) Surface-responsive materials. Science 297:964
55. Descalzo AB, Martínez-Máñez R, Sancenon F, Hoffmann K, Rurack K (2006) The supramolecular chemistry of organic–inorganic hybrid materials. Angew Chem Int Ed 45:5924
56. Becer CR, Hahn S, Fijten MW, Thijs HM, Hoogenboom R, Schubert US (2008) Libraries of methacrylic acid and oligo (ethylene glycol) methacrylate copolymers with LCST behavior. J Polym Sci A Polym Chem 46:7138
57. Ladmiral V, Legge TM, Zhao Y, Perrier S (2008) "Click" chemistry and radical polymerization: potential loss of orthogonality. Macromolecules 41:6728

58. Nurmi L, Lindqvist J, Randev R, Syrett J, Haddleton DM (2009) Glycopolymers via catalytic chain transfer polymerisation (CCTP), Huisgens cycloaddition and thiol–ene double click reactions. Chem Commun 2727
59. Liu YL, Chen YW (2007) Thermally reversible cross-linked polyamides with high toughness and self-repairing ability from maleimide-and furan-functionalized aromatic polyamides. Macromol Chem Phys 208:224
60. Oehlenschlaeger KK, Mueller JO, Brandt J, Hilf S, Lederer A, Wilhelm M, Graf R, Coote ML, Schmidt FG, Barner-Kowollik C (2014) Adaptable hetero Diels–Alder networks for fast self-healing under mild conditions. Adv Mater 26:3561
61. Klukovich HM, Kean ZS, Iacono ST, Craig SL (2011) Mechanically induced scission and subsequent thermal remending of perfluorocyclobutane polymers. J Am Chem Soc 133:17882
62. Yang Y, Urban MW (2013) Self-healing polymeric materials. Chem Soc Rev 42:7446
63. Deng G, Tang C, Li F, Jiang H, Chen Y (2010) Covalent cross-linked polymer gels with reversible sol–gel transition and self-healing properties. Macromolecules 43:1191
64. Nicolaÿ R, Kamada J, Van Wassen A, Matyjaszewski K (2010) Responsive gels based on a dynamic covalent trithiocarbonate cross-linker. Macromolecules 43:4355
65. Arisawa M, Yamaguchi M (2003) Rhodium-catalyzed disulfide exchange reaction. J Am Chem Soc 125:6624
66. Yoon JA, Kamada J, Koynov K, Mohin J, Nicolaÿ R, Zhang Y, Balazs AC, Kowalewski T, Matyjaszewski K (2011) Self-healing polymer films based on thiol–disulfide exchange reactions and self-healing kinetics measured using atomic force microscopy. Macromolecules 45:142
67. Amamoto Y, Otsuka H, Takahara A, Matyjaszewski K (2012) Self-healing of covalently cross-linked polymers by reshuffling thiuram disulfide moieties in air under visible light. Adv Mater 24:3975
68. Kantor SW, Grubb WT, Osthoff RC (1954) The mechanism of the acid-catalyzed and base-catalyzed equilibration of siloxanes. J Am Chem Soc 76:5190
69. Zheng P, McCarthy TJ (2012) A Surprise from 1954: siloxane equilibration is a simple, robust, and obvious polymer self-healing mechanism. J Am Chem Soc 134:2024
70. Maes F, Montarnal D, Cantournet S, Tournilhac F, Corté L, Leibler L (2012) Activation and deactivation of self-healing in supramolecular rubbers. Soft Matter 8:1681
71. Montarnal D, Tournilhac F, Hidalgo M, Couturier J-L, Leibler L (2009) Versatile one-pot synthesis of supramolecular plastics and self-healing rubbers. J Am Chem Soc 131:7966
72. Faghihnejad A, Feldman KE, Yu J, Tirrell MV, Israelachvili JN, Hawker CJ, Kramer EJ, Zeng H (2014) Adhesion and surface interactions of a self-healing polymer with multiple hydrogen-bonding groups. Adv Funct Mater 24:2322
73. Wilson GO, Caruso MM, Schelkopf SR, Sottos NR, White SR, Moore JS (2011) Adhesion promotion via noncovalent interactions in self-healing polymers. ACS Appl Mater Interfaces 3:3072
74. Schubert US, Eschbaumer C, Hien O, Andres PR (2001) 4′-Functionalized 2,2′, 6′,2-″-terpyridines as building blocks for supramolecular chemistry and nanoscience. Tetrahedron Lett 42:4705
75. Burnworth M, Tang L, Kumpfer JR, Duncan AJ, Beyer FL, Fiore GL, Rowan SJ, Weder C (2011) Optically healable supramolecular polymers. Nature 472:334
76. Holten-Andersen N, Harrington MJ, Birkedal H, Lee BP, Messersmith PB, Lee KYC, Waite JH (2011) pH-Induced metal-ligand cross-links inspired by mussel yield self-healing polymer networks with near-covalent elastic moduli. PNAS 108:2651
77. Krogsgaard M, Behrens MA, Pedersen JS, Birkedal H (2013) Self-healing mussel-inspired multi-pH-responsive hydrogels. Biomacromolecules 14:297
78. Burattini S, Greenland BW, Merino DH, Weng W, Seppala J, Colquhoun HM, Hayes W, Mackay ME, Hamley IW, Rowan SJ (2010) A healable supramolecular polymer blend based on aromatic π–π stacking and hydrogen-bonding interactions. J Am Chem Soc 132:12051

79. Greenland BW, Burattini S, Hayes W, Colquhoun HM (2008) Design, synthesis and computational modelling of aromatic tweezer-molecules as models for chain-folding polymer blends. Tetrahedron 64:8346
80. Fox J, Wie JJ, Greenland BW, Burattini S, Hayes W, Colquhoun HM, Mackay ME, Rowan SJ (2012) High-strength, healable, supramolecular polymer nanocomposites. J Am Chem Soc 134:5362
81. Buenger D, Topuz F, Groll J (2012) Hydrogels in sensing applications. Prog Polym Sci 37:1678
82. Roy I, Gupta MN (2003) Smart polymeric materials: emerging biochemical applications. Chem Biol 10:1161
83. Robinson DN, Peppas NA (2002) Preparation and characterization of pH-responsive poly (methacrylic acid-g-ethylene glycol) nanospheres. Macromolecules 35:3668
84. Ruan C, Zeng K, Grimes CA (2003) Anal Chim Acta 497:123
85. Bashir R, Hilt J, Elibol O, Gupta A, Peppas N (2002) Micromechanical cantilever as an ultrasensitive pH microsensor. Appl Phys Lett 81:3091
86. Xia Y, Gates B, Yin Y, Lu Y (2000) Monodispersed colloidal spheres: old materials with new applications. Adv Mater 12:693
87. Weissman JM, Sunkara HB, Tse AS, Asher SA (1996) Thermally switchable periodicities and diffraction from mesoscopically ordered materials. Science 274:959
88. Yeh P (1988) Optical waves in layered media. Wiley, New York
89. Hu L, Serpe MJ (2013) Controlling the response of color tunable poly (N-isopropylacrylamide) microgel-based etalons with hysteresis. Chem Commun 49:2649
90. Schacher FH, Rupar PA, Manners I (2012) Functional block copolymers: nanostructured materials with emerging applications. Angew Chem Int Ed 51:7898
91. Ye X, Qi L (2011) Two-dimensionally patterned nanostructures based on monolayer colloidal crystals: controllable fabrication, assembly, and applications. Nano Today 6:608
92. Lee K, Asher SA (2000) Photonic crystal chemical sensors: pH and ionic strength. J Am Chem Soc 122:9534
93. Marchetti M, Prager S, Cussler EL (1990) Thermodynamic predictions of volume changes in temperature-sensitive gels. 1. Theory. Macromolecules 23:1760
94. Xu X, Goponenko AV, Asher SA (2008) Polymerized polyHEMA photonic crystals: pH and ethanol sensor materials. J Am Chem Soc 130:3113
95. Mafé S, Manzanares JA, English AE, Tanaka T (1997) Multiple phases in ionic copolymer gels. Phys Rev Lett 79:3086
96. Shin J, Braun PV, Lee W (2010) Fast response photonic crystal pH sensor based on templated photo-polymerized hydrogel inverse opal. Sensor Actuat B Chem 150:183
97. Griffete N, Frederich H, Maître A, Chehimi MM, Ravaine S, Mangeney C (2011) Photonic crystal pH sensor containing a planar defect for fast and enhanced response. J Mater Chem 21:13052
98. Sorrell CD, Carter MCD, Serpe MJ (2011) Color tunable poly (N-isopropylacrylamide)-co-acrylic acid microgel–Au hybrid assemblies. Adv Funct Mater 21:425
99. Sorrell CD, Carter MCD, Serpe MJ (2011) A "paint-on" protocol for the facile assembly of uniform microgel coatings for color tunable etalon fabrication. ACS Appl Mater Interfaces 3:1140
100. Islam MR, Serpe MJ (2013) Polyelectrolyte mediated intra and intermolecular crosslinking in microgel-based etalons for sensing protein concentration in solution. Chem Commun 49:2646
101. Islam MR, Serpe MJ (2013) Penetration of polyelectrolytes into charged poly (N-isopropylacrylamide) microgel layers confined between two surfaces. Macromolecules 46:1599
102. Hu L, Serpe MJ (2012) Color modulation of spatially isolated regions on a single poly (N-isopropylacrylamide) microgel based etalon. J Mater Chem 22:8199

103. Sorrell CD, Serpe MJ (2011) Reflection order selectivity of color-tunable poly(N-isopropylacrylamide) microgel based etalons. Adv Mater 23:4088
104. Gopich IV, Szabo A (2007) Single-molecule FRET with diffusion and conformational dynamics. J Phys Chem B 111:12925
105. Hong SW, Kim KH, Huh J, Ahn C-H, Jo WH (2005) Design and synthesis of a new pH sensitive polymeric sensor using fluorescence resonance energy transfer. Chem Mater 17:6213
106. Hong SW, Ahn C-H, Huh J, Jo WH (2006) Synthesis of a PEGylated polymeric pH sensor and its pH sensitivity by fluorescence resonance energy transfer. Macromolecules 39:7694
107. Paek K, Chung S, Cho C-H, Kim BJ (2011) Fluorescent and pH-responsive diblock copolymer-coated core–shell CdSe/ZnS particles for a color-displaying, ratiometric pH sensor. Chem Commun 47:10272
108. Paek K, Yang H, Lee J, Park J, Kim BJ (2014) Efficient colorimetric pH sensor based on responsive polymer–quantum dot integrated graphene oxide. ACS Nano 8:2848
109. Xie D, Jiang Y, Pan W, Li D, Wu Z, Li Y (2002) Fabrication and characterization of polyaniline-based gas sensor by ultra-thin film technology. Sensor Actuat B Chem 81:158
110. Matsuguchi M, Tamai K, Sakai Y (2001) SO_2 gas sensors using polymers with different amino groups. Sensor Actuat B Chem 77:363
111. Nanto H, Dougami N, Mukai T, Habara M, Kusano E, Kinbara A, Ogawa T, Oyabu T (2000) A smart gas sensor using polymer-film-coated quartz resonator microbalance. Sensor Actuat B Chem 66:16
112. Zhang JT, Wang L, Luo J, Tikhonov A, Kornienko N, Asher SA (2011) 2-D array photonic crystal sensing motif. J Am Chem Soc 133:9152
113. Asher SA, Holtz J, Liu L, Wu Z (1994) Self-assembly motif for creating submicron periodic materials. Polymerized crystalline colloidal arrays. J Am Chem Soc 116:4997
114. Holtz JH, Asher SA (1997) Polymerized colloidal crystal hydrogel films as intelligent chemical sensing materials. Nature 389:829
115. Staples CA, Dome PB, Klecka GM, Oblock ST, Harris LR (1998) A review of the environmental fate, effects, and exposures of bisphenol A. Chemosphere 36:2149
116. Wu Z, Ca T, Lin C, Shen D, Li G (2008) Label-free colorimetric detection of trace atrazine in aqueous solution by using molecularly imprinted photonic polymers. Chem A Eur J 14:11358
117. Guo C, Zhou C, Sai N, Ning B, Liu M, Chen H, Gao Z (2012) Detection of bisphenol A using an opal photonic crystal sensor. Sensor Actuat B Chem 166:17
118. Clark LC, Lyons C (1962) Electrode systems for continuous monitoring in cardiovascular surgery. Ann N Y Acad Sci 102:29
119. Khimji I, Kelly EY, Helwa Y, Hoang M, Liu J (2013) Visual optical biosensors based on DNA-functionalized polyacrylamide hydrogels. Methods 64:292
120. Yin B-C, Ye B-C, Wang H, Zhu Z, Tan W (2012) Colorimetric logic gates based on aptamer-crosslinked hydrogels. Chem Commun 48:1248
121. Dave N, Chan MY, Huang P-JJ, Smith BD, Liu J (2010) Regenerable DNA-functionalized hydrogels for ultrasensitive, instrument-free mercury(II) detection and removal in water. J Am Chem Soc 132:12668
122. Rahman MM, X-b L, Kim J, Lim BO, Ahammad A, Lee J-J (2014) A cholesterol biosensor based on a bi-enzyme immobilized on conducting poly (thionine) film. Sensor Actuat B Chem 202:536
123. Lee E, Kim J, Myung J, Kang Y (2013) Modification of block copolymer photonic gels for colorimetric biosensors. Macromol Res 20:1219
124. Islam MR, Serpe MJ (2013) Label-free detection of low protein concentration in solution using a novel colorimetric assay biosensor. Bioelectron 49:133
125. Islam MR, Serpe MJ (2014) Polymer-based devices for the label-free detection of DNA in solution: low DNA concentrations yield large signals. Anal Bioanal Chem 406:4777
126. Islam MR, Serpe MJ (2014) A novel label-free colorimetric assay for DNA concentration in solution. Anal Chim Acta 843:83

Index